

**Development of novel compounds for the molecular imaging of hypoxia:  
<sup>18</sup>F-labeled nitroimidazoles and hypoxia inducible factor 1 alpha (HIF-1 $\alpha$ )-  
targeting compounds**

by

Jenilee Dawn Woodfield

A thesis submitted in partial fulfillment of the requirements for the degree of

Doctor of Philosophy

in

Cancer Sciences

Department of Oncology  
University of Alberta

## **Abstract**

Imaging of hypoxia has been previously achieved using positron emission tomography (PET) with radiotracers such as [<sup>18</sup>F]fluoroazomycin arabinoside ([<sup>18</sup>F]FAZA) [1] or [<sup>18</sup>F]fluoromisonidazole ([<sup>18</sup>F]FMISO) [2]. These typical nitroimidazole containing compounds are reductively trapped in hypoxic areas. Herein, we propose two novel ways to imaging hypoxia, one with a novel 2-nitroimidazole of *N*-(4-[<sup>18</sup>F]fluorobenzyl)-2-(2-nitro-1*H*-imidazol-1-yl)-acetamide ([<sup>18</sup>F]FBNA). Secondly, we propose to directly image the master regulator of hypoxia of hypoxia inducible factor 1 alpha (HIF-1 $\alpha$ ). We will comparatively assess the imaging of HIF-1 $\alpha$  versus traditional imaging agents of [<sup>18</sup>F]FMISO, [<sup>18</sup>F]FAZA and the novel 2-nitroimidazole imaging agent of [<sup>18</sup>F]FBNA.

We have developed two lead structures that bind to HIF-1 $\alpha$ , and have radiolabelled them using [<sup>18</sup>F]fluorine prosthetic group chemistry. [<sup>18</sup>F]SFB-link-*c*-(Ppg)LLFVY was prepared using the prosthetic group of [<sup>18</sup>F]SFB and the primary amine containing peptide link-*c*-(Ppg)LLFVY. [<sup>18</sup>F]SFB-link-*c*-(Ppg)LLFVY was prepared in  $66.2 \pm 5.4\%$  decay corrected recovered radiochemical yield from [<sup>18</sup>F]fluoride (n=8) with a purity >99%. [<sup>18</sup>F]FPeP4 was prepared using Pd-mediated SONOGASHIRA cross-coupling reaction between [<sup>18</sup>F]FPA and *N*-(4-iodophenyl)-4-((4-(pyridine-3-ylmethyl)piperazin-1-yl)methyl)benzamide. [<sup>18</sup>F]FPeP4 was prepared in  $5 \pm 2\%$  decay corrected recovered radiochemical yield from [<sup>18</sup>F]fluoride (n=5) with a purity >99%. Novel nitroimidazole [<sup>18</sup>F]FBNA was synthesized starting from the prosthetic group of [<sup>18</sup>F]FBAmine. [<sup>18</sup>F]FBNA was prepared in  $47.4 \pm 5.4\%$  decay corrected recovered radiochemical yield from [<sup>18</sup>F]FBAmine (n=8) with a purity >99%.

Radiopharmacological profile of [<sup>18</sup>F]FPeP4, [<sup>18</sup>F]SFB-link-*c*-(Ppg)LLFVY and [<sup>18</sup>F]FBNA were evaluated in comparison to [<sup>18</sup>F]FAZA and [<sup>18</sup>F]FMISO using triple negative breast cancer cell line MDA-MB-231. In HIF-1 $\alpha$  overexpressing MDA-MB-231 cells, cellular uptake of [<sup>18</sup>F]SFB-

link-*c*-(Ppg)LLFVY reached an internalized maximum of 30% applied radioactivity/mg protein at 120 min and [<sup>18</sup>F]FPeP4 reached an internalized maximum of 400% applied radioactivity/mg protein at 120 min. In non-transfected hypoxic MDA-MB-231 cells, [<sup>18</sup>F]FBNA reached an internalized maximum of 9% applied radioactivity/mg protein at 120 min in hypoxic conditions.

Radiopharmacological evaluation of all compounds included small animal PET imaging. Small animal PET studies of both HIF-1 $\alpha$  targeting radiotracers demonstrated poor tumor uptake compared to [<sup>18</sup>F]FAZA, [<sup>18</sup>F]FMISO and [<sup>18</sup>F]FBNA. This was due to the poor pharmacokinetics of these radiotracers *in vivo*, with both radiotracers exhibiting large amounts of first pass liver trapping. [<sup>18</sup>F]FPeP4 demonstrated a SUV<sub>max</sub> of 0.3 in MCF7 tumor bearing NIH-III mice compared to [<sup>18</sup>F]FBNA which had a SUV<sub>max</sub> of 0.75. Tumor to muscle ratio of [<sup>18</sup>F]FBNA in MFC-7 tumor model was 3 which was equal to [<sup>18</sup>F]FPeP4 at 3. Yet, [<sup>18</sup>F]FBNA was found to be metabolically unstable, whereas [<sup>18</sup>F]FPeP4 was metabolically stable.

[<sup>18</sup>F]SFB-link-*c*-(Ppg)LLFVY and [<sup>18</sup>F]FPeP4 are the first novel radiotracers to be designed that bind to HIF-1 $\alpha$ . Their *in vitro* uptake showed increased uptake in HIF-1 $\alpha$  overexpressing cells, yet their biodistribution *in vivo* is currently poor. Improvements to the delivery of these radiotracers *in vivo* could improve their future usage as radiotracers targeting HIF-1 $\alpha$ .

## **Preface**

This thesis is an original work by Jenilee Dawn Woodfield. The animal studies described in this thesis complied with the Canadian Council of Animal Care as approved by the local animal care committee (Cross Cancer Institute, University of Alberta, Protocol number: AC17231 and AC21259). There are two different protocol numbers due to the extended period of animal use.

Chapter 3 of this thesis is published as follows: Arian Pérez Nario, Jenilee Woodfield, Sofia Nascimento dos Santos, Cody Bergman, Melinda Wuest, Yasniel Babí Araújo, André Luis Lapolli, Frederick G. West, Frank Wuest, and Emerson Soares Bernardes. “*Synthesis of a 2-nitroimidazole derivative N-(4-[<sup>18</sup>F]fluorobenzyl)-2-(2-nitro-1H-imidazol-1-yl)-acetamide ([<sup>18</sup>F]FBNA) as PET radiotracer for imaging tumor hypoxia.*” EJNMMI Radiopharm Chem., 2022, 7, 13.

I was involved in numerous aspects of the above published work. I completed the automated radiochemistry experiments, specific activity calculations and curves, and helped in the preparation of the manuscript. Arian Pérez Nario and Cody Bergman completed all the chemistry and some of the radiochemistry experiments. Sofia Nascimento dos Santos completed all *in vitro* analyses. This whole work was created in collaboration with the Nuclear and Energy Research Institute (IPEN/CNEN - SP), São Paulo, SP CEP 05508-000 Brazil. All co-authors contributed to manuscript edits.

Chapter 4 of this thesis is currently in preparation as follows: Sofia Nascimento dos Santos, Melinda Wuest, Hans-Soenke Jans, Jenilee Woodfield, Arian Pérez Nario, Daniel Krysz, Jennifer Dufour, Darryl Glubrecht, Cody Bergman, Emerson Soares Bernardes, Frank Wuest. “*Systematic comparison of three <sup>18</sup>F-labeled 2-nitroimidazoles for imaging hypoxia in breast cancer xenografts: [<sup>18</sup>F]FBNA, [<sup>18</sup>F]FAZA and [<sup>18</sup>F]FMISO.*”

I was responsible for the radiosynthesis of [<sup>18</sup>F]FAZA, [<sup>18</sup>F]FMISO and [<sup>18</sup>F]FBAmine, and some of the *in vitro* analysis in the above publication. Sofia Nascimento dos Santos, Jennifer Dufour and Daniel Krysz completed all other *in vitro* analyses. Melinda Wuest completed all *in vivo* analyses. Hans-Soenke Jans completed kinetic analysis experiments. Arian Pérez Nario and Cody Bergman completed the synthesis of [<sup>18</sup>F]FBNA. Darryl Glubrecht completed the immunohistochemistry analysis. This work was created in collaboration with the Nuclear and Energy Research Institute

(IPEN/CNEN - SP), São Paulo, SP CEP 05508-000 Brazil. All co-authors contributed to manuscript edits.

Chapter 5 of this thesis is published as follows: Jenilee D. Woodfield, Atul Bhardwaj, Cody Bergman, and Frank Wuest. “*Synthesis, Binding Affinity Analysis, and <sup>18</sup>F Radiosynthesis of Small-Molecular-Weight HIF-1 $\alpha$ -Binding Compounds.*” ChemMedChem, 2021, 17, 1, e202100544.

I was involved in numerous aspects of the above published work. I completed all the chemistry, radiochemistry, and microscale thermophoresis experiments, and wrote the manuscript. Cody Bergman completed the synthesis of some of the peptide derivatives. Atul Bhardwaj completed all *in silico* analyses. All co-authors contributed to manuscript edits.

## **Acknowledgements**

I would like to thank the following people, for without them my Ph.D. thesis would not have been possible. Dr. Frank Wuest, my supervisor, for his many years of support, guidance, and encouragement in my project. He has been a wonderful teacher and mentor and helped me through the many perils of my thesis. Dr. Melinda Wuest, whose knowledge and expertise in small animal PET imaging are unparalleled. She has helped me learn the ins and outs of animal handling and imaging, for which I am extremely grateful. Jennifer Dufour and Monica Wang for their help in cell culture and *in vitro* experiments. Dr. Ingrid Hamann for her help in teaching me western blot analysis. Cody Bergman for his help with chemistry, peptide synthesis and radiochemistry. I would also like to thank and acknowledge all former and present members of the Wuest Lab for their helpful discussion and support, especially, Dr. Melinda Wuest, Dr. Vincent Bouvet, Dr. Susan Richter, Dr. Ingrid Hamann, Dr. Atul Bhardwaj, Dr. Jatinder Kaur, Cody Bergman, Jennifer Dufour, Samantha Leier, Richard Yuen, and Monica Wang. Special thanks and acknowledgement must go to all those who worked on the HIF-1 $\alpha$  project.

I would like to thank Dr. Lynne Postovit and Dr. Scott Findlay for their help in the transfection of the HIF-1 $\alpha$  overexpressing MDA-MB-231 cells.

Thank you to the members of my Ph.D. committee, Dr. Afsaneh Lavasanifar, Dr. Lynne Postovit, and Dr. Todd McMullen, for their scientific input and advice.

Acknowledgements and thanks go to the Cyclotron staff including Dave Clendening, Lloyd Barker and Blake Lazurko from the Edmonton PET Centre for radionuclide production and excellent technical support, as well as Gail Hipperson and Dan McGinn from the Vivarium of the Cross Cancer Institute for supporting the animal work.

I would also like to thank the Alberta Innovates Health Solution and Alberta Cancer Foundation for their financial assistance.

My thanks also go out to the Department of Oncology for their support with regard to funding and registration and special thanks to Jen Freund and Yvette Labiuk. I am very grateful to Dr. Ing Swie Going, Dr. Kristi Baker, and Dr. Roseline Godbout for serving on my candidacy committee.

Finally, and most importantly, I would like to thank my entire family. Especially, my husband Sion Woodfield for his continuous support. To my mother and father, Kathy and Eugene Way, thank you for your support for my whole life! To my two girls, Emma and Alice mommy loves you!

## **Table of Contents**

Abstract.....	ii
Preface.....	iv
Acknowledgements.....	vi
Table of Contents.....	viii
List of Tables .....	xx
List of Figures.....	xxiv
List of Symbols.....	xxxix
Glossary of Terms.....	xli
Chapter 1: Introduction.....	1
1.1    Molecular imaging.....	1
1.2    Breast cancer and breast cancer imaging with positron emission tomography .....	5
1.3    Hallmarks of cancer .....	7
1.4    Tumor microenvironment and hypoxia .....	8
1.5    Molecular imaging of hypoxia.....	10
1.6    Novel biomarkers for triple-negative breast cancer (TNBC) .....	12
1.7    Hypoxia-inducible factor 1 alpha (HIF-1 $\alpha$ ).....	12
1.7.1    From erythropoietin (EPO) to HIF-1 .....	13
1.7.2    HIF-1 expression in hypoxia.....	13

1.7.3	From HIF-1 to HIF-1 $\alpha$ .....	14
1.7.4	HIF-1 $\alpha$ regulation and structure .....	15
1.7.5	HIF-1 $\alpha$ /aryl hydrocarbon receptor nuclear translocator interactions and regulation	16
1.7.6	HIF-1 $\alpha$ cellular localization and gene activation .....	17
1.7.7	HIF-1 $\alpha$ in deregulating cellular energetics .....	17
1.7.8	HIF-1 $\alpha$ inhibitors .....	18
1.8	Hypothesis and aims/goals.....	19
Chapter 2: Methods, techniques, instrumentation, and chemicals.....		21
2.1	Instrumentation .....	21
2.1.1	High-performance liquid chromatography and flash chromatography.....	21
2.1.1.1	FIB HPLC method .....	21
2.1.1.2	FAZA HPLC method.....	21
2.1.1.3	FMISO HPLC method .....	21
2.1.1.4	Cu_peptides HPLC method .....	21
2.1.1.5	Cu_peptides_fast HPLC method.....	22
2.1.1.6	HIF-1 $\alpha$ compounds HPLC method.....	22
2.1.1.7	HIF-1 $\alpha$ compounds Iso HPLC method.....	22
2.1.1	Nuclear magnetic resonance and LC-MS .....	22
2.1.2	Radio-thin-layer chromatography, dose calibrator and gamma counter.....	22

2.1.3	Centrifugation, thermoshaker, oil bath, rotary evaporation and lyophilization .....	22
2.1.4	Microscale thermophoresis (MST) and potential of hydrogen (pH) meter .....	23
2.1.5	Plate reader, confocal microscope, and western blot.....	23
2.2	Chemicals.....	23
2.2.1	ELISA buffer (200 mL) .....	24
2.2.2	EMSA Buffer .....	24
2.2.3	In-house K.2.2.2./K <sub>2</sub> CO <sub>3</sub> solution.....	24
2.2.4	10X Running buffer solution .....	24
2.2.5	10X Transfer buffer solution .....	24
2.2.6	TBS-T buffer solution.....	24
2.2.7	RIPA buffer solution.....	25
2.2.8	Glycine buffer solution .....	25
2.2.9	Krebs buffer solution .....	25
2.2.10	Dulbecco's PBS buffer solution.....	25
2.2.11	PBS-T.....	25
2.2.12	4% Paraformaldehyde solution.....	25
2.3	Methods and techniques.....	26
2.3.1	Linear peptide synthesis and overall peptide purification .....	26
2.3.2	Plate-based assay (PBA) methodologies for HIF-1 $\alpha$ binding detection.....	26

2.3.2.1	PBA method A .....	26
2.3.2.2	PBA method B .....	26
2.3.3	In-solution charcoal-based assay for HIF-1 $\alpha$ binding .....	27
2.4	General microscale thermophoresis procedure .....	27
2.4.1	HIF-1 $\alpha$ fragment protein labelling .....	27
2.4.2	HIF-1 $\alpha$ fragment thermophoresis analysis .....	28
2.4.3	HIF-1 $\alpha$ full-length protein labelling .....	28
2.4.4	HIF-1 $\alpha$ full-length thermophoresis analysis .....	29
2.5	Computational analyses .....	29
2.6	Radiolabelling procedures .....	30
2.6.1	Production of n.c.a. [ $^{18}\text{F}$ ]fluoride .....	30
2.6.2	Fully automated synthesis .....	30
2.7	Biochemistry techniques and methods .....	30
2.7.1	Cell culture .....	30
2.7.2	Cell line transfection .....	31
2.7.3	Western blot .....	31
2.7.3.1	HIF-1 $\alpha$ antibody procedure .....	32
2.7.3.2	B-actin antibody procedure .....	32
2.7.4	Bicinchoninic acid (BCA) assay .....	33

2.7.5	Confocal analysis of Compound <b>33</b> (NBD-link-c-(Ppg)LLFVY).....	33
2.7.6	Cell uptake studies for HIF-1 $\alpha$ binding compounds .....	34
2.7.7	Cell uptake for nitroimidazole compounds using the hypoxia chamber.....	36
2.7.8	Silencing RNA transfection of MDA-MB-231 cells .....	38
2.7.9	<i>In vivo</i> metabolic stability .....	38
2.7.10	Dynamic PET imaging.....	39
2.8	Summary of synthesized chemicals .....	40
Chapter 3: Synthesis of radiolabelled nitroimidazole compounds .....		47
3.1	Fully automated synthesis.....	47
3.2	Radiosynthesis of [ $^{18}\text{F}$ ]fluoromisonidazole ([ $^{18}\text{F}$ ]FMISO).....	48
3.3	Radiosynthesis of [ $^{18}\text{F}$ ]fluoroazomycin arabinoside ([ $^{18}\text{F}$ ]FAZA).....	51
3.4	Radiosynthesis of 4-[ $^{18}\text{F}$ ]fluorobenzylamine ([ $^{18}\text{F}$ ]FBAmine).....	54
3.5	Radiosynthesis of N-(4-[ $^{18}\text{F}$ ]fluorobenzyl)-2-(2-nitro-1H-imidazol-1-yl)-acetamide ([ $^{18}\text{F}$ ]FBNA).....	55
3.6	Molar activity calculations for nitroimidazole compounds .....	58
3.6.1	Molar activity for [ $^{18}\text{F}$ ]FAZA .....	58
3.6.2	Molar activity for [ $^{18}\text{F}$ ]FMISO .....	59
3.6.3	Molar activity for [ $^{18}\text{F}$ ]FBNA.....	60
3.7	Partition Coefficient (logP) calculation for [ $^{18}\text{F}$ ]FBNA .....	61

3.8	Summary for the synthesis of radiolabelled nitroimidazole compounds.....	61
Chapter 4: <i>In vitro</i> and <i>in vivo</i> analysis of 2-nitroimidazole compounds.....		63
4.1	In vitro cell uptake of 2-nitroimidazole compounds.....	64
4.1.1	<i>In vitro</i> cell uptake of [ <sup>18</sup> F]FBNA.....	64
4.1.2	Comparative analysis of [ <sup>18</sup> F]FBNA, [ <sup>18</sup> F]FAZA and [ <sup>18</sup> F]FMISO cell uptake .....	66
4.2	In vivo metabolic stability and blood distribution of 2-nitroimidazoles.....	68
4.3	Dynamic PET imaging of 2-nitroimidazoles .....	69
4.4	Summary for the In vitro and in vivo analysis of 2-nitroimidazole compounds .....	75
Chapter 5: Synthesis and evaluation of novel HIF-1 $\alpha$ binding compounds.....		76
5.1	HIF-1 $\alpha$ binding derivatives chemical synthesis .....	77
	Compound 1: <i>p</i> -((4-((3-Pyridyl)methyl)-1-piperazinyl)methyl)benzoic acid .....	78
	Compound 2: <i>N-p</i> -Ethynylphenyl <i>p</i> -((4-((3-pyridyl)methyl)-1-piperazinyl)methyl)benzamide .....	79
	Compound 3: <i>N-p</i> -Ethynylphenyl <i>p</i> -(chloromethyl)benzamide .....	79
	Compound 4: <i>N-p</i> -Ethynylphenyl <i>p</i> -((4-((3-pyridyl)methyl)-1-piperazinyl)methyl)benzamide .....	80
	Compound 5: <i>N</i> -( <i>p</i> -(2-( <i>p</i> -Fluorophenyl)ethynyl)phenyl) <i>p</i> -((4-[(3-pyridyl)methyl)-1-piperazinyl)methyl)benzamide .....	81
	Synthesis route compound 5A: .....	81
	Synthesis route compound 5B: .....	82

Synthesis route compound 5C: .....	82
Synthesis route compound 5D: .....	82
Synthesis route compound 5E:.....	82
Synthesis route compound 5F:.....	83
Compound <b>6</b> : <i>p</i> -(2-( <i>p</i> -Fluorophenyl)ethynyl)aniline .....	84
Compound <b>7</b> : <i>p</i> -(2-( <i>p</i> -Fluorophenyl)ethynyl)aniline .....	85
Compound <b>8</b> : <i>N-p</i> -Iodophenyl <i>p</i> -((4-((3-pyridyl)methyl)-1-piperazinyl)methyl)benzamide	85
General reaction scheme for compound <b>9</b> to compound <b>20</b> .....	86
Compound <b>9</b> : N-(4-(1-ethynyl-4-fluorophenyl)phenyl)-4-((4-(pyridine-3-ylmethyl)piperazin-1-yl)methyl)benzamide .....	88
Compound <b>10</b> : N-(4-(4-ethynylanisole)phenyl)-4-((4-(pyridine-3-ylmethyl)piperazin-1-yl)methyl)benzamide.....	88
Compound <b>11</b> : N-(4-(4-ethynylaniline)phenyl)-4-((4-(pyridine-3-ylmethyl)piperazin-1-yl)methyl)benzamide.....	89
Compound <b>12</b> : N-(4-(4-ethynylbiphenyl)phenyl)-4-((4-(pyridine-3-ylmethyl)piperazin-1-yl)methyl)benzamide.....	89
Compound <b>13</b> : N-(4-(4-ethynyltoluene)phenyl)-4-((4-(pyridine-3-ylmethyl)piperazin-1-yl)methyl)benzamide.....	89
Compound <b>14</b> : N-(4-(4- <i>tert</i> -butylphenylacetylene)phenyl)-4-((4-(pyridine-3-ylmethyl)piperazin-1-yl)methyl)benzamide.....	90
Compound <b>15</b> : N-(4-(1-chloro-4-ethynylbenzene)phenyl)-4-((4-(pyridine-3-ylmethyl)piperazin-1-yl)methyl)benzamide.....	90

Compound <b>16</b> : N-(4-(1-bromo-4-ethynylbenzene)phenyl)-4-((4-(pyridine-3-ylmethyl) piperazin-1-yl)methyl)benzamide .....	91
Compound <b>17</b> : N-(4-(Phenylethynyl)phenyl)-4-([4-(3-pyridinyl-methyl)-1-piperazinyl)methyl) benzamide (ER-400-583-00).....	91
Compound <b>18</b> : N-(4-(1-ethynyl-4-nitrobenzene)phenyl)-4-((4-(pyridine-3-ylmethyl) piperazin-1-yl)methyl)benzamide.....	92
Compound <b>19</b> : N-(4-(4-ethynyl-N,N-dimethylaniline)phenyl)-4-((4-(pyridine-3-ylmethyl) piperazin-1-yl)methyl)benzamide.....	92
Compound <b>20</b> : N-(4-(1-ethynyl-4-(trifluoromethyl)benzene)-phenyl)-4-((4-(pyridine-3-ylmethyl) piperazin-1-yl)methyl)-benzamide.....	92
Compound <b>21</b> : <i>l</i> -(PPg)LLFVY .....	93
Compound <b>22</b> : <i>l</i> -C(StBu)LLFVY .....	93
Compound <b>23</b> : <i>c</i> -(Ppg)LLFVY.....	93
Compound <b>24</b> : <i>c</i> -C(StBu)LLFVY .....	94
Compound <b>25</b> : <i>c</i> -CLLFVY.....	94
Compound <b>26</b> : link- <i>c</i> -(Ppg)LLFVY .....	94
Compound <b>27</b> : azido-PEG-4-fluorobenzamide .....	95
Compound <b>28</b> : [ <sup>19</sup> F]SFB-link- <i>c</i> -(Ppg)LLFVY .....	95
5.2 HIF-1 $\alpha$ binding assays.....	95
Plate Assay # 1: Concentrations of HIF-1 $\alpha$ , method A.....	96
Plate Assay # 2, Competitive blocking, plate pre-blocking and solvent effects, method A.	97

Plate Assay # 3: Concentrations of HIF-1 $\alpha$ , method B .....	98
Plate Assay # 4: Purity of Gallium-68 radiolabelled peptide, method B.....	99
Plate Assay # 5 ID: Blocking with cold reference and DMSO concentrations effects, method B.....	100
Plate Assay # 6 Concentration of HIF-1 $\alpha$ , method B.....	100
Plate Assay # 7: Binding of a fluorescent compound to plate assay, method B.....	100
Plate Assay # 8 ID: SFB-labelled peptide and HIF-1 $\alpha$ concentrations, method B .....	101
Plate Assay # 9: Binding of SFB-labelled peptide in triplicate, method B.....	101
Solution Assay # 1: Charcoal assay with varying concentrations of protein in solution....	102
Solution Assay # 2: Charcoal assay with concentrated reaction solutions. ....	103
Solution Assay #3: Varying charcoal concentration and radiotracer concentration –no protein .....	104
Solution Assay #4: Charcoal assay with varying protein concentration.....	104
5.3 Microscale thermophoresis of HIF-1 $\alpha$ binding compounds.....	105
5.4 In Silico analysis of HIF-1 $\alpha$ binding compounds.....	108
5.5 Computational design of additional novel HIF-1a binding compounds.....	111
5.6 Summary for synthesis and evaluation of novel HIF-1 $\alpha$ binding compounds .....	113
Chapter 6: Synthesis of radiolabelled HIF-1 $\alpha$ binding compounds .....	115
6.1 [ <sup>18</sup> F]SFB-link-c-(Ppg)LLFVY (JDW00117) .....	115

6.2	[ <sup>68</sup> Ga]Gallium radiolabelling of cyclic peptide.....	117
	Compound <b>29</b> : NOTA-Bn-SCN-link-c-(Ppg)LLFVY.....	117
	Compound <b>30</b> : DOTA-link-c-(Ppg)LLFVY.....	117
	Compound <b>31</b> : <sup>69</sup> Ga-DOTA-link-c-(Ppg)LLFVY.....	118
6.2.1	[ <sup>68</sup> Ga]NOTA-Bn-SCN-link-c-(Ppg)LLFVY (JDW00316).....	118
6.2.2	[ <sup>68</sup> Ga]DOTA-link-c-(Ppg)LLFVY (JDW00816).....	120
6.2.3	[ <sup>64</sup> Cu]NOTA-Bn-SCN-(Ppg)LLFVY (JDW02415).....	121
6.3	Fluorescent labelling of cyclic peptide.....	123
	Compound <b>32</b> : N-[2-(2-{2-(2-Azidoethoxy)ethoxy}ethoxy)ethyl]-7-nitro-2,1,3-benzoxadiazol-4-amine.....	123
	Compound <b>33</b> : NBD-link-c-(Ppg)LLFVY.....	123
6.4	[ <sup>18</sup> F]Fluorine radiolabelling of small-molecular HIF-1 $\alpha$ targeting compounds.....	124
	Compound <b>34</b> : ( <i>p</i> -Ethynylphenyl)trimethylammonium.....	124
	Compound <b>35</b> : <i>p</i> -(2-( <i>p</i> -( <i>p</i> -((4-[(3-Pyridyl)methyl]-1-piperaziny)methyl)benzylamino]phenyl) ethynyl)(trimethylammonio)benzene.....	125
6.4.1	Direct radiolabelling to achieve [ <sup>18</sup> F]Compound <b>9</b> ([ <sup>18</sup> F]FPeP4).....	126
6.4.2	Prosthetic group approach for the synthesis of [ <sup>18</sup> F]compound <b>9</b> ([ <sup>18</sup> F]FPeP4).....	129
6.4.2.1	Synthesis of 4-[ <sup>18</sup> F]fluorophenylacetylene ([ <sup>18</sup> F]FPA).....	129
6.4.2.2	Sonogashira cross coupling reactions with [ <sup>18</sup> F]FPA.....	132
	Compound <b>36</b> : 1-((4-fluorophenyl)ethynyl)-2,4-dimethoxybenzene.....	132

6.5	Molar activity calculations for HIF-1 $\alpha$ targeting compound.....	141
6.5.1	Molar activity of [ <sup>18</sup> F]SFB-link-c-(Ppg)LLFVY .....	141
6.5.2	Molar activity of [ <sup>18</sup> F]FPeP4 .....	142
6.6	LogD calculations for HIF-1 $\alpha$ targetting compound [ <sup>18</sup> F]FPeP4.....	143
6.7	Summary for radiolabelling of HIF-1 $\alpha$ targeting compounds.....	144
Chapter 7: HIF-1 $\alpha$ in TNBC cell lines and <i>in vitro</i> analysis .....		145
7.1	Western blot analysis of HIF-1 $\alpha$ expression in EMT6 cells .....	145
7.2	In vitro analysis of HIF-1 $\alpha$ targetting compounds in EMT6 cells .....	146
7.3	Western blot and PET radiotracer analysis of the HIF-1 $\alpha$ transfected cell lines .....	153
7.3.1	Western blot of transfected MDA-MB-231 cell lines.....	153
7.3.2	<i>In vitro</i> analysis of PET radiotracers in transfected MDA-MB-231 cell lines .....	154
7.4	In vitro analysis of HIF-1 $\alpha$ targetting compounds in transfected MDA-MB-231 cells 157	
7.5	HIF-1 $\alpha$ silenced cell lines and western blot analysis .....	162
7.6	In vitro analysis of HIF-1 $\alpha$ targetting compounds in MCF10a .....	164
7.7	In vitro analysis of HIF-1 $\alpha$ targetting compounds in silenced MDA-MB-231 cells..	167
7.8	Confocal microscopy (CM) of HIF-1 $\alpha$ .....	170
7.8.1	CM of compound <b>33</b> (NBD-link-c-(PPg)LLFVY) in EMT6 cells .....	170
7.8.2	CM of compound <b>33</b> (NBD-link-c-(PPg)LLFVY) in HIF-1 $\alpha$ transfected cells.....	172

7.8.3	CM of HA Antibody in HIF-1 $\alpha$ transfected cells.....	174
7.9	Summary for the in vitro analysis of HIF-1 $\alpha$ binding radiotracers.....	175
Chapter 8: <i>In vivo</i> analysis of HIF-1 $\alpha$ binding compounds.....		176
8.1	Testing of transfected cell lines in NIH-III mice.....	176
8.2	PET imaging of HIF-1 $\alpha$ derivatives.....	176
8.3	Plasma stability of HIF-1 $\alpha$ derivative [ <sup>18</sup> F]FPeP4.....	182
8.4	Summary for the in vivo analysis of HIF-1 $\alpha$ targeting radiotracers.....	183
Chapter 9: Summary of results.....		185
9.1	Novel compounds targeting HIF-1 $\alpha$ and their analysis.....	185
9.2	Radiolabelling of HIF-1 $\alpha$ targeting compounds and 2-nitroimidazoles.....	187
9.3	In vitro analysis of HIF-1 $\alpha$ targeting compounds and 2-nitroimidazoles.....	189
9.4	In vivo metabolic stability and blood distribution of HIF-1 $\alpha$ targeting compounds and 2-nitroimidazoles.....	193
9.5	In vivo dynamic PET imaging of HIF-1 $\alpha$ targeting compounds and 2-nitroimidazoles	194
Chapter 10: Conclusion, outlook and significance.....		197
References.....		199
Appendix.....		213
Appendix Table of Contents.....		213

## **List of Tables**

Table 1.1. Summary of molecular imaging modalities, including SPECT (single photon emission computed tomography), PET (positron emission tomography), BLI (bioluminescence), FLI (fluorescence imaging), FMT (fluorescence molecular tomography), and Photoacoustic imaging. Including sensitivity, spatial resolution, and imaging depth for all modalities. *Spatial resolution is strongly depth-dependent. ....	1
Table 1.2. Common radioisotopes used in PET and SPECT imaging. Including the radioisotope half life, decay pathway, percentage of main decay pathway, maximum strength of emission and typical route of production [16]. ....	3
Table 2.1. Time points chart, for the in vitro analysis of HIF-1 $\alpha$ binding compounds. Including both cell uptake and BCA assay lysis time points. * This is not a lysis time point, but an incubation time point with the BCA reagents. ....	35
Table 2.2. Time points chart for nitroimidazole cell uptake with BCA assay. Each time point is an individual 12-well plate, where 3 of the wells are for the BCA assay and 3 wells are for radiotracer cell uptake analysis. Plates are subjected to 24 hours of normoxic/hypoxic treatment, before radiotracer addition. ....	37
Table 2.3. Complete summary of all synthesized compounds, including compound ID, structure and page number location in the thesis document. ....	40
Table 3.1. Molar activity calculations from the synthesis of [ $^{18}\text{F}$ ]FAZA using the formula of (Absorbance-3.0934)/529.13=molar amount). ....	58
Table 3.2. Molar activity calculations from the synthesis of [ $^{18}\text{F}$ ]FMISO using the formula of (Absorbance-3.3869)/587.41=molar amount). ....	59
Table 3.3. Molar activity calculations from the synthesis of [ $^{18}\text{F}$ ]FBNA using the formula of (Absorbance)/1854.9=molar amount). ....	60

Table 3.4. Partition coefficient replicates from the synthesis of [ <sup>18</sup> F]FBNA. ....	61
Table 4.1. Summary for the in vitro and in vivo analysis of 2-nitroimidazole compounds. Listed data is classified into either A) MDA-MB-231 cells or B) MCF-7 cells. Where “H” is hypoxic in vitro cell uptake and “N” is normoxic in vitro cell uptake. Additionally, standardized uptake value (SUV) and tumor to muscle ratio (TMR) are reported for xenografts using both cell lines. ....	75
Table 5.1. Reaction compositions for the synthesis of Compound <b>5.D</b> . Catalysts used including tetrakis(triphenylphosphine)palladium(0) (Pd(PPh <sub>3</sub> ) <sub>4</sub> ), bis(dibenzylideneacetone)palladium(0) (Pd(dba) <sub>2</sub> ), palladium(II) nitrate (Pd(NO <sub>3</sub> ) <sub>2</sub> ), 3,3',3''-Phosphanetriyltris(benzenesulfonic acid) trisodium salt (tppts)[119].....	83
Table 5.2. Summary data for the production of compound <b>9</b> to compound <b>20</b> . Including compound ID (Cmpd), “X” moiety as demonstrated in Figure 5.9, HPLC retention time, synthesis yield, compound isolated purity and physical properties.....	87
Table 5.3. Dilutions of HIF-1α to obtain required concentrations of protein in designated well.	96
Table 5.4. List of experiment well, along with corresponding reaction conditions.....	97
Table 5.5. Microscale thermophoresis data with truncated HIF-1α. *Note: Compound 7 is <85% pure, results are approximate. ....	106
Table 5.6. Microscale thermophoresis data with full-length HIF-1α. *Note: Compound 7 is <85% pure, results are approximate. ....	108
Table 5.7. Computational docking studies with novel HIF-1α binding compounds.....	111
Table 6.1. Summary of radiolabelling data for [ <sup>68</sup> Ga]DOTA-link-c-(Ppg)LLFVY (JDW00816). Including reaction ID, peptide mass, sodium acetate (NaOAc) volume, volume of gallium eluent, temperature, time and yield.....	121

Table 6.2. Summary of radiolabelling data for [ <sup>64</sup> Cu]NOTA-Bn-SCN-(Ppg)LLFVY (JDW02415).....	122
Table 6.3. Summary of data for the radiolabelling of compound <b>35</b> precursor. Including reaction ID, solvent for fluorination, compound 35 concentration, temperature, time and purity as determined by TLC. ....	127
Table 6.4. Summary of HPLC data for the radiolabelling of compound <b>35</b> precursor. Including HPLC injection ID, retention time of product peak, and solvent composition.....	127
Table 6.5. Loading scheme for the ASU for the synthesis of [ <sup>18</sup> F]FPA. ....	130
Table 6.6. Testing parameters for the radiosynthesis on the ASU for [ <sup>18</sup> F]FPA.....	131
Table 6.7. Complete testing reactions for FPEdMO. Notes: Pd(OAc) <sub>2</sub> is 1.5 mg in 100 μL DMF, Pd(PPh <sub>3</sub> ) <sub>4</sub> is 1.5 mg in 100 μL DMF, PdCl <sub>2</sub> (PPh <sub>3</sub> ) <sub>2</sub> is 1.4 mg in 100 μL DMF, CuI is added in 100 μL DMF solution, [ <sup>18</sup> F]FPA is added to each reaction with 150 μL of DMF. 25 μL of TEA is added to each reaction. Precursor is present as 6 mg in 100 μL DMF. ....	133
Table 6.8. Complete testing reactions for [ <sup>18</sup> F]FPeP4. Notes: Pd(OAc) <sub>2</sub> is 2.7 mg in 1 mL DMSO, Pd(Cl <sub>2</sub> )(PPh <sub>3</sub> ) <sub>2</sub> is 1.1 mg in 1 mL DMSO, Pd(PPh <sub>3</sub> ) <sub>4</sub> is 3.7 mg in 1 mL DMSO, Pd(OAc) <sub>2</sub> +dppf is 5.2 mg + 25.5 mg in 1 mL DMSO, Pd(OAc) <sub>2</sub> +Diphos is 6.8 mg + 35.0 mg in 1 mL DMSO, 50 μL of TEA is added to each reaction. Precursor is present as 10.2 mg in 1mL DMSO.....	136
Table 6.9. Molar activity calculations from the synthesis of [ <sup>18</sup> F]SFB-link-c-(Ppg)LLFVY using the formula of (Absorbance-37.064)/52758=molar amount).....	141
Table 6.10. Molar activity calculations from the synthesis of [ <sup>18</sup> F]FPeP4 using the formula of “Absorbance=1202.6x <sup>2</sup> +1779.3x-66.195”, where x=molar amount. Polynomial equation was solved in Excel using goal seek. ....	142
Table 7.1. Western blot intensity analysis for HIF-1α and B-Actin in 18955, 18949 and GFP cell lines (n=3). ....	154

Table 9.1. Summary data for the production of compound **9** to **20**, derivatized from the lead structure from the literature of ER-400583-00. ID is the compound identification number and \*‘‘ps’’ is shorthand for powdery solid..... 185

Table 9.2. Microscale thermophoresis data with full-length HIF-1 $\alpha$ . \*Note: Compound **7** is <85% pure, results are approximate. .... 186

## **List of Figures**

Figure 1.1. Various radiotracers for the PET imaging of breast cancer. Including: A) [ <sup>18</sup> F]FDG, B)[ <sup>18</sup> F]FDF, C) [ <sup>18</sup> F]RGD, D) [ <sup>18</sup> F]FLT and E) [ <sup>18</sup> F]FES. ....	6
Figure 1.2. The original six hallmarks of cancer as presented by Hanahan and Weinberg[35]. ...	7
Figure 1.3. “The Tumor Microenvironment at a Glance” as presented by Balkwill et al.[40].....	9
Figure 1.4. Mechanism of nitroimidazole metabolism in hypoxia using nitroreductase enzymes. ....	10
Figure 1.5. Previously developed PET imaging agents for the imaging of hypoxia. Including: A) [ <sup>18</sup> F]FMISO, B) [ <sup>18</sup> F]FAZA, C) [ <sup>18</sup> F]EF5, D) [ <sup>64</sup> Cu]ATSM, [ <sup>18</sup> F]FRP-170, and E) [ <sup>18</sup> F]DiFA..	11
Figure 1.6. Compounds that inhibit interactions with HIF-1 $\alpha$ protein directly. Including: A) EZN-2968 oligonucleotide, B) acriflavine, C) Cyclo-CLLFVY, D) Chaetocin, and E) ER-400583-00. ....	18
Figure 3.1. GE TRACERlab Fx automated synthesis unit modifications to convert a two synthesis FDG unit into a one synthesis two reactor ASU. ....	47
Figure 3.2. Radiosynthesis pathway for the synthesis of [ <sup>18</sup> F]FMISO. ....	48
Figure 3.3. HPLC analysis of [ <sup>19</sup> F]FMISO, non-radioactive reference compound for [ <sup>18</sup> F]FMISO. Three UV channels are shown, including: 325 nm in green, 254 nm in purple and 210 nm in blue. Positive absorbance only observed in the 325 nm channel.....	48
Figure 3.4. Typical HPLC analysis of [ <sup>18</sup> F]FMISO as produced on the ASU. Three UV channels are shown, including: 325 nm in green, 254 nm in blue and 210 nm in purple. HERM radioactivity channel is shown in pink.....	49
Figure 3.5. Quality control injection of [ <sup>18</sup> F]FMISO, from HPLC purified product. One UV channels shown as 325 nm in green, showing unknown non-radioactive contaminant. HERM radioactivity channel is shown in pink.....	50

Figure 3.6. Co-injection of HPLC purified [<sup>18</sup>F]FMISO and [<sup>19</sup>F]FMISO. Three UV channels are shown, including: 325 nm in green, 254 nm in blue and 210 nm in purple. HERM radioactivity channel is shown in pink..... 50

Figure 3.7. Radiosynthesis pathway for the synthesis of [<sup>18</sup>F]FAZA..... 51

Figure 3.8. HPLC analysis of [<sup>19</sup>F]FAZA, non-radioactive reference compound for [<sup>18</sup>F]FAZA. Three UV channels are shown, including: 325 nm in green, 254 nm in purple and 210 nm in blue. Positive absorbance only observed in the 325 nm channel..... 51

Figure 3.9. Typical HPLC analysis of [<sup>18</sup>F]FAZA as produced on the ASU. Three UV channels are shown, including: 325 nm in green, 254 nm in blue and 210 nm in purple. HERM radioactivity channel is shown in pink..... 52

Figure 3.10. Quality control injection of [<sup>18</sup>F]FAZA, from HPLC purified product. One UV channels shown as 325 nm in green, showing known non-radioactive contaminant of [<sup>19</sup>F]FAZA. HERM radioactivity channel is shown in pink. .... 53

Figure 3.11. Co-injection of HPLC purified [<sup>18</sup>F]FAZA and [<sup>19</sup>F]FAZA. Three UV channels are shown, including: 325 nm in green, 254 nm in blue and 210 nm in purple. HERM radioactivity channel is shown in pink..... 53

Figure 3.12. Radiosynthesis pathway for the synthesis of [<sup>18</sup>F]FBAmine. .... 54

Figure 3.13. Typical HPLC analysis of [<sup>18</sup>F]FBAmine as produced on the ASU. Three UV channels are shown, including: 325 nm in green, 254 nm in blue and 210 nm in purple. HERM radioactivity channel is shown in pink. HPLC method used is “FAZA”. .... 55

Figure 3.14. Radiosynthesis pathway for the synthesis of [<sup>18</sup>F]FBNA..... 55

Figure 3.15. HPLC analysis of [<sup>19</sup>F]FBNA, non-radioactive reference compound for [<sup>18</sup>F]FBNA. Three UV channels are shown, including: 325 nm in green, 254 nm in blue and 210 nm in purple. Positive absorbance observed in the 325 nm and 210 nm channels. .... 56

Figure 3.16. Typical HPLC analysis of [ <sup>18</sup> F]FBNA as produced manually. Three UV channels are shown, including: 325 nm in green, 254 nm in blue and 210 nm in purple. HERM radioactivity channel is shown in pink.....	57
Figure 3.17. Quality control injection of [ <sup>18</sup> F]FBNA, from HPLC purified product. One UV channels shown as 325 nm in green, showing known non-radioactive contaminant of [ <sup>19</sup> F]FBNA. HERM radioactivity channel is shown in pink. ....	57
Figure 3.19. Molar activity curve for [ <sup>19</sup> F]FAZA non-radioactive reference.....	58
Figure 3.20. Molar activity curve for [ <sup>19</sup> F]FMISO non-radioactive reference. ....	59
Figure 3.21. Molar activity curve for [ <sup>19</sup> F]FBNA non-radioactive reference.....	60
Figure 4.1. Cell uptake of [ <sup>18</sup> F]FAZA into MDA-MB-231, MCF7 and MCF10a cells under both normoxic and hypoxic conditions [117]. ....	63
Figure 4.2. In vivo small animal PET imaging of [ <sup>18</sup> F]FAZA in MDA-MB-231 and MCF7 xenograft models [117]. ....	63
Figure 4.3. Cell uptake of [ <sup>18</sup> F]FBNA into MDA-MB-231 cells under both normoxic and hypoxic conditions. Data is presented with percent uptake in normoxic conditions normalized to 100% n=(9/3). ....	64
Figure 4.4. Cell uptake of [ <sup>18</sup> F]FBNA into MCF7 cells under both normoxic and hypoxic conditions. Data is presented with percent uptake in normoxic conditions normalized to 100% n=(6/2). ....	65
Figure 4.5. In vitro cell uptake of A) [ <sup>18</sup> F]FBNA in MCF7 cells (n=6/2) and MDA-MB-231 cells (n=9/3), B) [ <sup>18</sup> F]FMISO in MCF7 cells (n=9/3) and MDA-MB-231 cells (n=9/3), C) [ <sup>18</sup> F]FAZA in MCF7 cells (n=9/3) and MDA-MB-231 cells (n=9/3). ....	67
Figure 4.6. Metabolic stability and blood distribution of [ <sup>18</sup> F]FBNA (n=3), [ <sup>18</sup> F]FAZA (n=1), and [ <sup>18</sup> F]FMISO (n=1) in normal female BALB/C mice. ....	68

Figure 4.7. Dynamic PET imaging of [ <sup>18</sup> F]FBNA in NIH-III tumor-bearing mice. A)MDA-MB-231 xenograft model B) MCF7 xenograft model. Measured tumors were between 5 mm <sup>2</sup> to 10 mm <sup>2</sup> , with SUV analysis completed in n=3 mice. ....	70
Figure 4.8. Dynamic PET imaging of [ <sup>18</sup> F]FMISO in NIH-III tumor-bearing mice. A)MDA-MB-231 xenograft model B) MCF7 xenograft model. Measured tumors were between 5 mm <sup>2</sup> to 10 mm <sup>2</sup> , with SUV analysis completed in n=4 mice. ....	71
Figure 4.9. Dynamic PET imaging of [ <sup>18</sup> F]FAZA in NIH-III tumor-bearing mice. A)MDA-MB-231 xenograft model B) MCF7 xenograft model. Measured tumors were between 5 mm <sup>2</sup> to 10 mm <sup>2</sup> , with SUV analysis completed in n=4 mice. ....	72
Figure 4.10. Time activity curve of [ <sup>18</sup> F]FBNA in NIH-III tumor-bearing mice with a MDA-MB-231 xenograft (black data points) or a MCF7 xenograft (red data points). Closed circle data points indicate the tumor uptake, whereas open circle data points indicate muscle uptake (n=3). ....	73
Figure 4.11. Time activity curve of [ <sup>18</sup> F]FMISO in NIH-III tumor bearing mice with a MDA-MB-231 xenograft (black data points) or a MCF7 xenograft (red data points). Closed circle data points indicate the tumor uptake, whereas open circle data points indicate muscle uptake (n=4). ....	74
Figure 4.12. Time activity curve of [ <sup>18</sup> F]FAZA in NIH-III tumor-bearing mice with a MDA-MB-231 xenograft (black data points) or a MCF7 xenograft (red data points). Closed circle data points indicate the tumor uptake, whereas open circle data points indicate muscle uptake (n=4). ....	74
Figure 5.1. Reaction scheme for the synthesis of compound <b>1</b> from the commercially available starting materials. ....	78
Figure 5.2. Reaction scheme for the synthesis of compound <b>2</b> from compound <b>1</b> and commercially available 4-ethynylaniline. ....	79

Figure 5.3. Reaction scheme for the synthesis of compound <b>3</b> from commercially available starting materials.....	79
Figure 5.4. Reaction scheme for the synthesis of compound <b>4</b> from compound <b>3</b> and commercially available 1-pyridin-3-ylmethyl-piperazine. ....	80
Figure 5.5. Reaction scheme for the synthesis of compound <b>5</b> from compound <b>4</b> and commercially available 4-fluoriodobenzene.....	81
Figure 5.6. Reaction scheme for the synthesis of compound <b>6</b> from commercially available starting materials.....	84
Figure 5.7. Reaction scheme for the synthesis of compound <b>7</b> from commercially available starting materials.....	85
Figure 5.8. Reaction scheme for the synthesis of compound <b>8</b> from compound <b>7</b> and commercially available 1-pyridin-3-ylmethyl-piperazine. ....	86
Figure 5.9. General reaction scheme for the production of compound <b>9</b> to compound <b>20</b> from compound <b>8</b> and commercially available 4-phenylacetylene derivatives.....	86
Figure 5.10. [ <sup>68</sup> Ga]NOTA-Bn-SCN-link-c-(Ppg)LLFVY response to various amounts of HIF-1 $\alpha$ protein loading concentrations in a plate based assay (n=1).....	99
Figure 5.11. JDW00315 concentration versus UV absorbance curve for a plate-based assay...	100
Figure 5.12. [ <sup>18</sup> F]SFB-link-c-(Ppg)LLFVY binding response to HIF-1 $\alpha$ protein at various concentrations of loading (n=1).....	101
Figure 5.13. [ <sup>18</sup> F]SFB-link-c-(Ppg)LLFVY binding to HIF-1 $\alpha$ protein at various concentrations of loading (n=3). ....	102
Figure 5.14. [ <sup>18</sup> F]SFB-link-c-(Ppg)LLFVY binding to HIF-1 $\alpha$ protein in solution with charcoal, assay #1 (n=3).....	102

Figure 5.15. [ <sup>18</sup> F]SFB-link-c-(Ppg)LLFVY binding to HIF-1 $\alpha$ protein in solution with charcoal, assay #2 (n=3).	103
Figure 5.16. [ <sup>18</sup> F]SFB-link-c-(Ppg)LLFVY binding to charcoal solution as varying concentrations (n=3).	104
Figure 5.17 [ <sup>18</sup> F]SFB-link-c-(Ppg)LLFVY binding to HIF-1 $\alpha$ in a charcoal solution assay (n=3).	105
Figure 5.18. a) P3 Binding pocket predicted for molecular docking analyses in HIF-1 $\alpha$ . The cavity is highlighted in purple mesh, and key residues are displayed. b) Molecular docking of compound <b>17</b> in HIF-1 $\alpha$ . Predicted binding mode of compound <b>17</b> in HIF-1 $\alpha$ ( $E_{\text{Intermolecular}} = -10.79$ kcal/mol).	109
Figure 5.19. Molecular docking of compound <b>9</b> in HIF-1 $\alpha$ . Predicted binding mode of compound ( <b>9</b> ) in HIF-1 $\alpha$ ( $E_{\text{Intermolecular}} = -11.94$ kcal/mol) and dotted oval highlights key residues of the binding pocket. For clarity, the carbon atoms of compound ( <b>9</b> ) are colored in orange, and key residues indicated in lines.	109
Figure 5.20. Molecular docking of SFB-link-c-(Ppg)LLFVY <b>3</b> in HIF-1 $\alpha$ . Predicted binding mode of [ <sup>19</sup> F]SFB-link-c-(Ppg)LLFVY <b>28</b> in HIF-1 $\alpha$ ( $E_{\text{Intermolecular}} = -10.11$ kcal/mol). The carbon atoms of the ligand are colored gray and key residues are highlighted in salmon-colored lines.	110
Figure 6.1. Radiosynthesis of [ <sup>18</sup> F]SFB-link-c-(Ppg)LLFVY using prosthetic group [ <sup>18</sup> F]SFB.	115
Figure 6.2. Typical HPLC of [ <sup>18</sup> F]SFB-link-c-(Ppg)LLFVY (JDW00117). Two UV channels are shown, including: 254 nm in green (171 Channel 1) and 210 nm in blue (171 Channel 2). HERM radioactivity channel is shown in pink.	116
Figure 6.3. Quality control HPLC of [ <sup>18</sup> F]SFB-link-c-(Ppg)LLFVY (JDW00117). Two UV channels are shown, including: 254 nm in green (171 Channel 1) and 210 nm in blue (171 Channel 2). HERM radioactivity channel is shown in pink.	116

Figure 6.4. HPLC co-injection of [ <sup>19</sup> F]SFB-link-c-(Ppg)LLFVY <b>28</b> and [ <sup>18</sup> F]SFB-link-c-(Ppg)LLFVY (JDW00117). Two UV channels are shown, including: 254 nm in green (171 Channel 1) and 210 nm in blue (171 Channel 2). HERM radioactivity channel is shown in pink. .....	117
Figure 6.5. Reaction scheme for the radiolabelling of [ <sup>68</sup> Ga]NOTA-Bn-SCN-link-c-(Ppg)LLFVY (JDW00316). .....	118
Figure 6.6. HPLC with degradation products of [ <sup>68</sup> Ga]NOTA-Bn-SCN-link-c-(Ppg)LLFVY (JDW00316). Two UV channels are shown, including: 254 nm in green (171 Channel 1) and 210 nm in blue (171 Channel 2). HERM radioactivity channel is shown in pink. ....	119
Figure 6.7. Reaction scheme for the radiolabelling of [ <sup>68</sup> Ga]DOTA-link-c-(Ppg)LLFVY (JDW00816). .....	120
Figure 6.8. Reaction scheme for the radiolabelling of [ <sup>64</sup> Cu]NOTA-Bn-SCN-(Ppg)LLFVY (JDW02415). .....	121
Figure 6.9. HPLC for the radiolabelling of [ <sup>64</sup> Cu]NOTA-Bn-SCN-(Ppg)LLFVY (JDW02415). Two UV channels are shown, including: 254 nm in green (171 Channel 1) and 210 nm in blue (171 Channel 2). HERM radioactivity channel is shown in pink. ....	122
Figure 6.10. Reaction scheme for the synthesis of compound <b>32</b> from commercially available starting materials. .....	123
Figure 6.11. Reaction scheme for the synthesis of compound <b>33</b> , from compound <b>32</b> (see section 6.3.) and compound <b>23</b> (see section 5.1.). ....	124
Figure 6.12. Reaction scheme for the synthesis of compound <b>34</b> from commercially available starting materials. .....	124
Figure 6.13. Reaction scheme for the synthesis of compound <b>35</b> , from compound <b>8</b> (see section 5.1.) and compound <b>34</b> (see section 6.3.). ....	125

Figure 6.14. Reaction scheme for the radiolabelling of [<sup>18</sup>F]compound **9** ([<sup>18</sup>F]FPeP4), from previously synthesized compound **35**. ..... 126

Figure 6.15. Typical HPLC chromatogram of [<sup>18</sup>F]FPeP4 reaction. Two UV channels are shown, including: 254 nm in green (171 Channel 1) and 210 nm in blue (171 Channel 2). HERM radioactivity channel is shown in pink..... 128

Figure 6.16. Typical HPLC of [<sup>19</sup>F]compound **9** reference compound. Two UV channels are shown, including: 254 nm in green (171 Channel 1) and 210 nm in blue (171 Channel 2). HERM radioactivity channel is shown in pink..... 128

Figure 6.17. Reaction scheme for the synthesis of 4-[<sup>18</sup>F]fluorophenylacetylene from the previously synthesized compound **34**. ..... 129

Figure 6.18. Percent yield on TLC for the radiolabelling of [<sup>18</sup>F]FPA in various solvents and temperatures (n=1). ..... 130

Figure 6.19. Reaction scheme for the synthesis of compound **36** from commercially available starting materials. .... 132

Figure 6.20. Typical HPLC injection of [<sup>18</sup>F]FPEdMO. Two UV channels are shown, including: 254 nm in green and 210 nm in blue. HERM radioactivity channel is shown in pink. .... 134

Figure 6.21. Non-radioactive reference compound of [<sup>19</sup>F]FPEdMO on HPLC. Two UV channels are shown, including: 254 nm in green and 210 nm in blue. .... 134

Figure 6.22. Synthesis of [<sup>18</sup>F]FPeP4 using palladium catalyzed cross-coupling reaction with [<sup>18</sup>F]FPA and compound **8**. .... 135

Figure 6.23. HPLC radiotracer for the impurity of [<sup>18</sup>F]FPA-Pd at 32.2 minutes. Two UV channels are shown, including: 254 nm in green and 210 nm in blue. HERM radioactivity channel is shown in pink. .... 137

Figure 6.24. HPLC radiotracer for the impurity of [<sup>18</sup>F]FPA-Pd-**8** at 15 minutes. Two UV channels are shown, including: 254 nm in green and 210 nm in blue. HERM radioactivity channel is shown in pink..... 137

Figure 6.25. HPLC chromatogram for co-injection of [<sup>18</sup>F]FPeP4 and compound **9**. Two UV channels are shown, including: 254 nm in green and 210 nm in blue. HERM radioactivity channel is shown in pink..... 138

Figure 6.26. HPLC chromatogram for synthesis of [<sup>18</sup>F]FPeP4 using PdCl<sub>2</sub>(PPh<sub>3</sub>)<sub>2</sub>. Two UV channels are shown, including: 254 nm in green and 210 nm in blue. HERM radioactivity channel is shown in pink..... 138

Figure 6.27. Crude purification of ASU synthesized [<sup>18</sup>F]FPeP4. Two UV channels are shown, including: 254 nm in green and 210 nm in blue. HERM radioactivity channel is shown in pink.  
..... 140

Figure 6.28. HPLC co-injection of [<sup>18</sup>F]FPeP4 (HERM) and [<sup>19</sup>F]compound **9**. Two UV channels are shown, including: 254 nm in green and 210 nm in blue. HERM radioactivity channel is shown in pink..... 140

Figure 6.29. Molar activity curve for [<sup>19</sup>F]SFB-link-c-(Ppg)LLFVY non-radioactive reference.  
..... 141

Figure 6.30. Molar activity curve for [<sup>19</sup>F]compound **9** non-radioactive reference for [<sup>18</sup>F]FPeP4.  
..... 142

Figure 6.31. LogD curve for [<sup>18</sup>F]FPeP4 at various pH points..... 143

Figure 7.1. Western blot of EMT6 cells for the expression of HIF-1a (100 kDa band) under normoxic and hypoxic conditions over time with B-actin staining (42 kDa band). Lane 1 was protein ladder, lane 2 – 24 hrs hypoxia, lane 3 – 10 hrs hypoxia, lane 4 – 8 hrs hypoxia, lane 5 – 6 hrs hypoxia, lane 6 – 4 hrs hypoxia, lane 7 – 2 hrs hypoxia, lane 8 – 24 hrs normoxia. .... 145

Figure 7.2. Cell uptake of [<sup>68</sup>Ga]NOTA-Bn-SCN-link-c-(Ppg)LLFVY in EMT6 cells under both hypoxic and normoxic conditions (n=5). \*\*Upon completion of these experiments, it was found that the analyzed compound was likely [<sup>68</sup>Ga]NOTA-Bn-SCN not [<sup>68</sup>Ga]NOTA-Bn-SCN-link-c-(Ppg)LLFVY..... 147

Figure 7.3. Cell uptake of [<sup>68</sup>Ga]NOTA-Bn-SCN in EMT6 cells under both hypoxic and normoxic conditions (n=1)..... 148

Figure 7.4. Combined cell uptake data of [<sup>68</sup>Ga]DOTA-link-c-(Ppg)LLFVY, [<sup>68</sup>Ga]NOTA-Bn-SCN and [<sup>68</sup>Ga]NOTA-Bn-SCN-link-c-(Ppg)LLFVY in EMT6 cells under both hypoxic and normoxic conditions (n=10)..... 149

Figure 7.5. Cell uptake of [<sup>18</sup>F]SFB-link-c-(Ppg)LLFVY in EMT6 cells under both hypoxic and normoxic conditions (n=1)..... 149

Figure 7.6. Cell uptake of [<sup>18</sup>F]SFB-link-c-(Ppg)LLFVY in EMT6 cells under both hypoxic (100 mM CoCl<sub>2</sub>, 4 hours) and normoxic conditions (n=1). ..... 150

Figure 7.7. Cytotoxicity of CoCl<sub>2</sub> treatment to EMT6 cells under various conditions for 2-hour incubation..... 151

Figure 7.8. Cell uptake of [<sup>18</sup>F]SFB-link-c-(Ppg)LLFVY in EMT6 cells under various hypoxic and normoxic conditions (n=1). Concentrations listed are for CoCl<sub>2</sub>..... 152

Figure 7.9. [<sup>18</sup>F]FDG cell uptake in transfected and natural MDA-MB-231 cells. Including MDA-MB-231 GFP cells, MDA-MB-231 18949 cells, MDA-MB-231 18955 cells and non-transfected MDA-MB-231 control (n=3)..... 154

Figure 7.10. [<sup>18</sup>F]FLT cell uptake in transfected MDA-MB-231 cells. Including MDA-MB-231 GFP control cells, MDA-MB-231 18949 cells, and MDA-MB-231 18955 cells (n=3)..... 155

Figure 7.11. [<sup>18</sup>F]FAZA cell uptake in transfected MDA-MB-231 cells. Including MDA-MB-231 GFP control cells, MDA-MB-231 18949 cells, and MDA-MB-231 18955 cells (n=2)..... 156

Figure 7.12. [ <sup>18</sup> F]SFB-link-c-(Ppg)LLFVY cell uptake in transfected MDA-MB-231 cells. Including MDA-MB-231 GFP control cells, MDA-MB-231 18949 cells, and MDA-MB-231 18955 cells (n=5). .....	157
Figure 7.13. [ <sup>18</sup> F]SFB-link-c-(Ppg)LLFVY cell uptake in transfected MDA-MB-231 cells at 60 minutes. Including MDA-MB-231 GFP control cells, MDA-MB-231 18949 cells, and MDA-MB-231 18955 cells (n=5). .....	158
Figure 7.14. [ <sup>18</sup> F]SFB-link-c-(Ppg)LLFVY cell uptake in transfected MDA-MB-231 cells. Including MDA-MB-231 GFP control cells, MDA-MB-231 18949 cells, and MDA-MB-231 18955 cells (n=6). .....	159
Figure 7.15. [ <sup>18</sup> F]SFB-link-c-(Ppg)LLFVY in HIF-1a transfected cells at 90 min. Including MDA-MB-231 GFP control cells, MDA-MB-231 18949 cells, and MDA-MB-231 18955 cells (n=4). .....	159
Figure 7.16. [ <sup>18</sup> F]SFB-link-c-(Ppg)LLFVY cell uptake in transfected MDA-MB-231 cells for four different cell passages, with glycine-HCl washes. A) passage 4, B) passage 13, C) passage 17, D) passage 21. Including MDA-MB-231 GFP control cells, MDA-MB-231 18949 cells, and MDA-MB-231 18955 cells (n=1). .....	160
Figure 7.17. [ <sup>18</sup> F]SFB-link-c-(Ppg)LLFVY cell uptake in transfected MDA-MB-231 cells at passage 20. Including MDA-MB-231 GFP control cells, MDA-MB-231 18949 cells, and MDA-MB-231 18955 cells (n=4). .....	161
Figure 7.18. [ <sup>18</sup> F]FPeP4 cell uptake in transfected MDA-MB-231 cells at passage 20. Including MDA-MB-231 GFP control cells, MDA-MB-231 18949 cells, and MDA-MB-231 18955 cells (n=3). .....	161
Figure 7.19. [ <sup>18</sup> F]FPeP4 cell uptake in transfected MDA-MB-231 cells at passage 20 and time point of 60 minutes. Including MDA-MB-231 GFP control cells, MDA-MB-231 18949 cells, and MDA-MB-231 18955 cells (n=9/3). .....	162

Figure 7.20. HIF-1 $\alpha$  silencing was completed in MDA-MB-231 cells in 6 well plates. Treatment groups are as follows: A) 48 hours Opti-MEM, B) 48 hours HIF-1 $\alpha$  siRNA, C) 48 hours scrambled siRNA, D) 24 hours Opti-MEM, E) 24 hours HIF-1 $\alpha$  siRNA, and F) 24 hours scrambled siRNA. PageRuler Plus molecular weight ladder on the left in kDa (cat #26619). HIF-1 $\alpha$  protein bands are highlighted in the blue box. B-actin bands are seen at 43 kDa..... 163

Figure 7.21. [ $^{18}\text{F}$ ]SFB-link-c-(Ppg)LLFVY cell uptake in MDA-MB-231 and MCF10a cells, under both normoxic and hypoxic conditions (n=3/1)..... 164

Figure 7.22. HIF-1 $\alpha$  western blot using MDA-MB-231, MCF7, MCF10a, and EMT6 cells with variable loading where lane 1 of a given cell line is 5  $\mu\text{L}$  of lysate, lane 2 is 10  $\mu\text{L}$  of lysate and lane 3 is 15  $\mu\text{L}$  of lysate (n=1)..... 165

Figure 7.23. Confocal analysis of HIF-1 $\alpha$  in MCF10a and MDA-MB-231 18955 cell lines. The top row is the MDA-MB-231 18955 cells, bottom row is the MCF10a cells. The left column is the CFL-488 signal. The center column is the DAPI signal. The right column is an overlay of the left and center columns. .... 166

Figure 7.24. [ $^{18}\text{F}$ ]SFB-link-c-(Ppg)LLFVY cellular uptake in MDA-MB-231 cells silenced with HIF-1 $\alpha$  siRNA. Including MDA-MB-231 with HIF-1 $\alpha$  siRNA, MDA-MB-231 cells with scrambled siRNA, and control MDA-MB-231 cells in opti-MEM media with lipofectamine (n=9/3). .... 167

Figure 7.25. Western blot analysis of BCA protein samples from the cellular uptake of [ $^{18}\text{F}$ ]FPeP4 in MDA-MB-231 cells. Gel loading is 0.5  $\mu\text{g}$  protein per well. Lane 1 is protein ladder with 100kDa band being stained, lanes 2,3, and 4 are HIF-1 $\alpha$  siRNA treatment, lanes 5 and 6 are scrambled siRNA treatment, lanes 7 and 8 are opti-MEM blank and lanes 9, 10 and 11 are 100  $\mu\text{M}$  CoCl $_2$  treatment. PageRuler Plus protein ladder as seen in the fluorescence channels is seen on the left with kDa measurements. HIF-1 $\alpha$  protein is present at 120 kDa. .... 168

Figure 7.26. [ $^{18}\text{F}$ ]FPeP4 cellular uptake in MDA-MB-231 cells silenced with HIF-1 $\alpha$  siRNA. Including MDA-MB-231 with HIF-1 $\alpha$  siRNA, MDA-MB-231 cells with scrambled siRNA,

MDA-MB-231 cells with 100  $\mu$ M CoCl<sub>2</sub> treatment, and control MDA-MB-231 cells in opti-MEM media with lipofectamine (n=9/3). ..... 169

Figure 7.27. NBD-link-c-(PPg)LLFVY in fixed EMT6 cells using confocal microscopy. Side 1 is the procedural blank containing no compound 33. Side 2 contains compound 33. A)DAPI staining B)Fluorescence is seen in the FITC CHANNEL C)Optical channel D)Overlay of channels A, B, and C..... 170

Figure 7.28. NBD-link-c-(PPg)LLFVY in fixed EMT6 cells using confocal microscopy. Side A is the hypoxic (1% O<sub>2</sub> and 5% CO<sub>2</sub>) slide with compound 33. Slide B is the normoxic slide with compound 33. A) IntDensity = 1622303.364 B) IntDensity = 1355969.154. .... 171

Figure 7.29. NBD-link-c-(PPg)LLFVY in fixed EMT6 cells using confocal microscopy. Side A is the hypoxic (CoCl<sub>2</sub>) slide with compound 33. Slide B is the normoxic slide with compound 33. A) Int Density = 8877025.981 B) IntDen = 8538546.676..... 172

Figure 7.30. NBD-link-c-(PPg)LLFVY in fixed MDA-MB-231 cells using confocal microscopy. Row A is the MDA-MB-231 GFP cells, Row B is the MDA-MB-231 18949 cells and Row C is the MDA-MB-231 18955 cell line. Column 1 is DAPI staining, Column 2 is the NBD-link-c-(PPg)LLFVY peptide, column 3 is the transmission image, and column 4 is the overlay of all other columns..... 173

Figure 7.31. pAb anti-HA tag in fixed MDA-MB-231 cells using confocal microscopy. Row A is the MDA-MB-231 GFP cells, Row B is the MDA-MB-231 18949 cells and Row C is the MDA-MB-231 18955 cell line. Column 1 is DAPI staining, Column 2 is the HA-tag, column 3 is the transmission image, and column 4 is the overlay of all other columns. .... 174

Figure 8.1. A)[<sup>18</sup>F]FAZA uptake in MDA-MB-231 18955 tumor model in NIH-III mice (n=2), showing both tumor and muscle uptake time activity curves. B) [<sup>18</sup>F]FAZA uptake in MDA-MB-231 tumor model in NIH-III mice (n=4), showing both tumor and muscle uptake time activity curves. .... 176

Figure 8.2. [ <sup>18</sup> F]FPeP4 uptake in MDA-MB-231 18955 tumor model and MCF7 tumor model in NIH-III mice, showing maximum intensity projection (MIP) at 5, 60 and 120 minutes post-injection.....	177
Figure 8.3. [ <sup>18</sup> F]FPeP4 time activity curves in MDA-MB-231 18955 tumor model in NIH-III mice, showing standardized uptake values from radiotracer injection to 120 minutes post injection.....	178
Figure 8.4. [ <sup>18</sup> F]FPeP4 uptake in non-tumor bearing NIH-III mice, showing maximum intensity projection (MIP) at 5 and 60 minutes, for two different formulations of [ <sup>18</sup> F]FPeP4.....	179
Figure 8.5. [ <sup>18</sup> F]FPeP4 time activity curves in non-tumor bearing NIH-III mice, showing standardized uptake values from radiotracer injection to 120 minutes post-injection.....	180
Figure 8.6. [ <sup>18</sup> F]SFB-link-c-(Ppg)LLFVY uptake in MCF7 tumor model in NIH-III mice, showing maximum intensity projection (MIP) at 5, 60 and 120 minutes post-injection.....	181
Figure 8.7. [ <sup>18</sup> F]FPeP4 and [ <sup>18</sup> F]SFB-link-c-(Ppg)LLFVY time activity curves in MCF-7 and MDA-MB-231 18955 tumor-bearing NIH-III mice, showing standardized uptake values from radiotracer injection to 120 minutes post-injection. ....	182
Figure 8.8. [ <sup>18</sup> F]FPeP4 metabolic stability in non-tumor bearing female BALB/c mice (n=1).	183
Figure 9.1. Lead compounds from the literature that inhibit interactions with HIF-1 $\alpha$ directly. a) ER-400583-00 and b) Cyclo-CLLFVY .....	185
Figure 9.2. A) Molecular docking of compound <b>9</b> in HIF-1 $\alpha$ . Predicted binding mode of compound ( <b>9</b> ) in HIF-1 $\alpha$ ( $E_{\text{Intermolecular}} = -11.94$ kcal/mol) and dotted oval highlights key residues of the binding pocket. B) Molecular docking of SFB-link-c-(Ppg)LLFVY <b>3</b> in HIF-1 $\alpha$ . Predicted binding mode of [ <sup>19</sup> F]SFB-link-c-(Ppg)LLFVY <b>28</b> in HIF-1 $\alpha$ ( $E_{\text{Intermolecular}} = -10.11$ kcal/mol). .....	187
Figure 9.3. Radiosynthesis pathway for the synthesis of [ <sup>18</sup> F]FMISO.....	187

Figure 9.4. Radiosynthesis pathway for the synthesis of [ <sup>18</sup> F]FAZA.....	188
Figure 9.5. Radiosynthesis pathway for the synthesis of [ <sup>18</sup> F]FBNA.....	188
Figure 9.6. Radiosynthesis of [ <sup>18</sup> F]SFB-link-c-(Ppg)LLFVY using prosthetic group [ <sup>18</sup> F]SFB.....	189
Figure 9.7. Synthesis of [ <sup>18</sup> F]FPeP4 using cross-coupling with [ <sup>18</sup> F]FPA. [ <sup>18</sup> F]FPA is synthesized in reactor 1 of the ASU, with cross-coupling occurring in reactor 2.....	189
Figure 9.8. Cell uptake of [ <sup>18</sup> F]FBNA, [ <sup>18</sup> F]FMISO, and [ <sup>18</sup> F]FAZA in MDA-MB-231 cells at 180 minutes, under both normoxic and hypoxic (1% O <sub>2</sub> , 5% CO <sub>2</sub> ) conditions.....	190
Figure 9.9. Standard radiotracer uptake in HIF-1a transfected MDA-MB-231 cell lines. A) [ <sup>18</sup> F]FDG (n=3), B) [ <sup>18</sup> F]FLT (n=3), C) [ <sup>18</sup> F]FAZA (n=2). .....	191
Figure 9.10. Internalized cell uptake in HIF-1a transfected cells. A) [ <sup>18</sup> F]SFB-link-c-(Ppg)LLFVY at 90 min (n=4). B) [ <sup>18</sup> F]FPeP4 at 60 minutes (n=3). .....	191
Figure 9.11. Internalized cell uptake in HIF-1a silenced cells. A) [ <sup>18</sup> F]SFB-link-c-(Ppg)LLFVY at 120 min (n=9/3). B) [ <sup>18</sup> F]FPeP4 at 120 minutes (n=9/3).....	192
Figure 9.12. In vivo metabolic stability of [ <sup>18</sup> F]FPeP4, [ <sup>18</sup> F]FBNA, [ <sup>18</sup> F]FAZA, and [ <sup>18</sup> F]FMISO in normal female BALB/C mice. ....	193
Figure 9.13. Blood component distribution of [ <sup>18</sup> F]FPeP4, [ <sup>18</sup> F]FBNA, [ <sup>18</sup> F]FAZA, and [ <sup>18</sup> F]FMISO in normal female BALB/C mice. ....	194
Figure 9.14. Time activity curves for the uptake of hypoxia imaging agents in MDA-MB-231 and MCF-7 tumor-bearing NIH-III mice. A) [ <sup>18</sup> F]FMISO, B) [ <sup>18</sup> F]FAZA, C) [ <sup>18</sup> F]FPeP4, D) [ <sup>18</sup> F]SFB-link-c-(Ppg)LLFVY, E) [ <sup>18</sup> F]FBNA.....	195

## **List of Symbols**

Angstrom	Å
Becquerels	Bq
Calories	cal
counts per minute	cpm
counts per sec	cps
Degree	°
Degree celcius	°C
Fentomolar	fM
Fentomoles	fmol
Gigabequerels	GBq
Hertz	Hz
Hours	hrs
Kilobequerels	kBq
Kilocalories	kcal
Kilodalton	kDa
Kiloelectron volt	keV
Liter	L
Megabequerels	MBq
Megahertz	MHz
Microliter	μL
Micromolar	μM

Micromoles	$\mu\text{mol}$
Milliamperes	mA
Milligram	mg
Milliliter	mL
Millimeter	mm
Millimeters of mercury	mmHg
Millimolar	mM
Millimoles	mmol
Minutes	min
Molar	M
Moles	mol
Nanomolar	nM
Nanomoles	nmol
Percent	%
Picomolar	pM
Picomoles	pmol
Thousand	k
Volts	V

## Glossary of Terms

[ <sup>62</sup> Cu]Copper-diacetyl-bis(N4-methylthiosemi-carbazone)	[ <sup>62</sup> Cu]ATSM
(( <sup>2</sup> H <sub>3</sub> )Methanesulfinyl)( <sup>2</sup> H <sub>3</sub> )methane	DMSO-d <sub>6</sub>
[ <sup>18</sup> F]fluoroazomycin arabinoside	[ <sup>18</sup> F]FAZA
[ <sup>18</sup> F]fluoromisonidazole	[ <sup>18</sup> F]FMISO
[ <sup>18</sup> F]sodium fluoride	[ <sup>18</sup> F]NaF
[ <sup>64</sup> Cu]Copper-diacetyl-bis(N4-methylthiosemi-carbazone)	[ <sup>64</sup> Cu]ATSM
1-((4-[ <sup>18</sup> F]fluorophenyl)ethynyl)-2,4-dimethoxybenzene	[ <sup>18</sup> F]FPedMO
1-(2,2-dihydroxymethyl-3-[ <sup>18</sup> F]fluoropropyl)-2-nitroimidazole	[ <sup>18</sup> F]DiFA
1-(2-[ <sup>18</sup> F]fluoro-1[hydroxymethyl]ethoxy)methyl-2-nitroimidazole	[ <sup>18</sup> F]FRP170
1,1'-bis(diphenylphosphino)ferrocene	dppf
16α-[ <sup>18</sup> F]-fluoro-17β-estradiol	[ <sup>18</sup> F]FES
1H-imidazole-1-propanol	NITTP
2-(2-nitro-1H-imidazol-1-yl)-N-(2,2,3,3,3-pentafluoropropyl)-acetamide	[ <sup>18</sup> F]EF5
2,2',2''-(1,4,7-triazacyclononane-1,4,7-triyl)triacetic acid	NOTA
2,2',2'',2'''-(1,4,7,10-Tetraazacyclododecane-1,4,7,10-tetrayl)tetraacetic acid	DOTA
2-deoxy-2-[ <sup>18</sup> F]fluoro-D-glucose	[ <sup>18</sup> F]FDG

3,3',3''-Phosphanetriyltris(benzenesulfonic acid) trisodium salt	tppts
3'-deoxy-3'-[ <sup>18</sup> F]-fluorothymidine	[ <sup>18</sup> F]FLT
4,7,13,16,21,24-Hexaoxa-1,10-diazabicyclo[8.8.8]hexacosane	K.2.2.2.
4-[ <sup>18</sup> F]fluorobenzonitrile	[ <sup>18</sup> F]FBN
4-[ <sup>18</sup> F]fluorobenzylamine	[ <sup>18</sup> F]FBAmine
4-[ <sup>18</sup> F]fluoroiodobenzene	[ <sup>18</sup> F]FIB
4-[ <sup>18</sup> F]fluorophenylacetylene	[ <sup>18</sup> F]FPA
4-[ <sup>18</sup> F]fluorophenylacetylene	[ <sup>18</sup> F]FPA
4',6-diamidino-2-phenylindole	DAPI
4-fluoroiodobenzene	FIB
4-fluorophenylacetylene	FPA
5'-GCCCTACGTGCTGTCTCA-3'	W18
6-[ <sup>18</sup> F]Fluoro-L-3,4-dihydroxyphenylalanine	[ <sup>18</sup> F]FDPOA
6-deoxy-6-[ <sup>18</sup> F]fluoro-D-fructose	[ <sup>18</sup> F]FDF
Acetonitrile	CH <sub>3</sub> CN
Acetyl-coenzyme A	acetyl-CoA
Adenosine triphosphate	ATP

Aldolase A	ALDA
Alpha	$\alpha$
Amino Acid	AA
Ammonia	NH <sub>3</sub>
Ammonium acetate	NH <sub>4</sub> OAc
Amyloid beta protein	Ab
Applied radioactivity per mg protein	AR/mgP
Arginine	Arg
Arginine-glycine-aspartic acid	RDG
Aryl hydrocarbon receptor nuclear translocator protein	ARNT
Aryl hydrocarbon receptor protein	AHR
Asparagine	Asn
ASU purification cartridge side 1	C18#1
ASU purification cartridge side 2	C18#2
Automated synthesis unit	ASU
Basic helix-loop-helix family, member e41	SHARP1
Basic-helix-loop-helix protein	bHLH

B-cell lymphoma 2	BCL2
BCL2/adenovirus E1B 19-kDa protein-interacting protein 3	BNIP3
Beta	$\beta$
Beta particle	b
Bicinchoninic acid	BCA
binding pocket three	P3
Bioluminescence	BLI
Bis(dibenzylideneacetone)palladium(0)	$\text{Pd}(\text{dba})_2$
Bis(triphenylphosphine)palladium(II) dichloride	$\text{PdCl}_2(\text{PPh}_3)_2$
Bovine serum albumin	BSA
Breast cancer type 1 susceptibility protein	BRCA1
Calcium chloride dihydrate	$\text{CaCl}_2 \cdot 2\text{H}_2\text{O}$
Calcium tungstate	$\text{CaWO}_4$
Calcium-44	$^{44}\text{Ca}$
Calculated	calcd
Canadian council on animal care	CCAC
Carbon dioxide	$\text{CO}_2$

Carbon monoxide	CO
Carbon nuclear magnetic resonance	<sup>13</sup> C-NMR
Carbon-11	<sup>11</sup> C
Carbon-12	<sup>12</sup> C
Carbonic anhydrase IX	CAIX
Cardiac implantable electronic device	CIED
Cell division control protein 53 homolog	Cdc53
Chemical shift	δ
Chinese hamster ovary	CHO
Chromosome 14 position 21	14q21
Chromosome 14 position 24	14q24
Cobalt chloride	CoCl <sub>2</sub>
Confocal microscopy	CM
Copper (I) iodide	CuI
Copper(II) acetate	Cu(OAc) <sub>2</sub>
Copper-64	<sup>64</sup> Cu
Coronary artery disease	CAD

Counts per minute	cpm
Coupling constant	J
Cross cancer institute	CCI
Cullin-2	Cul2
Cyclin-dependent kinase inhibitor 1	p21
Cyclized	<i>c</i>
Cysteine	C
Cytochrome c oxidase subunit 4 isoform 1	COX4-1
Cytochrome c oxidase subunit 4 isoform 2	COX4-2
Decay corrected yield	dcy
Deferoxamine	DFO
Deoxyribonucleic acid	DNA
Deuteron	d
Dichloromethane	CH <sub>2</sub> Cl <sub>2</sub>
Dimethyl sulfoxide	DMSO
Dissociation constant	K <sub>D</sub>
DL-Dithiothreitol	DTT

Doublet	d
Doublet of doublets	dd
Doublet of triplets	dt
Drosophila protein	Per
Dulbeccos's phosphate-buffered saline with 0.05% Tween-20	DPBS-T
Electron	b <sup>-</sup>
electrophoretic mobility shift assay	EMSA
Electrospray ionization	ESI
Energy for the intermolecular interaction in silico	$E_{intermolecular}$
Enolase 1	ENO1
Enzyme-linked immunosorbent assay	ELISA
Epithelial-mesenchymal transition	EMT
Erythropoietin	EPO
Estrogen receptor	ER
Ethanol	EtOH
Ethyl acetate	EtOAc
Ethyl cyanoglyoxylate-2-oxime	Oxyma

Ethylenediaminetetraacetic acid	EDTA
Fetal bovine serum	FBS
Fifty nucleotide	50-nt
Fluorescence molecular tomography	FMT
Fluorescence imaging	FLI
Fluorine-18	<sup>18</sup> F
forkhead box 3A	Fox03A
Gallium-68	<sup>68</sup> Ga
Gamma	g
Gene of tumor protein P53	TP53
Genetecin	G418
Glucose transporter 1	Glut 1
Glucose transporter 5	Glut 5
Glutathione S-transferase	GST
Half maximal inhibitory concentration	IC50
Helix-loop-helix protein	HLH
Heme oxygenase-1	HO-1

Henrietta Lacks	HeLa
Hexane	Hex
High-performance liquid chromatography	HPLC
Histone acetyltransferase p300	p300 HAT
Human embryonic kidney	HEK
Human epidermal growth factor receptor 2	HER2
Human immunodeficiency virus	HIV
Human serum albumin	HAS
Hydrochloric acid	HCl
Hydrogen peroxide	H <sub>2</sub> O <sub>2</sub>
Hypoxia induced factors	HIFs
Hypoxia inducible factor 1	HIF-1
Hypoxia inducible factor 1 alpha	HIF-1 $\alpha$
Hypoxia inducible factor 1 beta	HIF-1 $\beta$
Hypoxia inducible factor 2	HIF-2
Hypoxia inducible factor 2 alpha	HIF-2 $\alpha$
Hypoxia inducible factor 3 alpha	HIF-3 $\alpha$

Hypoxia-inducible enhancer binding site 1	HIE-BS1
Infective Endocarditis	IE
Inhibitory domain	ID
Inositol polyphosphate-4-phosphatase	INPP4B
Iodine-131	<sup>131</sup> I
Lacking thymidine kinase	Ltk
Lactate dehydrogenase	LDH
Lactate dehydrogenase A	LDHA
Langerhans cell histiocytosis	LCH
Leucine	L
Locked nucleic acid	LNA
Log of partition coefficient	LogD
Low-resolution mass spectrometry	LR-MS
Magnesium chloride	MgCl <sub>2</sub>
Magnesium sulphate	MgSO <sub>4</sub>
Mass	M
Mass to charge ratio	m/z

Matrix-assisted laser desorption/ionization	MALDI
Maximum a posteriori	MAP
<i>MAX</i> -interacting protein	MXI-1
Messenger ribonucleic acid	mRNA
Methanol	MeOH
MicroRNA	miRNA
Microscale thermophoresis	MST
Minutes	min
Molecular imaging	MI
Molybdenum-100	<sup>100</sup> Mo
Multiplet	m
<i>Myelocytomatosis</i>	<i>Myc</i>
N-(3-dimethylaminopropyl)-N-ethylcarbodiimide hydrochloride	EDC
N-(4-(1-ethynyl-4-[ <sup>18</sup> F]fluorophenyl)phenyl)-4-((4-(pyridine-3-ylmethyl)piperazin-1-yl)methyl)benzamide	[ <sup>18</sup> F]FPeP4
<i>N</i> -(4-[ <sup>18</sup> F]fluorobenzyl)-2-(2-nitro-1 <i>H</i> -imidazol-1-yl)-acetamide	[ <sup>18</sup> F]FBNA
N,N-diisopropylethylamine	DIPEA
N,N-dimethylformamide	DMF

N,N-dimethylpyridin-4-amine	DMAP
Natural killer cells	NK
Natural killer T cells	NKT
Neutron	n
Nickel coated	Ni-coated
Nickel-64	$^{64}\text{Ni}$
Nitrogen-13	$^{13}\text{N}$
Nitrogen-14	$^{14}\text{N}$
No carrier added	n.c.a.
<i>N</i> -succinimidyl-4- $^{18}\text{F}$ fluorobenzoate	$^{18}\text{F}$ SFB
<i>N</i> -succinimidyl-4- $^{19}\text{F}$ fluorobenzoate	$^{19}\text{F}$ SFB
Nuclear magnetic resonance	NMR
Oxygen	$\text{O}_2$
Oxygen dependent destruction domain	ODDD
Oxygen-15	$^{15}\text{O}$
Oxygen-18	$^{18}\text{O}$
Palladium (II) acetate	$\text{Pd}(\text{OAc})_2$

Palladium (II) nitrate	Pd(NO <sub>3</sub> ) <sub>2</sub>
Partial pressure of oxygen	pO <sub>2</sub>
Partition coefficient	D
Passage number 17	p17
Penicillin-streptomycin	PS
Per-ARNT-AHR-Sim domains	PAS
Peroxisome proliferator-activated receptor $\gamma$ coactivator 1 $\beta$	PGC-1 $\beta$
Phenylalanine	F
Phosphatase and tensin homolog	PTEN
Phosphate buffered saline	PBS
Phosphatidylinositol-4,5-bisphosphate 3-kinase, catalytic subunit alpha	PIK3CA
Phosphofructokinase-liver type	PFKL
Phosphoglycerate kinase 1	PGK1
Phosphoinositide 3-kinases	PI(3)K
Pittsburgh Compound-B	PiB
Platelet-derived growth factor subunit B	PDGF-b,
Polyvinylidene fluoride	PVDF

Positron	b+
Positron emission tomography	PET
Positron emission transaxial tomography	PETT
Positron emitting	PE
Positron emitting radiopharmaceuticals	PERs
Potassium carbonate	$K_2CO_3$
Potassium chloride	KCl
Potassium dihydrogen phosphate	$KH_2PO_4$
Potential of hydrogen	pH
Progesterone receptor	PgR
Propargylglycine	Ppg
Proton	p
Proton nuclear magnetic resonance	$^1H$ -NMR
pVHL-ElonginB-ElonginC	VBC
pVHL-ElonginC-ElonginB-Cul2-Rbx1	VCBCR
Pyruvate dehydrogenase kinase 1	PK1
Pyruvate kinase-muscle type	PKM

Quality Control	QC
Quaternary ammonium anion	QMA
Radioimmunoprecipitation assay	RIPA
Rat sarcoma virus	Ras
Reactor 1	R1
Reactor 2	R2
Regions of interest	ROI
Retention factor	Rf
Retention time	$t_R$
Retinoblastoma protein 1	RB1
Ribonucleic acid	RNA
RING-Box protein 1	Rbx1
Rotations per minute	rpm
Saturated	sat.
Scandium-44g	$^{44g}\text{Sc}$
Signal to noise ratio	S/N
Single photon emission computed tomography	SPECT

Single-minded protein	Sim
Singlet	s
Skp1-Cdc53- F-box protein	SCF
Small interfering RNA	siRNA
Sodium	Na
Sodium acetate	NaOAc
Sodium bicarbonate	NaHCO <sub>3</sub>
Sodium chloride	NaCl
Sodium dodecyl sulfate	SDS
Sodium hydroxide	NaOH
Sodium Iodide	NaI
Sodium sulfate	Na <sub>2</sub> SO <sub>4</sub>
Solid-phase peptide synthesis	SPPS
S-phase kinase-associated protein 1	Skp1
Standardized uptake value	SUV
Standardized uptake value at 180 minutes	SUV <sub>180min</sub>
Standardized uptake value at 5 minutes	SUV <sub>5min</sub>

Standardized uptake value maximum	$SUV_{\max}$
Technetium-99m	$^{99m}\text{Tc}$
Tellurium-130	$^{130}\text{Te}$
Tellurium-131	$^{131}\text{Te}$
Tetrahydrofuran	THF
Tetrakis(triphenylphosphine)palladium(0)	$\text{Pd}(\text{PPh}_3)_4$
thin-layer chromatography	TLC
Three-dimensional image	3D-image
Time-activity curves	TACs
Transactivation domain	TAD-N
Tricarboxylic acid	TCA
Trideuteroacetonitrile	$\text{CD}_3\text{CN}$
Triethylamine	TEA
Trifluoroacetic acid	TFA
Triphenylphosphine	$\text{PPh}_3$
Triple negative breast cancer	TNBC
Triplet	t

Triplet of doublets	td
Triplet of triplets	tt
Tris buffered saline with Tween-20	TBS-T
Tris hydrochloride	Tris-HCl
Tris-buffered saline	TBS
Tumor protein P53	p53
Tumor to muscle ratio	TMR
Tumor-associated macrophages	TAMs
Two times	2X
Tyrosine	Y
Ubiquitin ligase	E3-ligase
Valine	V
Vascular endothelial growth factor	VEGF
Vial 1	V1
Vial 10	V10
Vial 11	V11
Vial 12	V12

Vial 2	V2
Vial 3	V3
Vial 4	V4
Vial 5	V5
Vial 6	V6
Von hippel–lindau tumor suppressor	pVHL
Water	H <sub>2</sub> O
Western blot	WB
X-box binding protein 1	XBP1
Yittrium-89	<sup>89</sup> Y
Zinc-68	<sup>68</sup> Zn
Zirconium-89	<sup>89</sup> Zr

## **Chapter 1: Introduction**

### *1.1 Molecular imaging*

Molecular imaging is defined as a non-invasive assessment technique of a biological process at the cellular and molecular level in real-time [3]. Modern molecular imaging often employs a combination of molecular imaging probes with sophisticated instrumentation, using advanced analytical systems [4]. Various imaging modalities that are included in molecular imaging are summarized in *Table 1.1*. [4].

*Table 1.1. Summary of molecular imaging modalities, including SPECT (single photon emission computed tomography), PET (positron emission tomography), BLI (bioluminescence), FLI (fluorescence imaging), FMT (fluorescence molecular tomography), and Photoacoustic imaging. Including sensitivity, spatial resolution, and imaging depth for all modalities. \*Spatial resolution is strongly depth-dependent.*

Imaging Modality	Detection source	Sensitivity	Spatial resolution	Imaging depth
SPECT				
Clinical	Single gamma ray	nM-pM	10-15 mm	Unrestricted
Pre-clinical	Single gamma ray	nM-pM	0.5 mm	Unrestricted
PET				
Clinical	Coincidence gamma rays	pM	5-10 mm	Unrestricted
Pre-clinical	Coincidence gamma rays	pM	1 mm	Unrestricted
BLI	Light (luciferin/luciferase)	fM	0.1-2 mm*	Few mm
FLI	Fluorescence	pM	0.1-2 mm*	Few mm
FMT	Fluorescence	pM	1 mm	1-2 cm
Photoacoustic	Ultrasound waves	pM	0.01-1 mm*	Several cm

Although modern molecular imaging uses advanced technology, the birth of molecular imaging comes from a much more simplistic nature. Molecular imaging can trace its roots to the field of nuclear medicine.

Nuclear medicine uses radioactive elements, and traces the position of these radioactive elements in a living organism, by analyzing their emissions. In the field of nuclear medicine these special radioactive elements are often called radiotracers. Where a radiotracer consists of the combination of a radioactive isotope plus a targeting compound.

The advent of nuclear medicine began back in 1923, when George de Hevesy measured the uptake of lead isotopes in plants using an electroscope [5]. Next in 1934, Irene Curie and Fredrick Joliot discovered that using an alpha particle emitted from polonium, they could alter the three elements of aluminum, boron, and magnesium, such that the products as well continued to be sources of radiation [6]. This led to the discovery by researchers at the University of California Berkeley that they could use their cyclotron developed by Ernest O. Lawrence between 1930 and 1936, for the transmutation of elements [7]. From the cyclotron, the most important radioisotopes that were first synthesized were carbon-11 ( $^{11}\text{C}$ ) [7, 8], nitrogen-13 ( $^{13}\text{N}$ ) [8], oxygen-15 ( $^{15}\text{O}$ ) [9] and fluorine-18 ( $^{18}\text{F}$ ) [10].

After the discovery of these important positron-emitting (PE) radioisotopes, one of the first reported use of positron-emitting radiopharmaceuticals (PERs) was in 1945, where [ $^{11}\text{C}$ ]CO was inhaled by patients with oxygen and the exhaled [ $^{11}\text{C}$ ]CO<sub>2</sub> was measured [11]. Yet, due to the short half-lives of PET radioisotopes, the world began to focus on the use of radioisotopes with longer half-lives. One such isotope which was first synthesized by the Berkeley cyclotron was iodine-131 ( $^{131}\text{I}$ ) [12]. Although the first synthesized  $^{131}\text{I}$  was completed on a cyclotron, it also caused a lot of iodine by-products. Thus, it was not until the beginning of nuclear reactor fission with the Manhattan Project at Oak Ridge, Tennessee, that pure- $^{131}\text{I}$  was synthesized.

After the first radioisotopes were synthesized, next began the evolution of imaging technology. Starting in the late 1940s doctors used handheld Geiger meters to measure the biodistribution of  $^{131}\text{I}$  in living subjects without the production of a corresponding image. They would simply analyze the counts of radioactivity and varying distance to determine the biodistribution of  $^{131}\text{I}$  in the

thyroid of human patients [13]. After this, the first instrument to image organs was developed in 1950, called the rectilinear scanner by Benedict Cassen [14]. This instrument contained a calcium tungstate ( $\text{CaWO}_4$ ) crystal as the radiation detector element and was capable of printing the collected data on photographic film. This instrument was also used to image the thyroid of patients with  $^{131}\text{I}$  [14]. This was further modified over time to use a gamma camera containing a sodium iodide ( $\text{NaI}$ ) crystal. This is also known as the modern gamma camera or Anger camera [15].

*Table 1.2. Common radioisotopes used in PET and SPECT imaging. Including the radioisotope half life, decay pathway, percentage of main decay pathway, maximum strength of emission and typical route of production [16].*

Radionuclide	Half-Life	Decay Path	Percent of decay	Maximum strength of emission	Mode of production
Carbon-11	20.4 min	$\beta^+$	99.750%	960.5 keV	$^{14}\text{N}(p,\alpha)^{11}\text{C}$
Copper-64	12.7 hrs	$\beta^+$	17.52%	653.1 keV	$^{64}\text{Ni}(p,n)^{64}\text{Cu}$
Fluorine-18	109.73 min	$\beta^+$	96.86%	633.9 keV	$^{18}\text{O}(p,n)^{18}\text{F}$
Gallium-68	67.83 min	$\beta^+$	87.68%	1899.1 keV	$^{68}\text{Zn}(p,n)^{68}\text{Ga}$
Iodine-131	8.02 days	$\beta^-$	89.4%	606.3 keV	$^{130}\text{Te}(n,\gamma)^{131}\text{Te} \rightarrow ^{131}\text{I}$
Nitrogen-13	9.97 min	$\beta^+$	99.8%	1198.45 keV	$^{12}\text{C}(d,n)^{13}\text{N}$
Oxygen-15	2.04 min	$\beta^+$	99.885%	1735 keV	$^{14}\text{N}(d,n)^{15}\text{O}$
Scandium-44g	3.97 hrs	$\beta^+$	94.27%	1474.3 keV	$^{44}\text{Ca}(p,n)^{44g}\text{Sc}$
Technetium-99m	6.00 hrs	$\gamma$	88.5%	140.511 keV	$^{100}\text{Mo}(p,2n)^{99m}\text{Tc}$
Zirconium-89	78.42 hrs	$\beta^+$	22.8%	902 keV	$^{89}\text{Y}(p,n)^{89}\text{Zr}$

Finally, with the culmination of the gamma camera and advanced computer systems including a rotating detection system, the single photon emission computed tomography (SPECT) system was born in 1976 by John Keyes. This first system was named the Humongotron [17]. SPECT can detect gamma ray-emitting radioisotopes that emit a single photon of energy, providing a 3D image of the radioactive biodistribution using advanced computer technology [18].

Moving from SPECT to positron emission tomography (PET), a system was also developed to detect PE radioisotopes using a positron camera with the coincidence detection of gamma rays. This system developed by Anger and Gottschalk contained no scanning motion [19]. Again, leading to the first PETT I/II devices, which detected coincidence annihilation events on a NaI scintillation camera with a computer-controlled turntable [20-22].

Since, the development of the PET imaging system, the use of PET radiotracers has significantly expanded. *Table 1.2.* provides an overview of various important radioisotopes used in PET and SPECT imaging [16]. Focusing solely on PET, a radiolabelled molecular probe of interest is first synthesized using radiochemistry techniques. This radiotracer is often designed to interact with a biological process of interest and is either trapped in a cell or binds to a protein/transporter. Once the radiotracer is allowed to interact with a living organism, the biodistribution of the radioactivity is measured using a PET system. A positron-emitting isotope will decay via positron emission, releasing a positron, that annihilates immediately in the surrounding tissues with an electron. This annihilation event creates two 511 keV gamma rays that are ejected 180° from each other. These gamma rays are then detected on a coincidence scintillation detector, that records an event only when two gamma rays are detected simultaneously. After numerous detection events are recorded, an advanced computer system generates a 3D image of the biodistribution of radioactivity. Since all PET radiotracers rely on the interaction with a given biological process or a biomarker within or on the cell surface, current research focuses heavily on developing novel radiotracers that image biomarkers [23].

Lastly, it should be noted that radiotracers must follow the radiotracer principle as discovered by George de Hevesy. This principle states that although radiotracers are a class of drugs, they must exert no biological effect on the system of interest, due to their extremely small mass amount.

Therefore, a radiotracer is truly only used to observe a system of interest due to the emitted positron radiation. This earned George de Hevesy the Nobel Prize in 1943.

### *1.2 Breast cancer and breast cancer imaging with positron emission tomography*

As determined by the Canadian Cancer Society [24], 2 in 5 Canadian will develop cancer over their lifetime with 26 % of all new female patients presenting with breast cancer. Additionally, breast cancer is the second leading cause of cancer-related deaths in Canadian females with a 13.8% mortality [24]. It should be noted that although breast cancer is predominately found in females, there are cases that have been reported in males.

Breast cancer is a heterogeneous disease with currently four distinct subtypes. These subtypes are comprised of *luminal-A*, *luminal-B*, *Erb-B2* overexpression and *basal-like* breast cancers [25]. Luminal cancers are divided into *luminal-A* that have the following characteristics of estrogen receptor (ER) positive, progesterone receptor (PgR) positive, human epidermal growth factor receptor 2 (HER2) negative, and low expression of proliferation genes. Whereas luminal-B breast cancers have the characteristics of ER-positive, PgR negative or low, HER2 negative or overexpressed, and high expression of proliferation genes [25]. Next, the *Erb-B2* overexpression subtype is ER-negative, PgR-negative, and HER2-positive. Lastly, *basal-like* breast cancers comprise approximately 25 % of all breast cancers and are ER-negative, PgR-negative, and HER2-negative, also being called the “triple negative” breast cancers (TNBC) [25].

TNBC is associated with poor clinical outcomes and some of the characteristics also include: high nuclear grade, high expression of proliferation markers and accumulation of p53, as well as basal-like cells undergoing the epithelial-mesenchymal transition (EMT) more rapidly, leading to increased metastatic and aggressive cancers [26].

Breast cancer imaging using PET has been achieved using many different radiotracers. The most commonly used radiotracer is [<sup>18</sup>F]FDG (see *Figure 1.1.*), which is transported into the cell via glucose transporters most notably the Glut-1 transporter in breast cancer [27]. Trying to utilize a different glucose transporter of Glut-5, 6-deoxy-6-[<sup>18</sup>F]fluoro-D-fructose ([<sup>18</sup>F]FDF) was developed by Wuest *et al.* [28]. Both of these radiotracers are used as indicators of tumor metabolism. Moving to another mechanism 3'-deoxy-3'-[<sup>18</sup>F]-fluorothymidine ([<sup>18</sup>F]FLT) is used

as a biomarker for proliferation in primary breast cancer [29]. Yet another small molecule that is used as a biomarker for estrogen receptors is 16 $\alpha$ -[<sup>18</sup>F]-fluoro-17 $\beta$ -estradiol ([<sup>18</sup>F]FES) [30].

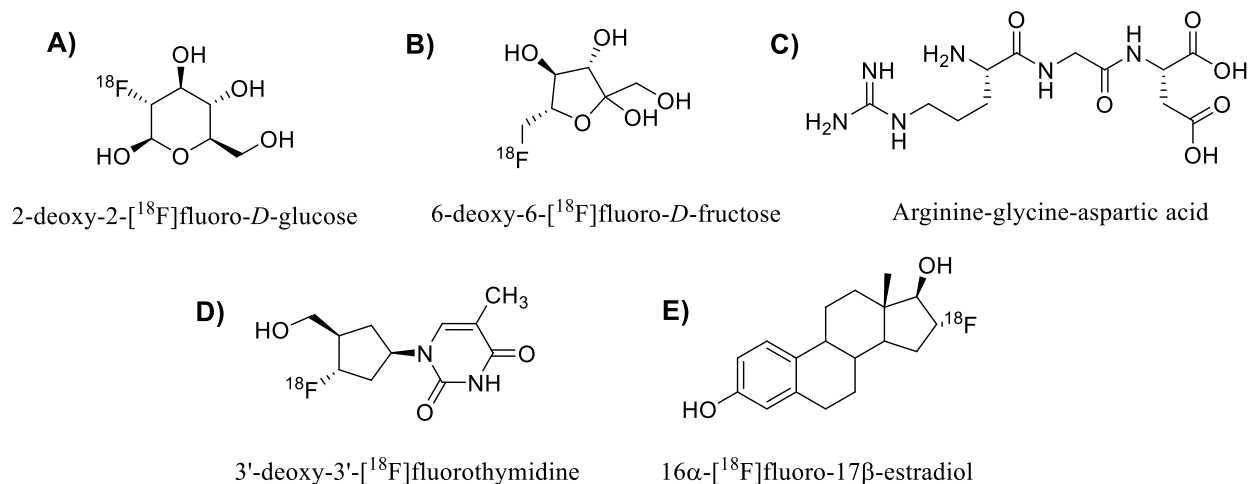


*Figure 1.1. Various radiotracers for the PET imaging of breast cancer. Including: A) [<sup>18</sup>F]FDG, B) [<sup>18</sup>F]FDF, C) [<sup>18</sup>F]RGD, D) [<sup>18</sup>F]FLT and E) [<sup>18</sup>F]FES.*

Breast cancer imaging using PET has been achieved using many different radiotracers. The most commonly used radiotracer is [<sup>18</sup>F]FDG (see *Figure 1.1.*), which is transported into the cell via glucose transporters most notably the Glut-1 transporter in breast cancer [27]. Trying to utilize a different glucose transporter of Glut-5, 6-deoxy-6-[<sup>18</sup>F]fluoro-*D*-fructose ([<sup>18</sup>F]FDF) was developed by Wuest *et al.* [28]. Both of these radiotracers are used as indicators of tumor metabolism. Moving to another mechanism 3'-deoxy-3'-[<sup>18</sup>F]-fluorothymidine ([<sup>18</sup>F]FLT) is used as a biomarker for proliferation in primary breast cancer [29]. Yet another small molecule that is used as a biomarker for estrogen receptors is 16 $\alpha$ -[<sup>18</sup>F]-fluoro-17 $\beta$ -estradiol ([<sup>18</sup>F]FES) [30].

Finally, moving from small molecules to biomolecules, peptides such as arginine-glycine-aspartic acid (RGD) peptide have been radiolabelled with <sup>68</sup>Ga and used for breast cancer imaging [31]. Increasing in molecular weight an affibody entitled [<sup>18</sup>F]GE-226, was used for the imaging of HER-2 [32]. Also, full-length Trastuzumab antibodies labelled with <sup>64</sup>Cu-DOTA have been used for imaging of breast cancer [33]. Lastly, [<sup>18</sup>F]sodium fluoride ([<sup>18</sup>F]NaF) can also be used to visualize bone metastases from primary breast cancer [34]. Currently approved for routine use by

the US Food and Drug Administration (FDA) are only three radiotracers for breast cancer. These include [ $^{18}\text{F}$ ]FDG, [ $^{18}\text{F}$ ]NaF, and [ $^{18}\text{F}$ ]FES.

All these radiotracers for the imaging of breast cancer target different facets of the hallmarks of cancer. Overall trying to exploit the overexpressed biomarkers present in cancer cells. In the development of novel radiotracers, it is important to understand these hallmarks of cancer and the tumor microenvironment.

### 1.3 Hallmarks of cancer

In 2000, Hanahan and Weinberg wrote one of the most influential publications entitled “The Hallmarks of Cancer” [35]. Here they highlight that there are six important hallmarks of cancer cells. This includes evading apoptosis, self-sufficiency in growth signals, insensitivity to anti-growth signals, sustained angiogenesis, limitless replicative potential, and tissue invasion & metastasis.

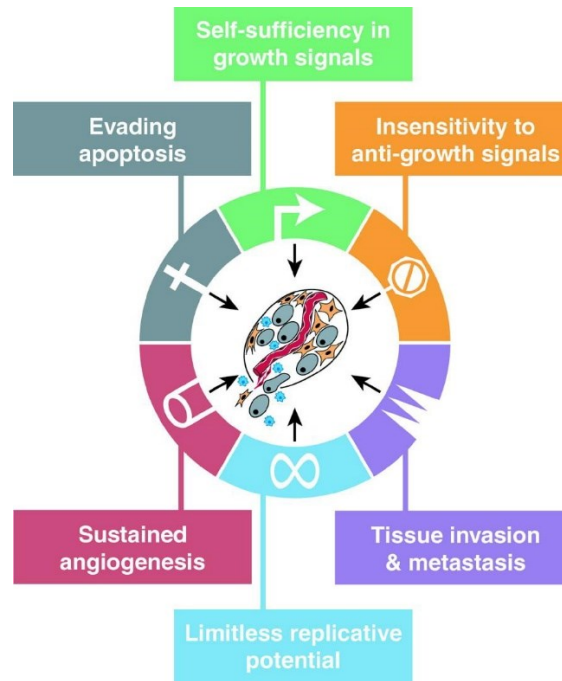


Figure 1.2. The original six hallmarks of cancer as presented by Hanahan and Weinberg[35].

*Figure 1.2.* shows their original publication figure with the six hallmarks of cancer [35]. These hallmarks emphasized that both cellular and environmental forces present in the tumor microenvironment help to shape tumor growth. Moving forward over the past eleven years Hanahan and Weinberg have expanded on their hallmarks to include four new emerging hallmarks of cancer [36]. These emerging hallmarks include deregulation of cellular energetics, avoiding immune detection, genomic instability and mutation, and tumor-promoting inflammation [36].

Exploiting some of the hallmarks of cancer, notable radiotracers that have been developed include [<sup>18</sup>F]FDG, which is a glucose-analog used to measure tumor cell metabolism and exploiting the deregulation of cellular energetics [37]. [<sup>18</sup>F]FLT has been used to measure tumor cell proliferation through limitless replicative potential [38]. [<sup>89</sup>Zr]Bevacizumab has been used to measure increased levels of vascular endothelial growth factor which is obtained through sustained angiogenesis [39]. Overall, by targeting various facets of the hallmarks of cancer, we can try to better image cancer using PET.

#### *1.4 Tumor microenvironment and hypoxia*

One very important point from the hallmarks of cancer is the importance of the tumor microenvironment on the growth and survival of tumor cells. The tumor microenvironment is a complex system of native cells as well as malignant cells.

This can include but is not exclusive to T-lymphocytes, B-lymphocytes, NK/NKT cells, tumor-associated macrophages (TAMs), myeloid-derived suppressor cells, dendritic cells, tumor-associated neutrophils, cancer-associated fibroblasts, adipocytes, vascular endothelial cells, pericytes and lymphatic endothelial cells, see *Figure 1.3.* [40].

The tumor microenvironment also includes areas of hypoxia, which are represented as beige areas in *Figure 1.3.* It is of note that these hypoxic cells are not only present in the interior of the tumor but can present on a leading edge as well [40]. A lower-than-normal oxygen concentration in tissues is termed hypoxia. To be specific, an oxygen (O<sub>2</sub>) concentration less than 2% O<sub>2</sub> is defined as hypoxic, with severe hypoxia (anoxia) being lower than 0.02% O<sub>2</sub> [41]. Adapting to the oxygen deprivation in cancer cells, hypoxia alters cellular energetics using several methods. Hypoxia can alter the following functions: glucose metabolism, mitochondrial respiration, glutamine

metabolism, and lipid metabolism. In most of these functions, the master regulators of these processes are often the hypoxia-induced factors (HIFs) [41]. There are two HIFs, HIF-1, and HIF-2 both of which contain an alpha ( $\alpha$ ) and a beta ( $\beta$ ) subunit. There also is a third  $\alpha$ -subunit in HIF-3 $\alpha$ , altogether the HIF-1 $\alpha$ , HIF-2 $\alpha$  and HIF-3 $\alpha$  subunits contain a high degree of sequence identity, as demonstrated by their ability to all bind the HIF-1 $\beta$  subunit [42].

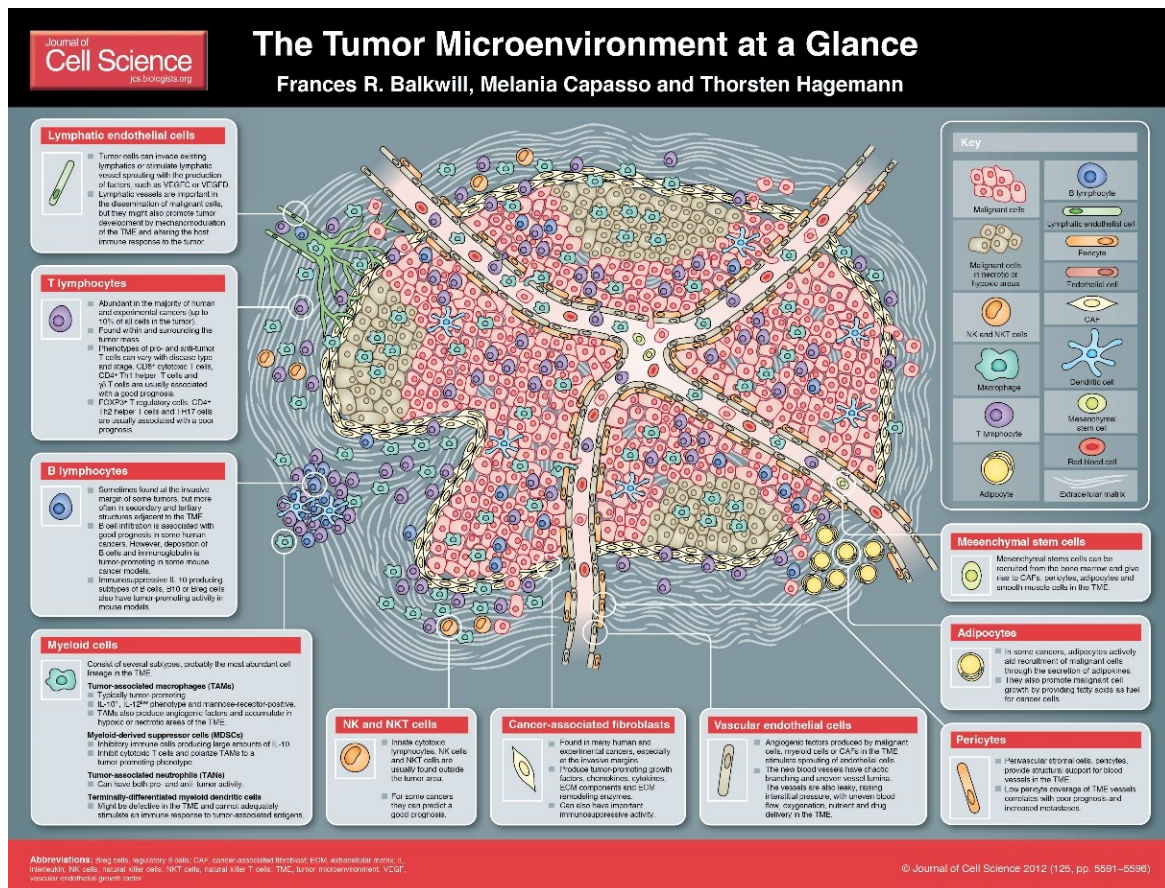


Figure 1.3. “The Tumor Microenvironment at a Glimpse” as presented by Balkwill et al. [40].

To understand the hypoxic areas of tumors, we must first look at the effect of the deregulation of cellular energetics on hypoxia. Firstly, the Warburg effect, which is a shift in the energy requirements of the cell from oxidative phosphorylation to glycolysis. In this change to glycolysis, the glucose-6-phosphate that is converted to pyruvate does not go through the energy-efficient oxidative phosphorylation cycles. Instead, pyruvate gets converted into lactate and exported from the cell [43]. Thus, only 2-4 ATP are obtained from the conversion of glucose-6-phosphate into

pyruvate instead of 36. Therefore, cancer cells have a higher requirement for glucose, due to the low efficiency in energy conversion. Overall, the use of glycolysis is linked to the shortage of oxygen (anaerobic conditions) in tumors [43]. Hypoxia in the tumor microenvironment can additionally be caused by rapid tumor growth causing improper tumor vasculature. Leading to a lack of proper oxygenation of the tumor tissue and thus hypoxic areas. These hypoxic areas of tumor tissue are often chemo-resistant and radio-resistant, often leading to poor prognosis [44]. This resistance shows that the tracking of hypoxic regions *in vivo* is of strong importance to provide the best treatment possible.

### 1.5 Molecular imaging of hypoxia

Molecular imaging of hypoxia using positron-emitting isotopes began with [<sup>18</sup>F]Fluoromisonidazole ([<sup>18</sup>F]FMISO) [2], which is a nitroimidazole-containing compound. In hypoxic environments, nitroreductase enzymes will process nitroaromatics to their amine equivalents, to trap the compound in the hypoxic environment [45]. It should be noted that this class of compounds was first developed as radiosensitizers [46] and their *in vivo* use was discontinued due to significant neurotoxicity [47]. Additionally, one very important nitroimidazole is pimonidazole. Pimonidazole is often used in histochemistry and correlates strongly to the level of hypoxia in the cells [48].

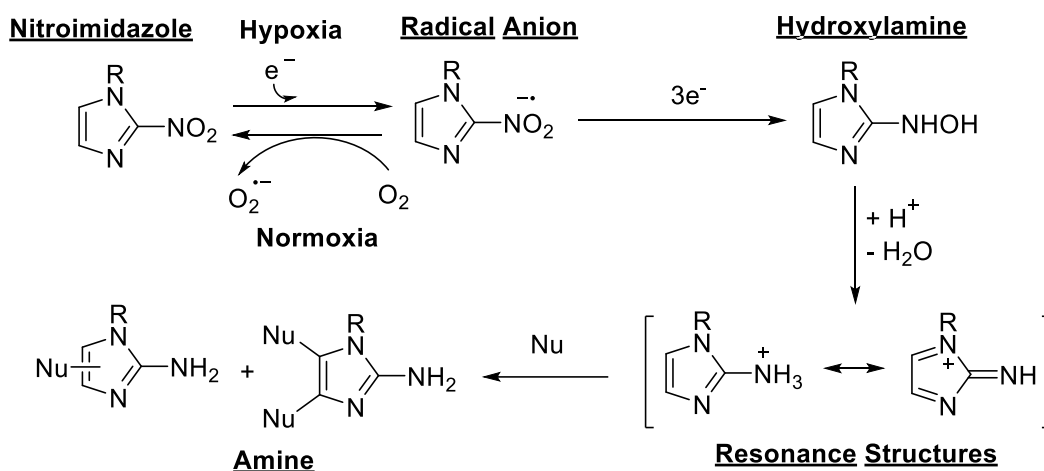


Figure 1.4. Mechanism of nitroimidazole metabolism in hypoxia using nitroreductase enzymes.

Throughout history many different nitroimidazole derivatives have also been created such as 2-(2-nitro-1H-imidazol-1-yl)-N-(2,2,3,3,3-pentafluoropropyl)-acetamide ( $[^{18}\text{F}]\text{EF5}$ ) [49],  $[^{18}\text{F}]\text{Fluor-oazomycin arabinoside}$  ( $[^{18}\text{F}]\text{FAZA}$ ) [1], 1-(2- $[^{18}\text{F}]\text{fluoro-1-[hydroxymethyl]-ethoxy)methyl-2-nitroimidazole}$  ( $[^{18}\text{F}]\text{FRP170}$ ) [50], and 1-(2,2-dihydroxymethyl-3- $[^{18}\text{F}]\text{fluoropropyl)-2-nitroimidazole}$  ( $[^{18}\text{F}]\text{DiFA}$ ) [51].

Although nitroimidazoles have previously been used to image hypoxia, they do have some shortcomings. Downsides of  $[^{18}\text{F}]\text{FMISO}$  and  $[^{18}\text{F}]\text{FAZA}$  include a low lipophilicity, slow tumor specific accumulation, slow clearance from normoxic tissue, and large digestive track clearance. Therefore other hypoxia imaging agents have been developed that were more lipophilic such as  $[^{64}\text{Cu}]\text{Copper-diacetyl-bis(N4-methylthiosemi-carbazone)}$  ( $[^{64}\text{Cu}]\text{ATSM}$ ) [52]. All of these compounds try to better image hypoxia by improving the pharmacokinetics profile of the radiotracer.

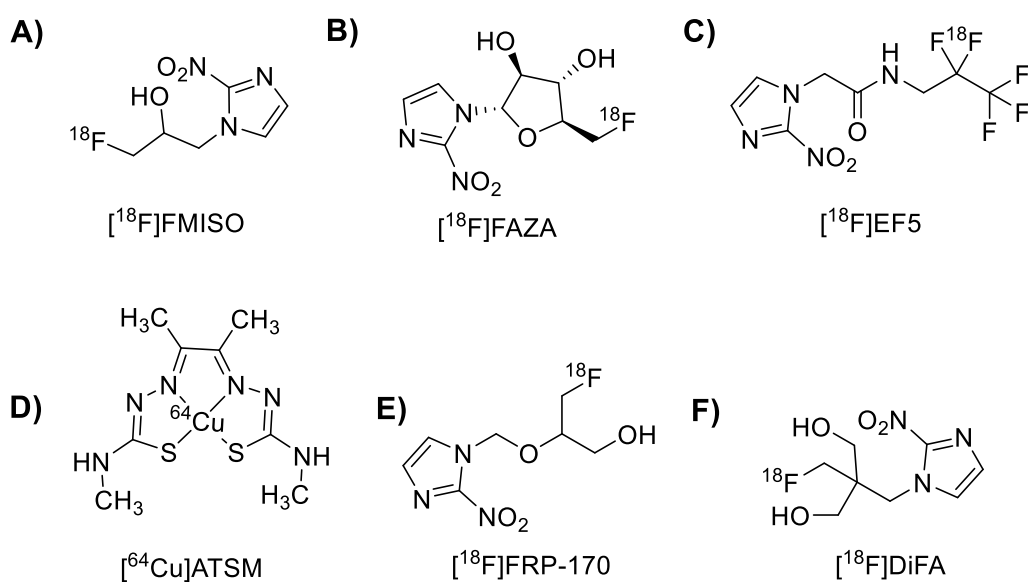


Figure 1.5. Previously developed PET imaging agents for the imaging of hypoxia.

Including: A)  $[^{18}\text{F}]\text{FMISO}$ , B)  $[^{18}\text{F}]\text{FAZA}$ , C)  $[^{18}\text{F}]\text{EF5}$ , D)  $[^{64}\text{Cu}]\text{ATSM}$ ,  $[^{18}\text{F}]\text{FRP-170}$ , and E)  $[^{18}\text{F}]\text{DiFA}$ .

Additionally, the correlation between  $[^{18}\text{F}]\text{FMISO}$ ,  $[^{64}\text{Cu}]\text{ATSM}$ , pimonidazole staining, partial pressure of oxygen ( $\text{pO}_2$ ), radiosensitivity and HIF-1 $\alpha$  expression was shown by Chia *et al.* [53]. Where they demonstrated that the cellular uptake of  $[^{18}\text{F}]\text{FMISO}$  and  $[^{64}\text{Cu}]\text{ATSM}$  happened

rapidly below 1 mmHg, pimonidazole staining was strong up to around 10 mmHg, cells became more radioresistant below 25 mmHg and HIF-1 $\alpha$  expression increased markedly below 50 mmHg [53]. Concluding that the increased expression of HIF-1 $\alpha$ , more closely relates to the level of pO<sub>2</sub> that correlates to radio-resistance. Thus, the expression level of HIF-1 $\alpha$  is a more direct measurement for hypoxia. Also it should be noted that the conversion between mmHg and %O<sub>2</sub> in tissues is dependent on the pH of the tissues[54], and cannot be converted in the context of this work.

### *1.6 Novel biomarkers for triple-negative breast cancer (TNBC)*

Recently, there has been significant effort to try and find biological markers (biomarkers) that could be used for the diagnosis and treatment of TNBC. Some recent hallmarks of TNBC that are emerging include XBP1 which was found to control the hypoxia-induced factor 1 alpha (HIF-1 $\alpha$ ) transcription pathway [55]. Also, SHARP1 was found to inhibit HIF-1 $\alpha$  by binding to HIF-1 $\alpha$  and promoting HIF-1 $\alpha$  proteasomal degradation [56].

TNBC has also been shown to have a high frequency of TP53 mutations, inferring mostly with loss of TP53 function [57]. Other gene expressions that are lost are RB1 and BRCA1, with another gene of PI(3)K being amplified. This PI(3)K activation can be due to loss of PTEN or INPP4B or amplification of PIK3CA [57]. Overall a couple of these genetic signatures are known to overlap with the function of HIF-mediated tumorigenesis, possibly emerging as an attractive molecular target for the imaging and treatment of TNBC [58].

### *1.7 Hypoxia-inducible factor 1 alpha (HIF-1 $\alpha$ )*

Highlighting the overall importance of cellular oxygenation, the 2019 Nobel Prize in Physiology or Medicine was awarded to Gregg L. Semenza, William G. Kaelin, and Sir Peter J. Ratcliffe “for their discoveries in how cells sense and adapt to oxygen availability [59].” Looking at cellular oxygen availability started in 1906 when Carnot and Deflandre first named “hemopoietic” as a blood-soluble factor responsible for erythropoiesis in anoxia [60]. Many years later, researchers began to acknowledge this specific factor as erythropoietin (EPO) in relationship to anemia as

detected in human serum [61]. Finally, the regulation of EPO production was the work completed by the above 2019 Nobel Prize winners.

#### 1.7.1 From erythropoietin (EPO) to HIF-1

In 1990, Semenza *et al.* found that in transgenic mice models the production of EPO required a specific regulatory element [62]. Binding to the EPO regulatory sequence at the 3' end of the EPO gene were proteins designated as “hypoxia-inducible nuclear factors” [63]. Further study of the expression of EPO found that EPO gene transcription was specifically mediated in hypoxia with an inducible enhancer region. This region contained a unique fifty nucleotide (50-nt) sequence that could bind at least three different transcription factors [64]. Through mutation studies of this 50-nt sequence, one sequence from nucleotide 4 to 12 was found to be imperative for the activity in hypoxia and was thus named the “hypoxia-inducible enhancer binding site 1” (HIE-BS1) [64]. Further work developed an oligonucleotide sequence (W18 – 5'-GCCCTACGTGCTGTCTCA-3') that specifically binds to the nuclear factor designated by Semenza *et al.* as hypoxia-inducible factor 1 (HIF-1). HIF-1 was found to be critical to the gene transcription of EPO through binding to the HIE-BS1 [64]. Lastly, HIF-1 was only detectable under hypoxic conditions using electrophoretic mobility shift assay (EMSA), suggesting it must be created through de novo protein synthesis [64].

#### 1.7.2 HIF-1 expression in hypoxia

Since HIF-1 was only found under hypoxic conditions, Wang *et al.* searched for chemically induced methodologies for the increased production of HIF-1. They found deferoxamine (DFO) could increase the expression of HIF-1 leading to the induction of EPO gene expression [65]. This was consistent with the observation that cobalt chloride (CoCl<sub>2</sub>), also increased the expression of HIF-1 [66]. Wang *et al.* built on the knowledge of a nuclear factor HIF-1 required for EPO activation, by proving HIF-1 activation in a variety of cell lines that had EPO expression removed. From this, HIF-1 was still found to be present in mouse Ltk-fibroblasts, CHO cells, Rat1 fibroblasts, human embryonic kidney 293 cells, HeLa cells, C<sub>2</sub>C<sub>12</sub> mouse myoblasts, and Hep3B [66].

Determination of the binding of HIF-1 to DNA was done through phosphorylation, methylation, and temperature studies. Concluding the half-life of binding/dissociation for HIF-1 to DNA to be less than one minute [67]. Also, HIF-1 required phosphorylation for DNA binding; additionally, methylation studies showed HIF-1 interacts primarily with the major groove of DNA at the site sequence 5'-TACGTGCT-3' [67]. Expanding from EPO regulation, the role of HIF-1 in the transcriptional regulation of glycolytic enzymes was determined [68]. From this work it was determined that HIF-1 was responsible for the regulation of aldolase A (ALDA), phosphoglycerate kinase 1 (PGK1), phosphofructokinase-liver type (PFKL), pyruvate kinase-muscle type (PKM), lactate dehydrogenase A (LDHA) and Enolase 1 (ENO1) in the family of glycolytic genes [68]. The binding site consensus sequence as determined from ALDA, ENO1, and LDHA was determined to be 5'-RCGTG-3' [69].

### 1.7.3 From HIF-1 to HIF-1 $\alpha$

To better understand the function of HIF-1, Wang *et al.* [70] purified and characterized the HIF-1 protein using CoCl<sub>2</sub> induction in Hela S3 cells. The overexpressed protein was purified on Sepharose CL-6B columns using the W18 DNA binding sequence. The purified protein in SDS page showed that the HIF-1 protein contains four peptides of apparent mass of 120, 94, 93, and 91 KDa [70]. Using further tryptic peptide mapping it was determined that HIF-1 is comprised of two subunits, HIF-1 $\alpha$  at 120 kDa and HIF-1 $\beta$  at 91/93/94 KDa. Once the subunits were identified it was noted that although both the alpha and beta subunits can bind DNA, the alpha subunit binds DNA more strongly than the beta subunit [70]. Lastly, they found that in solution HIF-1 $\alpha$  and HIF-1 $\beta$  mostly exist as the HIF-1 dimer at the molecular weight of 200-220 kDa [70].

DNA-binding activity of HIF-1 can be altered depending on the redox state of the cellular environment. Wang *et al.* [71] used both the reducing agent of Dithiothreitol (DTT) and the oxidizing agent of hydrogen peroxide (H<sub>2</sub>O<sub>2</sub>) in order to alter DNA binding of HIF-1. From these experiments, they determined that the regulation of the subunits of HIF-1 must be achieved using a different mechanisms. Both DTT and H<sub>2</sub>O<sub>2</sub> had some effect on the DNA binding of HIF-1, but only the expressed levels of HIF-1 $\alpha$  seemed to be affected by their treatments [71]. They further “suggested that the reduction of one or more cysteine residues of HIF-1 $\alpha$  is necessary for its association with DNA” [71]. The authors furthered this conclusion with an assay that alkylates

cysteine residues in an already bound HIF-1, finding that they could disturb the DNA binding of HIF-1 $\alpha$  [71]. Overall concluding that the redox state of cysteine residues is important, in the Per-ARNT-AHR-Sim (PAS) domain of HIF-1 $\alpha$ . Additionally, the cellular localization of HIF-1 $\alpha$  was only found accumulated in nuclear extracts and was not found in cytoplasmic extracts [72].

#### 1.7.4 HIF-1 $\alpha$ regulation and structure

Going beyond the redox state, Wang *et al.* [73] looked into the effect of protein kinase and phosphatase inhibitors on the expression of HIF-1. They found that serine/threonine kinase inhibitors only partially blocked HIF-1 DNA binding, while serine/threonine phosphatase inhibitors completely blocked HIF-1 DNA binding and Protein Kinase C inhibitors had no effect [73]. From this, they concluded that “tyrosine phosphorylation is required for hypoxia signal transduction” [73]. Later in 1995, Wang *et al.* [72] looked further into the structure of HIF-1 $\alpha$  and found it is a basic-helix-loop-helix (bHLH)-PAS protein. PAS proteins contain structural similarities to three different protein sequences, including: the Per protein from the *Drosophila* proteins period, the Sim protein from the single-minded proteins, and the AHR protein from the mammalian aryl hydrocarbon receptor protein. [72]. It should be noted that typically HLH motifs are often dimerization motifs. Also, Wang *et al.* confirmed that the HIF-1 receptor on DNA contains the binding sequence of 5'-BACGTGCK-3'[72]. HIF-1 $\alpha$  also is known to bind to adaptor protein p300 to increase the transcription provided as a HIF-1 complex in hypoxia [74].

The genetic location of human HIF-1 $\alpha$  was assigned to chromosomes 14q21 to 14q24, where HIF-1 $\beta$  was assigned to chromosome 1q21 [75]. Looking at the protein domains required for the heterodimerization of HIF-1 and its DNA binding and transcriptional activation; Jiang *et al.* [76] used an EMSA assay to test the binding of GST-tagged purified proteins to the W18 and M18 oligonucleotides. In their assay they used buffer containing DTT (5mM) and glycerol (20%), finding that HIF-1 does bind W18 with *in vitro* heterodimerization of HIF-1 $\alpha$  and HIF-1 $\beta$  [76]. In creating mutant proteins of HIF-1 $\alpha$ , they determined that HIF-1 $\alpha$  lacking the basic domain could still bind to HIF-1 $\beta$ . Overall they determined the region required for heterodimerization was AA 1-166 (bHLH-PasA) and the regions required to maintain DNA binding required AA 1-390 (bHLH-PAS) [76]. The structure of HIF-1 $\alpha$  contains “two separate and independent

transactivation domains [77]”, they are termed TAD-N (AA 531-575) and TAD-N (AA 786-785). HIF-1 $\alpha$  also contains an inhibitory domain termed ID (AA 576-785) [77].

#### 1.7.5 HIF-1 $\alpha$ /aryl hydrocarbon receptor nuclear translocator interactions and regulation

Wood *et al.* using aryl hydrocarbon receptor nuclear translocator (ARNT) deficient cells, found that HIF-1 expression was strongly related to the expression level of HIF-1 $\beta$ /ARNT [78]. Also, the downstream gene products of HIF-1 including LDH-A, PGK-1, GLUT-1, VEGF, and PDGF- $\beta$ , were all downregulated in the absence of ARNT. Showing that the HIF-1 complex in hypoxia is responsible for the upregulation of those genes [78]. Further information into the regulation of HIF-1, showed that HIF-1 $\alpha$  was the oxygen-sensitive component versus HIF-1 $\beta$  [79]. Additionally, within HIF-1 $\alpha$  it was found that amino acid 530 – 826 are responsible for the hypoxic activation of HIF-1 $\alpha$  using 1% O<sub>2</sub>, DFO and CoCl<sub>2</sub> induction [79]. Further work into the regulation of HIF-1 $\alpha$  in hypoxia had Maxwell *et al.* set out to determine the regulation of HIF-1 $\alpha$  by pVHL (von Hippel-Lindau protein) [80]. Using VHL-deficient cells, they determined that pVHL was responsible for the proteasomal degradation of HIF-1 $\alpha$  in normoxic conditions. Also, they determined that under hypoxic conditions, or with cells lacking pVHL that the degradation of HIF-1 $\alpha$  would not occur [80]. pVHL forms an E3-ligase complex with several proteins, Elongin B and C [81], Cul2 [82] and Rbx1 [83].

Elongin B and C are part of the Elongin (SIII) complex which is responsible for the elongation of RNA by RNA polymerase II [84]. In the complex of Elongin (SIII), elongin A is the subunit that is responsible for the action concerning RNA pol II. It is thought that pVHL acts as an inhibitor to the elongation of RNA by binding to Elongin B and C [84]. Rbx1 (RING-Box protein 1) is a 16 kDa protein that forms an SCF (Skp1-Cdc53- F-box protein) like complex with pVHL to perform ubiquitination of VHL target proteins [83]. Cul<sub>2</sub> is a member of the cullins family of proteins, like Cdc53 it is thought to be part of the SCF complex that interacts strongly in the cytoplasm with pVHL-ElonginB-ElonginC (VBC) complex [82]. Taken all together the pVHL-ElonginC-ElonginB-Cul2-Rbx1 (VCBCR) complex is responsible for targeting HIF-1 $\alpha$  in the oxygen-dependent destruction domain (ODDD) with the b-domain of pVHL specifically [85].

### 1.7.6 HIF-1 $\alpha$ cellular localization and gene activation

The localization of HIF-1 expression in the human and mouse bodies was analyzed by Wiener *et al.* [86] who found that HIF-1 $\alpha$  mRNA expression under normoxic conditions was in all organs analyzed, including heart, brain, placenta, lung, liver, skeletal muscle, kidney and pancreas. Whereas in mice, the levels of HIF-1 $\alpha$  mRNA were barely detectable under normoxic conditions, and increased significantly under hypoxic conditions [86].

Although HIF-1 $\alpha$  was shown to have numerous target genes including EPO, ALDA, etc., other genes are also activated by HIF-1 $\alpha$ . Glut-1 mRNA expression was found to be increased under hypoxia (1% O<sub>2</sub>), DFO and CoCl<sub>2</sub> treatments. The removal of the hypoxia response element in the Glut-1 gene leads to a drastic decrease in the hypoxic activation of Glut-1 through HIF-1 $\alpha$  [87]. Another gene target of HIF-1 $\alpha$  includes vascular endothelial growth factor (VEGF). HIF-1 $\alpha$  has been shown to bind to the 5'-flanking sequence of the VEGF gene and thus activate transcription of VEGF [88]. Also, HIF-1 $\alpha$  was shown to transcriptionally activate Heme Oxygenase-1 (HO-1) in mice under hypoxic conditions, through the increased expression of HIF-1 [89].

### 1.7.7 HIF-1 $\alpha$ in deregulating cellular energetics

HIF-1 $\alpha$  induces dramatic changes in cellular energetics. As a master regulator, HIF-1 $\alpha$  can induce glycolysis and inhibit mitochondrial respiration [41]. HIF-1 $\alpha$  induces the target gene for the synthesis of carbonic anhydrase IX [90].

HIF-1 $\alpha$  cooperates with oncogenes; *Ras* induces glycolysis through the upregulation of HIF-1 $\alpha$  [91] and *Myc* also increases HIF-1 $\alpha$  expression to induce metabolic changes [92],[93]. HIF-1 $\alpha$  prevents mitochondrial respiration by preventing the entry of acetyl-CoA into the TCA cycle [94]. HIF-1 $\alpha$  also prevents mitochondrial respiration through the activation of the pyruvate dehydrogenase kinase 1 (PDK1) [94]. HIF-1 $\alpha$  induces *MAX*-interacting protein (MXI-1) which is a repressor of *Myc* and then the *Myc*-*MAX* complex inhibits the peroxisome proliferator-activated receptor  $\gamma$  coactivator 1 $\beta$  (PGC-1 $\beta$ ) which inhibits overall the mitochondrial biogenesis [95]. HIF-1 $\alpha$  induces forkhead box 3A (*Fox03A*), which also represses *Myc* function [96]. HIF-1 $\alpha$  activates mitochondrial autophagy by induction of BCL2/adenovirus E1B 19-kDa protein-interacting

protein 3 (BNIP3) [97]. HIF-1 $\alpha$  causes the switch of cytochrome c oxidase subunits of COX4-1 to COX4-2 [98]. HIF-1 $\alpha$  upregulated the transcription of microRNA miR-210, leading to the inhibition of the TCA cycle and oxidative phosphorylation [99]. HIF-1 $\alpha$  activation in breast cancer cells leads to a shift in energy generation towards aerobic glycolysis [100]. HIF-1 $\alpha$  prevents H-Ras-induced senescence and also downregulates p53 and 21 [101].

### 1.7.8 HIF-1 $\alpha$ inhibitors

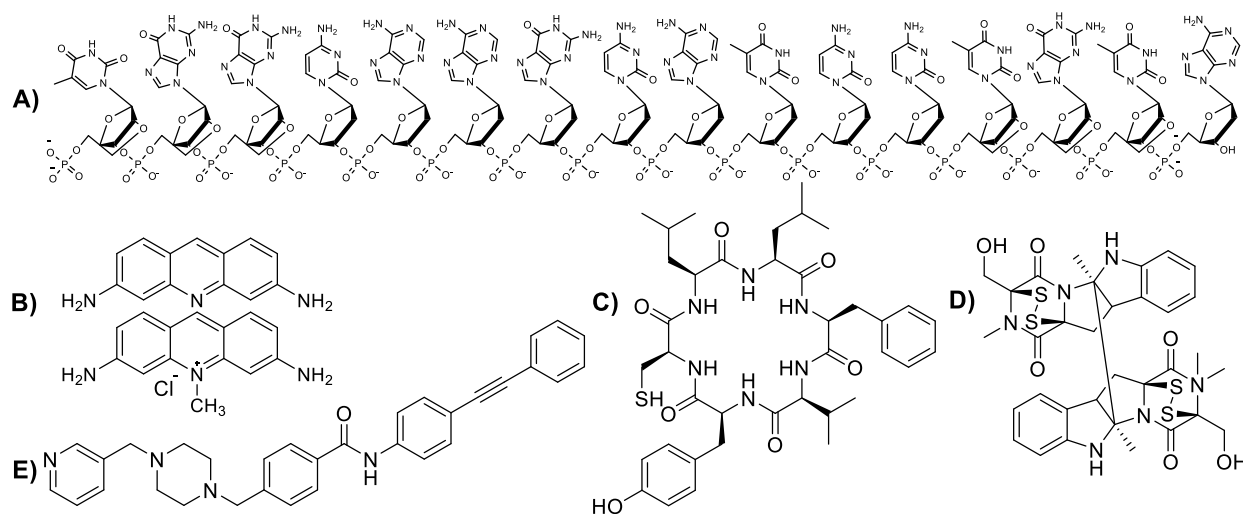


*Figure 1.6. Compounds that inhibit interactions with HIF-1 $\alpha$  protein directly. Including: A) EZN-2968 oligonucleotide, B) acriflavine, C) Cyclo-CLLFVY, D) Chaetocin, and E) ER-400583-00.*

HIF-1 $\alpha$  has been shown to mediate resistance to chemotherapy, therefore the development of chemicals that can inhibit the function of HIF-1 $\alpha$  is of extreme importance in the fight against cancer [102],[103]. There are numerous small molecule inhibitors of HIF-1 $\alpha$ , although their modes of inhibition vary numerously. Methods of inhibition of previous small molecule inhibitors include inhibition of HIF-1 $\alpha$  translation from RNA, HIF-1 $\alpha$  degradation, inhibition of HIF-1 $\alpha$  transcriptional activity, inhibition of DNA binding, HIF-1 $\alpha$  protein accumulation, inhibition of HIF-1 dimerization, promotion of HIF-1 $\beta$  degradation, and promotion of HIF-1 $\alpha$  degradation [104]. Most of these do not act specifically on HIF-1 $\alpha$  and instead act in the paths above and below HIF-1 $\alpha$  [41]. Some compounds are found to directly interact with HIF-1 $\alpha$ . One compound that targets the HIF-1 $\alpha$  mRNA is EZN-2968 (*Figure 1.6.A.*) which is an oligonucleotide sequence of

5'-TGGcaagcatccTGTA-3', where uppercase and lowercase indicate LNA or DNA residues, respectively. The IC<sub>50</sub> value of this compound is reported to be between 1-5 nM [105].

Compounds that target the PAS-B subdomain of HIF-1 $\alpha$ , such as acriflavine (*Figure 1.6.B.*); although the IC<sub>50</sub> value of this compound is fairly poor at 1  $\mu$ M [106]. Another compound binding to PAS-B subdomain of HIF-1 $\alpha$  is *cyclo*-CLLFVY (*Figure 1.6.C.*). The affinity of this peptide to HIF-1 $\alpha$  was found to be 124 nM [107]. A naturally occurring compound Chaetocin (*Figure 1.6.D.*), inhibits the binding of p300 to HIF-1 $\alpha$ ; but each mechanism of this complexation inhibition is yet to be fully elucidated. Additionally, the IC<sub>50</sub> value for Chaetocin is very low at 12.5  $\mu$ M [108]. A small molecule labeled ER-400583-00 (*Figure 1.6.E.*) was shown to localize to the same area using confocal microscopy as HIF-1 $\alpha$ , and was determined to act on HIF-1 $\alpha$  by affecting HIF-1 $\alpha$  degradation through the proline-hydroxylation-dependent ubiquitination pathway [109]. Overall there seems to be a large number of small molecule inhibitors for HIF-1 $\alpha$ , but a lot of the mechanisms of action are not fully elucidated [104].

### *1.8 Hypothesis and aims/goals*

In this work, we hypothesize that imaging hypoxia-inducible factor 1 alpha (HIF-1 $\alpha$ ) in breast cancer using positron emission tomography (PET) will provide a higher tumor-to-muscle ratio (TMR) and standardized uptake (SUV) compared to conventional hypoxia radiotracers. To achieve the above hypothesis, we have the following 8 aims.

Aim 1: Radiolabelling of nitroimidazole compounds for imaging hypoxia.

Aim 2: *In vitro* and *in vivo* analysis of radiolabelled nitroimidazole compounds.

Aim 3: Synthesis of novel HIF-1 $\alpha$  binding compounds.

Aim 4: Determination of binding affinity of HIF-1 $\alpha$  targeting compounds to HIF-1 $\alpha$  protein.

Aim 5: Radiolabelling of HIF-1 $\alpha$  targeted compounds using various methodologies.

Aim 6: *In vitro* analysis of radiolabelled HIF-1 $\alpha$  binding compounds.

Aim 7: *In vivo* analysis of radiolabelled HIF-1 $\alpha$  binding compounds.

Aim 8: Comparative analysis for the *in vivo* imaging of hypoxia.

## **Chapter 2: Methods, techniques, instrumentation, and chemicals.**

### *2.1 Instrumentation*

#### *2.1.1 High-performance liquid chromatography and flash chromatography*

High-performance liquid chromatography (HPLC) purification and analysis were performed using a Phenomenex LUNA<sup>®</sup> C18(2) column (100 Å, 250 x 10 mm, 10 mm) or a Phenomenex LUNA<sup>®</sup> Omega Polar C18 column (100 Å, 250 x 10 mm, 5 mm) using gradient elution, specific to the given compound of interest (Gilson 321 pump, 171 diode array detector, Berthold Technologies Herm LC). Flash Chromatography was done using a Yamazen Smart Flash AKROS, equipped with Green Flash “Prep AI” software and both universal silica columns and reversed-phase “ODS” columns. Gradient elution described below are done using CH<sub>3</sub>CN concentrations only. Aqueous component is either water or 0.2% trifluoroacetic acid (TFA) in water and can be varied depending on the purification procedure.

##### *2.1.1.1 FIB HPLC method*

Starting at 50% CH<sub>3</sub>CN from 0 to 8 minutes, ramping up to 80% CH<sub>3</sub>CN at 13 minutes, ramp up to 100% CH<sub>3</sub>CN till 30 minutes. 3 mL/min elution speed.

##### *2.1.1.2 FAZA HPLC method*

Isocratic elution 8% ethanol in water, 3 mL/min elution speed.

##### *2.1.1.3 FMISO HPLC method*

Starting at 5% CH<sub>3</sub>CN from 0 to 4 minutes, ramp up to 90% CH<sub>3</sub>CN at 23.90 and hold at 90% CH<sub>3</sub>CN for 35 minutes. 3 mL/min elution speed.

##### *2.1.1.4 Cu\_peptides HPLC method*

Starting at 10% CH<sub>3</sub>CN from 0 to 10 minutes, ramp up to 50% CH<sub>3</sub>CN at 25 minutes, ramp up to 90% CH<sub>3</sub>CN till 30 minutes, and hold at 90% CH<sub>3</sub>CN till 41 minutes. 2 mL/min elution speed.

#### 2.1.1.5 *Cu* peptides fast HPLC method

Starting at 5% CH<sub>3</sub>CN from 0 to 15 minutes, immediately up to 90% CH<sub>3</sub>CN and hold till 41 minutes. 2 mL/min elution speed.

#### 2.1.1.6 HIF-1 $\alpha$ compounds HPLC method

Starting at 20% CH<sub>3</sub>CN from 0 to 4 minutes, ramp up to 95% CH<sub>3</sub>CN at 24.10 minutes hold at 95% CH<sub>3</sub>CN to 35 minutes. 3 mL/min elution speed.

#### 2.1.1.7 HIF-1 $\alpha$ compounds Iso HPLC method

Isocratic elution at 40% CH<sub>3</sub>CN, 3 mL/min elution speed.

### 2.1.1 Nuclear magnetic resonance and LC-MS

Nuclear Magnetic Resonance (NMR) data were collected using a Bruker Ascend™ 600 MHz. Data were analyzed using TopSpin 4.1.0. High-resolution Mass Spectroscopy was achieved with an Agilent Technologies 6220 oa TOF. Data were analyzed using MassHunter Analytical Studio.

### 2.1.2 Radio-thin-layer chromatography, dose calibrator and gamma counter

Radio-TLC was performed using either EMD Merck F254 silica gel 60 aluminum-backed thin layer chromatography (TLC) plates or Analtech RP18 with UV254 aluminum-backed TLC plates. Radio-TLC plates were analyzed on a Bioscan AR-2000. Quantification of radioactive samples during chemistry was achieved using a Biodex ATOMLAB™ 400 dose calibrator. Quantification of radioactive samples for *in vivo* and *in vitro* work was achieved using a Hidex Gamma Counter with Hidex AMG software or a WIZARD2 Automatic gamma counter.

### 2.1.3 Centrifugation, thermoshaker, oil bath, rotary evaporation and lyophilization

Centrifugation of non-radioactive samples was achieved with a Hettich Zentrifugen Rotina 35R, whereas <sup>18</sup>F-radiolabelled samples were centrifuged on a Fisher Scientific Mini Centrifuge. Chemistry reaction parameters were screened using an Eppendorf Thermomixer R and an IKAMAG® Ret-G Stir plate with an oil bath. The final formulation of the final <sup>18</sup>F-radiolabelled

products for animal injection was done using glassware kept in an Isotemp Vacuum Oven Model 285A and a rotary evaporator of a Buchi HB 140 Rotavapor-M with a Fisher Maxima C Plus Model M8C pump. Non-radiochemistry rotary evaporation was done using a Heidolph Laborota 4000 equipped with a Vacuubrand PC 500 series pump. Lyophilization was done on a Labconco Freezone 4.5 with an Edwards RV5 pump.

#### 2.1.4 Microscale thermophoresis (MST) and potential of hydrogen (pH) meter

MST was completed using all Eppendorf® LoBind materials, including tips and microcentrifuge tubes on a Nanotemper Monolith NT.115 Labelled Instrument. pH was determined on a Fisherbrand accumet AE150 instrument equipped with a 13-620-108B probe.

#### 2.1.5 Plate reader, confocal microscope, and western blot

96 well plates are analyzed using a Molecular Devices SeptraMax 340PC equipped with SoftMax Pro software for analysis. Confocal. Western blot membranes are analyzed using a LICOR Odyssey® XF scanner. Cells were imaged with a Zeiss 710 Confocal Microscope using the 40x/1.3 Oil DIC M27 magnification setting. Images were analyzed with Zen 2011 SP3 software (Carl Zeiss Microscopy), saved, and optimized using Adobe Photoshop for noise and brightness levels (standardized between all three channels).

### 2.2 *Chemicals*

1-Pyridine-3-yl-methyl-piperazine was obtained from Combi Blocks (USA). DOTA-NHS-Ester was obtained from Macrocyclics (USA). 1-Ethynyl-4-fluorobenzene, 4-ethynylanisole, 1-chloro-4-ethynylbenzene, 1-bromo-4-ethynylbenzene, 1-ethynyl-4-(trifluoromethyl)benzene, and 4,7,13,16,21,24-Hexaoxa-1,10-diazabicyclo[8.8.8]hexacosane (K.2.2.2.) were obtained from TCI America (USA). Radiolabelling precursors 1H-imidazole-1-propanol (NITTP) and 1-(2,3-Diacetyl-5-tosyl-( $\alpha$ -D-arabinofuranosyl)-2-nitroimidazole were from ABX advanced biochemical compounds. All other chemicals were obtained from Sigma-Aldrich® and used without further purification. Water was obtained from a Barnstead Nanopure water filtration system (Barnstead Diamond Nanopure pack organic free RO/DIS).

### 2.2.1 ELISA buffer (200 mL)

Contained the following: 10 mM Tris-HCl (315.2 mg, 2 mmol), 50 mM KCl (745.5 mg, 10 mmol), 50 mM NaCl (584.4 mg, 10 mmol), 5 mM DTT (154.25 mg, 1 mmol), 1 mM MgCl<sub>2</sub> (40.66 mg, 0.2 mmol), 1 mM EDTA (74.44 mg, 0.2 mmol), and 10% glycerol (20 mL).

### 2.2.2 EMSA Buffer

EMSA buffer was the addition of BSA (0.2 mg) into a solution of ELISA buffer (1.0 mL).

### 2.2.3 In-house K.2.2.2./K<sub>2</sub>CO<sub>3</sub> solution

In-house K.2.2.2./K<sub>2</sub>CO<sub>3</sub> solution was prepared using K<sub>2</sub>CO<sub>3</sub> (92.3 mg) dissolved into H<sub>2</sub>O (7 mL) in a 50 mL volumetric flask. To the volumetric flask, K.2.2.2 (500 mg) was added and the solution was completed with CH<sub>3</sub>CN (43 mL).

### 2.2.4 10X Running buffer solution

Contained the following: 25 mM Tris-HCl (60.4 g), 192 mM glycine (288 g) and 0.1% SDS (20 g) for a 2-litre stock solution in Barnstead water.

### 2.2.5 10X Transfer buffer solution

Contained the following: 25 mM Tris-HCl (60.4 g) and 192 mM glycine (288 g) for a 2 L stock solution in Barnstead water.

### 2.2.6 TBS-T buffer solution

Contained the following: 50 mM Tris-HCl (6.05 g) and 150 mM NaCl (8.76 g) in 950 mL Barnstead water. The solution was pH adjusted to 7.4 and then Tween-20 (1 mL, 0.1%) was added to the mixture. Lastly, the solution was topped up to 1 L total volume.

### 2.2.7 RIPA buffer solution

Contained the following: Tris-HCl (6.04 g), NaCl (8.76 g), SDS (1 g), Sodium deoxycholate (5 g), Triton X-100 (5 mL) all into 1 L of Barnstead water.

### 2.2.8 Glycine buffer solution

Glycine (7.5 g, 0.1 M) is added into 950 mL of Barnstead water. HCl (37% solution) is added dropwise until a pH of 3.0 is obtained. The solution is topped up to 1 L and the 0.1 M Glycine wash, pH 3.0 solution is ready for use.

### 2.2.9 Krebs buffer solution

Into 950 mL Barnstead water was weighed the following: 120 mM NaCl (7.01 g), 25 mM NaHCO<sub>3</sub> (2.1 g), 4 mM KCl (0.3 g), 1.2 mM KH<sub>2</sub>PO<sub>4</sub> (0.16 g), 2.5 mM MgSO<sub>4</sub> (0.3 g), 70 μM CaCl<sub>2</sub> · 2H<sub>2</sub>O (10.3 mg). The solution was pH adjusted to 7.4 and the solution topped up to 1 L total volume.

### 2.2.10 Dulbecco's PBS buffer solution

Into 950 mL Barnstead water was weighed the following: NaCl (8 g), 25 mM Na<sub>2</sub>HPO<sub>4</sub> anhydrous (1.15 g), KCl (0.2 g), KH<sub>2</sub>PO<sub>4</sub> (0.2 g), MgCl<sub>2</sub> · 6H<sub>2</sub>O (100 mg), CaCl<sub>2</sub> · 2H<sub>2</sub>O (133 mg). The solution was pH adjusted to 7.6 and the solution topped up to 1 L total volume [110].

### 2.2.11 PBS-T

Phosphate-buffered saline (PBS) solution was prepared from a pre-packaged Sigma (P3818) package with pH adjusted to 7.3. Triton-X100 dilutions were prepared in PBS solution to obtain final Triton-X100 concentrations from 0.5% to 0.1%.

### 2.2.12 4% Paraformaldehyde solution

4% paraformaldehyde in PBS was prepared by the addition of paraformaldehyde (4.0 g) to PBS solution (100 mL). This mixture was allowed to stir on a hot plate until the paraformaldehyde was completely dissolved, and the PBS mixture was never allowed to boil. Once the solution had

cooled, the batch (100 mL) was aliquoted into fractions (15 mL) and stored at -80 °C for up to one month.

### 2.3 Methods and techniques

#### 2.3.1 Linear peptide synthesis and overall peptide purification

Linear peptides were prepared as per Richter *et al.* [111]. This peptide coupling was performed using solid-phase peptide synthesis (SPPS) on a Syro I (MultiSynTech/Biotage). High-performance liquid chromatography (HPLC) purification and analysis of products were performed using a Phenomenex JUPITER® Proteo column (90 Å, 250 x 10 mm, 4 mm) using gradient elutions specific to the given compound (Gilson 321 pump, UV/VIS-155 dual wavelength detector).

#### 2.3.2 Plate-based assay (PBA) methodologies for HIF-1 $\alpha$ binding detection

##### 2.3.2.1 PBA method A

Pierce Ni-coated plates (Prod #15142, clear 8 well strip plates) were loaded with a required concentration of HIF-1 $\alpha$  protein (Sino Biological (cat. #11977-H07E) N-terminal segment (Arg 575 to Asn826)) in EMSA buffer (50  $\mu$ L) and incubated at ambient temperature for 1 hour. After incubation, the excess protein is removed using ELISA buffer (3 x 200 mL) washes.

Next, the desired radiotracer is allowed to react with the immobilized protein for 1 hour at room temperature. Excess radiotracer is again removed using ELISA buffer (3 x 200 mL) washes. Clear 8 well strips are broken apart and individual wells' radioactivity is recorded using a gamma counter.

##### 2.3.2.2 PBA method B

HIF-1 $\alpha$  protein from LifeSpan BioSciences (LS-G12857/213, AA 218 – 506), was reconstituted in 20 mM Tris (2.4 mg, 0.02 mmol) and 150 mM NaCl (pH 8.0, 8.8 mg, 0.15 mmol) to a total volume of 1 mL of water. This achieved a final concentration of 5  $\mu$ g/50  $\mu$ L, which was frozen at -80°C for long-term storage. HIF-1 $\alpha$  protein (5  $\mu$ g) was diluted in Tris-buffer saline (TBS, 516  $\mu$ L) to create desired 27 pmol stock solution in a 100  $\mu$ L aliquot. Further dilution can achieve desired concentrations of 27, 18, 15, 12, 9, 6, 3 and 0 pmol per well. The solution was allowed to

rock for 1 hour at ambient temperature in nickel-coated plates (Pierce Ni-coated plates, Prod #15142, Lot #PH204843, clear 8 well strip plates). Plates are stated to have a max binding capacity of 9 pmol of protein per well. Excess protein was removed, and wells were washed with wash solution (TBS with 0.05% Tween-20, 3 x 200  $\mu$ L). The radiolabelled compound was added for assay (100  $\mu$ L) and let stand for 1 hour at ambient temperature. Remove excess radiolabelled compound and wash wells with wash solution (TBS with 0.05% Tween-20, 3 x 200  $\mu$ L). Add the required blocking compound for assay (100  $\mu$ L) and let stand for 1 hour at ambient temperature. Remove the blocking compound and wash wells with wash solution (TBS with 0.05% Tween-20, 3 x 200  $\mu$ L). If blocking was not required, proceed to the counting of the wells after the previous wash step. Break apart wells and place them in scintillation vials for detection on the gamma counter.

### 2.3.3 In-solution charcoal-based assay for HIF-1 $\alpha$ binding

As per, Fothergill and Nairn the addition of charcoal in solution to remove unbound residual radiolabelled peptide from the HIF-1 $\alpha$  protein in solution was tested [112]. HIF-1 $\alpha$  protein was to be diluted in TBS to a maximum volume (100  $\mu$ L) per Lobind Eppendorf tube. Radiolabelled compound was added to the Eppendorf tube and allowed to react for 1 hour at 37  $^{\circ}$ C in the Thermoshaker at 300 rpm.

A charcoal solution of Charcoal-Dextran Coated (Sigma C6241, 50 mg) in water (15 mL) was created and vortexed before use, in which a small aliquot (10 - 80  $\mu$ L) is added to each reaction tube. Next, the reaction was diluted with additional TBS (200  $\mu$ L) and allowed to react for an additional 30 minutes at 37  $^{\circ}$ C in the Thermoshaker at 300 rpm. Finally, the reaction tubes were centrifuged at 14,000 rpm for 15 minutes at 4  $^{\circ}$ C and the supernatant (170  $\mu$ L) was removed to a clean microcentrifuge tube. Both the supernatant and pellet are counted on the gamma counter.

## 2.4 *General microscale thermophoresis procedure*

### 2.4.1 HIF-1 $\alpha$ fragment protein labelling

From recombinant human HIF-1 $\alpha$  protein (LSBio, LS-G12857) an aliquot of 20  $\mu$ g (5  $\mu$ L) of protein was removed and added to a solution containing Dulbeccos's phosphate-buffered saline

with 0.05% Tween-20 and 1mM DTT (DPBS-T, 925  $\mu$ L) in a 1.5 mL Eppendorf® LoBind microcentrifuge tube. To this solution, DMSO (50  $\mu$ L) and the NanoTemper Monolith His-tag Labelling Kit RED-tris NTA (20  $\mu$ L) were added. The labelling occurred in the Thermoshaker (600 rpm) for 30 minutes at ambient temperature and once completed the solution was centrifuged to remove any insoluble material. As per manufacture specifications, MST-optimized NT-647 dye (RED-tris-NTA) with nanomolar affinity does not require purification of the labelled protein.

#### 2.4.2 HIF-1 $\alpha$ fragment thermophoresis analysis

All materials used for both tips and microcentrifuge tubes were Eppendorf LoBind quality to ensure low binding of protein and small molecular weight compounds. Stock solutions of all small molecular compounds and peptides were made in pure DMSO at a concentration of 2 mM. The stock solutions (1.25  $\mu$ L) were then diluted into DPBS-T (23.75  $\mu$ L) to achieve the final concentration of 100  $\mu$ M solutions for all compounds in 5% DMSO. Serial dilutions of the 100  $\mu$ M solutions were prepared for a total of 16 dilutions, in a total remaining volume of 5  $\mu$ L in each microcentrifuge tube. To these prepared dilutions, 5  $\mu$ L of fluorescently-labelled protein were added and the 10  $\mu$ L reactions were allowed to stand for 5 minutes at ambient temperature before being removed into standard NanoTemper capillaries and detected in a Monolith NT.115 instrument. The overall reaction solution for experiments contained DPBS with 0.05% Tween-20, 1 mM DTT, and 5% DMSO.

#### 2.4.3 HIF-1 $\alpha$ full-length protein labelling

From recombinant human HIF-1 $\alpha$  protein (Abcam, ab154478) an aliquot of 10  $\mu$ g (33.4  $\mu$ L) of protein was removed and added to a solution containing Dulbeccos's phosphate-buffered saline with Tween-20 (0.1%), DTT (2 mM), MgCl<sub>2</sub> (10 mM), and NaCl (150 mM) (Buffer A, 896.6 mL) in a 1.5 mL Eppendorf®LoBind microcentrifuge tube. To this solution, DMSO (50  $\mu$ L) and the NanoTemper Monolith His-tag Labelling Kit RED-tris NTA (20  $\mu$ L) was added. The labelling occurred in the Thermoshaker (600 rpm) for 30 minutes at ambient temperature and once completed the solution was centrifuged to remove any insoluble material. As per manufacture specifications, MST-optimized NT-647 dye (RED-tris-NTA) with nanomolar affinity does not require purification of the labelled protein.

#### 2.4.4 HIF-1 $\alpha$ full-length thermophoresis analysis

All materials used for both tips and microcentrifuge tubes were Eppendorf LoBind quality to ensure low binding of protein and small molecular weight compounds. Stock solutions of all small molecular compounds and peptides were made in pure DMSO at a concentration of 2 mM. Buffer B was prepared with the addition of bovine serum albumin (0.5 mg/mL) to Buffer A. Finally, Buffer C was prepared with the addition of glycerol (40%) to the prepared Buffer B solution. The stock solutions of DMSO (30  $\mu$ L) were then diluted into Buffer C (70  $\mu$ L) to achieve the final desired concentration of 600 mM solutions for all compounds in 30% DMSO. Serial dilutions of the 600 mM solutions were prepared for a total of 16 dilutions, in a total remaining volume of 5  $\mu$ L in each microcentrifuge tube. To these prepared dilutions 5  $\mu$ L of fluorescently-labelled protein in Buffer A were added and the 10  $\mu$ L reactions were allowed to stand for 5 minutes at room temperature before being removed in standard NanoTemper capillaries and detection in a Monolith NT.115 instrument. Overall reaction solution for experiments contained DPBS with Tween-20 (0.071%), DTT (1.42 mM), MgCl<sub>2</sub> (7.1 mM), NaCl (106.5 mM), DMSO (17.5%), glycerol (14%), and BSA (0.105 mg/mL).

#### 2.5 *Computational analyses*

The coordinates from the X-ray crystal structure of HIF-1 $\alpha$  (PDB ID: 4H6J, 1.52 Å) were retrieved from the RCSB Protein Data Bank server. The ligands were built with the builder toolkit and energy was minimized using the semi-empirical quantum mechanical method PM3 in ArgusLab 4.0.1 package. The crystallized ligand was docked first for validating the computational method. The receptor structure was selected and properly protonated, and geometry was optimized and minimized. The molecule to be docked in the receptor binding site was inserted into the workspace carrying the structure of the receptor. The docking program implements an efficient grid-based docking algorithm, which approximates an exhaustive search within the free volume of the binding site cavity. The conformational space was measured by the geometry optimization of the flexible ligand (rings are treated as rigid) in combination with the incremental construction of the ligand torsions. Therefore, docking occurred between the flexible parts of the ligand and receptor. The ligand orientation was determined by a shape-scoring function based on  $A_{\text{score}}$  and the final positions were ranked by lowest interaction energy values. The  $E_{\text{intermolecular}}$  value is the sum of the

energies involved in hydrogen bond interactions, hydrophobic interactions, and van der Waals interactions. Each molecular docking experiment was repeated three times to confirm the reproducibility.

## *2.6 Radiolabelling procedures*

### *2.6.1 Production of n.c.a. [<sup>18</sup>F]fluoride*

N.c.a. [<sup>18</sup>F]fluoride was produced via the <sup>18</sup>O(p,n)<sup>18</sup>F nuclear reaction from [<sup>18</sup>O]H<sub>2</sub>O (Rotem Industries Ltd, Hyox oxygen-18 enriched water, min. 98%) on an ACSI TR19/9 Cyclotron (Advanced Cyclotron Systems Inc., Richmond, Canada). Cyclotron-produced [<sup>18</sup>F]fluoride was trapped on a Waters SepPak<sup>®</sup> light QMA anion exchange cartridge (primed with 8 mL 0.5M K<sub>2</sub>CO<sub>3</sub> solution followed by 12 mL Barnstead water) or a Waters SepPak<sup>®</sup> QMA carbonate anion exchange cartridge (primed with 4 mL 0.5M K<sub>2</sub>CO<sub>3</sub> solution followed by 6 mL Barnstead water).

### *2.6.2 Fully automated synthesis*

Fully automated radiosynthesis were performed on a GE TRACERlab<sup>™</sup> FX (General Electric Company, Fairfield, Connecticut, United States) fully automated synthesis unit (ASU). ASU is contained within a fully sealed Comcer Hot Cell with ventilation into a gas-holdup system located within the Cyclotron Vault.

## *2.7 Biochemistry techniques and methods*

### *2.7.1 Cell culture*

EMT6 cells a murine mammary epithelial cell line were grown in DMEM/F12 medium (in-house preparation) supplemented with 10% fetal bovine serum (FBS) (Gibco<sup>®</sup> cat#A7364.01), 2 mM l-glutamine (Invitrogen) and 1% Gibco<sup>™</sup> Penicillin-Streptomycin (10,000 µg/mL) (cat#15140-122). MDA-MB-231 cells (ATCC) a human triple-negative breast cancer cell line was grown in DMEM/F12 medium (in-house preparation) supplemented with 10% fetal bovine serum (FBS) (Gibco<sup>®</sup> cat#A7364.01) and 1% Gibco<sup>™</sup> Penicillin-Streptomycin (10,000 µg/mL) (cat#15140-122). EMT6 and MDA-MB-231 cells were incubated at 37 °C in a humidified incubator with a 5% (v/v) CO<sub>2</sub> atmosphere (ThermoForma Series II Water Jacketed CO<sub>2</sub> Incubator). Cells were

kept for a maximum of 20 passages, with the cell growth medium being changed every other day and routinely reseeded once 90% confluency was achieved.

### 2.7.2 Cell line transfection

Plasmids were obtained from Addgene. HA-HIF1alpha P402A/P564A-pcDNA3 was a gift from William Kaelin (Addgene plasmid # 18955 ; <http://n2t.net/addgene:18955>; RRID:Addgene\_18955) [113] and HA-HIF1alpha-pcDNA3 was a gift from William Kaelin (Addgene plasmid # 18949 ; <http://n2t.net/addgene:18949> ; RRID:Addgene\_18949) [114].

MDA-MB-231 cells were incubated with the above plasmids and Genetecin (G418) to select for those cells expressing the plasmid. Blank transfection was done with GFP-containing plasmid.

### 2.7.3 Western blot

Cell lysate protein content was determined by BCA Analysis. Western blot samples were prepared at the desired protein loading with dilution with 2X Laemmli buffer solution (Sigma, cat# S3401) in a microcentrifuge tube. Samples were then denaturation at 95 °C for 5 minutes on the Thermoshaker at 400 rpm. Pre-manufactured Mini-Protean TGX 4-15%, 15 well combs, 15 mL/well (Cat# 4561086) gels from Bio-rad were then loaded into a Mini-Protean Tetra cell. Running buffer prepared as per **section 2.2.4** and loaded into the tetra cell up to the designated lines. Samples were then loaded into the designated wells. ThermoScientific PageRuler™ Plus Prestained Protein Ladder, 10 to 250 kDa (Cat# 26619) was loaded in well 1 (5 µL). SDS-PAGE was then allowed to run at 200 V for 30-40 minutes at ambient temperature.

Upon completion, the gel was removed from its plastic container and washed with running buffer for 5 minutes, before western transfer. The wet transfer was completed in the Mini-protean tetra cell at 300 mA for 3 hours at ambient temperature with transfer buffer as per **section 2.2.5**. The transfer stack was built with extra thick blot paper (BioRad, cat# 1703965) and PVDF Immun-Blot membrane (BioRad, cat#162-0177). PDVF membrane before use was cut to size and washed with methanol for 10 minutes, followed by transfer buffer for 10 minutes before use in the transfer stack. Blot transfer was run at 300 mA for three hours at room temperature using an ice pack in

the tetra cell. Once completed the blot was removed from the stack and washed with TBS-T (3 x 5 mL, 5-minute washes).

#### *2.7.3.1 HIF-1 $\alpha$ antibody procedure*

Washed blots from **section 2.7.3** were blocked using 10% milk in TBS-T for 1 hour. Multiple HIF-1 $\alpha$  antibodies were used throughout the evolution of this procedure, this procedure contains the best methodology achieved to date. Primary HIF-1 alpha Antibody (Novus Biologicals, NB100-479) was applied in a 1:1000 dilution in 10% BSA in PBS (1  $\mu$ g/mL final concentration). The HIF-1 $\alpha$  antibody was allowed to incubate for 24 hours at 4 °C on a rocker. After incubation, the primary antibody was removed and saved for future blots (used up to 4 times). The membrane was washed with TBS-T (3 x 5 mL, 5-minute washes), followed by the application of the secondary antibody. WesternSure® Goat anti-Rabbit HRP Secondary Antibody (LICOR, cat# 926-80011) was applied in a 1:2000 dilution in 10% milk in TBS-T and allowed to rock at ambient temperature for two hours. After incubation, the secondary antibody was removed and saved for future blots (used up to 7 times). The membrane was again washed with TBS-T (3 x 5 mL, 5-minute washes) and then placed onto a LICOR Odyssey® XF Imaging Tray. Once mounted on the Odyssey imaging drawer, the drawer was left open and the BioRad Clarity Western ECL solution (2 mL, cat #170-5060) was added to the membrane. The drawer was left open for five minutes, to allow for exposure to the chemiluminescent substrate. After exposure was complete the drawer was closed, and the blot was scanned for the required time.

#### *2.7.3.2 B-actin antibody procedure*

Washed blot from **section 2.7.3** was blocked using 10% milk in TBS-T for 1 hour. Primary Anti-Actin (20-33) antibody produced in rabbits (SigmaAldrich, A5060) was applied in a 1:2000 dilution in 2.5% BSA in PBS. B-actin antibody was allowed to incubate for 2 hours at ambient temperature on a rocker. After incubation, the primary antibody was removed and saved for future blots (used up to 8 times). The membrane was washed with TBS-T (3 x 5 mL, 5-minute washes), followed by the application of the secondary antibody. WesternSure® Goat anti-Rabbit HRP Secondary Antibody (LICOR, cat# 926-80011) was applied in a 1:5000 dilution in 2.5% milk in TBS-T and allowed to rock at ambient temperature for two hours. After incubation, the secondary

antibody was removed and saved for future blots (used up to 7 times). The membrane was again washed with TBS-T (3 x 5 mL, 5-minute washes) and then placed onto a LICOR Odyssey® XF Imaging Tray. Once mounted on the Odyssey imaging drawer, the drawer was left open and the BioRad Clarity Western ECL solution (2 mL, cat #170-5060) was added to the membrane. The drawer was left open for five minutes, to allow for exposure to the chemiluminescent substrate. After exposure was complete the drawer was closed, and the blot was scanned for the required time.

#### 2.7.4 Bicinchoninic acid (BCA) assay

Samples for BCA assay were prepared with RIPA lysates. Lysates in microcentrifuge tubes were manually agitated three times with a syringe (1 mL) and a 16G needle (blue color code). Samples were then centrifuged at 14,000 rpm, 4 °C for 15 minutes. The supernatant was removed (20 µL) and placed into 96 well plates for analysis. A standard protein curve was created using an albumin standard (2 mg/mL) to the desired concentrations in RIPA buffer. Typical curve concentrations were as follows; 1000, 800, 600, 500, 400, 300, 200, 100, 50 and 0 µg/mL. Standard curve samples and unknown samples are all plated in duplicate. To each plated sample BCA working solution (1:50, 200 µL) was applied from the Pierce™ BCA Protein Assay Kit (cat # 23227). 96-well plate was then covered with parafilm and allowed to incubate at 37 °C for 30 minutes. The developed 96-well plate was then analyzed using a Molecular Devices plate reader. The protein content is determined in µg/mL.

#### 2.7.5 Confocal analysis of Compound 33 (NBD-link-c-(Ppg)LLFVY)

Cells were grown on coverslips placed into 6 well plates. The growth medium was removed by washing the wells with ambient temperature PBS (4 x 2 mL/well). Once washed the cells were fixed to the coverslip at ambient temperature for 25 minutes using 4% paraformaldehyde in PBS (2 mL/well). After fixation, wells were once again washed with PBS (4 x 2 mL/well). Following fixation, cells were permeabilized at ambient temperature over 5 minutes with 0.5% Triton X-100 in PBS (2 mL/well). After permeabilization, wells were once again washed with PBS (4 x 2 mL/well). Cells were then blocked with 10% BSA in PBS for 1 hour at ambient temperature. The blocking solution was then removed and the peptide of interest (compound 33, 500 µL of a 100

$\mu\text{M}$  solution) was administered and allowed to incubate at ambient temperature for 60 minutes. After peptide incubation, the wells were washed with PBS containing 0.1% Triton X-100 (4 x 2 mL/well), followed by washing with plain PBS (4 x 2 mL/well). Finally, the cells were mounted using Mowiol mounting medium containing DAPI as required (20  $\mu\text{L}$ ). Mounted slides were then carefully inverted onto glass slides and placed in a drawer overnight. Slides were imaged one day after preparation.

#### 2.7.6 Cell uptake studies for HIF-1 $\alpha$ binding compounds

The required cell line was grown to confluency in T75 flask (Nunc EasyFlask Nunclon Delta). Cells were trypsinized with 0.25% Gibco™ Trypsin-EDTA (cat# 25200-072) for 5 – 15 minutes at 37 °C. Once detached from the flask, 9 mL of cell culture media was added and mixed thoroughly. Cells were removed from the flask (9 mL) to a 15 mL falcon tube, with 0.5 mL of the mixture being placed in a microcentrifuge tube. The small aliquot in the microcentrifuge tube was used for cell counting to determine the number of cells per mL of media. Cells were then further diluted in a 50 mL falcon tube with cell culture media to the desired concentration for plating (50k to 150k cells/mL). Cells were plated into 12-well plates 48 hours before the start of the assay using fresh growth medium (1 mL), so that cells reach 95% confluency before use.

After radiotracer synthesis, the required radioactivity was diluted to achieve 0.3 MBq of radiolabelled product per well in Krebs buffer (300  $\mu\text{L}$ ). Once the radiotracer dilution was completed, the starting radioactivity for the assay is recorded on a dose calibrator with the total activity amount and time recorded. Before radiotracer addition to the cells, the growth medium was removed and the cells were rinsed with room temperature Krebs buffer (3 x 500  $\mu\text{L}$ ). Then the radiotracer solution (300  $\mu\text{L}$ ) can be added to each well at a specific time according to *Table 2.1*. This time chart was only a demonstration of a typical cell uptake experiment and can be modified to the given time points required. Plates were then incubated at 37°C for various time points and oxygen conditions.

Upon completion of the time point, the radiotracer was removed and the wells were rinsed with ice-cold PBS buffer (3 x 500  $\mu\text{L}$ ) to stop the uptake. Additional rinses may be completed as

required including glycine-HCl wash (2 x 500  $\mu$ L, 5 minutes wait in-between) or 10% DMSO in Krebs wash (500  $\mu$ L)

*Table 2.1. Time points chart, for the in vitro analysis of HIF-1 $\alpha$  binding compounds. Including both cell uptake and BCA assay lysis time points. \* This is not a lysis time point, but an incubation time point with the BCA reagents.*

<b>Time point and oxygen variable</b>	<b>Radiotracer Start time (min)</b>	<b>Radiotracer End time (min)</b>	<b>Lyse cell Start time (min)</b>	<b>Lyse cells End time (min)</b>
120 min, Normoxic	0	120	121	131
120 min, Hypoxic	1	121	122	132
90 min, Normoxic	2	92	93	103
90 min, Hypoxic	3	93	94	104
60 min, Normoxic	4	64	65	75
60 min, Hypoxic	5	65	66	76
30 min, Normoxic	6	36	37	47
30 min, Hypoxic	7	37	38	48
15 min, Normoxic	8	23	24	34
15 min, Hypoxic	9	24	25	35
5 min, Normoxic	10	15	16	26
5 min, Hypoxic	11	16	17	27
1 min, Normoxic	12	13	14	24
1 min, Hypoxic	13	14	15	25
BCA Assay, Normoxic	n/a	n/a	65	75
BCA Assay, Hypoxic	n/a	n/a	66	76
BCA Incubation	n/a	n/a	91*	116*

Once the wells are thoroughly washed the cells were lysed with RIPA buffer (400  $\mu$ L) in each well. The RIPA solution was allowed to sit on the cells for a minimum of 10 minutes. Cell lysates were then removed with scraping and mixing of the lysate in the wells. Cell lysate (300  $\mu$ L) was removed from each well into labelled scintillation vials for gamma counting. For protein

quantification by BCA assay, 3 wells on one 12-well plate were used. On these wells, no radiotracer will be placed, instead, Krebs buffer was added until the cells were lysed.

Acquired gamma counter data along with BCA data was then analyzed to obtain the percent applied radiotracer uptake per mg protein. For experiments completed under hypoxic conditions, the medium was preconditioned for 3–4 h in a special hypoxia chamber at 1% O<sub>2</sub> and 5% CO<sub>2</sub> at 37 °C, before radiotracer addition. For experiments completed with chemical overexpression of HIF-1 $\alpha$ , CoCl<sub>2</sub> or DFO were allowed to incubate in the medium at normoxic conditions at 37 °C.

#### 2.7.7 Cell uptake for nitroimidazole compounds using the hypoxia chamber

The required cell line was grown to confluency in T75 flask (Nunc EasyFlask Nunclon Delta). Cells were trypsinized with 0.25% Gibco™ Trypsin-EDTA (cat# 25200-072) for 5 – 15 minutes at 37 °C. Once detached from the flask, 9 mL of cell culture media was added and mixed thoroughly. Cells were removed from the flask (9 mL) to a 15 mL falcon tube, with 0.5 mL of the mixture being placed in a microcentrifuge tube. The small aliquot in the microcentrifuge tube was used for cell counting to determine the number of cells per mL of media. Cells were then further diluted in a 50 mL falcon tube with cell culture media to the desired concentration for plating (100k cells/mL). Cells were plated into 12-well plates 48 hours before the start of the assay using fresh growth medium (1 mL), so that cells reach 95% confluency before treatment. Cells for hypoxia time points are seeded only one 6-well per 12-well plate, so each time point is isolated to one plate. 24 hours before the addition of the nitroimidazole radiotracer, the cell media was removed and the cells were washed with Krebs (3x1 mL). New Opti-MEM media is then applied to the cells and the plates were placed into the normoxic and hypoxic incubators (1% O<sub>2</sub> and 5% CO<sub>2</sub>) for 24 hours before radiotracer addition.

After radiotracer synthesis, the required radioactivity was diluted to achieve 0.3 to 0.6 MBq of radiolabelled product per well in Krebs buffer with 5% ethanol (250  $\mu$ L). Once the radiotracer dilution was completed, the starting radioactivity for the assay was recorded on a dose calibrator with the total activity amount and time recorded. Before radiotracer addition to the cells, the growth medium was removed and the cells were rinsed with room temperature Krebs buffer (3 x 500  $\mu$ L). Then the radiotracer solution (250  $\mu$ L) was added to each well at specific times according

to *Table 2.2*. This time sheet was only a demonstration of a typical cell uptake experiment and can be modified to the given time points required.

Plates were then incubated at 37°C for various time points and oxygen conditions. At each time points, the radiotracer was removed and the wells were rinsed with ice-cold PBS buffer (3 x 500 µL) to stop the uptake. Once the wells were thoroughly washed the cells were lysed with RIPA buffer (400 µL) in each well. The RIPA solution was allowed to sit on the cells for a minimum of 10 minutes. Cell lysates were then removed with scraping and mixing of the lysate in the wells. Cell lysate (300 µL) was removed from each well into labelled scintillation vials for gamma counting.

For protein quantification by BCA assay, 3 wells on one 12-well plate will be used. On these wells, no radiotracer will be placed, instead, Krebs buffer with 5% ethanol was added until the cells were lysed.

*Table 2.2. Time points chart for nitroimidazole cell uptake with BCA assay. Each time point is an individual 12-well plate, where 3 of the wells are for the BCA assay and 3 wells are for radiotracer cell uptake analysis. Plates are subjected to 24 hours of normoxic/hypoxic treatment, before radiotracer addition.*

<b>Time point and oxygen variable</b>	<b>Wash cells (min)</b>	<b>Radiotracer Start time (min)</b>	<b>Radiotracer End time (min)</b>	<b>Lyse cell Start time (min)</b>	<b>Lyse cells End time (min)</b>
1 min Hypoxia	0	1	2	3	13
60 min Hypoxia	5	6	66	67	77
120 min Hypoxia	7	8	128	129	139
180 min Hypoxia	9	10	190	191	201
1 min Normoxia	12	13	14	15	25
60 min Normoxia	17	18	78	79	89
120 min Normoxia	19	20	140	141	151
180 min Normoxia	21	22	202	203	213

Acquired gamma counter data along with BCA data was then analyzed in-order to obtain the percent applied radiotracer uptake per mg protein.

#### 2.7.8 Silencing RNA transfection of MDA-MB-231 cells

For analysis of silencing, testing was completed in 6 well plates. The procedure was adapted from “Lipofectamine® RNAiMAX Transfection Procedure” found on the ThermoFisher Scientific website. Briefly, Gibco Opti-MEM media (Cat# 31985-070) (150  $\mu$ L) is combined with Invitrogen lipofectamine RNAiMax (Cat# 56531) (9  $\mu$ L) as solution A. Solution B was prepared with Opti-MEM (150  $\mu$ L) and siRNA (30 pmol). Two siRNA were used for this solution, either Invitrogen Silencer Select Negative Control #1 siRNA (cat# 4390843) or Invitrogen HIF1 $\alpha$  Silencer Select Validated siRNA (cat# s6541). Solutions A and B were combined and allowed to sit at ambient temperature for 5 minutes. Once 5 minutes had passed, the media was removed from the cells in the 6-well plate. The 6-well plate was then washed with Krebs (3 x 1 mL) and the transfection solution (300  $\mu$ L) was then added to each well. Cells were incubated for 24 hours at 37 °C. Once silencing was completed, the transfection reagent was removed, and cells were washed with Krebs (3 x 1 mL). Cells were then either subjected to radiotracer addition, or cells were lysed with RIPA buffer (100  $\mu$ L) containing protease inhibitor (0.1  $\mu$ L) for protein analysis with western blot.

#### 2.7.9 In vivo metabolic stability

A normal female BALB/c mouse was put under isoflurane anesthesia. A radiotracer solution of interest containing ~20 to 25 MBq of radioactivity was injected intravenously. For [<sup>18</sup>F]FBNA, [<sup>18</sup>F]FMISO or [<sup>18</sup>F]FAZA, the radiotracer injection solution was 8% Ethanol in saline. For [<sup>18</sup>F]FPeP4, the radiotracer injection solution was 5% propylene glycol in saline. Blood samples (20 – 40  $\mu$ L) are removed from the tail vein at designated time points. Time points collected for [<sup>18</sup>F]FBNA, [<sup>18</sup>F]FMISO or [<sup>18</sup>F]FAZA included 5, 15, 30, 45, and 60 minutes post-injection. Time points collected for [<sup>18</sup>F]FPeP4 included 5, 15, and 30 minutes post-injection.

Blood samples were placed in a microcentrifuge tube and the plasma was separated using centrifugation (13,000g, 5 minutes). Plasma was removed into an additional microcentrifuge tube and methanol (100 mL) was used to subsequently precipitate the protein from the solution.

Additional centrifugation of the sample was completed (13,000g, 5 minutes) and the methanol was removed to a final microcentrifuge tube. The methanol supernatant was tested using radio TLC, with developed TLC plates being analyzed using a Bioscan AR-2000. For [ $^{18}\text{F}$ ]FBNA, [ $^{18}\text{F}$ ]FMISO or [ $^{18}\text{F}$ ]FAZA the mobile phase was 1:1 Ethanol : EtOAc. For [ $^{18}\text{F}$ ]FPeP4 the mobile phase was 1:8 MeOH:CH<sub>2</sub>Cl<sub>2</sub>. Additionally, blood components in the microcentrifuge tubes were analyzed using a HIDEX gamma counter.

#### 2.7.10 Dynamic PET imaging

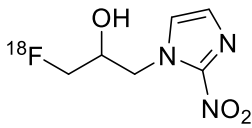
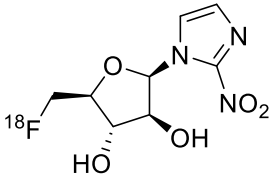
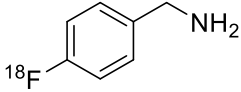
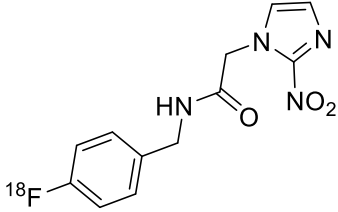
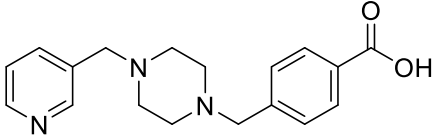
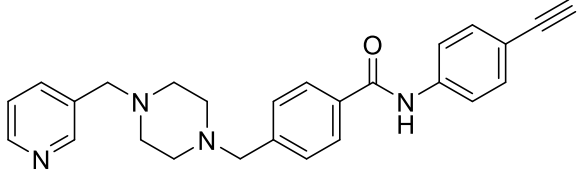
All animal experiments were carried out following the guidelines of the Canadian Council on Animal Care (CCAC) and approved by the local animal care committee of the Cross Cancer Institute. Human MCF7 cells ( $5 \times 10^6$  cells in 100  $\mu\text{L}$  PBS/Matrigel 50:50), triple-negative MDA-MB-231 cells ( $5 \times 10^6$  cells in 100  $\mu\text{L}$  PBS) and HIF-1 $\alpha$  transfection MDA-MB-231 18955 cells ( $5 \times 10^6$  cells in 100  $\mu\text{L}$  PBS +matrigel) were injected subcutaneously into the left shoulder of 8–10-week-old female NIH-III nude mice (Charles River, Saint-Constant, QC, Canada). MCF7-bearing mice also received a subcutaneously implanted 0.72 mg/pellet containing estrogen in a 60-day release preparation (Innovative Research of America, Sarasota, FL, USA) into the upper right flank. Tumors were grown for 3 to 4 weeks, reaching sizes of 300–500 mm<sup>3</sup>.

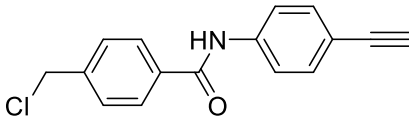
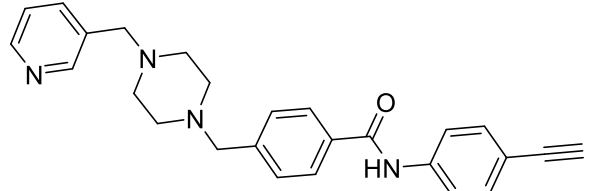
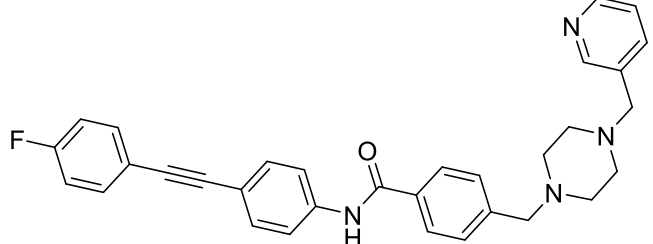
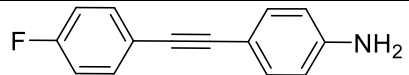
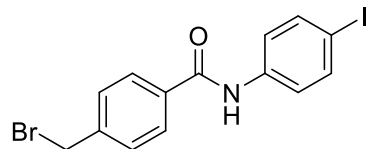
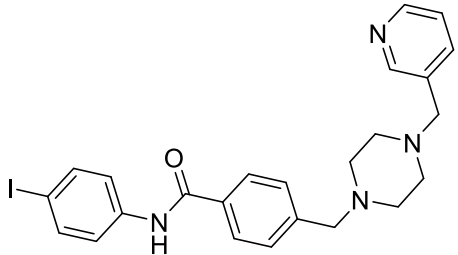
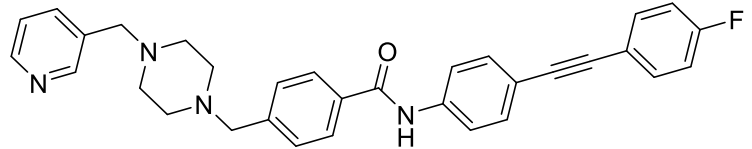
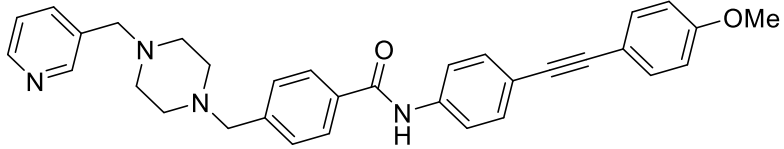
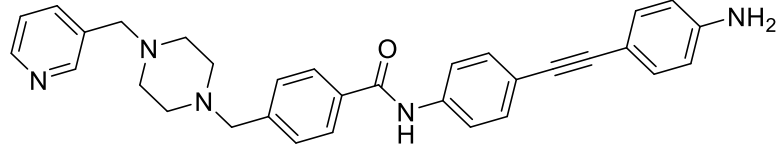
General anesthesia of tumor-bearing mice was induced with inhalation of isoflurane in 40% oxygen/60% nitrogen (gas flow = 1 mL/min), and the mice were subsequently fixed in the prone position. The body temperature was kept constant at 37 °C for the entire experiment. The mice were positioned in a prone position in the center of the field of view. A transmission scan for attenuation correction was not acquired. Injections were completed with  $\sim 4\text{--}7$  MBq of either [ $^{18}\text{F}$ ]FBNA, [ $^{18}\text{F}$ ]FMISO or [ $^{18}\text{F}$ ]FAZA in 100–200  $\mu\text{L}$  of saline (0.9%) containing 8 to 10% ethanol or  $\sim 4\text{--}7$  MBq of either [ $^{18}\text{F}$ ]SFB-link-c-(Ppg)LLFVY and [ $^{18}\text{F}$ ]FPeP4 in 100–200  $\mu\text{L}$  of saline (0.9%) containing 5% propylene glycol through a tail vein catheter. Data acquisition was performed over 180 min in a 3D list mode. The dynamic list mode data were sorted into sinograms with 65 time frames (10 x 2, 8 x 5, 6 x 10, 6 x 20, 8 x 60, 10 x 120, 5 x 300, and 12 x 600 s). The frames were reconstructed using maximum a posteriori (MAP) as reconstruction mode. The pixel size was 0.085 x 0.085 x 0.121 mm<sup>3</sup> (256 x 256 x 63), and the resolution in the center of the field of view was 1.8 mm. No correction for partial volume effects was applied. The image files were

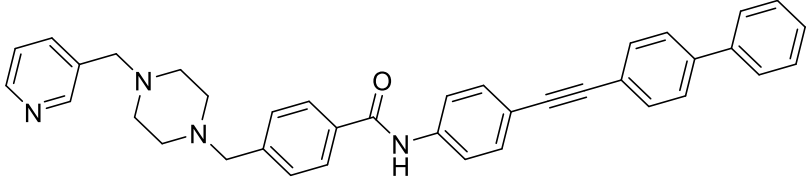
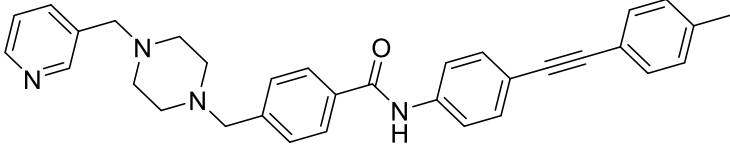
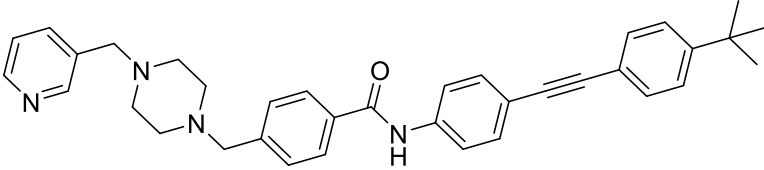
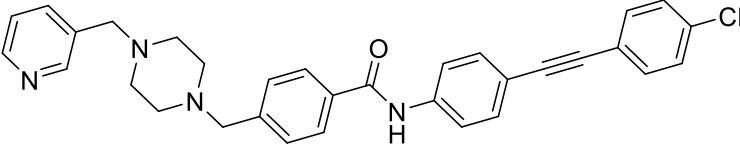
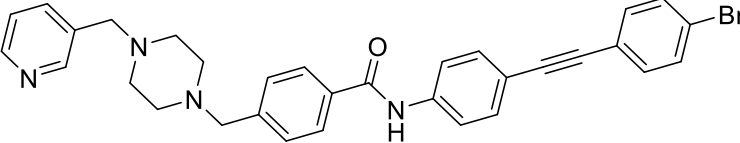
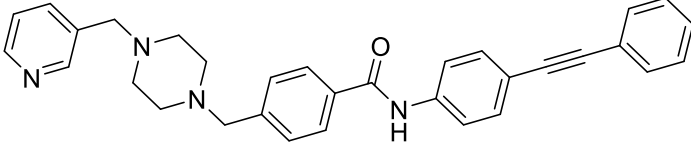
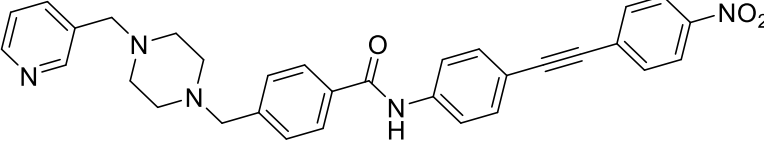
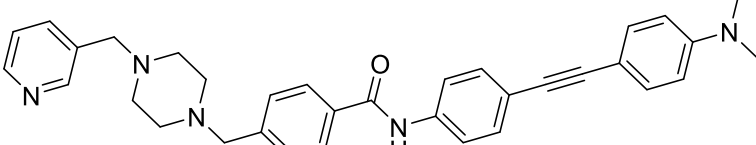
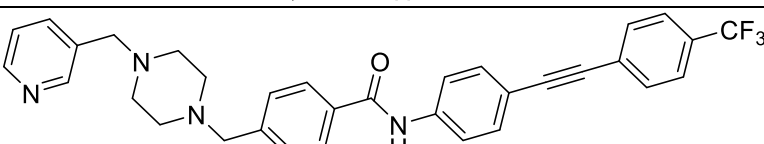
processed using the ROVER v 2.0.51 software (ABX GmbH, Radeberg, Germany). Masks defining 3D regions of interest (ROI) were set and the ROIs were defined by thresholding. Mean standardized uptake values  $[SUV]_{\text{mean}} = (\text{activity/mL tissue})/(\text{injected activity/body weight})$ , mL/g, were calculated for each ROI. All semi-quantified PET data are presented as means  $\pm$  SEM. TACs Time-activity curves (TACs) were constructed using Graph-Pad Prism 5.0 (GraphPad Software).

## 2.8 Summary of synthesized chemicals

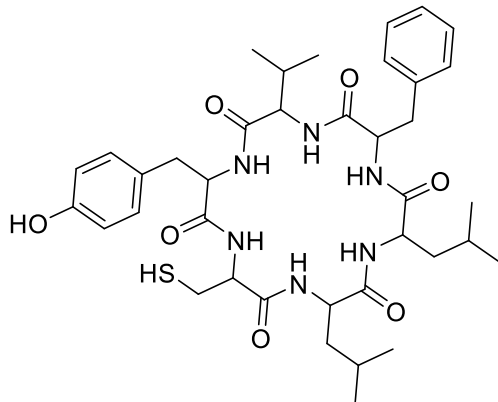
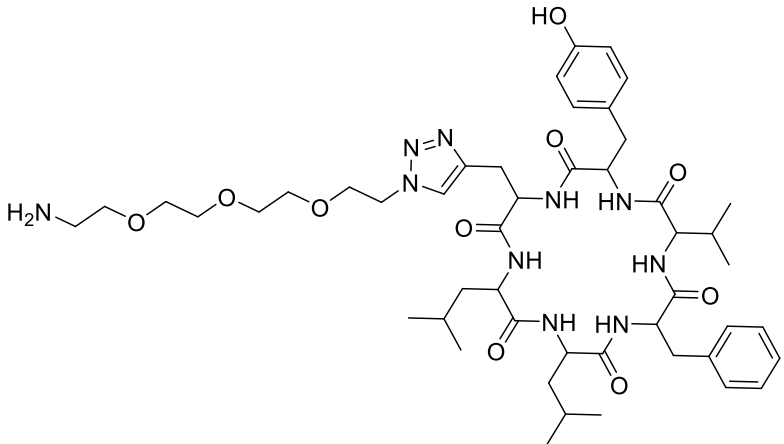
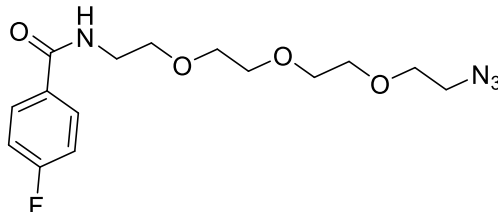
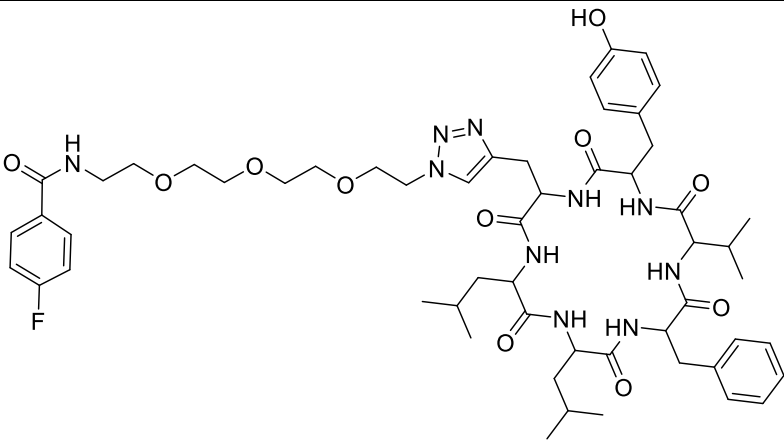
Table 2.3. Complete summary of all synthesized compounds, including compound ID, structure and page number location in the thesis document.

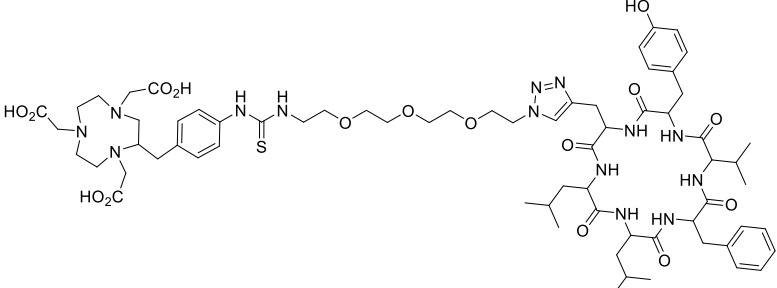
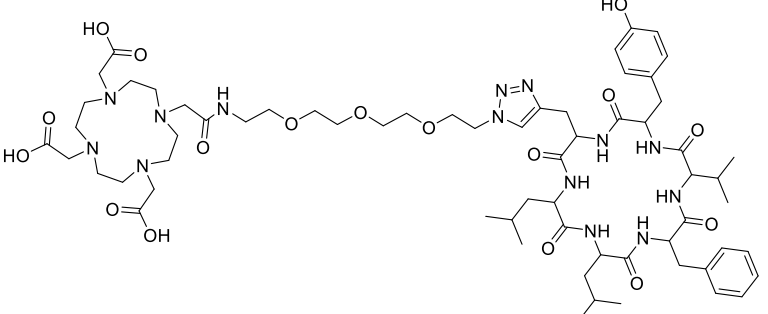
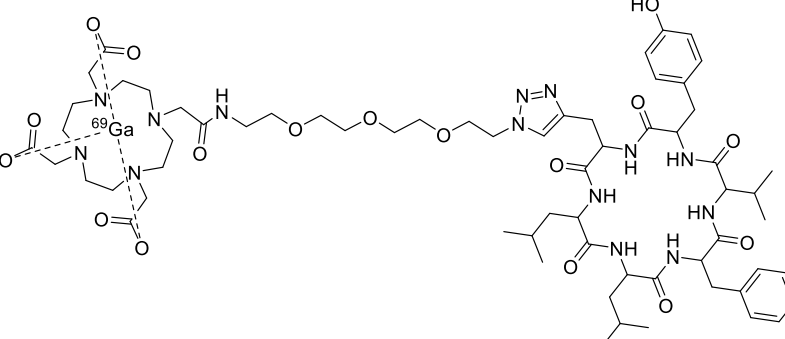
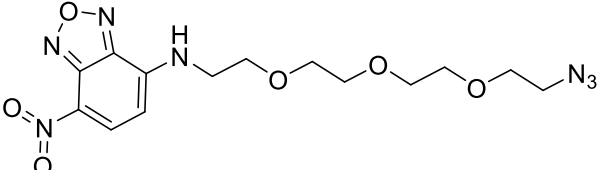
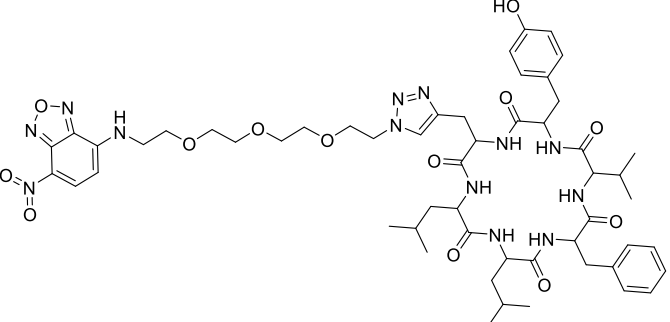
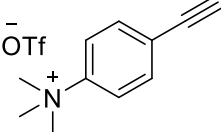
Compound ID	Structure	Page number
[ <sup>18</sup> F]FMISO		48
[ <sup>18</sup> F]FAZA		51
[ <sup>18</sup> F]FBAmine		54
[ <sup>18</sup> F]FBNA		55
1		78
2		79

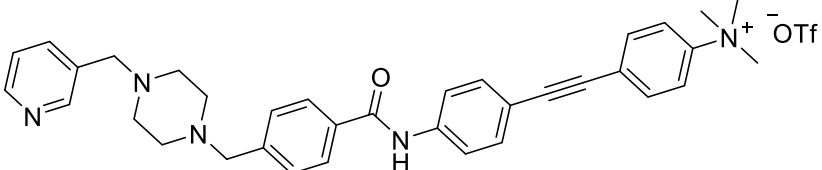
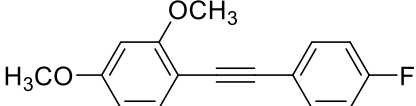
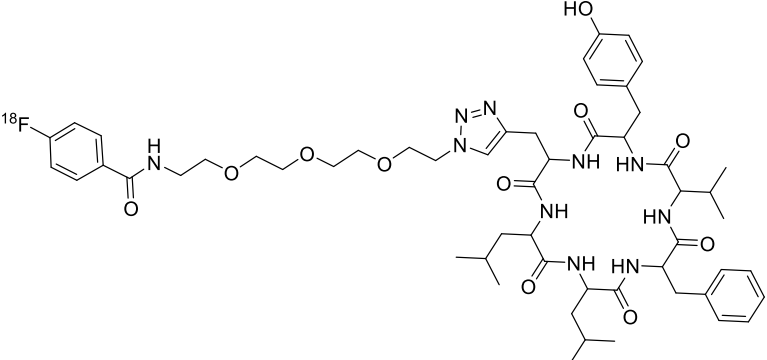
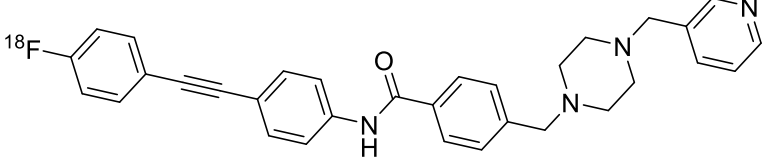
3		79
4		80
5		81
6		84
7		85
8		85
9		88
10		88
11		89

12		89
13		89
14		90
15		90
16		91
17		91
18		92
19		92
20		92

21		93
22		93
23		93
24		94

25		94
26		94
27		95
28		95

29		117
30		117
31		118
32		123
33		123
34		124

35		125
36		132
[ <sup>18</sup> F]SFB-link-c-(Ppg)LLVY		115
[ <sup>18</sup> F]FPeP4		135

## Chapter 3: Synthesis of radiolabelled nitroimidazole compounds

Herein, we report the synthesis of [ $^{18}\text{F}$ ]FMISO and [ $^{18}\text{F}$ ]FAZA, as two traditional hypoxia imaging agents. Additionally, we also synthesize a novel nitroimidazole hypoxia radiotracer, *N*-(4-[ $^{18}\text{F}$ ]fluorobenzyl)-2-(2-nitro-1*H*-imidazol-1-yl)-acetamide ([ $^{18}\text{F}$ ]FBNA). The novel nitroimidazole compound was designed to have a higher lipophilicity than both [ $^{18}\text{F}$ ]FMISO and [ $^{18}\text{F}$ ]FAZA, in order to improve the pharmacokinetics and biodistribution.

### 3.1 Fully automated synthesis

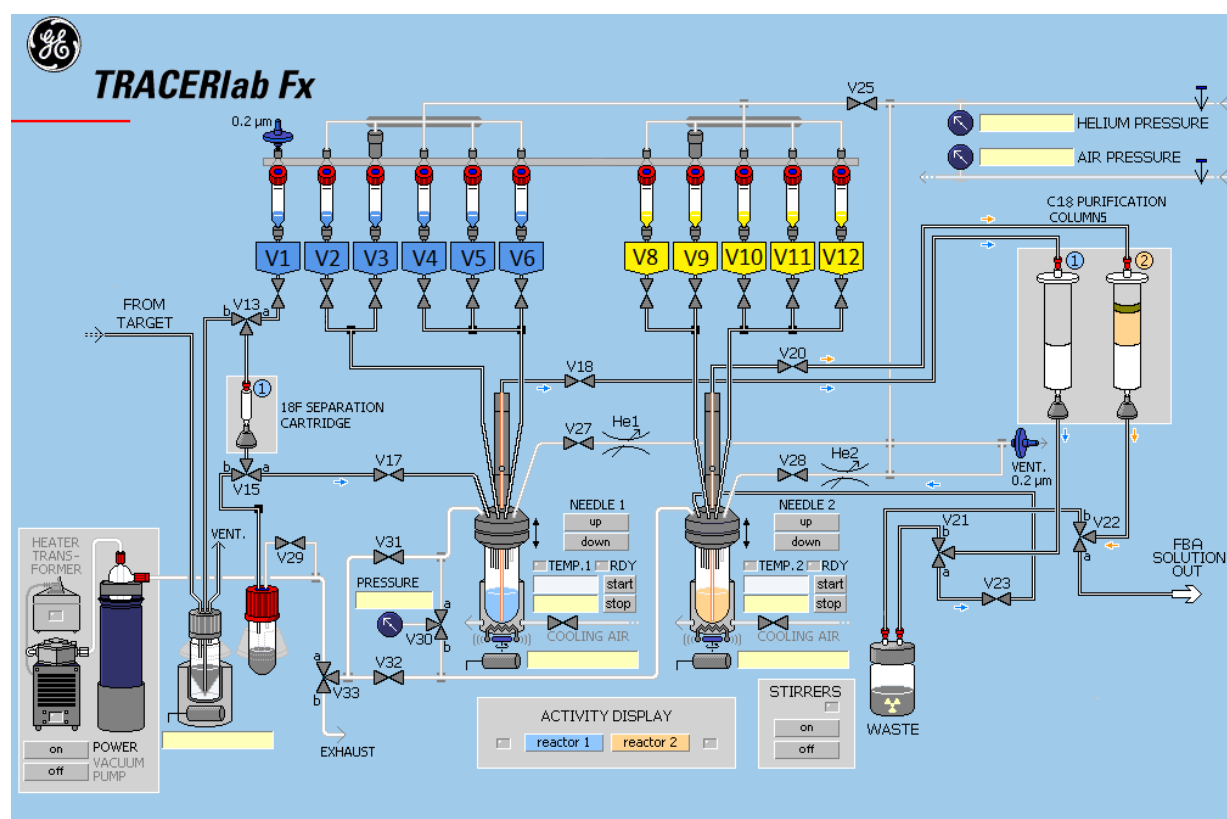


Figure 3.1. GE TRACERlab Fx automated synthesis unit modifications to convert a two synthesis FDG unit into a one synthesis two reactor ASU.

Radiosynthesis of [ $^{18}\text{F}$ ]fluoroazomycin arabinoside ([ $^{18}\text{F}$ ]FAZA), [ $^{18}\text{F}$ ]fluoromisonidazole ([ $^{18}\text{F}$ ]FMISO), and 4-[ $^{18}\text{F}$ ]fluorobenzylamine ([ $^{18}\text{F}$ ]FBAmine) were performed on a GE TRACERlab™ FX (General Electric Company, Fairfield, Connecticut, United States) fully automated synthesis unit (ASU). Synthesis of *N*-(4-[ $^{18}\text{F}$ ]fluorobenzyl)-2-(2-nitro-1*H*-imidazol-1-

yl)-acetamide ( $[^{18}\text{F}]\text{FBNA}$ ) was performed manually from the starting material of  $[^{18}\text{F}]\text{FBAmine}$ . All automated syntheses were done as per our published procedure [115], with modifications to the ASU shown in *Figure 3.1*.

### 3.2 Radiosynthesis of $[^{18}\text{F}]\text{fluoromisonidazole}$ ( $[^{18}\text{F}]\text{FMISO}$ )

Non-radioactive FMISO reference was tested on HPLC using the FMISO method to evaluate product retention time on a Luna C18(2) column, see *Figure 3.3*. Once completed the radiosynthesis was optimized on an automated synthesis unit.

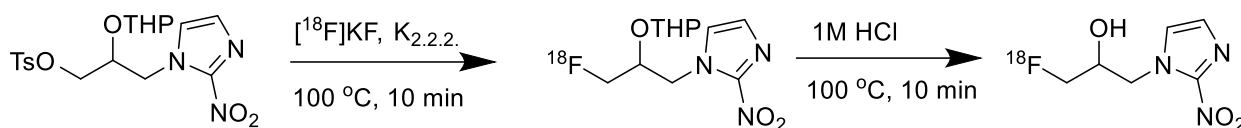


*Figure 3.2. Radiosynthesis pathway for the synthesis of  $[^{18}\text{F}]\text{FMISO}$ .*

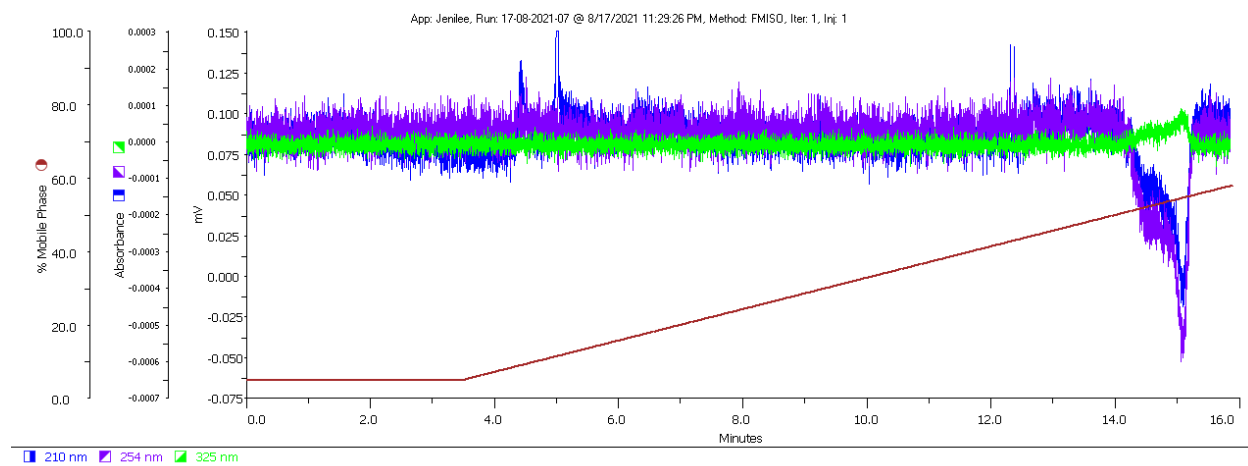


*Figure 3.3. HPLC analysis of  $[^{19}\text{F}]\text{FMISO}$ , non-radioactive reference compound for  $[^{18}\text{F}]\text{FMISO}$ . Three UV channels are shown, including: 325 nm in green, 254 nm in purple and 210 nm in blue. Positive absorbance only observed in the 325 nm channel.*

Synthesis of  $[^{18}\text{F}]\text{FMISO}$  was completed as follows:  $[^{18}\text{F}]\text{fluoride}$  in water was trapped on a Waters SepPak QMA carbonate (46 mg) cartridge (primed with 4 mL 0.5 M  $\text{K}_2\text{CO}_3$  solution, followed by 6 mL Barnstead water). Vial 1 (V1) containing an in-house solution of  $\text{K}_2.2.2./\text{K}_2\text{CO}_3$  in 86%  $\text{CH}_3\text{CN}:\text{H}_2\text{O}$  (V1: 1 mL) was used to elute the QMA cartridge into reactor 1 (R1).  $[^{18}\text{F}]\text{KF}$  was

dried azeotropically (V2: 1.5 mL CH<sub>3</sub>CN) under nitrogen flow and vacuum at 85 °C for 15 minutes. Once dried, NITTP precursor (5 mg) in CH<sub>3</sub>CN (V3: 1 mL) was added, and the fluorination reaction was allowed to proceed for 10 minutes at 100 °C. Upon completion, the reactor was cooled to 30 °C and then 1 M hydrochloric acid solution (V4: 1 mL) was added to reactor 1 and the deprotection was allowed to proceed for 10 minutes at 100 °C.

Again reactor 1 was allowed to cool to 30 °C and then 30% w/v sodium acetate solution in water (V5: 1 mL) was added to neutralize the reaction. The final mixture was pushed through a Waters SepPak Alumina N light cartridge (primed with 12 mL water) into a product vial containing a vent needle. Collected ASU eluent (3 mL) was directly injected onto HPLC using an isocratic elution of 8% Ethanol in water at 2 mL/min on a Luna C18(2) column. The product was collected in fractions to achieve the best concentrations for direct animal injection. Retention time on HPLC is 14.5 to 17.4 min, the product is a very wide peak that drastically overloads the detector, see *Figure 3.4*.

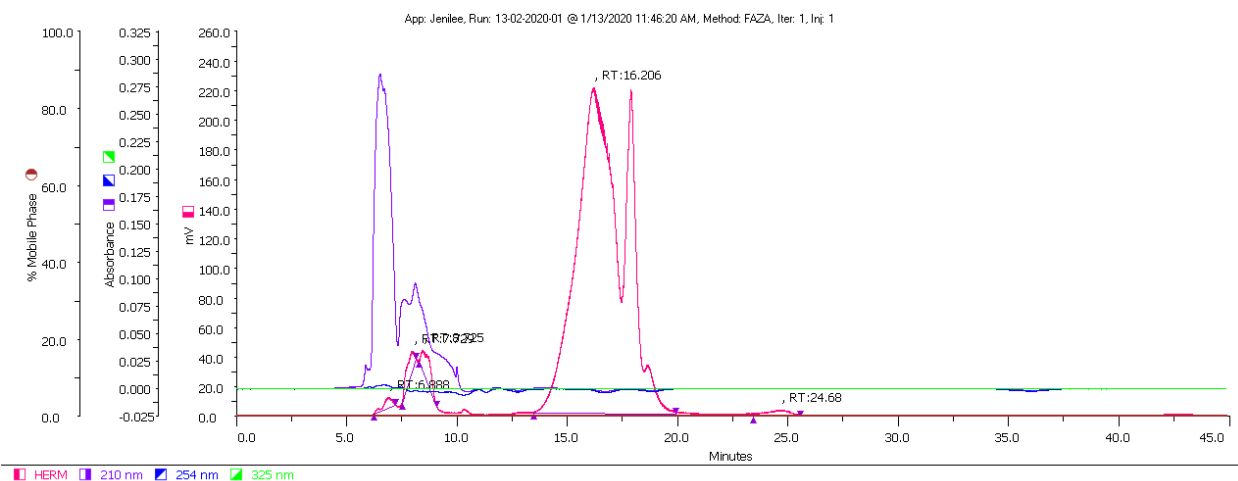


*Figure 3.4. Typical HPLC analysis of [<sup>18</sup>F]FMISO as produced on the ASU. Three UV channels are shown, including: 325 nm in green, 254 nm in blue and 210 nm in purple. HERM radioactivity channel is shown in pink.*

Quality control (QC) injection was done using gradient elution (FMISO method) in water:CH<sub>3</sub>CN, leading to a retention time of 15.4 min, see *Figure 3.5*. Overall [<sup>18</sup>F]FMISO could be achieved in 58.1 ± 17.9% dcy., from starting [<sup>18</sup>F]fluoride after a total synthesis time of 140 min (n=8). Purity

was >99% as determined by HPLC. Co-injection of non-radioactive reference compound and [ $^{18}\text{F}$ ]FMISO was completed as seen in *Figure 3.6*. It should be noted that [ $^{18}\text{F}$ ]FMISO, should not be dried to be reconstituted. Under all tested rotary evaporation conditions >10% defluorination was witnessed, when [ $^{18}\text{F}$ ]FMISO was volume reduced from the HPLC collected eluent.

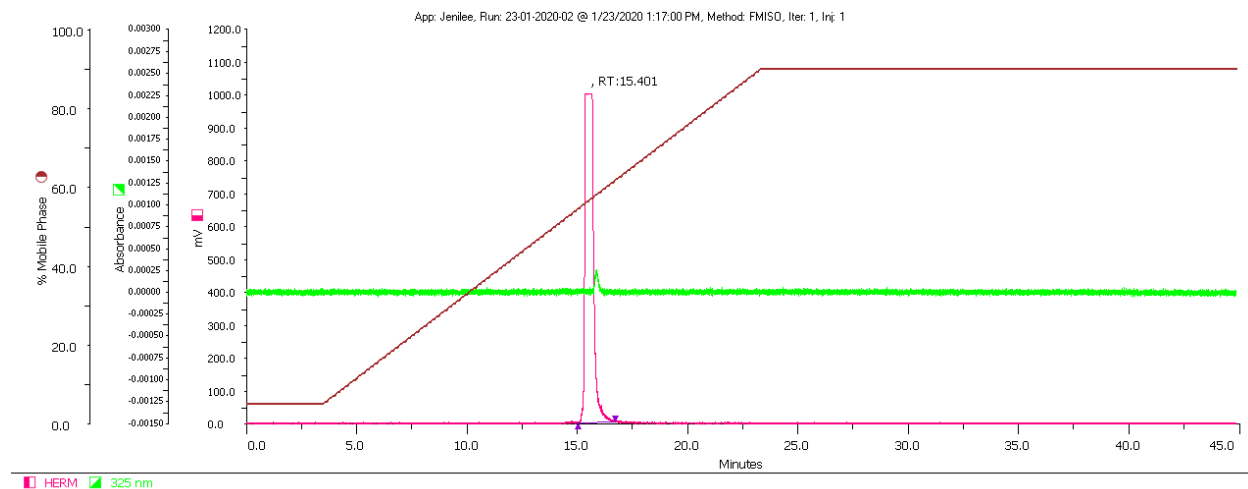


*Figure 3.5. Quality control injection of [ $^{18}\text{F}$ ]FMISO, from HPLC purified product. One UV channels shown as 325 nm in green, showing unknown non-radioactive contaminant. HERM radioactivity channel is shown in pink.*

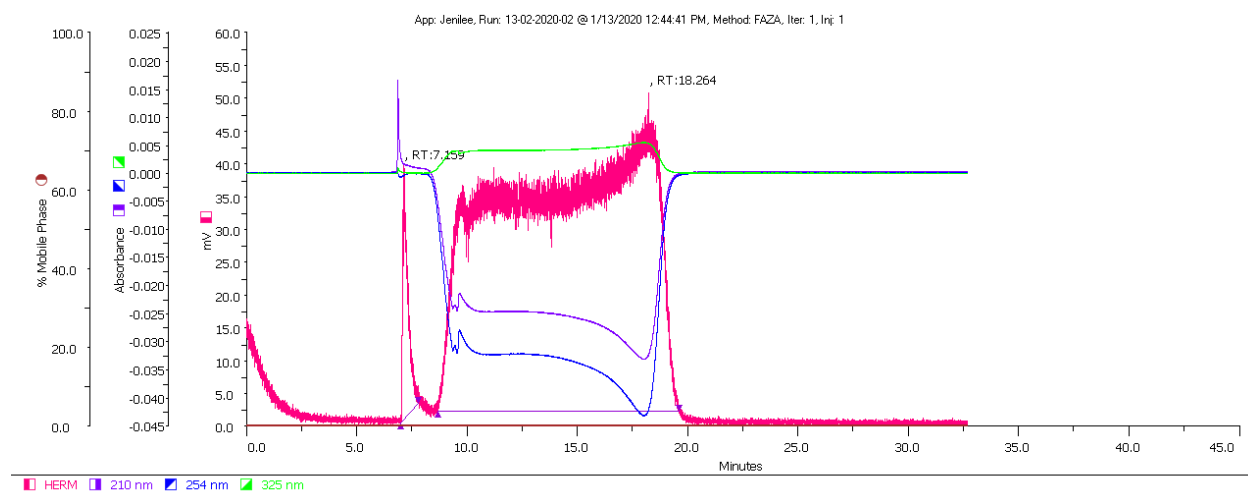


*Figure 3.6. Co-injection of HPLC purified [ $^{18}\text{F}$ ]FMISO and [ $^{19}\text{F}$ ]FMISO. Three UV channels are shown, including: 325 nm in green, 254 nm in blue and 210 nm in purple. HERM radioactivity channel is shown in pink.*

### 3.3 Radiosynthesis of [ $^{18}\text{F}$ ]fluoroazomycin arabinoside ([ $^{18}\text{F}$ ]FAZA)

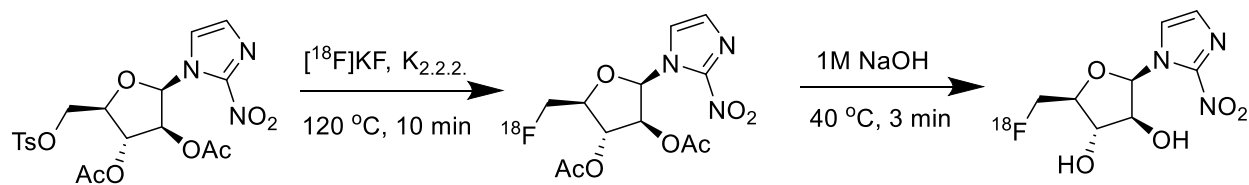


Figure 3.7. Radiosynthesis pathway for the synthesis of [ $^{18}\text{F}$ ]FAZA.

Non-radioactive FAZA reference was tested on HPLC using the FMISO method to evaluate product retention time on a Luna C18(2) column, see Figure 3.8. Once completed the radiosynthesis was optimized on an automated synthesis unit.

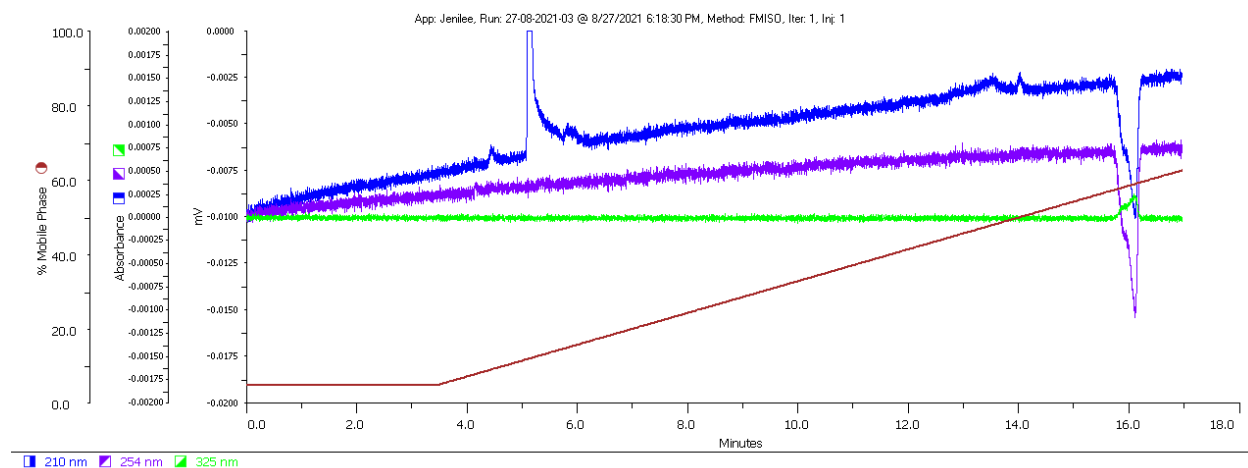
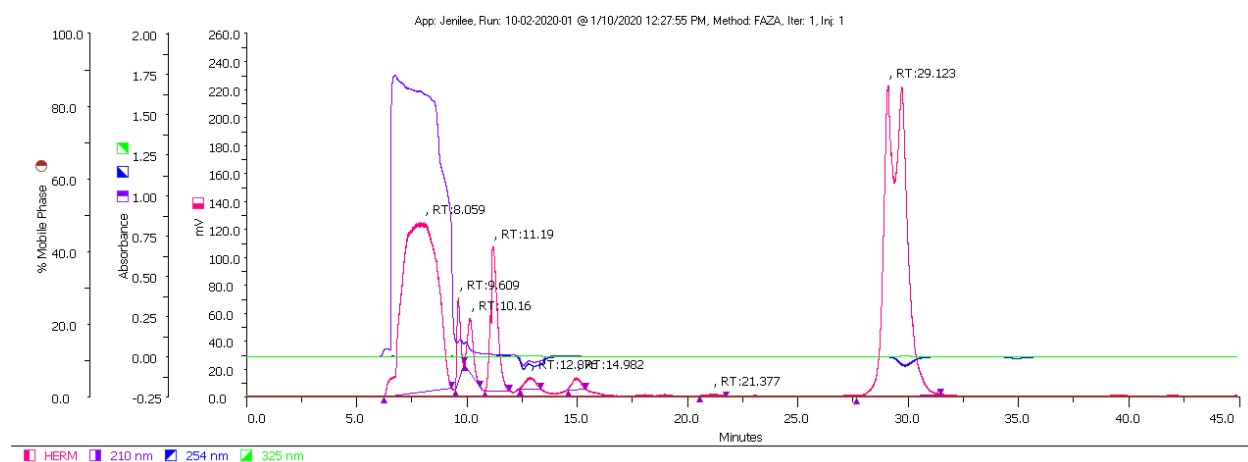


Figure 3.8. HPLC analysis of [ $^{19}\text{F}$ ]FAZA, non-radioactive reference compound for [ $^{18}\text{F}$ ]FAZA. Three UV channels are shown, including: 325 nm in green, 254 nm in purple and 210 nm in blue. Positive absorbance only observed in the 325 nm channel.

Synthesis of [ $^{18}\text{F}$ ]FAZA was completed as follows: [ $^{18}\text{F}$ ]fluoride in water was trapped on a Waters SepPak QMA carbonate (46 mg) cartridge (primed with 4 mL 0.5M K<sub>2</sub>CO<sub>3</sub> solution, followed by 6 mL Barnstead water). Vial 1 (V1) containing an in-house solution of K<sub>2.2.2</sub>/K<sub>2</sub>CO<sub>3</sub> in 86% CH<sub>3</sub>CN:H<sub>2</sub>O (V1: 0.8 mL) was used to elute the QMA cartridge into reactor 1 (R1). [ $^{18}\text{F}$ ]KF was dried azeotropically (V2: 1.5 mL CH<sub>3</sub>CN) under nitrogen flow and vacuum at 85 °C for 15 minutes. Once dried, ABX FAZA precursor (5 mg) in DMSO (V3: 0.8 mL) was added, and the

fluorination reaction was allowed to proceed for 10 minutes at 120 °C. Upon completion, the reactor was cooled to 30 °C and then 0.1 M sodium hydroxide solution (V4: 1 mL, freshly prepared) was added to reactor 1 and the deprotection was allowed to proceed for 3 minutes at 35 °C. Again reactor 1 was allowed to cool to 30 °C and then 0.2 M Acetic Acid (V5: 1.5 mL) was added to neutralize the reaction. The final mixture was pushed through a Waters SepPak Alumina N light cartridge (primed with 12 mL water) into a product vial containing a vent needle. Collected ASU eluent (3.3 mL) was directly injected onto HPLC using an isocratic elution of 8% Ethanol in water at 2 mL/min. The product was collected in fractions to achieve the best concentrations for direct animal injection. Retention time on HPLC is 31 to 34 min, the product is a very wide peak that drastically overloads both the detectors, see *Figure 3.9*.



*Figure 3.9. Typical HPLC analysis of [<sup>18</sup>F]FAZA as produced on the ASU. Three UV channels are shown, including: 325 nm in green, 254 nm in blue and 210 nm in purple. HERM radioactivity channel is shown in pink.*

Quality control (QC) injection was done using gradient elution (FMISO method) in water:CH<sub>3</sub>CN, leading to a retention time of 13.7 min, see *Figure 3.10*. Overall [<sup>18</sup>F]FAZA could be achieved in  $24.8 \pm 7.4\%$  dcy., from starting [<sup>18</sup>F]fluoride after a total synthesis time of 120 min (n=8). Purity was >99% as determined by HPLC. Co-injection of non-radioactive reference compound and [<sup>18</sup>F]FAZA was completed as seen in *Figure 3.11*. It should be noted that [<sup>18</sup>F]FAZA, should not be dried to be reconstituted. Under all tested rotary evaporation conditions >5% defluorination was witnessed, when [<sup>18</sup>F]FAZA was volume reduced from the HPLC collected eluent.

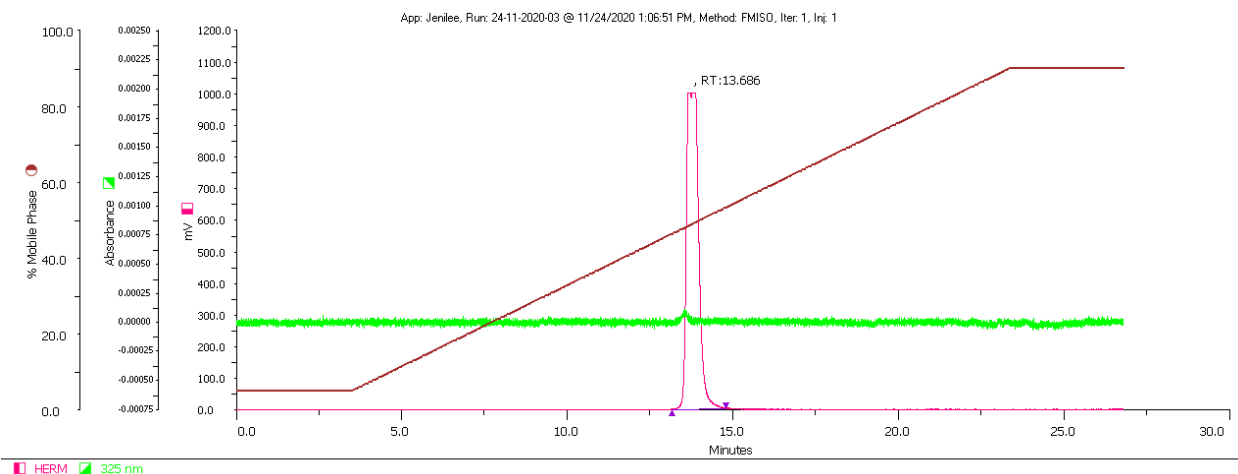


Figure 3.10. Quality control injection of  $[^{18}\text{F}]\text{FAZA}$ , from HPLC purified product. One UV channels shown as 325 nm in green, showing known non-radioactive contaminant of  $[^{19}\text{F}]\text{FAZA}$ . HERM radioactivity channel is shown in pink.

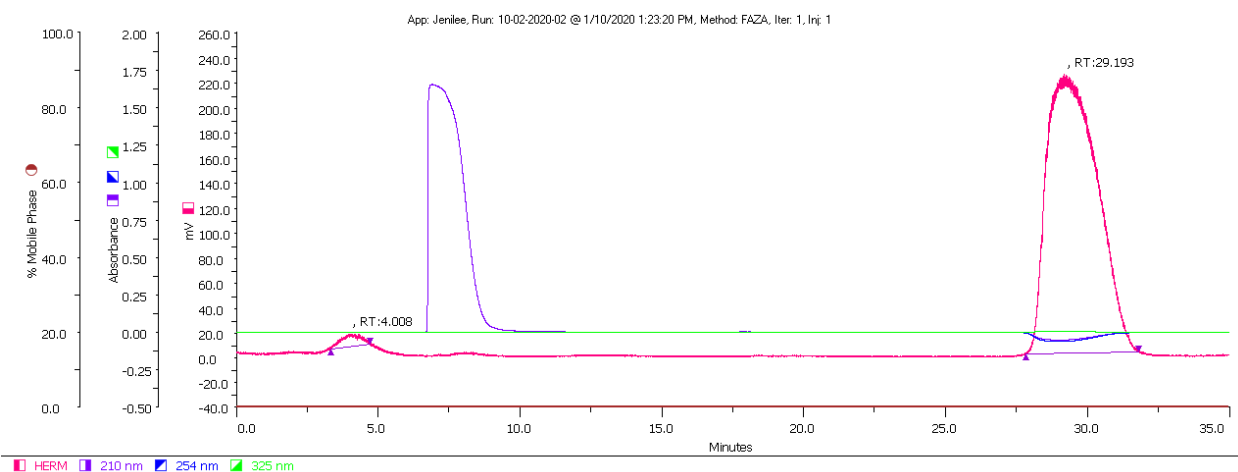


Figure 3.11. Co-injection of HPLC purified  $[^{18}\text{F}]\text{FAZA}$  and  $[^{19}\text{F}]\text{FAZA}$ . Three UV channels are shown, including: 325 nm in green, 254 nm in blue and 210 nm in purple. HERM radioactivity channel is shown in pink.

### 3.4 Radiosynthesis of 4- $^{18}\text{F}$ fluorobenzylamine ( $^{18}\text{F}$ FBAmine)

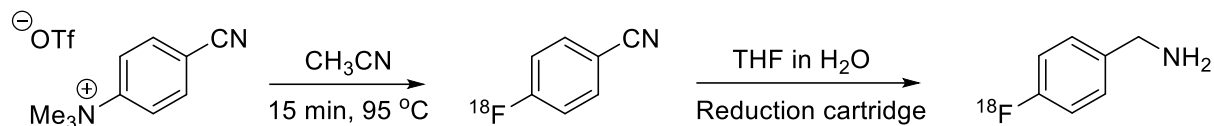


Figure 3.12. Radiosynthesis pathway for the synthesis of  $^{18}\text{F}$ FBAmine.

Synthesis of  $^{18}\text{F}$ FBAmine was completed as per our published procedure [116], briefly  $^{18}\text{F}$ fluoride in water was trapped on a Waters SepPak QMA Plus light cartridge (primed with 10 mL 0.5M K<sub>2</sub>CO<sub>3</sub> solution, followed by 12 mL Barnstead water). Vial 1 (V1) containing an in-house solution of K<sub>2</sub>.2.2./K<sub>2</sub>CO<sub>3</sub> in 86% CH<sub>3</sub>CN:H<sub>2</sub>O (V1: 1.5 mL) was used to elute the QMA cartridge into reactor 1 (R1).  $^{18}\text{F}$ KF was dried azeotropically (V2: 1.5 mL CH<sub>3</sub>CN) under nitrogen flow and vacuum at 85 °C for 15 minutes. Once dried, 4-cyano-*N,N,N*-trimethylanilinium trifluoromethanesulfonate (5 mg) in CH<sub>3</sub>CN (V3: 1.0 mL) is added, and the fluorination reaction allowed to proceed for 15 minutes at 95 °C. Once the reaction was completed, the mixture was diluted with water (V5, 12 mL) before being pushed through a Phenomenex Strata<sup>®</sup> C18-U cartridge (500 mg). The cartridge (C18#1) was washed with additional water (V6, 10 mL) and 4- $^{18}\text{F}$ fluorobenzonitrile ( $^{18}\text{F}$ FBN) was allowed to remain on the cartridge while the activation of the reducing cartridge was completed. Next, an additional Phenomenex Strata<sup>®</sup> C18-U cartridge (500 mg) containing BER (700 mg) and NiCl<sub>2</sub> (30 mg) (reducing cartridge, C18#2) was primed with water (V10, 3.0 mL). This cartridge was then allowed to sit for 3 min until the resin has completely activated. After activation, tetrahydrofuran (THF) (V4, 2.0 mL) was used to elute  $^{18}\text{F}$ FBN off C18#1 into another reactor (reactor 2, R2). The  $^{18}\text{F}$ FBN in R2 was then diluted with water (V11, 12 mL) and pushed through the activated C18#2. Finally,  $^{18}\text{F}$ FBAmine was eluted off C18#2 using THF (V12, 4.0 mL) into a product vial containing a vent needle. Collected ASU eluent (4.0 mL) was directly used for additional coupling experiments. Overall achieving a  $69.4 \pm 8.8\%$  dcy. from  $^{18}\text{F}$ fluoride after a total synthesis time of 90 min (n=7). Purity was  $84.2 \pm 14.8\%$  as determined by radio-TLC analysis.

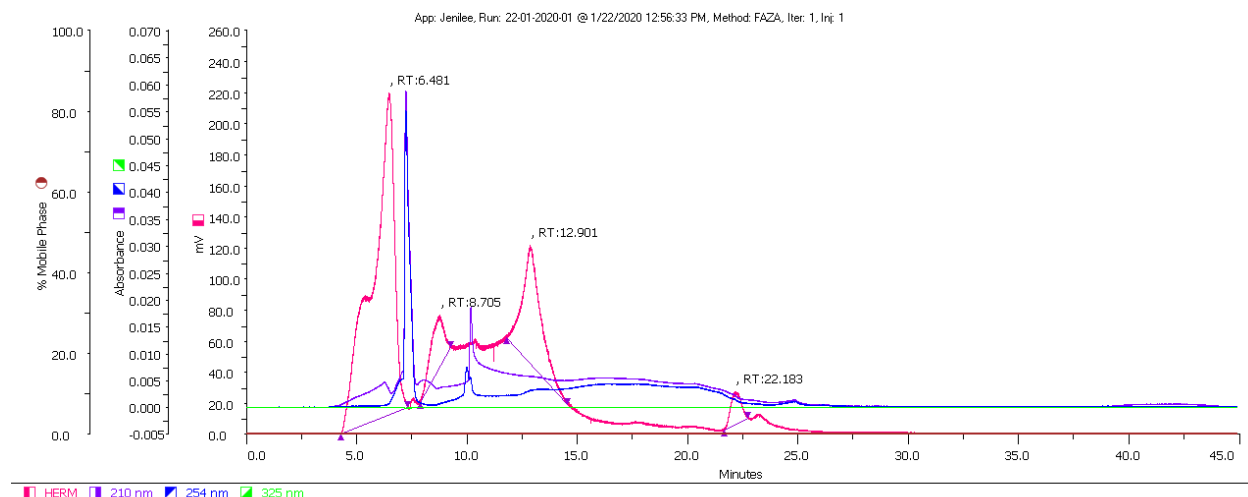


Figure 3.13. Typical HPLC analysis of  $[^{18}\text{F}]$ FBAmine as produced on the ASU. Three UV channels are shown, including: 325 nm in green, 254 nm in blue and 210 nm in purple. HERM radioactivity channel is shown in pink. HPLC method used is “FAZA”.

### 3.5 Radiosynthesis of $N$ -(4- $[^{18}\text{F}]$ fluorobenzyl)-2-(2-nitro-1H-imidazol-1-yl)-acetamide ( $[^{18}\text{F}]$ FBNA)

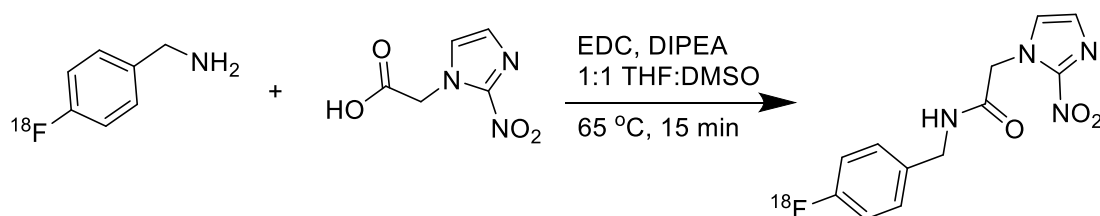


Figure 3.14. Radiosynthesis pathway for the synthesis of  $[^{18}\text{F}]$ FBNA.

Non-radioactive FBNA reference was tested on HPLC using the FMISO method to evaluate product retention time on a Luna C18(2) column, see Figure 3.15. Once completed, the radiosynthesis was optimized using manual prosthetic group coupling procedures.

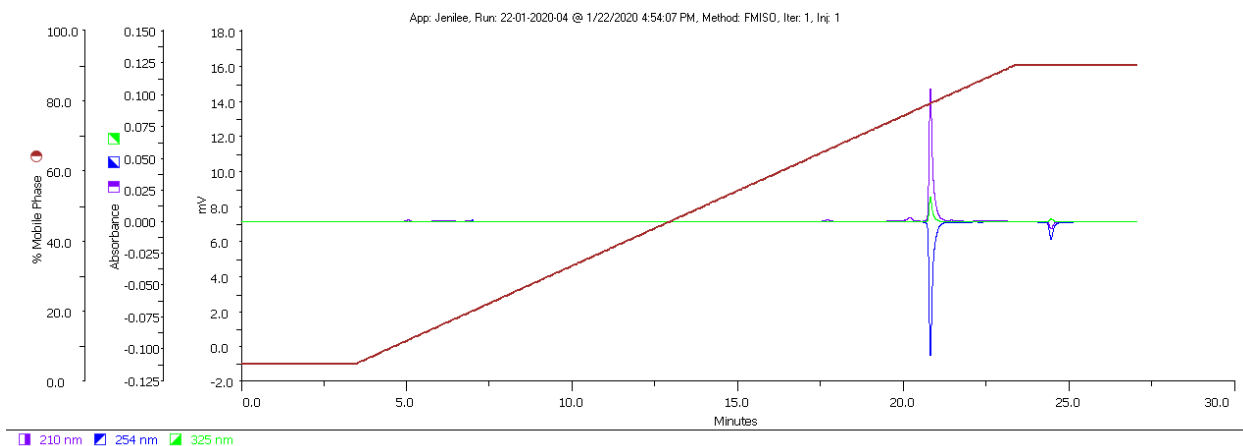


Figure 3.15. HPLC analysis of [ $^{19}\text{F}$ ]FBNA, non-radioactive reference compound for [ $^{18}\text{F}$ ]FBNA. Three UV channels are shown, including: 325 nm in green, 254 nm in blue and 210 nm in purple. Positive absorbance observed in the 325 nm and 210 nm channels.

[ $^{18}\text{F}$ ]FBAmine in THF from the fully automated synthesis was used directly as received in the product vial. In a 1.5 mL Eppendorf Lobind microcentrifuge tube the following were combined, [ $^{18}\text{F}$ ]FBAmine (500  $\mu\text{L}$ ), DMSO (500  $\mu\text{L}$ ), 1-ethyl-3-(3-dimethylaminopropyl)carbodiimide (EDC, 4.5 mg), DIPEA (25  $\mu\text{L}$ ), and (2-Amino-1-imidazolyl)acetic acid (5 mg). The microcentrifuge tube was then sealed with parafilm and placed on the Thermoshaker to react at 65  $^{\circ}\text{C}$  for 15 minutes at 1050 rpm. Once the reaction was completed the mixture was diluted with water (1 mL) and directly injected onto HPLC using the FMISO method, see Figure 3.16. The solvent composition of the reaction mixture was tested to determine if more ASU eluent could be used compared to the volume of DMSO solvent. In all tested parameters the yields were drastically lower in all other compositions except, 1:1 THF:DMSO.

The collected eluent from HPLC with the retention time of 20 to 21 minutes was collected into a pear-shaped flask and dried using rotary evaporation. Dried [ $^{18}\text{F}$ ]FBNA was then reconstituted into 8% ethanol in saline for both *in vivo* and *in vitro* use. Quality control (QC) injection is done using gradient elution (FMISO method) in water:CH<sub>3</sub>CN, leading to a retention time of 20.8 min, see Figure 3.17. Overall [ $^{18}\text{F}$ ]FBNA could be achieved in  $47.4 \pm 5.4\%$  dcy., from starting

[<sup>18</sup>F]FBAmine after a total synthesis time of 70 min (n=8). Purity was >99% as determined by HPLC QC injection.

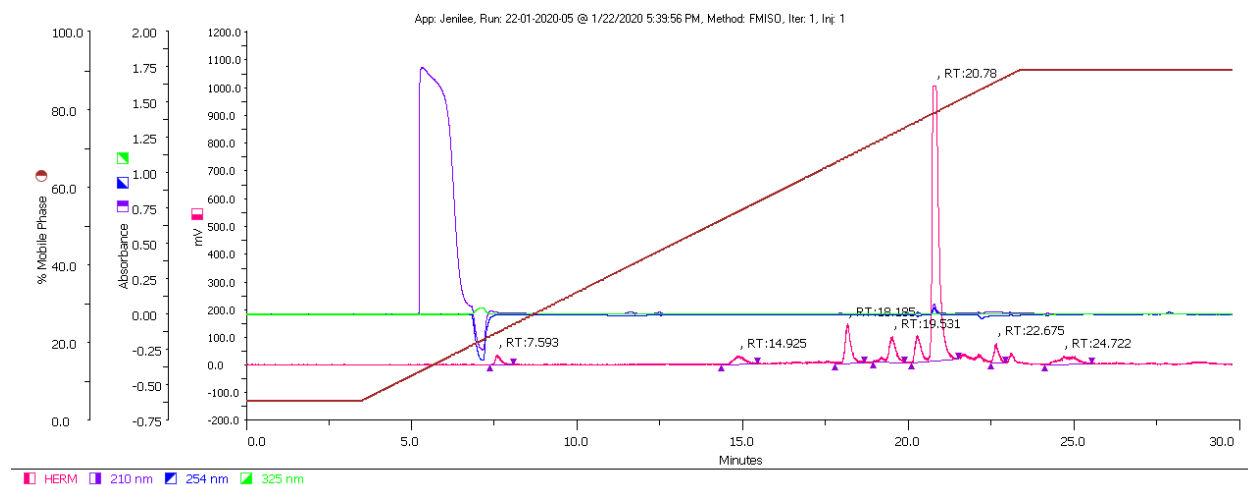


Figure 3.16. Typical HPLC analysis of [<sup>18</sup>F]FBNA as produced manually. Three UV channels are shown, including: 325 nm in green, 254 nm in blue and 210 nm in purple. HERM radioactivity channel is shown in pink.

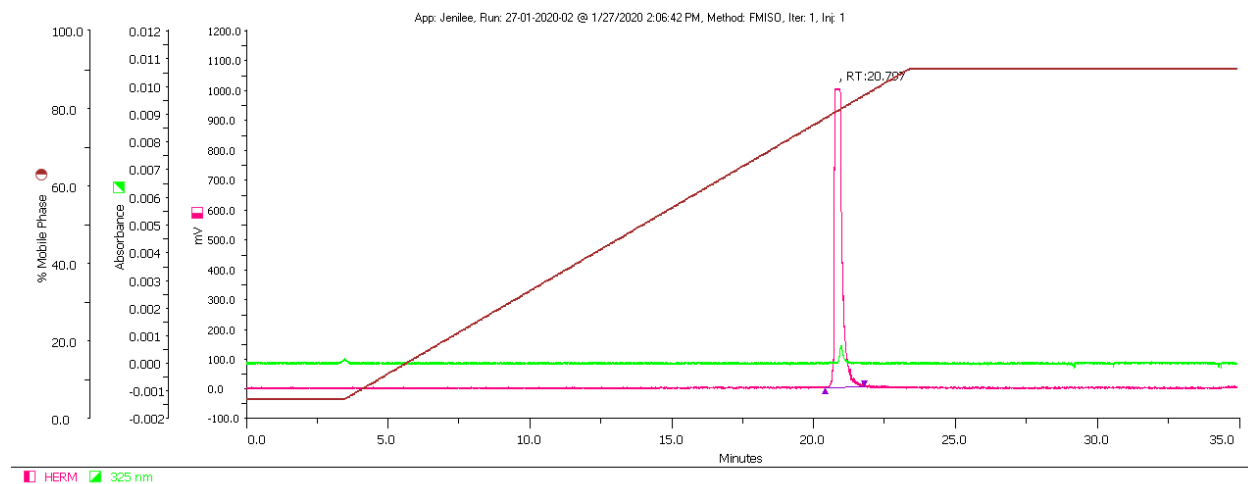
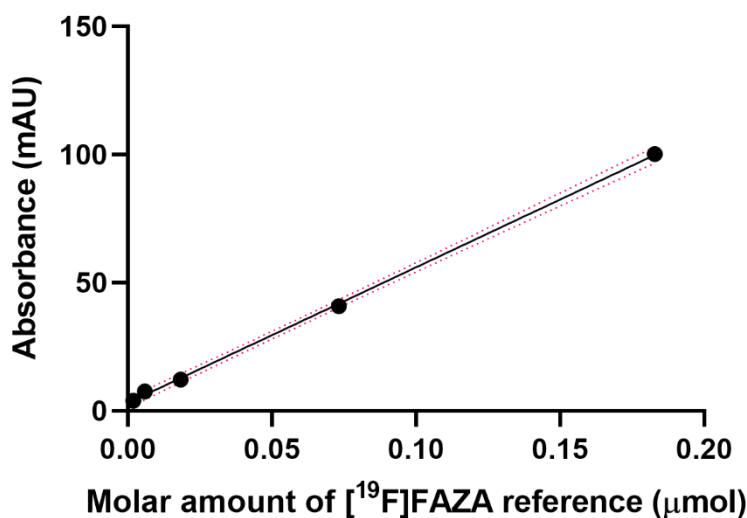


Figure 3.17. Quality control injection of [<sup>18</sup>F]FBNA, from HPLC purified product. One UV channels shown as 325 nm in green, showing known non-radioactive contaminant of [<sup>19</sup>F]FBNA. HERM radioactivity channel is shown in pink.

### 3.6 Molar activity calculations for nitroimidazole compounds

#### 3.6.1 Molar activity for [<sup>18</sup>F]FAZA

Various amounts of [<sup>19</sup>F]FAZA (0.45 to 45 μg) were solubilized into 10% ethanol in water (500 μL) and then injected onto the HPLC using the FMISO HPLC method. The area under the curve for the 325 nm wavelength channel was computed and a molar activity curve was created, see *Figure 3.19*. Using quality control injections for [<sup>18</sup>F]FAZA synthesis runs, known amounts of radioactivity are correlated to the absorbance under the UV peak in the 325 nm channel. Overall, yielding a molar activity of greater than 300 GBq/μmol (n=3); calculations seen in *Table 3.1*.



*Figure 3.19. Molar activity curve for [<sup>19</sup>F]FAZA non-radioactive reference.*

*Table 3.1. Molar activity calculations from the synthesis of [<sup>18</sup>F]FAZA using the formula of (Absorbance-3.0934)/529.13=molar amount).*

FAZA Synthesis ID	Absorbance (mAU)	Calculated molar amount (μmol)	Injected activity (GBq)	Calculated molar activity (GBq/umol)
FAZA0520	3.7938	0.001324	0.401	302.9428
FAZA0620	3.2898	0.000371	0.309	832.4907
FAZA0720	3.3454	0.000476	0.278	583.7228

### 3.6.2 Molar activity for [<sup>18</sup>F]FMISO

Various amounts of [<sup>19</sup>F]FMISO (0.35 to 70 μg) were solubilized into 10% ethanol in water (500 μL) and then injected onto the HPLC using the FMISO HPLC method. The area under the curve for the 325 nm wavelength channel was computed and a molar activity curve was created, see *Figure 3.20*. Using quality control injections for [<sup>18</sup>F]FMISO synthesis runs, known amounts of radioactivity are correlated to the absorbance under the UV peak in the 325 nm channel. Overall, yielding a molar activity of greater than  $34 \pm 12$  GBq/μmol (n=6); calculations seen in *Table 3.2*.

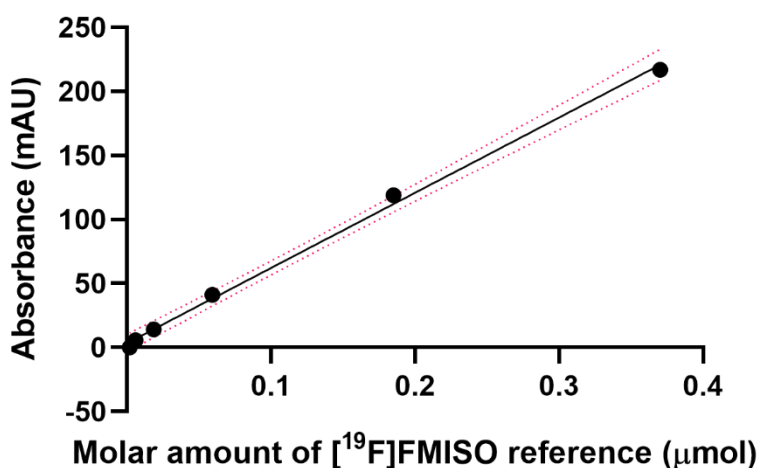


*Figure 3.20. Molar activity curve for [<sup>19</sup>F]FMISO non-radioactive reference.*

*Table 3.2. Molar activity calculations from the synthesis of [<sup>18</sup>F]FMISO using the formula of (Absorbance-3.3869)/587.41=molar amount).*

FMISO Synthesis ID	Absorbance (mAU)	Calculated molar amount (μmol)	Injected activity (GBq)	Calculated molar activity (GBq/umol)
FMISO0220	13.459	0.0171466	0.477	27.81888
FMISO0320	8.0966	0.0080177	0.2845	35.48382
FMISO0420	7.3515	0.0067493	0.131	19.40945
FMISO0520	8.4282	0.0085823	0.331	38.56797
FMISO0720	9.4878	0.0103861	0.558	53.72564
FMISO0820	12.6749	0.0158118	0.447	28.27005

### 3.6.3 Molar activity for [<sup>18</sup>F]FBNA

Various amounts of [<sup>19</sup>F]FBNA (15 to 500 μg) were solubilized into 30% CH<sub>3</sub>CN in 0.2% TFA in water (1000 μL) and then injected onto the HPLC using the FMISO HPLC method. The area under the curve for the 210 nm wavelength channel was computed and a molar activity curve was created, see *Figure 3.21*. Using quality control injections for [<sup>18</sup>F]FBNA synthesis runs, known amounts of radioactivity are correlated to the absorbance under the UV peak in the 210 nm channel.

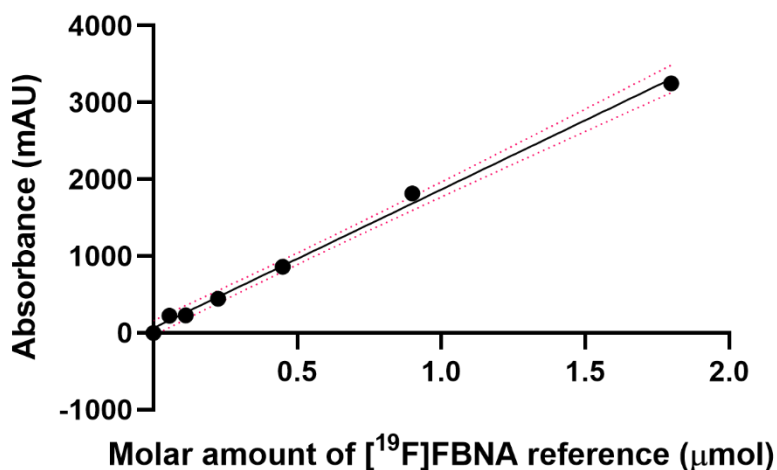


*Figure 3.21. Molar activity curve for [<sup>19</sup>F]FBNA non-radioactive reference.*

*Table 3.3. Molar activity calculations from the synthesis of [<sup>18</sup>F]FBNA using the formula of (Absorbance)/1854.9=molar amount).*

HPLC QC Injection ID	Absorbance (mAU)	Calculated molar amount (μmol)	Injected activity (GBq)	Calculated molar activity (GBq/μmol)
2022-11-04-02	8.53	0.00460	0.0265	5.77
2022-10-28-02	20.79	0.01121	0.0025	0.22
2022-10-06-02	153.50	0.08275	0.0110	0.13
2022-09-29-02	0.00	0.05619	0.0010	0.02
2022-09-20-02	4.07	0.00220	0.0153	6.97

Overall, yielding a maximum molar activity of 7 GBq/ $\mu$ mol, with calculations seen in *Table 3.3*. The molar activity calculations are very limited by the amount of radioactivity injected. For [ $^{18}\text{F}$ ]FBNA, the maximum injected radioactivity was 26.5 MBq.

### 3.7 Partition Coefficient ( $\log P$ ) calculation for [ $^{18}\text{F}$ ]FBNA

Nitroimidazole [ $^{18}\text{F}$ ]FBNA was prepared in a stock solution of saline. Aqueous PBS solution (500  $\mu\text{L}$ , pH 7.4) is then combined in a Lobind Eppendorf tube (1.5 mL) with octanol (500  $\mu\text{L}$ ) and 20  $\mu\text{L}$  of the radiotracer stock solution. Reactions are vigorously mixed and allowed to stand for 5 minutes, before sample removal. Removed from each layer is 50  $\mu\text{L}$  three times, into labelled microcentrifuge tubes. Samples are counted on a HIDEX gamma counter and replicates are shown in *Table 3.4*. below.

*Table 3.4. Partition coefficient replicates from the synthesis of [ $^{18}\text{F}$ ]FBNA.*

Synthesis ID	LogD
FBNA0620	0.92
FBNA0720	0.83
FBNA0820	1.03
FBNA0920	1.05
Overall Average	0.96
Standard deviation	0.10

Overall, [ $^{18}\text{F}$ ]FBNA was found to have a LogD value of  $0.96 \pm 0.10$  ( $n=9/3$ ). This is more favorable compared to the more hydrophilic compounds of [ $^{18}\text{F}$ ]FAZA and [ $^{18}\text{F}$ ]FMISO which have LogD values of -0.43 and 0.36 respectively [115].

### 3.8 Summary for the synthesis of radiolabelled nitroimidazole compounds

[ $^{18}\text{F}$ ]FMISO could be synthesized in  $58.1 \pm 17.9\%$  dcy., from starting [ $^{18}\text{F}$ ]fluoride after a total synthesis time of 140 min ( $n=8$ ). The purity of [ $^{18}\text{F}$ ]FMISO was  $>99\%$  as determined by HPLC with a molar activity of greater than  $34 \pm 12$  GBq/ $\mu$ mol ( $n=6$ ).

[<sup>18</sup>F]FAZA could be synthesized in  $24.8 \pm 7.4\%$  dcy., from starting [<sup>18</sup>F]fluoride after a total synthesis time of 120 min (n=8). The purity of [<sup>18</sup>F]FAZA was >99% as determined by HPLC with a molar activity of greater than 300 GBq/μmol (n=3).

[<sup>18</sup>F]FBNA could be synthesized in  $47.4 \pm 5.4\%$  dcy., from starting [<sup>18</sup>F]FBAmine after a total synthesis time of 70 min (n=8). The purity of [<sup>18</sup>F]FBNA was >99% as determined by HPLC with a maximum molar activity of 7 GBq/μmol (n=5). [<sup>18</sup>F]FBNA was found to have a LogD value of  $0.96 \pm 0.10$  (n=9/3).

The synthesis for [<sup>18</sup>F]FMISO, [<sup>18</sup>F]FAZA, and [<sup>18</sup>F]FBNA were all found to be robust, reproducible, and high yielding. Allowing for the routine production of these radiotracers.

## Chapter 4: *In vitro* and *in vivo* analysis of 2-nitroimidazole compounds

Previous work in our group has looked at the *in vitro* and *in vivo* analysis of [ $^{18}\text{F}$ ]FAZA in MDA-MB-231 and MCF-7 cells and tumor xenograft models [117]. Here, Dr. Ingrid Hamann found that [ $^{18}\text{F}$ ]FAZA had an increased uptake under hypoxic conditions at 180 minutes in all cell lines tested. Additionally, the statistical significance between hypoxia and normoxia was not seen at 60 minutes (see Figure 4.1).

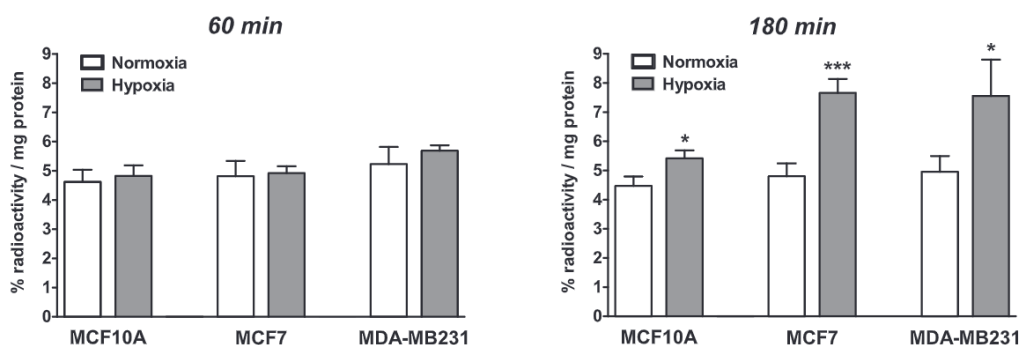


Figure 4.1. Cell uptake of [ $^{18}\text{F}$ ]FAZA into MDA-MB-231, MCF7 and MCF10a cells under both normoxic and hypoxic conditions [117].

Additionally, using small animal PET imaging they found that [ $^{18}\text{F}$ ]FAZA had an increased uptake in MDA-MB-231 xenografts versus MCF-7 xenografts (see Figure 4.2.). Here, they found a standardized uptake value at 180 minutes ( $\text{SUV}_{180}$ ) of 0.18 in MDA-MB-231 tumors and a  $\text{SUV}_{180}$  of 0.10 in MCF7 tumors. Also their tumor to muscle ratio (TMR) was found to be approximately 7.5 in MDA-MB-231 tumors and 2.5 in MCF7 tumors [117].

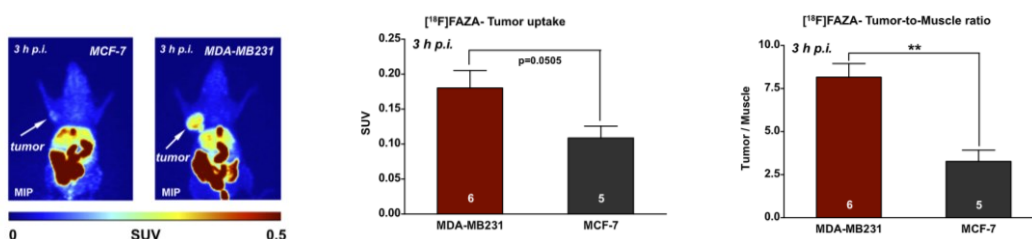


Figure 4.2. *In vivo* small animal PET imaging of [ $^{18}\text{F}$ ]FAZA in MDA-MB-231 and MCF7 xenograft models [117].

From these established models in our research group, herein we look at the *in vivo* and *in vitro* analysis of newly synthesized nitroimidazole radiotracers.

#### 4.1 *In vitro* cell uptake of 2-nitroimidazole compounds

Cell uptake of all three 2-nitroimidazoles was completed as per **section 2.7.7**. *In vitro* analysis was carried out in both human estrogen receptor-positive MCF7 cells as well as the human triple-negative MDA-MB-231 cells under normoxic and hypoxic (1% O<sub>2</sub>) conditions. Hypoxic conditions were achieved in a specially designed incubator, with hypoxia pre-incubation of the cells done for 24 hours before radiotracer addition.

##### 4.1.1 *In vitro* cell uptake of [<sup>18</sup>F]FBNA

Cell uptake of [<sup>18</sup>F]FBNA was carried out under normoxic and hypoxic (1% O<sub>2</sub>) conditions, with radiotracer uptake being monitored at the following time points of 1 minute, 60 minutes, 120 minutes and 180 minutes. The first cell line to be analyzed was MDA-MB-231 (see *Figure 4.3*).

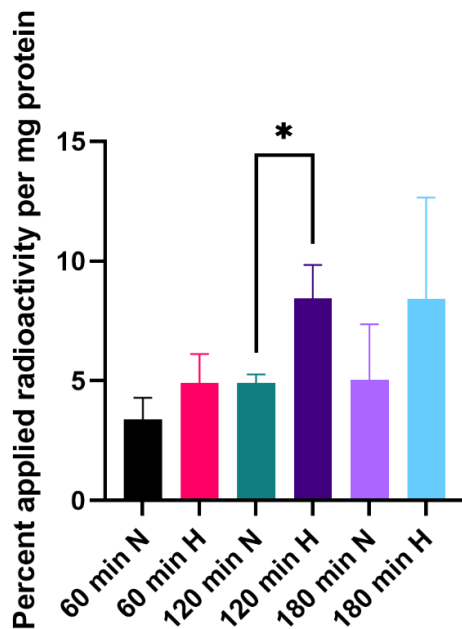


*Figure 4.3. Cell uptake of [<sup>18</sup>F]FBNA into MDA-MB-231 cells under both normoxic and hypoxic conditions. Data is presented with percent uptake in normoxic conditions normalized to 100% n=(9/3).*

In MDA-MB-231 cells, the uptake of [ $^{18}\text{F}$ ]FBNA was substantially increased under hypoxic conditions. At 60 minutes, the uptake of [ $^{18}\text{F}$ ]FBNA in hypoxia was twice that of the normoxic conditions. Moving to 180 minutes, the uptake of [ $^{18}\text{F}$ ]FBNA under hypoxic conditions increases to more than three times the value found in normoxic conditions.

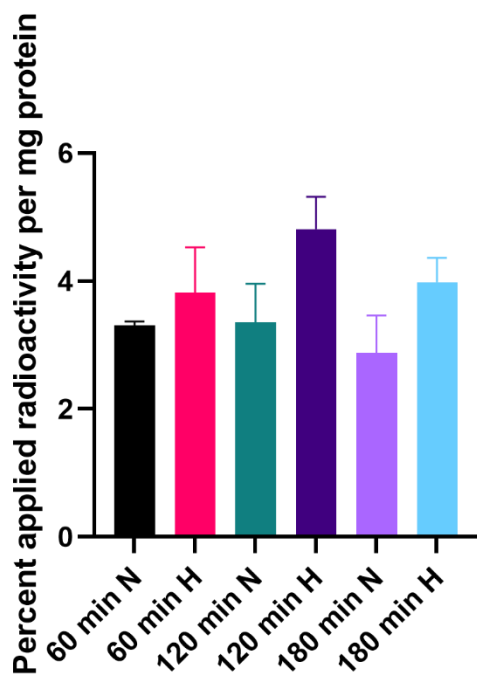


*Figure 4.4. Cell uptake of [ $^{18}\text{F}$ ]FBNA into MCF7 cells under both normoxic and hypoxic conditions. Data is presented with percent uptake in normoxic conditions normalized to 100%  $n=(6/2)$ .*

Cell uptake of [ $^{18}\text{F}$ ]FBNA was also tested in MCF7 cells, where the differences in uptake between normoxic and hypoxic were not as drastic. Even at 120 minutes the increase in uptake from normoxia to hypoxia was only a 40% increase from normoxia in MCF7 cells. This was compared to over a 150% increase in uptake in hypoxia in MDA-MB-231 cells. Comparing specifically the value at 120 minutes, in MDA-MB-231 cells under hypoxia we find an uptake of  $8.4 \pm 1.4\%$  applied radioactivity per mg protein (AR/mgP) ( $n=9/3$ ). Whereas in MCF7 cells under hypoxia we find an uptake of  $4.8 \pm 0.5\%$  AR/mgP ( $n=6/2$ ). Now looking at normoxia MDA-MB-231 cells under normoxia we find an uptake of  $4.9 \pm 0.4\%$  AR/mgP ( $n=9/3$ ). Whereas in MCF7 cells under normoxia we find an uptake of  $3.4 \pm 0.6\%$  AR/mgP ( $n=6/2$ ). In all experiments, n-numbers as

recorded as  $n=x/y$ , where  $y$  is the number of experiments and  $x$  is the number of data points total. Typically one experiment will include 3 data points.

#### 4.1.2 Comparative analysis of [ $^{18}\text{F}$ ]FBNA, [ $^{18}\text{F}$ ]FAZA and [ $^{18}\text{F}$ ]FMISO cell uptake

Cell uptake of [ $^{18}\text{F}$ ]FAZA and [ $^{18}\text{F}$ ]FMISO was carried out under normoxic and hypoxic (1%  $\text{O}_2$ ) conditions, with radiotracer uptake being monitored at the following time points of 1 minute, 60 minutes, 120 minutes and 180 minutes. Using MCF7 cells at 180 minutes, [ $^{18}\text{F}$ ]FMISO had a cell uptake of  $1.26 \pm 0.22\%$  AR/mgP ( $n=9/3$ ) in normoxic conditions and an uptake of  $1.39 \pm 0.18\%$  AR/mgP ( $n=9/3$ ) in hypoxic conditions (see *Figure 4.5.B*). Also in MCF7 cells at 180 minutes, [ $^{18}\text{F}$ ]FAZA had a cell uptake of  $4.80 \pm 0.44\%$  AR/mgP ( $n=9/3$ ) in normoxic conditions and an uptake of  $7.66 \pm 0.48\%$  AR/mgP ( $n=9/3$ ) in hypoxic conditions (see *Figure 4.5.C*). Both of these increases due to hypoxic conditions are statistically significant ( $p<0.05$ ) and demonstrate that both [ $^{18}\text{F}$ ]FMISO and [ $^{18}\text{F}$ ]FAZA have increased retention in hypoxic MCF7 cells.

Additional cell uptakes were also completed using MDA-MB-231 cells. At 180 minutes, [ $^{18}\text{F}$ ]FMISO had a cell uptake of  $3.02 \pm 0.81\%$  AR/mgP ( $n=9/3$ ) in normoxic conditions and an uptake of  $4.74 \pm 1.34\%$  AR/mgP ( $n=9/3$ ) in hypoxic conditions (see *Figure 4.5.B*). Also in MDA-MB-231 cells at 180 minutes, [ $^{18}\text{F}$ ]FAZA had a cell uptake of  $4.96 \pm 0.54\%$  AR/mgP ( $n=9/3$ ) in normoxic conditions and an uptake of  $7.56 \pm 1.24\%$  AR/mgP ( $n=9/3$ ) in hypoxic conditions (see *Figure 4.5.C*). Again, both of these increases due to hypoxic conditions are statistically significant ( $p<0.05$ ) and demonstrate that both [ $^{18}\text{F}$ ]FMISO and [ $^{18}\text{F}$ ]FAZA have increased retention in hypoxic MDA-MB-231 cells.

Compared to the cellular uptake of [ $^{18}\text{F}$ ]FBNA in MCF7 and MDA-MB-231 cells, [ $^{18}\text{F}$ ]FBNA has a very similar uptake profile to that of [ $^{18}\text{F}$ ]FAZA. Both had a significant uptake in hypoxic MDA-MB-231 cells of around  $\sim 8\%$  AR/mgP, with a normoxic uptake of around  $\sim 4.5\%$  AR/mgP. This was interesting as [ $^{18}\text{F}$ ]FBNA is the most hydrophobic nitroimidazole and [ $^{18}\text{F}$ ]FAZA is the most hydrophilic nitroimidazole, yet both seem to act very similarly *in vitro*.

Overall [ $^{18}\text{F}$ ]FBNA seems to perform comparatively to both [ $^{18}\text{F}$ ]FAZA and [ $^{18}\text{F}$ ]FMISO in both MCF7 cells and MDA-MB-231 cells *in vitro*. All three hypoxia radiotracers performed statistically significantly in the detection of hypoxic cells.

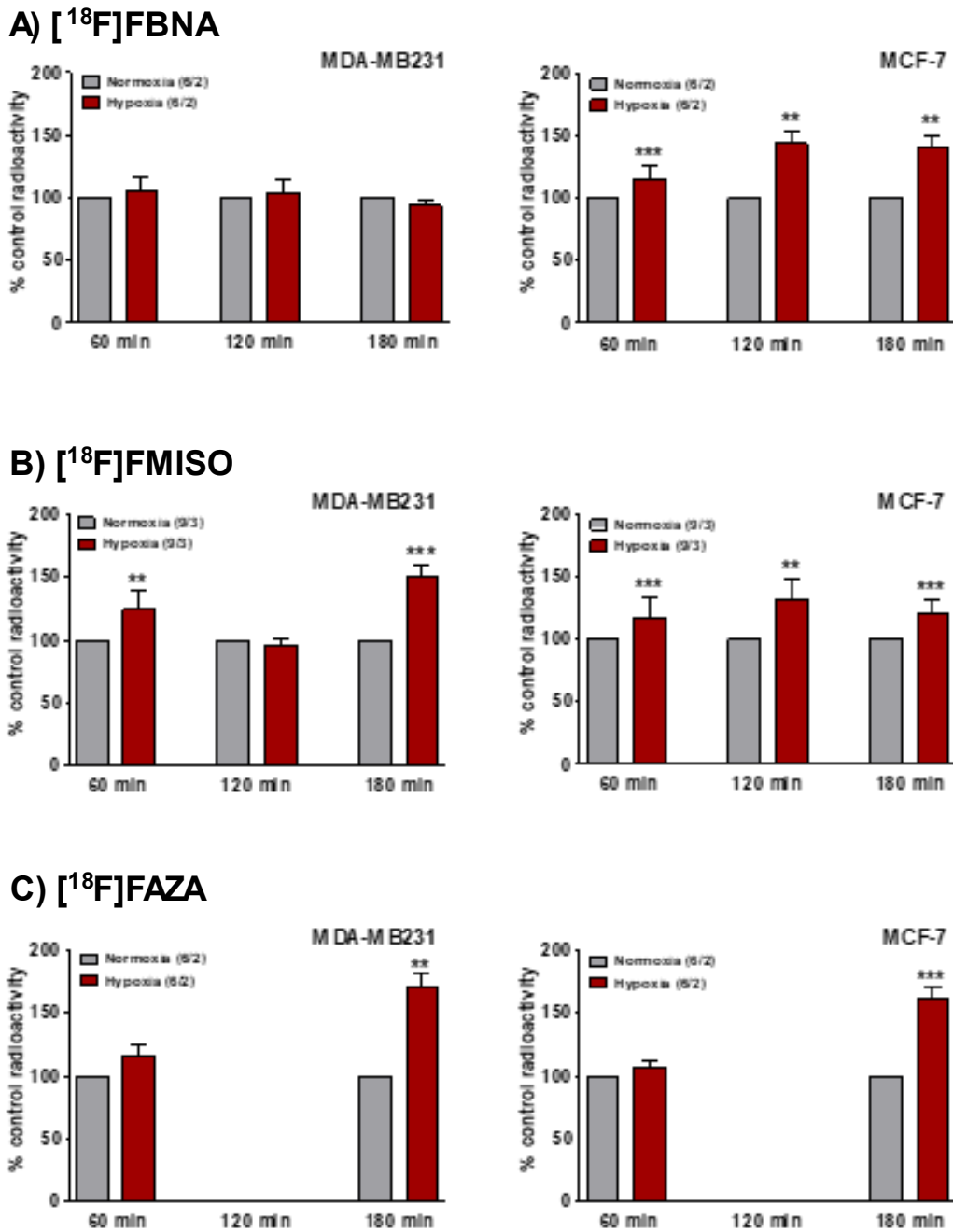


Figure 2

Figure 4.5. In vitro cell uptake of A)  $[^{18}\text{F}]$ FBNA in MCF7 cells ( $n=6/2$ ) and MDA-MB-231 cells ( $n=9/3$ ), B)  $[^{18}\text{F}]$ FMISO in MCF7 cells ( $n=9/3$ ) and MDA-MB-231 cells ( $n=9/3$ ), C)  $[^{18}\text{F}]$ FAZA in MCF7 cells ( $n=9/3$ ) and MDA-MB-231 cells ( $n=9/3$ ).

## 4.2 In vivo metabolic stability and blood distribution of 2-nitroimidazoles

In vivo metabolic stability was performed as per section 2.7.9. Data for [ $^{18}\text{F}$ ]FBNA was analyzed and comparatively analyzed to [ $^{18}\text{F}$ ]FMISO and [ $^{18}\text{F}$ ]FAZA (see Figure 4.6.).

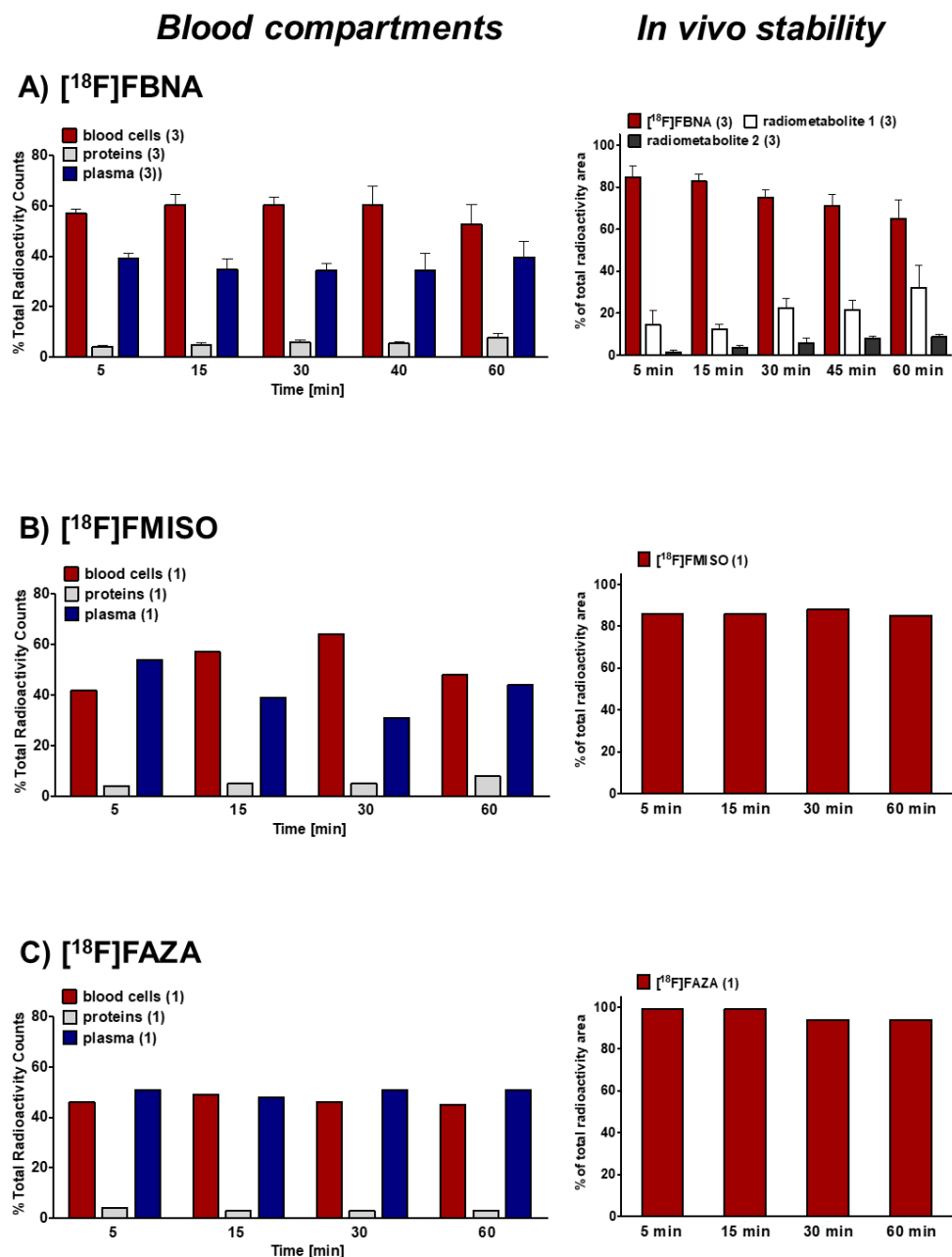


Figure 4.6. Metabolic stability and blood distribution of [ $^{18}\text{F}$ ]FBNA ( $n=3$ ), [ $^{18}\text{F}$ ]FAZA ( $n=1$ ), and [ $^{18}\text{F}$ ]FMISO ( $n=1$ ) in normal female BALB/C mice.

[<sup>18</sup>F]FBNA was found to be fairly metabolically unstable compared to the metabolic stable [<sup>18</sup>F]FMISO and [<sup>18</sup>F]FAZA. Within 5 minutes post injection, [<sup>18</sup>F]FBNA already was only 80% intact, progressing overtime to 65 ± 9 % intact after 60 minutes. At this 60 minute post injection timepoint [<sup>18</sup>F]FBNA was found to have two metabolites, existing as 32 ± 11 % radiometabolite-1 and 9 ± 1 % radiometabolite-2 (all n=3). We theorize that the metabolic instability could be due to the peptide-like amide bond found in the [<sup>18</sup>F]FBNA structure.

Blood distribution was performed as per section **section 2.7.9**. Data for [<sup>18</sup>F]FBNA was analyzed and comparatively analyzed to [<sup>18</sup>F]FMISO and [<sup>18</sup>F]FAZA (see *Figure 4.6.*).

It was found that [<sup>18</sup>F]FBNA is detected more in blood cells (~60%) versus plasma (~35-40%) not changing much over time. While [<sup>18</sup>F]FAZA is found at similar levels in blood cells and plasma at about 50% each. Analysis of [<sup>18</sup>F]FMISO, revealed slightly more variable results over time. This is likely to be accounted by the n=1 experiment only. Overall after 60 min post injection the protein-bound fraction was ~8% for [<sup>18</sup>F]FBNA which was similar to [<sup>18</sup>F]FMISO but higher than [<sup>18</sup>F]FAZA (~3%).

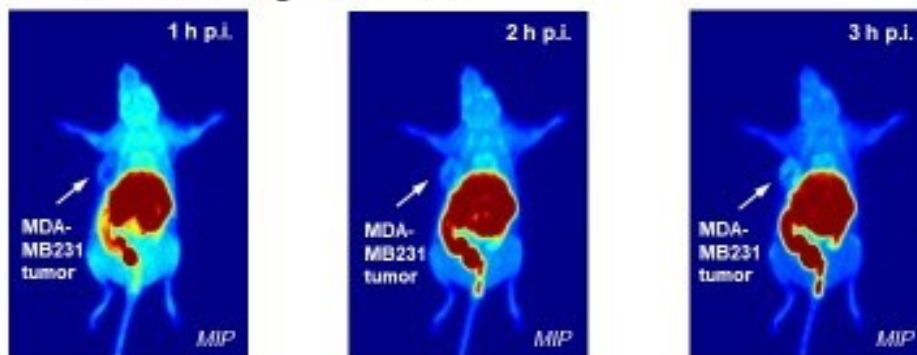
#### *4.3 Dynamic PET imaging of 2-nitroimidazoles*

Dynamic positron emission tomography (PET) imaging was performed as per **section 2.7.9**. [<sup>18</sup>F]FBNA was tested in both MCF7 and MDA-MB-231 NIH-III tumor-bearing mice (see *Figure 4.7.*).

*Figure 4.7.*, shows the dynamic PET images for [<sup>18</sup>F]FBNA at 1, 2, and 3 hours post-injection. Overall, as the radiotracer was distributed through the animal model, the retention in muscle tissue was high. Yet as time increases to three hours, the clearance from the muscle tissue increase and the tumors become more visible while using [<sup>18</sup>F]FBNA. At 5 min post-injection [<sup>18</sup>F]FBNA reached a SUV<sub>5min</sub> value of 0.56 ± 0.06 in MCF7 tumors versus only 0.30 ± 0.07 in MDA-MB-231 tumors (both n=3; p < 0.05). Looking to the longest time point at 180 min, the following SUV<sub>180min</sub> values were determined for [<sup>18</sup>F]FBNA 0.78 ± 0.01 in MCF-7 and 0.61 ± 0.04 in MDA-MB-231 tumors (both n=3; p < 0.05).

## [<sup>18</sup>F]FBNA

### A) MDA-MB231 tumor bearing NIH-III mice



### B) MCF-7 tumor bearing NIH-III mice

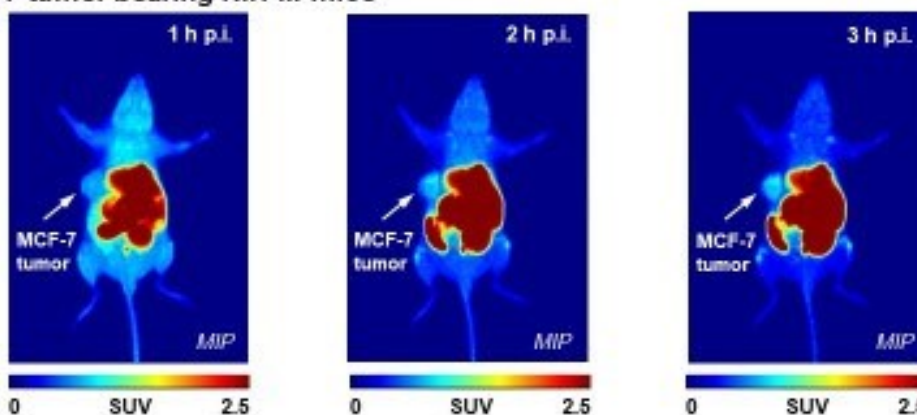


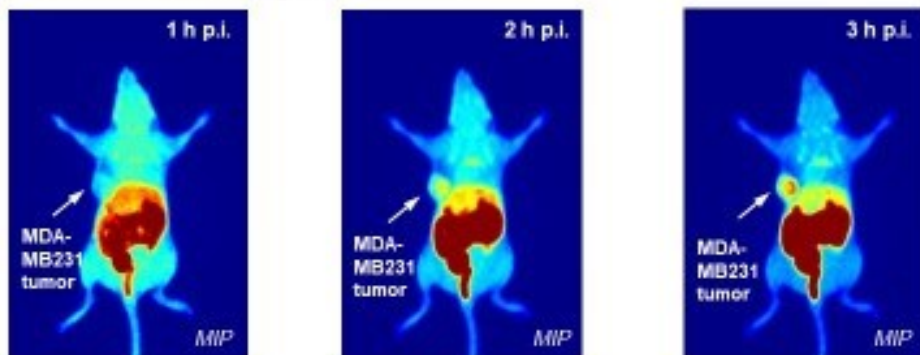
Figure 4.7. Dynamic PET imaging of [<sup>18</sup>F]FBNA in NIH-III tumor-bearing mice.

A) MDA-MB-231 xenograft model B) MCF7 xenograft model. Measured tumors were between 5 mm<sup>2</sup> to 10 mm<sup>2</sup>, with SUV analysis completed in n=3 mice.

[<sup>18</sup>F]FMISO was also tested in both MCF7 and MDA-MB-231 NIH-III tumor-bearing mice (see Figure 4.8). [<sup>18</sup>F]FMISO displayed similar muscle uptake and clearance as witnessed for [<sup>18</sup>F]FBNA. Yet even after 180 minutes, [<sup>18</sup>F]FMISO was not completely cleared from the muscle tissue. Yet the final tumor uptake values for [<sup>18</sup>F]FMISO were much higher than that for [<sup>18</sup>F]FBNA. After injection of [<sup>18</sup>F]FMISO a SUV<sub>5min</sub> value of 0.72 ± 0.03 was determined in MCF-7 tumors and 0.48 ± 0.04 in MDA-MB-231 tumors (both n=4; p < 0.01). Looking at the longer time point of 180 min, [<sup>18</sup>F]FMISO had and SUV<sub>180min</sub> of 1.36 ± 0.04 in MCF-7 and 1.23 ± 0.08 in MDA-MB-231 tumors (both n=4; p > 0.05).

## [<sup>18</sup>F]FMISO

### A) MDA-MB231 tumor bearing NIH-III mice



### B) MCF-7 tumor bearing NIH-III mice

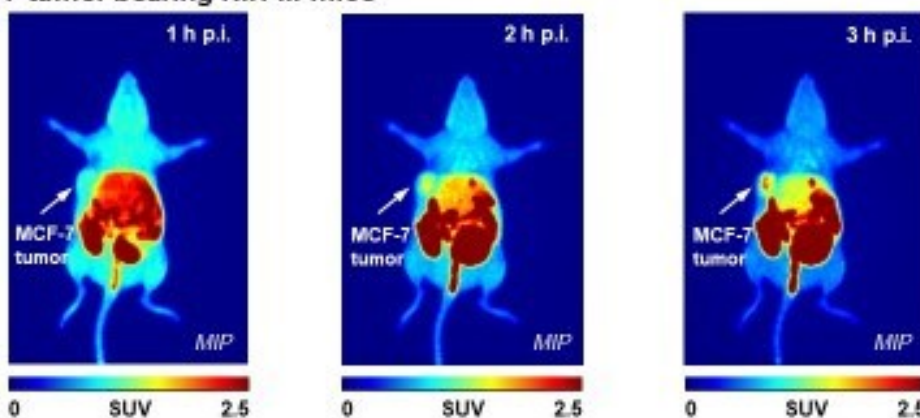


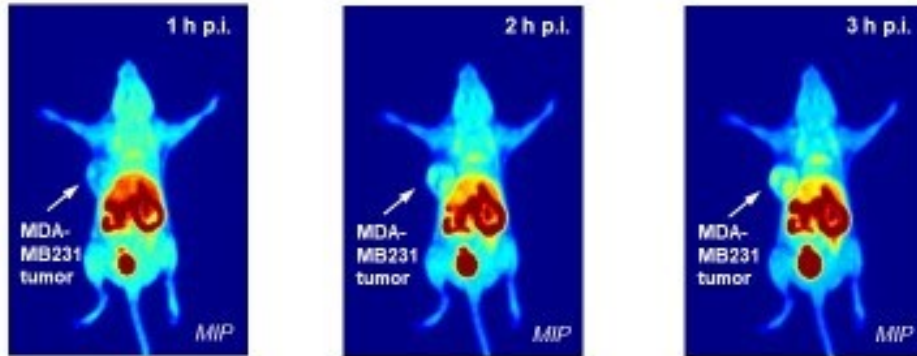
Figure 4.8. Dynamic PET imaging of [<sup>18</sup>F]FMISO in NIH-III tumor-bearing mice.

A) MDA-MB-231 xenograft model B) MCF7 xenograft model. Measured tumors were between 5 mm<sup>2</sup> to 10 mm<sup>2</sup>, with SUV analysis completed in n=4 mice.

Finally, [<sup>18</sup>F]FAZA was also tested in both MCF-7 and MDA-MB-231 NIH-III tumor-bearing mice (see Figure 4.9.). [<sup>18</sup>F]FAZA displayed similar muscle uptake and clearance as witnessed for [<sup>18</sup>F]FMISO. Both have a slower muscle clearance than witnessed for [<sup>18</sup>F]FBNA. Yet the final tumor uptake values for [<sup>18</sup>F]FAZA were not as high as for [<sup>18</sup>F]FMISO. After injection of [<sup>18</sup>F]FAZA a SUV<sub>5min</sub> was 0.54 ± 0.05 in MCF7 and 0.33 ± 0.02 in MDA-MB-231 tumors (both n=4; p < 0.05). Looking at the longer time point of 180 min, [<sup>18</sup>F]FAZA had a SUV<sub>180min</sub> of 0.66 ± 0.11 in MCF7 and 0.63 ± 0.14 in MDA-MB-231 tumors (both n=4; n.s.).

## [<sup>18</sup>F]FAZA

### A) MDA-MB231 tumor bearing NIH-III mice



### B) MCF-7 tumor bearing NIH-III mice

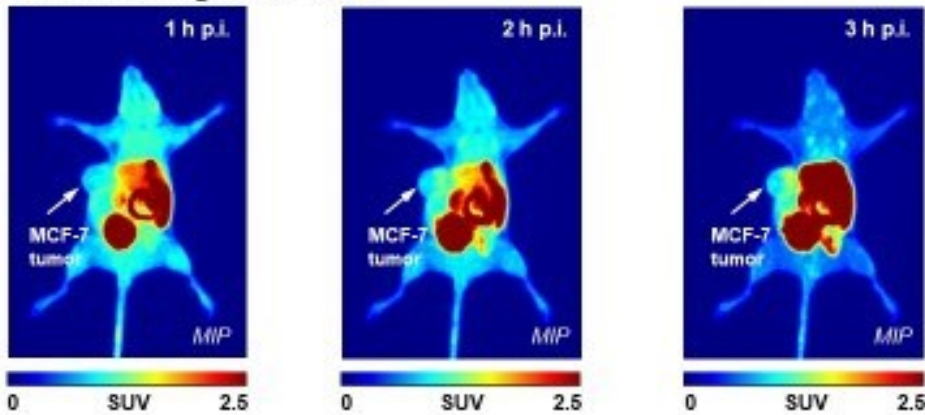


Figure 4.9. Dynamic PET imaging of [<sup>18</sup>F]FAZA in NIH-III tumor-bearing mice. A) MDA-MB-231 xenograft model B) MCF7 xenograft model. Measured tumors were between 5 mm<sup>2</sup> to 10 mm<sup>2</sup>, with SUV analysis completed in n=4 mice.

Looking specifically at the time activity curves for the uptake of [<sup>18</sup>F]FBNA (see Figure 4.10.), we see a very similar muscle uptake and clearance curve in both tumor models of MCF7 and MDA-MB-231. In the MDA-MB-231 tumor model the uptake of [<sup>18</sup>F]FBNA is much slower achieving a SUV<sub>max</sub> of 0.6 at 175 minutes. Compared to the MCF7 tumor model the uptake of [<sup>18</sup>F]FBNA is much more rapid and then reaches a plateau at 25 minutes post-injection at a SUV<sub>max</sub> of 0.75. Overall, [<sup>18</sup>F]FBNA achieves a tumor-to-muscle ratio (TMR) of 2 in MDA-MB-231 tumors and a TMR of 3 in MCF-7 tumors. Additionally, the plateau in the MCF7 tumor uptake curve for [<sup>18</sup>F]FBNA suggests that reductive trapping has stopped after only 25 minutes of uptake.

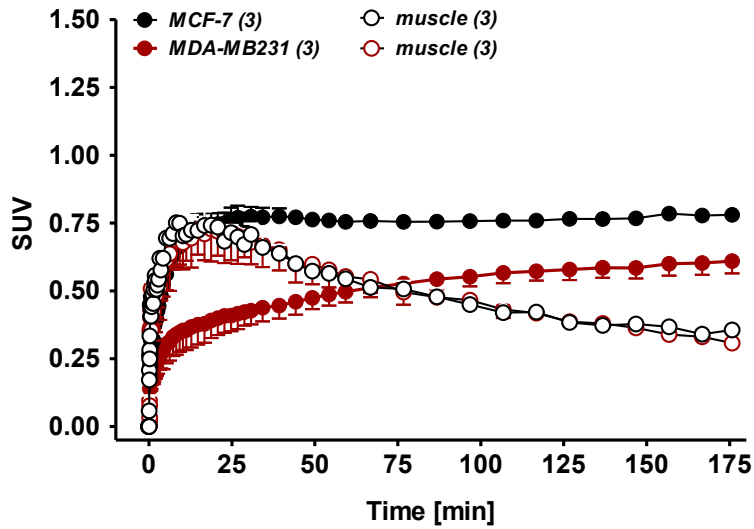


Figure 4.10. Time activity curve of  $[^{18}\text{F}]$ FBNA in NIH-III tumor-bearing mice with a MDA-MB-231 xenograft (black data points) or a MCF7 xenograft (red data points). Closed circle data points indicate the tumor uptake, whereas open circle data points indicate muscle uptake ( $n=3$ ).

The time activity curves for  $[^{18}\text{F}]$ FMISO (see Figure 4.11.), show a very similar trend in muscle clearance for both tumor models. As, similar to  $[^{18}\text{F}]$ FBNA,  $[^{18}\text{F}]$ FMISO also has a slower uptake in MDA-MB-231 tumors compared to MCF7 tumors. Yet both tumor uptake curves for  $[^{18}\text{F}]$ FMISO seem to both exponentially increase over time, up to a  $\text{SUV}_{\text{max}}$  of 1.25 in MCF7 and a  $\text{SUV}_{\text{max}}$  of 1.15 in MDA-MB-231. Overall  $[^{18}\text{F}]$ FMISO gives a very large TMR of  $\sim 3.5$  in both tumor models.

Lastly, the time activity curves for  $[^{18}\text{F}]$ FAZA (see Figure 4.12.), show again very similar muscle clearance from the MCF7 to the MDA-MB-231 tumor models. Also, again the uptake of  $[^{18}\text{F}]$ FAZA is much slower in the MDA-MB-231 tumor compared to the MCF7 tumor; yet both tumor models after 180 minutes reach the same  $\text{SUV}_{\text{max}}$  of 0.70. Just like in the  $[^{18}\text{F}]$ FBNA uptake, the uptake of  $[^{18}\text{F}]$ FAZA in MCF7 tumors has a rapid increase followed by a plateau after 20 minutes. Overall,  $[^{18}\text{F}]$ FAZA has a TMR of 3 in both tumor models.

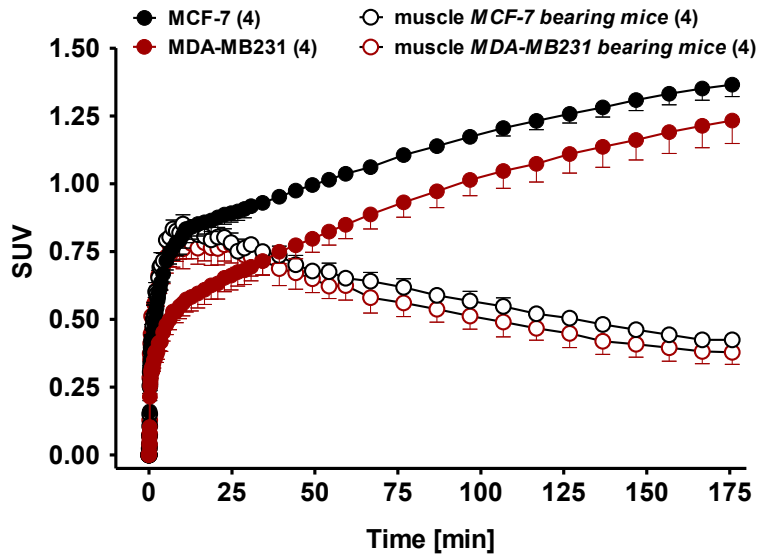


Figure 4.11. Time activity curve of  $[^{18}\text{F}]\text{FMISO}$  in NIH-III tumor bearing mice with a MDA-MB-231 xenograft (black data points) or a MCF7 xenograft (red data points). Closed circle data points indicate the tumor uptake, whereas open circle data points indicate muscle uptake ( $n=4$ ).

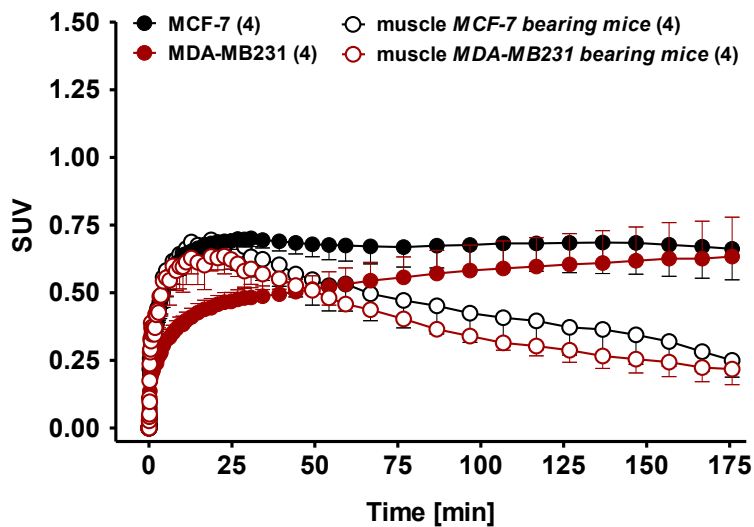


Figure 4.12. Time activity curve of  $[^{18}\text{F}]\text{FAZA}$  in NIH-III tumor-bearing mice with a MDA-MB-231 xenograft (black data points) or a MCF7 xenograft (red data points). Closed circle data points indicate the tumor uptake, whereas open circle data points indicate muscle uptake ( $n=4$ ).

Comparing the three nitroimidazoles, [<sup>18</sup>F]FMISO has the highest SUV<sub>max</sub> of up to 1.25, but its muscle clearance only ever drops to 0.35 after 180 minutes. Whereas, both [<sup>18</sup>F]FAZA and [<sup>18</sup>F]FBNA have medium tumor uptake with SUV<sub>max</sub> ~0.7 and a muscle clearance that falls below an SUV of 0.25. All of the nitroimidazoles have similar TMR ratios of ~3, with [<sup>18</sup>F]FMISO having the highest TMR of 3.5. Therefore it can be concluded that in these experimental studies, [<sup>18</sup>F]FMISO is likely the best nitroimidazole compound for the imaging of hypoxia in MCF7 and MDA-MB-231 tumor model in NIH-III mice.

#### 4.4 Summary for the In vitro and in vivo analysis of 2-nitroimidazole compounds

Table 4.1. Summary for the in vitro and in vivo analysis of 2-nitroimidazole compounds. Listed data is classified into either A) MDA-MB-231 cells or B) MCF-7 cells. Where “H” is hypoxic in vitro cell uptake and “N” is normoxic in vitro cell uptake. Additionally, standardized uptake value (SUV) and tumor to muscle ratio (TMR) are reported for xenografts using both cell lines.

Radiotracers	A) H	A) N	B) H	B) N	A) SUV	B) SUV	A) TMR	B) TMR
[ <sup>18</sup> F]FBNA	8.4%	4.9%	4.8%	3.4%	0.61	0.78	2	3
[ <sup>18</sup> F]FAZA	7.56%	4.96%	7.66%	4.80%	0.63	0.66	3	3
[ <sup>18</sup> F]FMISO	4.74%	3.02%	1.39%	1.26%	1.23	1.36	3.5	3.5

## **Chapter 5: Synthesis and evaluation of novel HIF-1 $\alpha$ binding compounds**

From literature, we choose two lead structures in order to model our HIF-1 $\alpha$  binding compounds. The first structure was a hexacyclic peptide designed by Miranda *et al.* [107] called *c*-CLLFVY. This structure was determined by a colony growth experiment using a HIF-1 bacterial reverse two-hybrid system. In brief, *E. coli* cells were forced to express both mutant P22-HIF-1 $\alpha$  and mutant 434-HIF-1 $\beta$ . Then using a SICLOPPS expression system, any expressed peptide that inhibited the interaction of 434-HIF-1 $\beta$  and P22-HIF-1 $\alpha$  would allow the *E. coli* cells to grow in culture. From observed colonies, they isolated their plasmids, and determined that their peptide structure inhibiting the binding of HIF-1 $\alpha$  to HIF-1 $\beta$  was *c*-CLLFVY. They then made a modified hexacyclic peptide *c*-(PpA)LLFVY in which the cysteine residue has been modified to a propargylalanine (PpA) residue. To the PpA they then added a linker with a biotin-PEG-azide in order to synthesize their full compound of biotin-PEG-triazole-*cyclo*-ALLFVY, that then they used to pull either His-HIF-1 $\alpha$ <sub>1-350</sub> or GST-HIF-1 $\beta$ <sub>1-474</sub> out of solution. Here they found that HIF-1 $\alpha$  was the only protein that bound to their cyclic peptide. Even further research by Miranda *et al.* showed that *c*-CLLFVY was specifically interacting with HIF-1 $\alpha$  and not HIF-2 $\alpha$  [107]. Overall *c*-CLLFVY was shown to have an IC<sub>50</sub> value of 1.3  $\mu$ M against HIF-1 $\alpha$ . Additionally, from these works it was shown that modification of the cysteine amino acid has little impact on the binding to HIF-1 $\alpha$ .

The second structure we choose was designed by Okamoto *et al.*, as a small molecular weight compound entitled ER-400583-00 [109]. Here they looked at developing compounds that bound to HIF-1 $\alpha$  using a PLAP reporter gene attached to VEGF expression. This work was completed using high throughput screening of over 43,000 compounds. From their analysis they found that ER-400583-00 inhibited the PLAP-HIF-1 reporter activity with an IC<sub>50</sub> value of 7.9 nM [109]. Further work showed that ER-400583-00 did not alter the level of HIF-1 $\alpha$  mRNA, but during hypoxia ER-400583-00 did repress the amount of HIF-1 $\alpha$  protein with a IC<sub>50</sub> value of 3.7 nM [109]. Overall the authors predicted that ER-400583-00 affects HIF-1 $\alpha$  degradation through the proline-hydroxylation-dependent ubiquitination pathway. Additionally, we choose to work with this structure, due to its theoretical ability to be modified using current radiochemistry practices in our laboratory.

Previous work has shown that the prosthetic group 4-<sup>18</sup>F]fluoroiodobenzene can be easily synthesized using an automated synthesis unit [118] and its subsequent use in Pd-mediated SONOGASHIRA reaction has been documented in alkyne-carbon bond formation [119]. Herein, we included the synthesis and analysis of novel HIF-1 $\alpha$  binding compounds based on the above two literature scaffolds.

### 5.1 HIF-1 $\alpha$ binding derivatives chemical synthesis

To achieve the structure of ER-400583-00, as shown in *Figure 1.6.e*, two separate synthesis paths were attempted. The first synthetic route looked at achieving the SONOGASHIRA cross-coupling using 4-fluoroiodobenzene (FIB) as the building block. Firstly, compound **1** was synthesized but the next coupling to create compound **2** could not be achieved. Thus, a new strategy was tested, by first synthesizing compound **3** and then finally compound **4** was obtained as the alkyne-containing precursor to be cross-coupled to FIB. Numerous Sonogashira parameters were tested on compound **4** using FIB, and this synthetic route (compound **5**) was unable to achieve the desired library of compounds. To fully determine the reason for the failure of this Sonogashira reaction, the simple reaction for compound **6** was tested. Overall, it was a low-yielding reaction, that demonstrated the electron-donating effect of the amine substitution hindered the alkyne in the Sonogashira reaction mechanism.

The second route then removed the alkyne from the large electron-donating structure of compound **4**. Instead, the Sonogashira cross-coupling reaction using 4-fluorophenylacetylene (FPA) was explored. Firstly, compound **7** was synthesized and further modified to create the iodo-containing compound **8**. Compound **8** as the iodine-containing precursor was then cross-coupled to FPA. Leading overall to the synthesis of a small library of compounds **9 – 20**. Additionally, several cyclic peptide structures were synthesized based on Cyclo-CLLFVY, as shown in *Figure 1.6.c*. Overall leading to a library of compounds that require further analysis in their ability to bind HIF-1 $\alpha$ .

Compound 1: *p*-((4-((3-Pyridyl)methyl)-1-piperazinyl)methyl)benzoic acid

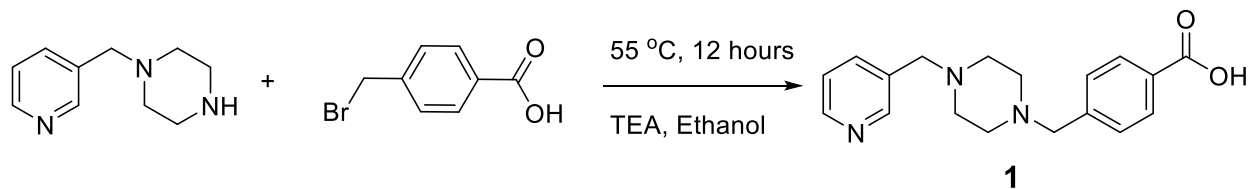


*Figure 5.1. Reaction scheme for the synthesis of compound 1 from the commercially available starting materials.*

1-Pyridin-3-ylmethyl-piperazine (100 mg, 0.565 mmol) along with triethylamine (TEA) (63  $\mu$ L, 0.45 mmol) were combined in ethanol (EtOH) (15 mL) and added dropwise to a solution of 4-(bromomethyl)benzoic acid (120.9 mg, 0.565 mmol) in EtOH (7 mL). Once the addition was completed, the reaction was left at 55 °C for 12 hours. The reaction mixture was extracted into ethyl acetate (EtOAc), and the EtOAc layer was washed with brine and dried over sodium sulphate ( $\text{Na}_2\text{SO}_4$ ). Next, the product was rotavaped down to near dryness and a large excess of water was added to precipitate the product of interest out of the solution. Yield: 50.9 mg (30%) as a creamy white colored crystalline solid. Thin-layer chromatography (TLC):  $R_f = 0.5$  (1:4, EtOAc:Hex). LR-MS  $m/z$  (ESI):  $\text{C}_{18}\text{H}_{21}\text{N}_3\text{O}_2$  ( $[\text{M}+\text{Na}]^+$ ) calcd. 334.15, found 334 (*figure S1*).  $^1\text{H-NMR}$  (600 MHz,  $\text{CD}_3\text{CN}$ ):  $\delta$ 2.91(t,  $J = 8.45$  Hz, 2H), 3.96 (t,  $J = 8.45$  Hz, 2H), 7.01 (td,  $J = 7.47$  and 0.99 Hz, 1H), 7.15 (dd,  $J = 7.45$  and 0.63 Hz, 1H), 7.22 (m, 1H), 7.53 (dd,  $J = 8.20$  and 7.49 Hz, 2H), 7.58 (dd,  $J = 8.11$  and 0.43 Hz, 1H), 7.65 (tt,  $J = 7.49$  and 1.22 Hz, 1H), 7.83 (dd,  $J = 8.52$  and 1.23 Hz, 2H) (*figure S2*).  $^{13}\text{C-NMR}$  (150 MHz,  $\text{CD}_3\text{CN}$ ):  $\delta$ 27.4, 50.2, 114.7, 117.3, 124.0, 125.4, 127.3, 127.5, 129.2, 132.5, 133.6, 136.6, 141.7 (*figure S3*).

Compound 2: *N-p*-Ethynylphenyl*p*-((4-((3-pyridyl)methyl)-1-piperazinyl)methyl)benzamide

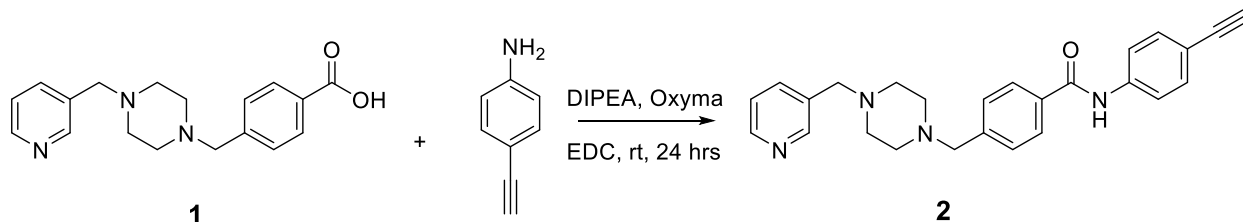


Figure 5.2. Reaction scheme for the synthesis of compound 2 from compound 1 and commercially available 4-ethynylaniline.

To a solution of Compound 1 (40 mg, 0.129 mmol) in N,N-dimethylformamide (DMF) (3.0 mL), 4-ethynylaniline (45.3 mg, 0.387 mmol) was added along with N,N-diisopropylethylamine (DIPEA) (224  $\mu$ L, 1.29 mmol), ethyl cyanoglyoxylate-2-oxime (Oxyma) (91.6 mg, 0.65 mmol) and N-(3-dimethylaminopropyl)-N-ethylcarbodiimide hydrochloride (EDC) (124 mg, 0.65 mmol). The reaction was left stirring at ambient temperature for 24 hours, after which the mixture was extracted into dichloromethane (CH<sub>2</sub>Cl<sub>2</sub>) and 2N hydrochloric acid (HCl). The combined CH<sub>2</sub>Cl<sub>2</sub> fractions were washed over brine, dried with Na<sub>2</sub>SO<sub>4</sub> and rotavaped to dryness to yield an orange-red oil. No true product could be isolated.

Compound 3: *N-p*-Ethynylphenyl*p*-(chloromethyl)benzamide

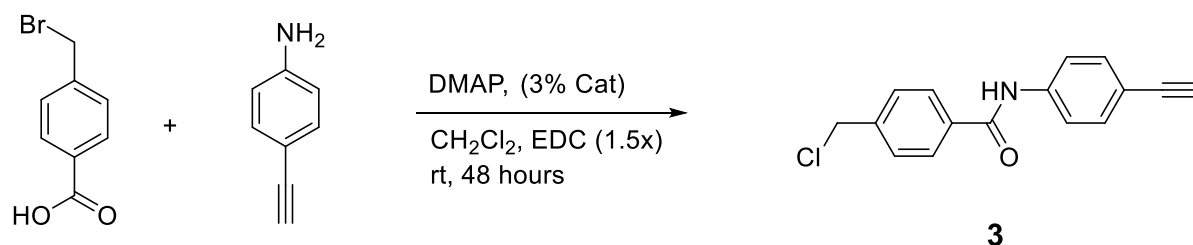
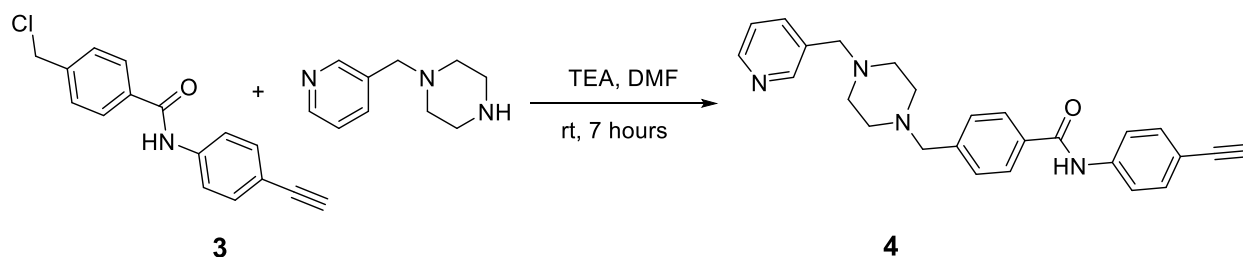


Figure 5.3. Reaction scheme for the synthesis of compound 3 from commercially available starting materials.

A mixture of 4-(bromomethyl)benzoic acid (2.0 g, 9 mmol), 4-ethynylaniline (1.09 g, 9 mmol), EDC (2.59 g, 14 mmol), and N,N-dimethylpyridin-4-amine (DMAP) (33 mg, 0.27 mmol) in CH<sub>2</sub>Cl<sub>2</sub> (200 mL) was allowed to stir at ambient temperature for 48 hours. Upon completion, the

reaction mixture was extracted with 2N HCl and sat. NaHCO<sub>3</sub>, and dried over Na<sub>2</sub>SO<sub>4</sub>. The CH<sub>2</sub>Cl<sub>2</sub> layer was then reduced to complete dryness to yield a creamy white powdery solid. (775 mg, 28% yield). LR-MS m/z (ESI): C<sub>16</sub>H<sub>12</sub>ClNO ([M+Na]<sup>+</sup>) calcd. 292.05, found 292.0 (*figure S4*). HR-MS m/z (ESI): C<sub>16</sub>H<sub>12</sub>ClNO ([M+Na]<sup>+</sup>) calcd. 292.05, found 292.0499 (*figure S5*). <sup>1</sup>H-NMR (600 MHz, DMSO-d<sub>6</sub>): δ4.12 (s, 1H), 4.85 (s, 2H), 7.48 (d, J = 8.74 Hz, 2H), 7.60 (d, J = 8.51 Hz, 2H), 7.82 (d, J = 8.83 Hz, 2H), 7.96 (d, J = 8.42 Hz, 2H), 10.43 (s, 1H) (*figure S6*). <sup>13</sup>C-NMR (150 MHz, DMSO-d<sub>6</sub>): δ45.9, 80.5, 84.0, 117.0, 120.5, 128.6, 129.3, 132.7, 135.0, 140.1, 141.7, 165.7 (*figure S7*).

**Compound 4:** *N-p-Ethynylphenylp-((4-((3-pyridyl)methyl)-1-piperazinyl)methyl)benzamide*



*Figure 5.4. Reaction scheme for the synthesis of compound 4 from compound 3 and commercially available 1-pyridin-3-ylmethyl-piperazine.*

*N-p-Ethynylphenylp-(chloromethyl)benzamide* (0.77 g, 2.7 mmol) was combined with 1-pyridin-3-ylmethyl-piperazine (350 μL, 2.1 mmol) and TEA (370 mL, 2.7 mmol) in DMF (5 mL) and allowed to react for 7 hours at ambient temperature. Upon completion, the reaction was diluted with CH<sub>2</sub>Cl<sub>2</sub> and extracted firstly into 2N HCl. The aqueous layers were collected and basified with 5N sodium hydroxide (NaOH), once basified the aqueous layer was extracted back into CH<sub>2</sub>Cl<sub>2</sub>. Now the CH<sub>2</sub>Cl<sub>2</sub> layers were reduced to complete dryness to yield the product as a light yellow solid (0.8113 g, 93% yield). LR-MS m/z (ESI): C<sub>26</sub>H<sub>26</sub>N<sub>4</sub>O ([M+H]<sup>+</sup>) calcd. 411.22, found 411.2, ([M+Na]<sup>+</sup>) calcd. 433.20, found 433.2. (*figure S8*) HR-MS m/z (ESI): C<sub>26</sub>H<sub>26</sub>N<sub>4</sub>O ([M+H]<sup>+</sup>) calcd. 411.2179, found 411.2171, ([M+Na]<sup>+</sup>) calcd. 433.1999, found 433.1995. (*figure S9*) <sup>1</sup>H-NMR (600 MHz, DMSO-d<sub>6</sub>): δ4.12 (s, 1H), 4.85 (s, 2H), 7.48 (d, J = 8.74 Hz, 2H), 7.60 (d, J = 8.51 Hz, 2H), 7.82 (d, J = 8.83 Hz, 2H), 7.96 (d, J = 8.42 Hz, 2H), 10.43 (s, 1H) (*figure S10*). <sup>13</sup>C-

NMR (150 MHz, DMSO- $d_6$ ):  $\delta$ 45.9, 80.5, 84.0, 117.0, 120.5, 128.6, 129.3, 132.7, 135.0, 140.1, 141.7, 165.7. (*figure S11*).

Compound 5: *N*-(*p*-(2-(*p*-Fluorophenyl)ethynyl)phenyl)*p*-((4-[(3-pyridyl)methyl]-1-piperazinyl)methyl)benzamide

The reaction scheme as shown in *figure 5.5.*, was tested using six different palladium-catalyzed Sonogashira reactions to attempt the synthesis of compound **5**.

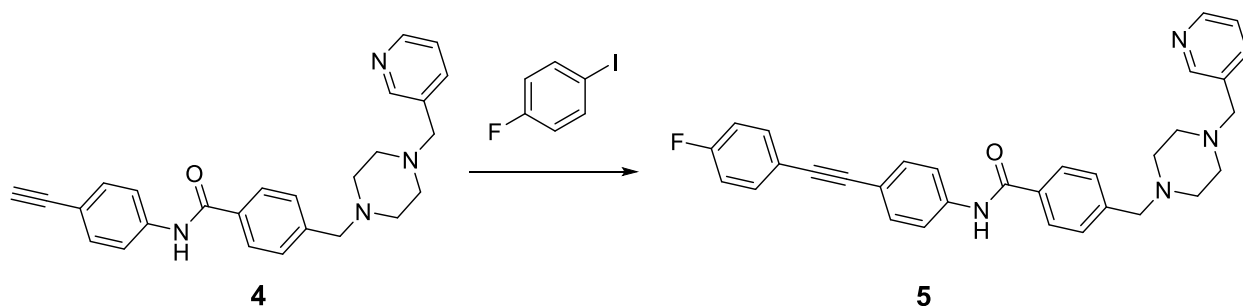


*Figure 5.5. Reaction scheme for the synthesis of compound 5 from compound 4 and commercially available 4-fluoroiodobenzene.*

#### *Synthesis route compound 5A:*

Compound **4** (105 mg, 0.26 mmol) along with FIB (36  $\mu$ L, 0.31 mmol) were combined with the catalyst system of bis(triphenylphosphine)palladium(II) dichloride (PdCl<sub>2</sub>(PPh<sub>3</sub>)<sub>2</sub>) (9.0 mg, 0.013 mmol), copper (I) iodide (CuI) (2.4 mg, 0.013 mmol), and TEA (36  $\mu$ L, 0.26 mmol) in a solution of DMF (3 mL) and the reaction was stirred in an oil bath at 75 °C for 6 hours. The reaction was monitored every 60 minutes with TLC and upon completion, the reaction mixture was diluted with 2N HCl and then extracted back into CH<sub>2</sub>Cl<sub>2</sub> and the aqueous extract was kept. Next, the acidic aqueous layer was basified with 5N NaOH; which turned the aqueous layer from a dark orange color to yellowy-white color. Finally, the basified aqueous layer was extracted back with CH<sub>2</sub>Cl<sub>2</sub> and this organic layer was rotavaped down to reveal a yellow residue. The product was purified using Silica gel Column Chromatography (1:4 MeOH:CH<sub>2</sub>Cl<sub>2</sub>) and fractions 31 to 39 were combined to give a yellow powder after rotary evaporation. The fine yellow powder (15.3 mg), was determined to not be the correct product of interest.

*Synthesis route compound 5B:*

From Zhong *et al.*, this experiment is a copper-free Sonogashira reaction with nitrogen-containing ligands and TEA [120]. Compound **4** (10 mg, 0.024 mmol) along with FIB (10  $\mu$ L, 0.086 mmol) were combined with the catalyst system of PdCl<sub>2</sub>(PPh<sub>3</sub>)<sub>2</sub> (2.0 mg, 2.8  $\mu$ mol) and TEA (50  $\mu$ L, 0.26 mmol) in a solution of DMF (400  $\mu$ L) and the reaction was shaken on the Thermoshaker at 85 °C for 30 minutes. Upon completion, the reaction was acidified with 2N HCl (600  $\mu$ L) and centrifuged. The resulting liquid layers were tested by HPLC and no products could be determined.

*Synthesis route compound 5C:*

Compound **4** (2 mg, 5  $\mu$ mol) along with FIB (0.4  $\mu$ L, 0.003 mmol) were combined with the catalyst system of palladium (II) acetate (Pd(OAc)<sub>2</sub>) (0.01 mg, 0.045  $\mu$ mol), and TEA (1.4  $\mu$ L, 0.01 mmol) in a solution of water (2.0  $\mu$ L) and the reaction was shaken on the Thermoshaker at 25 °C for 6 hours under nitrogen. Upon completion, the reaction was acidified with 2N HCl (1.0 mL) and CH<sub>3</sub>CN (1.0 mL) was added to the reaction mixture to increase solubility. The reaction was centrifuged, and the resulting liquid layers were tested by HPLC and no products could be determined.

*Synthesis route compound 5D:*

Compound **4** along with FIB were combined with different catalyst systems as shown in *Table 5.1*. All reactions were shaken on the Thermoshaker at 80 °C and tested for completion on TLC (1:4 MeOH: CH<sub>2</sub>Cl<sub>2</sub>) at 1, 5, 30, 60 and 90 minutes. Upon completion, the only reaction demonstrating a change was reaction compound **5.D.4**. This reaction was then acidified with 2N HCl (1.0 mL) and centrifuged. The resulting liquid layers were tested by HPLC and no products were observed.

*Synthesis route compound 5E:*

From Hierso *et al.*, this experiment used ferrous catalysts alongside palladium catalysts in a Sonogashira reaction [121]. Compound **4** (35.3 mg, 0.085 mmol) along with FIB (12  $\mu$ L, 0.102 mmol) were combined with the catalyst system of PdCl<sub>2</sub>(PPh<sub>3</sub>)<sub>2</sub> (0.6  $\mu$ g, 0.85  $\mu$ mol), CuI (3.1 mg, 0.016 mmol), 1,1'-bis(diphenylphosphino)ferrocene (dppf) (1.3 mg, 2.3  $\mu$ mol), and potassium

carbonate ( $K_2CO_3$ ) (31.2 mg, 0.23 mmol) in a solution of DMF (5.0 mL) and the reaction was stirred in an oil bath at 130 °C for 20 hours under nitrogen. Upon completion, the reaction mixture was worked up with dilution of 2N HCl and then extracted back into  $CH_2Cl_2$  and the aqueous extract was kept. Next, the acidic aqueous layer was basified with 5N NaOH and finally, the basified aqueous layer was extracted back with  $CH_2Cl_2$  and this organic layer was rotavaped down to give a brown powder. The product was tested using TLC and NMR and was determined to not be the correct product of interest.

*Table 5.1. Reaction compositions for the synthesis of Compound 5.D. Catalysts used including tetrakis(triphenylphosphine)palladium(0) ( $Pd(PPh_3)_4$ ), bis(dibenzylideneacetone)palladium(0) ( $Pd(dba)_2$ ), palladium(II) nitrate ( $Pd(NO_3)_2$ ), 3,3',3''-Phosphanetriyltris(benzenesulfonic acid) trisodium salt ( $tppts$ )[119].*

<b>Reaction ID</b>	<b>Palladium Catalyst</b>	<b>Pd (mg)</b>	<b>CuI (mg)</b>	<b>Compound 4 (mg)</b>	<b>TEA (<math>\mu</math>L)</b>	<b><math>CH_3CN</math> (<math>\mu</math>L)</b>	<b><math>H_2O</math> (<math>\mu</math>L)</b>	<b>FIB (<math>\mu</math>L)</b>
<b>C.5.D.1</b>	$PdCl_2(PPh_3)_2$	1.0	2.5	2.6	5.0	500	0	1.0
<b>C.5.D.2</b>	$Pd(PPh_3)_4$	1.3	6.1	3.0	5.0	500	0	1.0
<b>C.5.D.3</b>	$Pd(OAc)_2$	1.2	3.0	2.1	5.0	500	0	1.0
<b>C.5.D.4</b>	$Pd(dba)_2$	1.2	4.3	4.1	5.0	500	0	1.0
<b>C.5.D.5</b>	$Pd(NO_3)_2$	1.4	2.4	2.1	5.0	300	200	1.0
<b>C.5.D.6</b>	$Pd(tppts)_4$	1.0	3.2	2.7	5.0	300	200	1.0

*Synthesis route compound 5F:*

From Okamoto *et al.*, this experiment was done using NEAT conditions [122]. Compound 4 (32.8 mg, 0.080 mmol) along with FIB (7  $\mu$ L, 0.060 mmol) were combined with the catalyst system of  $Pd(OAc)_2$  (3.1  $\mu$ g, 0.014  $\mu$ mol), CuI (3.1 mg, 0.016 mmol), triphenylphosphine ( $PPh_3$ ) (1.6 mg, 6.1  $\mu$ mol), and TEA (304  $\mu$ L, 2.2 mmol) and the reaction was left shaking at ambient temperature for 72 hours under nitrogen. Upon completion, the reaction mixture was acidified with 2N HCl and then extracted with  $CH_2Cl_2$ . The aqueous extract was kept was then basified with 5N NaOH and finally, the basified aqueous layer was extracted back with  $CH_2Cl_2$ . The organic layer was then washed with saturated  $NaHCO_3$  and rotavaped to complete dryness. The residue was then re-

suspended in CH<sub>3</sub>CN and tested with HPLC. Collected peaks on HPLC were tested using LC-MS and no products could be determined.

Compound 6: *p*-(2-(*p*-Fluorophenyl)ethynyl)aniline

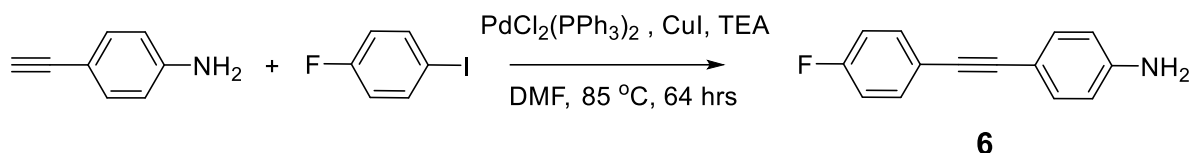


*Figure 5.6. Reaction scheme for the synthesis of compound 6 from commercially available starting materials.*

4-Ethynylaniline (257.4 mg, 2.2 mmol) was combined with FIB (494  $\mu$ L, 4.3 mmol) and the catalyst system of PdCl<sub>2</sub>(PPh<sub>3</sub>)<sub>2</sub> (5.3 mg, 7.6  $\mu$ mol), CuI (3.3 mg, 0.017 mmol), and TEA (446  $\mu$ L, 3.2 mmol) in a solution of DMF (10 mL) and the reaction was stirred in an oil bath at 85°C for 64 hours. Upon completion, the reaction mixture was acidified with 2N HCl and extracted three times into CH<sub>2</sub>Cl<sub>2</sub>. The combined CH<sub>2</sub>Cl<sub>2</sub> fractions were rotavaped to near dryness and the residue was purified by silica column chromatography using a gradient of CH<sub>2</sub>Cl<sub>2</sub> to EtOAc. The product was in the pure EtOAc extracts with a TLC R<sub>f</sub>=0.85 (50:50 EtOAc:Hexane). Overall the product was a pinkish-red oil (79 mg, 17% yield) LR-MS m/z (ESI): C<sub>14</sub>H<sub>10</sub>FN ([M+H]<sup>+</sup>) calcd. 212.25, found 212.1. (*figure S12*) HR-MS m/z (ESI): C<sub>14</sub>H<sub>10</sub>FN ([M+H]<sup>+</sup>) calcd. 212.087, found 212.0869. (*figure S13*) <sup>1</sup>H-NMR (600 MHz, DMSO-d<sub>6</sub>):  $\delta$ 5.58 (s, 1H), 4.85 (s, 2H), 6.56 (d, J = 8.68 Hz, 2H), 7.19 (d, J = 8.68 Hz, 2H), 7.23 (t, J = 8.95 Hz, 2H), 7.51 (dd, J = 8.92 and 5.48 Hz, 2H) (*figure S14*). <sup>13</sup>C-NMR (150 MHz, DMSO-d<sub>6</sub>):  $\delta$ 85.8, 91.4, 108.4, 114.1, 116.2, 116.4, 120.3, 133.0, 133.4, 133.5, 150.0, 161.1. (*figure S15*). <sup>19</sup>F-NMR (600MHz, DMSO-d<sub>6</sub>):  $\delta$ 112.1. (*figure S16*).

Compound 7: *p*-(2-(*p*-Fluorophenyl)ethynyl)aniline

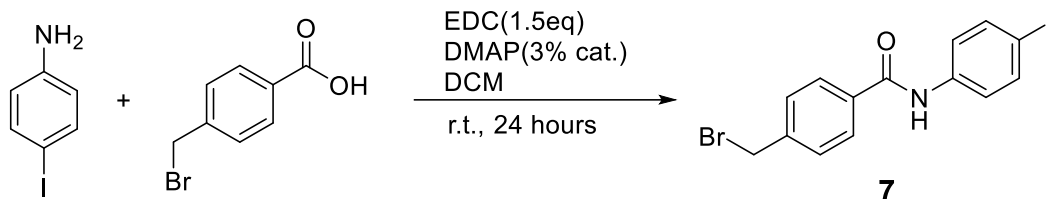


Figure 5.7. Reaction scheme for the synthesis of compound 7 from commercially available starting materials.

4-Iodoaniline (1.49 g, 6.8 mmol) was combined with 4-(bromomethyl)benzoic acid (1.46 g, 6.8 mmol), along with the catalyst system of EDC (1.96 g, 10.0 mmol) and DMAP (24.9 mg, 0.204 mmol) in CH<sub>2</sub>Cl<sub>2</sub> (25mL). The reaction was allowed to stir at ambient temperature for 24 hours, during this time the reaction mixture became increasingly cloudy as the product of interest began to precipitate from the solution. Upon completion, the reaction mixture was simply filtered to remove the product of interest as a fine white powder (1.87 g, 66% yield). LR-MS *m/z* (ESI): C<sub>14</sub>H<sub>11</sub>BRINO ([M+Cl]<sup>-</sup>) calcd. 449.88, found 449.88., ([M+Br]<sup>-</sup>) calcd. 493.82, found 493.82. (figure S17) HR-MS *m/z* (ESI): C<sub>14</sub>H<sub>11</sub>BRINO ([M-H]<sup>-</sup>) calcd. 413.8996, found 413.8987, ([M+Cl]<sup>-</sup>) calcd. 449.8763, found 449.8751, ([M+Br]<sup>-</sup>) calcd. 493.8258, found 493.8249. (figure S18) <sup>1</sup>H-NMR (600 MHz, DMSO-d<sub>6</sub>): δ4.81 (d, *J* = 41.3 Hz, 2H), 7.60 (dd, *J* = 8.45 and 3.80 Hz, 2H), 7.63 (dd, *J* = 8.97 and 2.34 Hz, 2H), 7.70 (dd, *J* = 8.89 and 0.73 Hz, 2H), 7.93 (dd, *J* = 15.50 and 8.40 Hz, 2H), 10.36 (d, *J* = 3.29 Hz, 1H) (figure S19). <sup>13</sup>C-NMR (150 MHz, DMSO-d<sub>6</sub>): δ62.8, 87.9, 122.9, 126.5, 128.0, 128.6, 129.3, 129.7, 135.0, 137.7, 139.4, 141.7, 142.1, 165.7. (figure S20).

Compound 8: *N*-*p*-Iodophenyl-*p*-((4-((3-pyridyl)methyl)-1-piperazinyl)methyl)benzamide

*p*-(2-(*p*-Fluorophenyl)ethynyl)aniline (1.2 g, 2.9 mmol) was combined with 1-pyridin-3-ylmethylpiperazine (0.46 g, 2.6 mmol) in a solution of TEA (404 μL, 2.9 mmol) and DMF (7.0 mL). The reaction was allowed to stir at ambient temperature for 1 hour and the product as it was completed would precipitate out of the solution. This precipitate was simply filtered from the filtrate and lyophilized overnight to yield the product as a fine white powder (0.61 g, 46% yield).

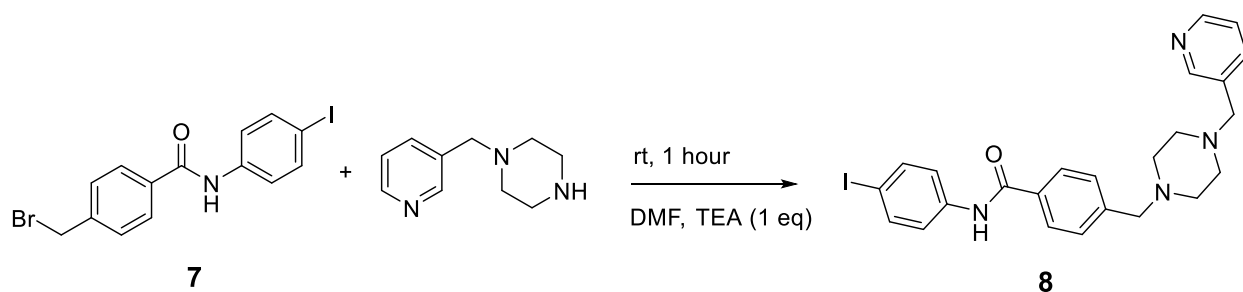


Figure 5.8. Reaction scheme for the synthesis of compound **8** from compound **7** and commercially available 1-pyridin-3-ylmethyl-piperazine.

LR-MS  $m/z$  (ESI):  $C_{24}H_{25}IN_4O$  ( $[M+H]^+$ ) calcd. 513.12, found 513, ( $[M+Na]^+$ ) calcd. 535.10, found 535. (figure S21) HR-MS  $m/z$  (ESI):  $C_{24}H_{25}IN_4O$  ( $[M+H]^+$ ) calcd. 513.1146, found 513.1137. (figure S22)  $^1H$ -NMR (600 MHz,  $DMSO-d_6$ ):  $\delta$  2.40 (s, 8H), 3.50 (s, 2H), 3.54 (s, 2H), 7.35 (dd,  $J = 7.72$  and  $4.79$  Hz, 1H), 7.44 (d,  $J = 8.24$  Hz, 2H), 7.63 (d,  $J = 8.86$  Hz, 2H), 7.69 (m, 3H), 7.89 (d,  $J = 8.27$  Hz, 2H), 8.46 (dd,  $J = 4.75$  and  $1.63$  Hz, 1H), 8.48 (d,  $J = 1.65$  Hz, 1H), 10.30 (s, 1H) (figure S23).  $^{13}C$ -NMR (150 MHz,  $DMSO-d_6$ ):  $\delta$  52.9, 53.0, 59.6, 62.0, 87.7, 122.9, 123.9, 128.1, 129.1, 133.8, 134.0, 137.0, 137.7, 139.5, 142.8, 148.7, 150.5, 166.0 (figure S24). Analytical Luna HPLC,  $t_R = 14.98$  min, >99 % purity (figure S25).

#### General reaction scheme for compound **9** to compound **20**

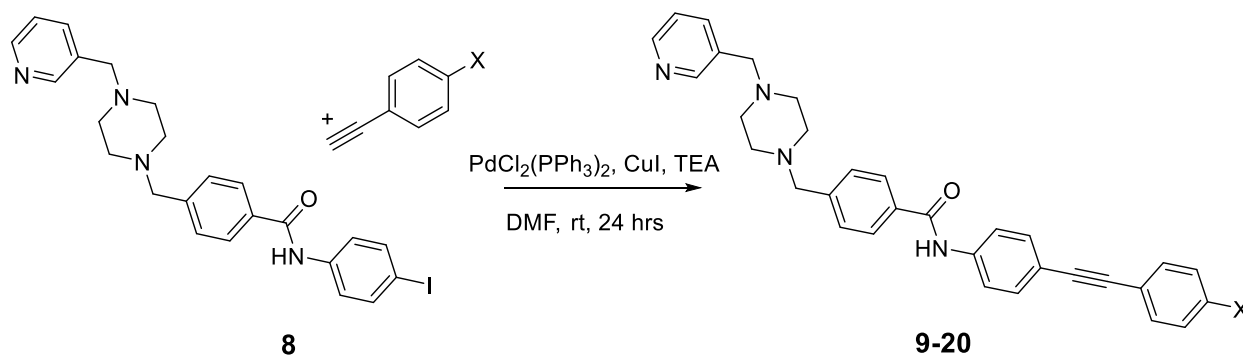


Figure 5.9. General reaction scheme for the production of compound **9** to compound **20** from compound **8** and commercially available 4-phenylacetylene derivatives.

This synthesis was modified from Nagao *et al.* [123] with all reactions being completed in a 1.5 mL Eppendorf® Lobind microcentrifuge tube. The reaction was left shaking at 1100 rpm on the

Thermoshaker for 24 hours at ambient temperature under a nitrogen atmosphere. The catalyst system of PdCl<sub>2</sub>(PPh<sub>3</sub>)<sub>2</sub> (3.1 mg, 0.0044 mmol), CuI (1.7 mg, 0.0089 mmol), and triethylamine (36.8 μL, 0.27 mmol) in a solution of DMF (500 μL) was used. Upon completion, the reaction mixture was diluted with EtOAc (2 mL), THF (2.0 mL) and H<sub>2</sub>O (4.0 mL). Next, the aqueous layer was removed and the organic layer was washed twice more with additional water. The organic layer was then rotary evaporated to complete dryness and purified using silica gel chromatography in a pipette tip. The column was firstly equilibrated with simply CH<sub>2</sub>Cl<sub>2</sub> and the sample was dissolved in MeOH:CH<sub>2</sub>Cl<sub>2</sub> (1:8, 500 mL) for injection. Fractions were eluted with CH<sub>2</sub>Cl<sub>2</sub> followed by MeOH:CH<sub>2</sub>Cl<sub>2</sub> (1:8), and fractions were tested on RP-TLC using CH<sub>3</sub>CN:H<sub>2</sub>O (80:20) as the mobile phase. Products of interest were identified, and the fractions rotavaped to reveal the final product. All products were confirmed using HPLC on a LUNA analytical column as well as NMR and Mass. Analytical HPLC analysis of products was performed using a Phenomenex Luna<sup>®</sup> C18(2) column (100 Å, 250 x 4.6 mm, 10 mm) using gradient elutions specific to the given compound (Gilson 321 pump, UV/VIS-155 dual-wavelength detector). *Table 3.2* includes a summary of the synthesis for compounds **9** to **20**. It should be noted that CuI amount varies overtime, due to the degradation of the chemical.

*Table 5.2. Summary data for the production of compound 9 to compound 20. Including compound ID (Cmpd), "X" moiety as demonstrated in Figure 5.9, HPLC retention time, synthesis yield, compound isolated purity and physical properties.*

<b>Cmpd</b>	<b>X</b>	<b>HPLC t<sub>R</sub> (min)</b>	<b>Yield (%)</b>	<b>Mass (mg)</b>	<b>Purity (%)</b>	<b>Physical properties</b>
<b>9</b>	F	14.98	51	16.0	>99	Light yellow powdery solid
<b>10</b>	OMe	18.43	24	11.0	>99	Dark grey powdery solid
<b>11</b>	NH <sub>2</sub>	17.92	61	26.5	>99	Burnt red powdery solid
<b>12</b>	Ph	12.24	13	6.3	>84	Light brown tan powdery solid
<b>13</b>	Me	23.65	26	11.3	>99	Bright orange red powdery solid
<b>14</b>	C(CH <sub>3</sub> ) <sub>3</sub>	20.21	46	22.1	>99	Light orange powdery solid
<b>15</b>	Cl	25.49	32	14.4	>99	Light brown powdery solid
<b>16</b>	Br	21.29	29	14.2	>99	Light yellow powdery solid
<b>17</b>	H	21.89	59	26.1	>95	Dark brown powdery solid
<b>18</b>	NO <sub>2</sub>	18.48	38	17.4	>99	Brown grainy solid
<b>19</b>	N(CH <sub>3</sub> ) <sub>2</sub>	18.3	41	37.9	>95	Bright teal green powdery solid
<b>20</b>	CF <sub>3</sub>	14.15	43	21.1	>95	Dark brownish grey powdery solid

Compound 9: N-(4-(1-ethynyl-4-fluorophenyl)phenyl)-4-((4-(pyridine-3-ylmethyl)piperazin-1-yl)methyl)benzamide

*N*-(4-iodophenyl)-4-((4-(pyridine-3-ylmethyl)piperazin-1-yl)methyl)-benzamide (31.8 mg, 0.062 mmol) was combined with 1-ethynyl-4-fluorobenzene (21.8 mg, 0.18 mmol) and the catalyst system as shown in the general scheme, The product was a light yellow solid (16.0 mg, 51% yield). LR-MS *m/z* (ESI): C<sub>32</sub>H<sub>29</sub>FN<sub>4</sub>O ([M+H]<sup>+</sup>) calcd. 505.24, found 505.2. (*figure S26*). HR-MS *m/z* (ESI): C<sub>32</sub>H<sub>29</sub>FN<sub>4</sub>O ([M+H]<sup>+</sup>) calcd. 505.2398, found 505.2399. (*figure S27*). <sup>1</sup>H-NMR (600 MHz, CDCl<sub>3</sub>): δ 2.51 (s, 8H), 3.55 (s, 2H), 3.60 (s, 2H), 7.07 (t, *J* = 8.75 Hz, 2H), 7.27 (m, 1H), 7.48 (d, *J* = 8.34 Hz, 2H), 7.54 (m, 4H), 7.68 (m, 3H), 7.84 (d, *J* = 8.32 Hz, 2H), 8.53 (dd, *J* = 4.80 and 1.67 Hz, 1H), 8.56 (d, *J* = 1.57 Hz, 1H). (*figure S28*). <sup>13</sup>C-NMR (150 MHz, CDCl<sub>3</sub>): δ 53.0, 53.1, 60.2, 62.5, 88.1, 88.8, 115.6, 115.7, 118.9, 119.6, 119.4, 123.3, 127.0, 129.4, 132.4, 133.4, 133.5, 133.6, 136.7, 138.0, 143.0, 148.6, 150.5, 161.6, 163.3, 165.4. (*figure S29*). <sup>19</sup>F-NMR (600MHz, CDCl<sub>3</sub>): δ 111.1. (*figure S30*). Analytical Luna HPLC, *t<sub>R</sub>* = 18.43 min, >99 % purity. (*figure S31*).

Compound 10: N-(4-(4-ethynylanisole)phenyl)-4-((4-(pyridine-3-ylmethyl)piperazin-1-yl)methyl)benzamide

*N*-(4-iodophenyl)-4-((4-(pyridine-3-ylmethyl)piperazin-1-yl)methyl)-benzamide (45.0 mg, 0.088 mmol) was combined with 4-ethynylanisole (34.3 mg, 0.26 mmol) and the catalyst system as shown in the general scheme. The product was a dark grey powdery solid (11.0 mg, 26% yield). LR-MS *m/z* (ESI): C<sub>32</sub>H<sub>32</sub>N<sub>4</sub>O<sub>2</sub> ([M+H]<sup>+</sup>) calcd. 517.24, found 517.3. (*figure S32*). HR-MS *m/z* (ESI): C<sub>32</sub>H<sub>32</sub>N<sub>4</sub>O<sub>2</sub> ([M+H]<sup>+</sup>) calcd. 517.2598, found 517.2596. (*figure S33*). <sup>1</sup>H-NMR (600 MHz, CDCl<sub>3</sub>): δ 2.51 (s, 8H), 3.55 (s, 2H), 3.60 (s, 2H), 3.85 (s, 3H), 6.90 (d, *J* = 8.92 Hz, 2H), 7.27 (m, 1H), 7.48 (m, 4H), 7.54 (d, *J* = 8.81 Hz, 2H), 7.68 (m, 3H), 7.84 (d, *J* = 8.33 Hz, 2H), 8.53 (dd, *J* = 4.80 and 1.67 Hz, 1H), 8.56 (d, *J* = 1.55 Hz, 1H). (*figure S34*). <sup>13</sup>C-NMR (150 MHz, CDCl<sub>3</sub>): δ 53.0, 53.1, 55.3, 60.2, 62.5, 87.8, 89.2, 114.0, 115.4, 119.4, 119.6, 121.8, 123.3, 127.0, 129.4, 132.3, 133.0, 133.5, 133.6, 136.7, 137.6, 138.0, 142.9, 148.6, 150.5, 159.6, 165.3. (*figure S35*). Analytical Luna HPLC, *t<sub>R</sub>* = 17.92 min, >99 % purity. (*figure S36*).

Compound 11: N-(4-(4-ethynylaniline)phenyl)-4-((4-(pyridine-3-ylmethyl)piperazin-1-yl)methyl)benzamide

*N*-(4-iodophenyl)-4-((4-(pyridine-3-ylmethyl)piperazin-1-yl)methyl)-benzamide (45.0 mg, 0.088 mmol) was combined with 4-ethynylaniline (46.8 mg, 0.40 mmol) and the catalyst system as shown in the general scheme. The product was a burnt red powdery solid (26.5 mg, 61% yield). LR-MS *m/z* (ESI): C<sub>32</sub>H<sub>31</sub>N<sub>5</sub>O ([M+2H]<sup>2+</sup>) calcd. 251.82, found 251.7. (*figure S37*). <sup>1</sup>H-NMR (600 MHz, DMSO-d<sub>6</sub>): δ 2.39 (s, 8H), 3.55 (s, 2H), 3.58 (s, 2H), 5.53 (s, 2H), 6.55 (d, *J* = 8.62 Hz, 4H), 7.19 (d, *J* = 8.59 Hz, 2H), 7.44 (m, 4H), 7.80 (d, *J* = 8.80 Hz, 4H), 7.90 (d, *J* = 8.28 Hz, 2H), 10.32 (s, 1H). (*figure S38*). <sup>13</sup>C-NMR (150 MHz, DMSO-d<sub>6</sub>): δ 53.0, 53.1, 62.0, 87.0, 91.0, 108.8, 114.1, 118.7, 120.5, 128.1, 129.1, 131.8, 132.9, 134.0, 139.3, 142.7, 149.8, 166.0. (*figure S39*). Analytical Luna HPLC, *t<sub>R</sub>* = 12.24 min, 84 % purity. (*figure S40*).

Compound 12: N-(4-(4-ethynylbiphenyl)phenyl)-4-((4-(pyridine-3-ylmethyl)piperazin-1-yl)methyl)benzamide

*N*-(4-iodophenyl)-4-((4-(pyridine-3-ylmethyl)piperazin-1-yl)methyl)-benzamide (45.0 mg, 0.088 mmol) was combined with 4-ethynylbiphenyl (47.0 mg, 0.26 mmol) and the catalyst system as shown in the general scheme. The product was a light brown tan powdery solid (6.3 mg, 13% yield). LR-MS *m/z* (ESI): C<sub>38</sub>H<sub>34</sub>N<sub>4</sub>O ([M+2H]<sup>2+</sup>) calcd. 282.36, found 282.2. (*figure S41*). <sup>1</sup>H-NMR (600 MHz, DMSO-d<sub>6</sub>): δ 2.45 (s, 8H), δ 3.56 (s, 2H), 3.60 (s, 2H), 7.39 (t, *J* = 7.34 Hz, 1H), 7.48 (m, 4H), 7.56 (d, *J* = 8.57 Hz, 2H), 7.63 (d, *J* = 8.12 Hz, 2H), 7.72 (t, *J* = 9.71 Hz, 4H), δ 7.87 (d, *J* = 8.73 Hz, 2H), 7.92 (d, *J* = 8.14 Hz, 2H), 8.57 (bs, 3H), 10.39 (s, 1H). (*figure S42*). <sup>13</sup>C-NMR (150 MHz, DMSO-d<sub>6</sub>): δ 52.6, 52.7, 59.5, 61.8, 89.0, 90.8, 117.4, 120.5, 122.0, 127.1, 127.3, 128.2, 128.3, 129.3, 129.5, 132.3, 132.4, 134.0, 137.0, 139.6, 140.2, 140.5, 166.0. (*figure S43*). Analytical Luna HPLC, *t<sub>R</sub>* = 23.65 min, >95 % purity. (*figure S44*).

Compound 13: N-(4-(4-ethynyltoluene)phenyl)-4-((4-(pyridine-3-ylmethyl)piperazin-1-yl)methyl)benzamide

*N*-(4-iodophenyl)-4-((4-(pyridine-3-ylmethyl)piperazin-1-yl)methyl)-benzamide (45.0 mg, 0.088 mmol) was combined with 4-ethynyltoluene (33.5 mg, 0.29 mmol) and the catalyst system as shown in the general scheme. The product was a bright orange-red powdery solid (11.3 mg, 26%

yield). LR-MS  $m/z$  (ESI):  $C_{33}H_{32}N_4O$  ( $[M+2H]^{2+}$ ) calcd. 251.33, found 251.2. (*figure S45*).  $^1H$ -NMR (600 MHz, DMSO- $d_6$ ):  $\delta$  2.34 (s, 3H), 2.40 (s, 8H), 3.51 (s, 2H), 3.55 (s, 2H), 7.24 (d,  $J = 8.43$  Hz, 2H), 7.44 (m, 4H), 7.52 (d,  $J = 8.73$  Hz, 2H), 7.70 (s, 1H), 7.85 (d,  $J = 8.78$  Hz, 2H), 7.91 (d,  $J = 8.29$  Hz, 2H), 8.51 (bs, 3H), 10.38 (s, 1H). (*figure S46*).  $^{13}C$ -NMR (150 MHz, DMSO- $d_6$ ):  $\delta$  21.5, 53.0, 53.1, 59.6, 62.0, 89.3, 89.4, 117.6, 119.9, 120.5, 128.1, 129.1, 129.8, 131.6, 132.3, 133.9, 136.8, 138.8, 140.0, 142.8, 166.1. (*figure S47*). Analytical Luna HPLC,  $t_R = 20.21$  min, >99 % purity. (*figure S48*).

Compound 14: N-(4-(4-*tert*-butylphenylacetylene)phenyl)-4-((4-(pyridine-3-ylmethyl) piperazin-1-yl)methyl)benzamide

N-(4-iodophenyl)-4-((4-(pyridine-3-ylmethyl)piperazin-1-yl)methyl)-benzamide (45.0 mg, 0.088 mmol) was combined with 4-*tert*-butylphenylacetylene (47.6 mg, 0.30 mmol) and the catalyst as shown in the general scheme. The product was a light orange powdery solid (22.1 mg, 46% yield). LR-MS  $m/z$  (ESI):  $C_{36}H_{38}N_4O$  ( $[M+2H]^{2+}$ ) calcd. 272.36, found 272.3. (*figure S49*).  $^1H$ -NMR (600 MHz, DMSO- $d_6$ ):  $\delta$  1.29 (s, 9H), 2.40 (s, 8H), 3.53 (s, 2H), 3.54 (s, 2H), 7.48 (m, 6H), 7.53 (d,  $J = 8.73$  Hz, 2H), 7.74 (d,  $J = 5.95$  Hz, 1H), 7.85 (d,  $J = 8.80$  Hz, 2H), 7.90 (d,  $J = 8.27$  Hz, 2H), 8.77 (bs, 3H), 10.38 (s, 1H). (*figure S50*).  $^{13}C$ -NMR (150 MHz, DMSO- $d_6$ ):  $\delta$  31.4, 35.0, 53.0, 53.1, 60.0, 62.0, 89.2, 89.4, 117.6, 120.0, 120.5, 126.0, 128.1, 129.1, 131.5, 132.3, 133.9, 140.0, 142.8, 151.7, 166.1. (*figure S51*). Analytical Luna HPLC,  $t_R = 25.49$  min, >99 % purity. (*figure S52*).

Compound 15: N-(4-(1-chloro-4-ethynylbenzene)phenyl)-4-((4-(pyridine-3-ylmethyl) piperazin-1-yl)methyl)benzamide

N-(4-iodophenyl)-4-((4-(pyridine-3-ylmethyl)piperazin-1-yl)methyl)-benzamide (45.0 mg, 0.088 mmol) was combined with 1-chloro-4-ethynylbenzene (36.0 mg, 0.26 mmol) and the catalyst system as shown in the general scheme. The product was a light brown powdery solid (14.4 mg, 32% yield). LR-MS  $m/z$  (ESI):  $C_{32}H_{29}N_4OCl$  ( $[M+2H]^{2+}$ ) calcd. 261.54, found 261.2. (*figure S53*).  $^1H$ -NMR (600 MHz, DMSO- $d_6$ ):  $\delta$  2.41 (s, 8H), 3.51 (s, 2H), 3.55 (s, 2H), 7.37 (s, 1H), 7.45 (d,  $J = 8.33$ , 2H), 7.50 (d,  $J = 8.32$  Hz, 2H), 7.56 (m, 4H), 7.70 (d,  $J = 7.51$  Hz, 1H), 7.87 (d,  $J = 8.83$  Hz, 2H), 7.91 (d,  $J = 8.33$  Hz, 2H), 8.50 (bs, 2H), 10.40 (s, 1H). (*figure S54*).  $^{13}C$ -NMR (150

MHz, DMSO- $d_6$ ):  $\delta$  53.0, 53.1, 59.6, 62.0, 88.0, 91.1, 117.0, 120.5, 121.9, 128.2, 129.1, 129.4, 132.5, 133.4, 133.7, 133.9, 136.9, 140.4, 142.8, 166.1. (*figure S55*). Analytical Luna HPLC,  $t_R$  = 21.29 min, >99 % purity. (*figure S56*).

Compound 16: N-(4-(1-bromo-4-ethynylbenzene)phenyl)-4-((4-(pyridine-3-ylmethyl) piperazin-1-yl)methyl)benzamide

N-(4-iodophenyl)-4-((4-(pyridine-3-ylmethyl)piperazin-1-yl)methyl)-benzamide (45.0 mg, 0.088 mmol) was combined with 1-bromo-4-ethynylbenzene (47.8 mg, 0.26 mmol) and the catalyst system as shown in the general scheme. The product was a bright yellow powdery solid (14.2 mg, 29% yield). LR-MS  $m/z$  (ESI):  $C_{32}H_{29}N_4OBr$  ( $[M+2H]^{2+}$ ) calcd. 283.76, found 283.2. (*figure S57*).  $^1H$ -NMR (600 MHz, DMSO- $d_6$ ):  $\delta$  2.40 (s, 8H), 3.53 (s, 2H), 3.55 (s, 2H), 7.45 (d,  $J$  = 8.29 Hz, 2H), 7.50 (d,  $J$  = 8.64 Hz, 2H), 7.56 (d,  $J$  = 8.78 Hz, 2H), 7.63 (d,  $J$  = 8.64 Hz, 2H), 7.74 (s, 1H), 7.87 (d,  $J$  = 8.85 Hz, 2H), 7.91 (d,  $J$  = 8.30 Hz, 2H), 8.78 (bs, 3H), 10.40 (s, 1H). (*figure S58*).  $^{13}C$ -NMR (150 MHz, DMSO- $d_6$ ):  $\delta$  53.0, 59.8, 62.0, 88.1, 91.2, 117.0, 120.5, 122.2, 122.4, 128.1, 129.1, 131.9, 132.0, 132.1, 132.2, 132.3, 132.4, 132.5, 133.6, 133.8, 133.9, 140.4, 142.8, 162.7, 166.1. (*figure S59*). Analytical Luna HPLC,  $t_R$  = 21.89 min, >95 % purity. (*figure S60*).

Compound 17: N-(4-(Phenylethynyl)phenyl)-4-([4-(3-pyridinyl-methyl)-1-piperazinyl)methyl]benzamide (ER-400-583-00)

N-(4-iodophenyl)-4-((4-(pyridine-3-ylmethyl)piperazin-1-yl)methyl)-benzamide (45.0 mg, 0.088 mmol) was combined with phenylacetylene (29.0 mg, 0.28 mmol) and the catalyst system as shown in the general scheme. The product was a dark brown powdery solid (26.1 mg, 59% yield). LR-MS  $m/z$  (ESI):  $C_{32}H_{30}N_4O$  ( $[M+2H]^{2+}$ ) calcd. 244.32, found 244.2. (*figure S61*).  $^1H$ -NMR (600 MHz, DMSO- $d_6$ ):  $\delta$  2.40 (s, 8H), 3.52 (s, 2H), 3.55 (s, 2H), 7.44 (m, 5H), 7.55 (m, 4H), 7.72 (s, 1H), 7.87 (d,  $J$  = 7.82 Hz, 2H), 7.91 (d,  $J$  = 7.22 Hz, 2H), 8.62 (bs, 2H), 10.40 (s, 1H). (*figure S62*).  $^{13}C$ -NMR (150 MHz, DMSO- $d_6$ ):  $\delta$  53.0, 53.1, 60.0, 62.0, 89.1, 90.0, 117.4, 120.5, 123.0, 128.2, 129.0, 129.1, 129.2, 129.4, 131.7, 132.4, 132.9, 133.9, 136.8, 140.2, 142.8, 166.1. (*figure S63*). Analytical Luna HPLC,  $t_R$  = 18.48 min, >99 % purity. (*figure S64*).

Compound 18: N-(4-(1-ethylnyl-4-nitrobenzene)phenyl)-4-((4-(pyridine-3-ylmethyl) piperazin-1-yl)methyl)benzamide

N-(4-iodophenyl)-4-((4-(pyridine-3-ylmethyl)piperazin-1-yl)methyl)-benzamide (45.0 mg, 0.088 mmol) was combined with 1-ethylnyl-4-nitrobenzene (47.8 mg, 0.32 mmol) and the catalyst system as shown in the general scheme. The product was a brown grainy solid (17.4 mg, 38% yield). LR-MS m/z (ESI): C<sub>32</sub>H<sub>29</sub>N<sub>5</sub>O<sub>3</sub> ([M+2H]<sup>2+</sup>) calcd. 266.63, found 266.7. (*figure S65*). <sup>1</sup>H-NMR (600 MHz, DMSO-d<sub>6</sub>): δ 2.39 (s, 8H), 3.55 (s, 2H), 3.62 (s, 2H), 7.46 (d, J = 8.20 Hz, 2H), 7.62 (d, J = 8.78 Hz, 2H), 7.81 (d, J = 8.96 Hz, 2H), 7.91 (m, 5H), 8.28 (d, J = 8.93 Hz, 2H), 10.45 (s, 1H). (*figure S66*). <sup>13</sup>C-NMR (150 MHz, DMSO-d<sub>6</sub>): δ 53.0, 53.1, 62.0, 87.7, 95.2, 116.3, 120.5, 122.8, 124.4, 128.2, 129.1, 129.9, 132.8, 132.9, 133.8, 137.7, 141.0, 142.9, 147.1, 166.1. (*figure S67*). Analytical Luna HPLC, t<sub>R</sub> = 18.30 min, >95 % purity. (*figure S68*).

Compound 19: N-(4-(4-ethylnyl-N,N-dimethylaniline)phenyl)-4-((4-(pyridine-3-ylmethyl) piperazin-1-yl)methyl)benzamide

N-(4-iodophenyl)-4-((4-(pyridine-3-ylmethyl)piperazin-1-yl)-methyl)benzamide (90.0 mg, 0.18 mmol) was combined with 4-ethylnyl-N,N-dimethylaniline (76.7 mg, 0.53 mmol) and the catalyst system as shown in the general scheme. The product was a bright teal green powdery solid (37.9 mg, 41% yield). LR-MS m/z (ESI): C<sub>34</sub>H<sub>35</sub>N<sub>5</sub>O ([M+2H]<sup>2+</sup>) calcd. 265.85, found 265.8. (*figure S69*). <sup>1</sup>H-NMR (600 MHz, DMSO-d<sub>6</sub>): δ 2.41 (s, 8H), 2.96 (s, 6H), 3.51 (s, 2H), 3.55 (s, 2H), 6.72 (d, J = 9.14 Hz, 2H), 7.35 (m, 3H), 7.46 (m, 4H), δ 7.70 (d, J = 7.80 Hz, 1H), 7.82 (d, J = 8.85, 2H), 7.91 (d, J = 8.34 Hz, 2H), 8.48 (d, J = 10.00 Hz, 2H), 10.35 (s, 1H). (*figure S70*). <sup>13</sup>C-NMR (150 MHz, DMSO-d<sub>6</sub>): δ 40.2, 52.9, 53.0, 59.6, 62.0, 87.8, 90.6, 100.0, 109.2, 112.4, 118.5, 120.5, 123.9, 128.1, 129.1, 131.8, 132.7, 134.0, 137.0, 139.4, 142.8, 148.7, 150.5, 166.0. (*figure S71*). Analytical Luna HPLC, t<sub>R</sub> = 14.15 min, >95 % purity. (*figure S72*).

Compound 20: N-(4-(1-ethynyl-4-(trifluoromethyl)benzene)-phenyl)-4-((4-(pyridine-3-ylmethyl) piperazin-1-yl)methyl)-benzamide

N-(4-iodophenyl)-4-((4-(pyridine-3-ylmethyl)-piperazin-1-yl)methyl)benzamide (45.0 mg, 0.088 mmol) was combined with 1-ethynyl-4-(trifluoromethyl)benzene (43.1 mg, 0.25 mmol) and the catalyst system as shown in the general scheme. The product was a dark brownish-grey powdery

solid (21.1 mg, 43% yield). LR-MS  $m/z$  (ESI):  $C_{33}H_{29}N_4F_3$  ( $[M+H]^+$ ) calcd. 555.61, found 555.2, ( $[M+2H]^{2+}$ ) calcd. 278.31, found 278.2. (*figure S73*).  $^1H$ -NMR (600 MHz, DMSO- $d_6$ ):  $\delta$  2.40 (s, 8H), 3.55 (s, 4H), 7.45 (d,  $J = 8.30$  Hz, 2H), 7.60 (d,  $J = 8.79$  Hz, 2H), 7.78 (m, 5H), 7.90 (m, 5H), 8.79 (bs, 2H), 10.43 (s, 1H). (*figure S74*).  $^{13}C$ -NMR (150 MHz, DMSO- $d_6$ ):  $\delta$  53.0, 53.1, 62.0, 87.8, 92.7, 116.6, 120.5, 123.6, 125.4, 125.9, 126.0, 126.1, 126.2, 127.3, 128.2, 128.7, 129.1, 132.4, 132.7, 133.8, 140.7, 142.9, 166.1. (*figure S75*). Analytical Luna HPLC,  $t_R = 21.63$  min, >99% purity. (*figure S76*).

#### Compound 21: *l*-(Ppg)LLFVY

Peptide *l*-(Ppg)LLFVY was prepared with the N-terminus of the peptide containing the *L*-propargylglycine moiety. Overall the peptide was purified by HPLC purification followed by lyophilization to yield a fine fluffy white powder (7.1 mg, 15% yield). LR-MS  $m/z$  (MALDI):  $C_{40}H_{56}N_6O_8$  ( $[M+H]^+$ ) calcd. 749.43, found 749.1. (*figure S77*). HPLC purification  $t_R = 28.9$  min. (*figure S78*).

#### Compound 22: *l*-C(StBu)LLFVY

*l*-C(ALLOC)LLFVY was prepared with the N-terminus of the peptide containing the StBu-protected cysteine moiety. Overall the peptide was purified by HPLC purification followed by lyophilization to yield a fine fluffy white powder (17.7 mg, 33% yield). LR-MS  $m/z$  (MALDI):  $C_{42}H_{64}N_6O_8S_2$  ( $[M+H]^+$ ) calcd. 845.42, found 845.2. (*figure S79*). HPLC purification  $t_R = 29.5$  min. (*figure S80*).

#### Compound 23: *c*-(Ppg)LLFVY

From Miranda *et al.* [107] *l*-(Ppg)LLFVY (33.3 mg, 0.046 mmol) was combined with Oxyma (37.9 mg, 0.27 mmol) and EDC (25.6 mg, 0.13 mmol) in a solution of DMF (100 mL). The reaction was left shaking at ambient temperature for 24 hours and upon completion, the reaction volume was reduced by rotary evaporation. The DMF solution was prepared for HPLC injection by dilution with  $H_2O$  to give a DMF: $H_2O$  (75:25) mixture. The reaction was purified on HPLC, isolated and lyophilized and confirmed by MALDI to be the product of interest as a fluffy white

powder (15.0 mg, 46% yield). LR-MS  $m/z$  (MALDI):  $C_{40}H_{54}N_6O_7$  ( $[M+H]^+$ ) calcd. 731.42, found 731.3. (*figure S81*). HPLC purification  $t_R = 35.0$  min. (*figure S82 & S83*).

Compound 24: *c*-C(StBu)LLFVY

*l*-C(StBu)LLFVY (17.7 mg, 0.021 mmol) combined with Oxyma (18.5 mg, 0.13 mmol) and EDC (12.1 mg, 0.063 mmol) in a solution of DMF (15 mL). The reaction was stirred at ambient temperature for 24 hours, and upon completion, the reaction volume was reduced by rotary evaporation to near dryness. The reaction residue was prepared for HPLC injection by dilution with  $CH_3CN:2\%$  TFA in  $H_2O$  (1:1, 6 mL). The product was purified on HPLC, isolated, lyophilized and identity confirmed by MALDI. The desired product was obtained as a fluffy white powder (2.4 mg, 14 % yield) LR-MS  $m/z$  (MALDI):  $C_{42}H_{62}N_6O_7S_2$  ( $[M+H]^+$ ) calcd. 827.42, found 827.2. HPLC purification  $t_R = 38.9$  min. (*figure S84 & S85*).

Compound 25: *c*-CLLFVY

The deprotection of *c*-C(StBu)LLFVY (23.3 mg, 0.028 mmol) was completed in 2-mercaptoethanol (20%) in DMF containing additional *N*-methyl morpholine (0.1 M) at room temperature for 16 hours. Upon completion, the product was purified and collected by HPLC followed by lyophilization to yield a fluffy white powder (17.7mg, 85% yield) LR-MS  $m/z$ :  $C_{38}H_{54}N_6O_7S$  ( $[M+H]^+$ ) calcd. 739.39, found 739.4. (*figure S86*). HPLC purification  $t_R = 43.8$  min. (*figure S87*).

Compound 26: link-*c*-(Ppg)LLFVY

$Cu(OAc)_2$  (5.0 mg, 0.028 mmol) and sodium ascorbate (14.8 mg, 0.075 mmol) were first combined in a solution of  $H_2O$  (1.0 mL). This solution was then transferred into a Lobind Eppendorf® microcentrifuge tube containing 11-azido-3,6,9-trioxaundecan-1-amine **20** (2.6  $\mu$ L, 0.013 mmol) and *c*-(PPg)LLFVY (3.2 mg, 0.0044 mmol). Finally, the reaction mixture was topped up with a solution of *tert*.-butanol (1.0 mL). The reaction was allowed to shake at ambient temperature for 24 hours. Upon completion, the reaction was extracted with  $CH_2Cl_2$  (3X, 2 mL), and the collected organic phases were rotavaped to complete dryness to reveal a yellow residue. This residue was purified using HPLC, concentrated by rotary evaporation and lyophilization to reveal a fine white

powder (2.6 mg, 63 % yield) as confirmed by MALDI. LR-MS  $m/z$  (MALDI):  $C_{48}H_{72}N_{10}O_{10}$  ( $[M+H]^+$ ) calcd. 949.55, found 949.2. ( $[M+Na]^+$ ) calcd. 971.53, found 971.2. (*figure S88*). HPLC purification  $t_R$  = 26.0 min. (*figure S89*).

#### Compound 27: azido-PEG-4-fluorobenzamide

*N*-succinimidyl-4- $[^{19}F]$ fluorobenzoate ( $[^{19}F]$ SFB) (11.0 mg, 0.047 mmol) was combined with 11-azido-3,6,9-trioxaundecan-1-amine **20** (14.0  $\mu$ L, 0.070 mmol) in DMF (1 mL) and DIPEA (14  $\mu$ L, 0.008 mmol). The reaction was shaken at ambient temperature for 24 hours at 800 rpm on the Thermoshaker. Once completed, the reaction was diluted with  $CH_3CN:H_2O$  containing 0.2% TFA (1.0 mL, 10:90) and purified by HPLC. The product was collected and lyophilized to reveal a clear colorless oil (9.2 mg, 58% yield). LR-MS  $m/z$  (MALDI):  $C_{15}H_{21}FN_4O_4$  ( $[M+H]^+$ ) calcd. 341.16, found 341.2. (*figure S90*) HPLC purification  $t_R$  = 19.5 min.

#### Compound 28: $[^{19}F]$ SFB-link-*c*-(Ppg)LLFVY

$Cu(OAc)_2$  (11.3 mg, 0.062 mmol) and sodium ascorbate (83.8 mg, 0.42 mmol) were first combined in a solution of  $H_2O$  (3.0 mL). Next  $[^{19}F]$ SFB-link (9.1 mg, 0.024 mmol) was combined with *c*-(Ppg)LLFVY (9.2 mg, 0.013 mmol) in a solution of *tert.*-butanol (3.0 mL). Finally, both solutions were combined, and the reaction was allowed to stir at ambient temperature for 24 hours. Once completed the reaction was extracted with  $CH_2Cl_2$  and rotavaped to complete dryness. The dried product was re-dissolved in DMF (2 mL) and diluted with  $CH_3CN:H_2O$  containing 0.2% TFA (1.0 mL, 10:90) and purified by HPLC. The product was collected and lyophilized to reveal a fine yellowish-white powder (7.6 mg, 56% yield). LR-MS  $m/z$  (MALDI):  $C_{55}H_{75}FN_{10}O_{11}$  ( $[M+H]^+$ ) calcd. 1071.57, found 1071.4. (*figure S91*). HPLC purification  $t_R$  = 34.7 min. (*figure S92*).

### 5.2 HIF-1 $\alpha$ binding assays

To determine the binding of newly developed small molecules inhibitors of HIF-1 $\alpha$ , a radioactive plate-based assay and an in-solution charcoal assay were attempted. Using PBA method A, the binding of HIF-1 $\alpha$  protein to the wells was optimized first in assays #1 and #2. From these tests, it was determined that the originally bought protein was the incorrect sequence. This was due to human error in the ordering of the desired protein. Thus, PBA method B was developed with a

new HIF-1 $\alpha$  protein and an improved washing protocol. Leading to the tests as seen in assay #3-5, with again another problem being detected in the stability of the HIF-1 $\alpha$  targeting radiopeptide. Thus, the linker molecule in the peptide was modified and tested leading to assay #6-9 with various radioisotopes being tested. Overall, all the stable radiopeptide derivatives started to show a large proportion of non-specific binding, with an extremely low signal detected in all assays. Therefore the use of the in-solution charcoal-based assay was tested to remove these non-specific interactions and allow for use of a larger amount of peptide in the solution. Yet again the signal achieved was extremely low, thus the use of microscale thermophoresis will be investigated.

Plate Assay # 1: Concentrations of HIF-1 $\alpha$ , method A

HIF-1 $\alpha$  (5.88  $\mu$ g) was dissolved into EMSA buffer (207  $\mu$ L) to create a 10 $\mu$ M stock solution that was diluted as shown in *Table 5.3*. [<sup>68</sup>Ga]NOTA-Bn-SCN-link-c-(Ppg)LLFVY (JDW00316-3) was applied radiotracer of interest.

*Table 5.3. Dilutions of HIF-1 $\alpha$  to obtain required concentrations of protein in designated well.*

Well Number	Volume EMSA Buffer ( $\mu$ L)	Volume HIF-1 $\alpha$ solution ( $\mu$ L)	Final concentration HIF-1 $\alpha$ solution ( $\mu$ M)
1	50	0	0
2	25	25	5
3	47.5	2.5	0.5
4	45	5	1
5	37.5	12.5	2.5
6	25	25	5
7	12.5	37.5	7.5
8	0	50	10

Overall, there was a very high non-specific binding in the blank well at 851,050 counts per minute (cpm). Although there was an increased binding in all wells containing HIF-1 $\alpha$  protein. This signal increase was only from 47,000 cpm to a maximum of 131,000 cpm. Also, there was no obvious trend in the binding of JDW00316-3 versus the concentration of protein used. This leads to no definite conclusions on protein concentrations required for each well. Thus, all further testing will be done at 1 $\mu$ M protein to preserve precious HIF-1 $\alpha$  protein.

Plate Assay # 2, Competitive blocking, plate pre-blocking and solvent effects, method A

HIF-1 $\alpha$  (5.88  $\mu$ g) was dissolved into EMSA buffer (390  $\mu$ L) to create a 5 $\mu$ M stock solution. This was then further diluted into each well with additional EMSA buffer (40  $\mu$ L) as shown in *Table 5.4*.

*Table 5.4. List of experiment well, along with corresponding reaction conditions.*

Well Number	EMSA Buffer ( $\mu$ L)	HIF-1 $\alpha$ solution ( $\mu$ L)	Reaction conditions
1	50	0	Post - 50 $\mu$ M <i>c</i> -(Ppg)LLFVY inhibition
2	40	10	Post - 50 $\mu$ M <i>c</i> -(Ppg)LLFVY inhibition
3	50	0	Post - 5 $\mu$ M <i>c</i> -(Ppg)LLFVY inhibition
4	40	10	Post - 5 $\mu$ M <i>c</i> -(Ppg)LLFVY inhibition
5	50	0	Post - 500nM <i>c</i> -(Ppg)LLFVY inhibition
6	40	10	Post - 500nM <i>c</i> -(Ppg)LLFVY inhibition
7	50	0	Post - 50nM <i>c</i> -(Ppg)LLFVY inhibition
8	40	10	Post - 50nM <i>c</i> -(Ppg)LLFVY inhibition
9	50	0	Post - 5nM <i>c</i> -(Ppg)LLFVY inhibition
10	40	10	Post - 5nM <i>c</i> -(Ppg)LLFVY inhibition
11	50	0	Post - 500pM <i>c</i> -(Ppg)LLFVY inhibition
12	40	10	Post - 500pM <i>c</i> -(Ppg)LLFVY inhibition
13	25	0	Pre - 25 $\mu$ L of a 5% milk solution added
14	25	0	Pre - 25 $\mu$ L of a 5% BSA solution added
15	0	0	Pre - 50 $\mu$ L of a 10% milk solution added
16	0	0	Pre - 50 $\mu$ L of a 10% BSA solution added
17	50	0	Same - 40% DMSO solution in NH <sub>4</sub> OAc buffer
18	40	10	Same - 40% DMSO solution in NH <sub>4</sub> OAc buffer
19	50	0	Same - 50% DMSO solution in NH <sub>4</sub> OAc buffer
20	40	10	Same - 50% DMSO solution in NH <sub>4</sub> OAc buffer
21	50	0	Same - 10% DMSO solution in NH <sub>4</sub> OAc buffer
22	40	10	Same - 10% DMSO solution in NH <sub>4</sub> OAc buffer
23	50	0	Same - 20% DMSO solution in NH <sub>4</sub> OAc buffer
24	40	10	Same - 20% DMSO solution in NH <sub>4</sub> OAc buffer

Treatment of each well was completed post, pre or the same. Where “post” means the application of the treatment happened post-incubation with [<sup>64</sup>Cu]NOTA-Bn-SCN-link-*c*-(Ppg)LLFVY. Next, “pre” means the application of the treatment happened pre-incubation with [<sup>64</sup>Cu]NOTA-Bn-SCN-link-*c*-(Ppg)LLFVY, which is at the same time as the HIF-1 $\alpha$  application to the nickel-coated plates. Finally, “same” means the application of the treatment happens at the same time as the

application of [<sup>64</sup>Cu]NOTA-Bn-SCN-link-c-(Ppg)LLFVY. [<sup>64</sup>Cu]NOTAs-Bn-SCN-link-c-(Ppg)LLFVY (JDW02415-8) (50 μL) solution and various buffer solutions were allowed to sit at room temperature for 1 hour. All wells were diluted with additional NH<sub>4</sub>OAc buffer to a total volume of 200μL. Following JDW02415-8 reaction, wells 13 to 24 were washed with ELISA Buffer and broken apart and counted and wells 1 to 12 were treated with the corresponding cold competitive compound binding as per *Table 5.4*.

Overall the 5% BSA did provide the greatest inhibition of non-specific binding at only 16,000 cpm detected. Also, all the concentrations of DMSO significantly decreased the non-specific binding down to only 2,000 cpm, but this also drastically decreased the amount of signal seen for the radioactive compound binding. This is assumed to be due to protein denaturing at all concentrations of DMSO applied to the assay from 10-40 % DMSO in NH<sub>4</sub>OAc buffer. Finally, the cold peptide inhibitor provided no obvious trend in information as to the plate assay binding. In conclusion, this assay had numerous problems with no discernable data.

In an attempt to reconcile this data, it was determined that the HIF-1α protein purchased was the wrong recombinant protein and does not contain the PAS-B region, which is required for the binding to our peptide of interest. Thus, a new recombinant HIF-1α protein will need to be acquired.

### Plate Assay # 3: Concentrations of HIF-1α, method B

Protein was applied as per PBA method B. [<sup>68</sup>Ga]NOTA-Bn-SCN-link-c-(Ppg)LLFVY (JDW00316-13) was added to each well and overall there was a high non-specific binding in the blank well at 175,000 cpm. Although again there was an increased binding in all wells containing HIF-1α protein; this signal increase was only from approximately 1.5% applied radioactivity to a maximum of 5% applied radioactivity (*Figure 5.10*). Also, the binding plateaued at amounts above 12 pmol, thus this loading was chosen to move forward with the loading of HIF-1α into the well of the assay plate.

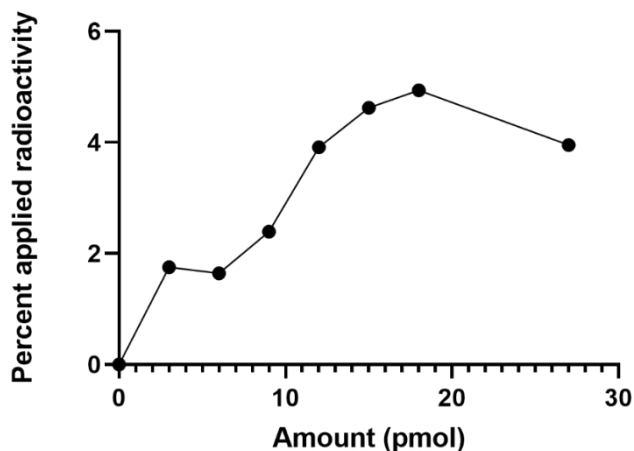


*Figure 5.10. [<sup>68</sup>Ga]NOTA-Bn-SCN-link-c-(Ppg)LLFVY response to various amounts of HIF-1 $\alpha$  protein loading concentrations in a plate based assay (n=1)*

Plate Assay # 4: Purity of Gallium-68 radiolabelled peptide, method B

Protein was applied as per PBA method B. [<sup>68</sup>Ga]NOTA-Bn-SCN-link-c-(Ppg)LLFVY (JDW00316-14) was synthesized and purified using HPLC to obtain three peaks. Each peak was tested at a protein loading of 12 pmol HIF-1 $\alpha$  and a blank of 0 pmol HIF-1 $\alpha$ . The first peak from HPLC contained a single peak on the baseline of the TLC. A second peak HPLC peak contained a split peak with a ratio of 50:50 positioned at the baseline and an Rf=0.2 on TLC. Finally, HPLC peak three predominately had an Rf=0.2 on TLC. In all of the tests, only the test for HPLC peak one had a binding greater than the background signal. Also, this was a very low binding of only 0.5% of the applied radiation dose. Overall it indicates that peptide may not be present in peaks 2 and 3. Upon further analysis of [<sup>68</sup>Ga]NOTA-Bn-SCN-link-c-(Ppg)LLFVY, it was determined through thorough HPLC analysis that the peptide is degrading in solution and that all the tested radioactive products were just NOTA. Thus, a new peptide was designed for further testing without the Bn-SCN-linkage.

Plate Assay # 5 ID: Blocking with cold reference and DMSO concentrations effects, method B

Protein was applied as per PBA method B. [<sup>68</sup>Ga]DOTA-link-c-(Ppg)LLFVY (JDW00816-14) was applied to wells for 1 hour at room temperature. After the binding of the radiotracer, treatments to wells included, TBS solution for blank, 20% to 100% DMSO, and cold c-(Ppg)LLFVY inhibitor. Overall, the amount of DMSO did not affect the radiolabeled peptide-protein interaction. Also, the binding was not affected by increased concentrations of blocking peptide. Concluding that no matter what parameter was tested all tests were between 1.7 to 1.8% applied radioactivity. Since no trends could be discerned the protein loading should be re-evaluated.

Plate Assay # 6 Concentration of HIF-1 $\alpha$ , method B

Protein was applied as per PBA method B. [<sup>68</sup>Ga]DOTA-link-c-(Ppg)LLFVY (JDW00816-15) was added to each well and allowed to bind over an additional hour. Overall, all the wells had the same binding as the background, this was even completed in triplicate. Yet each concentration of protein loading gave the same value of around 20,000 cpm.

Plate Assay # 7: Binding of a fluorescent compound to plate assay, method B

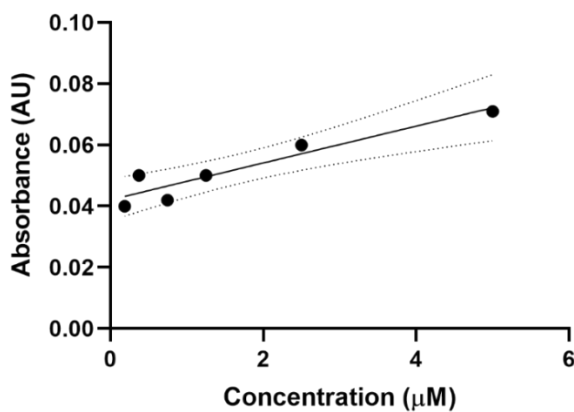


*Figure 5.11. JDW00315 concentration versus UV absorbance curve for a plate-based assay.*

Protein was applied as per PBA method B. Fluorescently-tagged peptide JDW00315 was then added. Additionally, a fluorescence curve without protein was also created on the Ni-coated plates

to quantify any possible binding (*Figure 5.11.*). Overall, all wells of fluorescent peptide had no binding over background absorbance values to the protein. Thus, this compound/methodology was not suitable for this assay.

Plate Assay # 8 ID: SFB-labelled peptide and HIF-1 $\alpha$  concentrations, method B

Protein was applied as per PBA method B and radiotracer addition was [ $^{18}\text{F}$ ]SFB-link-c-(Ppg)LLFVY (JDW00117-7). Using this radiotracer there was an increasing trend with applied radioactivity versus the applied protein concentration in each well.

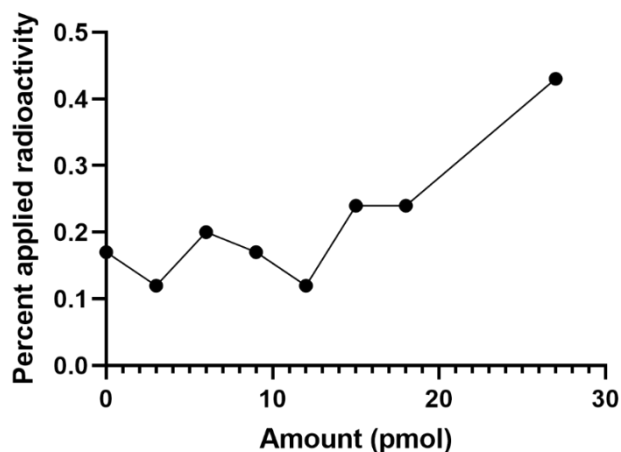


*Figure 5.12.* [ $^{18}\text{F}$ ]SFB-link-c-(Ppg)LLFVY binding response to HIF-1 $\alpha$  protein at various concentrations of loading ( $n=1$ ).

Showing that the required protein loading is likely higher than 15 pmol. Yet, overall the amount of signal-to-noise seen in this plate-based assay is very low with only a maximum of 0.40% applied radioactivity binding to the protein. (*Figure 5.12.*).

Plate Assay # 9: Binding of SFB-labelled peptide in triplicate, method B

Protein was applied as per PBA method B before the addition of the [ $^{18}\text{F}$ ]SFB-link-c-(Ppg)LLFVY (JDW00117-8) radiotracer. All samples were repeated in triplicate, and overall there was no significant response at increasing concentrations of protein. There is also a large non-specific binding that cannot be removed from the assay (*Figure 5.13.*).

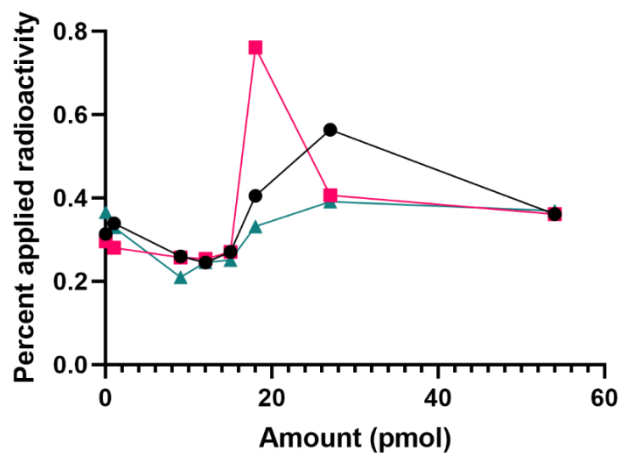


Figure 5.13. [ $^{18}\text{F}$ ]SFB-link-c-(Ppg)LLFVY binding to HIF-1 $\alpha$  protein at various concentrations of loading ( $n=3$ ).

Solution Assay # 1: Charcoal assay with varying concentrations of protein in solution

HIF-1 $\alpha$  (5  $\mu\text{g}$ ) was dissolved into TBS (100  $\mu\text{L}$ ) to create desired to create a stock solution. This was then diluted to achieve concentrations of 27, 12, and 0 pmol per tube.

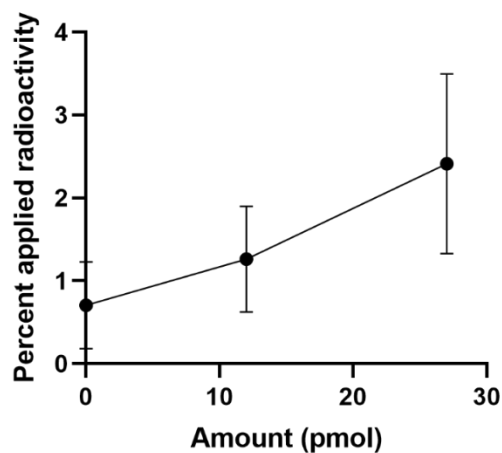
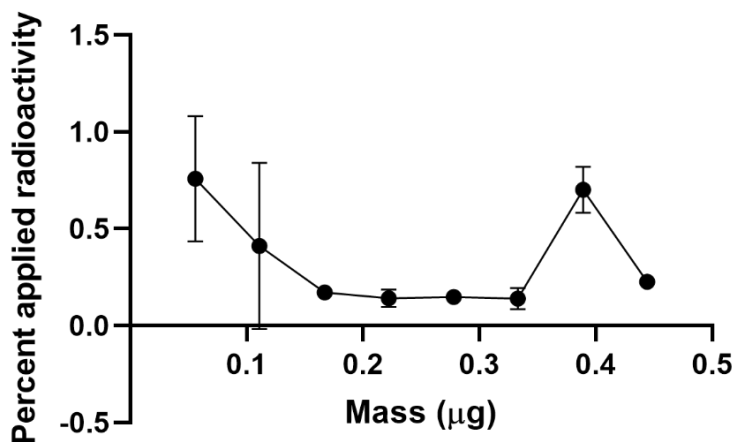


Figure 5.14. [ $^{18}\text{F}$ ]SFB-link-c-(Ppg)LLFVY binding to HIF-1 $\alpha$  protein in solution with charcoal, assay #1 ( $n=3$ ).

This was completed in triplicate with the addition of the [ $^{18}\text{F}$ ]SFB-link-c-(Ppg)LLFVY (JDW00117-8) radiotracer (100  $\mu\text{L}$ ). Overall, the charcoal did seem effective in removing the radioactivity from the solution, but the amount of radioactivity seen binding to the protein in the solution still produced very little signal. There was only 2% of the applied radioactivity in the solution bound to the protein at 27 pmol protein concentration (*Figure 5.14*). Possibly the reaction solutions are too dilute to allow proper interaction of peptide to protein.

Solution Assay # 2: Charcoal assay with concentrated reaction solutions.

HIF-1 $\alpha$  (5  $\mu\text{g}$ ) was dissolved into TBS (90  $\mu\text{L}$ ) to create desired stock solution. This was then diluted to achieve a mass of protein in solution from 0  $\mu\text{g}$  to 0.444  $\mu\text{g}$ . To these reaction tubes radiotracer [ $^{18}\text{F}$ ]SFB-link-c-(Ppg)LLFVY (JDW00117-9) (20  $\mu\text{L}$ ) was added along with the charcoal (20  $\mu\text{L}$ ). The more concentrated peptide protein reaction mixtures did not improve the amount of radioactivity that was bound to the protein in the solution. Overall the percent applied radioactivity in the supernatant was still less than 0.7%. (*Figure 5.15*).



*Figure 5.15. [ $^{18}\text{F}$ ]SFB-link-c-(Ppg)LLFVY binding to HIF-1 $\alpha$  protein in solution with charcoal, assay #2 (n=3).*

### Solution Assay #3: Varying charcoal concentration and radiotracer concentration –no protein

Varying amount of radiotracer [ $^{18}\text{F}$ ]SFB-link-c-(Ppg)LLFVY (JDW00117-10) was added to low bind Eppendorf along with varying volumes of charcoal solution to determine the efficiency of removing this radiotracer from solution.

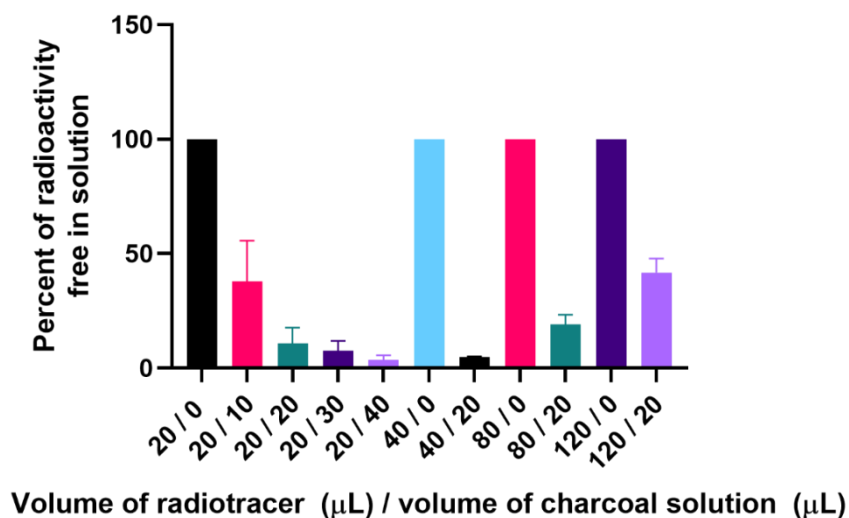


Figure 5.16. [ $^{18}\text{F}$ ]SFB-link-c-(Ppg)LLFVY binding to charcoal solution as varying concentrations ( $n=3$ ).

These results show that the radiotracer can efficiently be removed from the solution when applied in the amounts of 20 to 40 μL of the radiotracer. This was achieved with both 20 μL and 40 μL of charcoal solution. Also, at a larger amount of radioactivity (80 and 120 μL) the amount of radioactivity removed was not completed with only 20 μL charcoal solution (Figure 5.16.). Going forward it was decided to use 20 μL radiotracer with 40 μL charcoal solution.

### Solution Assay #4: Charcoal assay with varying protein concentration

HIF-1 $\alpha$  (5 μg) was dissolved into TBS (90 μL) to create desired to create a stock solution. This was then diluted to achieve concentrations from 30 to 300 nM per tube. This was completed in triplicate with the addition of the [ $^{18}\text{F}$ ]SFB-link-c-(Ppg)LLFVY (JDW00117-11) (20 μL). Followed by the charcoal being added as a 40 μL volume. Overall, there was found to be

radioactive peptide binding to the protein in solution, but the data was not consistent and even still at 0 nM protein there was a high background signal. (Figure 5.17.).

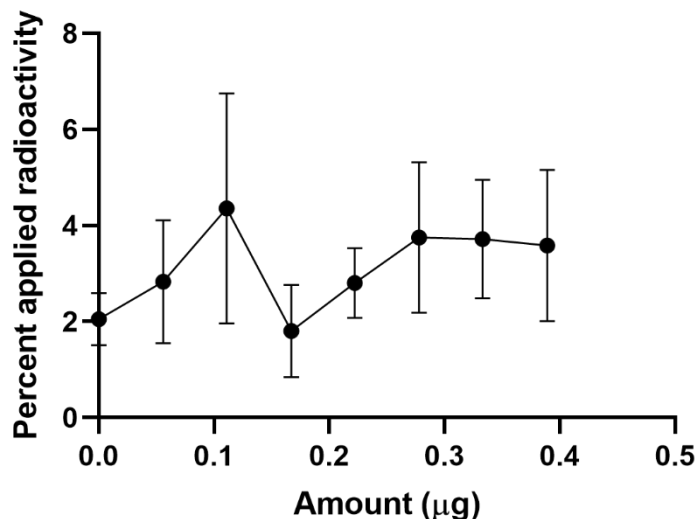


Figure 5.17  $[^{18}\text{F}]$ SFB-link-c-(Ppg)LLFVY binding to HIF-1 $\alpha$  in a charcoal solution assay ( $n=3$ ).

### 5.3 Microscale thermophoresis of HIF-1 $\alpha$ binding compounds

First, compounds were analyzed for their binding affinity to a truncated HIF-1 $\alpha$  containing only the PAS-B region. This recombinant protein contained AA 218-506 with a His-T7 tag. Each sample was run with a sixteen-point concentration curve in triplicate to obtain the reported  $K_D$  values (Table 5.5.). Signal-to-noise ratios (S/N) and the amplitude response are also reported. Amplitude response uses a threshold of greater than or equal to 6.0 as a cut-off point for the signal-to-noise ratio to determine that a binding event has occurred. As summarized in Table 5.5, all three tested cyclic peptides showed binding to truncated HIF-1 $\alpha$  exhibiting nanomolar  $K_D$  values for reference peptide c-CLLFVY **25** ( $52.8 \pm 31.2$  nM) and propargyl glycine-containing peptides  $[^{19}\text{F}]$ SFB-link-c-(Ppg)LLFVY (**28**) ( $7.1 \pm 3.4$  nM) and c-(Ppg)LLFVY (**23**) ( $29.9 \pm 19.0$  nM).

Table 5.5. Microscale thermophoresis data with truncated HIF-1 $\alpha$ . \*Note: Compound 7 is <85% pure, results are approximate.

Compound	X	K <sub>D</sub> (nM)	S/N	Amplitude response
c-CLLFVY	N/A	52.8 $\pm$ 31.2	8	10.1
c-(Ppg)LLFVY	N/A	29.9 $\pm$ 19.0	6	7.6
<b>28</b>	N/A	7.1 $\pm$ 3.4	6.4	6.4
Acriflavine	N/A	244 $\pm$ 295	9	16.2
PpgBBN1	N/A	No binding	1.8	N/A
ER-400-583-00	H	No binding	3.4	N/A
<b>9</b>	F	80.5 $\pm$ 49.0	6.4	4.4
<b>10</b>	OCH <sub>3</sub>	821.5 $\pm$ 434.0	6.4	6
<b>11*</b>	NH <sub>2</sub>	203.5 $\pm$ 105.3	6.4	4.4
<b>12</b>	Ph	No binding	3.2	N/A
<b>13</b>	CH <sub>3</sub>	581.9 $\pm$ 340.5	6.5	7.2
<b>14</b>	C(CH <sub>3</sub> ) <sub>3</sub>	9.2 $\pm$ 10.2	6.1	6
<b>15</b>	Cl	No binding	2.5	N/A
<b>16</b>	Br	157.9 $\pm$ 0.1	124	124
<b>18</b>	NO <sub>2</sub>	205.2 $\pm$ 114.0	6.4	11
<b>19</b>	N(CH <sub>3</sub> ) <sub>2</sub>	2468 $\pm$ 684	13.2	26
<b>20</b>	CF <sub>3</sub>	113.1 $\pm$ 73.1	6.0	5.2

The results also demonstrate that lead compound [<sup>19</sup>F]SFB-link-c-(Ppg)LLFVY displays higher binding affinity to truncated HIF-1 $\alpha$  and that replacement of the cysteine residue in reference compound c-CLLFVY with propargyl glycine had no detrimental effect on the binding affinity. The low nanomolar affinity of [<sup>19</sup>F]SFB-link-c-(Ppg)LLFVY to truncated HIF-1 $\alpha$  also confirms that the propargyl glycine residue is suitable for the introduction of additional side chains using click chemistry. We also tested reference compound acriflavine [106] and non-binding linear bombesin peptide **PpgBBN1** [119] as positive and negative controls, respectively. Small molecule HIF-1 $\alpha$  inhibitor acriflavine demonstrated a binding affinity of K<sub>D</sub> = 244  $\pm$  295 nM, while peptide **PpgBBN1** showed an S/N of 1.8, indicating no binding.

Additionally from Table 5.5., the literature reported small molecule inhibitor ER-400-583-00 **17** showed no detectable binding to truncated HIF-1 $\alpha$  with a low S/N of 3.4. This lack of binding to truncated HIF-1 $\alpha$  for compound **17** was possibly due to the low solubility of **17** in solution, with concentrations above 600  $\mu$ M causing aggregation and precipitation. Additionally, the chlorine

derivative also exhibits no detectable binding, likely due to the high lipophilicity of this compound and poor solubility in the aqueous binding solution.

Yet, fluorine-containing compound **9** with a  $K_D = 80.5 \pm 49$  nM to truncated HIF-1 $\alpha$  seemed to be a suitable candidate for the development of a  $^{18}\text{F}$ -labelled radioligand. It should be noted that thermophoresis analysis with truncated HIF-1 $\alpha$  was performed without a blocking agent in the solution. Thus, the reported values observed will be higher than the actual values. As well the protein fragment will likely allow for better spatial ability of the small molecules to bind into a pocket, that may be hindered in a larger protein fragment.

Thus, to get a more proper binding value, we modified the thermophoresis procedure to test out an almost full-length HIF-1 $\alpha$  protein in a fully blocked bovine serum albumin solution. From this we achieved binding with all three cyclic peptides **23**, **25**, and **28**, the acriflavine reference, and eleven of the small molecules tested. With the non-binding compounds being the negative control of the bombesin peptide derivative (*Table 5.6.*) and compounds (**15** and **16**) which contain the Cl and Br derivatives.

Overall our [ $^{19}\text{F}$ ]SFB-link-c-(PPg)LLFVY **28** peptide derivative still demonstrated a very favorable binding at  $K_D = 0.46 \pm 0.2$   $\mu\text{M}$ , which was comparable to the acriflavine standard reference of  $K_D = 0.12 \pm 0.09$   $\mu\text{M}$ . The reference peptide of c-CLLFVY **25** had a  $K_D > 1000$   $\mu\text{M}$ , since the concentration of peptide in solution could not be increased enough to witness the true  $K_D$  value, this is just an approximation off the top of the acquired thermophoresis curves. Lastly, the small molecule derivative reference ER-400-583-00 (**17**) showed an improved binding affinity of  $K_D = 0.32 \pm 0.19$   $\mu\text{M}$  compared to the data achieved from the protein fragment of HIF-1 $\alpha$ . This could be due to the composition of the thermophoresis solution helping to obtain a better representative binding. Also the  $\text{N}(\text{CH}_3)_2$  derivative **19** with a  $K_D = 1.3 \pm 1.0$   $\mu\text{M}$  and the fluorine-containing derivative **9** with a  $K_D = 7.8 \pm 3.4$   $\mu\text{M}$  showed very strong binding to the HIF-1 $\alpha$  protein.

In conclusion, we have synthesized over fourteen novel peptide and small molecule derivatives that show binding capabilities towards the HIF-1 $\alpha$  protein. These binding affinities were quantified using microscale thermophoresis. Peptide derivative [ $^{19}\text{F}$ ]SFB-link-c-(Ppg)LLFVY **28**

showed an affinity of  $K_D = 0.46 \pm 0.2 \mu\text{M}$ , and fluorine-containing small molecule **9** had an affinity of  $K_D = 7.8 \pm 3.4 \mu\text{M}$  towards the full-length HIF-1 $\alpha$  protein in solution.

We also predict that these small molecular compounds bind to HIF-1 $\alpha$  in the PAS-B region as analyzed by computational docking studies. Future studies will elucidate the true inhibitor capabilities of these small molecular compounds.

Table 5.6. Microscale thermophoresis data with full-length HIF-1 $\alpha$ . \*Note: Compound 7 is <85% pure, results are approximate.

Compound	X	$K_D$ ( $\mu\text{M}$ )	S/N	Amplitude response
c-(Ppg)LLFVY	N/A	$27.6 \pm 27.0$	7.1	20.3
<b>28</b>	N/A	$0.46 \pm 0.20$	8.7	12
c-CLLFVY	N/A	>1000	161	994.5
Acriflavine	N/A	$0.12 \pm 0.09$	6	55.4
PpgBBN1	N/A	No binding	0.4	N/A
ER-400-583-00	H	$0.32 \pm 0.20$	6	7.4
<b>9</b>	F	$7.8 \pm 3.4$	7.7	78.4
<b>10</b>	OCH <sub>3</sub>	$72.4 \pm 53.1$	7.4	104.3
<b>11*</b>	NH <sub>2</sub>	$47.8 \pm 30.2$	7.4	70.3
<b>12</b>	Ph	>1000	83.5	1054
<b>13</b>	CH <sub>3</sub>	$23.7 \pm 13.1$	7.1	22.8
<b>14</b>	C(CH <sub>3</sub> ) <sub>3</sub>	$77.5 \pm 1.2$	10.3	76.5
<b>15</b>	Cl	No binding	5.2	N/A
<b>16</b>	Br	No binding	1.0	N/A
<b>18</b>	NO <sub>2</sub>	$31.4 \pm 21.6$	6	17.5
<b>19</b>	N(CH <sub>3</sub> ) <sub>2</sub>	$1.3 \pm 1.0$	8.2	132.5
<b>20</b>	CF <sub>3</sub>	$24.5 \pm 19.2$	6.4	26.9

#### 5.4 In Silico analysis of HIF-1 $\alpha$ binding compounds

To predict the binding pocket for HIF-1 $\alpha$ , computational analyses were completed, along with the predictive binding of the reference compound **17**. Our computational analyses indicate that there are at least three binding pockets available for accommodating a synthetic ligand. Based on the cavity size and ligand accessibility, the binding pocket P3 (*Figure 5.18a.*) was selected for

molecular docking analyses. Binding to the P3 binding pocket of HIF-1 $\alpha$ , reference compound **17** showed predictive binding with a  $E_{\text{Intermolecular}} = -10.79$  kcal/mol, as shown in *Figure 5.18b*.

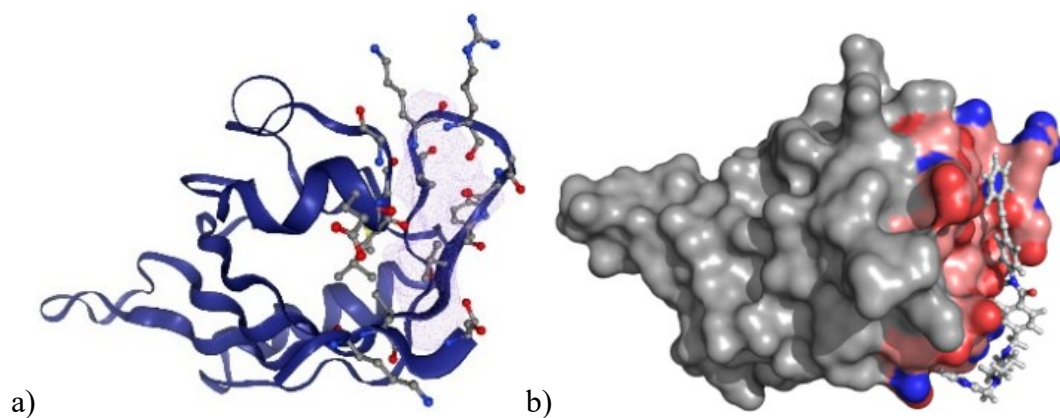


*Figure 5.18. a) P3 Binding pocket predicted for molecular docking analyses in HIF-1 $\alpha$ . The cavity is highlighted in purple mesh, and key residues are displayed. b) Molecular docking of compound **17** in HIF-1 $\alpha$ . Predicted binding mode of compound **17** in HIF-1 $\alpha$  ( $E_{\text{Intermolecular}} = -10.79$  kcal/mol).*

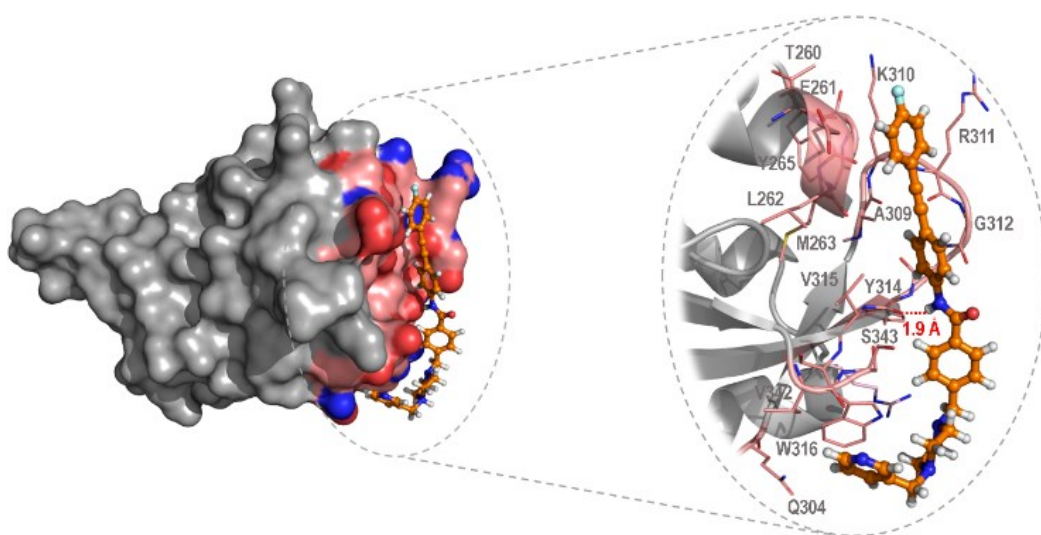


*Figure 5.19. Molecular docking of compound **9** in HIF-1 $\alpha$ . Predicted binding mode of compound (**9**) in HIF-1 $\alpha$  ( $E_{\text{Intermolecular}} = -11.94$  kcal/mol) and dotted oval highlights key residues of the binding pocket. For clarity, the carbon atoms of compound (**9**) are colored in orange, and key residues indicated in lines.*

Finally, with the help of molecular docking we attempted to find a potential binding mode of our lead compound (**5**), and of [<sup>19</sup>F]SFB-link-c-(Ppg)LLFVY (**28**) in the P3 HIF-1 $\alpha$  binding pocket. Similar to the predicted binding mode of the parent molecule (**17**, *Figure 5.18b*), the compound (**9**) attained a favourable binding mode in HIF-1 $\alpha$  binding pocket (*Figure 5.19*). The 4-fluorophenyl substituent was located in a subpocket lined by T260, E261, L262, M263, G264, Y265 residues, and Y314 indicated H-bonding interactions with one of the amide groups (NH---OH = 1.9Å). Moreover, the pyridine motif of compound **9** was also found engaged in  $\pi$ - $\pi$  interactions with W316 residue. In contrast to the positioning of 4-fluorophenyl substituent of compound **9**, the cyclic peptide portion of the [<sup>19</sup>F]SFB-link-c-(Ppg)LLFVY **28** was found positioned in the vicinity of E261, L262, M263, G264, and 4-hydroxyl group of the tyrosine indicated H-bonding with K310 residue (*Figure 5.20*).

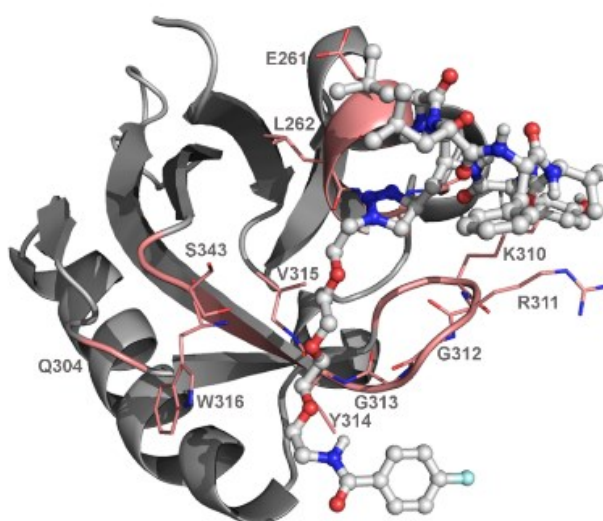


*Figure 5.20. Molecular docking of SFB-link-c-(Ppg)LLFVY **3** in HIF-1 $\alpha$ . Predicted binding mode of [<sup>19</sup>F]SFB-link-c-(Ppg)LLFVY **28** in HIF-1 $\alpha$  ( $E_{\text{Intermolecular}} = -10.11$  kcal/mol). The carbon atoms of the ligand are colored gray and key residues are highlighted in salmon-colored lines.*

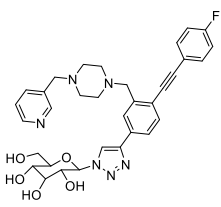
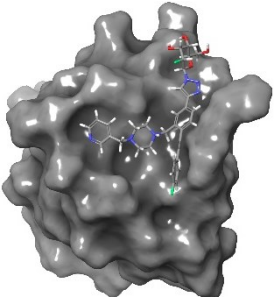
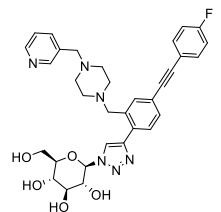
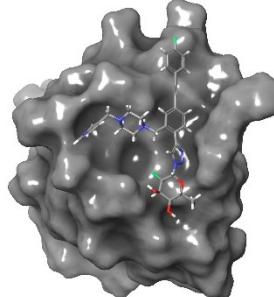
In conclusion, lead peptide derivative [<sup>19</sup>F]SFB-link-c-(Ppg)LLFVY **28** obtained a docking score of -10.11 kcal/mol, and small molecule inhibitor **9** had an E-intermolecular interaction score of -11.94 kcal/mol. Also, from the binding of lead peptide derivative [<sup>19</sup>F]SFB-link-c-(Ppg)LLFVY

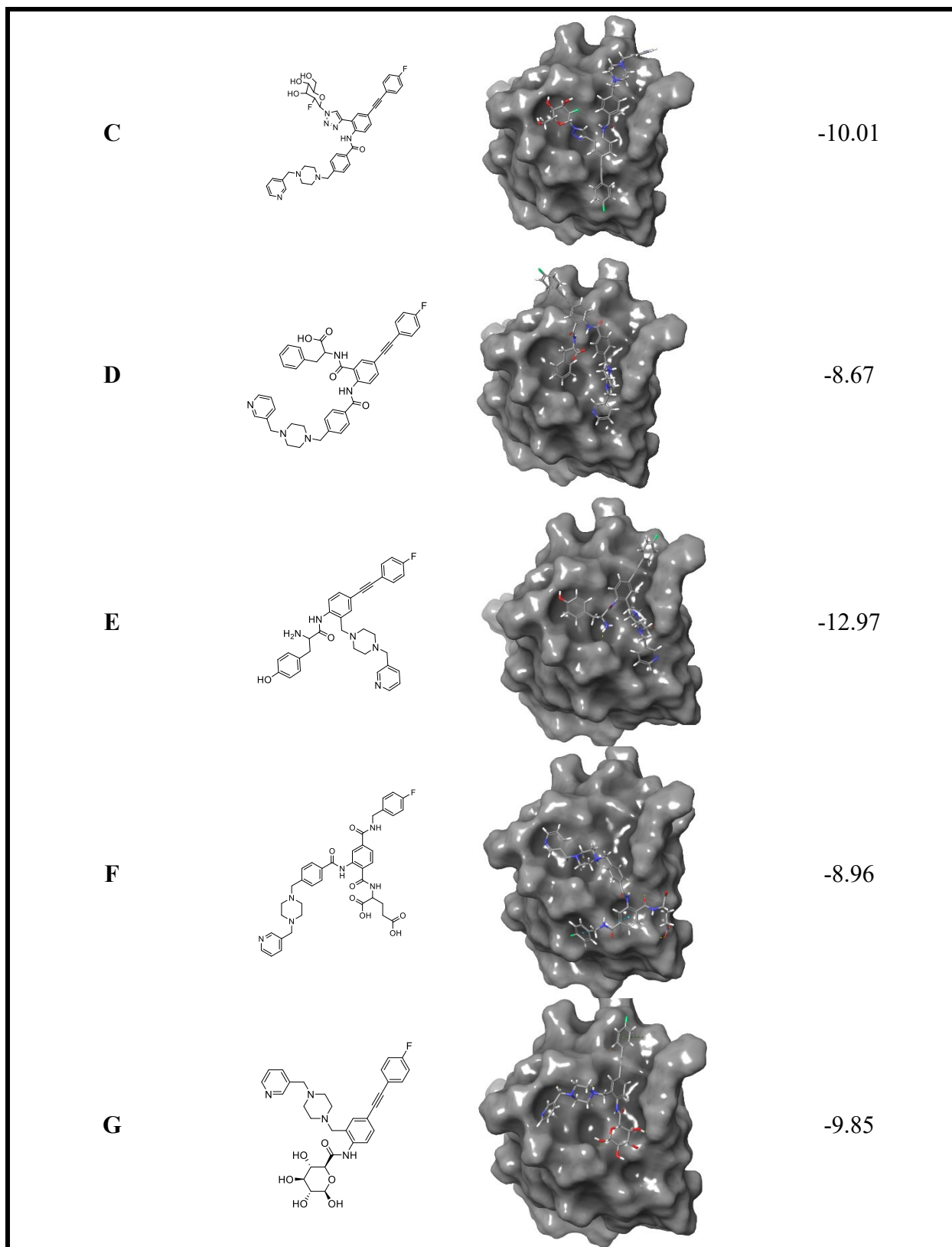
**28** and small molecule inhibitor **9** in the P3 binding pocket, we were able to determine an unused portion of the pocket which can be exploited in future HIF-1 $\alpha$  binding compound design.

### 5.5 Computational design of additional novel HIF-1 $\alpha$ binding compounds

Based on the structure of P3 binding pocket, several novel compounds targeting HIF-1 $\alpha$  were developed *in silico*. Structures were based on previously known HIF-1 $\alpha$  small molecule inhibitor **9**, improving pharmacokinetics by adding more hydrophilic groups and some small peptide-like structures. Nine additional compounds were designed with “Y” like structures to better exploit the geometry of the P3 binding pocket of HIF-1 $\alpha$ . Compounds **A** to **I** were then docked in the P3 HIF-1 $\alpha$  binding pocket, and the observed docking scores were calculated (Table 5.7).

Table 5.7. Computational docking studies with novel HIF-1 $\alpha$  binding compounds.

Compound ID	Structure	Computational Analysis Image	E-intermolecular docking score (kcal/mol)
<b>A</b>			-8.43
<b>B</b>			-9.91





Both of these lead compounds were also tested *in silico* for binding to the HIF-1 $\alpha$  PAS-B domain. Where our lead peptide derivative [<sup>19</sup>F]SFB-link-c-(Ppg)LLFVY **28** obtained a docking score of -10.11 kcal/mol, and small molecule inhibitor **9** had an E-intermolecular interaction score of -11.94 kcal/mol. Overall, we have two strong candidate compounds for future radiolabelling experiments.

## Chapter 6: Synthesis of radiolabelled HIF-1 $\alpha$ binding compounds

### 6.1 [ $^{18}\text{F}$ ]SFB-link-c-(Ppg)LLFVY (JDW00117)

Radiolabelling of c-(Ppg)LLFVY **23** was achieved using prosthetic group chemistry with [ $^{18}\text{F}$ ]SFB produced on a GE TracerLab FX automated synthesis unit [124]. Labeling precursor link-c-(Ppg)LLFVY **27** was prepared via click chemistry using cyclic peptide **23** and 11-azido-3,6,9-trioxaundecan-1-amine.

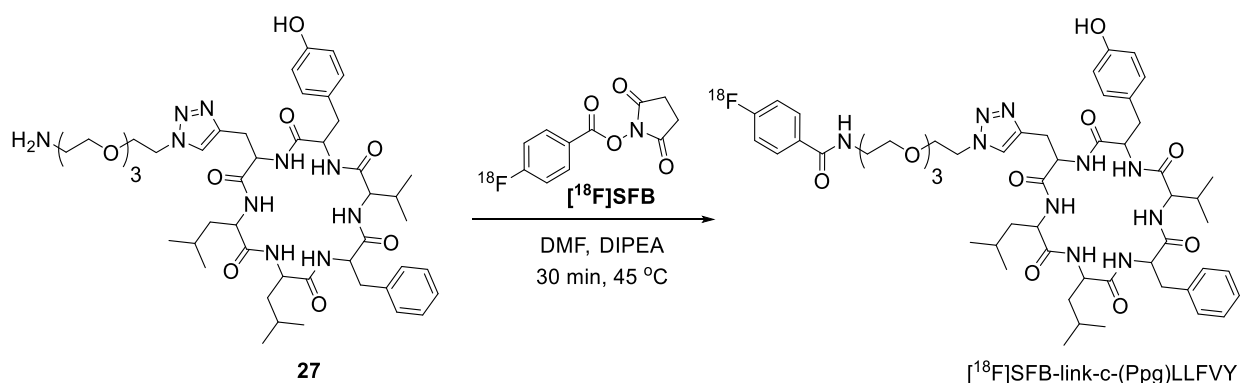


Figure 6.1. Radiosynthesis of [ $^{18}\text{F}$ ]SFB-link-c-(Ppg)LLFVY using prosthetic group [ $^{18}\text{F}$ ]SFB.

Link-c-(Ppg)LLFVY (**27**) (1.0 mg) was dissolved in DMF (100  $\mu\text{L}$ ) with DIPEA (30  $\mu\text{L}$ ) in a 1.5 mL Eppendorf® Lobind microcentrifuge tube. To this mixture [ $^{18}\text{F}$ ]SFB [124] (200  $\mu\text{L}$ ) from an automated synthesis unit was added and the reaction was agitated on the Thermoshaker at 45 °C for 30 minutes at 1050 rpm (Figure 6.1.). After the reaction, a mixture of  $\text{H}_2\text{O}:\text{CH}_3\text{CN}$  (90:10, 400  $\mu\text{L}$ ) was added, and the diluted product was injected into the HPLC for purification using a Phenomenex LUNA® C18(2) column. The correct product with a retention time of 37.3 minutes was collected and the eluent was removed using rotary evaporation. The radiolabeled peptide was then reconstituted with DMSO and diluted with buffer to a concentration of 0.1% DMSO. Achieving a  $66.2 \pm 5.4\%$  decay corrected recovered radiochemical yield from [ $^{18}\text{F}$ ]fluoride (n=8) with a purity >99%. A typical HPLC injection chromatogram is shown in Figure 6.2., quality control injection chromatogram is seen in Figure 6.3. and finally, product formation was confirmed with co-injection of reference standard [ $^{19}\text{F}$ ]SFB-link-c-(Ppg)LLFVY **28** (Figure 6.4.).

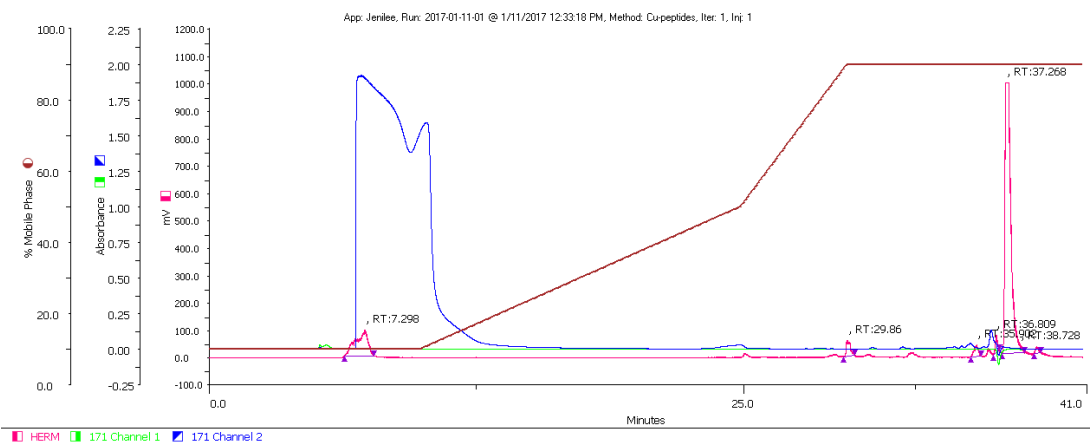


Figure 6.2. Typical HPLC of [ $^{18}\text{F}$ ]SFB-link-c-(Ppg)LLFVY (JDW00117). Two UV channels are shown, including: 254 nm in green (171 Channel 1) and 210 nm in blue (171 Channel 2). HERM radioactivity channel is shown in pink.

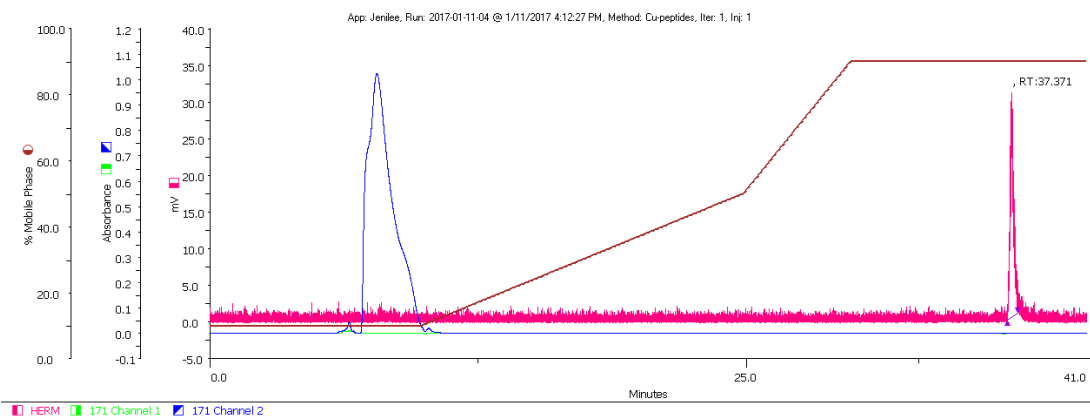


Figure 6.3. Quality control HPLC of [ $^{18}\text{F}$ ]SFB-link-c-(Ppg)LLFVY (JDW00117). Two UV channels are shown, including: 254 nm in green (171 Channel 1) and 210 nm in blue (171 Channel 2). HERM radioactivity channel is shown in pink.

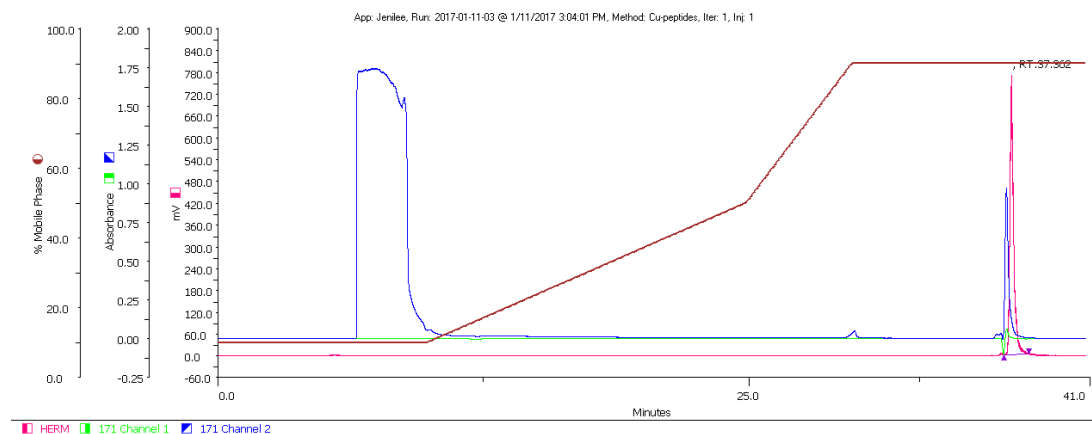


Figure 6.4. HPLC co-injection of [ $^{19}\text{F}$ ]SFB-link-c-(Ppg)LLFVY **28** and [ $^{18}\text{F}$ ]SFB-link-c-(Ppg)LLFVY (JDW00117). Two UV channels are shown, including: 254 nm in green (171 Channel 1) and 210 nm in blue (171 Channel 2). HERM radioactivity channel is shown in pink.

## 6.2 [ $^{68}\text{Ga}$ ]Gallium radiolabelling of cyclic peptide

Two separate cyclic peptide starting materials were synthesized with a NOTA chelator or a DOTA chelator. Both compound **29** and compound **30** were radiolabelled with [ $^{68}\text{Ga}$ ]gallium.

### Compound **29**: NOTA-Bn-SCN-link-c-(Ppg)LLFVY

Link-c-(Ppg)LLFVY (**27**) (3.9 mg, 4.1  $\mu\text{mol}$ ) and p-SCN-Bn-NOTA (2.8 mg, 5.0  $\mu\text{mol}$ ) were combined in a solution of  $\text{NaHCO}_3$  at pH 9.1 (1.0 mL). This reaction was agitated at ambient temperature for 24 hours. Upon completion, the reaction was diluted with  $\text{CH}_3\text{CN}$  (1.5 mL) and the NOTA-labelled cyclic-(PPg)LLFVY was purified using HPLC (figure S93). The collected fractions ( $t_{\text{R}}=38.34$  minutes) were lyophilized to give the product as a fine white powder (2.0 mg, 35% yield). LR-MS  $m/z$  (MALDI):  $\text{C}_{68}\text{H}_{98}\text{N}_{14}\text{O}_{16}\text{S}$  ( $[\text{M}+\text{H}]^+$ ) calcd. 1399.71, found 1399.3. (figure S94)

### Compound **30**: DOTA-link-c-(Ppg)LLFVY

Link-c-(Ppg)LLFVY (**27**) (2.0 mg, 2.1  $\mu\text{mol}$ ) and DOTA-NHS-Ester (2.1 mg, 2.7  $\mu\text{mol}$ ) were combined in a solution of DMF (0.5 mL) containing DIPEA (1  $\mu\text{L}$ ). This reaction was agitated at

ambient temperature for 24 hours. Upon completion, the reaction was diluted with CH<sub>3</sub>CN:H<sub>2</sub>O containing 0.2% TFA (3.0 mL, 10:90) and the DOTA-labelled cyclic-(PPg)LLFVY was purified using HPLC (*figure S95*). The collected fractions ( $t_R=24.5$  minutes) were lyophilized to give the product as a fine white powder (1.3 mg, 46% yield). LR-MS  $m/z$  (MALDI): C<sub>64</sub>H<sub>98</sub>N<sub>14</sub>O<sub>17</sub> ([M+H]<sup>+</sup>) calcd. 1335.73, found 1335.5. (*figure S96*).

### Compound 31: <sup>69</sup>Ga-DOTA-link-c-(Ppg)LLFVY

EDTA (4.0 mg) was combined in NaOAc buffer (1 mL, pH 4.5) and a small amount of gallium trichloride (50 mg) was transferred to the solution under a nitrogen atmosphere. This was allowed to stand at ambient temperature for 5 minutes and then a small aliquot of the solution (150 μL) was added to compound **30** (0.8 mg, 0.6 μmol) in NaOAc buffer (150 μL, pH 4.5). The reaction was heated to 90 °C for 3 hours, followed by ambient temperature for an additional 21 hours, for a total reaction time of 24 hours. Upon completion, the reaction was purified by HPLC. The collected fractions ( $t_R=39.4$  minutes, *figure S97*) were lyophilized to give the product as a fine white powder (1.3 mg, 100 % yield). LR-MS  $m/z$  (MALDI): C<sub>64</sub>H<sub>95</sub>GaN<sub>14</sub>O<sub>17</sub> ([M+H]<sup>+</sup>) calcd. 1401.64, found 1401.5. (*Figure S98*.)

### 6.2.1 [<sup>68</sup>Ga]NOTA-Bn-SCN-link-c-(Ppg)LLFVY (JDW00316)

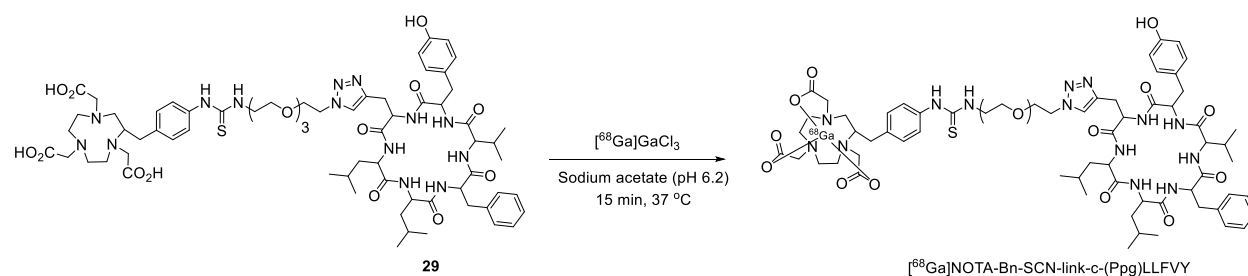


*Figure 6.5. Reaction scheme for the radiolabelling of [<sup>68</sup>Ga]NOTA-Bn-SCN-link-c-(Ppg)LLFVY (JDW00316).*

Compound **29** (0.1 mg to 250 ng, 7.1 mmol to 179 pmol) was dissolved into NH<sub>4</sub>OAc buffer (100 μL) in a 1.5 mL Lobind Eppendorf Tube. The [<sup>68</sup>Ga]GaCl<sub>3</sub> in saline solution (200 μL) was added to the reaction mixture and it was allowed to shake at 37 °C, with TLC (10 mM EDTA in NaOAc buffer, pH 5.6) reactions were tested at intervals of 5 and 15 minutes. Gallium-68 incorporation

was greater than 99%. Reactions were then challenged with EDTA (10  $\mu$ L, 10 mM EDTA in trace metal 100  $\mu$ M  $\text{NH}_4\text{OAc}$  buffer) added into the reaction and shaken for 5 minutes, still showing >98% chelation.

After cell uptake studies it was determined that more analysis for the radiolabeling of this product was required since degradation was suspected. [ $^{68}\text{Ga}$ ]NOTA-Bn-SCN-link-c-(Ppg)LLFVY was first tested for different solvent conditions (pH) for gallium incorporation. It was found that when compound **29** (250 ng, 100  $\mu$ L  $\text{H}_2\text{O}$ ) was added to  $\text{NH}_4\text{OAc}$  buffer (200  $\mu$ L) with the [ $^{68}\text{Ga}$ ]GaCl<sub>3</sub> in saline solution (200 $\mu$ L), the pH of 5 was achieved which was optimal for producing a single product on TLC and one peak on HPLC (tr = 8.3 minutes). An additional test was completed with a precursor that was freeze-dried from the stock solution. This reaction gave a TLC with a 50:50 peak at the baseline and only one peak on HPLC at 8.3 minutes. Suggesting that this compound is not stable in solution. It was concluded that in aqueous conditions the thiourea-bond was degrading and causing free NOTA to be released!

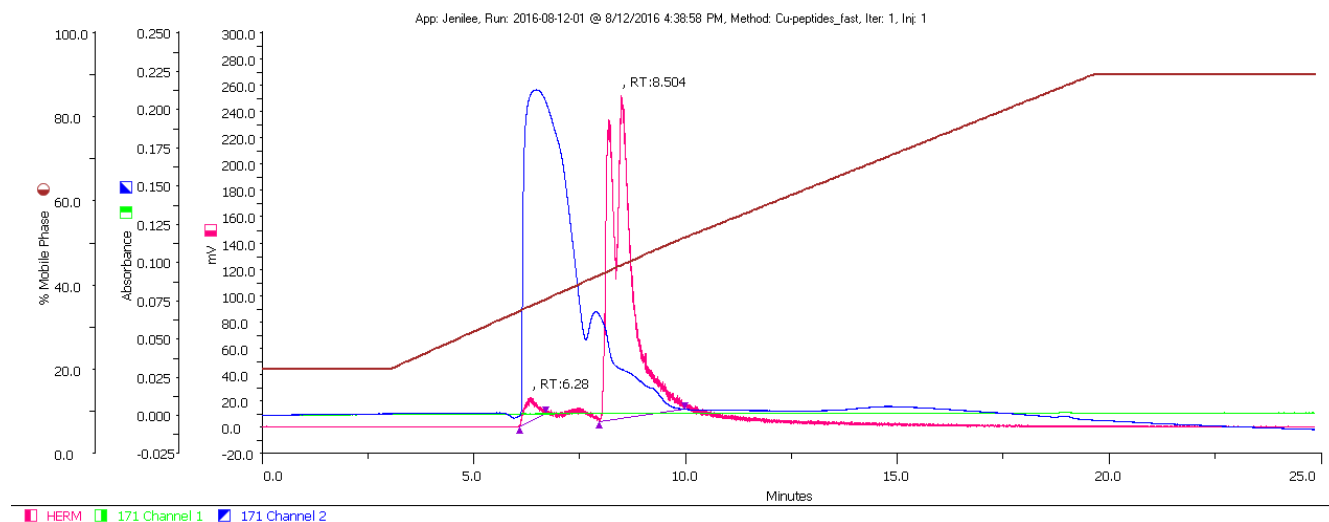


Figure 6.6. HPLC with degradation products of [ $^{68}\text{Ga}$ ]NOTA-Bn-SCN-link-c-(Ppg)LLFVY (JDW00316). Two UV channels are shown, including: 254 nm in green (171 Channel 1) and 210 nm in blue (171 Channel 2). HERM radioactivity channel is shown in pink.

## 6.2.2 [<sup>68</sup>Ga]DOTA-link-c-(Ppg)LLFVY (JDW00816)

A solution for radiolabeling experiments was prepared as per Mueller et al. [125], briefly 5 M NaCl/HCl solution was prepared with NaCl (14.6 mg), HCl (1.25 mL, 5.5 M), and H<sub>2</sub>O (50 mL). The 5.5M HCl solution was prepared with 37% HCl TraceMetal Grade (23 mL) and H<sub>2</sub>O (27 mL). 1M NaOAc pH 4.5 was prepared with NaOAc (4.1 g), 37% HCl TraceMetal Grade (1 mL) and H<sub>2</sub>O (50 mL), with 100% Acetic Acid to adjust the pH. Lastly phosphate buffer was made with Na<sub>2</sub>HPO<sub>4</sub>•7H<sub>2</sub>O (6.1 g) in H<sub>2</sub>O (40 mL).

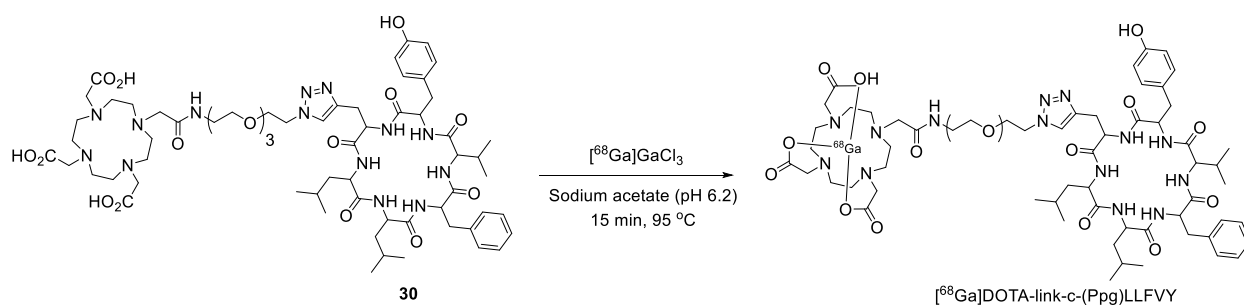


Figure 6.7. Reaction scheme for the radiolabelling of [<sup>68</sup>Ga]DOTA-link-c-(Ppg)LLFVY (JDW00816).

Firstly, the gallium-68 as received from the iThemba generator is purified using a PS-H+ cartridge from Macherey-Nagel. The eluent from the generator is directly trapped onto the cartridge and the product is eluted with 5M NaCl/HCl solution (1.0 mL) as described above.

Next, compound **30** (10.0 µg, 7.5 nmol) was combined in NaOAc buffer (75 µL, pH 4.5). To this peptide was added an aliquot of NaOAc buffer (150 µL, pH 4.5) and the <sup>68</sup>Ga in NaCl (150 µL). This was allowed to react at 95°C for 15 minutes and then the product was purified by HPLC using the Cu\_peptides method in **section 2.1.1.4**. (figure S99). The quality control sample of the reaction was directly injected into the HPLC to give a retention time of 34.7 minutes. If the product was sufficiently pure, the rest of the reaction aliquot was not injected onto the HPLC and instead used for *in vitro* assays. The product identity was confirmed by co-injection on HPLC with a cold reference compound **31** (figure S100).

To achieve this optimized synthesis above, numerous reaction parameters were tested as summarized in *Table 6.1*. Yields were calculated using aluminum-backed silica TLC plates developed using 10:90 NaOAc buffer: MeOH as the mobile phase, leading to a  $R_f=0$  from the radiolabeled peptide. Overall, the product could be achieved with a decay correct radiochemical yield of  $77 \pm 5 \%$  with a purity  $>99\%$  as determined by HPLC.

*Table 6.1. Summary of radiolabelling data for  $[^{68}\text{Ga}]\text{DOTA-link-c-(Ppg)LLFVY}$  (JDW00816). Including reaction ID, peptide mass, sodium acetate (NaOAc) volume, volume of gallium eluent, temperature, time and yield.*

Reaction ID	Peptide mass ( $\mu\text{g}$ )	NaOAc volume ( $\mu\text{L}$ )	Gallium volume ( $\mu\text{L}$ )	Temp. ( $^{\circ}\text{C}$ )	Time (minutes)	Yield (%)
JDW00816-1	18	200	200	100	30	23
JDW00816-2	18	200	200	100	30	0
JDW00816-3	40	350	500	95	45	98
JDW00816-4	10	75	25	95	8,13,18,24	20,30,20,15
JDW00816-5	10	75	50	95	15	99
JDW00816-6	10	75	500	95	15	11
JDW00816-7	10	225	150	95	14	99
JDW00816-8	10	225	150	95	15	99
JDW00816-9	2.5	75	50	95	15	93
JDW00816-10	2.5	225	150	95	15	62
JDW00816-11	10	150	150	95	15	67
JDW00816-12	10	450	300	95	15	60
JDW00816-13	10	675	450	95	15	43
JDW00816-14	10	75	50	95	15	99
JDW00816-15	10	75	50	95	15	99
JDW00816-16	10	225	150	95	15	99
JDW00816-17	10	225	150	95	15	99

### 6.2.3 $[^{64}\text{Cu}]\text{NOTA-Bn-SCN-(Ppg)LLFVY}$ (JDW02415)

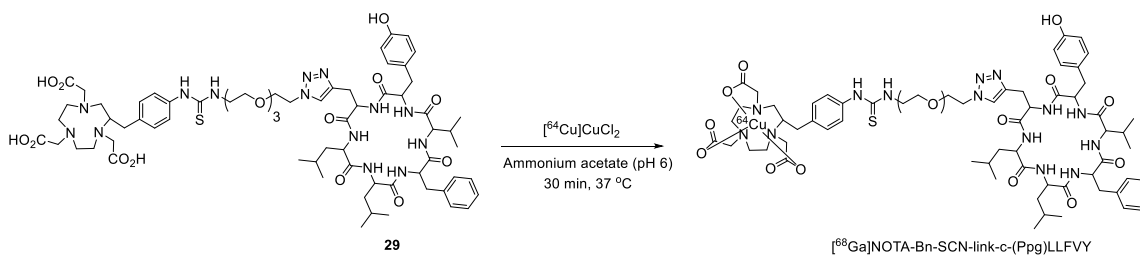


*Figure 6.8. Reaction scheme for the radiolabelling of  $[^{64}\text{Cu}]\text{NOTA-Bn-SCN-(Ppg)LLFVY}$  (JDW02415).*

Compound **29** (10  $\mu\text{g}$  to 25 ng, 7.1 nmol to 17.9 pmol) was dissolved into  $\text{NH}_4\text{OAc}$  buffer (50  $\mu\text{L}$ ) in a 1.5 mL Lobind Eppendorf Tube. The reaction mixture was shaken at 37  $^\circ\text{C}$  for 30 minutes, with TLC testing completed at the time intervals of 5, 15, and 30 minutes. Upon completion of the reaction, the reaction mixture was injected into HPLC using the method “Cu\_peptides\_Fast” (see **section 2.1.1.5.**), having a retention time of 18.6 minutes. Overall, the product was found to be greater than 99% (n=3) pure by HPLC with an overall recovered radiochemical yield of  $75 \pm 5\%$  (n=3) after HPLC. Also, the reaction proceeded optimally at 25 ng of peptide in 25  $\mu\text{L}$  of  $\text{NH}_4\text{OAc}$  buffer within 30 minutes; which was chosen since at lower concentrations of peptide (see *table 6.2*), the radiolabelled product could not be recovered from HPLC, due to the small mass causing retention time problems.

*Table 6.2. Summary of radiolabelling data for [ $^{64}\text{Cu}$ ]NOTA-Bn-SCN-(Ppg)LLFVY (JDW02415).*

Radiolabelling ID	Peptide mass ( $\mu\text{g}$ )	5 Minutes	15 Minutes	30 Minutes
JDW02415-1	10	92.9 %	95.9%	96.1%
JDW02415-2	2.5	99.2%	99.3%	99.1%
JDW02415-3	0.25	978.0%	99.0%	98.9%
JDW02415-6	0.025	89.3%	91.8%	95.1%
JDW02415-4	0.0025	72.2%	79.5%	72.4%
JDW02415-5	0.00025	61.9%	70.9%	79.6%

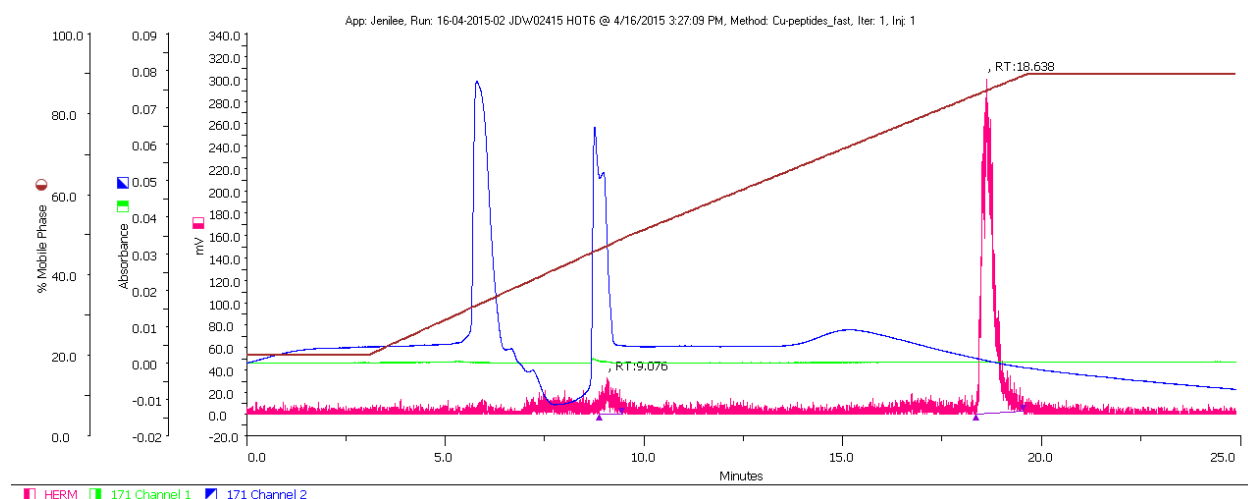


*Figure 6.9. HPLC for the radiolabelling of [ $^{64}\text{Cu}$ ]NOTA-Bn-SCN-(Ppg)LLFVY (JDW02415). Two UV channels are shown, including: 254 nm in green (171 Channel 1) and 210 nm in blue (171 Channel 2). HERM radioactivity channel is shown in pink.*

From JDW02415-6, the specific activity was calculated to be 51.5 GBq/ $\mu\text{mol}$  on 0.92 MBq of product and thus the limiting factor was the amount of radioactivity injected. If radiolabelling could be achieved on 300 MBq, this would equal 16787.9 GBq/ $\mu\text{mol}$ . Finally, since the molar activity is very good and the incorporation is complete, there is no need for HPLC purification. As even the UV absorbance on the HPLC cannot detect any starting peptide as seen in *Figure 6.9*.

### 6.3 Fluorescent labelling of cyclic peptide

**Compound 32:** N-[2-(2-{2-(2-Azidoethoxy)ethoxy}ethoxy)ethyl]-7-nitro-2,1,3-benzoxadiazol-4-amine

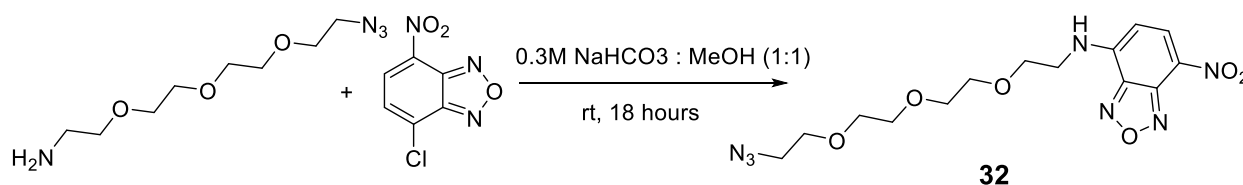


*Figure 6.10. Reaction scheme for the synthesis of compound 32 from commercially available starting materials.*

As per Berchel *et al.* [126], 11-Azido-3,6,9-trioxaundecan-1-amine (220  $\mu\text{L}$ , 1.11 mmol) in a solution of  $\text{NaHCO}_3$  (0.3 M, 2.5 mL) was combined with 4-chloro-7-nitrobenzofurazan (147.7 mg, 0.74 mmol) in methanol (MeOH) (7.5 mL). The reaction was allowed to proceed for 18 hours at ambient temperature. Upon completion, the reaction volume was reduced by rotavap and the residue was purified using flash chromatography (1:1, EtOAc:Hex). Fractions were collected and the product was isolated as an orange-yellow solid.  $^1\text{H-NMR}$  (600 MHz,  $\text{CDCl}_3$ ):  $\delta$ 3.39 (t,  $J = 5.00$  Hz, 2H), 3.70 (m, 12H), 3.89 (dd,  $J = 5.60$  and 4.61 Hz, 2H), 5.31 (s, 1H), 6.20 (d,  $J = 8.68$  Hz, 1H), 8.46 (d,  $J = 8.66$  Hz, 1H) (*figure S101*).  $^{13}\text{C-NMR}$  (150 MHz,  $\text{CDCl}_3$ ):  $\delta$ 68.1, 70.5, 70.6, 70.7, 70.7, 98.8, 123.6, 136.6, 143.9, 144.3 (*figure S102*).

**Compound 33:** NBD-link-c-(Ppg)LLFVY

Compound **32** (1.15 mg 3.0  $\mu\text{mol}$ ) was combined with *c*-(Ppg)LLFVY **23** (2.0 mg, 2.7  $\mu\text{mol}$ ),  $\text{Cu}(\text{OAc})_2$  (5.0 mg, 2.6  $\mu\text{mol}$ ), and sodium ascorbate (2.5 mg, 12.6  $\mu\text{mol}$ ) in a mixture of *t*-

butanol:water (50:50, 1.5 mL). The reaction was left stirring at ambient temperature for 24 hours and upon completion, the mixture was extracted three times in CH<sub>2</sub>Cl<sub>2</sub> (2 mL). The organic layers were combined, and the volume was reduced using nitrogen flow. The concentrated sample was purified using preparatory TLC (9:1 CH<sub>2</sub>Cl<sub>2</sub>: MeOH) R<sub>f</sub>=0.66. Here the silica was removed from the plate and extracted using CH<sub>2</sub>Cl<sub>2</sub>, the CH<sub>2</sub>Cl<sub>2</sub> was again removed using rotary evaporation to yield the product as a bright orange solid (2.9 mg, 95% yield) LR-MS m/z (ESI): C<sub>54</sub>H<sub>73</sub>N<sub>13</sub>O<sub>13</sub> ([M+H]<sup>+</sup>) calcd. 1112.55, found 1112.6. ([M+Na]<sup>+</sup>) calcd. 1134.54, found 1134.5. (*figure S103*) HR-MS m/z (ESI): C<sub>54</sub>H<sub>73</sub>N<sub>13</sub>O<sub>13</sub> ([M+H]<sup>+</sup>) calcd. 1112.5524, found 1112.5542. ([M+Na]<sup>+</sup>) calcd. 1134.54, found 1134.5356. (*figure s104*).

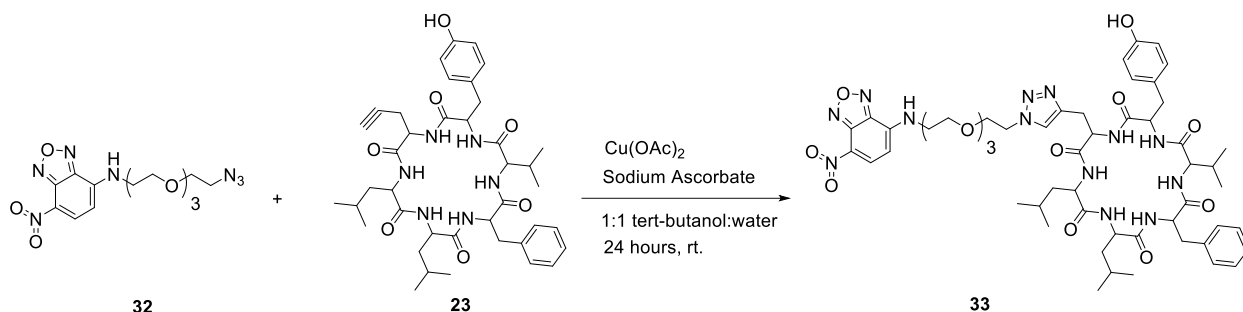


Figure 6.11. Reaction scheme for the synthesis of compound **33**, from compound **32** (see section 6.3.) and compound **23** (see section 5.1.).

#### 6.4 [<sup>18</sup>F]Fluorine radiolabelling of small-molecular HIF-1 $\alpha$ targeting compounds

##### Compound **34**: (*p*-Ethynylphenyl)trimethylammonium

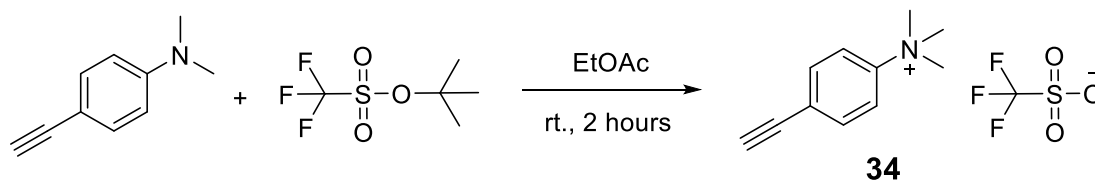
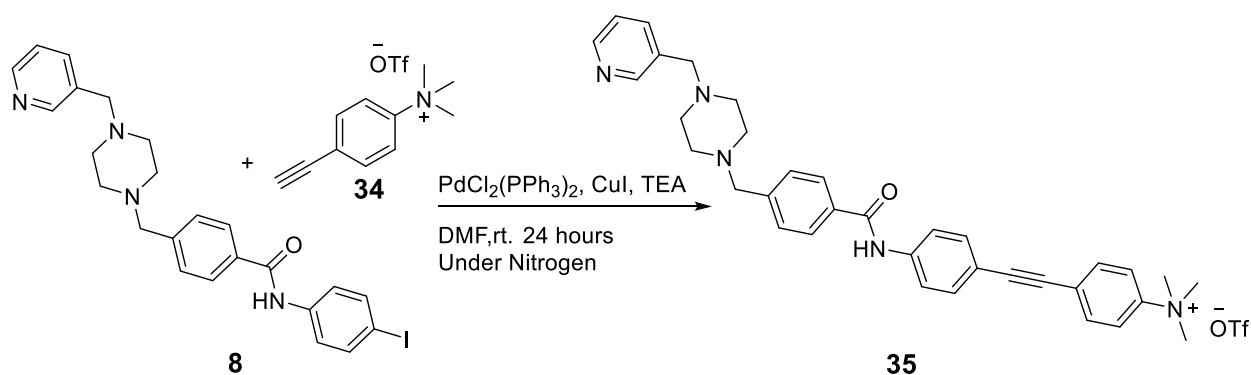


Figure 6.12. Reaction scheme for the synthesis of compound **34** from commercially available starting materials.

4-Ethynyl-N,N-dimethylaniline (99.7 mg, 0.69 mmol) was combined with methyl trifluoromethanesulfonate (100  $\mu$ L, 0.8 mmol) and allowed to stir at ambient temperature for 2

hours in ethyl acetate (2 mL). The product upon formation would precipitate out of the solution. Once the reaction was completed, the product was filtered and washed with ethyl acetate to yield the product of interest as a white powdery solid (110 mg, 100 % yield). LR-MS  $m/z$  (ESI):  $C_{11}H_{14}N$  ( $[M]^+$ ) calcd. 160.11, found 160.2 (*figure S105*).  $^1H$ -NMR (600 MHz,  $(CD_3)_2SO$ ):  $\delta$  3.92 (s, 9H), 3.95 (s, 1H), 7.78 (m, 2H), 8.15 (m, 2H) (*figure S106*).  $^{13}C$ -NMR (150 MHz,  $(CD_3)_2SO$ ):  $\delta$  56.8, 81.1, 81.2, 120.9, 124.6, 133.6, 147.2. (*figure S107*).

Compound 35: *p*-(2-(*p*-(*p*-((4-[(3-Pyridyl)methyl]-1-piperazinyl)methyl)benzylamino]phenyl)ethynyl)(trimethylammonio)benzene



*Figure 6.13. Reaction scheme for the synthesis of compound 35, from compound 8 (see section 5.1.) and compound 34 (see section 6.3.).*

Compound **8** (113.0 mg, 0.22 mmol) was combined with compound **34** (122.4 mg, 0.76 mmol) and the catalyst system of  $PdCl_2(PPh_3)_2$  (7.7 mg, 10.9  $\mu$ mol), CuI (5.3 mg, 27.8  $\mu$ mol), and triethylamine (100  $\mu$ L) in a solution of DMF (2.0 mL). After the reaction was completed, the product was extracted using  $CH_2Cl_2$  and water. The  $CH_2Cl_2$  layer was collected, and the volume was reduced using rotary evaporation. The dried product was again resolubilized in additional  $CH_2Cl_2$ , but the product would not dissolve back into the solution. This product was filtered to yield an orange-yellow powdery solid (123.5 mg, 100% yield). LR-MS  $m/z$  (ESI):  $C_{35}H_{38}N_5O^+$  ( $[M+H]^{2+}$ ) calcd. 272.66, found 272.7. (*figure S108*)  $^1H$ -NMR (600 MHz,  $D_2O$ ):  $\delta$  3.40 (s, 9H), 3.51 (s, 8H), 4.36 (s, 2H), 4.61 (s, 2H), 7.37 (s, 2H), 7.45 (d,  $J = 8.35$  Hz, 2H), 7.51 (d,  $J = 9.25$  Hz, 2H), 7.59 (d,  $J = 9.28$  Hz, 2H), 7.72 (d,  $J = 8.29$  Hz, 2H), 8.00 (dd,  $J = 8.13$  and 5.88 Hz, 2H), 8.64 (dt,  $J = 8.25$  and 1.62 Hz, 2H), 8.73 (d,  $J = 5.75$  Hz, 2H), 8.88 (s, 1H) (*figure S109*).  $^{13}C$ -



Table 6.3. Summary of data for the radiolabelling of compound 35 precursor. Including reaction ID, solvent for fluorination, compound 35 concentration, temperature, time and purity as determined by TLC.

Reaction ID	Solvent	Precursor conc. (mg/mL)	Temp. (°C)	Time (min)	Purity (%)
[ <sup>18</sup> F]FPeP4-1A	CH <sub>3</sub> CN	12	95	0	0.9
[ <sup>18</sup> F]FPeP4-1B	CH <sub>3</sub> CN	12	95	20	46.2
[ <sup>18</sup> F]FPeP4-2A	CH <sub>3</sub> CN	6	160	20	0.5
[ <sup>18</sup> F]FPeP4-3A	DMF	14	95	20	1.0
[ <sup>18</sup> F]FPeP4-3B	DMF	14	95	40	4.4
[ <sup>18</sup> F]FPeP4-4A	CH <sub>3</sub> CN	17	95	5	20.1
[ <sup>18</sup> F]FPeP4-4B	CH <sub>3</sub> CN	17	95	25	21.0
[ <sup>18</sup> F]FPeP4-4C	CH <sub>3</sub> CN	17	95	45	43.8
[ <sup>18</sup> F]FPeP4-4D	CH <sub>3</sub> CN	17	95	60	33.8
[ <sup>18</sup> F]FPeP4-5A	DMSO	13.5	95	20	35.2
[ <sup>18</sup> F]FPeP4-5B	DMSO	13.5	95	40	13.0
[ <sup>18</sup> F]FPeP4-6A	DMSO	25	95	5	3.1
[ <sup>18</sup> F]FPeP4-6B	DMSO	25	95	10	7.0
[ <sup>18</sup> F]FPeP4-6C	DMSO	25	95	15	5.8
[ <sup>18</sup> F]FPeP4-6D	DMSO	25	95	20	11.4
[ <sup>18</sup> F]FPeP4-6E	DMSO	25	95	30	12.4
[ <sup>18</sup> F]FPeP4-6F	DMSO	25	95	50	16.7
[ <sup>18</sup> F]FPeP4-7A	DMSO	27	95	45	0

Table 6.4. Summary of HPLC data for the radiolabelling of compound 35 precursor. Including HPLC injection ID, retention time of product peak, and solvent composition.

HPLC Injection ID	Retention time (min)	Radioactivity present (Yes/No)	TFA in HPLC H <sub>2</sub> O (Yes/No)
13-07-2016-01	21.97	No	No
13-07-2016-02	18.01	No	Yes
13-07-2016-03	22.99	Yes	Yes
13-07-2016-04	22.93	Yes	Yes
13-07-2016-05	18.5 + 22.30	co injection	Yes

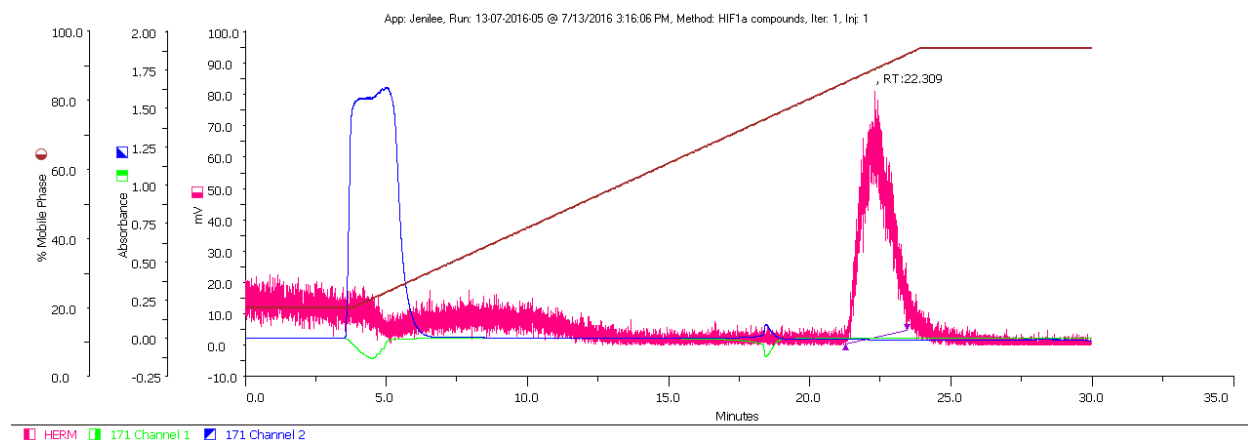


Figure 6.15. Typical HPLC chromatogram of  $[^{18}\text{F}]\text{FPeP4}$  reaction. Two UV channels are shown, including: 254 nm in green (171 Channel 1) and 210 nm in blue (171 Channel 2). HERM radioactivity channel is shown in pink.

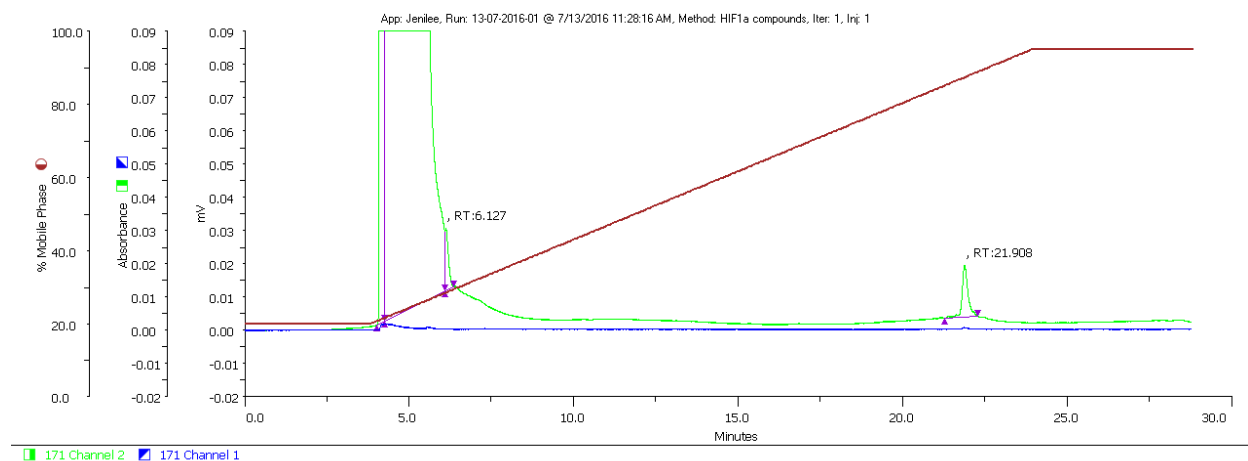


Figure 6.16. Typical HPLC of  $[^{19}\text{F}]\text{compound 9}$  reference compound. Two UV channels are shown, including: 254 nm in green (171 Channel 1) and 210 nm in blue (171 Channel 2). HERM radioactivity channel is shown in pink.

When reactions were further analyzed by HPLC, the radioactive product at 23 minutes could not be identified (Figures 6.15 and 6.16). This was because the co-injection of the radioactive compound and non-radioactive compound together never gave the same retention time (Table 6.4). Overall, the reaction must be forming a very similar compound, that has the same retention on TLC as the product of interest.

## 6.4.2 Prosthetic group approach for the synthesis of [<sup>18</sup>F]compound **9** ([<sup>18</sup>F]FPeP4)

### 6.4.2.1 Synthesis of 4-[<sup>18</sup>F]fluorophenylacetylene ([<sup>18</sup>F]FPA)

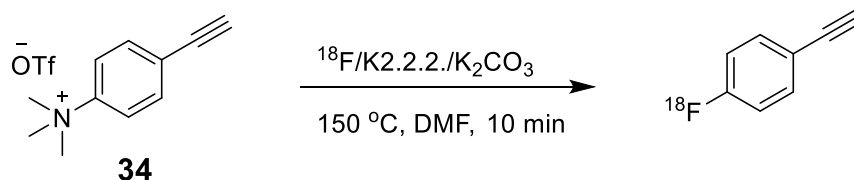
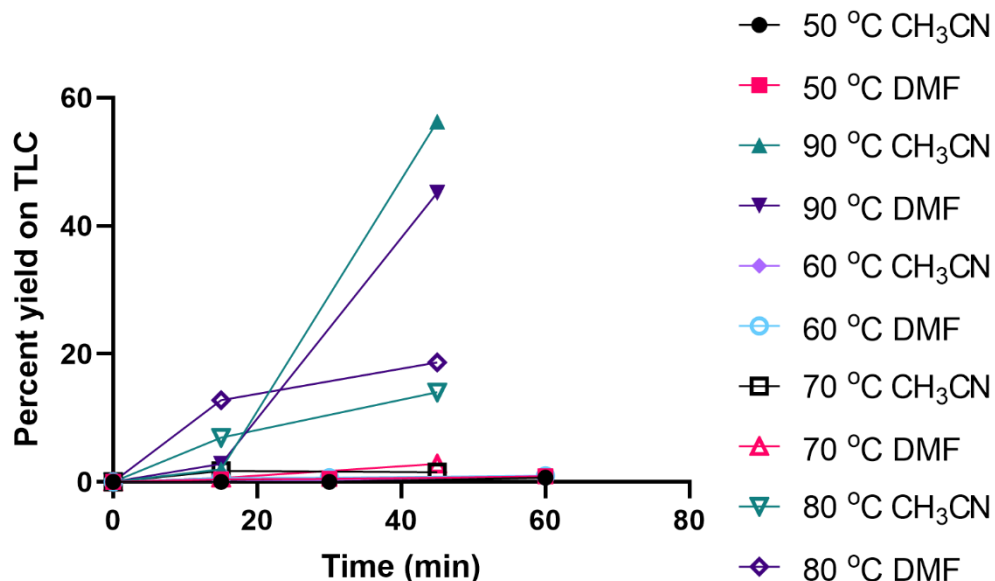


Figure 6.17. Reaction scheme for the synthesis of 4-[<sup>18</sup>F]fluorophenylacetylene from the previously synthesized compound **34**.

Manual optimization of radiolabelling parameters using compound **34** as radiolabelling precursor was completed by varying the concentration of the precursor, radiolabelling solvent used, temperature and time of reaction. The first reactions used a precursor concentration of 40 mg/mL of compound **34** in two solvents (DMF and CH<sub>3</sub>CN). Reactions were completed in 1.5 mL low-bind Eppendorf tubes shaking at 1050 rpm on a thermoshaker at 50, 60, 70, 80 and 90 °C for 15 to 60 minutes. Overall, the highest temperature of 90 °C produced the highest yields as determined by TLC (5:1, EtOAc, Hexane, R<sub>f</sub>=0.85), see Figure 6.18.

Also during these preliminary radiolabelling experiments, [<sup>18</sup>F]FPA was found to be extremely volatile. Even at ambient temperature (21 °C), the compound that was adhered to the silica on the TLC plate would slowly volatilize over 15 minutes completely into the air. Therefore, extreme care should be given to the timing of TLC plate reading and overall handling of this compound. The next experiments for the synthesis of [<sup>18</sup>F]FPA were completed at a precursor concentration of 13 mg/mL in both CH<sub>3</sub>CN and DMF at 110 and 120 °C for 45 minutes. Overall, from these experiments it was found that the yield did not increase over that which was achieved at 95 °C. This was due to constant volatility of the product being produced. Additionally, CH<sub>3</sub>CN was found to be higher yielding than the solvent of DMF. Therefore, the reaction parameters of 95 °C in CH<sub>3</sub>CN were carried forward for testing of the precursor concentration in solution. Concentrations from 0.8 to 13 mg/mL were tested to determine that at lower concentrations below 4 mg/mL the yield of the fluorination was optimal.

These manual radiolabelling procedures were then carried forward to the automated synthesis unit (ASU), a GE TracerLab FX. The loading of the ASU is shown in *Table 6.5*.



*Figure 6.18. Percent yield on TLC for the radiolabelling of [18F]FPA in various solvents and temperatures (n=1).*

*Table 6.5. Loading scheme for the ASU for the synthesis of [18F]FPA.*

ASU Component	Contents	Volume
V1	K2.2.2./K <sub>2</sub> CO <sub>3</sub> or TBA-HCO <sub>3</sub>	1.0 to 1.5 mL
V2	CH <sub>3</sub> CN	1.5 mL
V3	FPA precursor in solvent	1.0 mL
V4	Elution Solvent	3.0 mL
V5	Water	12.0 mL
V6	Water	12.0 mL
QMA	SepPak QMA or PS-HCO <sub>3</sub>	Primed 10 mL K <sub>2</sub> CO <sub>3</sub> /12 mL water
C18 #2	Various	Primed 5 mL EtOH/12 mL water

Testing parameters began with radiofluorinations at 85 °C, 45 minutes, 4 mg/mL in CH<sub>3</sub>CN, as per the manual optimization, which gave a very poor yield of only 4%. Sequential optimization was completed as per *Table 6.6*.

Table 6.6. Testing parameters for the radiosynthesis on the ASU for [ $^{18}\text{F}$ ]FPA.

Reaction ID	Precursor Conc. (mg/mL)	$^{18}\text{F}$ -source	Solvent	Temp. ( $^{\circ}\text{C}$ )	Time (min)	C18 cartridge	Yield (%)
1	4.0	K222/ $\text{K}_2\text{CO}_3$	$\text{CH}_3\text{CN}$	85	45	None	3.8
2	4.0	K222/ $\text{K}_2\text{CO}_3$	DMF	85	45	None	3.9
3	12.7	K222/ $\text{K}_2\text{CO}_3$	$\text{CH}_3\text{CN}$	85	45	None	4.0
4	12.8	K222/ $\text{K}_2\text{CO}_3$	DMF	85	45	None	4.4
5	14.3	K222/ $\text{K}_2\text{CO}_3$	DMF	150	15	Phenomenex Strata C18U	30.0
6	29.3	K222/ $\text{K}_2\text{CO}_3$	DMF	100	45	None	1.2
7	9.6	K222/ $\text{K}_2\text{CO}_3$	DMF	150	20	Phenomenex Strata C18U	14.7
8	12	K222/ $\text{K}_2\text{CO}_3$	DMF	150	20	Phenomenex Strata C18U	18.7
9	11.9	K222/ $\text{K}_2\text{CO}_3$	DMF	150	20	Phenomenex Strata C18U	9.9
10	12.9	K222/ $\text{K}_2\text{CO}_3$	DMF	150	20	Phenomenex Strata C18U	24.0
11	7.1	K222/ $\text{K}_2\text{CO}_3$	DMF	150	20	Phenomenex Strata C18U	17.4
12	14.1	K222/ $\text{K}_2\text{CO}_3$	DMF	140	30	Phenomenex Strata C18U	13.8
13	9.6	K222/ $\text{K}_2\text{CO}_3$	DMF	140	30	Phenomenex Strata C18U	12.1
14	6.9	K222/ $\text{K}_2\text{CO}_3$	DMF	140	30	Phenomenex Strata C18U	15.3
15	10.1	K222/ $\text{K}_2\text{CO}_3$	DMF	140	30	SepPak tC18 Plus	15.1
16	12.8	TBA- $\text{HCO}_3$	DMF	140	30	SepPak tC18 Plus	15.4

Overall, due to the required higher temperatures for fluorination, DMF was found to be the better solvent of choice. The concentration of the precursor from 5-15 mg/mL had very little influence on the radiochemical yield. Additionally, using either  $\text{K222}/\text{K}_2\text{CO}_3$  or  $\text{TBA-HCO}_3$  gave no difference in the radiochemical yield. Final ASU parameters were determined to be  $\sim 10$  mg/mL in DMF at  $140^{\circ}\text{C}$  for 30 minutes, obtaining a  $15.6 \pm 3.8\%$  radiochemical yield after 53 minutes from [ $^{18}\text{F}$ ]fluoride. Yields could not be raised further, due to the physical limitations on the ASU for

radiofluorination of an extremely volatile compound. In the GE Tracerlab FX, there is no distillation possible, thus there is very likely a large proportion of the product still in the gas phase or stuck at the top of the reactor. This has been witnessed, as there is volatile radioactivity that is not trapped on the C18 cartridge and instead is trapped in a radioactive gas waste exhaust bag.

#### 6.4.2.2 Sonogashira cross coupling reactions with [ $^{18}\text{F}$ ]FPA

##### Compound 36: 1-((4-fluorophenyl)ethynyl)-2,4-dimethoxybenzene

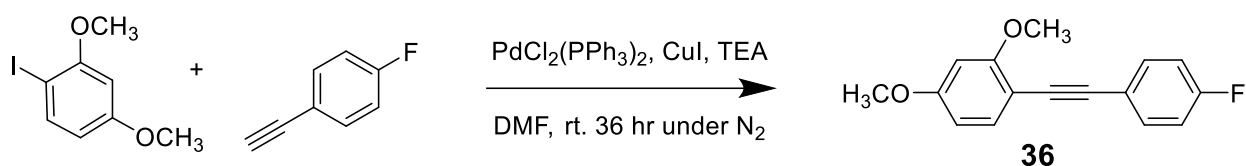


Figure 6.19. Reaction scheme for the synthesis of compound 36 from commercially available starting materials.

1-Iodo-2,4-dimethoxybenzene (45.7 mg) and 4-fluorophenylacetylene (22.1 mg) were combined in a 2 mL Lobind Eppendorf along with PdCl<sub>2</sub>(PPh<sub>3</sub>)<sub>2</sub> (2.0 mg), CuI (2.5 mg) and TEA (50  $\mu\text{L}$ ) all in 1 mL DMF. The reaction was purged under nitrogen, parafilm and agitated at ambient temperature over 36 hours at 1050 rpm. Once completed, the reaction was extracted into CH<sub>2</sub>Cl<sub>2</sub>, washed with water and the organic phase rotary evaporated to dryness. The dried reaction was resolubilized in EtOAc and purified using flash chromatography (5:1) Hex:EtOAc. Overall yielding a bright yellow oil (21.6 mg, 49%). Thin-layer chromatography (TLC): R<sub>f</sub> = 0.6 (1:5, EtOAc:Hex). LR-MS m/z (ESI): C<sub>16</sub>H<sub>13</sub>FO<sub>2</sub> ([M+Na]<sup>+</sup>) calcd. 256.10, found 256.2 (figure S111). <sup>1</sup>H-NMR (600 MHz, (CD<sub>3</sub>)<sub>2</sub>SO):  $\delta$ 3.81(s, 3H), 3.85 (s, 3H), 6.57 (m, 1H), 6.63 (d, J = 2.88 Hz, 1H), 7.25 (m, 2H), 7.40 (d, J = 8.18 Hz, 1H), 7.54 (m, 2H) (figure S112). <sup>13</sup>C-NMR (150 MHz, (CD<sub>3</sub>)<sub>2</sub>SO): 55.2, 55.9, 86.6, 90.8, 99.0, 103.9, 106.1, 116.4 (J<sub>F</sub> = 24 Hz), 120.1 (J<sub>F</sub> = 3.3 Hz), 133.8 (J<sub>F</sub> = 9 Hz), 134.4, 161.4, 161.7, 162.1 (J<sub>F</sub> = 246 Hz) (figure S114). <sup>19</sup>F-NMR (600MHz, (CD<sub>3</sub>)<sub>2</sub>SO):  $\delta$ -111.5. (figure S113).

#### 6.4.2.2.1 Synthesis of 1-((4-[<sup>18</sup>F]fluorophenyl)ethynyl)-2,4-dimethoxybenzene ([<sup>18</sup>F]FPEdMO)

[<sup>18</sup>F]FPA was synthesized on the ASU and used in the test Sonogashira reaction to synthesize 1-((4-[<sup>18</sup>F]fluorophenyl)ethynyl)-2,4-dimethoxybenzene ([<sup>18</sup>F]FPEdMO). Different palladium catalysts, copper-free/copper-present reactions were all tested in DMF at 95 °C for 30 minutes on the thermoshaker at 1050 rpm. Reactions were then tested on TLC (5:1 EtOAc:Hex, R<sub>f</sub>=0.78) versus a blank reaction to determine the size of the product peak. This is because [<sup>18</sup>F]FPA on TLC R<sub>f</sub>=0.8, yet when combined with a palladium source, most of the radioactivity will be present at R<sub>f</sub>=0. Hence the blank reaction identified the amount of unbound-[<sup>18</sup>F]FPA that can then be subtracted from the product peak percentage. The total reaction data is shown in *Table 6.7*.

*Table 6.7. Complete testing reactions for FPEdMO. Notes: Pd(OAc)<sub>2</sub> is 1.5 mg in 100 μL DMF, Pd(PPh<sub>3</sub>)<sub>4</sub> is 1.5 mg in 100 μL DMF, PdCl<sub>2</sub>(PPh<sub>3</sub>)<sub>2</sub> is 1.4 mg in 100 μL DMF, CuI is added in 100 μL DMF solution, [<sup>18</sup>F]FPA is added to each reaction with 150 μL of DMF. 25 μL of TEA is added to each reaction. Precursor is present as 6 mg in 100 μL DMF.*

Reaction ID	Palladium Catalyst	CuI (mg)	Total volume (μL)	Precursor (mg)	TLC Yield (%)	Overall Yield (%)
FPEdMO -1	Pd(OAc) <sub>2</sub>	2.9	475	6	62	39
FPEdMO -2	Pd(OAc) <sub>2</sub>	2.9	475	0	23	-
FPEdMO-3	Pd(OAc) <sub>2</sub>	0	375	6	75	61
FPEdMO-4	Pd(OAc) <sub>2</sub>	0	375	0	14	-
FPEdMO-5	Pd(PPh <sub>3</sub> ) <sub>4</sub>	2.9	475	6	92	42
FPEdMO-6	Pd(PPh <sub>3</sub> ) <sub>4</sub>	2.9	475	0	50	-
FPEdMO-7	Pd(PPh <sub>3</sub> ) <sub>4</sub>	0	375	6	82	47
FPEdMO-8	Pd(PPh <sub>3</sub> ) <sub>4</sub>	0	375	0	35	-
FPEdMO-9	PdCl <sub>2</sub> (PPh <sub>3</sub> ) <sub>2</sub>	2.9	475	6	66	14
FPEdMO-10	PdCl <sub>2</sub> (PPh <sub>3</sub> ) <sub>2</sub>	2.9	475	0	52	-
FPEdMO-11	PdCl <sub>2</sub> (PPh <sub>3</sub> ) <sub>2</sub>	0	375	6	58	37
FPEdMO-12	PdCl <sub>2</sub> (PPh <sub>3</sub> ) <sub>2</sub>	0	375	0	21	-

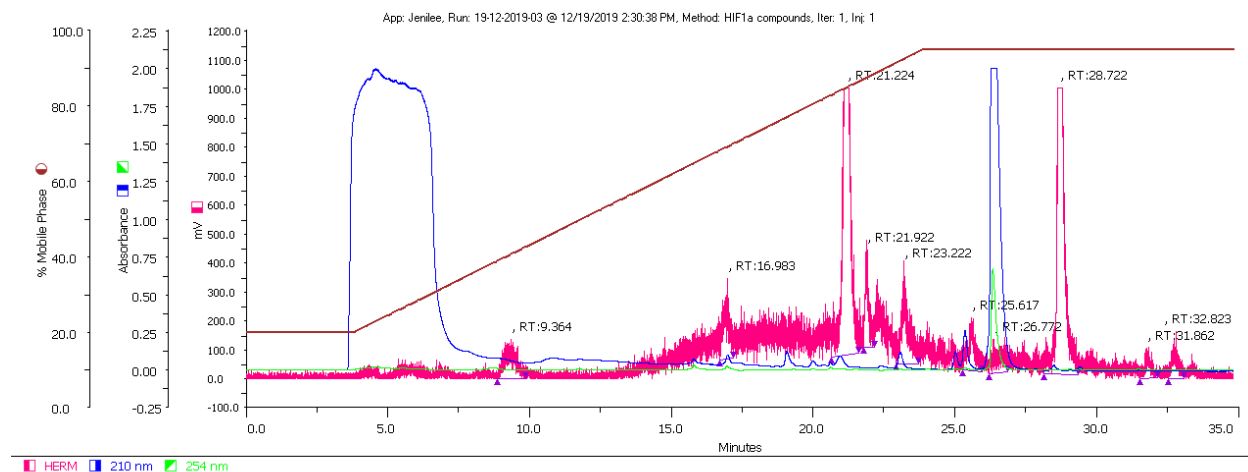


Figure 6.20. Typical HPLC injection of  $[^{18}\text{F}]\text{FPedMO}$ . Two UV channels are shown, including: 254 nm in green and 210 nm in blue. HERM radioactivity channel is shown in pink.

Overall it was found the reaction proceeds best with  $\text{Pd}(\text{OAc})_2$ , Cu-free, with TEA in DMF at 95 °C for 30 minutes. This reaction FPedMO-3 was confirmed using HPLC with the HIF-1 $\alpha$  compounds method to confirm the product peak at 29 minutes (Figure 6.20.). Cold reference compound **36** was found to have a retention time of 28.5 min on the same HPLC method (Figure 6.21.).

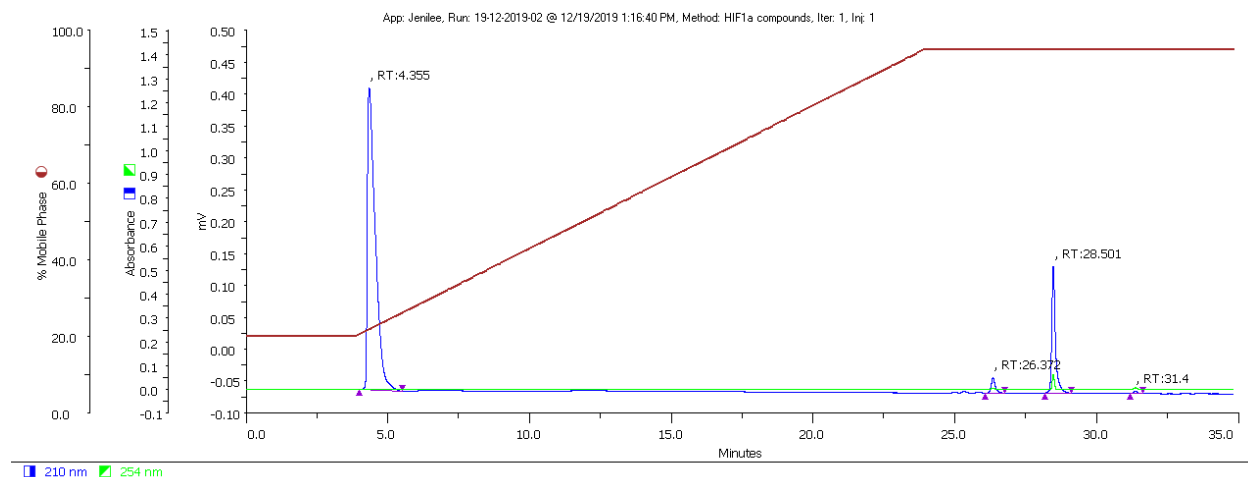


Figure 6.21. Non-radioactive reference compound of  $[^{19}\text{F}]\text{FPedMO}$  on HPLC. Two UV channels are shown, including: 254 nm in green and 210 nm in blue.

#### 6.4.2.2.2 Synthesis of [ $^{18}\text{F}$ ]compound **9** using [ $^{18}\text{F}$ ]FPA ([ $^{18}\text{F}$ ]FPeP4)

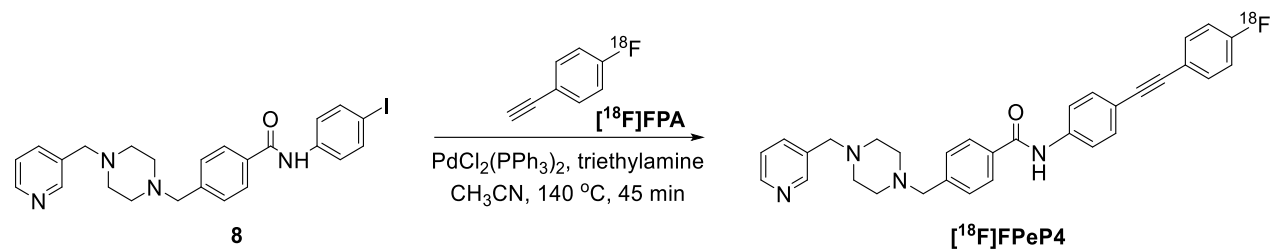


Figure 6.22. Synthesis of [ $^{18}\text{F}$ ]FPeP4 using palladium catalyzed cross-coupling reaction with [ $^{18}\text{F}$ ]FPA and compound **8**.

[ $^{18}\text{F}$ ]FPA was synthesized on the ASU and used in the Sonogashira reaction to synthesize [ $^{18}\text{F}$ ]compound **9**. Starting with the best reaction parameters from the [ $^{18}\text{F}$ ]FPeDMO synthesis which included  $\text{Pd}(\text{OAc})_2$ , Cu-free, with TEA in DMF at  $95\text{ }^\circ\text{C}$  for 30 minutes.

Cold reference compound **9** was found to have a retention time of 18.79 min on the HPLC HIF1 $\alpha$  compounds method. On the HIF1 $\alpha$  compound isocratic method, the retention time shifts to 16.1 minutes. Upon the first reaction, there was no witnessed product but several larger peaks were witnessed at 30 and 32 minutes on the HPLC.

To discern what is happening to the [ $^{18}\text{F}$ ]FPA in the Sonogashira reaction, several blank reactions were tested on HPLC. Using all three catalysts of  $\text{Pd}(\text{OAc})_2$ ,  $\text{PdCl}_2(\text{PPh}_3)_2$  and  $\text{Pd}(\text{PPh}_3)_4$ , the complex of [ $^{18}\text{F}$ ]FPA-Pd is the peak witnessed at a retention time of 32.2 minutes.

Next, the first round of complete optimization was completed as per *Table 6.8*. All reactions were completed in 2.0 mL Lobind Eppendorf tubes at  $95\text{ }^\circ\text{C}$  for 60 minutes in DMSO, with analysis completed by TLC (7:3, Hexane:EtOAc). Palladium added was 100  $\mu\text{L}$  of solution with 100  $\mu\text{L}$  of [ $^{18}\text{F}$ ]FPA from the ASU. Finally, yield values are determined from the difference on TLC from the blank using the solvent front peak on TLC as the product of interest.

Overall, there was very little product observed, with the largest yield of 9.8% of [ $^{18}\text{F}$ ]FPeP4 being found when using  $\text{Pd}(\text{PPh}_3)_4$ , in a copper-free Sonogashira reaction.

Table 6.8. Complete testing reactions for [<sup>18</sup>F]FPeP4. Notes: Pd(OAc)<sub>2</sub> is 2.7 mg in 1 mL DMSO, Pd(Cl<sub>2</sub>)(PPh<sub>3</sub>)<sub>2</sub> is 1.1 mg in 1 mL DMSO, Pd(PPh<sub>3</sub>)<sub>4</sub> is 3.7 mg in 1 mL DMSO, Pd(OAc)<sub>2</sub>+dppf is 5.2 mg + 25.5 mg in 1 mL DMSO, Pd(OAc)<sub>2</sub>+Diphos is 6.8 mg + 35.0 mg in 1 mL DMSO, 50 μL of TEA is added to each reaction. Precursor is present as 10.2 mg in 1 mL DMSO.

Reaction ID	Palladium Catalyst	CuI (mg)	Total volume (μL)	Precursor mass (mg)	TLC Yield (%)	Overall Yield (%)
[ <sup>18</sup> F]FPeP4-8	Pd(OAc) <sub>2</sub>	0	350	1.02	42.6	0
[ <sup>18</sup> F]FPeP4-9	Pd(OAc) <sub>2</sub>	0	350	0	45.8	-
[ <sup>18</sup> F]FPeP4-10	Pd(OAc) <sub>2</sub>	0.5	350	1.02	35.1	7.7
[ <sup>18</sup> F]FPeP4-11	Pd(OAc) <sub>2</sub>	1.2	350	0	27.4	-
[ <sup>18</sup> F]FPeP4-12	PdCl <sub>2</sub> (PPh <sub>3</sub> ) <sub>2</sub>	0	350	1.02	16.8	0
[ <sup>18</sup> F]FPeP4-13	PdCl <sub>2</sub> (PPh <sub>3</sub> ) <sub>2</sub>	0	350	0	17.11	-
[ <sup>18</sup> F]FPeP4-14	PdCl <sub>2</sub> (PPh <sub>3</sub> ) <sub>2</sub>	0.6	350	1.02	15.1	0
[ <sup>18</sup> F]FPeP4-15	PdCl <sub>2</sub> (PPh <sub>3</sub> ) <sub>2</sub>	0.7	350	0	16.1	-
[ <sup>18</sup> F]FPeP4-16	Pd(PPh <sub>3</sub> ) <sub>4</sub>	0	350	1.02	35.0	9.8
[ <sup>18</sup> F]FPeP4-17	Pd(PPh <sub>3</sub> ) <sub>4</sub>	0	350	0	25.2	-
[ <sup>18</sup> F]FPeP4-18	Pd(PPh <sub>3</sub> ) <sub>4</sub>	0.6	350	1.02	13.7	0
[ <sup>18</sup> F]FPeP4-19	Pd(PPh <sub>3</sub> ) <sub>4</sub>	0.7	350	0	15.0	-
[ <sup>18</sup> F]FPeP4-20	Pd(OAc) <sub>2</sub> +dppf	0	350	1.02	36.0	0
[ <sup>18</sup> F]FPeP4-21	Pd(OAc) <sub>2</sub> +dppf	0	350	0	40.0	-
[ <sup>18</sup> F]FPeP4-22	Pd(OAc) <sub>2</sub> +dppf	0.6	350	1.02	28.7	5.4
[ <sup>18</sup> F]FPeP4-23	Pd(OAc) <sub>2</sub> +dppf	0.9	350	0	23.3	-
[ <sup>18</sup> F]FPeP4-24	Pd(OAc) <sub>2</sub> +Diphos	0	350	1.02	40.1	3.9
[ <sup>18</sup> F]FPeP4-25	Pd(OAc) <sub>2</sub> +Diphos	0	350	0	36.2	-
[ <sup>18</sup> F]FPeP4-26	Pd(OAc) <sub>2</sub> +Diphos	0.7	350	1.02	20.5	0
[ <sup>18</sup> F]FPeP4-27	Pd(OAc) <sub>2</sub> +Diphos	0.6	350	0	20.4	-
[ <sup>18</sup> F]FPeP4-28	Pd(OAc) <sub>2</sub>	1.3	350	1.5	33.2	4
[ <sup>18</sup> F]FPeP4-29	Pd(OAc) <sub>2</sub>	0.9	350	0	29.2	-

Due to the low-yielding reaction in DMSO, the cross-coupling was attempted in DMF as the solvent. Reactions were completed in sealed glass reactor tubes at 140 °C for 45 minutes with 400 μL of [<sup>18</sup>F]FPA from the ASU and a varying amount of TEA base (100 – 400 μL). All of these reactions ([<sup>18</sup>F]FPeP4-30 to [<sup>18</sup>F]FPeP4-33) were completed with Pd(OAc)<sub>2</sub> in a copper-free Sonogashira reaction. Again, all reactions lead to a product at the retention time of 15 minutes, but none lead to the product of interest in [<sup>18</sup>F]FPeP4. Also when collected from the HPLC, this product has the color of the palladium catalyst, thus it can be assumed to be some sort of adduct

of [ $^{18}\text{F}$ ]FPA-Pd-8, since in a previous analysis [ $^{18}\text{F}$ ]FPA-Pd had a retention time of 32.5 minutes on HPLC.

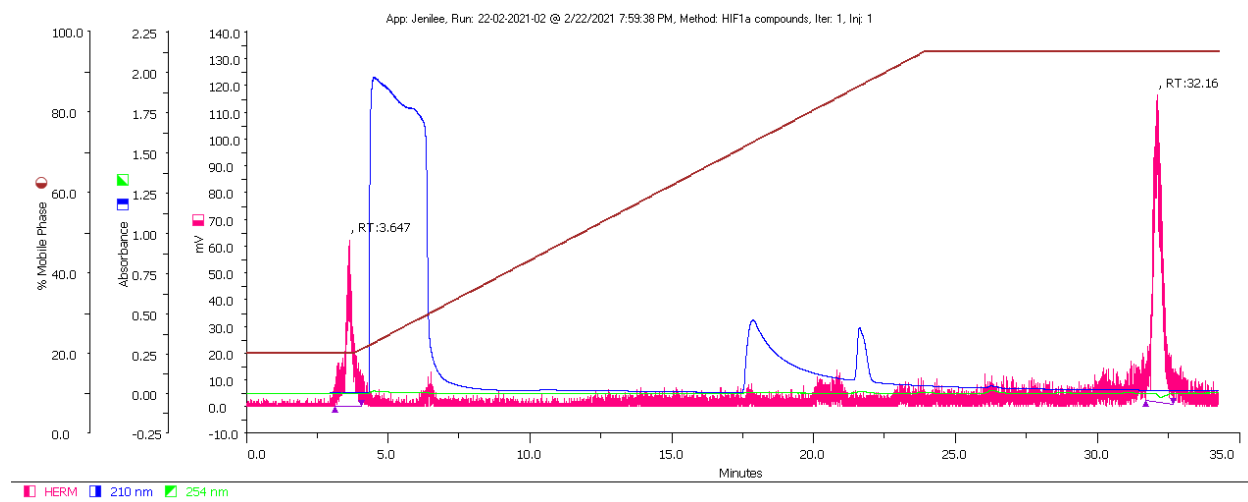


Figure 6.23. HPLC radiotracer for the impurity of [ $^{18}\text{F}$ ]FPA-Pd at 32.2 minutes. Two UV channels are shown, including: 254 nm in green and 210 nm in blue. HERM radioactivity channel is shown in pink.

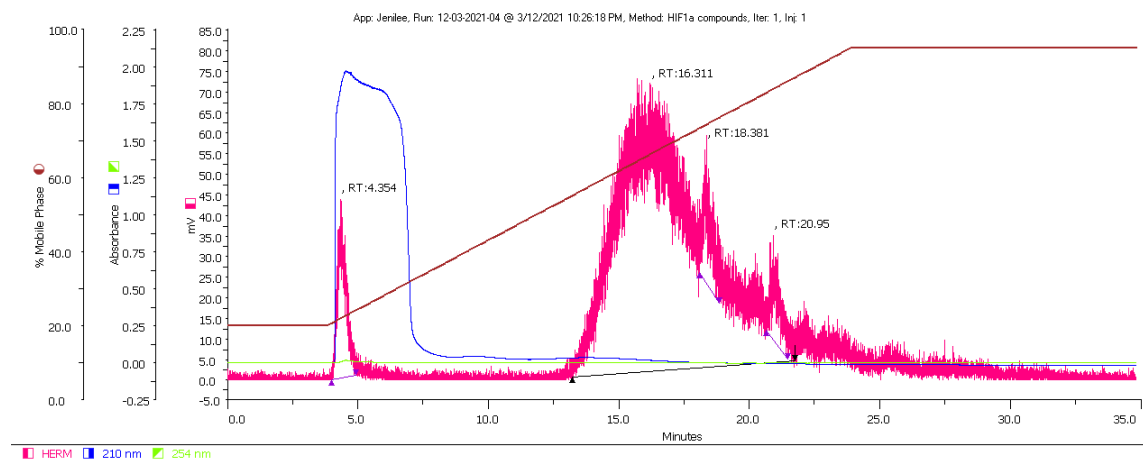


Figure 6.24. HPLC radiotracer for the impurity of [ $^{18}\text{F}$ ]FPA-Pd-8 at 15 minutes. Two UV channels are shown, including: 254 nm in green and 210 nm in blue. HERM radioactivity channel is shown in pink.

To further improve radiolabelling, [ $^{18}\text{F}$ ]FPeP4-34 was attempted in which  $\text{CH}_3\text{CN}$  was added to the above reaction mixture for [ $^{18}\text{F}$ ]FPeP4-30. [ $^{18}\text{F}$ ]FPeP4-34 lead to an increase in the yield up

to 10%, with the product of interest being able to be collected from HPLC at 18.6 minutes and co-injected with the cold reference compound **9**.

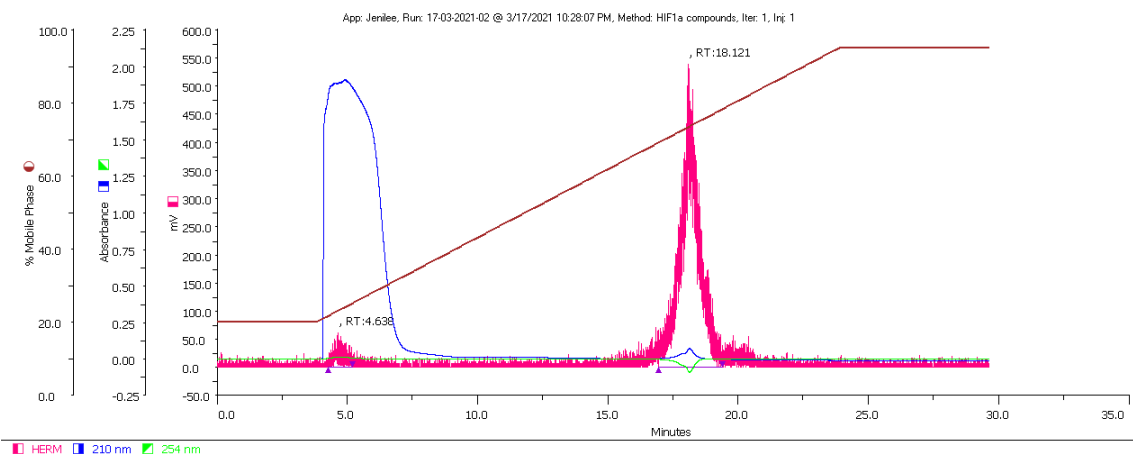


Figure 6.25. HPLC chromatogram for co-injection of  $[^{18}\text{F}]$ FPeP4 and compound **9**. Two UV channels are shown, including: 254 nm in green and 210 nm in blue. HERM radioactivity channel is shown in pink.

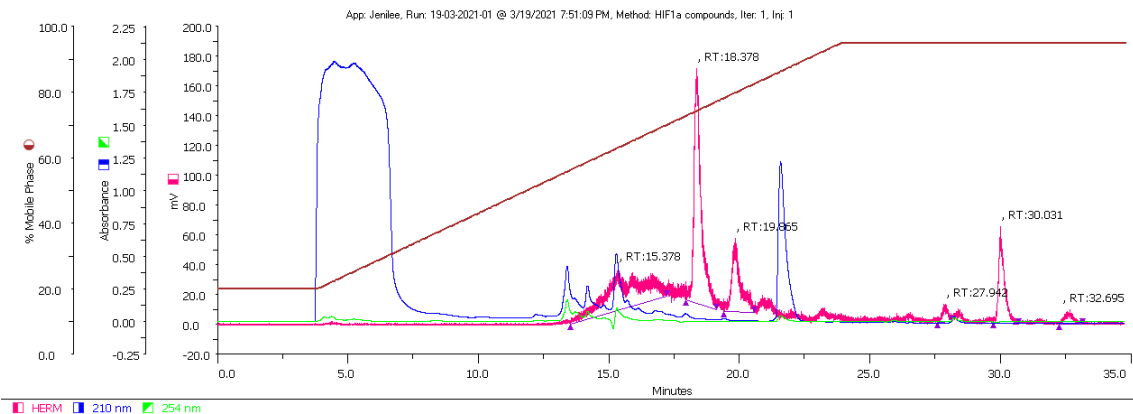


Figure 6.26. HPLC chromatogram for synthesis of  $[^{18}\text{F}]$ FPeP4 using  $\text{PdCl}_2(\text{PPh}_3)_2$ . Two UV channels are shown, including: 254 nm in green and 210 nm in blue. HERM radioactivity channel is shown in pink.

Lastly, manual testing sought to change the catalyst from  $\text{Pd}(\text{OAc})_2$  to  $\text{PdCl}_2(\text{PPh}_3)_2$ . Here  $[^{18}\text{F}]$ FPeP4-35 using 2.3 mg of compound **8**, 1.4 mg of  $\text{PdCl}_2(\text{PPh}_3)_2$ , 300 mL  $\text{CH}_3\text{CN}$ , 200 mL TEA, with 500 mL of  $[^{18}\text{F}]$ FPA in DMF. The reaction was heated in a sealed glass reactor at 140

°C for 45 minutes, giving a 20% recovered yield from HPLC, with the product peak eluting off HPLC at 18.4 minutes.

These parameters were then taken to a fully automated synthesis, performed on a GE TRACERlab™ FX automated synthesis unit (ASU). [<sup>18</sup>F]fluoride was firstly trapped on a Waters SepPak® light QMA cartridge and resolubilized using 86% Kryptofix® 2.2.2 (K<sub>222</sub>) solution (1.5 mL) containing both K<sub>222</sub> and potassium carbonate (K<sub>2</sub>CO<sub>3</sub>). [<sup>18</sup>F]fluoride/kryptofix complex was then dried azeotropically under vacuum and a steady stream of nitrogen at 50 °C and 85 °C. To the dried [<sup>18</sup>F]fluoride, 4-acetylene-*N,N,N*-trimethyl benzyl ammonium trifluoromethyl sulfonate (12 mg) in DMF (1 mL) was added and reacted for 25 minutes at 150 °C. Once the reaction was completed and thoroughly cooled to 25 °C, the reaction was diluted with water (12 mL) and passed through a Waters SepPak tC18 plus cartridge. This cartridge was then eluted with DMF (2 mL) into a second reactor already containing *N*-(4-iodophenyl)-4-((4-(pyridine-3-ylmethyl)piperazin-1-yl)methyl) benzamide (10 mg), PdCl<sub>2</sub>(PPh<sub>3</sub>)<sub>2</sub> (2 mg), CH<sub>3</sub>CN (500 mL) and triethylamine (1.5 mL). Reactor 2 mixture was then reacted at 140 °C for 45 minutes. Upon full cooling of the reactor to 40 °C, the reaction mixture was transferred into a product vial and purified without dilution before HPLC injection.

For HPLC injection, the ASU mixture (1 mL) was diluted with 0.2% TFA in water (1 mL) to inject 2 mL of volume. Purification was done with a Phenomenex LUNA® C18(2) Omega column with an isocratic elution with 40:60 CH<sub>3</sub>CN:(0.2% TFA in water). The product with a retention time of 18.5 minutes was collected and the eluent was removed using rotary evaporation. The radiolabeled small molecule was then reconstituted with ethanol and diluted with buffer to a concentration of 7% EtOH in a buffer. Overall achieving a 5 ± 2% decay corrected recovered radiochemical yield from [<sup>18</sup>F]fluoride (n=5) with a purity >99%.

It should be noted that the retention time of the compound on HPLC will change drastically, depending on the pH of the injection solution. Hence, it can be seen that the product of interest can shift between 16.2 to 18.6 minutes. Keeping the injection solution consistent at 50:50 Organic:0.2% TFA in water has led to a more consistent retention time at 18.5 minutes.

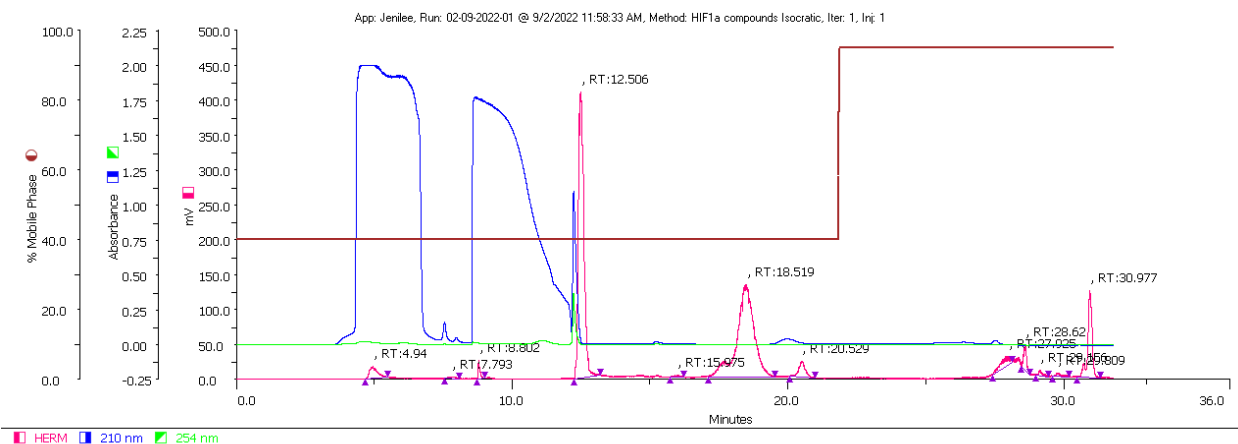


Figure 6.27. Crude purification of ASU synthesized  $[^{18}\text{F}]$ FPeP4. Two UV channels are shown, including: 254 nm in green and 210 nm in blue. HERM radioactivity channel is shown in pink.

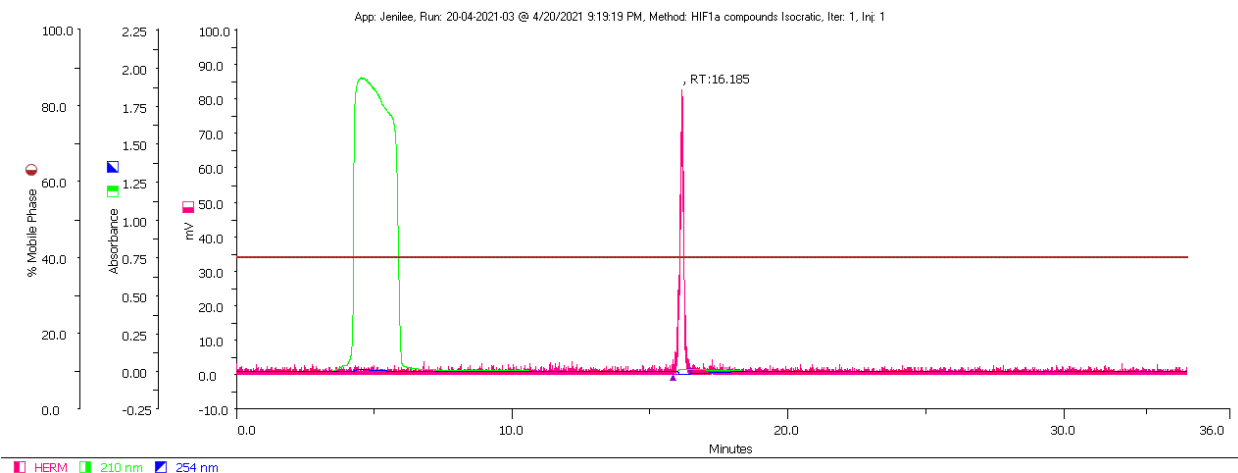


Figure 6.28. HPLC co-injection of  $[^{18}\text{F}]$ FPeP4 (HERM) and  $[^{19}\text{F}]$ compound **9**. Two UV channels are shown, including: 254 nm in green and 210 nm in blue. HERM radioactivity channel is shown in pink.

A major challenge for radiosynthesis of  $[^{18}\text{F}]$ FPeP4 on the ASU was the highly volatile nature of  $[^{18}\text{F}]$ FPA, which led to substantial losses of  $[^{18}\text{F}]$ FPA and subsequent low overall radiochemical yield. The formation of product  $[^{18}\text{F}]$ FPeP4 was confirmed by co-injection of reference compound *N*-(4-(1-ethynyl-4-fluorophenyl)phenyl)-4-((4-(pyridine-3-ylmethyl)piperazin-1-yl)-methyl)benzamide **9**.

## 6.5 Molar activity calculations for HIF-1 $\alpha$ targeting compound

### 6.5.1 Molar activity of [ $^{18}\text{F}$ ]SFB-link-c-(Ppg)LLFVY

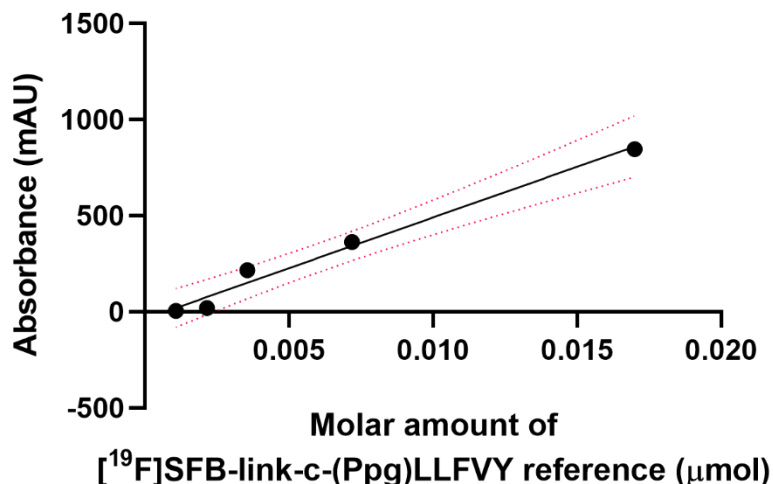


Figure 6.29. Molar activity curve for [ $^{19}\text{F}$ ]SFB-link-c-(Ppg)LLFVY non-radioactive reference.

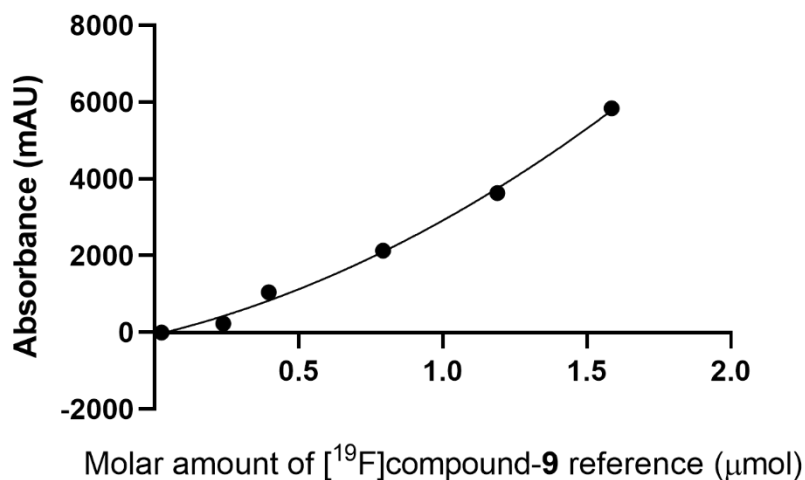
Various amounts of [ $^{19}\text{F}$ ]SFB-link-c-(Ppg)LLFVY (1 to 20  $\mu\text{g}$ ) were solubilized into 10% DMSO in 50:50  $\text{CH}_3\text{CN}$ :0.2% TFA in water (1000  $\mu\text{L}$ ) and then injected onto the HPLC using the Cu\_peptides HPLC method (see **section 2.1.1.4.**). The area under the curve for the 210 nm wavelength channel was computed and a molar activity curve was created as seen in *Figure 6.29*. Using quality control injections for [ $^{18}\text{F}$ ]SFB-link-c-(Ppg)LLFVY (JDW01121) synthesis runs, a known amount of radioactivity is correlated to the absorbance under the UV peak in the 210 nm channel.

Table 6.9. Molar activity calculations from the synthesis of [ $^{18}\text{F}$ ]SFB-link-c-(Ppg)LLFVY using the formula of  $(\text{Absorbance}-37.064)/52758=\text{molar amount}$ .

JDW01121 Synthesis ID	Absorbance (mAU)	Calculated molar amount ( $\mu\text{mol}$ )	Injected activity (GBq)	Calculated specific activity (GBq/ $\mu\text{mol}$ )
JDW01121-05	43.7764	0.001532287	0.0120	7.831
JDW01121-06	0	0.000702529	0.3000	427.029
JDW01121-08	0	0.000702529	0.0162	23.060
JDW01121-09	0	0.000702529	0.1000	142.343
JDW01121-10	0	0.000702529	0.0500	71.171

When the absorbance seen in *Table 6.9.* was shown to be 0, the calculated molar amount was assumed to be 0.7 nmol, which is the limit of the UV detector for [<sup>19</sup>F]SFB-link-c-(Ppg)LLFVY. Overall, we found a molar activity of between 8 to 425 GBq/μmol (n=5), with calculations seen in *Table 6.9.* These values are all strictly dependent on the injected activity amount which in the highest case was only 300 MBq, and yielded the highest molar activity of 427 GBq/μmol.

### 6.5.2 Molar activity of [<sup>18</sup>F]FPeP4



*Figure 6.30. Molar activity curve for [<sup>19</sup>F]compound 9 non-radioactive reference for [<sup>18</sup>F]FPeP4.*

*Table 6.10. Molar activity calculations from the synthesis of [<sup>18</sup>F]FPeP4 using the formula of “Absorbance=1202.6x<sup>2</sup>+1779.3x-66.195”, where x=molar amount. Polynomial equation was solved in Excel using goal seek.*

FPeP4 Synthesis ID	Absorbance (mAU)	Calculated molar amount (μmol)	Injected activity (GBq)	Calculated molar activity (GBq/umol)
FPeP4-51	9.9079	0.041601516	0.0387	0.930
FPeP4-52	17.483	0.045621854	0.0324	0.710
FPeP4-54	663.8178	0.334607813	0.1694	0.506
FPeP4-55	0	0.036311655	0.03	0.826
FPeP4-66	0	0.036311655	0.00441	0.121

Various amounts of [ $^{19}\text{F}$ ]compound **9** (120 to 800  $\mu\text{g}$ ) were solubilized into DMF (500  $\mu\text{L}$ ) and then injected onto the HPLC using the HIF-1 $\alpha$  compounds isocratic HPLC method. The area under the curve for the 254 nm wavelength channel was computed and a molar activity curve was created as seen in *Figure 6.30*. Using quality control injections for [ $^{18}\text{F}$ ]FPeP4 synthesis runs, a known amount of radioactivity is correlated to the absorbance under the UV peak in the 254 nm channel.

Overall, yielding a molar activity maximum of 1 GBq/ $\mu\text{mol}$  ( $n=5$ ), with calculations seen in *Table 6.10*. This is a very low molar activity and is limited by the amount of injected radioactivity in the quality control. Due to the low yield of the synthesis, this could not be better elucidated.

#### 6.6 LogD calculations for HIF-1 $\alpha$ targeting compound [ $^{18}\text{F}$ ]FPeP4

Small molecule inhibitor [ $^{18}\text{F}$ ]FPeP4 was prepared in a stock solution of 3.97 MBq in 900  $\mu\text{L}$  0.2% TFA in water. pH curve was created using 1 M acetic acid and 1M NaOH, to achieve the following pH values: 1.50, 4.16, 5.0, 6.14, 7.5, 8.73, 11.29, and 12.82. An aqueous solution (500  $\mu\text{L}$ ) is then combined in a Lobind Eppendorf tube (1.5 mL) with octanol (500  $\mu\text{L}$ ) and 20  $\mu\text{L}$  of the radiotracer stock solution. Reactions are vigorously mixed and allowed to stand for 5 minutes, before sample removal. Removed from each layer is 50  $\mu\text{L}$  three times, into labelled microcentrifuge tubes. Samples are compounded on a HIDEX gamma counter and plotted as seen below in *Figure 6.31*.

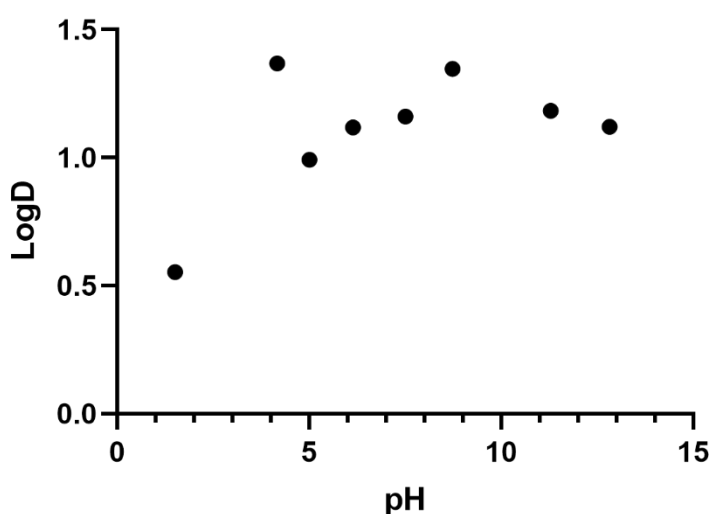


*Figure 6.31. LogD curve for [ $^{18}\text{F}$ ]FPeP4 at various pH points.*

Overall, from pH 4 to 12, [<sup>18</sup>F]FPeP4 has a LogP value of  $1.18 \pm 0.13$  (n=7). In very acidic conditions the LogD drops to 0.55, showing increased solubility in acidic aqueous solvents.

#### *6.7 Summary for radiolabelling of HIF-1 $\alpha$ targeting compounds*

Radiolabelling of lead peptide [<sup>18</sup>F]SFB-link-c-(Ppg)LLFVY was achieved in a  $66 \pm 5\%$  radiochemical yield using readily available prosthetic [<sup>18</sup>F]SFB. [<sup>18</sup>F]SFB-link-c-(Ppg)LLFVY had a maximum molar activity of 425 GBq/ $\mu$ mol on a 300 MBq quality control injection. Small molecule inhibitor [<sup>18</sup>F]FPeP4 was radiolabelled in radiochemical yields of  $5 \pm 2\%$  using a Sonogashira cross-coupling reaction with [<sup>18</sup>F]FPA. [<sup>18</sup>F]FPeP4 had a maximum molar activity of 1 GBq/ $\mu$ mol on a 40 MBq quality control injection. Both radiotracers will be tested for PET imaging of HIF-1 $\alpha$  in cancer models.

## **Chapter 7: HIF-1 $\alpha$ in TNBC cell lines and *in vitro* analysis**

Previous work completed by the Wuest research group, has used breast cancer cell lines: EMT6, MDA-MB-231 and MCF7, to investigate the effect of hypoxia on lysyl oxidase (LOX) enzymes. This work was completed using a LOX targeting radiopeptide [ $^{18}\text{F}$ ]FB-GGGDPKGGGGG-NH<sub>2</sub> [127]. During this work, EMT6 were analyzed for HIF-1 $\alpha$  expression and thus became our starting cell line model for our HIF-1 $\alpha$  binding compound.

### *7.1 Western blot analysis of HIF-1 $\alpha$ expression in EMT6 cells*

EMT6 cells were cultured in single well plates (7 plates) for 24 hours before hypoxia treatment. After adhering to the plates for 24 hours, the cells were subjected to various time points of hypoxia in reverse order (24, 10, 8, 6, 4, and 2 hours), as well as one normoxic blank for 24 hours. Upon completion of the treatments, plates were put on ice and lysed using RIPA buffer (100  $\mu\text{L}$ ) containing protease inhibitors (1  $\mu\text{L}$ ). From the determined protein content, 50  $\mu\text{g}$  of protein was loaded per well into the designated wells. The western blot was completed as per section 2.7.2., with the exception of nitrocellulose membrane (BioRad Nitrocellulose membrane 0.45  $\mu\text{M}$ , cat# 1620115) being used instead of PVDF.

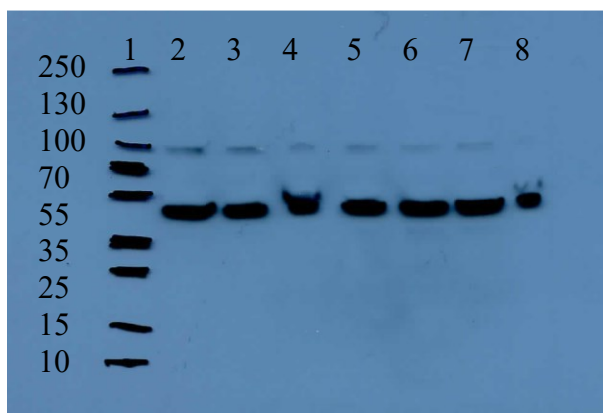


*Figure 7.1. Western blot of EMT6 cells for the expression of HIF-1 $\alpha$  (100 kDa band) under normoxic and hypoxic conditions over time with B-actin staining (42 kDa band). Lane 1 was protein ladder, lane 2 – 24 hrs hypoxia, lane 3 – 10 hrs hypoxia, lane 4 – 8 hrs hypoxia, lane 5 – 6 hrs hypoxia, lane 6 – 4 hrs hypoxia, lane 7 – 2 hrs hypoxia, lane 8 – 24 hrs normoxia.*

Specific antibodies and dilution used included, the primary HIF-1 $\alpha$  (28b) antibody (sc-13515) (12  $\mu$ L) was allowed to incubate on the blot in 5% milk solution with TBST (6 mL) overnight at 4°C. Secondary Goat anti-mouse IgG-HRP antibody (sc-2005) (1  $\mu$ L) was allowed to incubate on the blot in 5% milk solution with TBS-T (5 mL) for one hour. The blot was wrapped in saran film and 1 mL of BioRad clarity Western ECL substrate (cat # 170-5060) was added and allowed to sit for 5 minutes before film exposure. The film was exposed to the blot at the required time points and the film was processed using a film processing machine.

The obtained western blot gel was then stained for B-actin with a primary antibody of Anti-actin (20-33) rabbit antibody (Sigma A5060) and a secondary antibody of Anti-rabbit IgG (whole molecule)-peroxidase goat antibody (Sigma A0545). It should be noted that the actin blot was developed using Thermofisher Pico-Supersignal West PICO Chemiluminescent substrate (Prod #34080) instead of BioRad clarity Western ECL substrate.

Overall in EMT6 cells, we found that at 24 hours of hypoxia (1% O<sub>2</sub>), there was maximal HIF-1 $\alpha$  expression. This overexpression was roughly equal to the expression at 10 hours, yet the feasibility of the 10-hour time point in regards to radioactive cell uptake experiments excluded it from future use.

### *7.2 In vitro analysis of HIF-1 $\alpha$ targeting compounds in EMT6 cells*

EMT6 cells were plated onto 12 well plates as per **section 2.7.5**. There was no glycine wash in all these EMT6 cell experiments, all radioactivity reported is internalized and cell surface-bound. [<sup>68</sup>Ga]NOTA-Bn-SCN-link-c-(Ppg)LLFVY was prepared as per **section 4.2.1**. The initial experiment, JDW-EMT6-316-1, completed a full-time course experiment and it was found that the maximal uptake at 120 minutes was 5.0% applied radioactivity/mg protein corrected to 1-minute background uptake.

Continued testing of [<sup>68</sup>Ga]NOTA-Bn-SCN-link-c-(Ppg)LLFVY was completed in full-time course experiments (1, 5, 15, 30, 60, 90, and 120 minutes) under both normoxic and hypoxic conditions (n=5). Hypoxic 12 well plates were incubated in 1% CO<sub>2</sub> for 24 hours. Upon analysis of radioactive lysates, it was found that at 60 minutes there was an almost two-fold increased

uptake of the [ $^{68}\text{Ga}$ ]NOTA-Bn-SCN-link-c-(Ppg)LLFVY in hypoxic conditions versus normoxic conditions (see *Figure 7.2*).

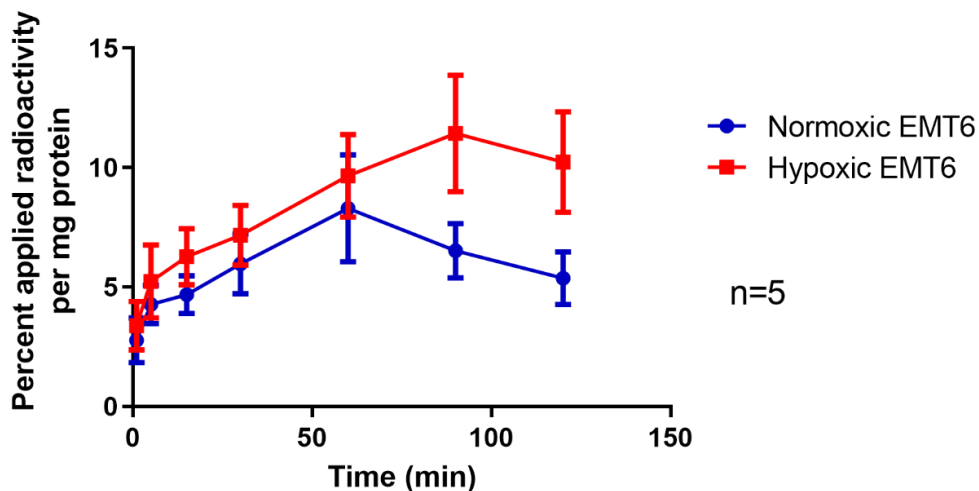


*Figure 7.2. Cell uptake of [ $^{68}\text{Ga}$ ]NOTA-Bn-SCN-link-c-(Ppg)LLFVY in EMT6 cells under both hypoxic and normoxic conditions (n=5). \*\*Upon completion of these experiments, it was found that the analyzed compound was likely [ $^{68}\text{Ga}$ ]NOTA-Bn-SCN not [ $^{68}\text{Ga}$ ]NOTA-Bn-SCN-link-c-(Ppg)LLFVY.*

Although, [ $^{68}\text{Ga}$ ]NOTA-Bn-SCN-link-c-(Ppg)LLFVY (see *Figure 7.2*. \*\*note) showed initial promise as a HIF-1 $\alpha$  targeting radiotracer, after extensive studies, it was found that the SCN-linkage in the NOTA-peptide was not stable after radiolabelling. The degraded radiotracer would simply become [ $^{68}\text{Ga}$ ]NOTA-Bn-SCN and link-c-(Ppg)LLFVY. Thus testing was also completed with just [ $^{68}\text{Ga}$ ]NOTA-Bn-SCN to determine if the link-c-(Ppg)LLFVY had any impact on the cellular uptake in both hypoxic and normoxic conditions. Using [ $^{68}\text{Ga}$ ]NOTA-Bn-SCN alone appeared to mimic the uptake pattern witnessed from the whole peptide (*Figure 7.3*). Thus it was determined that this unstable linkage could not be used for further assays, as the [ $^{68}\text{Ga}$ ]NOTA-Bn-SCN alone could be fully responsible for the uptake pattern seen in EMT6 cells.

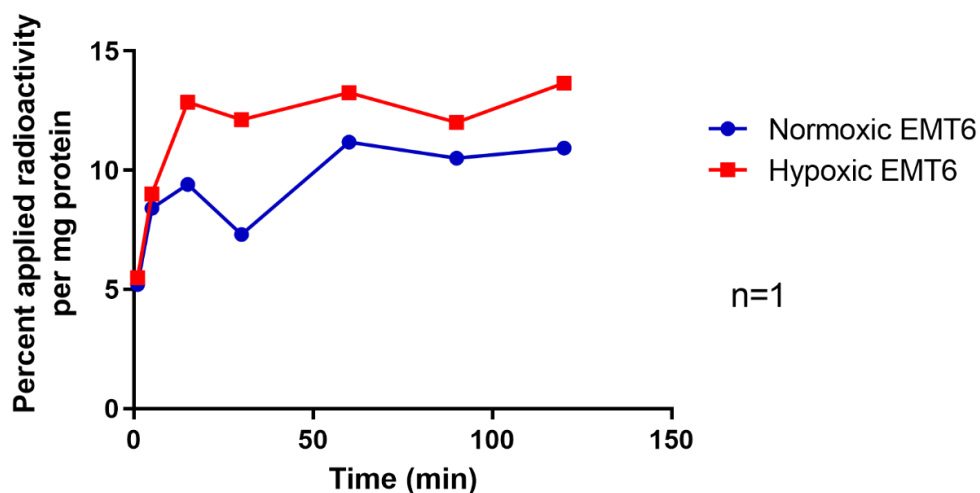


Figure 7.3. Cell uptake of  $[^{68}\text{Ga}]\text{NOTA-Bn-SCN}$  in EMT6 cells under both hypoxic and normoxic conditions ( $n=1$ ).

Another novel HIF-1 $\alpha$  targeting peptide was then tested in cell uptakes in EMT6 cells,  $[^{68}\text{Ga}]\text{DOTA-link-c-(Ppg)LLFVY}$  (section 6.2.2). Here the uptake in both normoxic and hypoxic conditions strongly mimicked that seen by all the other gallium-chelator-containing compounds (including both  $[^{68}\text{Ga}]\text{NOTA-Bn-SCN}$  and  $[^{68}\text{Ga}]\text{NOTA-Bn-SCN-link-c-(Ppg)LLFVY}$ ).

With an average uptake of  $\sim 12\%$  applied radioactivity per mg protein in hypoxic cells and an average uptake of  $\sim 6\%$  applied radioactivity per mg protein in normoxia at 120 minutes. ( $n=4$ ). Even combining all the gallium-chelated HIF-1 $\alpha$  targeted peptides into one graph with  $[^{68}\text{Ga}]\text{NOTA-Bn-SCN}$ , showed a strong correlation over all the replicates ( $n=10$ ), see Figure 7.4. Thus, it was suggested that the chelator-free radiotracer (such as a radiotracer containing  $^{18}\text{F}$ -fluoride) may need to be developed and tested in place of the current radiotracers. Since it appears that the chelator itself is affecting the uptake and possibly the binding to HIF-1 $\alpha$ .

The radiotracer we designed without a chelator is  $[^{18}\text{F}]\text{SFB-link-c-(Ppg)LLFVY}$  (section 6.1).  $[^{18}\text{F}]\text{SFB-link-c-(Ppg)LLFVY}$  was first tested for the full-time curve (1, 5, 15, 30, 60, 90, and 120 minutes) in normoxic and hypoxic EMT6 cells (Figure 7.5). Here again, there was a very similar trend seen in the chelator containing peptide radiotracers.

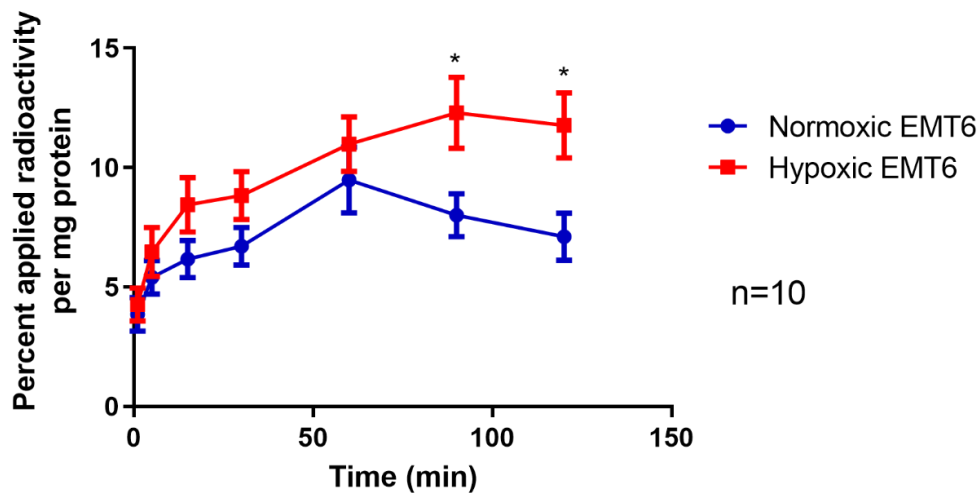


Figure 7.4. Combined cell uptake data of  $[^{68}\text{Ga}]\text{DOTA-link-c-(Ppg)LLFVY}$ ,  $[^{68}\text{Ga}]\text{NOTA-Bn-SCN}$  and  $[^{68}\text{Ga}]\text{NOTA-Bn-SCN-link-c-(Ppg)LLFVY}$  in EMT6 cells under both hypoxic and normoxic conditions ( $n=10$ ).

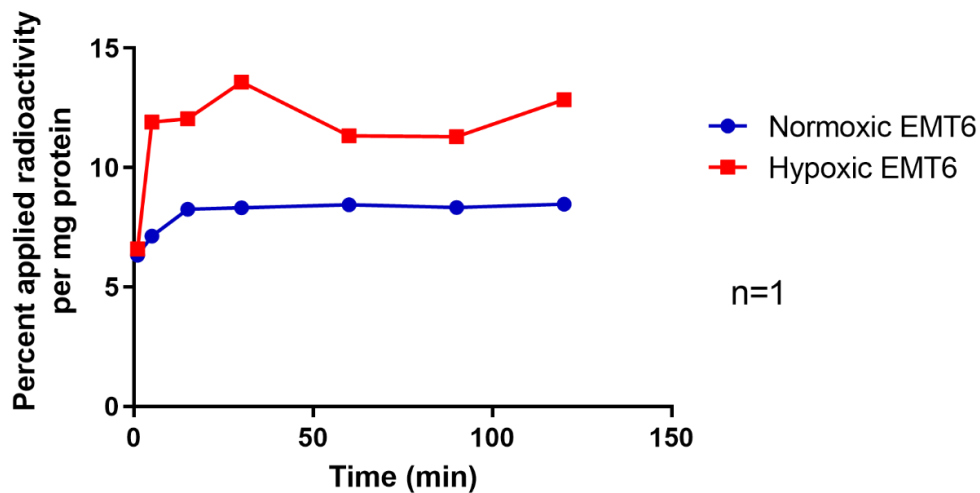
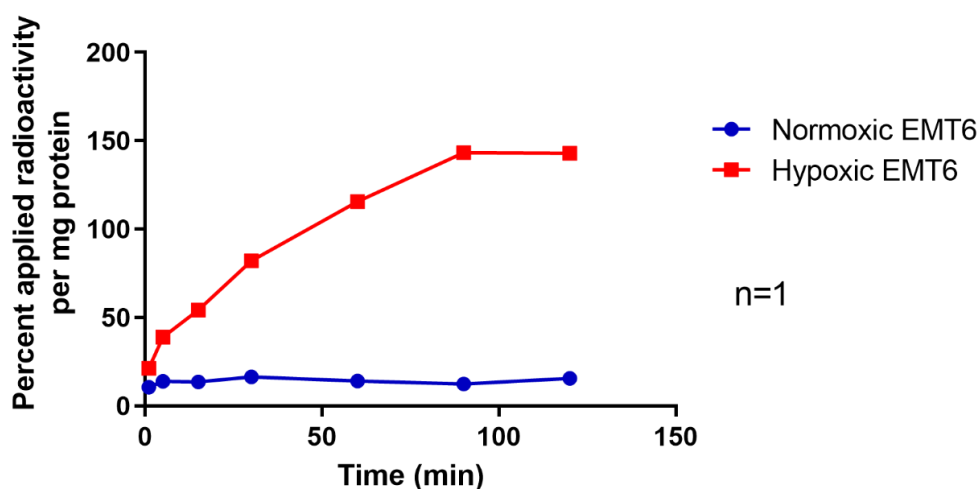


Figure 7.5. Cell uptake of  $[^{18}\text{F}]\text{SFB-link-c-(Ppg)LLFVY}$  in EMT6 cells under both hypoxic and normoxic conditions ( $n=1$ ).

Therefore, the differences in normoxic/hypoxic cell uptake that we are seeing, might be due to the methodology of the cell uptake. Current cell uptake methodology involves a hypoxia cell uptake

chamber that is within an incubator. Anytime that the 12-well plate was required to be manipulated, it must be removed from the hypoxia chamber/incubator. Thus, because to the short biological half-life of HIF-1 $\alpha$ , we may simply be destroying all the build-up of any HIF-1 $\alpha$  created under the hypoxic conditions. Therefore, we aimed to look at some chemically induced HIF-1 $\alpha$  models using cobalt chloride (CoCl<sub>2</sub>).

The first concentration of CoCl<sub>2</sub> HIF-1 $\alpha$  induction was 100  $\mu$ M for 4 hours prior to radiotracer addition. Here there was an extremely large uptake of [<sup>18</sup>F]SFB-link-c-(Ppg)LLFVY in CoCl<sub>2</sub> hypoxia. Maximal uptake went up to 143% applied radioactivity/mg protein at 90 minutes, whereas the uptake in normoxic cells was maximal at 16% applied radioactivity/mg protein (see *Figure 7.6*).



*Figure 7.6. Cell uptake of [<sup>18</sup>F]SFB-link-c-(Ppg)LLFVY in EMT6 cells under both hypoxic (100  $\mu$ M CoCl<sub>2</sub>, 4 hours) and normoxic conditions (n=1).*

Although this difference in *Figure 7.6* is large between normoxic and hypoxic cells, the amount of cells killed due to the CoCl<sub>2</sub> treatment was determined to be approximately 66%. Due to this, we decided to look at varying concentration of CoCl<sub>2</sub> treatment; to protect the % applied radioactivity/mg protein data from being skewed due to low protein content. The chosen various concentrations were 100  $\mu$ M, 1 mM, 30 mM, and 100 mM CoCl<sub>2</sub> treatment for 4 hours. For both

the 1 mM and 100  $\mu$ M treatment levels there was minimal impact on the protein content of the cells from the treatment (see *Figure 7.7.*).

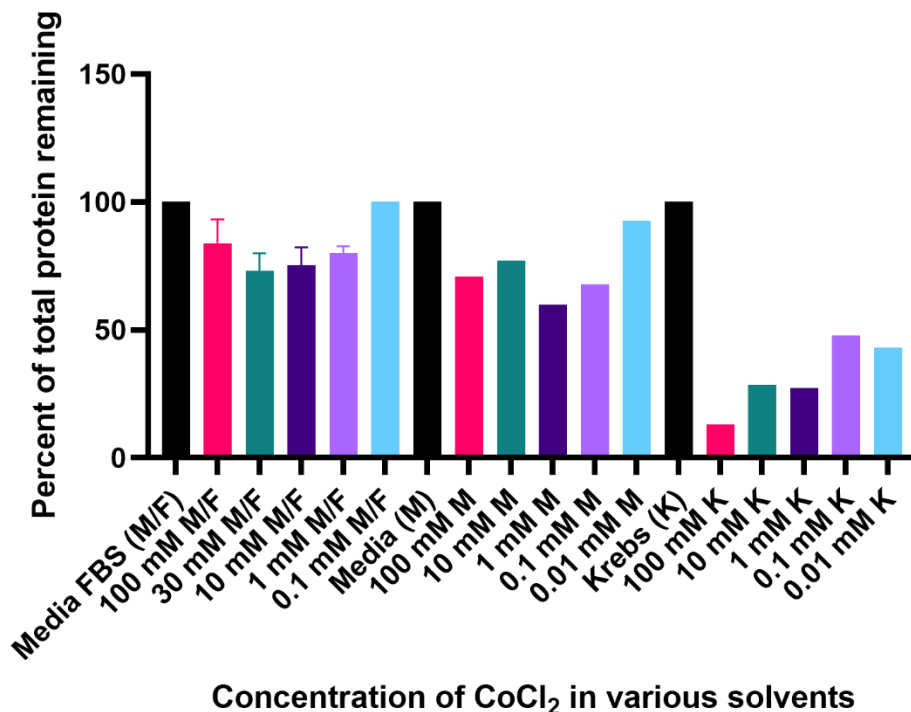


*Figure 7.7. Cytotoxicity of CoCl<sub>2</sub> treatment to EMT6 cells under various conditions for 2-hour incubation.*

Yet the 30 mM CoCl<sub>2</sub> treatment still reduced the protein content to 50% of the non-treated cells. To further understand the cytotoxic effects of CoCl<sub>2</sub> treatment on EMT6 cells, EMT6 cells were subjected to a variety of treatments for 2 hours, before determining the protein content of the wells.

Overall, all the CoCl<sub>2</sub> treatments in Krebs were very detrimental to the survival of the cells. Whereas, CoCl<sub>2</sub> treatment in media allowed for 80% of the cells to survive most of the treatment concentrations. In addition, the use of FBS with media had very little impact on the protein content of the cells compared to media without FBS.

Lastly, *in vitro* analysis of [<sup>18</sup>F]SFB-link-c-(Ppg)LLFVY cell uptake was completed in EMT6 cells, under both hypoxia and normoxia, as well as varying concentrations of CoCl<sub>2</sub> treatment (see

Figure 7.8.). Here we found that using 100  $\mu\text{M}$  of  $\text{CoCl}_2$  treatment in hypoxic cells produced a cell uptake of  $[^{18}\text{F}]\text{SFB-link-c-(Ppg)LLFVY}$   $\sim 25\%$  AR/mgP, compared to  $\sim 30\%$  AR/mgP in normoxia. Next, using 1 mM of  $\text{CoCl}_2$  treatment in hypoxic cells produced a cell uptake of  $[^{18}\text{F}]\text{SFB-link-c-(Ppg)LLFVY}$   $\sim 10\%$  AR/mgP, compared to  $\sim 5\%$  AR/mgP in normoxia. Lastly, using 30 mM of  $\text{CoCl}_2$  treatment in hypoxic cells produced a cell uptake of  $[^{18}\text{F}]\text{SFB-link-c-(Ppg)LLFVY}$   $\sim 45\%$  AR/mgP, compared to  $\sim 10\%$  AR/mgP in normoxia. Overall the cell uptake of  $[^{18}\text{F}]\text{SFB-link-c-(Ppg)LLFVY}$  was extremely variable depending on the concentration of  $\text{CoCl}_2$  treatment. Additionally, at both the 1 mM and 30 mM  $\text{CoCl}_2$  treatment levels, the cell uptake of  $[^{18}\text{F}]\text{SFB-link-c-(Ppg)LLFVY}$  was greater in hypoxic conditions compared to normoxic conditions.

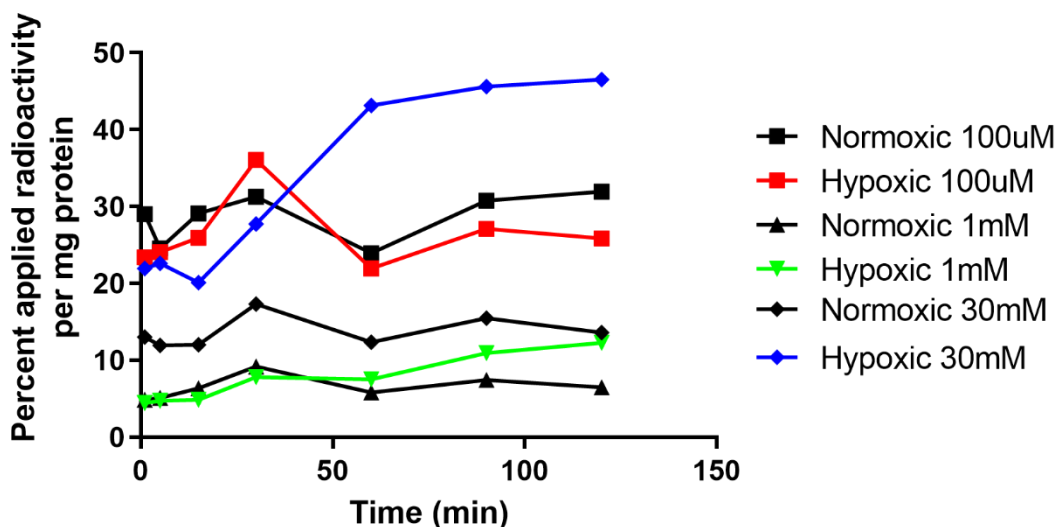


Figure 7.8. Cell uptake of  $[^{18}\text{F}]\text{SFB-link-c-(Ppg)LLFVY}$  in EMT6 cells under various hypoxic and normoxic conditions ( $n=1$ ). Concentrations listed are for  $\text{CoCl}_2$ .

Upon completion of these experiments, it was decided to switch the experimental model from the murine breast cancer cell line to a human triple-negative breast cancer cell line of MDA-MB-231. This was done to match the cell line used for the *in vitro* analysis of the 2-nitroimidazole compounds. Thus, we began our experimentation using a HIF-1 $\alpha$  transfection in MDA-MB-231 cells.

### 7.3 Western blot and PET radiotracer analysis of the HIF-1 $\alpha$ transfected cell lines

MDA-MB-231 cells were transfected as per **section 2.7.7**. Three cell lines were created, labelled as MDA-MB-231 18955, MDA-MB-231 18949, and MDA-MB-231 GFP. Where GFP was a blank transfection of the MDA-MB-231 cells, 18949 was an overexpression of a natural HIF-1 $\alpha$  protein and 18955 was an overexpression of an unnatural HIF-1 $\alpha$ , in which proline 402 and proline 564 have both been changed to alanine.

#### 7.3.1 Western blot of transfected MDA-MB-231 cell lines

The primary analysis of these novel cell lines included western blot expression levels of the HIF-1 $\alpha$  protein. For this data analysis, the three cell lines will be designated as follows: 18949 (MDA-MB-231 18949), 18955 (MDA-MB-231 18955), and GFP (MDA-MB-231 GFP). When lysates were prepared, they were prepared with RIPA buffer containing 1 mM CoCl<sub>2</sub> and 0.2% protease inhibitor. Cell lysate samples were loaded between 20 to 50  $\mu$ g per well. SDS-PAGE gels were blotted onto nitrocellulose membranes for two hours at 200 mA. Membranes were blocked with Pierce Clear Milk Blocking Buffer for 1 hour at ambient temperature. Primary HIF-1 $\alpha$  antibody (Novus Biologicals, NB100-449) was used at the concentration of 1:1000 in a special blocking solution, overnight at 4 °C. Secondary Goat anti-mouse AlexaFluor 680 (Invitrogen, A21057), 1:10,000 dilution in special blocking solution was incubated for 1 hour at ambient temperature. Membranes were analyzed on the Odyssey scanner and the band intensity for HIF-1 $\alpha$  and B-actin was quantified to determine the overexpression of HIF-1 $\alpha$  in the transfected cell lines (see *Table 7.1*).

For the calculation of overexpression, the amount of HIF-1 $\alpha$  in the GFP cell line was set as the baseline and all other values are compared to that standard expression. Overall, 18949 cell lines are found to have the highest overexpression of HIF-1 $\alpha$  compared to GFP cell line of  $90.3 \pm 50.6\%$ . Next, the 18955 cell line has an overexpression of HIF-1 $\alpha$  compared to GFP cell line of  $36.5 \pm 21.9\%$ .

Table 7.1. Western blot intensity analysis for HIF-1 $\alpha$  and B-Actin in 18955, 18949 and GFP cell lines (n=3).

Replicate	1	2	3	1	2	3	1	2	3
Cell line	GFP	GFP	GFP	18949	18949	18494	18955	18955	18955
HIF-1 $\alpha$ Band Intensity	2115	1663	2583	4721	5453	5010	2252	2737	3653
B-Actin Band Intensity	13099	9525	9010	10917	9995	9825	9893	10396	10016
Corrected HIF-1 $\alpha$ amount	2115	2117	3389	5508	6745	6261	2803	3302	4512
Percent of GFP				116.8	165.5	146.5	10.3	30.0	77.6
HIF-1 $\alpha$ Band Intensity	2589	2684	2868	4679	4526	5298	4253	4463	4957
B-Actin Band Intensity	21280	17214	13431	19443	12456	20825	21363	21344	21947
Corrected HIF-1 $\alpha$ amount	2589	3197	3926	5083	6402	5411	4236	4450	4802
Percent of GFP				57.0	97.8	67.2	30.9	37.5	48.3
HIF-1 $\alpha$ Band Intensity	3381	4478	3866	5559	6270	8142	4875	4954	3804
B-Actin Band Intensity	148629	134971	133290	178729	151305	138566	120517	108238	127005
Corrected HIF-1 $\alpha$ amount	3381	4890	4265	4433	6157	8694	5798	6301	4357
Percent of GFP				6.1	47.4	108.1	38.8	50.8	4.3
Percent Overexpression				90.3			36.5		
Standard deviation				50.6			21.9		

7.3.2 *In vitro* analysis of PET radiotracers in transfected MDA-MB-231 cell lines

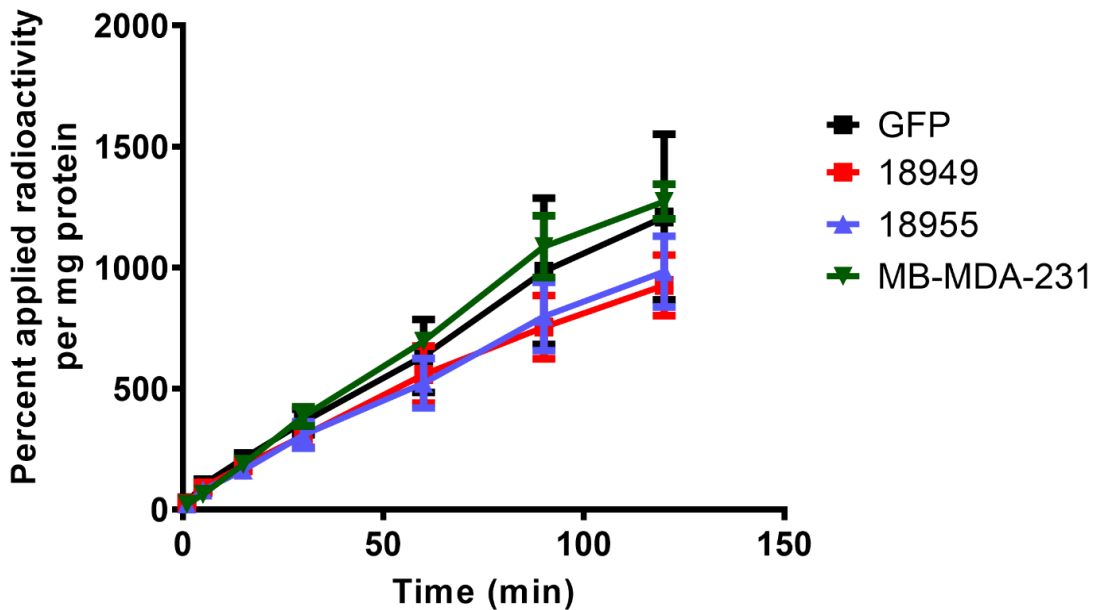
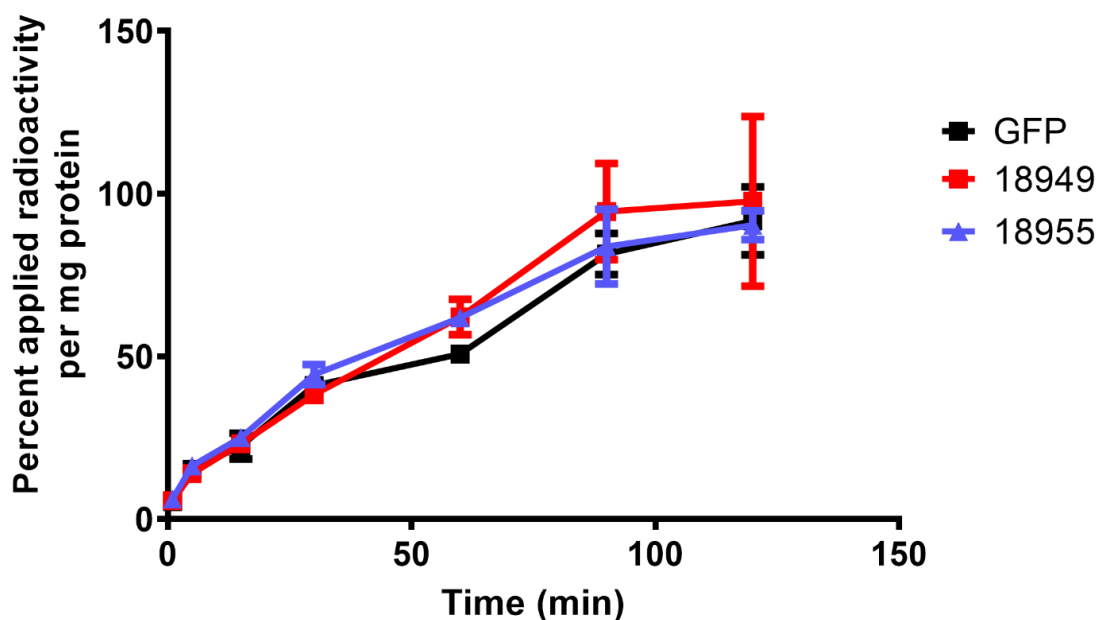


Figure 7.9. [ $^{18}\text{F}$ ]FDG cell uptake in transfected and natural MDA-MB-231 cells. Including MDA-MB-231 GFP cells, MDA-MB-231 18949 cells, MDA-MB-231 18955 cells and non-transfected MDA-MB-231 control (n=3).

Transfected MDA-MB-231 cells were plated at 75,000 cells per well into 12 well plates as per **section 2.7.5**. [ $^{18}\text{F}$ ]FDG, [ $^{18}\text{F}$ ]FLT and [ $^{18}\text{F}$ ]FAZA were obtained from the Edmonton Radiopharmaceutical Center (ERC) and produced onsite.

Transfected cell lines were initially tested using the radiotracers of [ $^{18}\text{F}$ ]FDG, [ $^{18}\text{F}$ ]FLT and [ $^{18}\text{F}$ ]FAZA. Using [ $^{18}\text{F}$ ]FDG (see *Figure 7.9*), both the natural MDA-MB-231 cells and the MDA-MB-231 GFP cell lines had a very similar high glucose metabolism of 1100% applied radioactivity/mg protein at 120 minutes. Compared to both MDA-MB-231 18955 and MDA-MB-231 18949 which has a slightly lower glucose metabolism at 120 minutes of 750% applied radioactivity/mg protein. This was slightly contrary to logic, as one would expect an overexpression of HIF-1 $\alpha$  to cause overexpression of Glut1; thus leading to an increased glucose uptake of [ $^{18}\text{F}$ ]FDG.



*Figure 7.10. [ $^{18}\text{F}$ ]FLT cell uptake in transfected MDA-MB-231 cells. Including MDA-MB-231 GFP control cells, MDA-MB-231 18949 cells, and MDA-MB-231 18955 cells ( $n=3$ ).*

Yet the upregulation of these pathways was not enough to overcome the deleterious effects of a HIF-1 $\alpha$  transfection. Changing the natural amount of HIF-1 $\alpha$  in the MDA-MB-231 cells causes

the cells to grow notably slower in culture. Using [ $^{18}\text{F}$ ]FLT (see *Figure 7.10*), all cell lines had a very similar uptake, suggesting that all the cell lines proliferate at similar rates. Maximal uptake at 120 minutes was approximately 80% applied radioactivity/mg protein. Thus, these results taken in combination with the [ $^{18}\text{F}$ ]FDG uptake, suggesting that the upregulation of HIF-1 $\alpha$  does not affect the proliferative capacity of the cells, but does affect their glucose metabolism.

Finally with [ $^{18}\text{F}$ ]FAZA (see *Figure 7.11.*), again all cell lines had a very similar uptake, suggesting that none of the cell lines are under hypoxia. Maximal uptake at 60 minutes was approximately 3.5% applied radioactivity/mg protein. Overall, this shows that although the transfected cells are overexpressing HIF-1 $\alpha$ , they are not a hypoxic environment allowing for the increased uptake of a 2-nitroimidazole radiotracer.

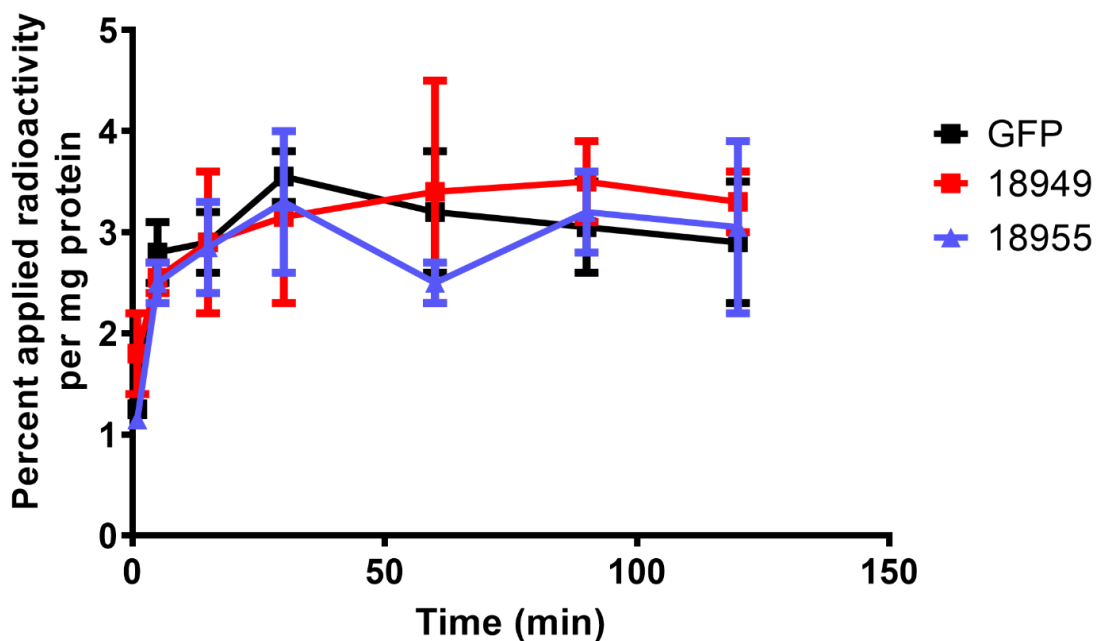


*Figure 7.11. [ $^{18}\text{F}$ ]FAZA cell uptake in transfected MDA-MB-231 cells. Including MDA-MB-231 GFP control cells, MDA-MB-231 18949 cells, and MDA-MB-231 18955 cells (n=2).*

#### 7.4 *In vitro* analysis of HIF-1 $\alpha$ targetting compounds in transfected MDA-MB-231 cells

Transfected MDA-MB-231 cells were plated at 75,000 cells per well into 12 well plates as per **section 2.7.5**. There was no glycine wash in all these beginning experiments, all radioactivity reported is internalized and cell surface-bound. Glycine-HCl washes will be used in certain experiments and will be stated to have been completed. [ $^{18}\text{F}$ ]SFB-link-c-(Ppg)LLFVY was prepared as per **section 6.1**.

Initial cell uptake with [ $^{18}\text{F}$ ]SFB-link-c-(Ppg)LLFVY (n=5) was completed without glycine wash. Thus a large amount of radioactivity was even initially bound to the cells at the 1-minute time point. There was a strong trend that the overall amount of radioactivity bound to the cells was higher in the HIF-1 $\alpha$  overexpressing cell lines. Yet this trend was not always obvious at all time points in the cellular uptake. Looking at the 60-minute time point alone, the average cell uptake in 18955 cells was 71.5% applied radioactivity/mg protein. Compared to the GFP cell line at 54.4% applied radioactivity/mg protein, this difference is statistically significant as seen in *Figure 7.13*.

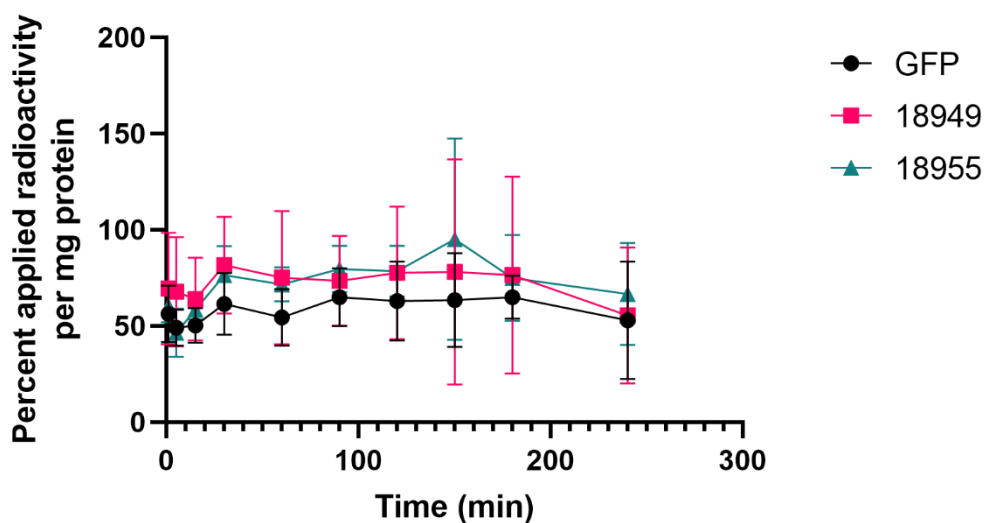


*Figure 7.12.* [ $^{18}\text{F}$ ]SFB-link-c-(Ppg)LLFVY cell uptake in transfected MDA-MB-231 cells. Including MDA-MB-231 GFP control cells, MDA-MB-231 18949 cells, and MDA-MB-231 18955 cells (n=5).

Although we were able to see some increased uptake in the HIF-1 $\alpha$  transfected cells for the radiotracer of [ $^{18}\text{F}$ ]SFB-link-c-(Ppg)LLFVY, the differences seen had large variability, especially in the 18949 cell line. The variable maybe caused by the overexpressed HIF-1a not being stabilized in the normoxic cellular environment. Whereas, the mutant-HIF-1a in the 18955 is not degraded in the normoxic cellular environment. Additionally, glycine-HCl washes were completed in the next sets of experiments to elucidate the amount of internalized radioactivity of [ $^{18}\text{F}$ ]SFB-link-c-(Ppg)LLFVY in the transfected cell lines.

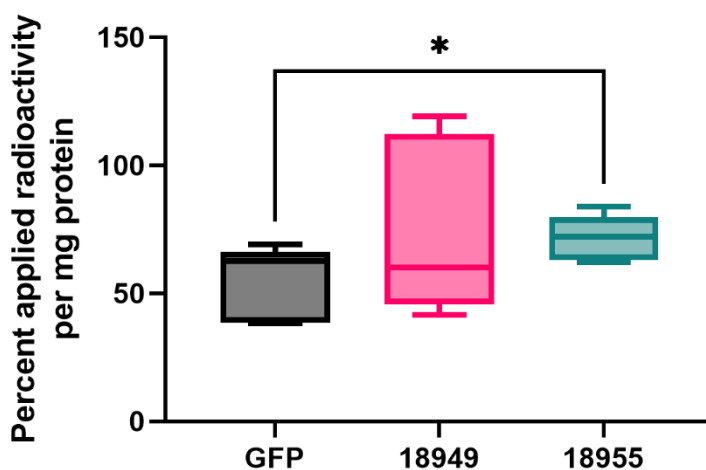


*Figure 7.13. [ $^{18}\text{F}$ ]SFB-link-c-(Ppg)LLFVY cell uptake in transfected MDA-MB-231 cells at 60 minutes. Including MDA-MB-231 GFP control cells, MDA-MB-231 18949 cells, and MDA-MB-231 18955 cells (n=5).*

From *Figure 7.14*, there appeared to be a statistically significant increase in uptake in the 18949 and 18955 cell lines, compared to the GFP cell lines. This was confirmed in *Figure 7.15*, to which the data was compared using a paired t-test ( $p < 0.05$ ).

Also, upon deeper inspection of the cell uptake data for [ $^{18}\text{F}$ ]SFB-c-link-(Ppg)LLFVY in transfected MDA-MB-231 cells with glycine-HCl washes, we saw some very interesting trends from one experiment to the next. As the passage number increased, the total percent of radioactivity applied per mg protein increased.

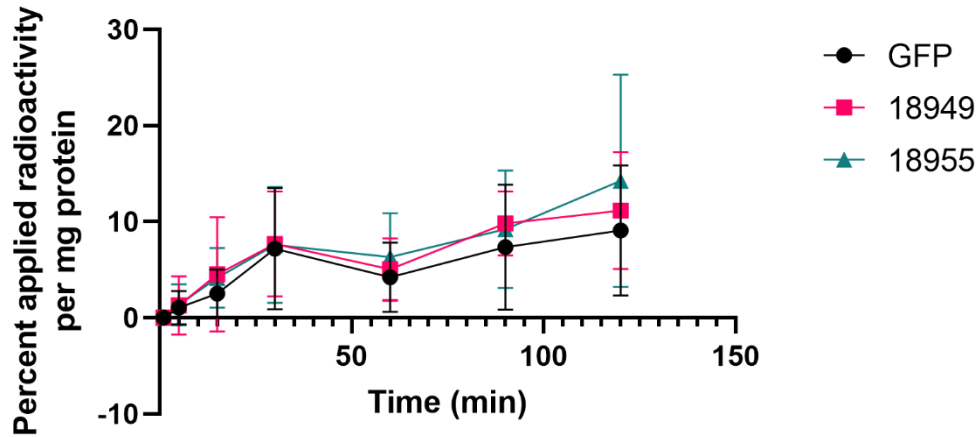


Figure 7.14.  $[^{18}\text{F}]$ SFB-link-c-(Ppg)LLFVY cell uptake in transfected MDA-MB-231 cells. Including MDA-MB-231 GFP control cells, MDA-MB-231 18949 cells, and MDA-MB-231 18955 cells ( $n=6$ ).

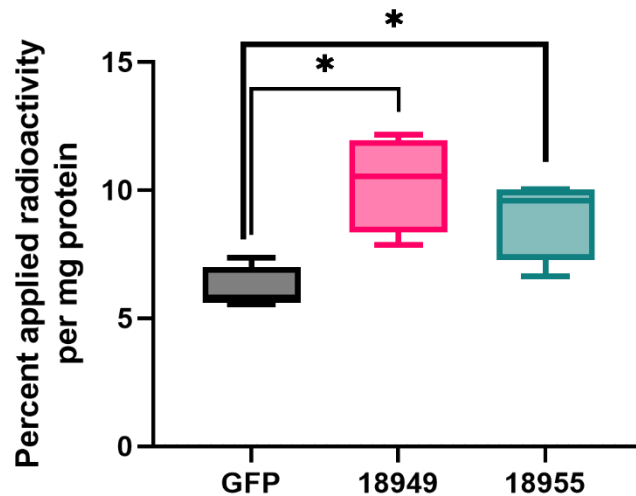


Figure 7.15.  $[^{18}\text{F}]$ SFB-link-c-(Ppg)LLFVY in HIF-1a transfected cells at 90 min. Including MDA-MB-231 GFP control cells, MDA-MB-231 18949 cells, and MDA-MB-231 18955 cells ( $n=4$ ).

From p4 (see Figure 7.16A), there is approximately 12% applied radioactivity/mg protein in the 18955 cells. Moving to p13 (see Figure 7.16B), there was equal uptake as approximately 14% applied radioactivity/mg protein in the 18955 cells. In even higher passage numbers of p17 (see

Figure 7.16D), there is increasing uptake as approximately 20% applied radioactivity/mg protein in the 18949 cells. Then finally, in the p21 (see Figure 7.16D) of the 18955 cells, there is uptake of 40% applied radioactivity/mg protein. Therefore, the stability of the transfection between passages was tested.

To confirm the radiotracer cell uptake with the levels of HIF-1 $\alpha$  protein, whole cell lysates at passage 27 and passage 4 were tested in a western blot. The western blot showed a 50% increased expression of HIF-1 $\alpha$  in the 18949 cell line from passage 4 to passage 27. Also in the 18955 cell line, there is only a 15% increased expression of HIF-1 $\alpha$  from passage 4 to passage 27.

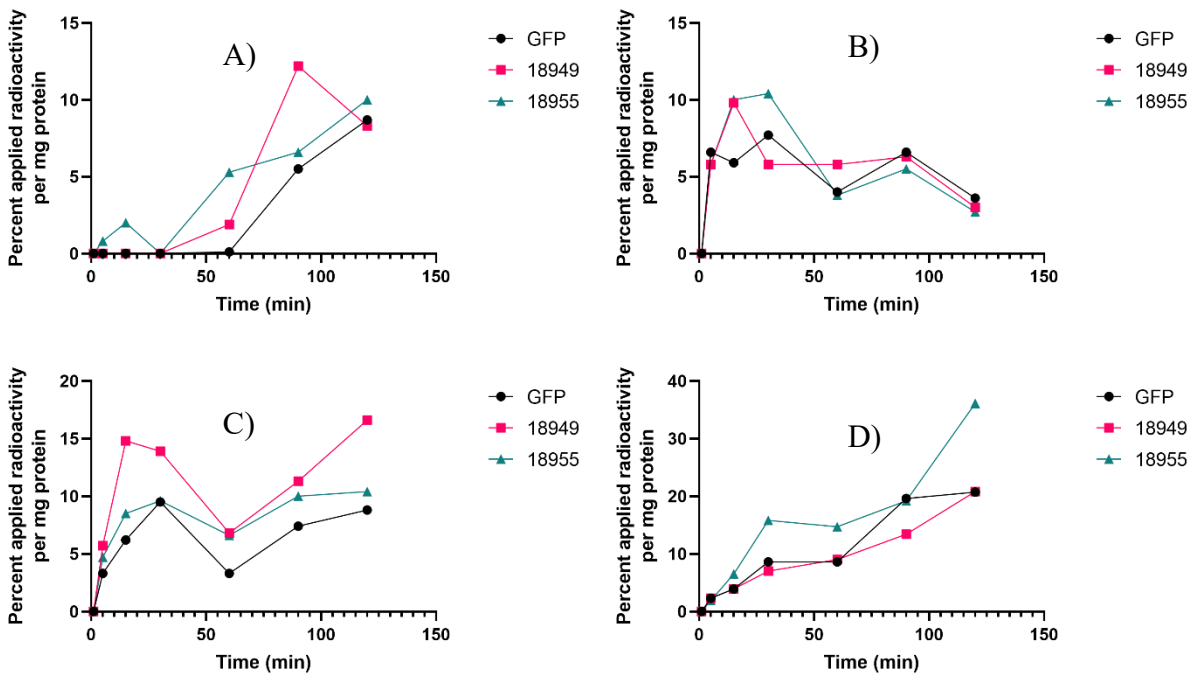
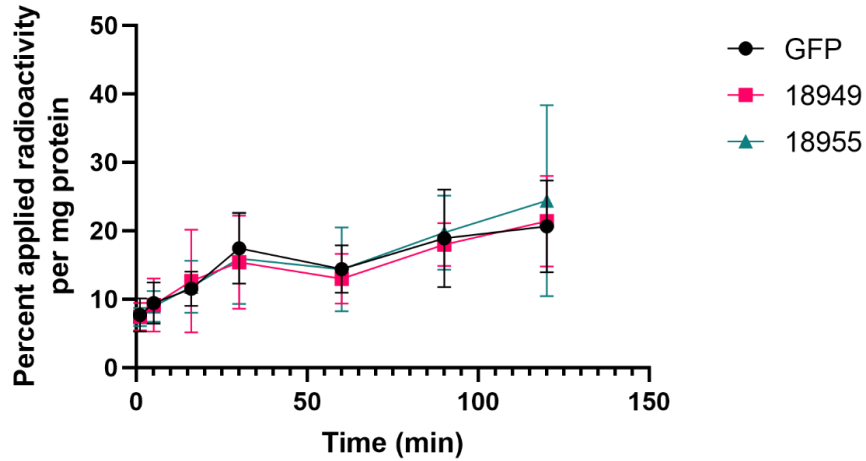


Figure 7.16.  $[^{18}\text{F}]$ SFB-link-c-(Ppg)LLFVY cell uptake in transfected MDA-MB-231 cells for four different cell passages, with glycine-HCl washes. A) passage 4, B) passage 13, C) passage 17, D) passage 21. Including MDA-MB-231 GFP control cells, MDA-MB-231 18949 cells, and MDA-MB-231 18955 cells ( $n=1$ ).

Therefore, for use of these cell lines in animals, a single passage number will be chosen to maintain consistency in the expression level of HIF-1 $\alpha$ . Passage 20 was chosen for future experiments, and the cell uptake of  $[^{18}\text{F}]$ SFB-c-link-(Ppg)LLFVY was tested in p20 MDA-MB-231 cells. Overall

the uptake of [ $^{18}\text{F}$ ]SFB-c-link-(Ppg)LLFVY in all three HIF-1 $\alpha$  transfected cells, showed no significant differences at any of the tested time points (see *Figure 7.17*).



*Figure 7.17.* [ $^{18}\text{F}$ ]SFB-link-c-(Ppg)LLFVY cell uptake in transfected MDA-MB-231 cells at passage 20. Including MDA-MB-231 GFP control cells, MDA-MB-231 18949 cells, and MDA-MB-231 18955 cells ( $n=4$ ).

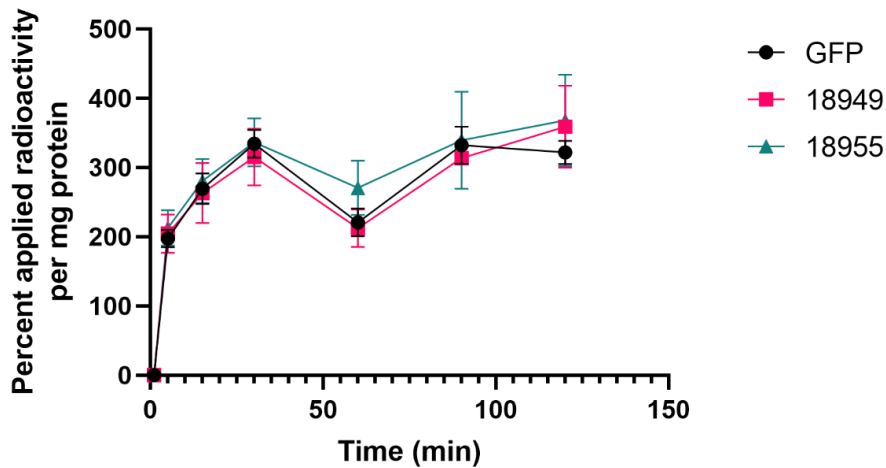


*Figure 7.18.* [ $^{18}\text{F}$ ]FPeP4 cell uptake in transfected MDA-MB-231 cells at passage 20. Including MDA-MB-231 GFP control cells, MDA-MB-231 18949 cells, and MDA-MB-231 18955 cells ( $n=3$ ).

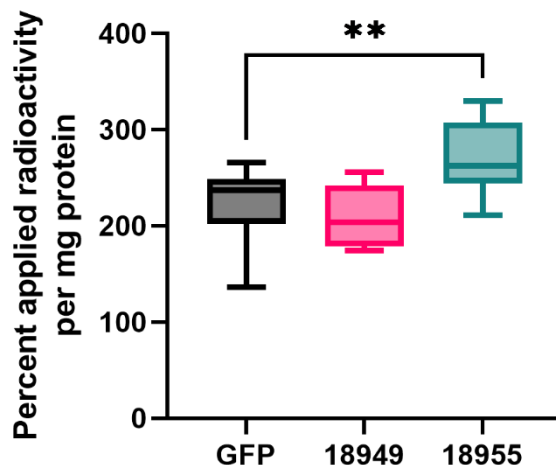


Figure 7.19. [ $^{18}\text{F}$ ]FPeP4 cell uptake in transfected MDA-MB-231 cells at passage 20 and time point of 60 minutes. Including MDA-MB-231 GFP control cells, MDA-MB-231 18949 cells, and MDA-MB-231 18955 cells ( $n=9/3$ ).

Compared to [ $^{18}\text{F}$ ]SFB-c-link-(Ppg)LLFVY, [ $^{18}\text{F}$ ]FPeP4 has a substantially higher uptake in the MDA-MB-231 cells, up to 370% applied radiotracer/mg protein. This internalized uptake value was over 10 times higher than the HIF-1 $\alpha$  targeting cyclic peptide. Taking the 60-minute time point there was a statistically significant increase in uptake from both the GFP and 18494 cell lines to the 18955 cell line (Figure 7.19).

### 7.5 HIF-1 $\alpha$ silenced cell lines and western blot analysis

MDA-MB-231 cells (250,000 cells) were placed into 6 well plates and allowed to attach for 24 hours. Silencing was completed for 24 and 48 and using HIF-1 $\alpha$  siRNA, scrambled siRNA, and Opti-MEM blank control. Lysed samples (10  $\mu\text{L}$ ) were loaded into a Mini-Protean TGX 4-15%, 15 well gel (Cat #456-1086) and run at 200 V for 35 minutes. The subsequent transfer was completed to a PVDF membrane and analyzed with HIF-1 $\alpha$  antibody as per **section 2.7.3.1**.

Measurements of the intensity of HIF-1 $\alpha$  and B-Actin bands on the blot were analyzed (Table S1). HIF-1 $\alpha$  intensity was then corrected to the amount of protein loaded using B-action as the control protein. The average of each treatment was then calculated and compared. After 24 hours the amount of HIF-1 $\alpha$  protein in the blot was 0.615, compared to 0.229 after 48 hours.

This is likely due to the prolonged treatment in Opti-MEM being detrimental to the survival of the cells. In both the 24 and 48 hour HIF-1 $\alpha$  siRNA treatment, the HIF-1 $\alpha$  was silenced 97% after 24 hours and 98.5% after 48 hours. Lastly, the scrambled siRNA had a slight unspecific decrease in the level of HIF-1 $\alpha$  with a 29.7% silencing after 24 hours and 39.6% after 48 hours. Overall, going forward silencing will be completed for the 24 hours treatment period.

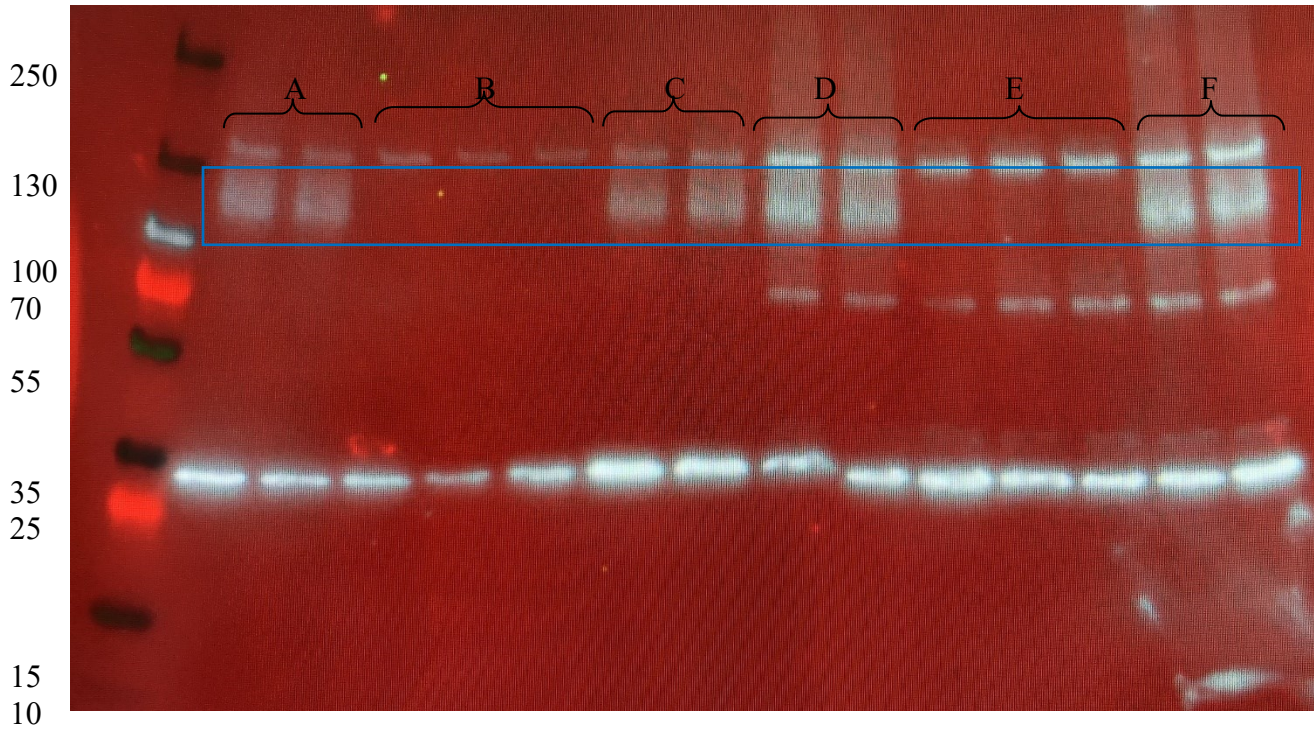


*Figure 7.20. HIF-1 $\alpha$  silencing was completed in MDA-MB-231 cells in 6 well plates. Treatment groups are as follows: A) 48 hours Opti-MEM, B) 48 hours HIF-1 $\alpha$  siRNA, C) 48 hours scrambled siRNA, D) 24 hours Opti-MEM, E) 24 hours HIF-1 $\alpha$  siRNA, and F) 24 hours scrambled siRNA. PageRuler Plus molecular weight ladder on the left in kDa (cat #26619). HIF-1 $\alpha$  protein bands are highlighted in the blue box.  $\beta$ -actin bands are seen at 43 kDa.*

7.6 *In vitro analysis of HIF-1 $\alpha$  targeting compounds in MCF10a*

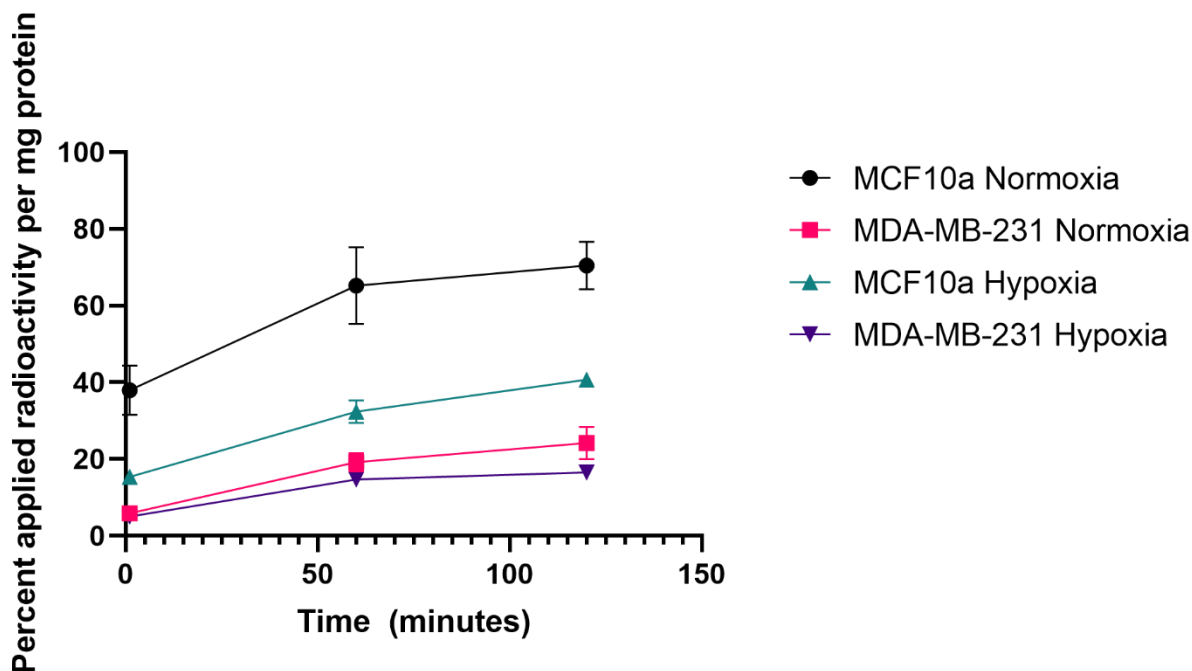


Figure 7.21. [ $^{18}\text{F}$ ]SFB-link-c-(Ppg)LLFVY cell uptake in MDA-MB-231 and MCF10a cells, under both normoxic and hypoxic conditions ( $n=3/1$ ).

To better achieve a zero value for the uptake of the HIF-1 $\alpha$  targeted radiotracers, we tried cellular uptake in MCF10a cells. This was due to previous research in our group reporting very low expression of HIF-1 $\alpha$  from western blot analysis. MDA-MB-231 and MCF-10a cells were plated at 100,000 cells per well into 12 well plates as per **section 2.7.5**. There was glycine wash in all these experiments, and all radioactivity reported was internalized. Additionally, hypoxia (1% O<sub>2</sub>, 5% CO<sub>2</sub>) was applied to the cells for four hours before radiotracer uptake. [ $^{18}\text{F}$ ]SFB-link-c-(Ppg)LLFVY was prepared as per **section 4.1** and was tested ( $n=3/1$ ) in both normoxic and hypoxic conditions in MCF10a and MDA-MB-231 cells.

These results were interesting and puzzling, as the normoxic conditions has higher radiotracer uptake than the hypoxic conditions. Additionally, the MCF10a cells had much higher uptake than the MDA-MB-231 cells. This suggested that the HIF-1 $\alpha$  level was higher in the MCF10a cells than that of the MDA-MB-231 cells.

To further confirm the protein level, MCF10a, EMT6, MCF7, and MDA-MB-231 whole flasks were lysed and samples (5, 10 and 15  $\mu$ L) were loaded into a Mini-Protean TGX 4-15%, 15 well gel (Cat #456-1086) and run at 200 V for 35 minutes. The subsequent transfer was completed to a PVDF membrane and analyzed with HIF-1 $\alpha$  antibody as per **section 2.7.3.1**.



*Figure 7.22. HIF-1 $\alpha$  western blot using MDA-MB-231, MCF7, MCF10a, and EMT6 cells with variable loading where lane 1 of a given cell line is 5  $\mu$ L of lysate, lane 2 is 10  $\mu$ L of lysate and lane 3 is 15  $\mu$ L of lysate ( $n=1$ ).*

Comparing the intensity of the bands, EMT6 and MDA-MB-231 both have fairly equivalent amounts of HIF-1 $\alpha$ . When the value for the expression of HIF-1 $\alpha$  in MDA-MB-231 cells was set to 100%, MCF7 has 172% and MCF10a has 233% expression of HIF-1  $\alpha$ . This was contrary to previous results from our research group. It should be noted that a different HIF-1  $\alpha$  antibody was used for my experiments, which maybe leading to more accurate results.

To try and further follow up on these western blot results, confocal analysis of HIF-1 $\alpha$  was completed in both MCF10a and MDA-MB-231 18955 cells. MDA-MB-231 18955 and MCF10a confocal slides were all prepared under normoxic conditions. All other methodologies were the same as seen in **section 2.7.5**, except for compound **33** was not applied. Instead, the primary antibody used was rabbit anti-HIF-1 $\alpha$  (NB100-479) at 1:200 concentration in 10% BSA in PBS at 4  $^{\circ}$ C for 24 hours. After primary antibody incubation, the antibody solution was removed, and the cells were washed with 1% BSA in PBS (3 x 10 min, 2 mL). After washes, the secondary antibody was added, goat-anti-rabbit CFL-488 at a 1:1000 dilution in 10% BSA in PBS with 0.01% Triton

X-100. The secondary antibody was allowed to incubate at room temperature for 2 hours, after which the solution was removed, and the slides were washed with 1% BSA in PBS (3 x 10 min, 2 mL) prior to mounting. Confocal slides were analyzed using ImageJ, color channels were separated, the threshold was set to Otsu and a mask was created. The mask was applied over the green channel and the integrated density was calculated for all cell lines.

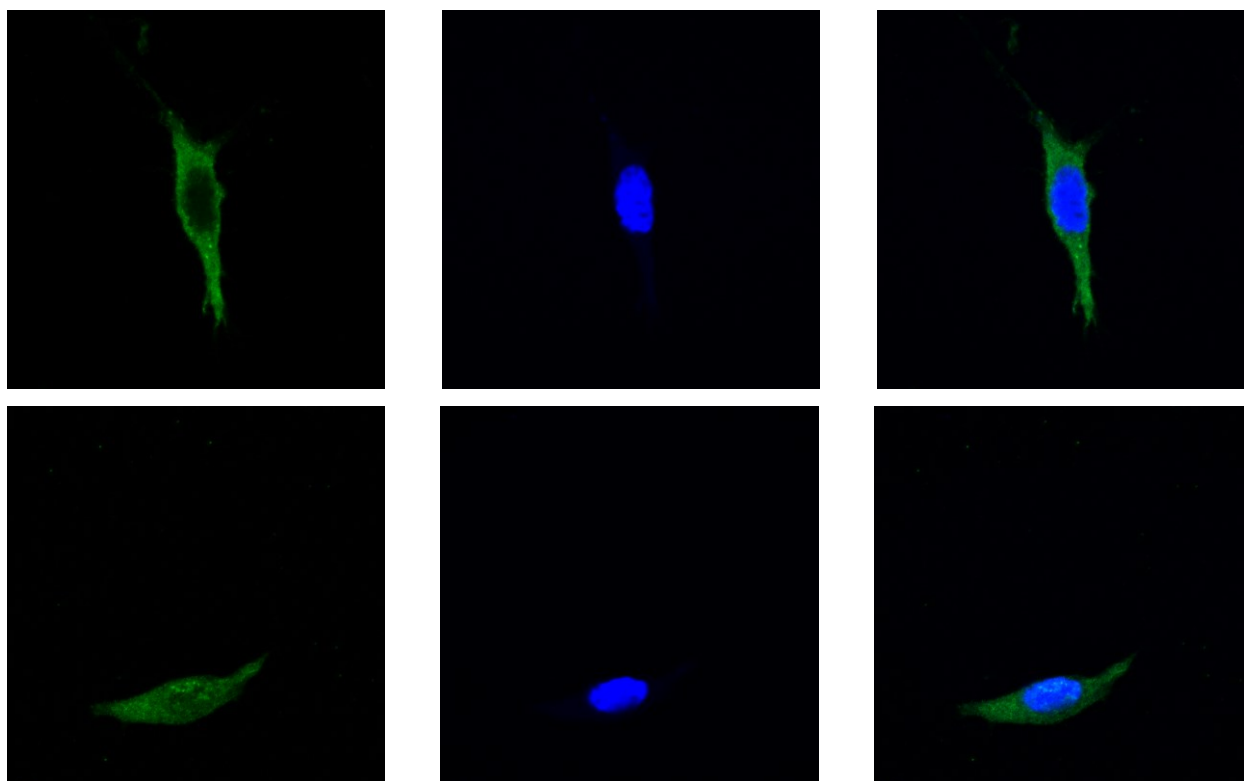


*Figure 7.23. Confocal analysis of HIF-1 $\alpha$  in MCF10a and MDA-MB-231 18955 cell lines. The top row is the MDA-MB-231 18955 cells, bottom row is the MCF10a cells. The left column is the CFL-488 signal. The center column is the DAPI signal. The right column is an overlay of the left and center columns.*

MDA-MB-231 18955 had an average integrated density per cell of 1,738,643, which was minus the secondary antibody blank. Whereas, MCF10a had an average integrated density per cell of 1,128,352, which was minus the secondary antibody blank. Overall there is an increased density of 54% in the MDA-MB-231 18955 cells, which does not fully reflect the western blot results.

Although the levels of HIF-1 $\alpha$  were not confirmed with these results, it did confirm that MCF10a cells do express HIF-1 $\alpha$  at a given level. Additionally, it was seen that the localization of HIF-1 $\alpha$  in the 18955 cells was mostly cytoplasmic, whereas the MCF10a had both cytoplasmic and nuclear localization of the HIF-1 $\alpha$ . In conclusion, another methodology for the silencing of HIF-1 $\alpha$  must be tested.

### 7.7 *In vitro analysis of HIF-1 $\alpha$ targetting compounds in silenced MDA-MB-231 cells*

MDA-MB-231 cells (100,000 cells) were placed into 12 well plates and allowed to attach for 48 hours. After 48 hours, the cells were silenced using siRNA silencing as per **section 2.7.8**. Silencing was completed for 24 hours using HIF-1 $\alpha$  siRNA, scrambled siRNA, and Opti-MEM blank control. Data were analyzed using no protein correction value for the different treatments and the percent applied radioactivity uptake values were strictly compared. This is due to the large killing effect of the treatment, causing a substantial decrease in cellular protein and thus enlarging the values which should be smaller.

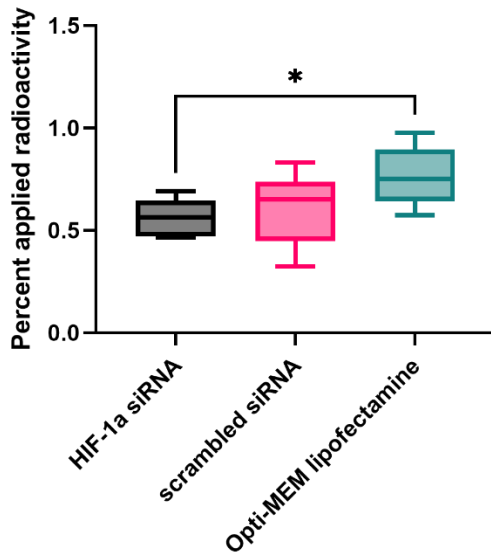
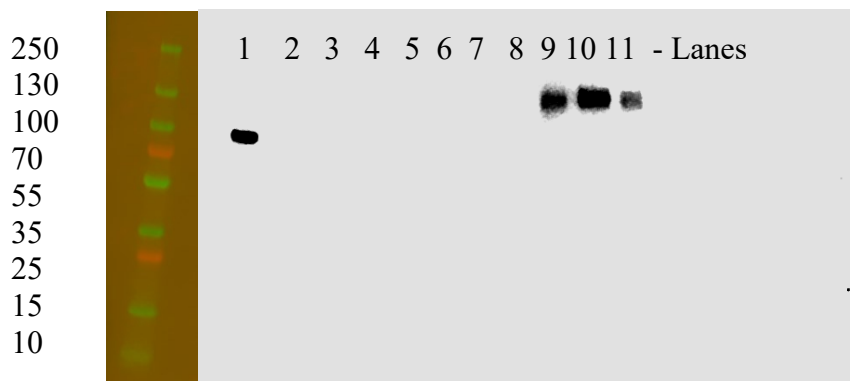


Figure 7.24. [ $^{18}F$ ]SFB-link-c-(Ppg)LLFVY cellular uptake in MDA-MB-231 cells silenced with HIF-1 $\alpha$  siRNA. Including MDA-MB-231 with HIF-1 $\alpha$  siRNA, MDA-MB-231 cells with scrambled siRNA, and control MDA-MB-231 cells in opti-MEM media with lipofectamine (n=9/3).

[<sup>18</sup>F]SFB-link-c-(Ppg)LLFVY was applied to the HIF-1 $\alpha$  silenced cells (n=3) and it was found that after 60 minutes, there was a statistically significant increase in uptake (p<0.05) in the Opti-MEM cells compared to the HIF-1 $\alpha$  silenced cells, see *Figure 7.24*. The uptake increased from  $0.59 \pm 0.09\%$  applied radioactivity to  $0.76 \pm 0.14\%$  applied radioactivity. This difference was very small and likely due to the poor uptake of the cyclic peptide in the MDA-MB-231 cells in combination with the low levels of HIF-1 $\alpha$  present in a 12-well plate assay.

Thus some modifications of this experiment were done in the cell uptake with [<sup>18</sup>F]FPeP4 to achieve better data. This includes an additional set of plates that were not subjected to silencing and was a HIF-1 $\alpha$  overexpression using CoCl<sub>2</sub> (100  $\mu$ M) for 24 hours. Additionally, protein levels of HIF-1 $\alpha$  were reconfirmed with western blot after the uptake to ensure levels of HIF-1 $\alpha$  were elevated in the CoCl<sub>2</sub> treatment group.



*Figure 7.25. Western blot analysis of BCA protein samples from the cellular uptake of [<sup>18</sup>F]FPeP4 in MDA-MB-231 cells. Gel loading is 0.5  $\mu$ g protein per well. Lane 1 is protein ladder with 100kDa band being stained, lanes 2,3, and 4 are HIF-1 $\alpha$  siRNA treatment, lanes 5 and 6 are scrambled siRNA treatment, lanes 7 and 8 are opti-MEM blank and lanes 9, 10 and 11 are 100  $\mu$ M CoCl<sub>2</sub> treatment. PageRuler Plus protein ladder as seen in the fluorescence channels is seen on the left with kDa measurements. HIF-1 $\alpha$  protein is present at 120 kDa.*

Cellular uptake of [<sup>18</sup>F]FPeP4 seemed to have a background uptake value of approximately 6% applied radioactivity, this is possibly contributed to non-specific interactions (n=9/3). Yet there was a statistically significant (p<0.01) increase in uptake in the CoCl<sub>2</sub> (100  $\mu$ M, 24 hours)

treatment group. Overall the average percent applied radioactivity in each group was  $6.6 \pm 1.2\%$  in HIF-1 $\alpha$  siRNA,  $6.6 \pm 0.9\%$  in the scrambled siRNA,  $6.1 \pm 0.8\%$  in the Opti-MEM, and  $7.6 \pm 1.1\%$  in the CoCl<sub>2</sub> treatment group. Additionally, for each of these experiments using [<sup>18</sup>F]FPeP4, the BCA well of the experiment was also used to run a western blot. In which the only lane to see any expression of HIF-1 $\alpha$  was the CoCl<sub>2</sub> treatment group. This is likely due to the low amount of cells per well, additionally, only 10  $\mu$ L of lysate was used per well, from an average 50  $\mu$ g/mL lysate solution. This equates to a gel loading of only 0.5  $\mu$ g.

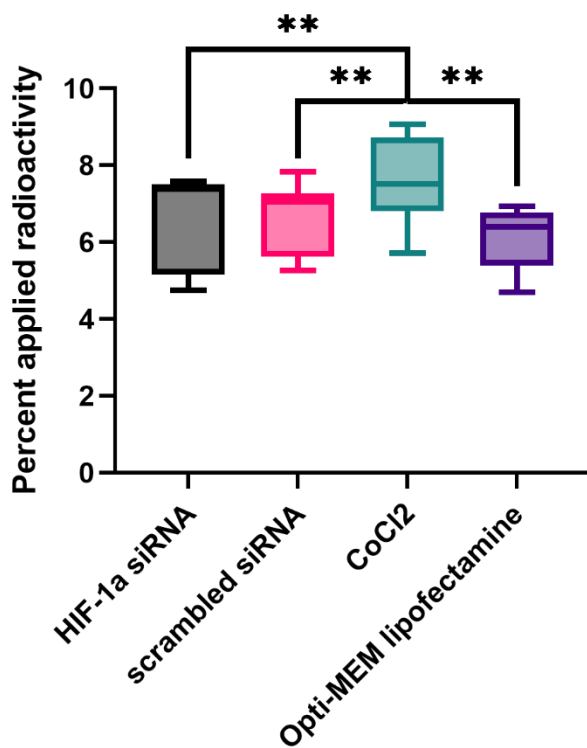
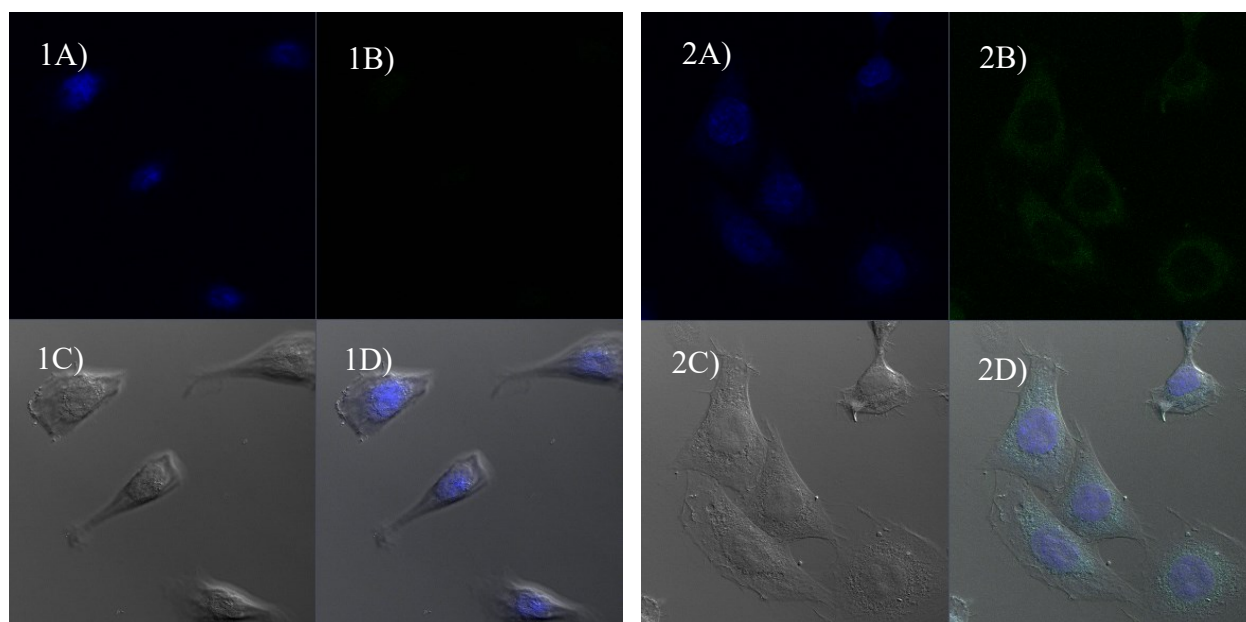


Figure 7.26. [<sup>18</sup>F]FPeP4 cellular uptake in MDA-MB-231 cells silenced with HIF-1 $\alpha$  siRNA. Including MDA-MB-231 with HIF-1 $\alpha$  siRNA, MDA-MB-231 cells with scrambled siRNA, MDA-MB-231 cells with 100  $\mu$ M CoCl<sub>2</sub> treatment, and control MDA-MB-231 cells in opti-MEM media with lipofectamine (n=9/3).

## 7.8 Confocal microscopy (CM) of HIF-1 $\alpha$

### 7.8.1 CM of compound 33 (NBD-link-c-(PPg)LLFVY) in EMT6 cells

Confocal microscopy tests were completed in EMT6 cells (passage 12). Cells were prepared under normoxic conditions. All slides were prepared as per **section 2.7.5**, except for the permeabilization step. Various permeabilization concentrations were tested from 0.5% Triton-X100 to 0.2% Triton-X100 in PBS. Overall, 0.5% Triton-X100 in PBS was found to be optimal, with the best signal-to-noise ratio. NBD-link-c-(PPg)LLFVY in EMT6 cells, showed cytoplasmic localization, with very little to no nuclear localization. *Figure 7.27.* shows both the procedural blank (1) and the compound **33** (2) slides.



*Figure 7.27. NBD-link-c-(PPg)LLFVY in fixed EMT6 cells using confocal microscopy. Side 1 is the procedural blank containing no compound 33. Side 2 contains compound 33. A)DAPI staining B)Fluorescence is seen in the FITC CHANNEL C)Optical channel D)Overlay of channels A, B, and C.*

EMT6 (passage 15) with NBD-link-c-(PPg)LLFVY was then tested under both hypoxic and normoxic conditions. Hypoxic conditions were achieved by pre-incubation of the EMT6 cells in a hypoxic incubator at 37 °C for 4 hours (1.0% O<sub>2</sub> and 5% CO<sub>2</sub>). All other methodologies can be

found in **section 2.7.5**. Cells were analyzed using ImageJ from Fiji, using the moment's threshold with signal converted to a mask and then counted to achieve the integrated density on a tile scan.

Unfortunately, the hypoxic chamber induction of hypoxia did not lead to a substantial increase in the binding of the fluorescent peptide (*Figure 7.28*). There was only an increased fluorescence signal of 17% from the normoxic to the hypoxic cells. Thus, other methods of induction of HIF-1 $\alpha$  were tested.

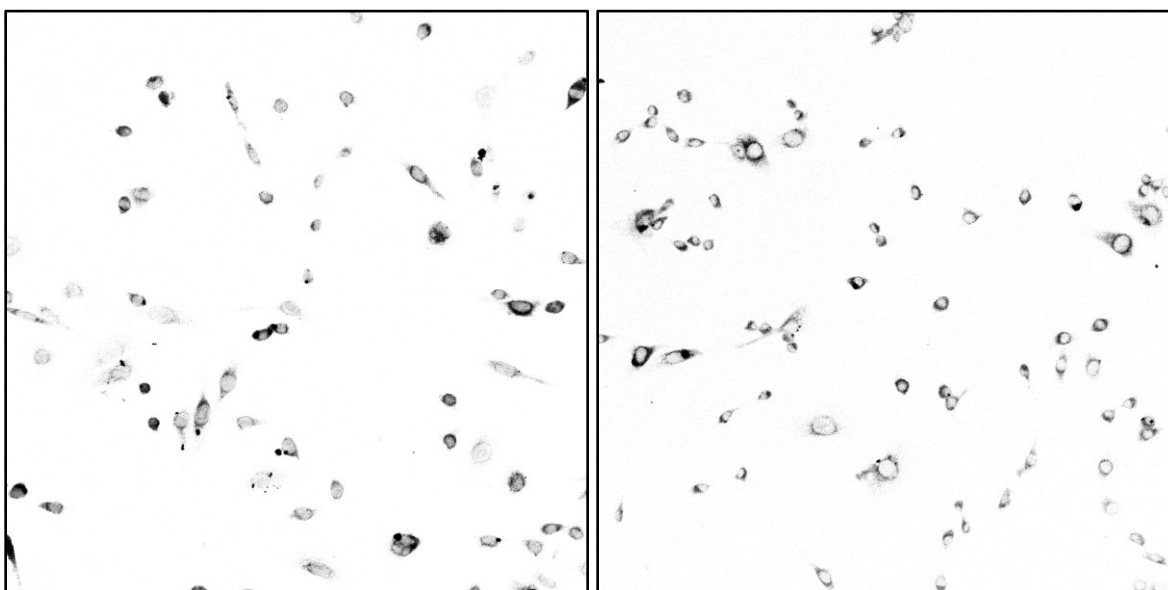


*Figure 7.28. NBD-link-c-(PPg)LLFVY in fixed EMT6 cells using confocal microscopy. Side A is the hypoxic (1% O<sub>2</sub> and 5% CO<sub>2</sub>) slide with compound 33. Slide B is the normoxic slide with compound 33. A) IntDensity = 1622303.364 B) IntDensity = 1355969.154.*

EMT6 (passage 17) with NBD-link-c-(PPg)LLFVY was then tested under both hypoxic and normoxic conditions. Hypoxic conditions were achieved by the addition of CoCl<sub>2</sub> solution (100  $\mu$ M, 3.0 mL) prepared in RPMI-1640 medium at 37  $^{\circ}$ C for 4 hours. All other methodologies can be found in **section 2.7.5**. Again, the expected increase in fluorescence in the hypoxic cells was not substantially observed. Instead, both the hypoxic and normoxic cells had fairly equivalent amounts of compound 33 bindings (see *Figure 7.29*). The numerical difference in the integrated density between the two panels is only a 4% increase in hypoxic EMT6 cells.

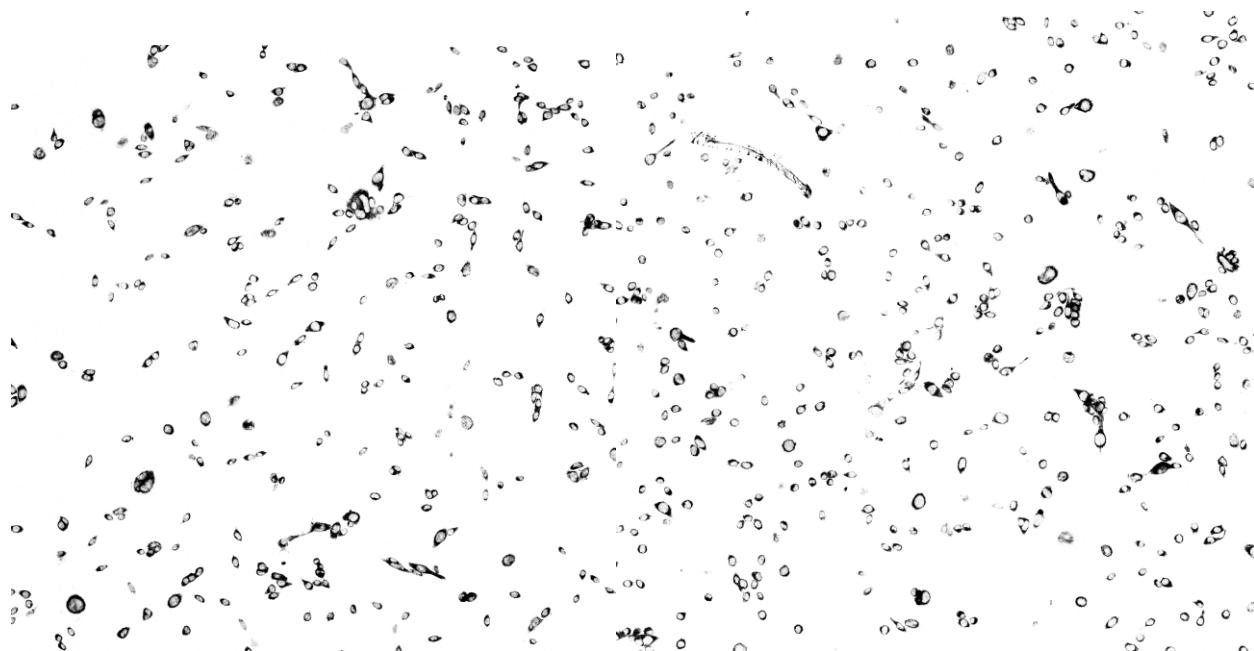


*Figure 7.29. NBD-link-c-(PPg)LLFVY in fixed EMT6 cells using confocal microscopy. Side A is the hypoxic (CoCl<sub>2</sub>) slide with compound 33. Slide B is the normoxic slide with compound 33. A) Int Density = 8877025.981 B) IntDen = 8538546.676*

#### 7.8.2 CM of compound 33 (NBD-link-c-(PPg)LLFVY) in HIF-1 $\alpha$ transfected cells

MDA-MB-231 HIF-1 $\alpha$  transfected cell lines (GFP, 18949 and 18955) confocal slides were all prepared under normoxic conditions. All other methodology is the same as seen in **section 2.7.5**. Confocal slides were analyzed using ImageJ, color channels were separated, the threshold was set to Otsu and a mask was created. The mask was applied over the green channel and the integrated density was calculated for all three cell lines, with slides containing three cells. MDA-MB-231 GFP had an integrated density of  $1.50 \times 10^6$ , MDA-MB-231 18949 had an integrated density of  $1.09 \times 10^6$  and MDA-MB-231 18955 had an integrated density of  $4.17 \times 10^6$ . This is the highest difference seen in the confocal slides analyzed.

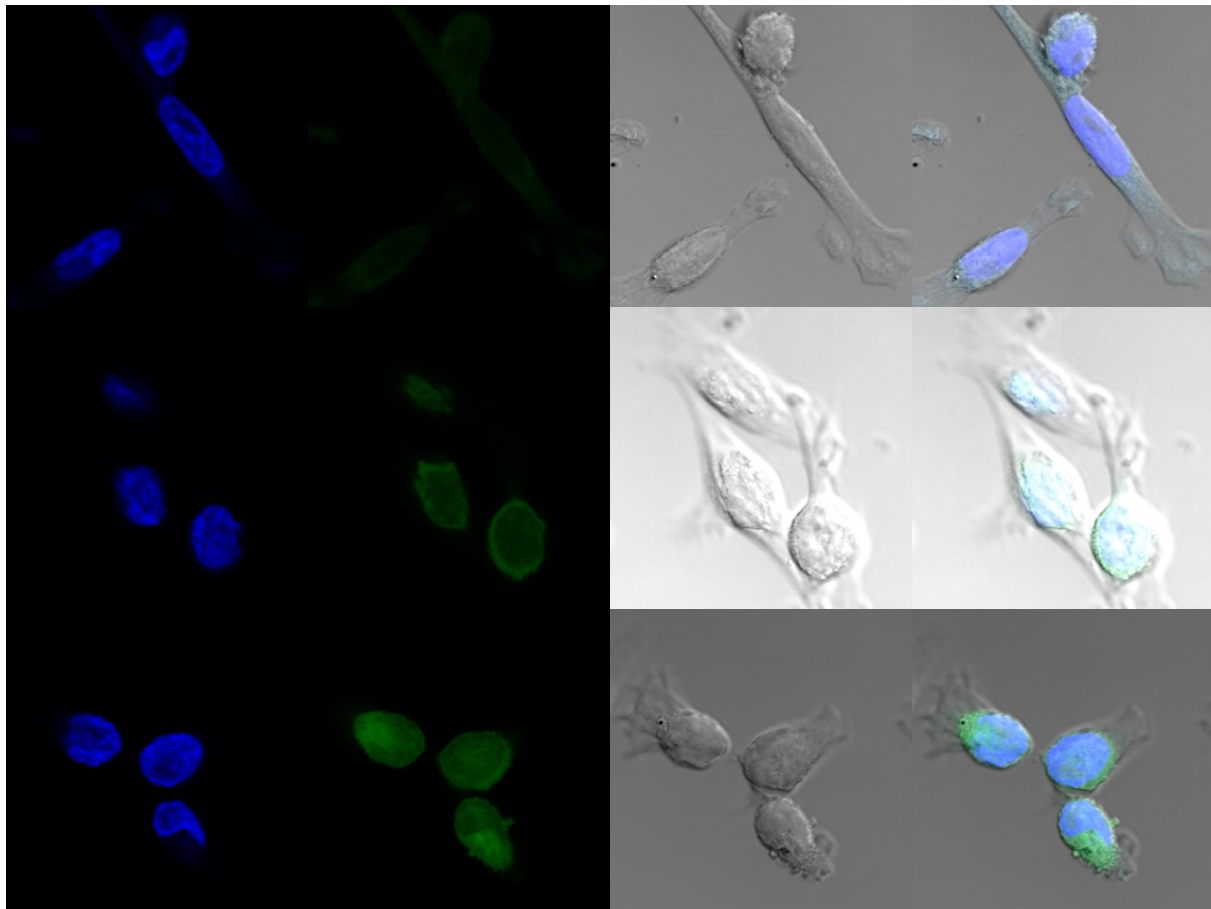


*Figure 7.30. NBD-link-c-(PPg)LLFVY in fixed MDA-MB-231 cells using confocal microscopy. Row A is the MDA-MB-231 GFP cells, Row B is the MDA-MB-231 18949 cells and Row C is the MDA-MB-231 18955 cell line. Column 1 is DAPI staining, Column 2 is the NBD-link-c-(PPg)LLFVY peptide, column 3 is the transmission image, and column 4 is the overlay of all other columns.*

Looking at a larger sampling of 15 random cells per slide, GFP had an integrated density of 418,402 per cell, 18949 had an integrated density of 935,981 per cell, and 18955 had an integrated density of 629,893 per cell. These numbers reflect the overexpression as seen in the western blot, there is a 123% increase in density in 18949 and a 51% increase in density in the 18955 cells. Additionally, the localization of the NBD-link-c-(PPg)LLFVY in the HIF-1 $\alpha$  transfected cells was primarily nuclear with some cytoplasmic portion of the fluorescent peptide. There was a larger proportion of cytoplasmic binding in the GFP cell line, compared to both 18949 and 18955.

### 7.8.3 CM of HA Antibody in HIF-1 $\alpha$ transfected cells

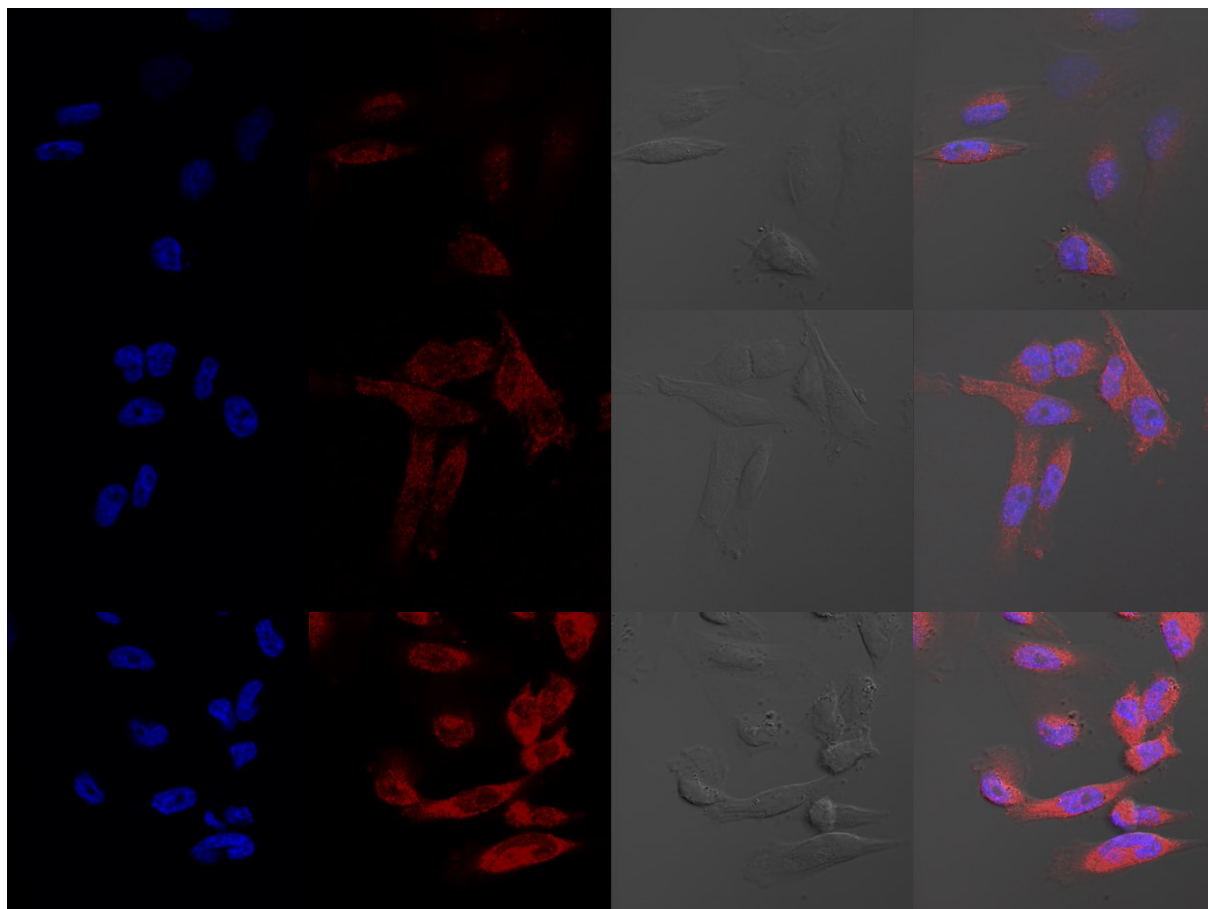


*Figure 7.31. pAb anti-HA tag in fixed MDA-MB-231 cells using confocal microscopy. Row A is the MDA-MB-231 GFP cells, Row B is the MDA-MB-231 18949 cells and Row C is the MDA-MB-231 18955 cell line. Column 1 is DAPI staining, Column 2 is the HA-tag, column 3 is the transmission image, and column 4 is the overlay of all other columns.*

MDA-MB-231 HIF-1 $\alpha$  transfected cell lines (GFP, 18949 and 18955) confocal slides were all prepared under normoxic conditions. All other methodologies are the same as seen in **section 2.7.5.**, except for the NBD-link-c-(PPg)LLFVY cyclic peptide. Instead, HA levels were analyzed using the primary antibody of pAb anti-HA-tag chicken antibody (Novus, NB600-361, 1:250), followed with the secondary antibody of goat anti-chicken dyelight 633 (Novus, NBP1-75706,

1:1000). Confocal slides were analyzed using ImageJ, color channels were separated, the threshold was set to Otsu and a mask was created.

The mask was applied over the red channel and the integrated density was calculated for all three cell lines, with a minimum of 17 cells being counted for each cell line.

Averaging the integrated density over 18 cells (see *Figure 7.31*), the GFP cell line had an integrated density of 11,018 per cell. Whereas the 18949 cell line had an integrated density of 14,482 per cell and the 18955 cell line had an integrated density of 15,579 per cell. If we assume all the binding to the GFP cells is non-specific, since there should be no expressed HA-antigen, we get values of 3,463 and 4,560 integrated density per cell for 18949 and 18955 cells. This leads to a 31% increased amount of HA-tag in the 18955 cells. Overall, the use of the HA antibody was deemed to have too large of a background signal to be used further.

#### *7.9 Summary for the in vitro analysis of HIF-1 $\alpha$ binding radiotracers*

[<sup>18</sup>F]SFB-c-link-(Ppg)LLFVY was found to have an *in vitro* cell uptake into MDA-MB-231 18955 cells of ~10% AR/mgP compared to the MDA-MB-231 GFP cells with a ~6% AR/mgP. This increased uptake correlated to the increased expression of HIF-1 $\alpha$  in the MDA-MB-231 18955 cells, and was stastically significant. [<sup>18</sup>F]FPeP4 was found to have an *in vitro* cell uptake into MDA-MB-231 18955 cells of ~280% AR/mgP compared to the MDA-MB-231 GFP cells with a ~220% AR/mgP. This increased uptake correlated to the increased expression of HIF-1 $\alpha$  in the MDA-MB-231 18955 cells, and was stastically significant.

Both HIF-1 $\alpha$  targetting radiotracers of [<sup>18</sup>F]SFB-c-link-(Ppg)LLFVY and [<sup>18</sup>F]FPeP4 were found to have a high proportion of non-specific binding. Yet, they were both able to detect changes in the level of HIF-1 $\alpha$  expression with a corresponding increased cellular uptake.

## Chapter 8: *In vivo* analysis of HIF-1 $\alpha$ binding compounds

### 8.1 Testing of transfected cell lines in NIH-III mice

MDA-MB-231 18955 tumors were grown in NIH-III mice as per **section 2.7.10**. [ $^{18}\text{F}$ ]FAZA was synthesized as per **section 4.3**, and injected into 18955 xenografts using the methodology in **section 2.7.10**. [ $^{18}\text{F}$ ]FAZA uptake in MDA-MB-231 18955 tumors (see *Figure 8.1.A*) was compared to uptake in normal MDA-MB-231 tumor models in NIH-III mice (see *Figure 8.1.B*).

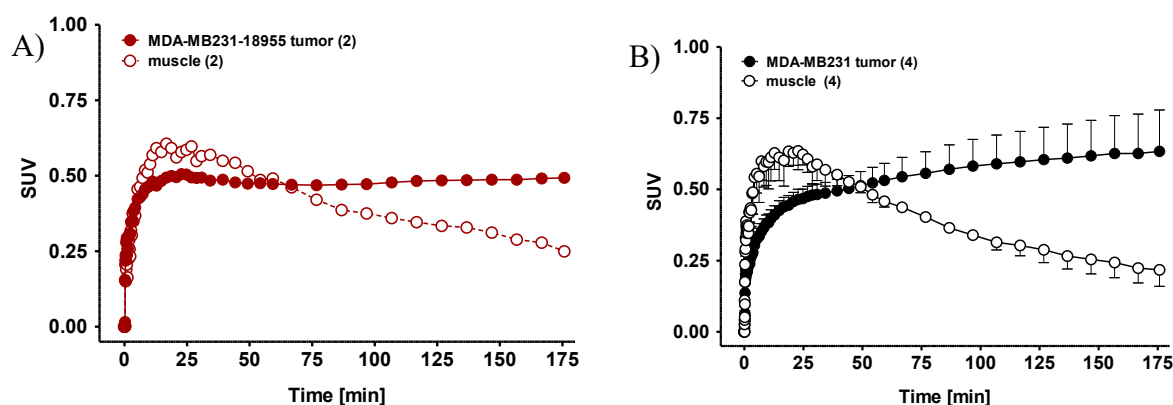


*Figure 8.1. A) [ $^{18}\text{F}$ ]FAZA uptake in MDA-MB-231 18955 tumor model in NIH-III mice (n=2), showing both tumor and muscle uptake time activity curves. B) [ $^{18}\text{F}$ ]FAZA uptake in MDA-MB-231 tumor model in NIH-III mice (n=4), showing both tumor and muscle uptake time activity curves.*

Overall both the MDA-MB-231 tumor model and MDA-MB-231 18955 tumor model have similar tumor uptake in the range of 0.5 to 0.6 SUV. Additionally, the retention in muscle for both tumor models is also very comparable leading to a tumor-to-muscle ratio of 2 at 175 minutes post injection. Therefore the transfection of the MDA-MB-231 cells does not appear to impact the uptake of [ $^{18}\text{F}$ ]FAZA.

### 8.2 PET imaging of HIF-1 $\alpha$ derivatives

MDA-MB-231 18955 tumors and MCF7 were grown in NIH-III mice as per **section 2.7.10**. [ $^{18}\text{F}$ ]SFB-link-c-(Ppg)LLFVY and [ $^{18}\text{F}$ ]FPeP4 was synthesized as per **section 6.1** and **6.4.2.2.2.**,

and injected into 18955 and MCF7 xenografts using methodology in **section 2.7.10**. [ $^{18}\text{F}$ ]FPeP4 uptake in MDA-MB-231 18955 tumors (see *Figure 8.2*.) was compared to the uptake in MCF7 tumors. [ $^{18}\text{F}$ ]FPeP4 was formulated with 5% propylene glycol in saline for animal injection.

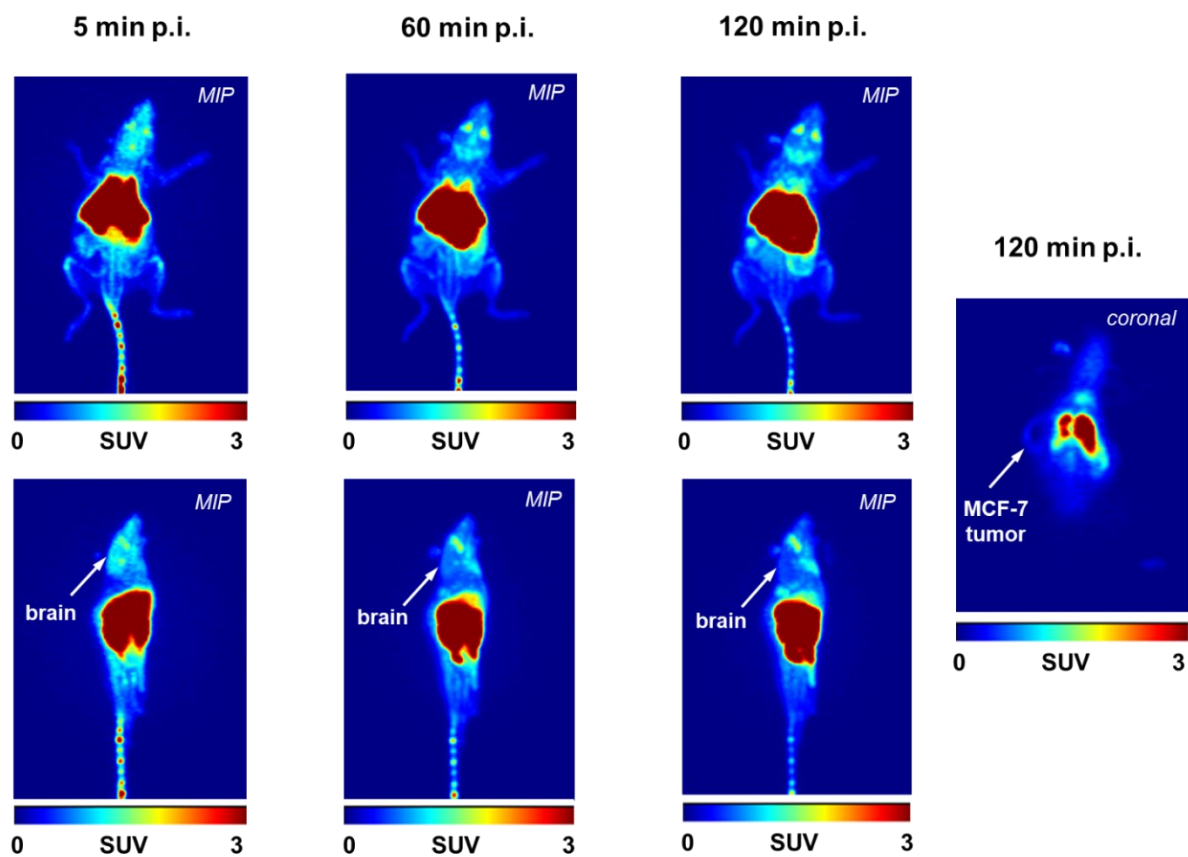


*Figure 8.2. [ $^{18}\text{F}$ ]FPeP4 uptake in MDA-MB-231 18955 tumor model and MCF7 tumor model in NIH-III mice, showing maximum intensity projection (MIP) at 5, 60 and 120 minutes post-injection.*

Uptake of [ $^{18}\text{F}$ ]FPeP4 in MCF7 tumor achieved a maximum of 0.3 SUV with a muscle uptake of 0.1 SUV after 120 minutes. This gives a tumor-to-muscle ratio (TMR) of 3, which is relatively good compared to the TMR for [ $^{18}\text{F}$ ]FAZA of 2.

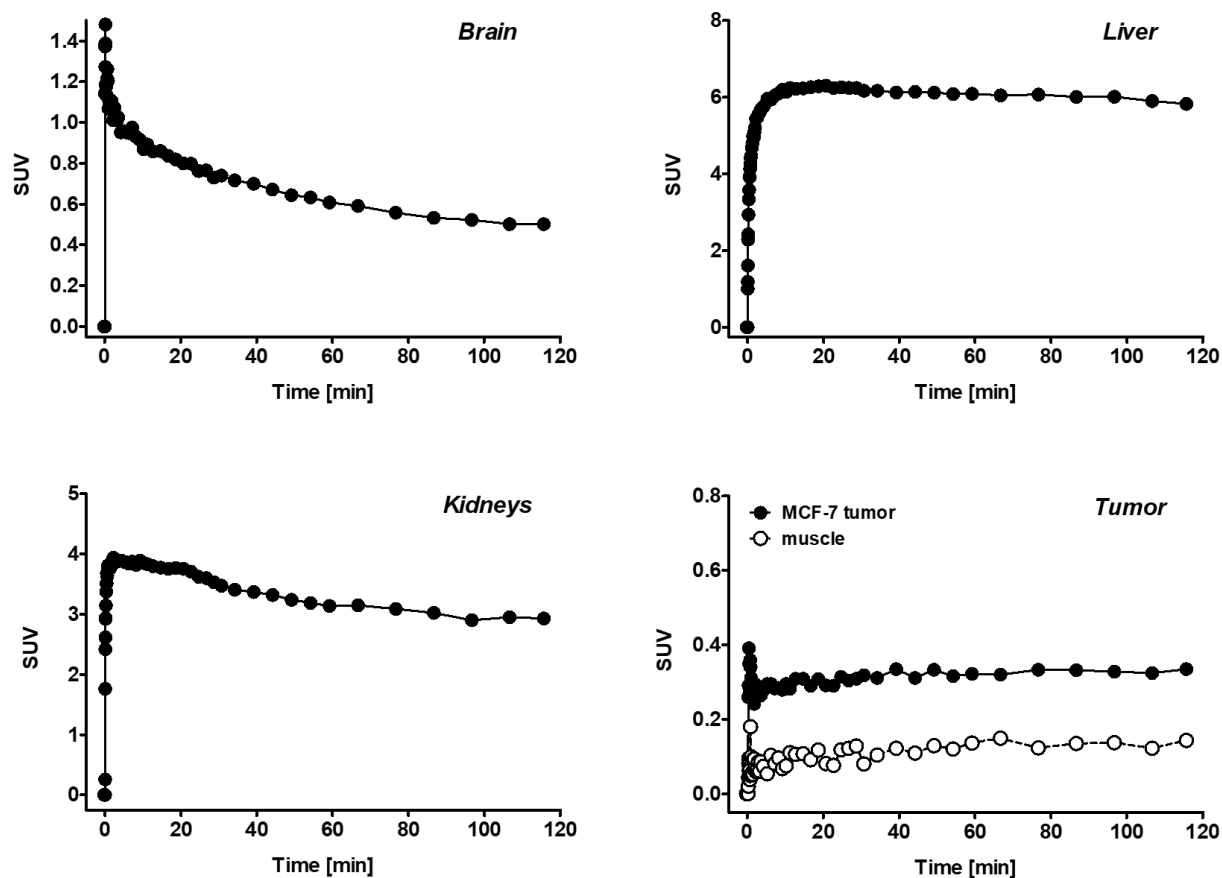


Figure 8.3.  $[^{18}\text{F}]\text{FPeP4}$  time activity curves in MDA-MB-231 18955 tumor model in NIH-III mice, showing standardized uptake values from radiotracer injection to 120 minutes post injection.

Although, there was detectable tumor uptake, the biodistribution of  $[^{18}\text{F}]\text{FPeP4}$  was not favorable. There was a large component of radiotracer that remained in the liver up to a SUV of 6, after only 5 minutes post-injection. Thus likely the radiotracer was trapped in the liver with the first pass through the circulation system. Additionally, we do observe renal clearance with  $[^{18}\text{F}]\text{FPeP4}$ , up to a SUV max of 4 at 5 minutes. Lastly,  $[^{18}\text{F}]\text{FPeP4}$  appears to pass the blood-brain-barrier and have some retention in the brain, even with an SUV of 0.5 after 120 minutes post-injection.

This suggests that possibly  $[^{18}\text{F}]\text{FPeP4}$  may be useful for imaging a tumor in the brain tissue. This possibility for glioblastoma imaging will be looked at in the future.

Attempting to achieve better biodistribution of the [ $^{18}\text{F}$ ]FPeP4 radiotracer, a formulation of 5% propylene glycol in saline with 3.5% HSA was attempted. Previous research has shown that a carrier for the radiotracer, such as HSA, can improve the first-pass pharmacokinetics of a radiotracer. This work was completed in non-tumor bearing NIH-III mice.

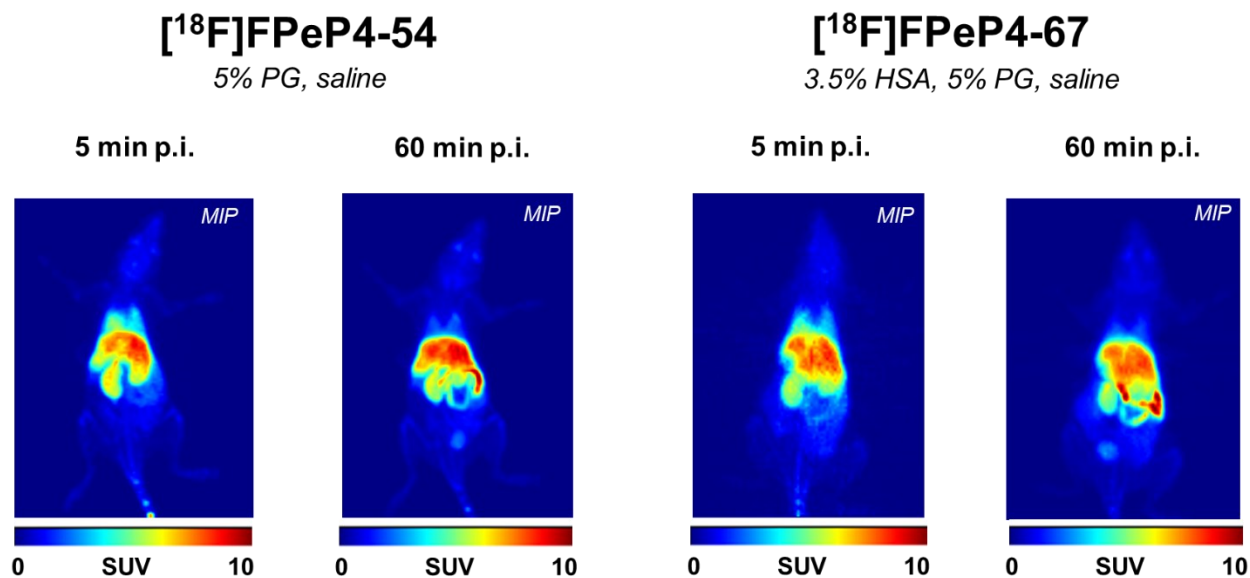


Figure 8.4. [ $^{18}\text{F}$ ]FPeP4 uptake in non-tumor bearing NIH-III mice, showing maximum intensity projection (MIP) at 5 and 60 minutes, for two different formulations of [ $^{18}\text{F}$ ]FPeP4.

Reformulation of [ $^{18}\text{F}$ ]FPeP4 into a solution containing 3.5% HAS did not improve the pharmacodynamics of the radiotracer. The first-pass trapping in the liver was still witnessed up to an SUV maximum of 7 after 5 minutes. Also, the SUV max in the kidneys increased from 4 to 5 with the addition of 3.5% HSA. Additionally, the use of HSA in the formulation decreased the amount of [ $^{18}\text{F}$ ]FPeP4 in the brain. Overall the addition of HSA did not improve [ $^{18}\text{F}$ ]FPeP4 biodistribution as seen from the time activity curves in Figure 8.5.

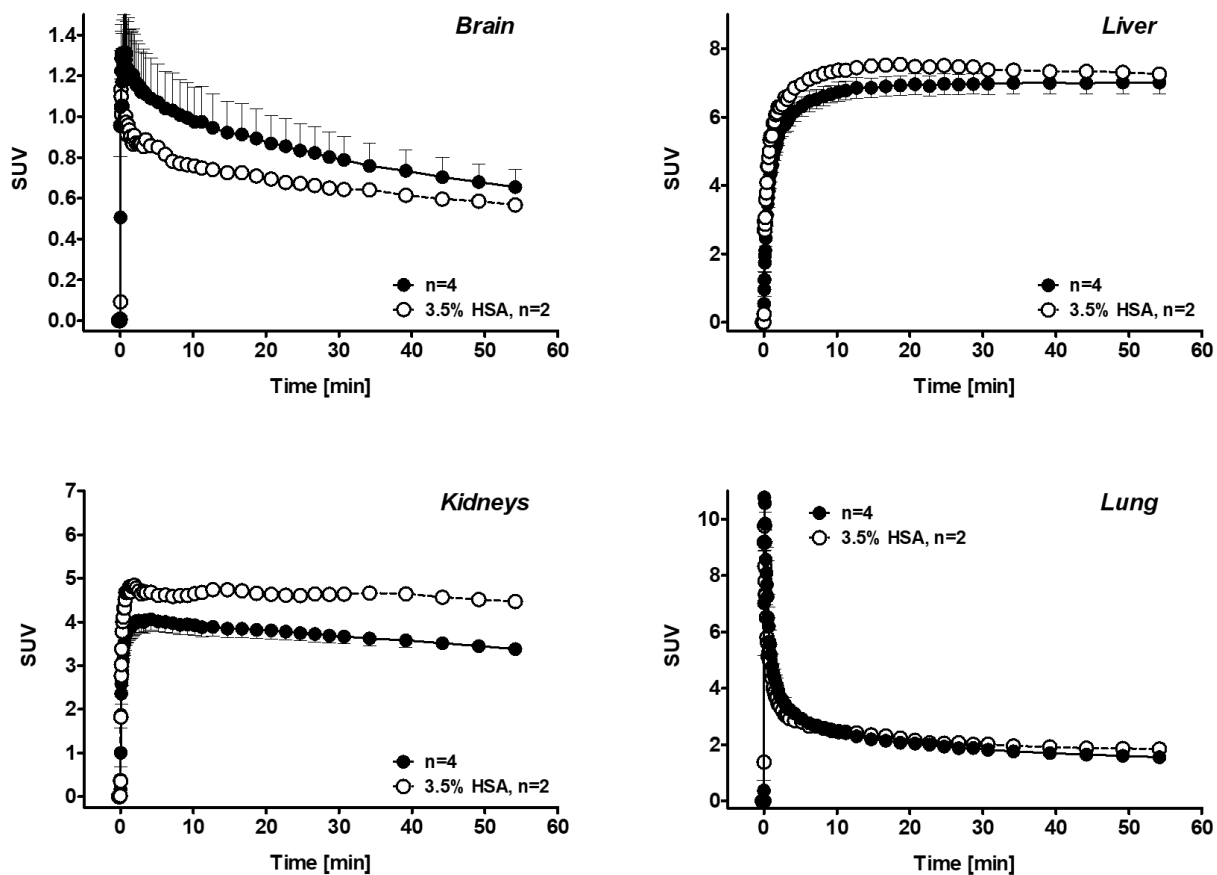


Figure 8.5.  $[^{18}\text{F}]$ FPeP4 time activity curves in non-tumor bearing NIH-III mice, showing standardized uptake values from radiotracer injection to 120 minutes post-injection.

The second HIF-1 $\alpha$  targeting compound of  $[^{18}\text{F}]$ SFB-link-c-(Ppg)LLFVY was also tested in MCF-7 tumor-bearing NIH-III mice (see Figure 8.6.). Using this radiotracer, there was very negligible tumor uptake and the biodistribution in the mouse model was very poor. Mostly all of the radiotracer was trapped in the liver first pass, this is likely due to the larger lipophilicity of this radiotracer compared to that of  $[^{18}\text{F}]$ FPeP4. Additionally, comparing side-by-side the time activity curves for both HIF-1 $\alpha$  targeting compounds, we can see that  $[^{18}\text{F}]$ SFB-link-c-(Ppg)LLFVY has no difference in the tumor versus muscle uptake curves. Thus,  $[^{18}\text{F}]$ SFB-link-c-(Ppg)LLFVY is not a promising HIF-1 $\alpha$  targeting compound.

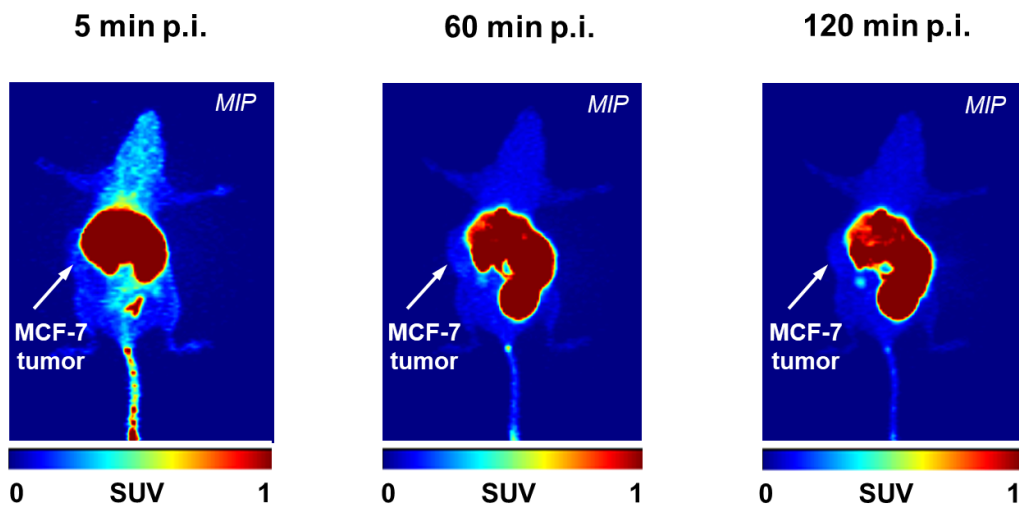


Figure 8.6.  $[^{18}\text{F}]$ SFB-link-c-(Ppg)LLFVY uptake in MCF7 tumor model in NIH-III mice, showing maximum intensity projection (MIP) at 5, 60 and 120 minutes post-injection.

Additionally in Figure 8.7, the time activity curves for  $[^{18}\text{F}]$ FPeP4 in both 18955 tumor models and MCF7 tumor models, had a tumor uptake of  $\text{SUV} = 0.2$ . Compared to the muscle uptake of  $\text{SUV} = 0.1$ , that resulted in a TMR of 2 in both tumor models. Whereas,  $[^{18}\text{F}]$ SFB-link-c-(Ppg)LLFVY in both 18955 tumor models and MCF7 tumor models, had a tumor uptake of  $\text{SUV} = 0.1$ . Compared to the muscle uptake of  $\text{SUV} = 0.1$ , that resulted in a TMR of 1 in both tumor models.

Although the uptake of  $[^{18}\text{F}]$ FPeP4 is not large, we do see an increased uptake in tumor tissue. According to Lipinski's rule of five,  $[^{18}\text{F}]$ FPeP4 is a fairly promising drug candidate, with a LogD of 1.18, 2 hydrogen bond donors, 5 hydrogen bond acceptors, and a molecular mass of 504.23. Yet, the major problem with this radiotracer is the biodistribution profile, which could not be optimized within the scope of this work.

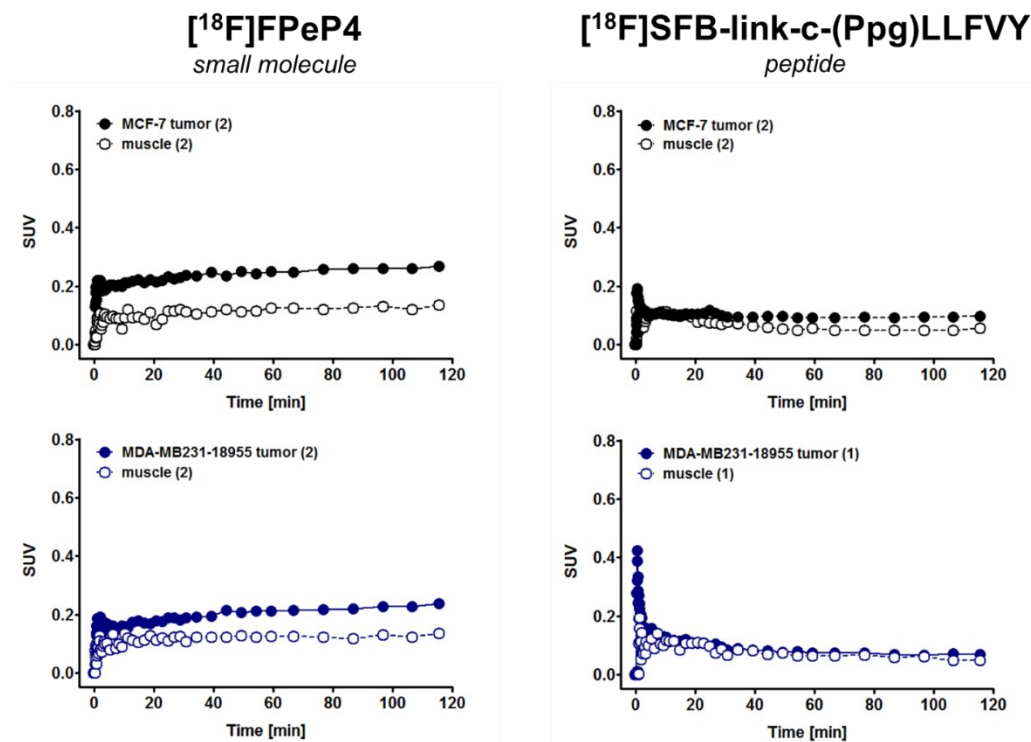


Figure 8.7.  $[^{18}\text{F}]\text{FPeP4}$  and  $[^{18}\text{F}]\text{SFB-link-c-(Ppg)LLFVY}$  time activity curves in MCF-7 and MDA-MB-231 18955 tumor-bearing NIH-III mice, showing standardized uptake values from radiotracer injection to 120 minutes post-injection.

### 8.3 Plasma stability of HIF-1 $\alpha$ derivative $[^{18}\text{F}]\text{FPeP4}$

*In vivo* metabolic stability was performed as per **section 2.7.9**. Data for  $[^{18}\text{F}]\text{FPeP4}$  was analyzed by TLC analysis using normal phase aluminum-backed TLC plates.  $[^{18}\text{F}]\text{FPeP4}$  was found to be extremely metabolically stable (see *Figure 8.8*). After 30 minutes, 92% of the radiotracer remained intact (n=1). Additionally, the amount intact may indeed be larger than reported. This is due to the extremely small amount of injected radioactivity. Typical amounts of injected radioactivity are ~20MBq, this test was done with 2 MBq, thus counts for the TLC plate were extended to 10 minutes.

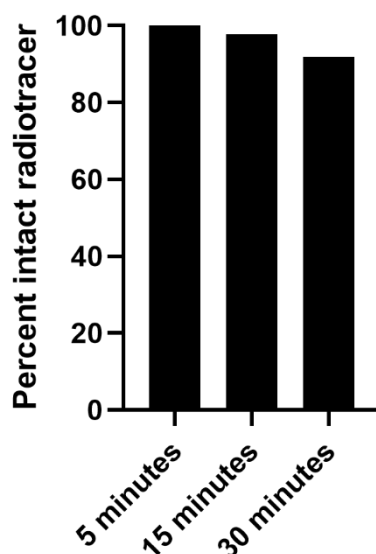


Figure 8.8.  $[^{18}\text{F}]\text{FPeP4}$  metabolic stability in non-tumor bearing female BALB/c mice ( $n=1$ ).

Blood distribution was performed as per section **section 2.7.9**. Data for  $[^{18}\text{F}]\text{FPeP4}$  was analyzed by a HIDEEX gamma counter.  $[^{18}\text{F}]\text{FPeP4}$  was found to be predominately bound to the blood with  $64 \pm 5\%$  ( $n=3$ ) of the radioactivity found in the first centrifuged blood fraction. Very little of the  $[^{18}\text{F}]\text{FPeP4}$  was found to be protein bound, with only  $1 \pm 1\%$  ( $n=3$ ) of the radioactivity being present in the precipitated protein. Finally,  $34 \pm 4\%$  ( $n=3$ ) of the radioactivity of  $[^{18}\text{F}]\text{FPeP4}$  was found to be in the plasma. Overall the blood distribution of  $[^{18}\text{F}]\text{FPeP4}$  was found to be very similar to that of  $[^{18}\text{F}]\text{FBNA}$ .

#### 8.4 Summary for the in vivo analysis of HIF-1a targetting radiotracers

In both 18955 tumor models and MCF7 tumor models,  $[^{18}\text{F}]\text{FPeP4}$  achieved a maximal tumor uptake of  $\text{SUV} = 0.2$ . When compared to the muscle uptake of  $\text{SUV} = 0.1$ , the resulting TMR was found to be 2. Additionally,  $[^{18}\text{F}]\text{SFB-link-c-(Ppg)LLFVY}$  in both 18955 tumor models and MCF7 tumor models, had a tumor uptake of  $\text{SUV} = 0.1$ . Compared to the muscle uptake of  $\text{SUV} = 0.1$ , that resulted in a TMR of 1 in both tumor models.

Both HIF-1 $\alpha$  targetting radiotracers of [<sup>18</sup>F]SFB-link-c-(Ppg)LLFVY and [<sup>18</sup>F]FPeP4 had very poor biodistribution with large amount of first pass liver trapping. Yet, these are the first known radiotracers to directly image HIF-1 $\alpha$  using positron emission tomography.

## Chapter 9: Summary of results

### 9.1 Novel compounds targeting HIF-1 $\alpha$ and their analysis

We synthesized a library of compounds targeting HIF-1 $\alpha$ , based on two structures from the literature (see *Figure 9.1.*). From the structure of ER-400583-00, twelve derivatives were made in the 4' aryl position from the alkyne bond (see *Table 9.1.*).

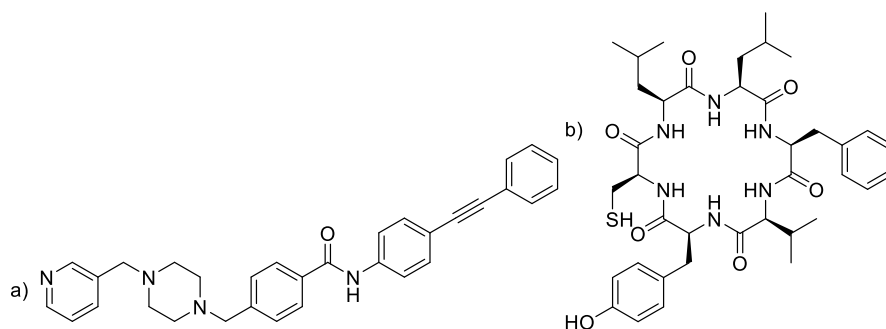


*Figure 9.1. Lead compounds from the literature that inhibit interactions with HIF-1 $\alpha$  directly. a) ER-400583-00 and b) Cyclo-CLLFVY*

*Table 9.1. Summary data for the production of compound 9 to 20, derivatized from the lead structure from the literature of ER-400583-00. ID is the compound identification number and \*‘ps’ is shorthand for powdery solid.*

ID	X	HPLC tr (min)	Yield (%)	Mass (mg)	Purity (%)	*Physical properties
9	F	14.98	51	16.0	>99	Light yellow ps
10	OMe	18.43	24	11.0	>99	Dark grey ps
11	NH <sub>2</sub>	17.92	61	26.5	>99	Burnt red ps
12	Ph	12.24	13	6.3	>84	Light brown ps
13	Me	23.65	26	11.3	>99	Bright orange ps
14	C(CH <sub>3</sub> ) <sub>3</sub>	20.21	46	22.1	>99	Light orange ps
15	Cl	25.49	32	14.4	>99	Light brown ps
16	Br	21.29	29	14.2	>99	Light yellow ps
17	H	21.89	59	26.1	>95	Dark brown ps
18	NO <sub>2</sub>	18.48	38	17.4	>99	Brown grainy solid
19	N(CH <sub>3</sub> ) <sub>2</sub>	18.3	41	37.9	>95	Bright teal green ps
20	CF <sub>3</sub>	14.15	43	21.1	>95	Dark brownish grey ps

Based on cyclo-CLLFVY, three peptide derivatives were synthesized and tested alongside the other small molecule inhibitors for binding to HIF-1 $\alpha$ . Microscale thermophoresis (MST), an in-solution assay with full-length HIF-1 $\alpha$  gave promising results for lead structures (see *Table 9.2.*). [<sup>19</sup>F]SFB-c-link-(Ppg)LLFVY had a dissociation constant of  $0.46 \pm 0.20$   $\mu$ M and [<sup>19</sup>F]FPeP4 had a dissociation constant of  $7.8 \pm 3.4$   $\mu$ M in the full-length HIF-1 $\alpha$  MST experiments.

*Table 9.2. Microscale thermophoresis data with full-length HIF-1 $\alpha$ . \*Note: Compound 7 is <85% pure, results are approximate.*

Compound	X	K <sub>D</sub> ( $\mu$ M)	S/N	Amplitude response
c-(Ppg)LLFVY	N/A	$27.6 \pm 27.0$	7.1	20.3
<b>28</b>	N/A	$0.46 \pm 0.20$	8.7	12
c-CLLFVY	N/A	>1000	161	994.5
Acriflavine	N/A	$0.12 \pm 0.09$	6	55.4
PpgBBN1	N/A	No binding	0.4	N/A
ER-400-583-00	H	$0.32 \pm 0.20$	6	7.4
<b>9</b>	F	$7.8 \pm 3.4$	7.7	78.4
<b>10</b>	OCH <sub>3</sub>	$72.4 \pm 53.1$	7.4	104.3
<b>11*</b>	NH <sub>2</sub>	$47.8 \pm 30.2$	7.4	70.3
<b>12</b>	Ph	>1000	83.5	1054
<b>13</b>	CH <sub>3</sub>	$23.7 \pm 13.1$	7.1	22.8
<b>14</b>	C(CH <sub>3</sub> ) <sub>3</sub>	$77.5 \pm 1.2$	10.3	76.5
<b>15</b>	Cl	No binding	5.2	N/A
<b>16</b>	Br	No binding	1.0	N/A
<b>18</b>	NO <sub>2</sub>	$31.4 \pm 21.6$	6	17.5
<b>19</b>	N(CH <sub>3</sub> ) <sub>2</sub>	$1.3 \pm 1.0$	8.2	132.5
<b>20</b>	CF <sub>3</sub>	$24.5 \pm 19.2$	6.4	26.9

Complementary in silico analysis of [<sup>19</sup>F]SFB-c-link-(Ppg)LLFVY and [<sup>19</sup>F]FPeP4 binding to HIF-1 $\alpha$  was also completed; giving a predicted binding with intermolecular energy of -11.94 kcal/mol for [<sup>19</sup>F]FPeP4 and -10.11 kcal/mol for [<sup>19</sup>F]SFB-c-link-(Ppg)LLFVY (see *Figure 9.2.*).

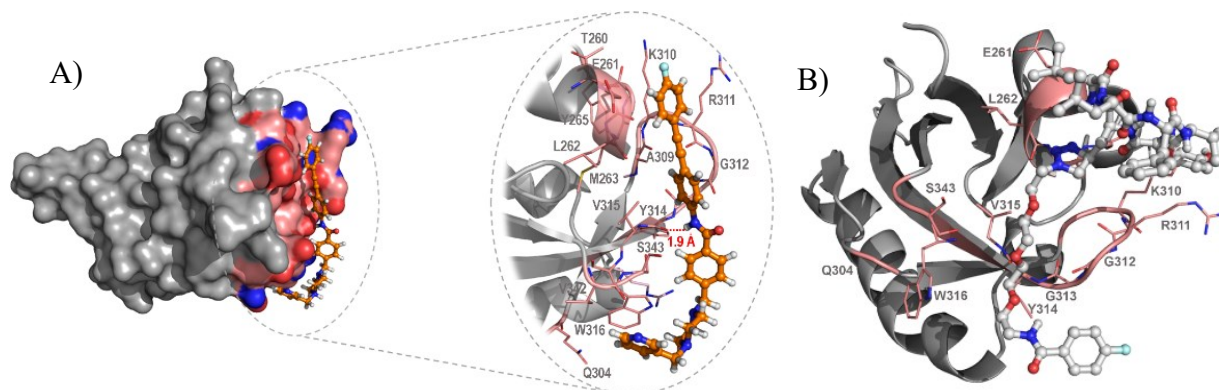


Figure 9.2. A) Molecular docking of compound **9** in HIF-1 $\alpha$ . Predicted binding mode of compound (**9**) in HIF-1 $\alpha$  ( $E_{\text{Intermolecular}} = -11.94$  kcal/mol) and dotted oval highlights key residues of the binding pocket. B) Molecular docking of SFB-link-c-(Ppg)LLFVY **3** in HIF-1 $\alpha$ . Predicted binding mode of [ $^{19}\text{F}$ ]SFB-link-c-(Ppg)LLFVY **28** in HIF-1 $\alpha$  ( $E_{\text{Intermolecular}} = -10.11$  kcal/mol).

## 9.2 Radiolabelling of HIF-1 $\alpha$ targeting compounds and 2-nitroimidazoles

Three 2-nitroimidazole compounds were synthesized using automated and manual radiolabelling procedures. [ $^{18}\text{F}$ ]FMISO was fully synthesized on an automated synthesis unit (ASU) in 140 minutes, with a decay corrected yield of  $58.1 \pm 17.9\%$  ( $n=8$ ) from starting [ $^{18}\text{F}$ ]fluoride (see Figure 9.3.).

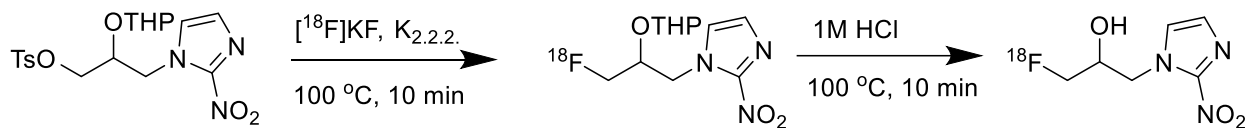


Figure 9.3. Radiosynthesis pathway for the synthesis of [ $^{18}\text{F}$ ]FMISO.

[ $^{18}\text{F}$ ]FAZA was fully synthesized on an automated synthesis unit (ASU) in 120 minutes, with a decay corrected yield of  $24.8 \pm 7.4\%$  ( $n=8$ ) from starting [ $^{18}\text{F}$ ]fluoride (see Figure 9.4.).

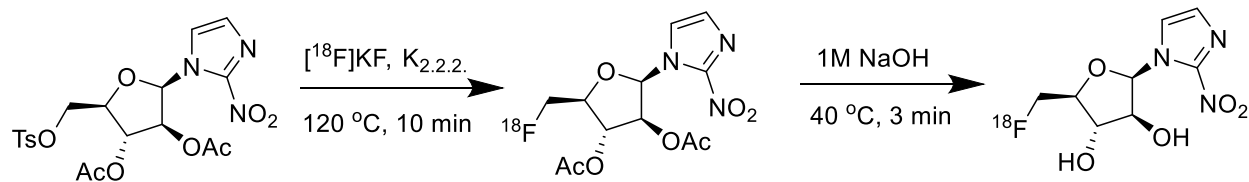


Figure 9.4. Radiosynthesis pathway for the synthesis of [ $^{18}\text{F}$ ]FAZA.

[ $^{18}\text{F}$ ]FBNA was synthesized in a two-step procedure. Firstly, [ $^{18}\text{F}$ ]FBAmine was synthesized on an automated synthesis unit (ASU) in 90 minutes, with a decay corrected yield of  $69.4 \pm 8.8\%$  ( $n=7$ ) from starting [ $^{18}\text{F}$ ]fluoride. Secondly, [ $^{18}\text{F}$ ]FBAmine was manually coupled with (2-Amino-1-imidazolyl)acetic acid precursor using EDC and DIPEA (see Figure 9.5.). Yielding [ $^{18}\text{F}$ ]FBNA in  $47.4 \pm 5.4\%$  decay corrected yield from starting [ $^{18}\text{F}$ ]FBAmine in a total synthesis time of 70 minutes ( $n=8$ ).

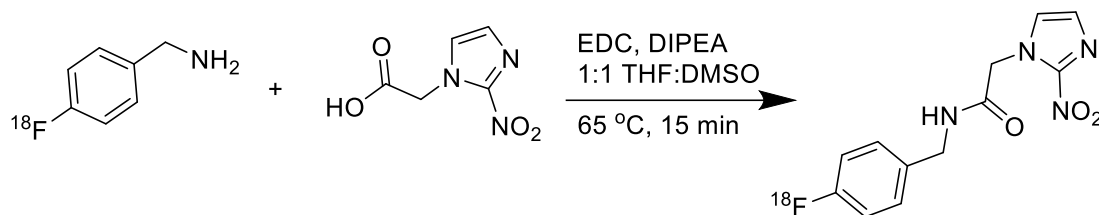
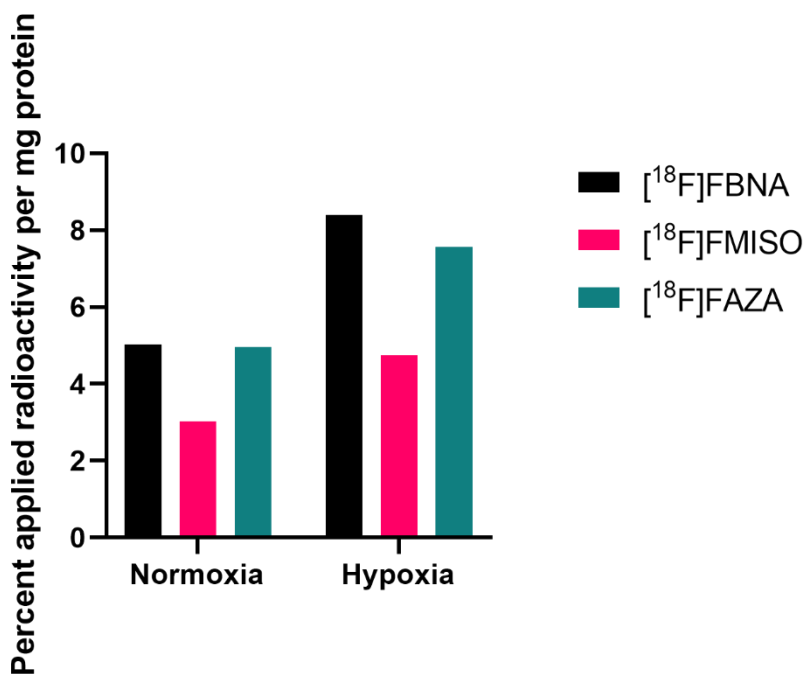


Figure 9.5. Radiosynthesis pathway for the synthesis of [ $^{18}\text{F}$ ]FBNA.

HIF-1 $\alpha$  targeting compound [ $^{18}\text{F}$ ]SFB-c-link-(Ppg)LLFVY was synthesized in a two-step procedure. Firstly, [ $^{18}\text{F}$ ]SFDB was synthesized on an ASU in 58 minutes, with a decay corrected yield of  $67 \pm 23\%$  ( $n=186$ ) from starting [ $^{18}\text{F}$ ]fluoride. Secondly, [ $^{18}\text{F}$ ]SFB was manually coupled with link-c-(Ppg)LLFVY precursor using DIPEA (see Figure 9.6.). Overall yielding [ $^{18}\text{F}$ ]SFB-c-link-(Ppg)LLFVY in  $66.2 \pm 5.4\%$  decay corrected yield from starting [ $^{18}\text{F}$ ]fluoride in a total synthesis time of 60 minutes ( $n=8$ ).



at 180 minutes (see *Figure 9.8*). Overall, the increase in uptake due to hypoxic conditions was between 2-3% applied radioactivity per mg protein for all three nitroimidazole compounds.



*Figure 9.8. Cell uptake of [<sup>18</sup>F]FBNA, [<sup>18</sup>F]FMISO, and [<sup>18</sup>F]FAZA in MDA-MB-231 cells at 180 minutes, under both normoxic and hypoxic (1% O<sub>2</sub>, 5% CO<sub>2</sub>) conditions.*

Cell uptake of HIF-1 $\alpha$  targeting compounds under standard hypoxic/normoxic cell uptake experimental conditions was not successful. Instead, MDA-MB-231 HIF-1 $\alpha$  transfected cell lines were designed, containing three different plasmids. MDA-MB-231 GFP was a blank transfection cell line, MDA-MB-231 18949 overexpresses natural HIF-1 $\alpha$ , and MDA-MB-231 18955 overexpresses a mutant HIF-1 $\alpha$  that is not subject to normoxic degradation. These transfected cell lines were tested with standard PET radiotracers (see *Figure 9.9*.) before cell uptake with [<sup>18</sup>F]SFB-link-c-(PPg)LLFVY and [<sup>18</sup>F]FPeP4.

All PET radiotracers, [<sup>18</sup>F]FDG, [<sup>18</sup>F]FLT and [<sup>18</sup>F]FAZA showed the cells were metabolically active, proliferating and non-hypoxic. [<sup>18</sup>F]SFB-link-c-(Ppg)LLFVY uptake in HIF-1 $\alpha$  transfected cells, showed a statistically significant increase in uptake ( $p < 0.05$ ) at 90 minutes post radiotracer application in both the HIF-1 $\alpha$  overexpressing cell lines versus the GFP blank (see *Figure 9.10.A*).

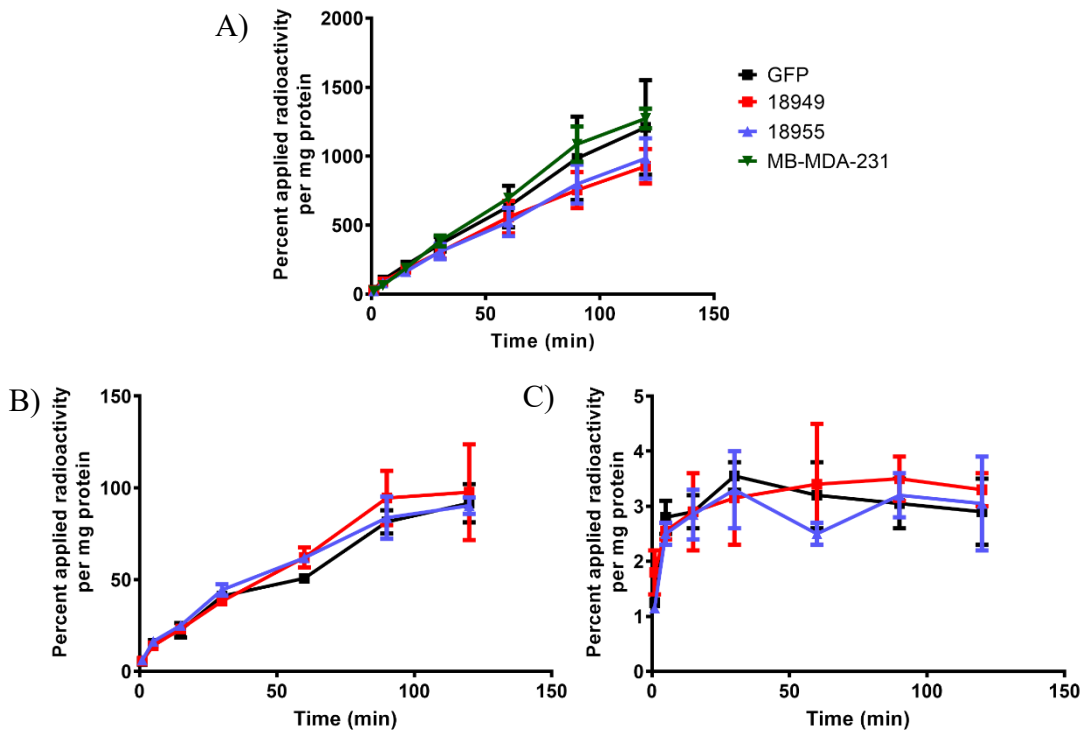


Figure 9.9. Standard radiotracer uptake in HIF-1a transfected MDA-MB-231 cell lines. A)  $[^{18}\text{F}]\text{FDG}$  ( $n=3$ ), B)  $[^{18}\text{F}]\text{FLT}$  ( $n=3$ ), C)  $[^{18}\text{F}]\text{FAZA}$  ( $n=2$ ).

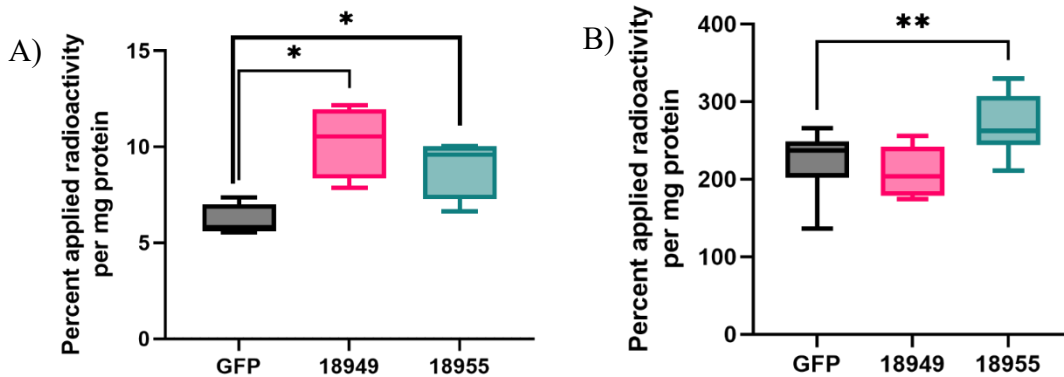
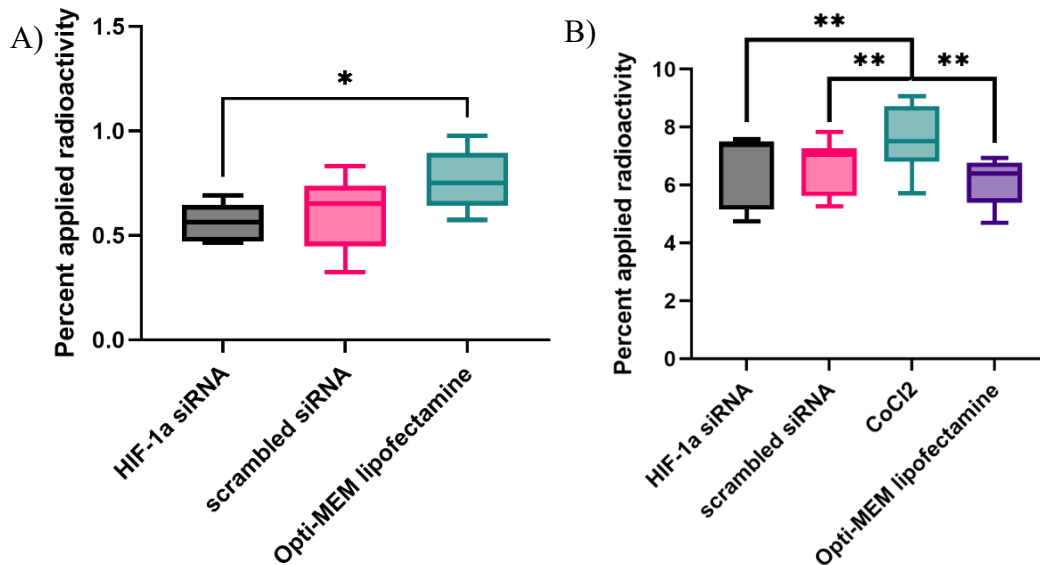


Figure 9.10. Internalized cell uptake in HIF-1a transfected cells. A)  $[^{18}\text{F}]\text{SFB-link-c-(Ppg)LLFVY}$  at 90 min ( $n=4$ ). B)  $[^{18}\text{F}]\text{FPeP4}$  at 60 minutes ( $n=3$ ).

[<sup>18</sup>F]FPeP4 uptake in HIF-1 $\alpha$  transfected cells, also showed a statistically significant increase in uptake ( $p < 0.05$ ) at 60 minutes post radiotracer application in the HIF-1 $\alpha$  overexpressing 18955 cell line versus the GFP blank (see *Figure 9.10.B*). Additionally, uptake of [<sup>18</sup>F]SFB-link-c-(Ppg)LLFVY reached an average of 9.5% applied radioactivity per mg protein in the 18955 cells, whereas [<sup>18</sup>F]FPeP4 reached an average of 275% applied radioactivity per mg protein in the 18955 cells.

Attempting to obtain a negative control for the expression of HIF-1 $\alpha$ , siRNA silencing was completed in normal MDA-MB-231 cells. The protein level of HIF-1 $\alpha$  in the silenced cell line was confirmed with a western blot. Western blot also confirmed the overexpression of HIF-1 $\alpha$  using CoCl<sub>2</sub> (100  $\mu$ M) treatment for 24 hours. [<sup>18</sup>F]SFB-link-c-(Ppg)LLFVY uptake in the Opti-MEM lipofectamine blank was statistically significant ( $p < 0.05$ ) to the HIF-1 $\alpha$  silencing (see *Figure 9.11.A*). [<sup>18</sup>F]FPeP4 uptake in the Opti-MEM lipofectamine blank was statistically significant ( $p < 0.05$ ) to the HIF-1 $\alpha$  silencing (see *Figure 9.11.A*).



*Figure 9.11. Internalized cell uptake in HIF-1 $\alpha$  silenced cells. A) [<sup>18</sup>F]SFB-link-c-(Ppg)LLFVY at 120 min ( $n = 9/3$ ). B) [<sup>18</sup>F]FPeP4 at 120 minutes ( $n = 9/3$ ).*

Since the differences in [ $^{18}\text{F}$ ]SFB-link-c-(Ppg)LLFVY uptake in silenced cells was very small, a HIF-1 $\alpha$  overexpression was introduced into the tests with [ $^{18}\text{F}$ ]FPeP4. [ $^{18}\text{F}$ ]FPeP4 uptake in the CoCl $_2$  treatment was statistically significant ( $p < 0.01$ ) to all other cell treatment groups (see *Figure 9.11.B*). Overall [ $^{18}\text{F}$ ]SFB-link-c-(Ppg)LLFVY appears to be more sensitive to smaller changes in HIF-1 $\alpha$  expression level since differences between HIF-1 $\alpha$  siRNA and Opti-MEM were witnessed. This is likely due to the decreased ability of the peptide to be up-taken by the cells, either by size constraints or lipophilicity. Also [ $^{18}\text{F}$ ]FPeP4 very clearly has a large component of unspecific binding ~5% applied radioactivity in all cell treatments.

#### 9.4 *In vivo metabolic stability and blood distribution of HIF-1 $\alpha$ targeting compounds and 2-nitroimidazoles*

[ $^{18}\text{F}$ ]FPeP4, [ $^{18}\text{F}$ ]FBNA, [ $^{18}\text{F}$ ]FMISO and [ $^{18}\text{F}$ ]FAZA were tested for metabolic stability and blood component distribution. [ $^{18}\text{F}$ ]FPeP4 was found to be metabolically stable up to 30 minutes. [ $^{18}\text{F}$ ]FMISO and [ $^{18}\text{F}$ ]FAZA were also both found to be metabolically stable up to 60 minutes. Lastly, [ $^{18}\text{F}$ ]FBNA was found to be metabolically unstable, with only 65% of intact radiotracer remaining after 60 minutes post-injection (see *Figure 9.12*).

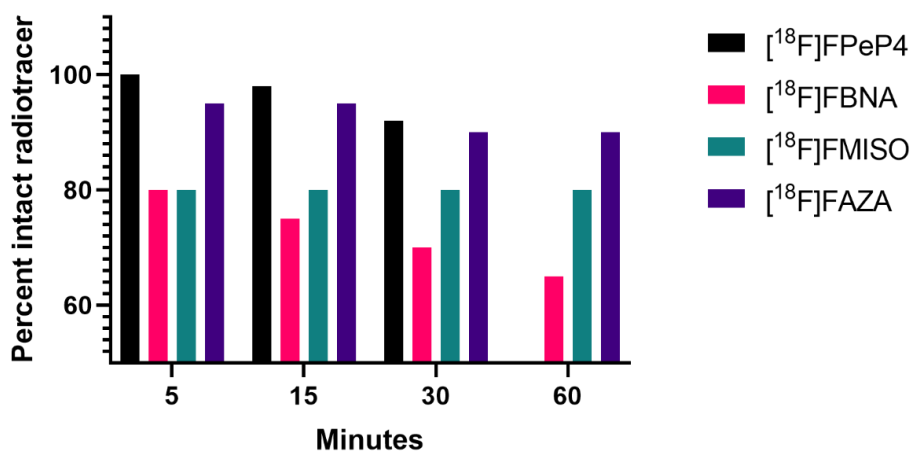


*Figure 9.12. In vivo metabolic stability of [ $^{18}\text{F}$ ]FPeP4, [ $^{18}\text{F}$ ]FBNA, [ $^{18}\text{F}$ ]FAZA, and [ $^{18}\text{F}$ ]FMISO in normal female BALB/C mice.*

Blood component distribution of [ $^{18}\text{F}$ ]FPeP4 was found predominately in the blood cells with 65% of radioactivity, 1% was protein bound and 34% was in the plasma (see *Figure 9.13*). This was very similar to [ $^{18}\text{F}$ ]FBNA in which 55% was blood bound, 5% was protein bound and 45% was in the plasma. Also, [ $^{18}\text{F}$ ]FMISO and [ $^{18}\text{F}$ ]FAZA were very similar with ~50% of the radioactivity in the blood-bound and plasma fractions.

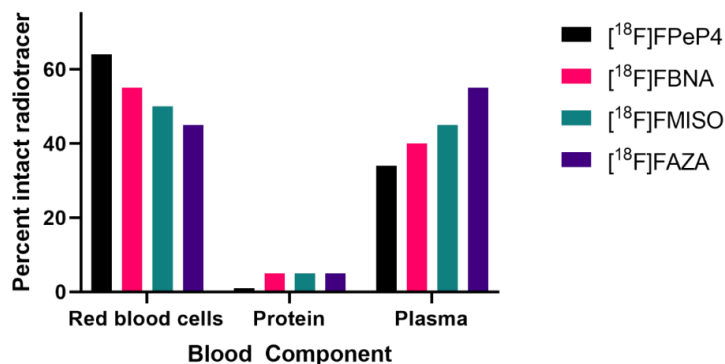


*Figure 9.13. Blood component distribution of [ $^{18}\text{F}$ ]FPeP4, [ $^{18}\text{F}$ ]FBNA, [ $^{18}\text{F}$ ]FAZA, and [ $^{18}\text{F}$ ]FMISO in normal female BALB/C mice.*

### 9.5 *In vivo dynamic PET imaging of HIF-1 $\alpha$ targeting compounds and 2-nitroimidazoles*

[ $^{18}\text{F}$ ]SFB-c-link-(Ppg)LLFVY showed very low uptake (SUV 0.1) in MCF-7 and MDA-MB-231 tumor models, with no differentiation between tumor and muscle tissue (see *Figure 9.14.D*). [ $^{18}\text{F}$ ]FPeP4 also had very low uptake (SUV 0.2) in MCF-7 and MDA-MB-231 tumor models, yet there was a difference between tumor and muscle tissue yielding a TMR of 2 (see *Figure 9.14.C*). [ $^{18}\text{F}$ ]FBNA also had median uptake (SUV 0.5 to 0.75) in MCF-7 and MDA-MB-231 tumor models, with a TMR of 3 in MCF-7 tumors (see *Figure 9.14.E*). [ $^{18}\text{F}$ ]FAZA also had median uptake (SUV 0.65) in MCF-7 and MDA-MB-231 tumor models, with a TMR of 3 (see *Figure 9.14.B*). [ $^{18}\text{F}$ ]FMISO also had the highest tumor uptake (SUV 1.25) in MCF-7 and MDA-MB-231 tumor models, with a TMR of 3.5 (see *Figure 9.14.A*).

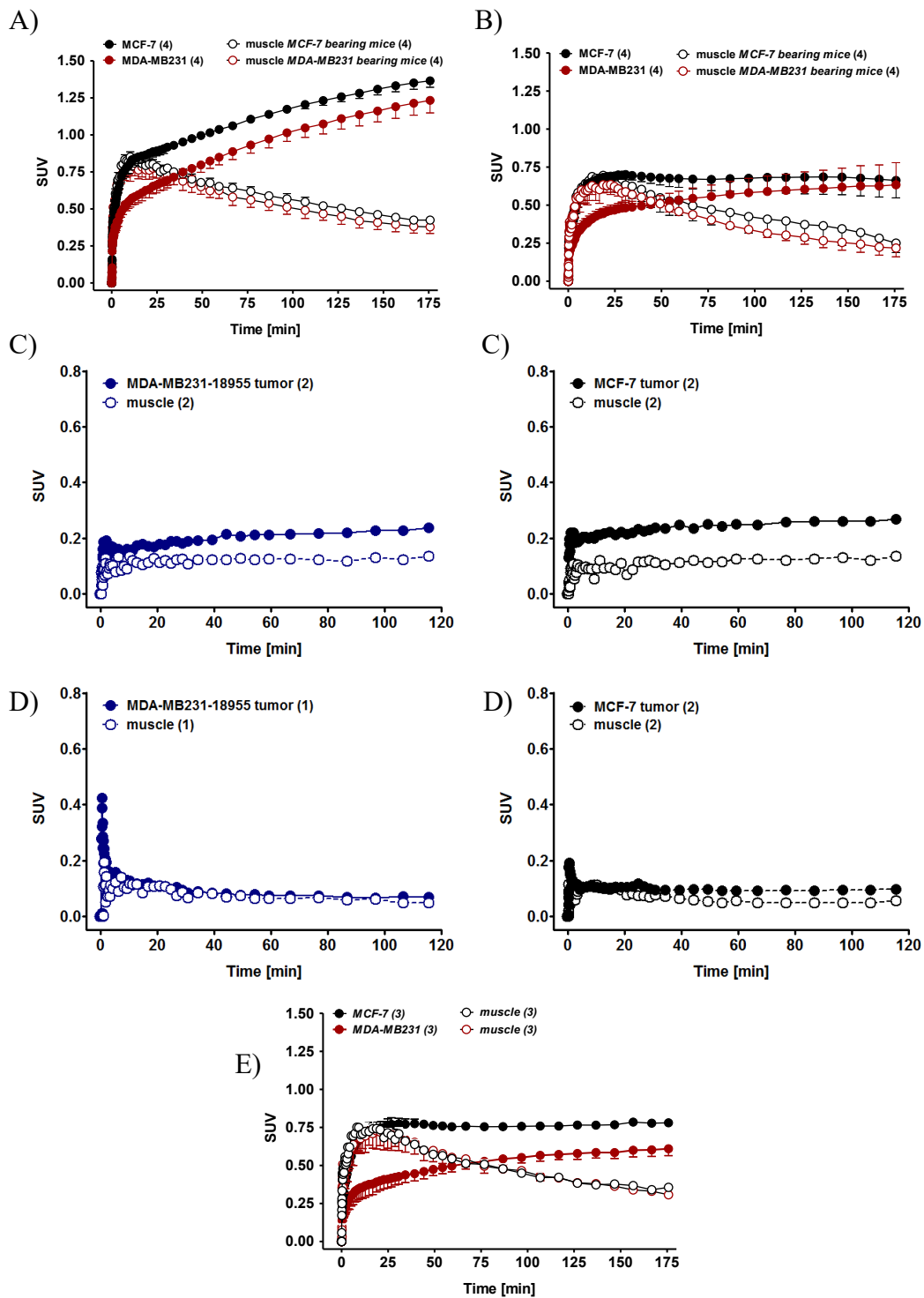


Figure 9.14. Time activity curves for the uptake of hypoxia imaging agents in MDA-MB-231 and MCF-7 tumor-bearing NIH-III mice. A)  $[^{18}\text{F}]\text{FMISO}$ , B)  $[^{18}\text{F}]\text{FAZA}$ , C)  $[^{18}\text{F}]\text{FPeP4}$ , D)  $[^{18}\text{F}]\text{SFB-link-c-(Ppg)LLFVY}$ , E)  $[^{18}\text{F}]\text{FBNA}$ .

Overall, [<sup>18</sup>F]SFB-c-link-(Ppg)LLFVY had very poor pharmacokinetics and was trapped by the liver first pass. [<sup>18</sup>F]FPeP4 had some ability to detect tumor versus muscle tissue, yet the SUV was very low and again the compound has poor pharmacokinetics. [<sup>18</sup>F]FBNA, [<sup>18</sup>F]FMISO and [<sup>18</sup>F]FAZA all performed well *in vivo*, but [<sup>18</sup>F]FMISO was the best-performing 2-nitroimidazole compound in our assays.

The increased lipophilicity of [<sup>18</sup>F]FBNA was designed to aid in the passive diffusion of nitroimidazoles into tissues. Yet the increase in lipophilicity was not enough to overcome the metabolic instability of [<sup>18</sup>F]FBNA *in vivo*.

## **Chapter 10: Conclusion, outlook and significance**

Twelve novel compounds targeting HIF-1 $\alpha$  were synthesized and tested for binding to HIF-1 $\alpha$  using microscale thermophoresis. Lead compounds [ $^{19}\text{F}$ ]SFB-link-c-(Ppg)LLFVY and [ $^{19}\text{F}$ ]FPeP4 were found to have dissociation constants in the  $\mu\text{M}$  range, thus their binding to HIF-1 $\alpha$  was further analyzed *in silico*. From the *in silico* analysis, the binding pocket in HIF-1 $\alpha$  was found to have a more “Y” like shape, that was not being fully utilized. Thus, nine chemical structures were designed and docked using the same *in silico* model of HIF-1 $\alpha$ . These new HIF-1 $\alpha$  binding compounds could be further investigated in future research. Leading to possibly better HIF-1 $\alpha$  binding compounds that may have better pharmacokinetics, as a possible future scientific direction.

Radiosynthesis of [ $^{18}\text{F}$ ]SFB-link-c-(Ppg)LLFVY used previously designed prosthetic groups, but the radiosynthesis of [ $^{18}\text{F}$ ]FPeP4 proved much more difficult. The synthesis of [ $^{18}\text{F}$ ]FPA had to first be accomplished in our research lab. The fully automated synthesis of this important building block opens the ability to radiolabel other compounds using this prosthetic group. Radiochemistry of traditional hypoxia imaging agents [ $^{18}\text{F}$ ]FAZA and [ $^{18}\text{F}$ ]FMISO was adapted for use in our automated synthesis unit. Additionally, the synthesis of the more novel 2-nitroimidazole [ $^{18}\text{F}$ ]FBNA was optimized using EDC-peptide chemistry. All radiochemistry procedures are robust, and reliable and can be easily produced when required using the procedures within this thesis. Thus, allowing compounds for the imaging of hypoxia to be easily produced in other research laboratories.

[ $^{18}\text{F}$ ]SFB-link-c-(Ppg)LLFVY and [ $^{18}\text{F}$ ]FPeP4 demonstrate that they are able to detect changes in HIF-1 $\alpha$  expression through increased cellular uptake *in vitro*. Yet their use *in vivo* is not optimal, due to their large first-pass liver binding. [ $^{18}\text{F}$ ]FPeP4 shows the most promise as a HIF-1 $\alpha$  binding radiotracer, as it does have detectable uptake into tumor tissue. Additionally, [ $^{18}\text{F}$ ]FPeP4 also shows blood-brain barrier passage, thus its use as a brain hypoxia imaging agent should be a future direction for research.

Traditional 2-nitroimidazole [ $^{18}\text{F}$ ]FMISO, using *in vitro* analysis was shown to have a cell uptake of approximately 1.7% applied radioactivity per mg protein increase from normoxia to hypoxia.

This is very low compared to the approximate 4% applied radioactivity per mg protein increase in [<sup>18</sup>F]SFB-link-c-(Ppg)LLFVY to detect increased HIF-1 $\alpha$  expression. Also, even though the increase is [<sup>18</sup>F]FPeP4 is even higher, approximately 25% applied radioactivity per mg protein increase to detect increased HIF-1 $\alpha$  expression. Therefore the targetting of HIF-1 $\alpha$  should not be discounted in future research.

Overall, the downside to imaging HIF-1 $\alpha$  appears to be in the biodistribution of the HIF-1 $\alpha$  targetting compounds. Five minutes post-injection, very little of the radiotracer is left circulating in the bloodstream. Additionally, attempts to improve this have not come to a successful conclusion. Yet, we do have some uptake into tumor tissue with an SUV of 0.2. If this value could be improved further the imaging of HIF-1 $\alpha$  may yet be an achievable target.

Imaging a transcription factor, was always a hard target to reach. Yet here we have shown the very first *in vitro* targetting of HIF-1 $\alpha$ , using HIF-1 $\alpha$  targetting radiolabelled compounds. Although, their full use in positron emission tomography has yet to surpass the use of traditional hypoxia imaging agents such as [<sup>18</sup>F]FMISO; this thesis provides the backbones to further research in targetting the transcription factor of hypoxia-inducible factor 1 alpha.

Contrary to our original hypothesis, traditional 2-nitroimidazole [<sup>18</sup>F]FMISO in this research was found to be the best hypoxia imaging agent *in vivo* for the imaging of breast cancer. This is attributed to its large tumor uptake, high tumor-to-muscle ratio and metabolic stability.

## References

1. Piert, M., et al., *F-18 labeled Fluoroazomycin arabinoside (FAZA): A novel marker of tumor tissue hypoxia*. JOURNAL OF NUCLEAR MEDICINE, 2001. **42**(5): p. 279P-279P.
2. Jerabek, P.A., et al., *Synthesis and biodistribution of 18F-labeled fluoronitroimidazoles: Potential in vivo markers of hypoxic tissue*. International Journal of Radiation Applications and Instrumentation. Part A. Applied Radiation and Isotopes, 1986. **37**(7): p. 599-605.
3. Pomper, M., et al., *What is molecular imaging?* Journal of Nuclear Medicine, 2008. **49**(supplement 1): p. 163P-163P.
4. Wells, R.G., *Instrumentation in molecular imaging*. Journal of Nuclear Cardiology, 2016. **23**(6): p. 1343-1347.
5. Hevesy, G., *The Absorption and Translocation of Lead by Plants: A Contribution to the Application of the Method of Radioactive Indicators in the Investigation of the Change of Substance in Plants*. The Biochemical journal, 1923. **17**(4-5): p. 439-445.
6. Joliot, F. and I. Curie, *Artificial Production of a New Kind of Radio-Element*. Nature, 1934(133): p. 201-202.
7. Henderson, M.C., M.S. Livingston, and E.O. Lawrence, *Artificial Radioactivity Produced by Deuteron Bombardment*. Phys. Rev., 1934. **45**: p. 428-429.
8. Crane, H.R. and C.C. Lauritsen, *Radioactivity from Carbon and Boron Oxide Bombardment with Deutons and the Conversion of Positrons into Radiation*. Phys. Rev., 1934. **45**: p. 430-432.
9. Edwin, M. and M.S. Livingston, *Artificial Radioactivity Produced by the Deuteron Bombardment of Nitrogen*. Phys. Rev., 1935. **47**: p. 452-457.
10. Snell, A.H., *A new radioactive isotope of fluorine*. Phys. Rev., 1937. **51**: p. 143.

11. Tobias, C.A., et al., *THE ELIMINATION OF CARBON MONOXIDE FROM THE HUMAN BODY WITH REFERENCE TO THE POSSIBLE CONVERSION OF CO TO CO<sub>2</sub>*. American Journal of Physiology-Legacy Content, 1945. **145**(2): p. 253-263.
12. Livingood, J.J. and G.T. Seaborg, *Radioactive Isotopes of Iodine*. Phys. Rev., 1938. **54**: p. 775-782.
13. ALLEN, H.C., JR., R.L. LIBBY, and B. CASSEN, *THE SCINTILLATION COUNTER IN CLINICAL STUDIES OF HUMAN THYROID PHYSIOLOGY USING I<sup>131</sup>\**. The Journal of Clinical Endocrinology & Metabolism, 1951. **11**(5): p. 492-511.
14. Blahd, W.H., *Ben cassen and the development of the rectilinear scanner*. Seminars in Nuclear Medicine, 1996. **26**(3): p. 165-170.
15. Anger, H.O., *Scintillation Counters for Radioactive Sample Measurement*. Review of Scientific Instruments, 1951. **22**(12): p. 912-914.
16. Be, M.-M., et al., *Table of Radionuclides*. Monographie BIPM-5. Vol. 8. 2016: Bureau International des Poids et Mesures.
17. Keyes, J.W., et al., *The Humongotron—A Scintillation-Camera Transaxial Tomograph*. Journal of Nuclear Medicine, 1977. **18**(4): p. 381-387.
18. Jaszczak, R.J., R.E. Coleman, and C.B. Lim, *SPECT: Single Photon Emission Computed Tomography*. IEEE Transactions on Nuclear Science, 1980. **27**(3): p. 1137-1153.
19. Anger, H.O. and A. Gottschalk, *LOCALIZATION OF BRAIN TUMORS WITH THE POSITRON SCINTILLATION CAMERA*. J Nucl Med, 1963. **4**: p. 326-30.
20. Phelps, M.E., et al., *Design Considerations for a Positron Emission Transaxial Tomograph (PETT III)*. IEEE Transactions on Nuclear Science, 1976. **23**(1): p. 516-522.
21. Ter-Pogossian, M.M., et al., *A Positron-Emission Transaxial Tomograph for Nuclear Imaging (PETT)*. Radiology, 1975. **114**(1): p. 89-98.

22. Phelps, M.E., et al., *Application of annihilation coincidence detection to transaxial reconstruction tomography*. J Nucl Med, 1975. **16**(3): p. 210-24.
23. James, M.L. and S.S. Gambhir, *A molecular imaging primer: modalities, imaging agents, and applications*. Physiol Rev, 2012. **92**(2): p. 897-965.
24. Advisory, C.C.S.s. and C.o.C. Statistics, *Canadian Cancer Statistics 2014*. 2014, Canadian Cancer Society: Toronto, ON.
25. Yersal, O. and S. Barutca, *Biological subtypes of breast cancer: Prognostic and therapeutic implications*. World Journal of Clinical Oncology, 2011. **5**(3): p. 412-424.
26. Heitz, F., et al., *Triple-negative and HER2-overexpressing breast cancers exhibit an elevated risk and an earlier occurrence of cerebral metastases*. European Journal of Cancer, 2009. **45**(16): p. 2792-2798.
27. Avril, N., et al., *Glucose metabolism of breast cancer assessed by 18F-FDG PET: histologic and immunohistochemical tissue analysis*. Journal of Nuclear Medicine, 2001. **42**(0161-5505 (Print)): p. 9-16.
28. Wuest, M., et al., *Radiopharmacological evaluation of 6-deoxy-6-[18F]fluoro-d-fructose as a radiotracer for PET imaging of GLUT5 in breast cancer*. Nuclear Medicine and Biology, 2011. **38**(4): p. 461-475.
29. Woolf, D.K., et al., *Evaluation of FLT-PET-CT as an imaging biomarker of proliferation in primary breast cancer*. Br J Cancer, 2014. **110**(12): p. 2847-2854.
30. van Kruchten, M., et al., *PET imaging of oestrogen receptors in patients with breast cancer*. The Lancet Oncology, 2013. **14**(11): p. e465-e475.
31. Yoon, H.-J., et al., *Correlation of breast cancer subtypes, based on estrogen receptor, progesterone receptor, and HER2, with functional imaging parameters from 68Ga-RGD*

- PET/CT and 18F-FDG PET/CT*. European Journal of Nuclear Medicine and Molecular Imaging, 2014. **41**(8): p. 1534-1543.
32. Trousil, S., et al., *Positron emission tomography imaging with 18F-labeled ZHER2:2891 affibody for detection of HER2 expression and pharmacodynamic response to HER2-modulating therapies*. Clin Cancer Res, 2014. **20**(6): p. 1632-43.
  33. Tamura, K., et al., *64Cu-DOTA-trastuzumab PET imaging in patients with HER2-positive breast cancer*. J Nucl Med, 2013. **54**(11): p. 1869-75.
  34. Grant, F.D., et al., *Skeletal PET with  $^{18}\text{F}$ -Fluoride: Applying New Technology to an Old Tracer*. Journal of Nuclear Medicine, 2008. **49**(1): p. 68.
  35. Hanahan, D. and R.A. Weinberg, *The Hallmarks of Cancer*. Cell, 2000. **100**(1): p. 57-70.
  36. Hanahan, D. and Robert A. Weinberg, *Hallmarks of Cancer: The Next Generation*. Cell, 2011. **144**(5): p. 646-674.
  37. Ido, T., et al., *Labeled 2-deoxy-D-glucose analogs. 18F-labeled 2-deoxy-2-fluoro-D-glucose, 2-deoxy-2-fluoro-D-mannose and 14C-2-deoxy-2-fluoro-D-glucose*. Journal of Labelled Compounds and Radiopharmaceuticals, 1978. **14**(2): p. 175-183.
  38. Grierson, J.R., A.F. Shields, and J.F. Eary, *Development of a Radiosynthesis for 3'-[18F]Fluoro-3'-Deoxy-Nucleosides*. Journal of Labelled Compounds and Radiopharmaceuticals, 1997. **40**(1): p. 60-62.
  39. Nagengast, W.B., et al., *In Vivo VEGF Imaging with Radiolabeled Bevacizumab in a Human Ovarian Tumor Xenograft*. Journal of Nuclear Medicine, 2007. **48**(8): p. 1313.
  40. Balkwill, F.R., M. Capasso, and T. Hagemann, *The tumor microenvironment at a glance*. J Cell Sci, 2012. **125**(Pt 23): p. 5591-6.

41. *Tumor Microenvironment and Cellular Stress: Signaling, Metabolism, Imaging, and Therapeutic Targets*. Advances in Experimental Medicine and Biology. Vol. 772. 2014: Springer.
42. Tian, H., S.L. McKnight, and D.W. Russell, *Endothelial PAS domain protein 1 (EPAS1), a transcription factor selectively expressed in endothelial cells*. Genes Dev, 1997. **11**(1): p. 72-82.
43. Garber, K., *Energy boost: the Warburg effect returns in a new theory of cancer*. J Natl Cancer Inst, 2004. **96**(24): p. 1805-6.
44. Harris, A.L., *Hypoxia — a key regulatory factor in tumour growth*. Nature Reviews Cancer, 2002. **2**(1): p. 38-47.
45. Kizaka-Kondoh, S. and H. Konse-Nagasawa, *Significance of nitroimidazole compounds and hypoxia-inducible factor-1 for imaging tumor hypoxia*. Cancer Science, 2009. **100**(8): p. 1366-1373.
46. Adams, G.E., et al., *Electron-Affinic Sensitization: VII. A Correlation between Structures, One-Electron Reduction Potentials, and Efficiencies of Nitroimidazoles as Hypoxic Cell Radiosensitizers*. Radiation Research, 1976. **67**(1): p. 9-20.
47. Coleman, C.N., *Hypoxic cell radiosensitizers: expectations and progress in drug development*. Int J Radiat Oncol Biol Phys, 1985. **11**(2): p. 323-9.
48. Kennedy, A.S., et al., *Proliferation and hypoxia in human squamous cell carcinoma of the cervix: First report of combined immunohistochemical assays*. International Journal of Radiation Oncology\*Biological\*Physics, 1997. **37**(4): p. 897-905.
49. Dolbier, W.J.R., et al., *[18F]-EF5, a marker for PET detection of hypoxia: synthesis of precursor and a new fluorination procedure*. Applied radiation and isotopes : including data, instrumentation and methods for use in agriculture, industry and medicine, 2001. **54** **1**: p. 73-80.

50. Wada, H., et al., *Synthesis of 1-[2-[18F]fluoro-1-(hydroxymethyl)-ethoxy]methyl-2-nitroimidazole ([18F]FENI), a potential agent for imaging hypoxic tissues by PET.* Journal of Labelled Compounds and Radiopharmaceuticals, 2000. **43**(8): p. 785-793.
51. Shimizu, Y., et al., *A Novel PET Probe “[18F]DiFA” Accumulates in Hypoxic Region via Glutathione Conjugation Following Reductive Metabolism.* Molecular Imaging and Biology, 2019. **21**(1): p. 122-129.
52. Fujibayashi, Y., et al., *Copper-62-ATSM: A New Hypoxia Imaging Agent with High Membrane Permeability and Low Redox Potential.* Journal of Nuclear Medicine, 1997. **38**(7): p. 1155.
53. Chia, K., et al., *Correlation of hypoxia PET tracer uptake with hypoxic radioresistance in cancer cells: PET biomarkers of resistance to stereotactic radiation therapy?* Nuclear Medicine and Biology, 2022. **110-111**: p. 10-17.
54. Collins, J.A., et al., *Relating oxygen partial pressure, saturation and content: the haemoglobin-oxygen dissociation curve.* Breathe (Sheff), 2015. **11**(3): p. 194-201.
55. Chen, X., et al., *XBPI promotes triple-negative breast cancer by controlling the HIF1[agr] pathway.* Nature, 2014. **508**(7494): p. 103-107.
56. Montagner, M., et al., *SHARPI suppresses breast cancer metastasis by promoting degradation of hypoxia-inducible factors.* Nature, 2012. **487**(7407): p. 380-384.
57. *The Cancer Genome Atlas Network. Comprehensive molecular portraits of human breast tumours.* Nature, 2012. **490**(7418): p. 61-70.
58. Bernardi, R. and L. Gianni, *Hallmarks of triple negative breast cancer emerging at last?* Cell Res, 2014. **24**(8): p. 904-905.
59. 2020, N.o.N.M.A. *The Nobel Prize in Physiology or Medicine 2019.* Wed. 18 Mar 2020; Available from: <<https://www.nobelprize.org/prizes/medicine/2019/summary/>>.

60. Carnot, P. and C. Deflandre, *Sur Tactivite hemopoietique du serum*. Compt. rend. Acad. dsc., 1906. **143**: p. 384.
61. Gurney, C.W., et al., *Demonstration of Erythropoietin in Human Plamsa*. The Journal of Clinical Investigation, 1957. **36**(6): p. 896-896.
62. Semenza, G.L., et al., *Human erythropoietin gene expression in transgenic mice: multiple transcription initiation sites and cis-acting regulatory elements*. Molecular and Cellular Biology, 1990. **10**(3): p. 930-938.
63. Semenza, G.L., et al., *Hypoxia-inducible nuclear factors bind to an enhancer element located 3' to the human erythropoietin gene*. Proceedings of the National Academy of Sciences of the United States of America, 1991. **88**(13): p. 5680-5684.
64. Semenza, G.L. and G.L. Wang, *A nuclear factor induced by hypoxia via de novo protein synthesis binds to the human erythropoietin gene enhancer at a site required for transcriptional activation*. Molecular and Cellular Biology, 1992. **12**(12): p. 5447-5454.
65. Wang, G. and G. Semenza, *Desferrioxamine induces erythropoietin gene expression and hypoxia-inducible factor 1 DNA-binding activity: implications for models of hypoxia signal transduction*. Blood, 1993. **82**(12): p. 3610-3615.
66. Wang, G.L. and G.L. Semenza, *General involvement of hypoxia-inducible factor 1 in transcriptional response to hypoxia*. Proceedings of the National Academy of Sciences of the United States of America, 1993. **90**(9): p. 4304-4308.
67. Wang, G.L. and G.L. Semenza, *Characterization of hypoxia-inducible factor 1 and regulation of DNA binding activity by hypoxia*. Journal of Biological Chemistry, 1993. **268**(29): p. 21513-21518.
68. Semenza, G.L., et al., *Transcriptional regulation of genes encoding glycolytic enzymes by hypoxia-inducible factor 1*. Journal of Biological Chemistry, 1994. **269**(38): p. 23757-23763.

69. Semenza, G.L., et al., *Hypoxia Response Elements in the Aldolase A, Enolase 1, and Lactate Dehydrogenase A Gene Promoters Contain Essential Binding Sites for Hypoxia-inducible Factor 1*. *Journal of Biological Chemistry*, 1996. **271**(51): p. 32529-32537.
70. Wang, G.L. and G.L. Semenza, *Purification and Characterization of Hypoxia-inducible Factor 1*. *Journal of Biological Chemistry*, 1995. **270**(3): p. 1230-1237.
71. Wang, G.L., B.H. Jiang, and G.L. Semenza, *Effect of Altered Redox States on Expression and DNA-Binding Activity of Hypoxia-Inducible Factor 1*. *Biochemical and Biophysical Research Communications*, 1995. **212**(2): p. 550-556.
72. Wang, G.L., et al., *Hypoxia-inducible factor 1 is a basic-helix-loop-helix-PAS heterodimer regulated by cellular O<sub>2</sub> tension*. *Proceedings of the National Academy of Sciences of the United States of America*, 1995. **92**(12): p. 5510-5514.
73. Wang, G.L., B.H. Jiang, and G.L. Semenza, *Effect of Protein Kinase and Phosphatase Inhibitors on Expression of Hypoxia-Inducible Factor 1*. *Biochemical and Biophysical Research Communications*, 1995. **216**(2): p. 669-675.
74. Arany, Z., et al., *An Essential Role for p300/CBP in the Cellular Response to Hypoxia*. *Proceedings of the National Academy of Sciences of the United States of America*, 1996. **93**(23): p. 12969-12973.
75. Semenza, G.L., et al., *Assignment of the Hypoxia-Inducible Factor 1 $\alpha$  Gene to a Region of Conserved Synteny on Mouse Chromosome 12 and Human Chromosome 14q*. *Genomics*, 1996. **34**(3): p. 437-439.
76. Jiang, B.-H., et al., *Dimerization, DNA Binding, and Transactivation Properties of Hypoxia-inducible Factor 1*. *Journal of Biological Chemistry*, 1996. **271**(30): p. 17771-17778.
77. Jiang, B.-H., et al., *Transactivation and Inhibitory Domains of Hypoxia-inducible Factor 1 $\alpha$ : MODULATION OF TRANSCRIPTIONAL ACTIVITY BY OXYGEN TENSION*. *Journal of Biological Chemistry*, 1997. **272**(31): p. 19253-19260.

78. Wood, S.M., et al., *The Role of the Aryl Hydrocarbon Receptor Nuclear Translocator (ARNT) in Hypoxic Induction of Gene Expression: STUDIES IN ARNT-DEFICIENT CELLS*. Journal of Biological Chemistry, 1996. **271**(25): p. 15117-15123.
79. Pugh, C.W., et al., *Activation of Hypoxia-inducible Factor-1; Definition of Regulatory Domains within the  $\alpha$  Subunit*. Journal of Biological Chemistry, 1997. **272**(17): p. 11205-11214.
80. Maxwell, P.H., et al., *The tumour suppressor protein VHL targets hypoxia-inducible factors for oxygen-dependent proteolysis*. Nature, 1999. **399**(6733): p. 271-275.
81. Duan, D., et al., *Inhibition of transcription elongation by the VHL tumor suppressor protein*. Science, 1995. **269**(5229): p. 1402-1406.
82. Pause, A., et al., *The von Hippel-Lindau tumor-suppressor gene product forms a stable complex with human CUL-2, a member of the Cdc53 family of proteins*. Proceedings of the National Academy of Sciences of the United States of America, 1997. **94**: p. 2156-61.
83. Kamura, T., et al., *Rbx1, a Component of the VHL Tumor Suppressor Complex and SCF Ubiquitin Ligase*. Science, 1999. **284**(5414): p. 657-661.
84. Aso, T., et al., *Elongin (SIII): a multisubunit regulator of elongation by RNA polymerase II*. Science, 1995. **269**(5229): p. 1439-1443.
85. Clifford, S.C., et al., *The pVHL-associated SCF ubiquitin ligase complex: Molecular genetic analysis of elongin B and C, Rbx1 and HIF-1 $\alpha$  in renal cell carcinoma*. Oncogene, 2001. **20**(36): p. 5067-5074.
86. Wiener, C.M., G. Booth, and G.L. Semenza, *In Vivo Expression of mRNAs Encoding Hypoxia-Inducible Factor 1*. Biochemical and Biophysical Research Communications, 1996. **225**(2): p. 485-488.

87. Ebert, B.L., J.D. Firth, and P.J. Ratcliffe, *Hypoxia and Mitochondrial Inhibitors Regulate Expression of Glucose Transporter-1 via Distinct Cis-acting Sequences*. *Journal of Biological Chemistry*, 1995. **270**(49): p. 29083-29089.
88. Forsythe, J.A., et al., *Activation of vascular endothelial growth factor gene transcription by hypoxia-inducible factor 1*. *Molecular and Cellular Biology*, 1996. **16**(9): p. 4604-4613.
89. Lee, P.J., et al., *Hypoxia-inducible Factor-1 Mediates Transcriptional Activation of the Heme Oxygenase-1 Gene in Response to Hypoxia*. *Journal of Biological Chemistry*, 1997. **272**(9): p. 5375-5381.
90. Tan, E.Y., et al., *The key hypoxia regulated gene CAIX is upregulated in basal-like breast tumours and is associated with resistance to chemotherapy*. *Br J Cancer*, 0000. **100**(2): p. 405-411.
91. Pylayeva-Gupta, Y., E. Grabocka, and D. Bar-Sagi, *RAS oncogenes: weaving a tumorigenic web*. *Nat Rev Cancer*, 2011. **11**(11): p. 761-74.
92. Dang, C.V., et al., *The interplay between MYC and HIF in cancer*. *Nat Rev Cancer*, 2008. **8**(1): p. 51-56.
93. Qing, G., et al., *Combinatorial regulation of neuroblastoma tumor progression by N-Myc and hypoxia inducible factor HIF-1alpha*. *Cancer Res*, 2010. **70**(24): p. 10351-61.
94. Kim, J.W., et al., *HIF-1-mediated expression of pyruvate dehydrogenase kinase: a metabolic switch required for cellular adaptation to hypoxia*. *Cell Metab*, 2006. **3**(3): p. 177-85.
95. Zhang, H., et al., *HIF-1 inhibits mitochondrial biogenesis and cellular respiration in VHL-deficient renal cell carcinoma by repression of C-MYC activity*. *Cancer Cell*, 2007. **11**(5): p. 407-20.

96. Jensen, K.S., et al., *FoxO3A promotes metabolic adaptation to hypoxia by antagonizing Myc function*. *Embo j*, 2011. **30**(22): p. 4554-70.
97. Zhang, H., et al., *Mitochondrial autophagy is an HIF-1-dependent adaptive metabolic response to hypoxia*. *J Biol Chem*, 2008. **283**(16): p. 10892-903.
98. Fukuda, R., et al., *HIF-1 regulates cytochrome oxidase subunits to optimize efficiency of respiration in hypoxic cells*. *Cell*, 2007. **129**(1): p. 111-22.
99. Favaro, E., et al., *MicroRNA-210 Regulates Mitochondrial Free Radical Response to Hypoxia and Krebs Cycle in Cancer Cells by Targeting Iron Sulfur Cluster Protein ISCU*. *PLoS ONE*, 2010. **5**(4): p. e10345.
100. Chiavarina, B., et al., *Metabolic reprogramming and two-compartment tumor metabolism: opposing role(s) of HIF1alpha and HIF2alpha in tumor-associated fibroblasts and human breast cancer cells*. *Cell Cycle*, 2012. **11**(17): p. 3280-9.
101. Kilic Eren, M. and V. Tabor, *The Role of Hypoxia Inducible Factor-1 Alpha in Bypassing Oncogene-Induced Senescence*. *PLoS ONE*, 2014. **9**(7): p. e101064.
102. Azam, F., S. Mehta, and A.L. Harris, *Mechanisms of resistance to antiangiogenesis therapy*. *Eur J Cancer*, 2010. **46**(8): p. 1323-32.
103. Moeller, B.J. and M.W. Dewhirst, *HIF-1 and tumour radiosensitivity*. *Br J Cancer*, 2006. **95**(1): p. 1-5.
104. Xia, Y., H.K. Choi, and K. Lee, *Recent advances in hypoxia-inducible factor (HIF)-1 inhibitors*. *Eur J Med Chem*, 2012. **49**: p. 24-40.
105. Greenberger, L.M., et al., *A RNA antagonist of hypoxia-inducible factor-1 $\alpha$ , EZN-2968, inhibits tumor cell growth*. *Molecular Cancer Therapeutics*, 2008. **7**(11): p. 3598-3608.

106. Lee, K., et al., *Acridine inhibits HIF-1 dimerization, tumor growth, and vascularization*. Proceedings of the National Academy of Sciences, 2009. **106**(42): p. 17910-17915.
107. Miranda, E., et al., *A Cyclic Peptide Inhibitor of HIF-1 Heterodimerization That Inhibits Hypoxia Signaling in Cancer Cells*. Journal of the American Chemical Society, 2013. **135**(28): p. 10418-10425.
108. De, M.S., et al., *Use of diketodithiopiperazine antibiotics for the preparation of antiangiogenic pharmaceutical compositions*. 2007, Google Patents.
109. Okamoto, K., et al., *Microregional antitumor activity of a small-molecule hypoxia-inducible factor 1 inhibitor*. International Journal of Molecular Medicine, 2012. **29**(4): p. 541-549.
110. Dulbecco, R. and M. Vogt *PLAQUE FORMATION AND ISOLATION OF PURE LINES WITH POLIOMYELITIS VIRUSES*. Journal of Experimental Medicine, 1954. **99**(2): p. 167-182.
111. Richter, S., et al., *Synthesis and radiopharmacological evaluation of a high-affinity and metabolically stabilized 18F-labeled bombesin analogue for molecular imaging of gastrin-releasing peptide receptor-expressing prostate cancer*. Nuclear Medicine and Biology, 2013. **40**(8): p. 1025-1034.
112. Fothergill, J.E. and R.C. Nairn, *Purification of Fluorescent Protein Conjugates : Comparison of Charcoal and 'Sephadex'*. Nature, 1961. **192**(4807): p. 1073-1074.
113. Yan, Q., et al., *The hypoxia-inducible factor 2alpha N-terminal and C-terminal transactivation domains cooperate to promote renal tumorigenesis in vivo*. Mol Cell Biol, 2007. **27**(6): p. 2092-102.
114. Kondo, K., et al., *Inhibition of HIF is necessary for tumor suppression by the von Hippel-Lindau protein*. Cancer Cell, 2002. **1**(3): p. 237-246.

115. Nario, A.P., et al., *Synthesis of a 2-nitroimidazole derivative N-(4-[18F]fluorobenzyl)-2-(2-nitro-1H-imidazol-1-yl)-acetamide ([18 F]FBNA) as PET radiotracer for imaging tumor hypoxia*. EJNMMI Radiopharmacy and Chemistry, 2022. **7**(1): p. 13.
116. Way, J. and F. Wuest, *Fully automated synthesis of 4-[18F]fluorobenzylamine based on borohydride/NiCl<sub>2</sub> reduction*. Nuclear Medicine and Biology, 2013. **40**(3): p. 430-436.
117. Hamann, I., et al., *Expression and function of hexose transporters GLUT1, GLUT2, and GLUT5 in breast cancer—effects of hypoxia*. The FASEB Journal, 2018. **32**(9): p. 5104-5118.
118. Way, J.D. and F. Wuest, *Automated radiosynthesis of no-carrier-added 4-[18F]fluoroiodobenzene: a versatile building block in 18F radiochemistry*. Journal of Labelled Compounds and Radiopharmaceuticals, 2014. **57**(2): p. 104-109.
119. Way, J.D., C. Bergman, and F. Wuest, *Sonogashira cross-coupling reaction with 4-[18F]fluoroiodobenzene for rapid 18F-labelling of peptides*. Chemical Communications, 2015. **51**(18): p. 3838-3841.
120. Zhong, H., et al., *The copper-free Sonogashira cross-coupling reaction promoted by palladium complexes of nitrogen-containing chelating ligands in neat water at room temperature*. Dalton Transactions, 2014. **43**(5): p. 2098-2103.
121. Hierso, J.-C., et al., *Catalytic Efficiency of a New Tridentate Ferrocenyl Phosphine Auxiliary: Sonogashira Cross-Coupling Reactions of Alkynes with Aryl Bromides and Chlorides at Low Catalyst Loadings of 10<sup>-1</sup> to 10<sup>-4</sup> Mol %*. Organic Letters, 2004. **6**(20): p. 3473-3476.
122. Okamoto, N., M. Ishikura, and R. Yanada, *Cleavage of Carbon–Carbon Triple Bond: Direct Transformation of Alkynes to Nitriles*. Organic Letters, 2013. **15**(11): p. 2571-2573.

123. Nagao, S., et al., *Synthesis and structure–activity relationships of novel, potent, orally active hypoxia-inducible factor-1 inhibitors*. *Bioorganic & Medicinal Chemistry*, 2014. **22**(19): p. 5513-5529.
124. Sharma, S.K., et al., *Synthesis and pre-clinical evaluation of an (18)F-labeled single-chain antibody fragment for PET imaging of epithelial ovarian cancer*. *American Journal of Nuclear Medicine and Molecular Imaging*, 2016. **6**: p. 185-98.
125. Mueller, D., et al., *Radiolabeling of DOTA-like conjugated peptides with generator-produced 68Ga and using NaCl-based cationic elution method*. *Nature Protocols*, 2016. **11**: p. 1057.
126. Berchel, M., et al., *Modular Construction of Fluorescent Lipophosphoramidates by Click Chemistry*. *European Journal of Organic Chemistry*, 2011. **2011**(31): p. 6294-6303.
127. Wuest, M., et al., *Targeting lysyl oxidase for molecular imaging in breast cancer*. *Breast Cancer Res*, 2015. **17**(1): p. 107.

## **Appendix**

### *Appendix Table of Contents*

<u>p-((4-((3-Pyridyl)methyl)-1-piperazinyl)methyl)benzoic acid, compound 1, supporting data.</u>	222
Figure S1. LR-MS for compound 1.....	222
Figure S2. <sup>1</sup> H-NMR for compound 1.....	222
Figure S3. <sup>13</sup> C-NMR for compound 1.....	222
<u>N-p-Ethynylphenylp-(chloromethyl)benzamide, compound 3, supporting data.</u>	223
Figure S4. LR-MS for compound 3.....	223
Figure S5. HR-MS for compound 3.....	223
Figure S6. <sup>1</sup> H-NMR for compound 3.....	224
Figure S7. <sup>13</sup> C-NMR for compound 3.....	224
<u>N-p-Ethynylphenylp-((4-((3-pyridyl)methyl)-1-piperazinyl)methyl)benzamide, compound 4 supporting data.</u>	225
Figure S8. LR-MS for compound 4.....	225
Figure S9. HR-MS for compound 4.....	225
Figure S10. <sup>1</sup> H-NMR for compound 4.....	226
Figure S11. <sup>13</sup> C-NMR for compound 4. ....	226
<u>p-(2-(p-Fluorophenyl)ethynyl)aniline, compound 6 supporting data.</u>	227
Figure S12. LR-MS for compound 6.....	227
Figure S13. HR-MS for compound 6.....	227

Figure S14. <sup>1</sup> H-NMR for compound <b>6</b> .....	228
Figure S15. <sup>13</sup> C-NMR for compound <b>6</b> .....	228
Figure S16. <sup>19</sup> F-NMR for compound <b>6</b> .....	229
<u>p-(2-(p-Fluorophenyl)ethynyl)aniline, compound <b>7</b> supporting data.</u> .....	230
Figure S17. LR-MS for compound <b>7</b> .....	230
Figure S18. HR-MS for compound <b>7</b> .....	230
Figure S19. <sup>1</sup> H-NMR for compound <b>7</b> .....	231
Figure S20. <sup>13</sup> C-NMR for compound <b>7</b> .....	231
<u>N-p-Iodophenylp-((4-((3-pyridyl)methyl)-1-piperazinyl)methyl)benzamide, compound <b>8</b> supporting data.</u> .....	232
Figure S21. LR-MS for compound <b>8</b> .....	232
Figure S22. HR-MS for compound <b>8</b> .....	232
Figure S23. <sup>1</sup> H-NMR for compound <b>8</b> .....	233
Figure S24. <sup>13</sup> C-NMR for compound <b>8</b> .....	233
Figure S25. Analytical HPLC for compound <b>8</b> .....	234
<u>N-(4-(1-ethynyl-4-fluorophenyl)phenyl)-4-((4-(pyridine-3-ylmethyl)piperazin-1- yl)methyl)benzamide ,compound <b>9</b> supporting data.</u> .....	235
Figure S26. LR-MS for compound <b>9</b> .....	235
Figure S27. HR-MS for compound <b>9</b> .....	235
Figure S28. <sup>1</sup> H-NMR for compound <b>9</b> .....	236

Figure S29. <sup>13</sup> C-NMR for compound <b>9</b> .	236
Figure S30. <sup>19</sup> F-NMR for compound <b>9</b> .	237
Figure S31. Analytical HPLC for compound <b>9</b> .	237
<u>N-(4-(4-ethynylanisole)phenyl)-4-((4-(pyridine-3-ylmethyl)piperazin-1-yl) methyl) benzamide, compound <b>10</b>, supporting data.</u>	238
Figure S32. LR-MS for compound <b>10</b> .	238
Figure S33. HR-MS for compound <b>10</b> .	238
Figure S34. <sup>1</sup> H-NMR for compound <b>10</b> .	239
Figure S35. <sup>13</sup> C-NMR for compound <b>10</b> .	239
Figure S36. Analytical HPLC for compound <b>10</b> .	240
<u>N-(4-(4-ethynylaniline)phenyl)-4-((4-(pyridine-3-ylmethyl)piperazin-1-yl) methyl) benzamide, compound <b>11</b>, supporting data.</u>	241
Figure S37. LR-MS for compound <b>11</b> .	241
Figure S38. <sup>1</sup> H-NMR for compound <b>11</b> .	241
Figure S39. <sup>13</sup> C-NMR for compound <b>11</b> .	242
Figure S40. Analytical HPLC for compound <b>11</b> .	242
<u>N-(4-(4-ethynylbiphenyl)phenyl)-4-((4-(pyridine-3-ylmethyl)piperazin-1-yl) methyl) benzamide, compound <b>12</b>, supporting data.</u>	243
Figure S41. LR-MS for compound <b>12</b> .	243
Figure S42. <sup>1</sup> H-NMR for compound <b>12</b> .	243

Figure S43. $^{13}\text{C}$ -NMR for compound <b>12</b> . .....	244
Figure S44. Analytical HPLC for compound <b>12</b> . .....	244
<u>N-(4-(4-ethynyltoluene)phenyl)-4-((4-(pyridine-3-ylmethyl)piperazin-1-yl) methyl) benzamide, compound <b>13</b>, supporting data.</u> .....	245
Figure S45. LR-MS for compound <b>13</b> . .....	245
Figure S46. $^1\text{H}$ -NMR for compound <b>13</b> . .....	245
Figure S47. $^{13}\text{C}$ -NMR for compound <b>13</b> . .....	246
Figure S48. Analytical HPLC for compound <b>13</b> . .....	246
<u>N-(4-(4-tert-butylphenylacetylene)phenyl)-4-((4-(pyridine-3-ylmethyl) piperazin-1-yl)methyl)benzamide, compound <b>14</b>, supporting data.</u> .....	247
Figure S49. LR-MS for compound <b>14</b> . .....	247
Figure S50. $^1\text{H}$ -NMR for compound <b>14</b> . .....	247
Figure S51. $^{13}\text{C}$ -NMR for compound <b>14</b> . .....	248
Figure S52. Analytical HPLC for compound <b>14</b> . .....	248
<u>N-(4-(1-chloro-4-ethynylbenzene)phenyl)-4-((4-(pyridine-3-ylmethyl) piperazin-1-yl)methyl)benzamide, compound <b>15</b>, supporting data.</u> .....	249
Figure S53. LR-MS for compound <b>15</b> . .....	249
Figure S54. $^1\text{H}$ -NMR for compound <b>15</b> . .....	249
Figure S55. $^{13}\text{C}$ -NMR for compound <b>15</b> . .....	250
Figure S56. Analytical HPLC for compound <b>15</b> . .....	250

<u>N-(4-(1-bromo-4-ethynylbenzene)phenyl)-4-((4-(pyridine-3-ylmethyl) piperazin-1-yl)methyl)benzamide, compound 16, supporting data.....</u>	251
Figure S57. LR-MS for compound 16.....	251
Figure S58. <sup>1</sup> H-NMR for compound 16.....	251
Figure S59. <sup>13</sup> C-NMR for compound 16.....	252
Figure S60. Analytical HPLC for compound 16.....	252
<u>N-(4-(Phenylethynyl)phenyl)-4-([4-(3-pyridinyl-methyl)-1-piperazinyl)methyl) benzamide compound 17, (ER-400-583-00) , supporting data.....</u>	253
Figure S61. LR-MS for ER-400-583-00.....	253
Figure S62. <sup>1</sup> H-NMR for ER-400-583-00.....	253
Figure S63. <sup>13</sup> C-NMR for ER-400-583-00.....	254
Figure S64. Analytical HPLC for ER-400-583-00.....	254
<u>N-(4-(1-ethynyl-4-nitrobenzene)phenyl)-4-((4-(pyridine-3-ylmethyl) piperazin-1-yl)methyl)benzamide, compound 18, supporting data.....</u>	255
Figure S65. LR-MS for compound 18.....	255
Figure S66. <sup>1</sup> H-NMR for compound 18.....	255
Figure S67. <sup>13</sup> C-NMR for compound 18.....	256
Figure S68. Analytical HPLC for compound 18.....	256
<u>N-(4-(4-ethynyl-N,N-dimethylaniline)phenyl)-4-((4-(pyridine-3-ylmethyl) piperazin-1-yl)methyl)benzamide, compound 19, supporting data.....</u>	257

Figure S69. LR-MS for compound <b>19</b> .	257
Figure S70. <sup>1</sup> H-NMR for compound <b>19</b> .	257
Figure S71. <sup>13</sup> C-NMR for compound <b>19</b> .	258
Figure S72. Analytical HPLC for compound <b>19</b> .	258
<u>N-(4-(1-ethynyl-4-(trifluoromethyl)benzene)-phenyl)-4-((4-(pyridine-3-ylmethyl) piperazin-1-yl)methyl)-benzamide, compound <b>20</b>, supporting data.</u>	259
Figure S73. LR-MS for compound <b>20</b> .	259
Figure S74. <sup>1</sup> H-NMR for compound <b>20</b> .	259
Figure S75. <sup>13</sup> C-NMR for compound <b>20</b> .	260
Figure S76. Analytical HPLC for compound <b>20</b> .	260
<u>l-(PPg)LLFVY, compound <b>21</b>, supporting data.</u>	261
Figure S77. MALDI spectra for l-(PPg)LLFVY.	261
Figure S78. Crude HPLC chromatogram of l-(PPg)LLFVY, product is 28.9 minutes.	261
<u>l-C(StBu)LLFVY, compound <b>22</b>, supporting data.</u>	262
Figure S79. MALDI spectra for l-C(StBu)LLFVY.	262
Figure S80. Crude HPLC chromatogram of l-C(StBu)LLFVY, product is 29.5 minutes.	262
<u>c-(Ppg)LLFVY, compound <b>23</b>, supporting data.</u>	263
Figure S81. MALDI spectra for c-(Ppg)LLFVY.	263
Figure S82. Crude HPLC chromatogram of c-(PPg)LLFVY, product is 35 minutes.	263

Figure S83. Pure HPLC UV spectra at 210 nm, including LCMS for c-(Ppg)LLFVY.....	264
<u>c-C(StBu)LLFVY, compound 24, supporting data.....</u>	265
Figure S84. Crude HPLC chromatogram of c-C(StBu)LLFVY, product is 38.9 minutes. ....	265
Figure S85. HPLC UV spectra at 254nm, including LCMS for c-C(StBu)LLFVY.....	265
<u>c-CLLFVY, compound 25 supporting data. ....</u>	266
Figure S86. LC-MS for c-CLLFVY. ....	266
Figure S87. Crude HPLC chromatogram of c-CLLFVY, product is 43.8 minutes.....	266
<u>link-c-(Ppg)LLFVY, compound 26, supporting data. ....</u>	267
Figure S88. MALDI spectra for link-c-(Ppg)LLFVY. ....	267
Figure S89. Crude HPLC chromatogram of link-c-(PPg)LLFVY, product is 26.4 minutes.....	267
<u>azido-PEG-4-fluorobenzamide, compound 27, supporting data.....</u>	268
Figure S90. LR-MS for azido-PEG-4-fluorobenzamide.....	268
<u>[<sup>19</sup>F]SFB-link-c-(Ppg)LLFVY, compound 28, supporting data. ....</u>	269
Figure S91. HPLC UV spectra at 254nm, including LCMS for [ <sup>19</sup> F]SFB-link-c-(Ppg)LLFVY. .....	269
Figure S92. Crude HPLC chromatogram of [ <sup>19</sup> F]SFB-link-c-(Ppg)LLFVY, product is 34.7 minutes.....	269
<u>NOTA-Bn-SCN-link-c-(Ppg)LLFVY, compound 29, supporting data.....</u>	270
Figure S93. HPLC purification for NOTA-Bn-SCN-link-c-(Ppg)LLFVY. ....	270
Figure S94. MALDI-MS for NOTA-Bn-SCN-link-c-(Ppg)LLFVY.....	270

<u>DOTA-link-c-(Ppg)LLFVY, compound 30, supporting data</u> .....	271
Figure S95. HPLC purification for DOTA-link-c-(Ppg)LLFVY. ....	271
Figure S96. LR-MS for DOTA-link-c-(Ppg)LLFVY. ....	271
<u>[<sup>69</sup>Ga]-DOTA-link-c-(Ppg)LLFVY, compound 31, supporting data</u> .....	272
Figure S97. HPLC purification for [ <sup>69</sup> Ga]-DOTA-link-c-(Ppg)LLFVY. ....	272
Figure S98. LR-MS for [ <sup>69</sup> Ga]-DOTA-link-c-(Ppg)LLFVY.....	272
<u>[<sup>68</sup>Ga]-DOTA-link-c-(Ppg)LLFVY, JDW00816, supporting data</u> .....	273
Figure S99. Typical HPLC example of [ <sup>68</sup> Ga]DOTA-link-c-(Ppg)LLFVY crude reaction. ....	273
Figure S100. Co-injection of [ <sup>68</sup> Ga]DOTA-link-c-(Ppg)LLFVY and [ <sup>69</sup> Ga]DOTA-link-c-(Ppg)LLFVY.....	273
<u>N-[2-(2-{2-(2-Azidoethoxy)ethoxy}ethoxy)ethyl]-7-nitro-2,1,3-benzoxadiazol-4-amine, compound 32, supporting data</u> .....	274
Figure S101. <sup>1</sup> H-NMR for compound 32.....	274
Figure S102. <sup>13</sup> C-NMR for compound 32. ....	274
<u>NBD-link-c-(Ppg)LLFVY, compound 33, supporting data</u> .....	275
Figure S103. LR-MS for compound 33. ....	275
Figure S104. HR-MS for compound 33.....	275
<u>(p-Ethynylphenyl)trimethylammonium, compound 34, supporting data</u> .....	276
Figure S105. LR-MS for compound 34. ....	276
Figure S106. <sup>1</sup> H-NMR for compound 34.....	276

Figure S107. <sup>13</sup> C-NMR for compound <b>34</b> . .....	277
<u>p-(2-(p-(p-((4-[3-Pyridyl)methyl]-1-piperazinyl)methyl)benzylamino]phenyl)ethynyl)(trimethylammonio)benzene, compound <b>35</b>, supporting data. ....</u>	278
Figure S108. LR-MS for compound <b>35</b> . .....	278
Figure S109. <sup>1</sup> H-NMR for compound <b>35</b> . .....	278
Figure S110. <sup>13</sup> C-NMR for compound <b>35</b> . .....	279
<u>1-((4-fluorophenyl)ethynyl)-2,4-dimethoxybenzene, compound <b>36</b>, supporting data. ....</u>	280
Figure S111. LR-MS for compound <b>36</b> . .....	280
Figure S112. <sup>1</sup> H-NMR for compound <b>36</b> . .....	280
Figure S113. <sup>19</sup> F-NMR for compound <b>36</b> . .....	281
Figure S114. <sup>13</sup> C-NMR for compound <b>36</b> . .....	281
<u>2-amino-4-[(4-fluorophenyl)ethynyl]benzoic acid, compound <b>37</b>, supporting data. ....</u>	282
Figure S115. LR-MS for compound <b>37</b> . .....	282
Table S1. Intensity calculations from HIF-1 $\alpha$ silencing in MDA-MB-231 cells. ....	283

p-((4-((3-Pyridyl)methyl)-1-piperazinyl)methyl)benzoic acid, compound 1, supporting data.

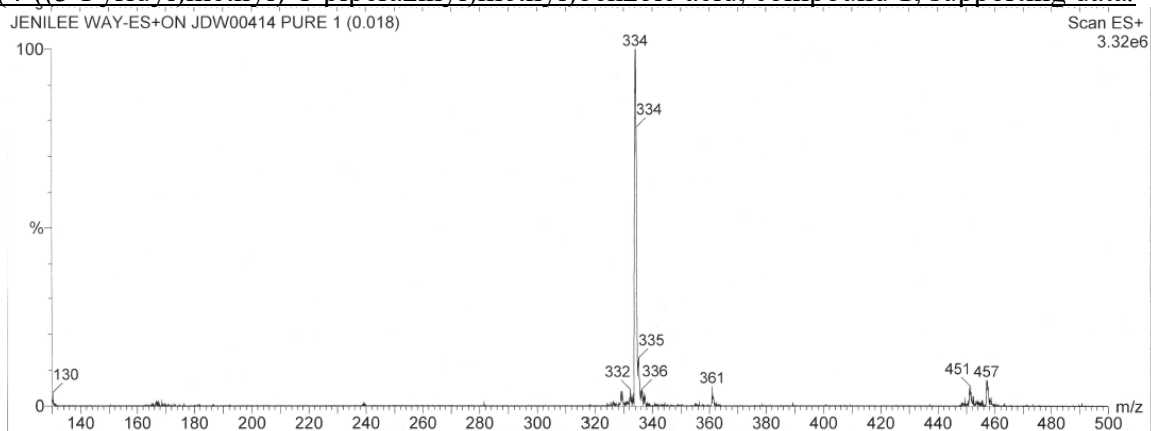


Figure S1. LR-MS for compound 1.

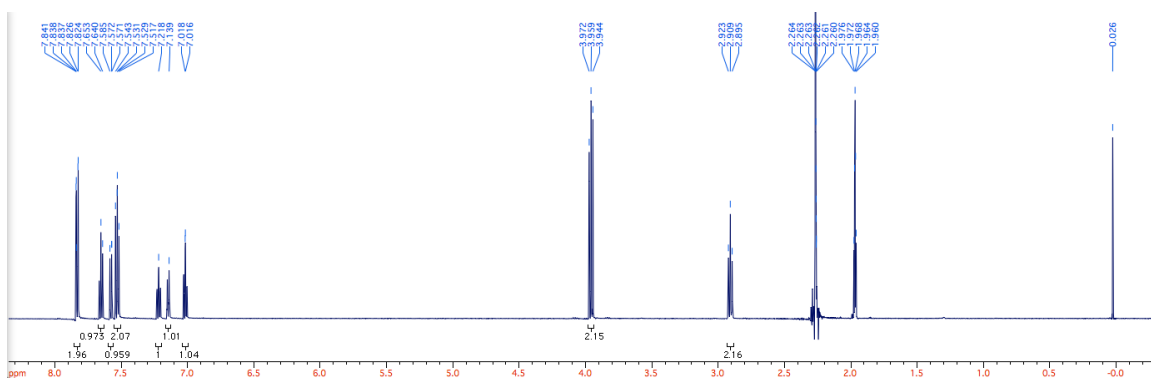


Figure S2. <sup>1</sup>H-NMR for compound 1.

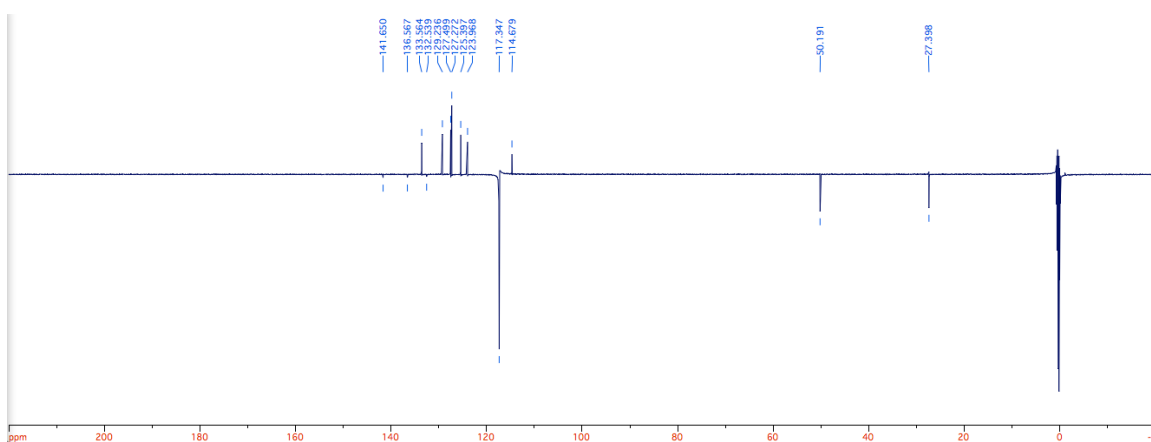


Figure S3. <sup>13</sup>C-NMR for compound 1.

N-p-Ethynylphenylp-(chloromethyl)benzamide, compound **3**, supporting data.

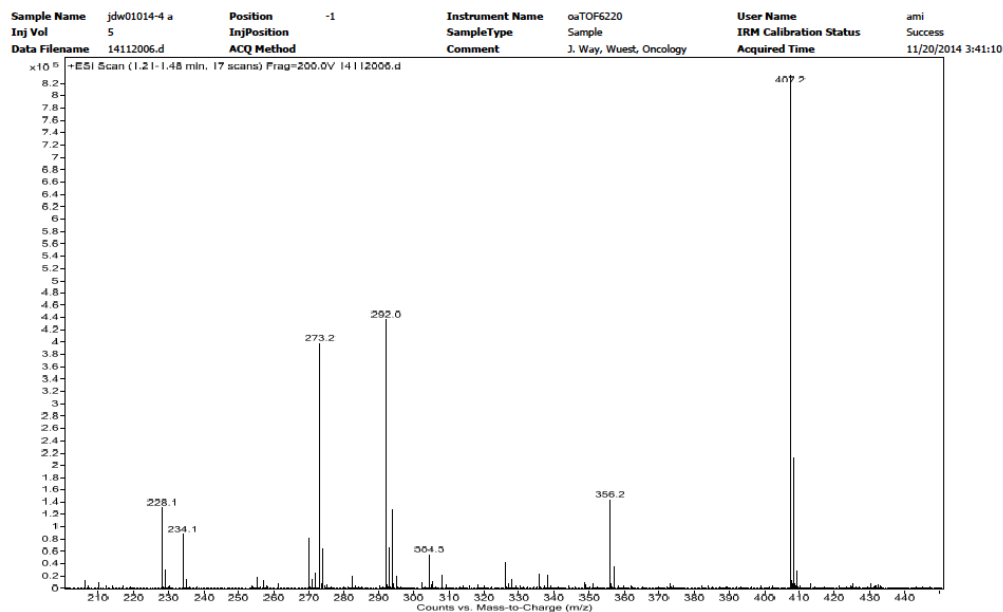


Figure S4. LR-MS for compound **3**.

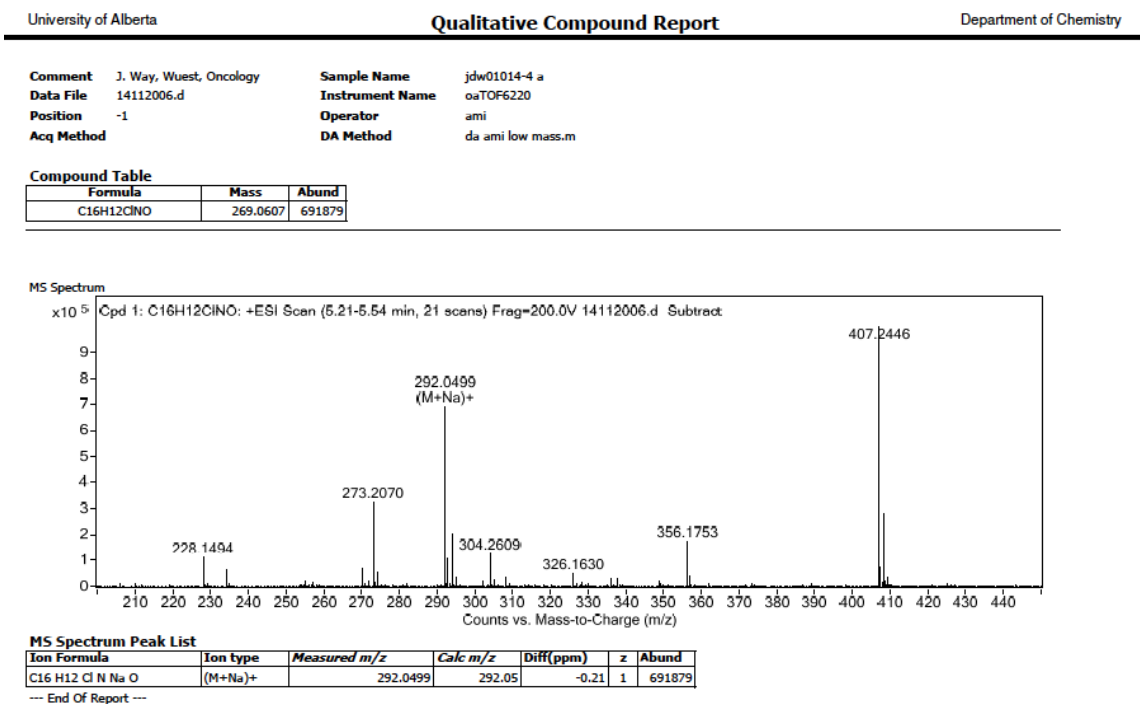


Figure S5. HR-MS for compound **3**.

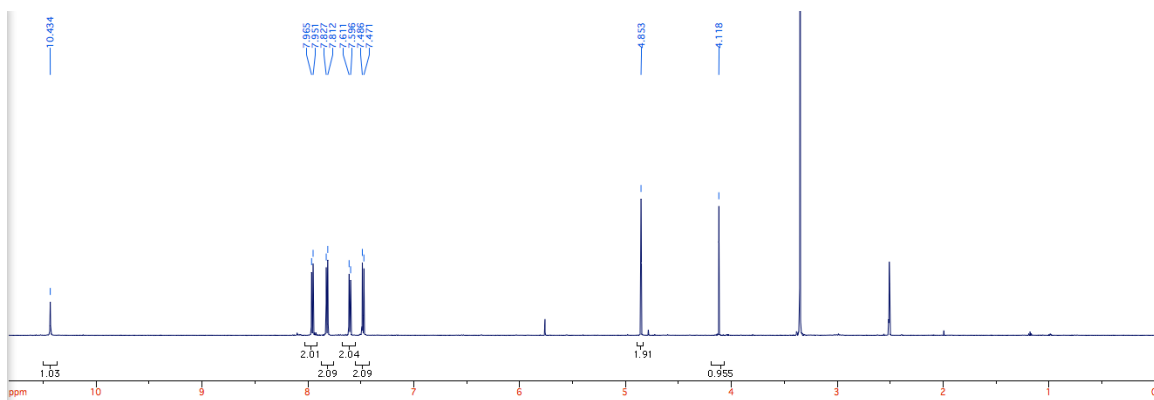


Figure S6.  $^1\text{H}$ -NMR for compound **3**.

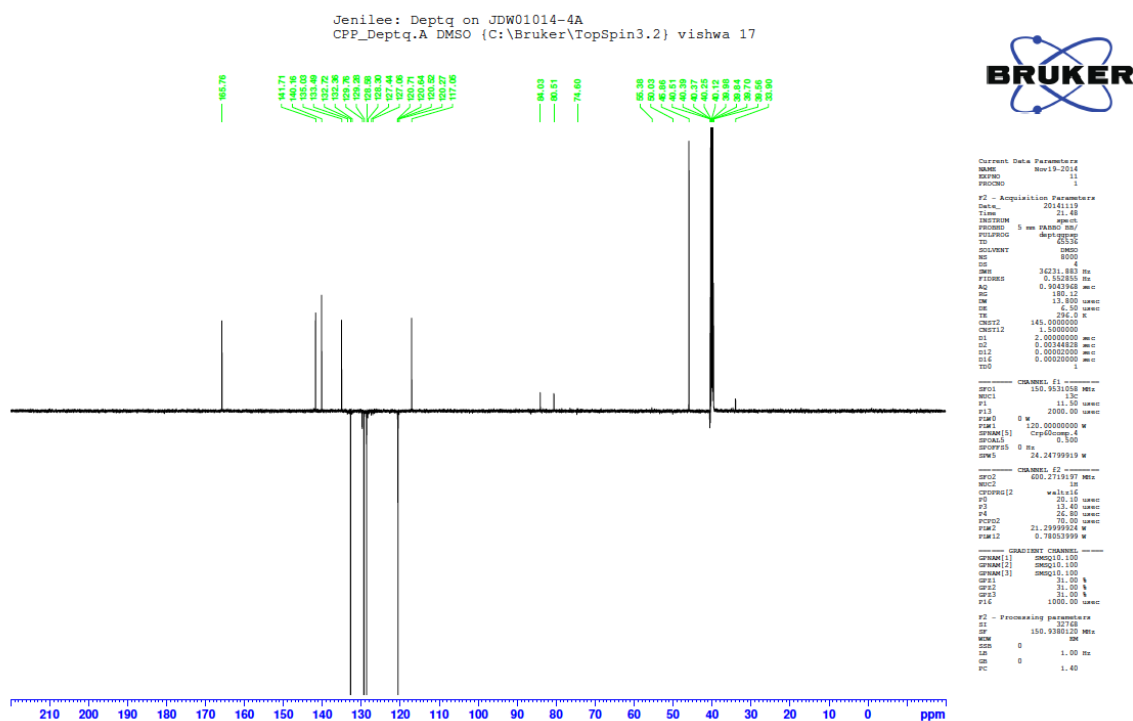


Figure S7.  $^{13}\text{C}$ -NMR for compound **3**.

N-p-Ethynylphenylp-((4-((3-pyridyl)methyl)-1-piperaziny1)methyl)benzamide, compound 4  
supporting data

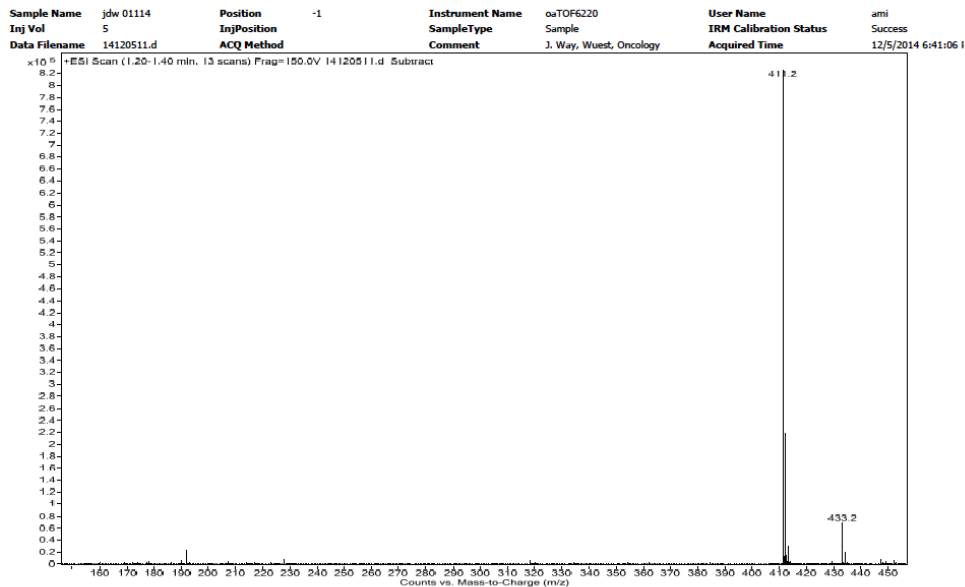


Figure S8. LR-MS for compound 4.

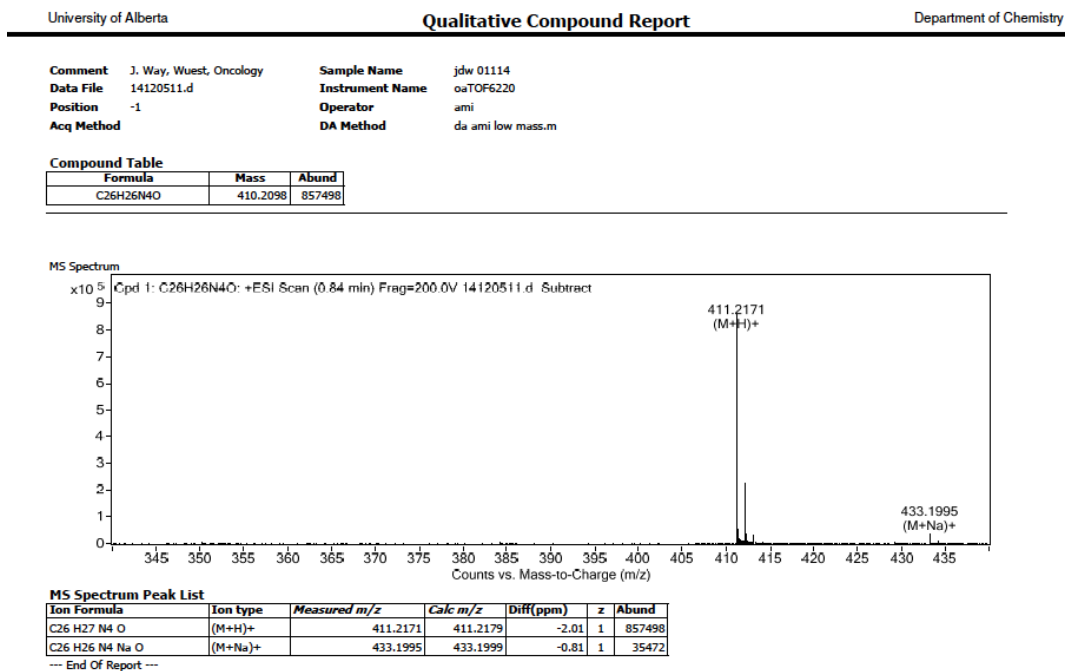


Figure S9. HR-MS for compound 4.

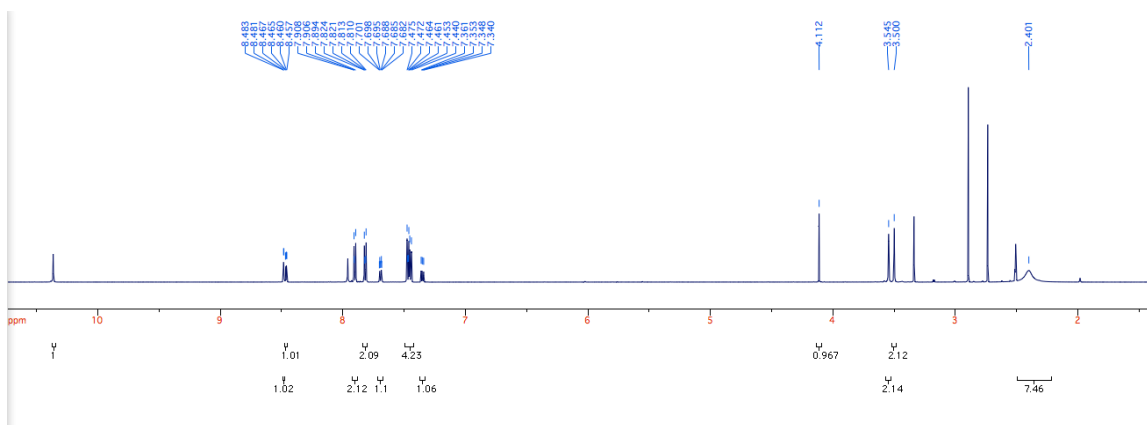


Figure S10.  $^1\text{H-NMR}$  for compound **4**.

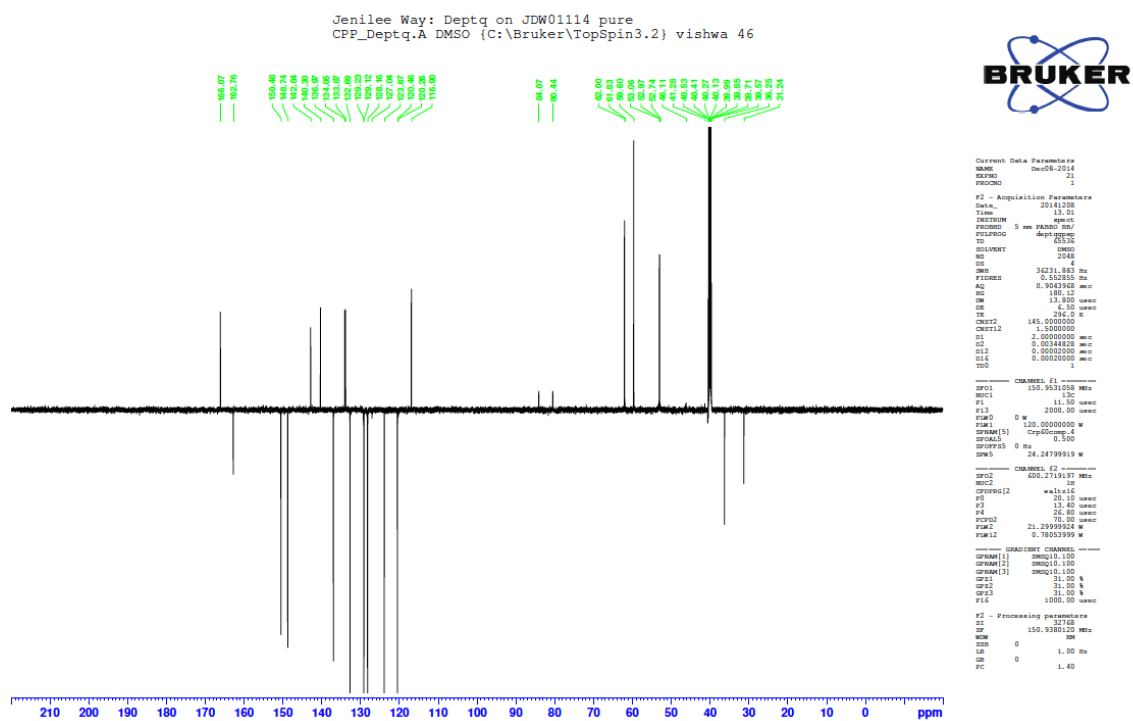


Figure S11.  $^{13}\text{C-NMR}$  for compound **4**.

p-(2-(p-Fluorophenyl)ethynyl)aniline, compound 6 supporting data.

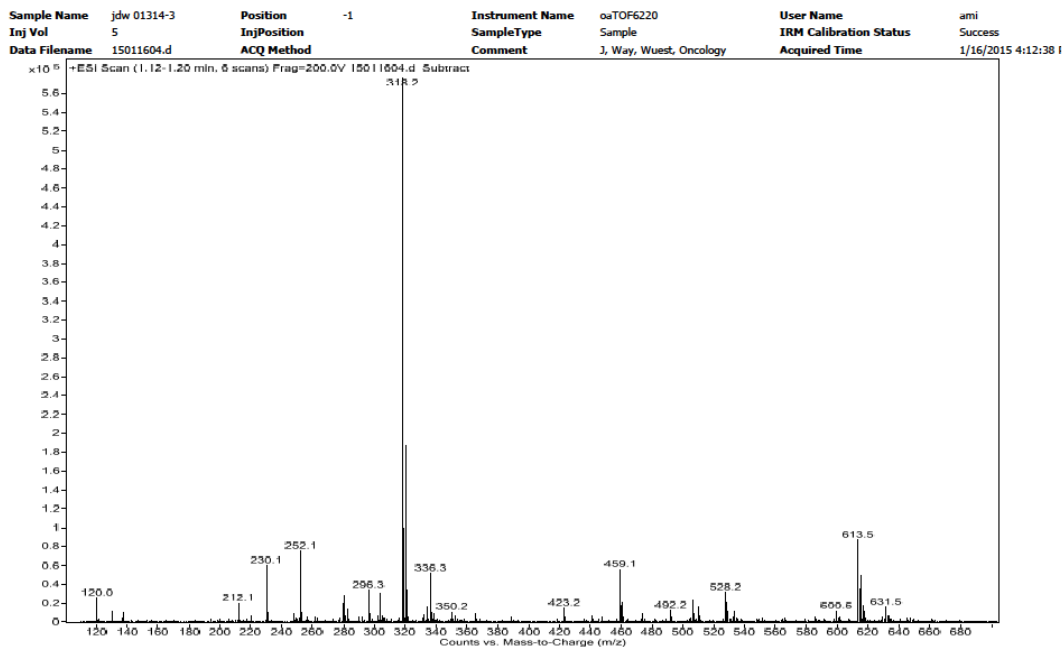


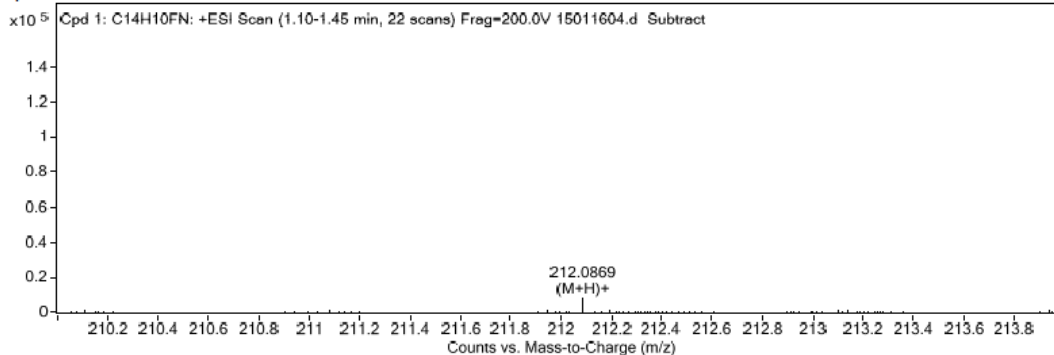
Figure S12. LR-MS for compound 6.

Comment	J. Way, Wuest, Oncology	Sample Name	jdw 01314-3
Data File	15011604.d	Instrument Name	oaTOF6220
Position	-1	Operator	ami
Acq Method		DA Method	da ami low mass.m

Compound Table

Formula	Mass	Abund
C14H10FN	211.0797	7631

MS Spectrum



MS Spectrum Peak List

Ion Formula	Ion type	Measured m/z	Calc m/z	Diff(ppm)	Abund
C14 H11 F N	(M+H)+	212.0869	212.087	-0.25	7631

--- End Of Report ---

Figure S13. HR-MS for compound 6.

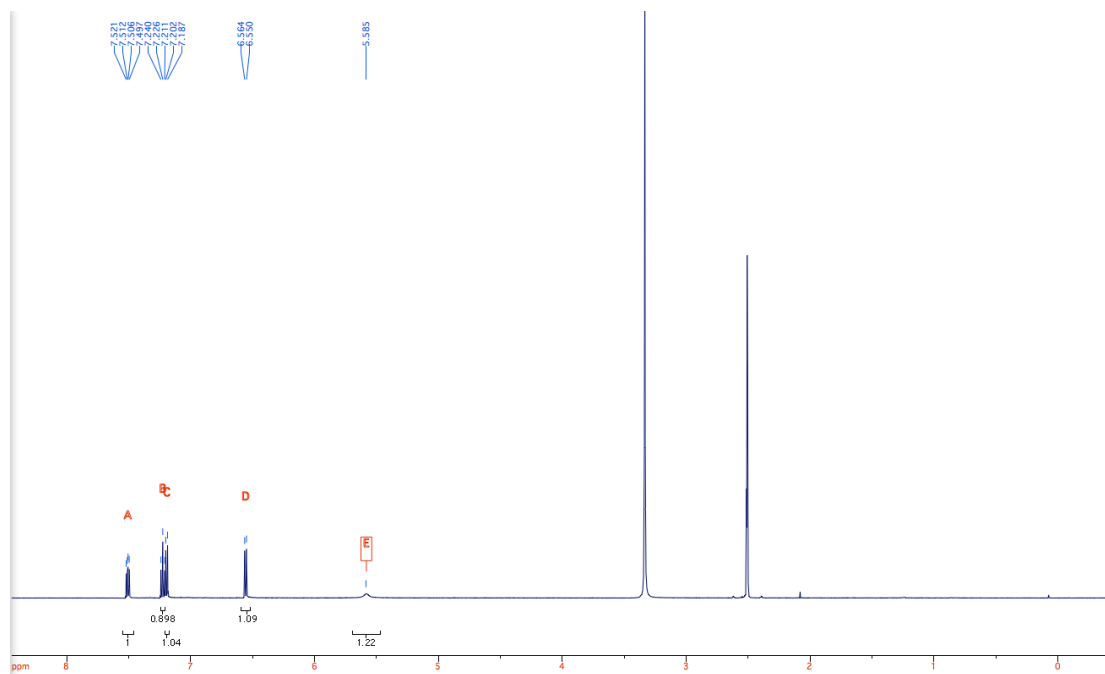


Figure S14.  $^1\text{H}$ -NMR for compound **6**.

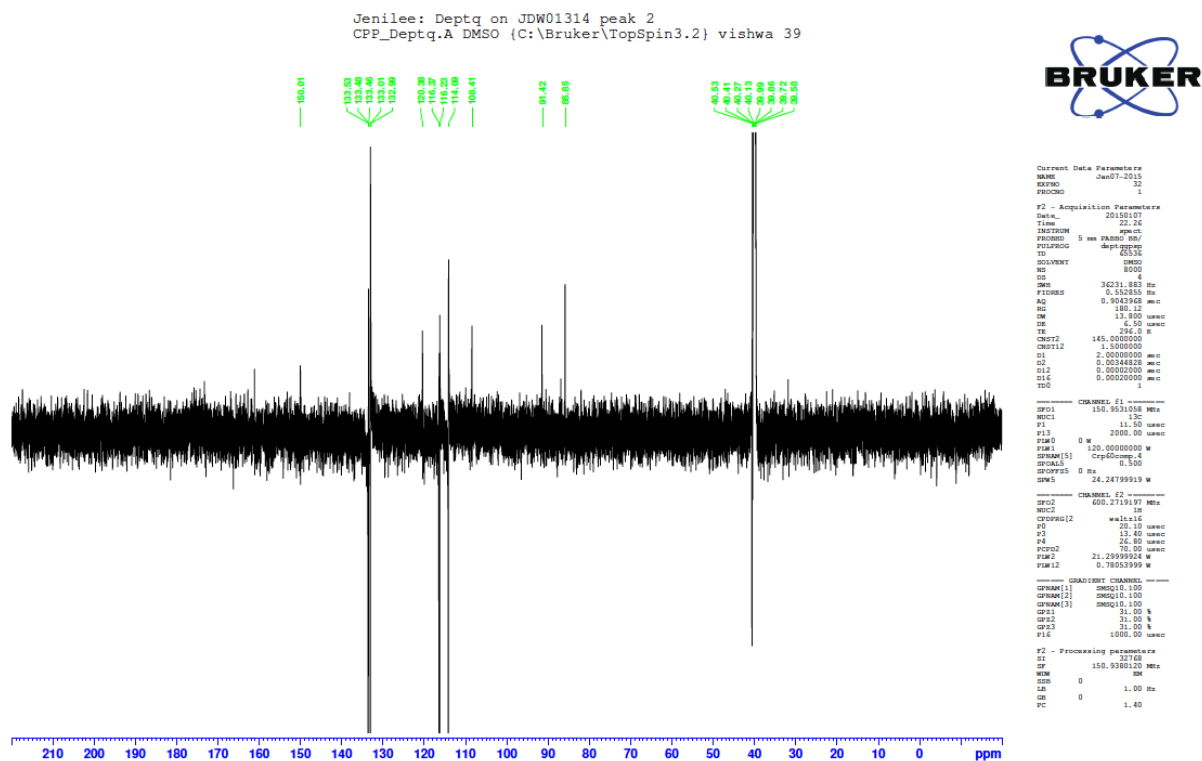


Figure S15.  $^{13}\text{C}$ -NMR for compound **6**.

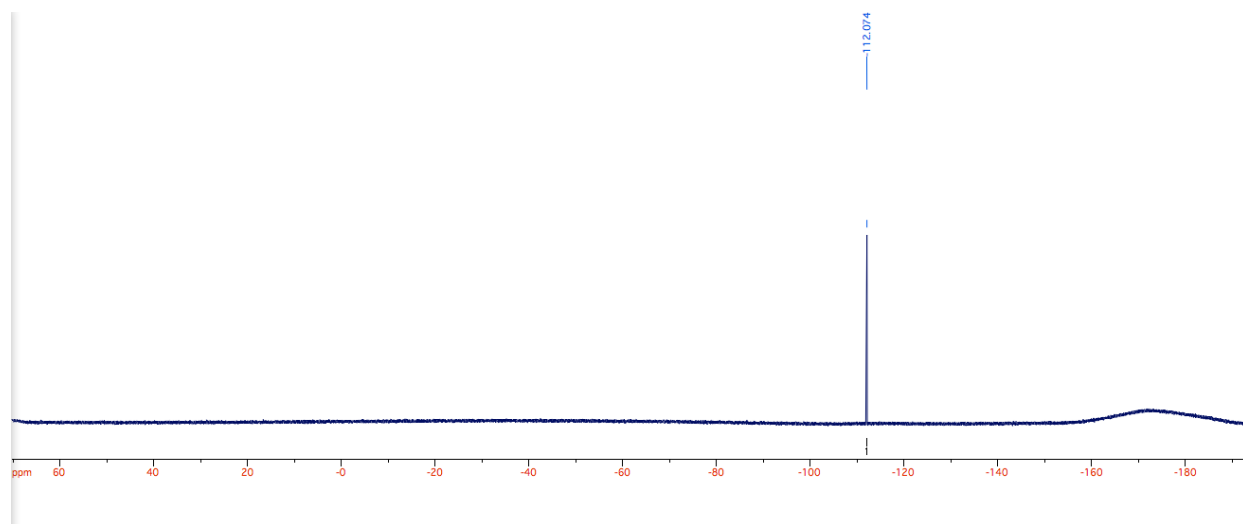


Figure S16.  $^{19}\text{F}$ -NMR for compound 6.

p-(2-(p-Fluorophenyl)ethynyl)aniline, compound 7 supporting data.

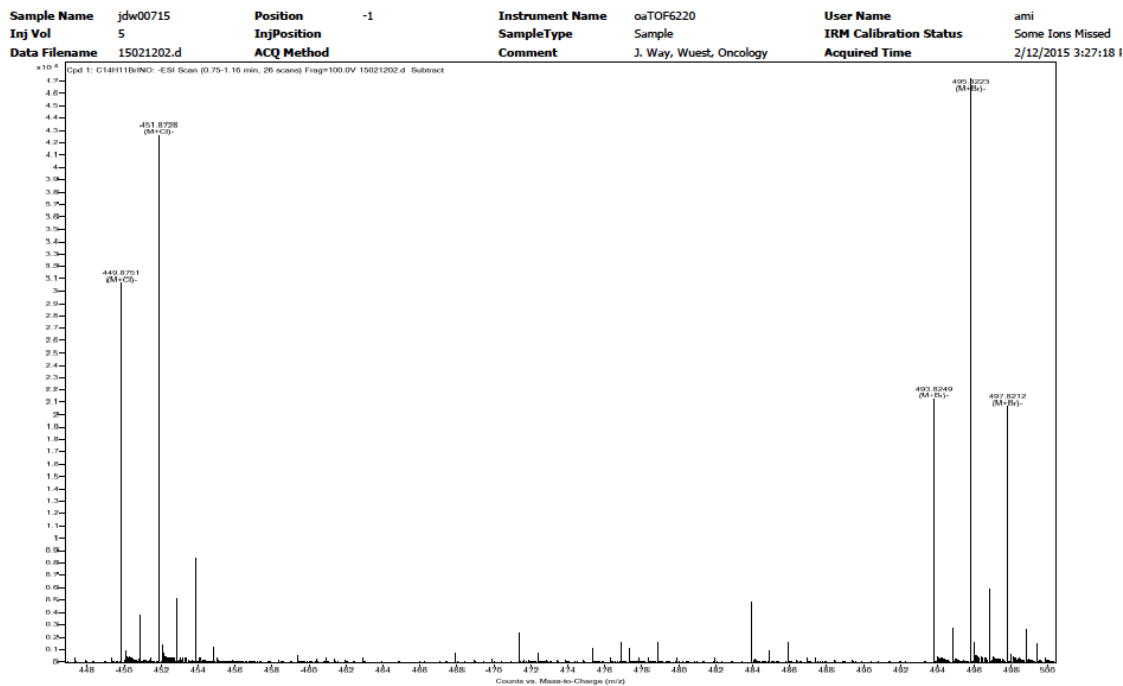


Figure S17. LR-MS for compound 7.

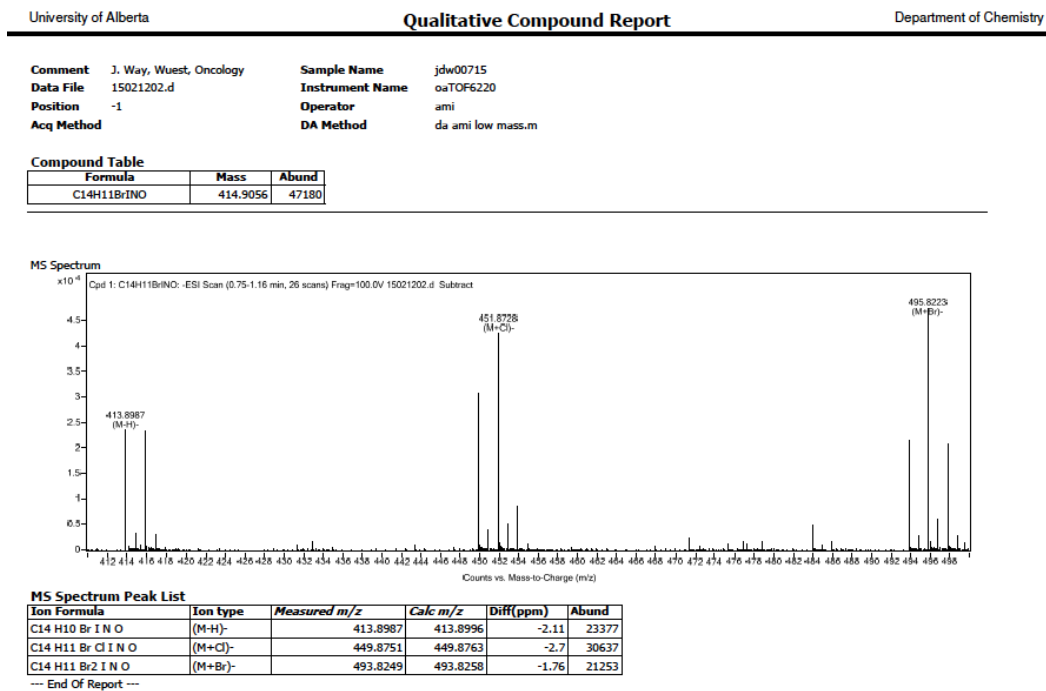


Figure S18. HR-MS for compound 7.

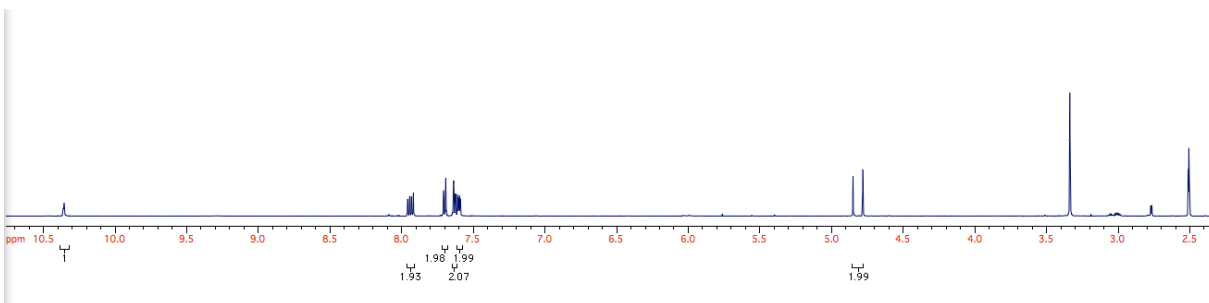


Figure S19.  $^1\text{H}$ -NMR for compound 7.

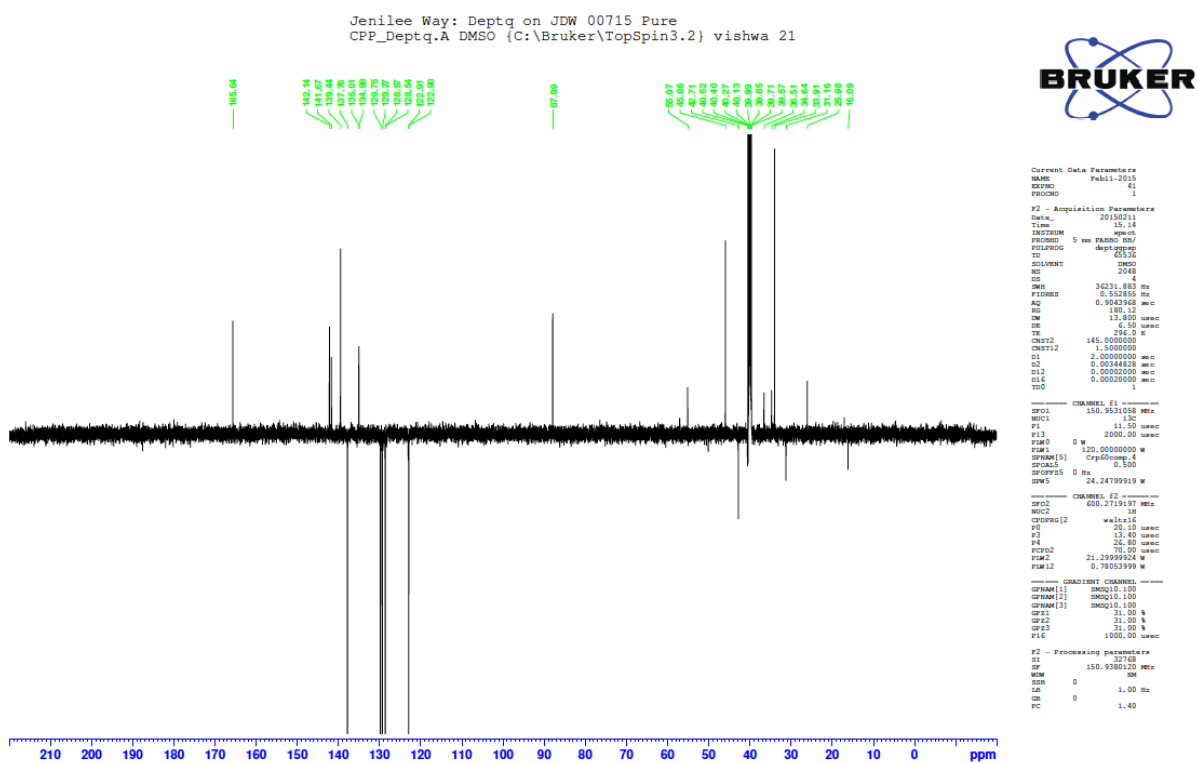


Figure S20.  $^{13}\text{C}$ -NMR for compound 7.

N-p-Iodophenylp-((4-((3-pyridyl)methyl)-1-piperazinyl)methyl)benzamide, compound 8  
supporting data.

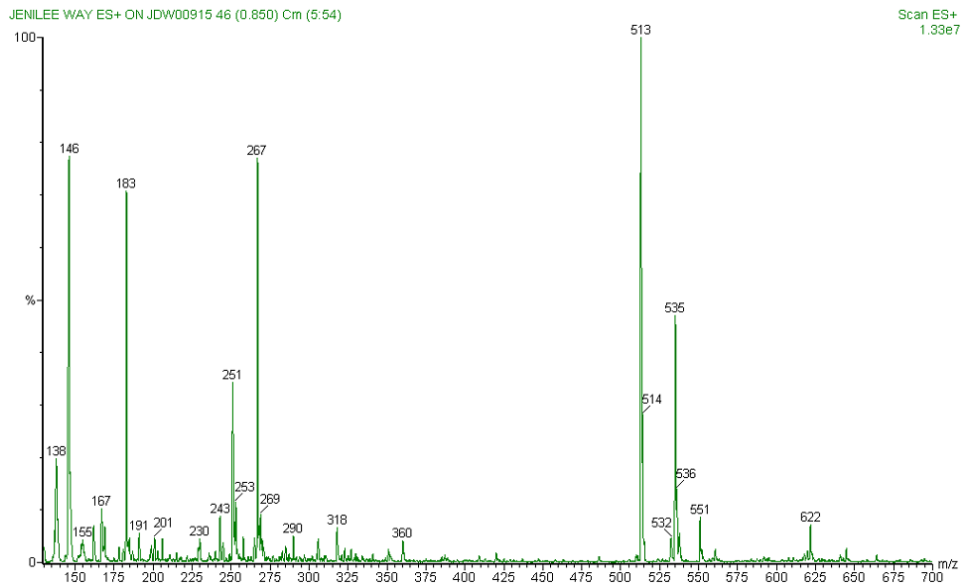


Figure S21. LR-MS for compound 8.

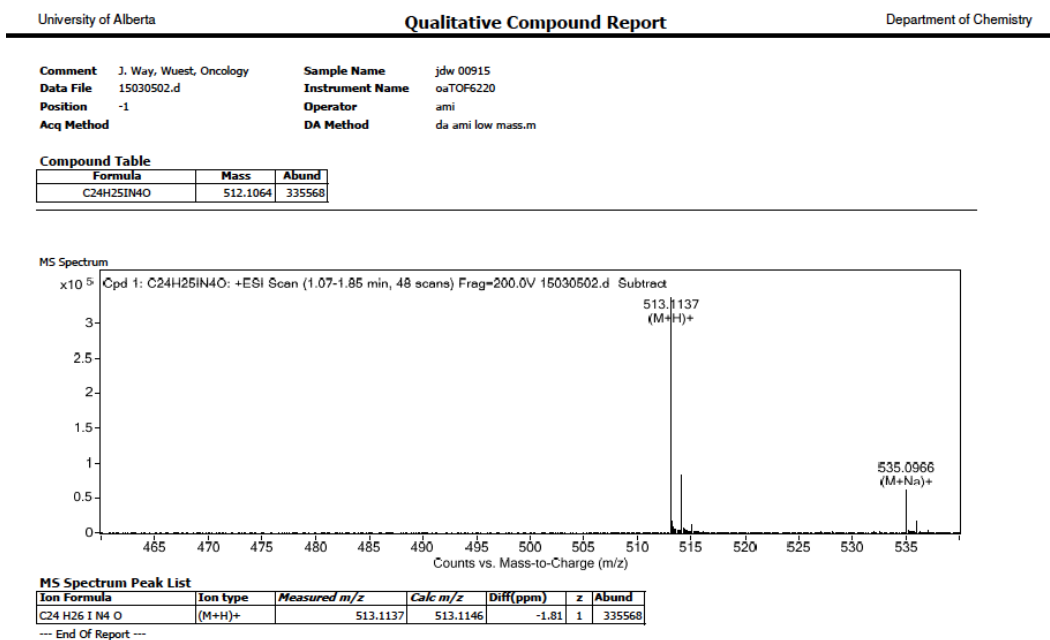


Figure S22. HR-MS for compound 8.

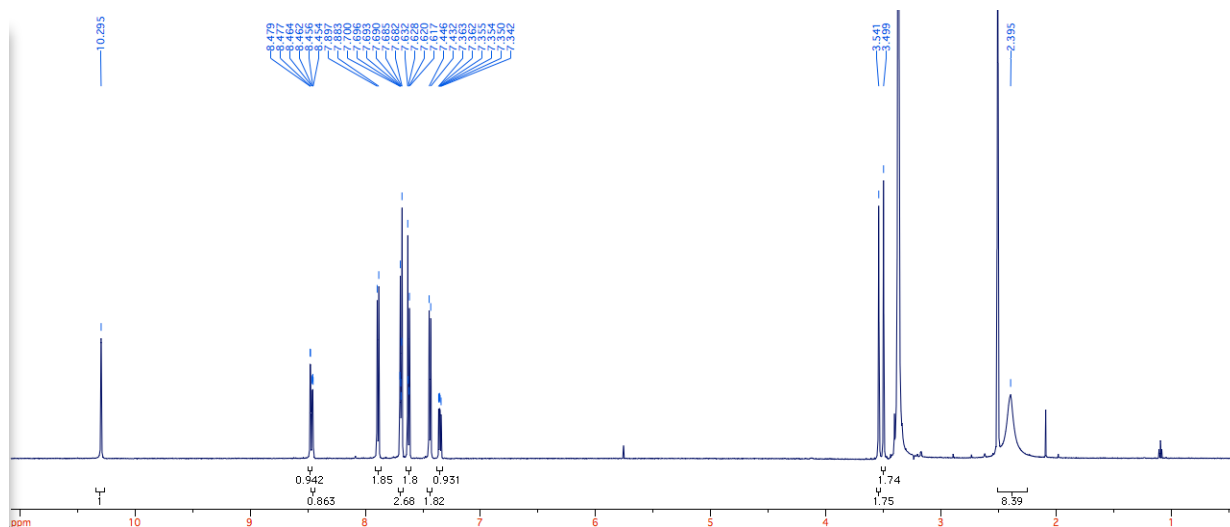


Figure S23.  $^1\text{H-NMR}$  for compound **8**.

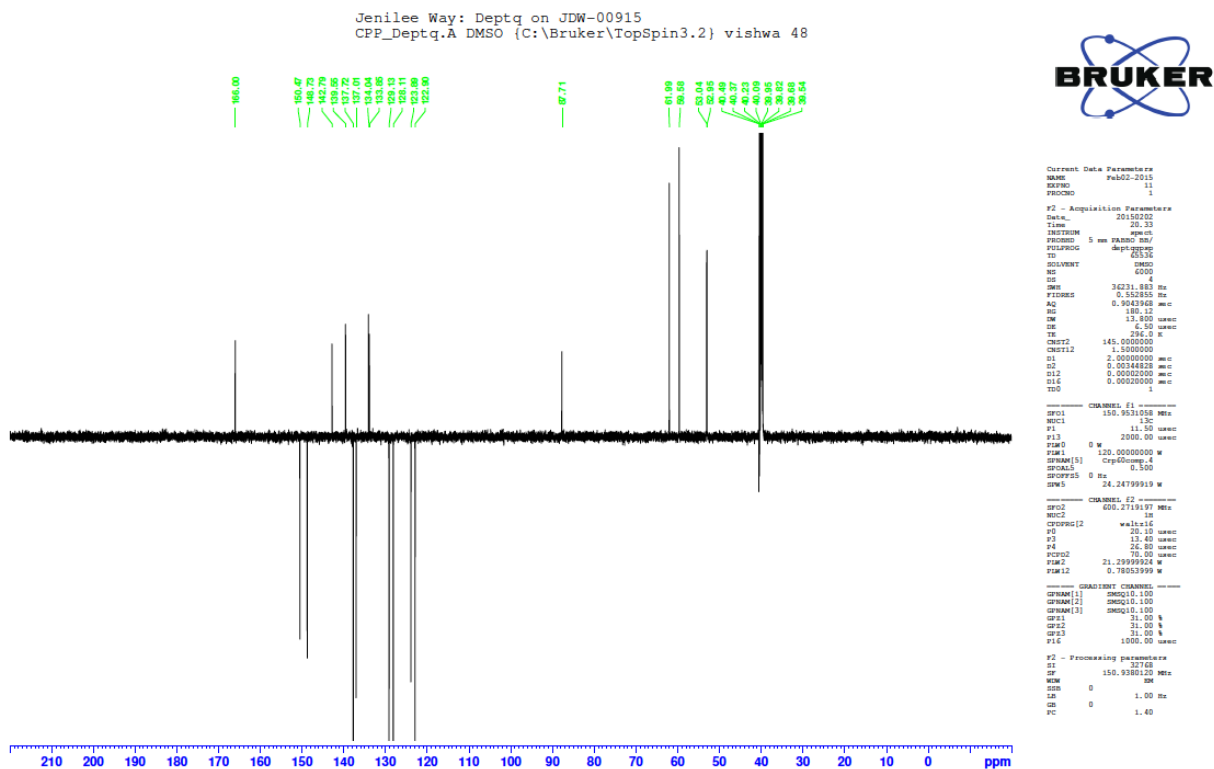


Figure S24.  $^{13}\text{C-NMR}$  for compound **8**.

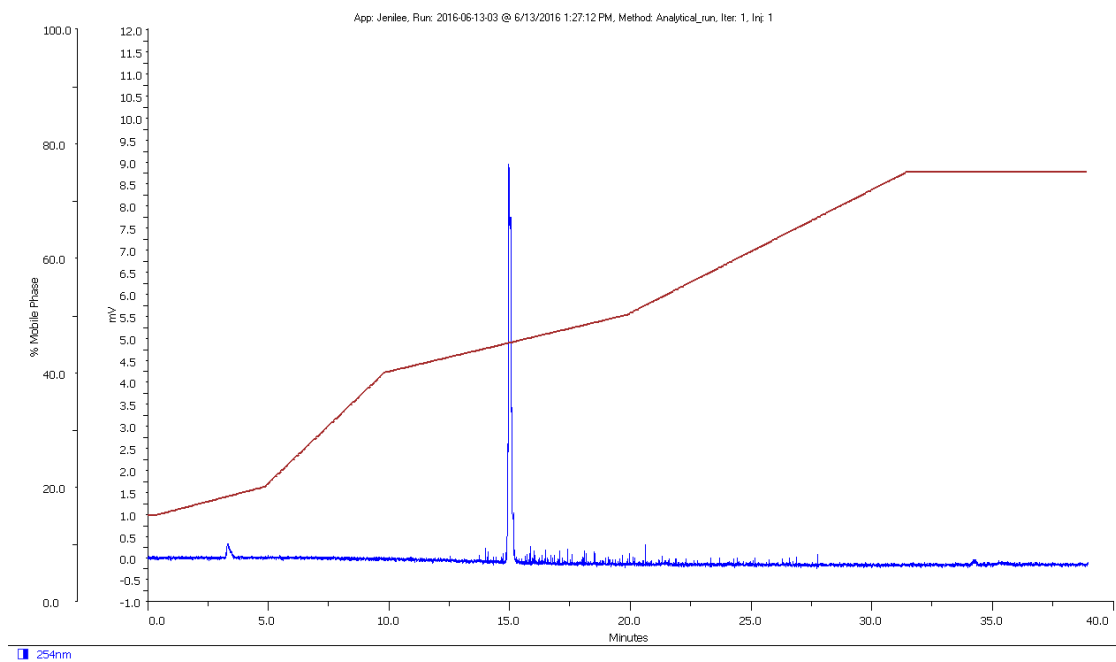


Figure S25. Analytical HPLC for compound **8**.

N-(4-(1-ethynyl-4-fluorophenyl)phenyl)-4-((4-(pyridine-3-ylmethyl)piperazin-1-yl)methyl)benzamide, compound 9 supporting data.

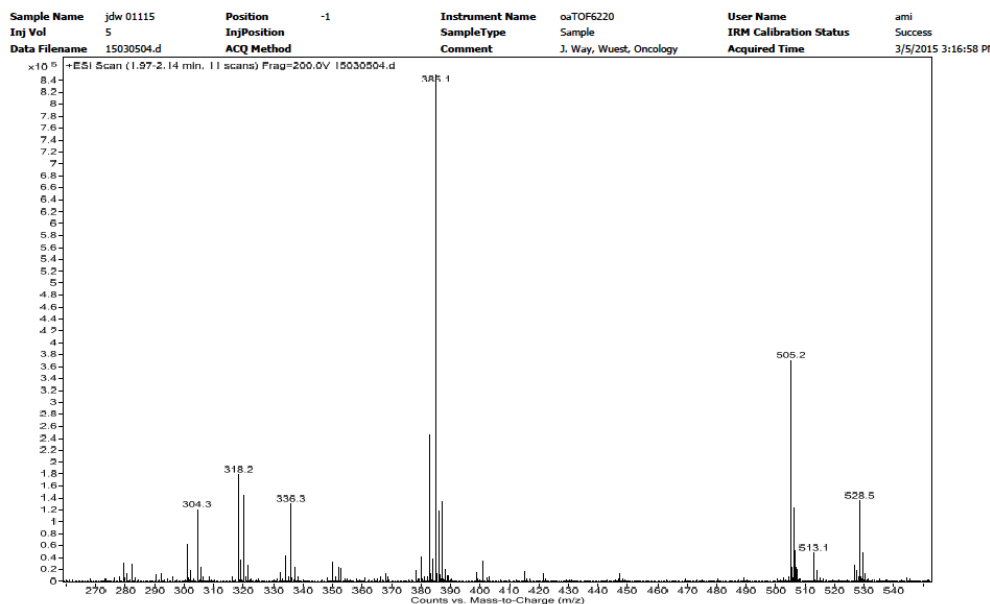


Figure S26. LR-MS for compound 9.

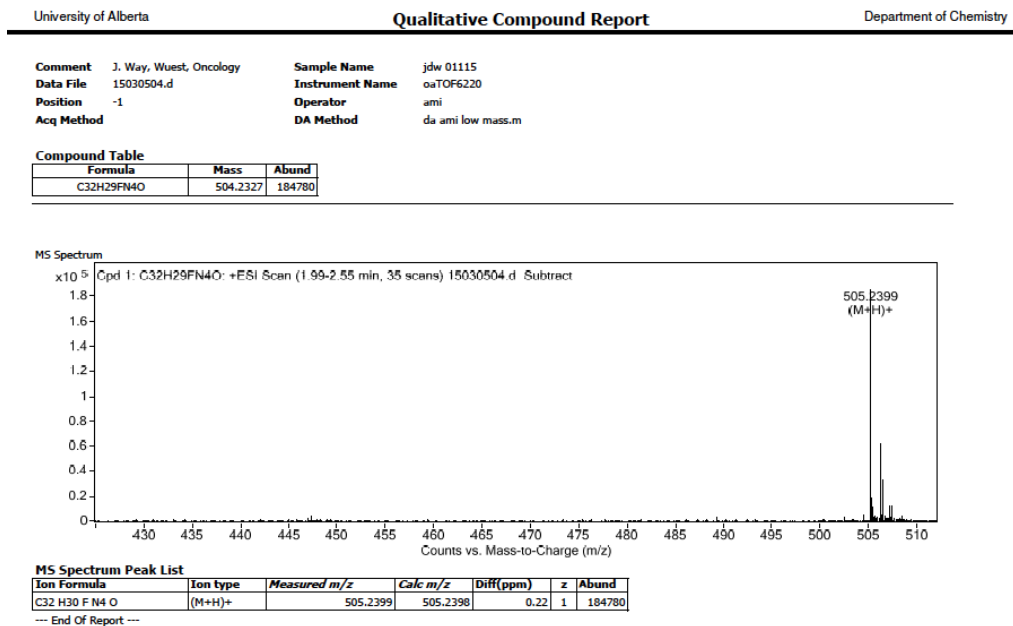


Figure S27. HR-MS for compound 9.

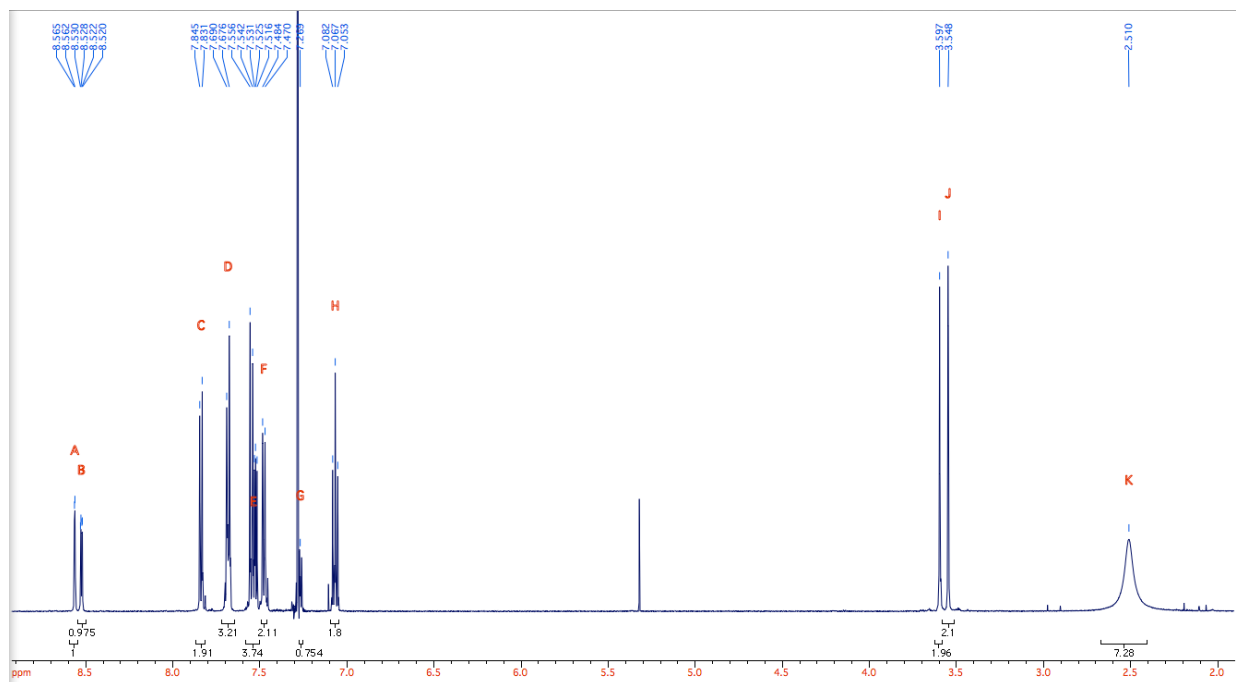


Figure S28.  $^1\text{H-NMR}$  for compound **9**.

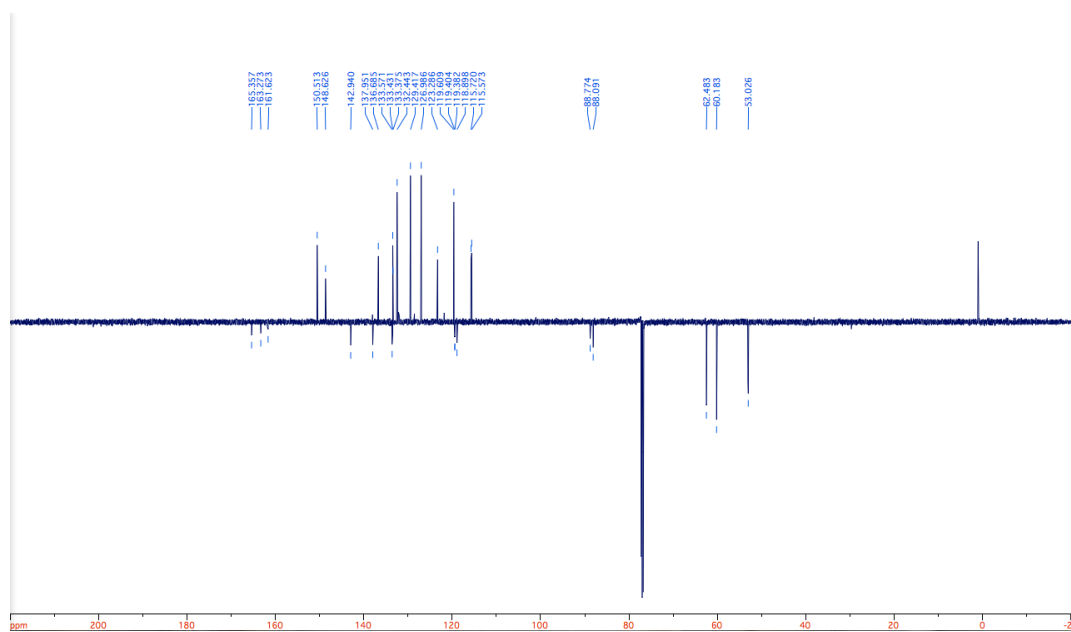


Figure S29.  $^{13}\text{C-NMR}$  for compound **9**.

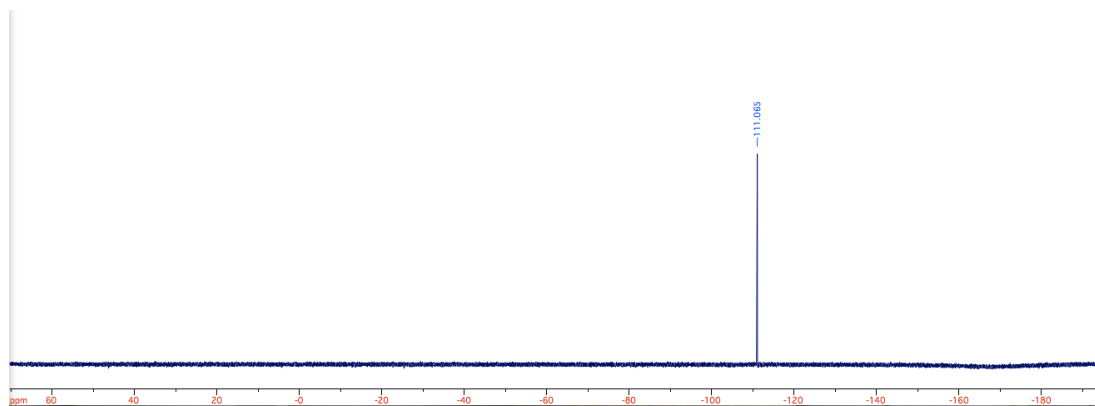


Figure S30.  $^{19}\text{F}$ -NMR for compound 9.

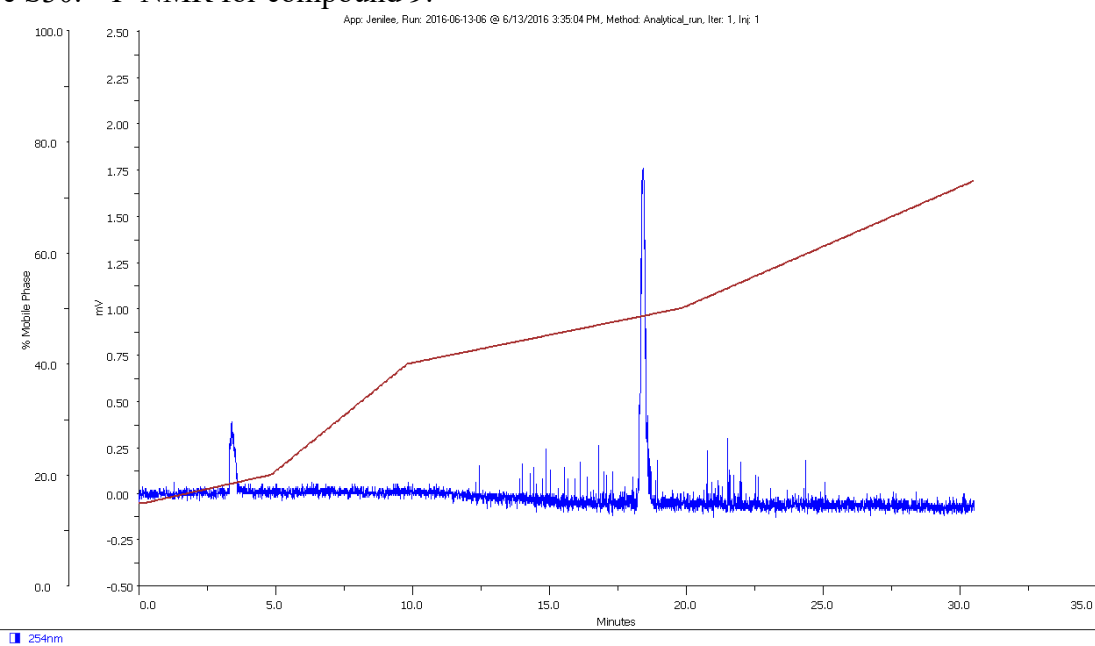


Figure S31. Analytical HPLC for compound 9.

N-(4-(4-ethynylanisole)phenyl)-4-((4-(pyridine-3-ylmethyl)piperazin-1-yl) methyl) benzamide, compound 10, supporting data.

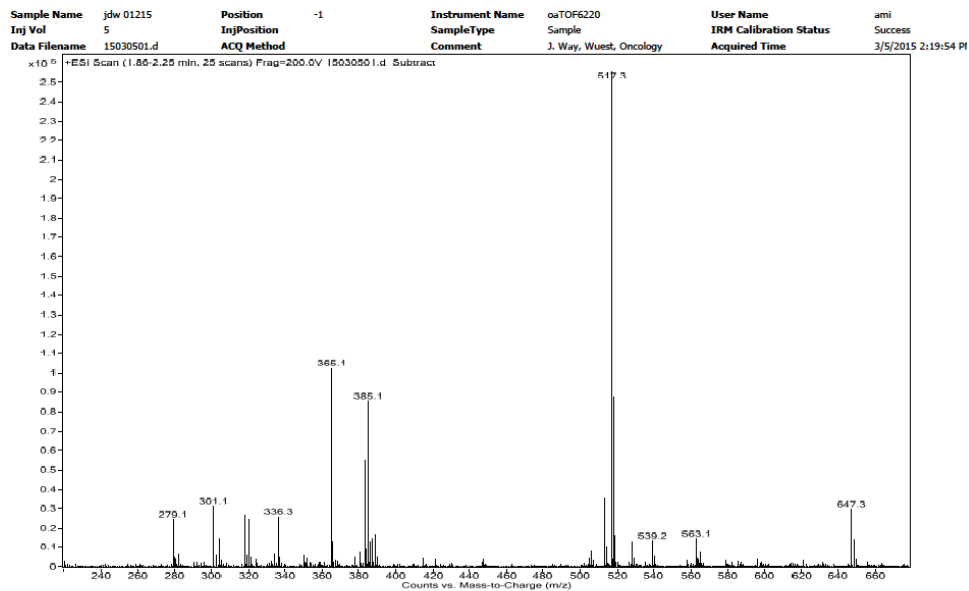


Figure S32. LR-MS for compound 10.

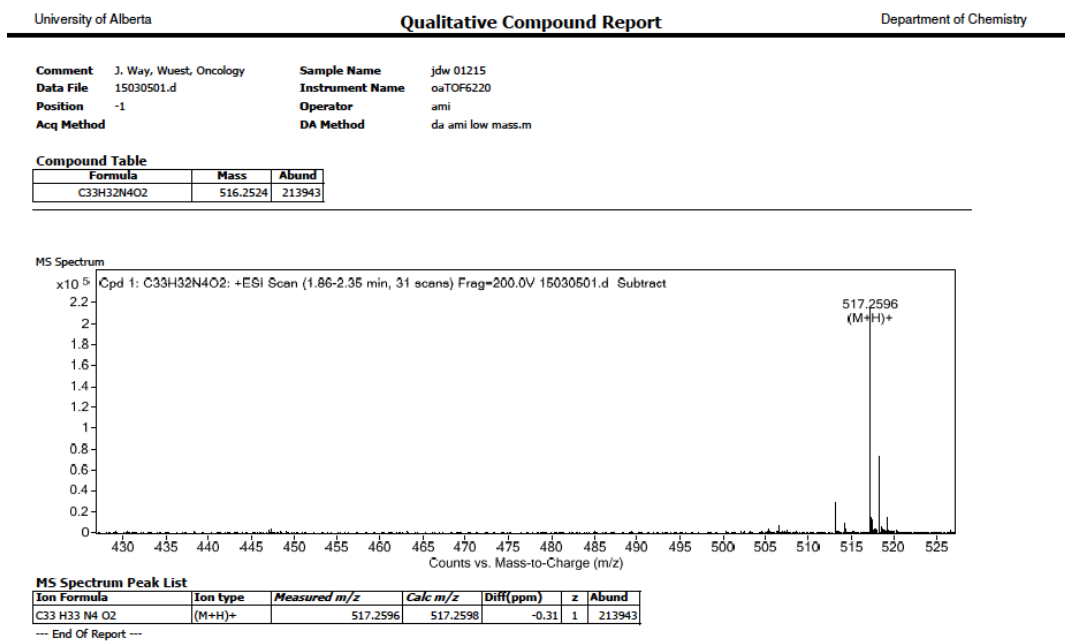


Figure S33. HR-MS for compound 10.

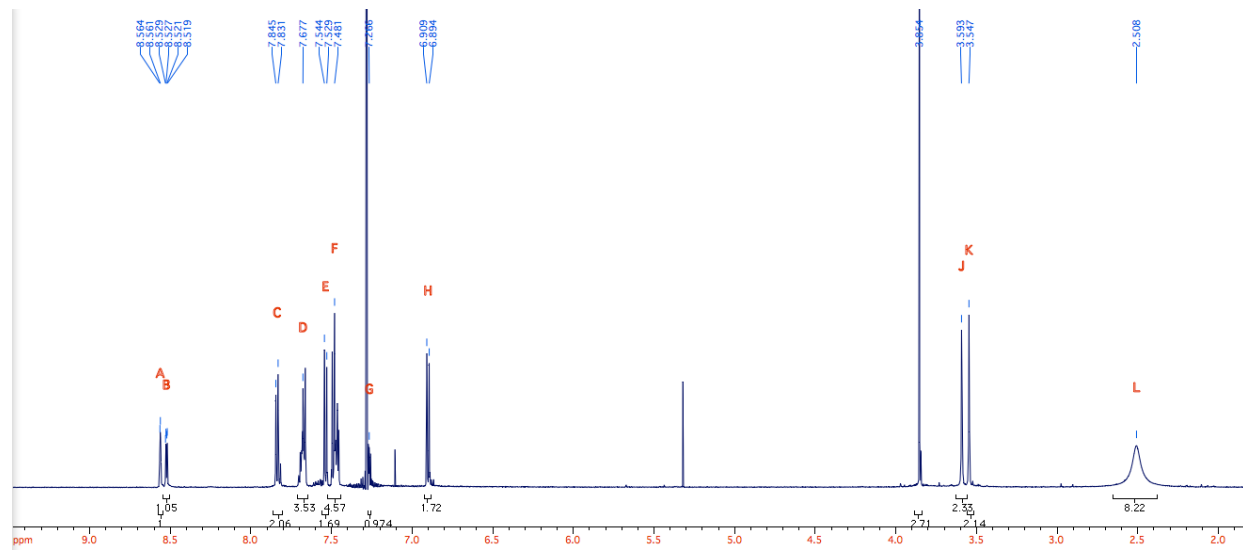


Figure S34.  $^1\text{H-NMR}$  for compound **10**.

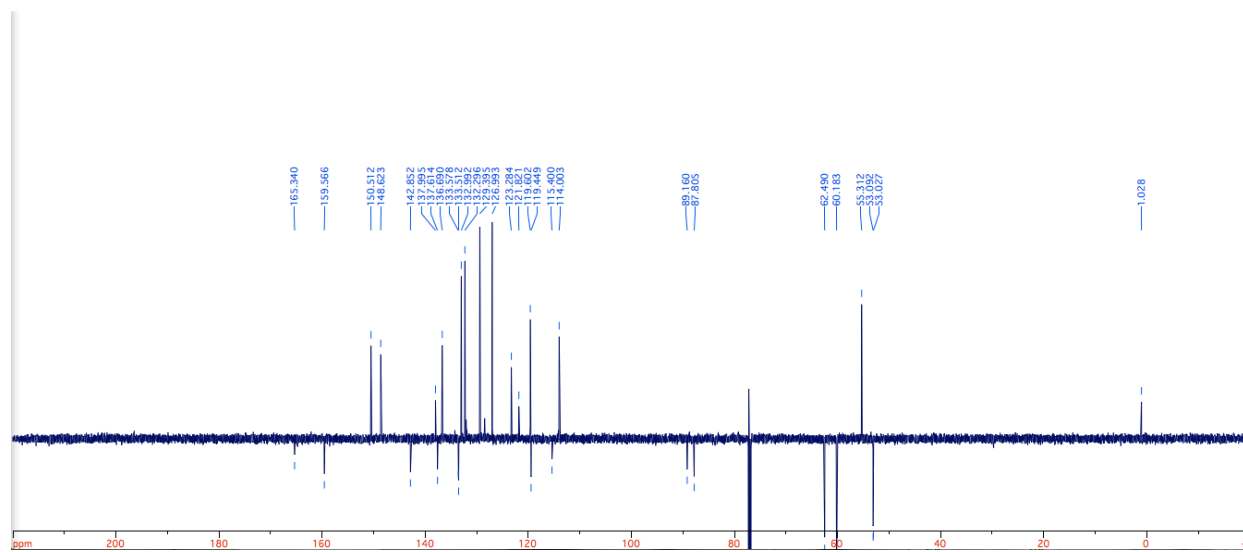


Figure S35.  $^{13}\text{C-NMR}$  for compound **10**.

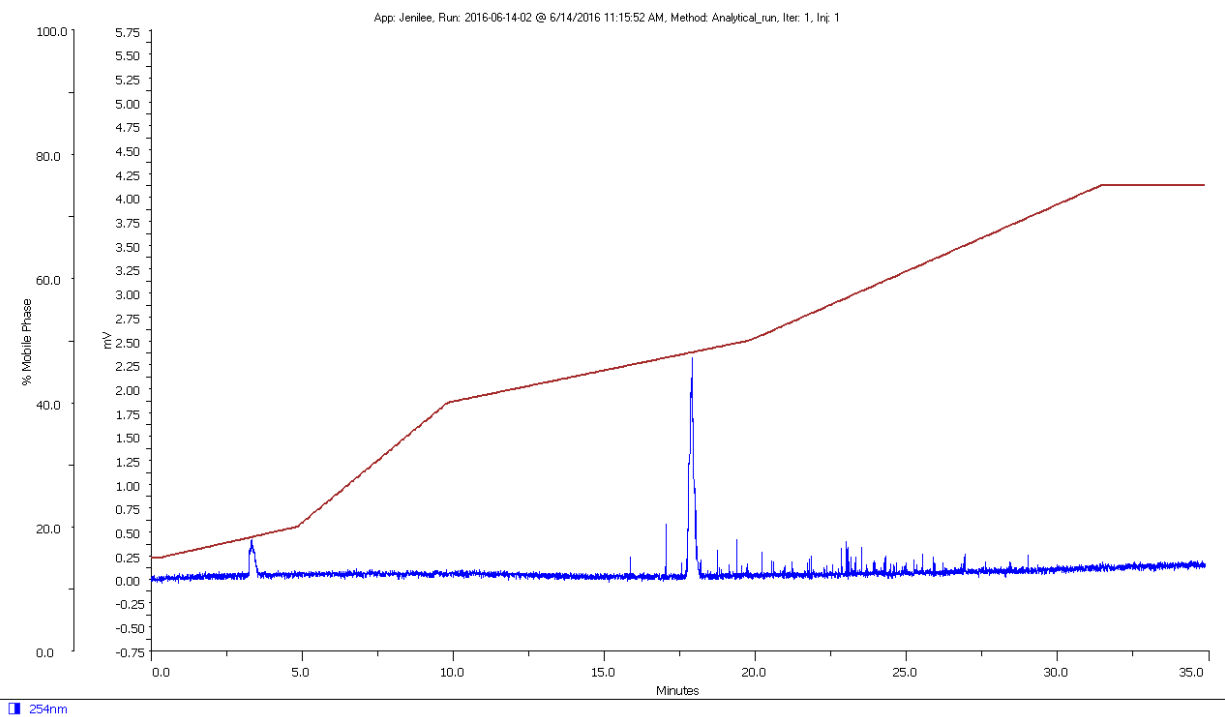


Figure S36. Analytical HPLC for compound **10**.

N-(4-(4-ethynylaniline)phenyl)-4-((4-(pyridine-3-ylmethyl)piperazin-1-yl) methyl) benzamide, compound 11, supporting data.

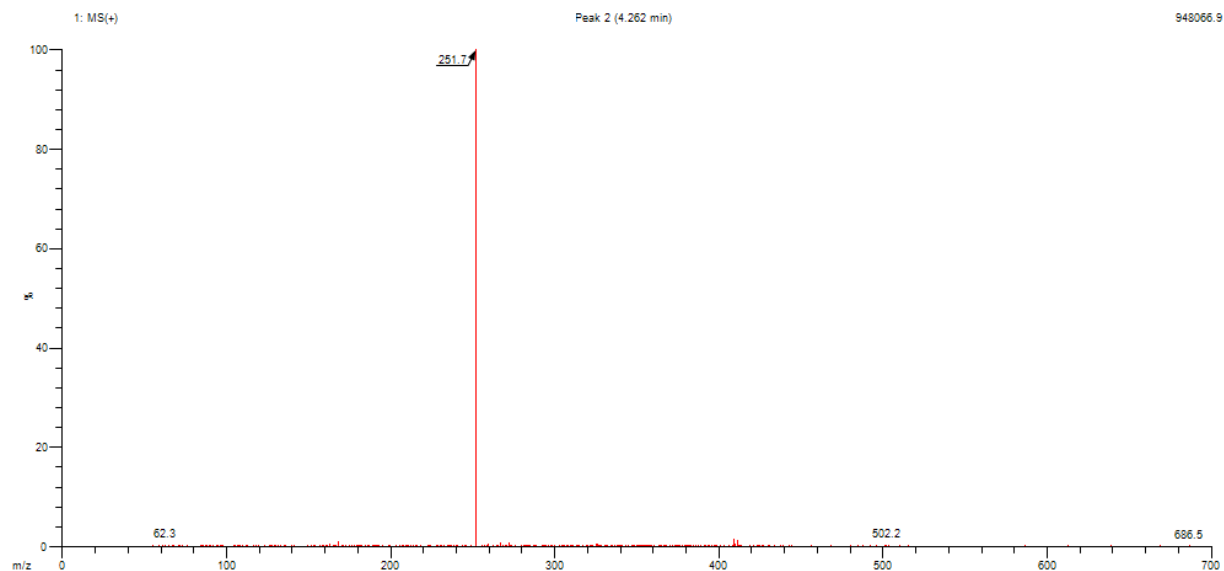


Figure S37. LR-MS for compound **11**.

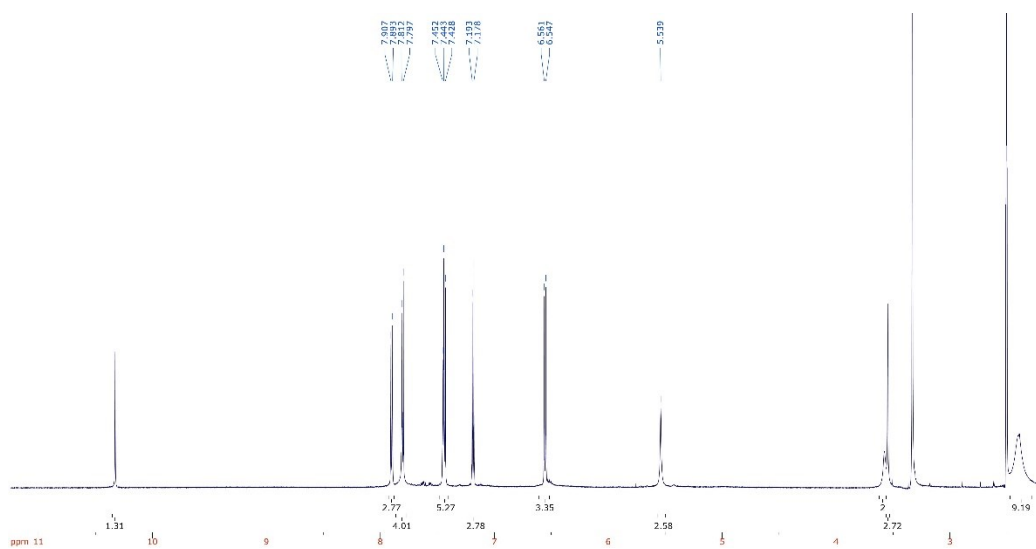


Figure S38.  $^1\text{H-NMR}$  for compound **11**.

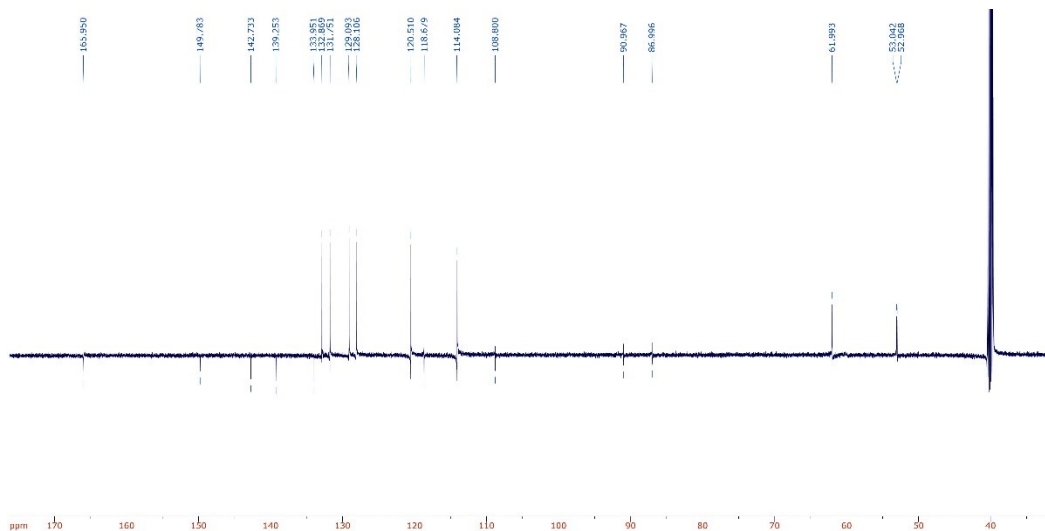


Figure S39.  $^{13}\text{C}$ -NMR for compound **11**.

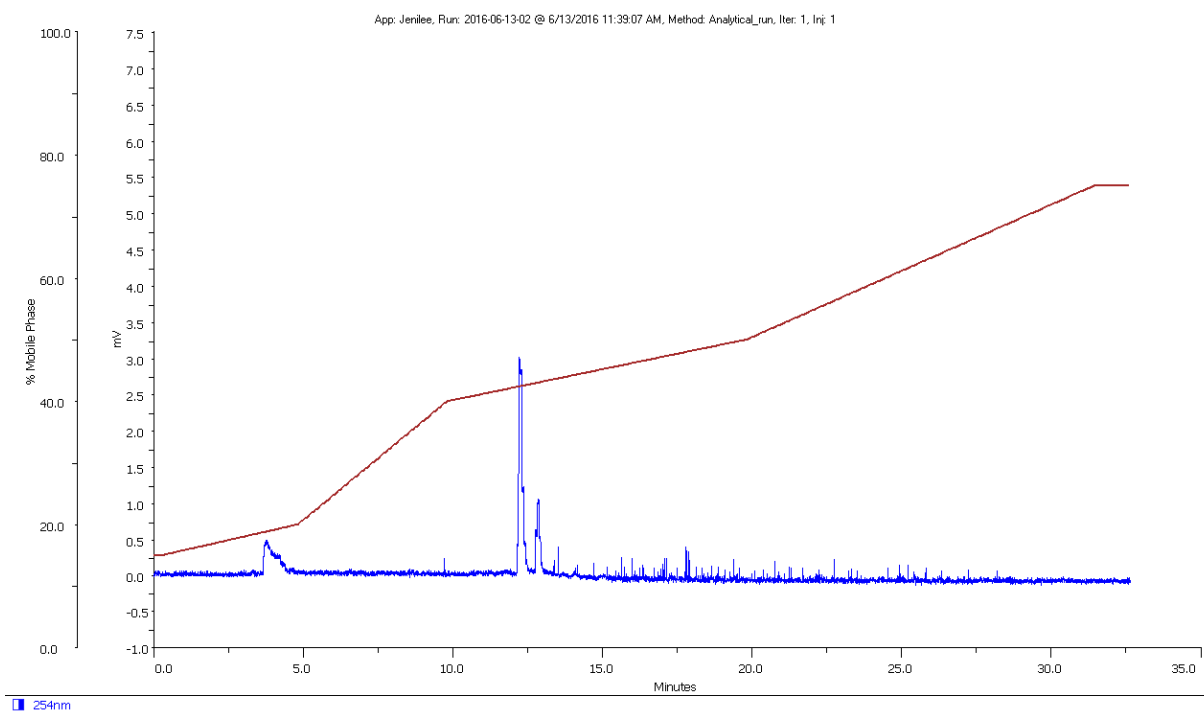


Figure S40. Analytical HPLC for compound **11**.

N-(4-(4-ethynylbiphenyl)phenyl)-4-((4-(pyridine-3-ylmethyl)piperazin-1-yl) methyl) benzamide, compound 12, supporting data.

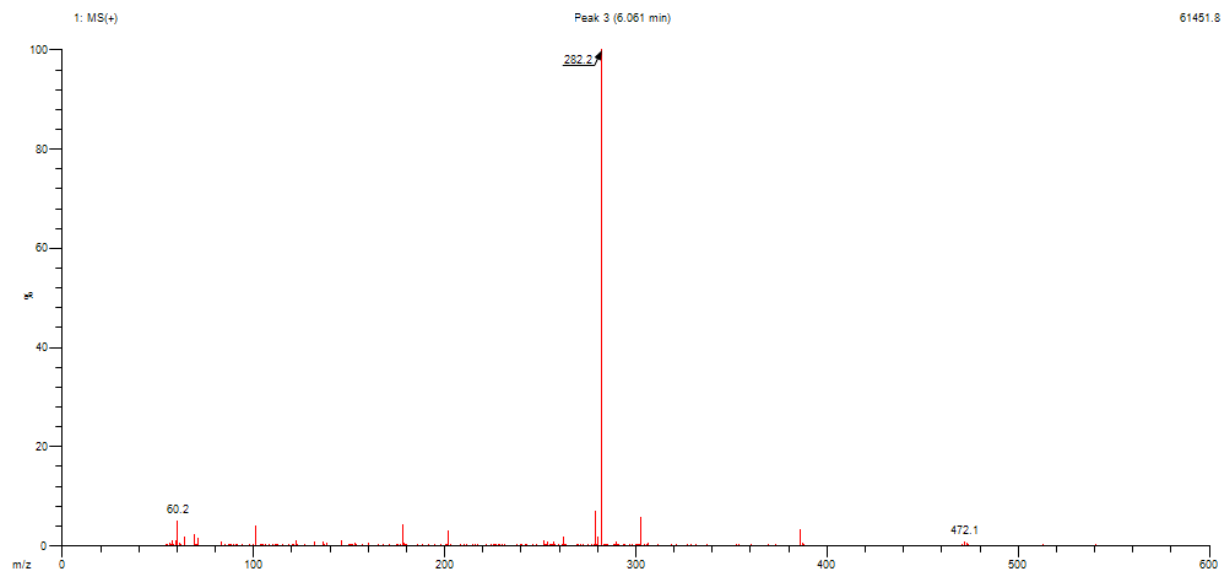


Figure S41. LR-MS for compound 12.

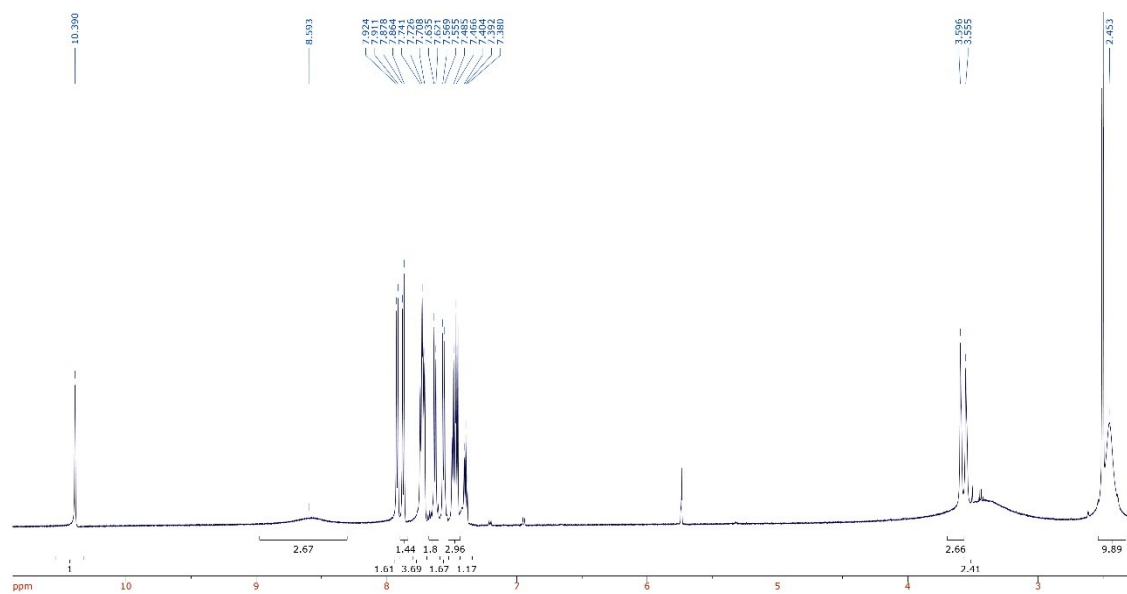


Figure S42.  $^1\text{H-NMR}$  for compound 12.

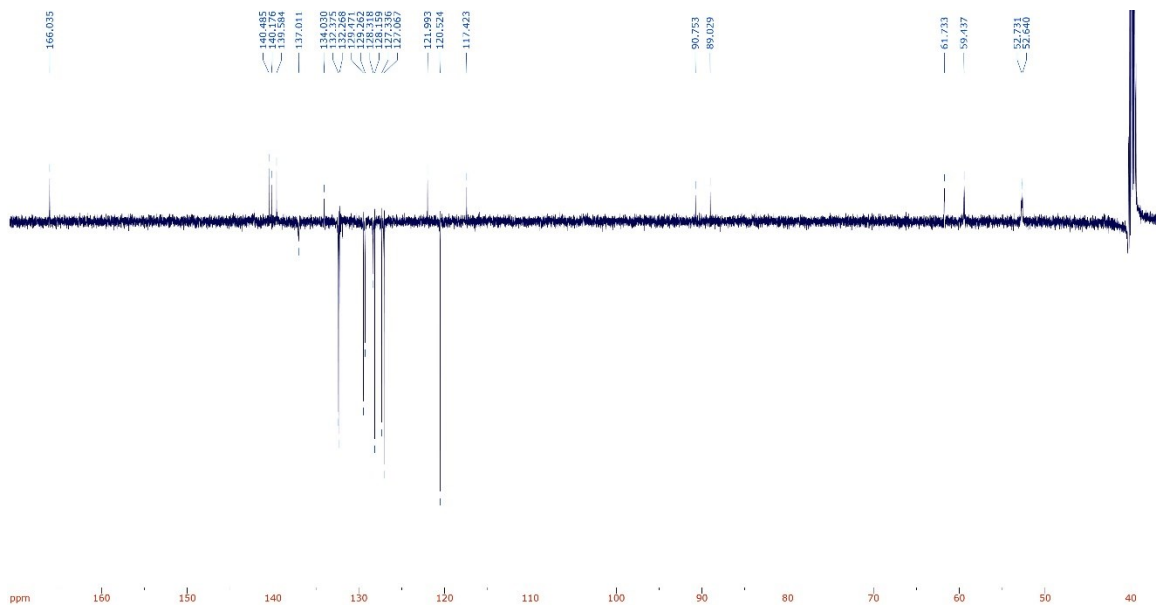


Figure S43.  $^{13}\text{C}$ -NMR for compound **12**.

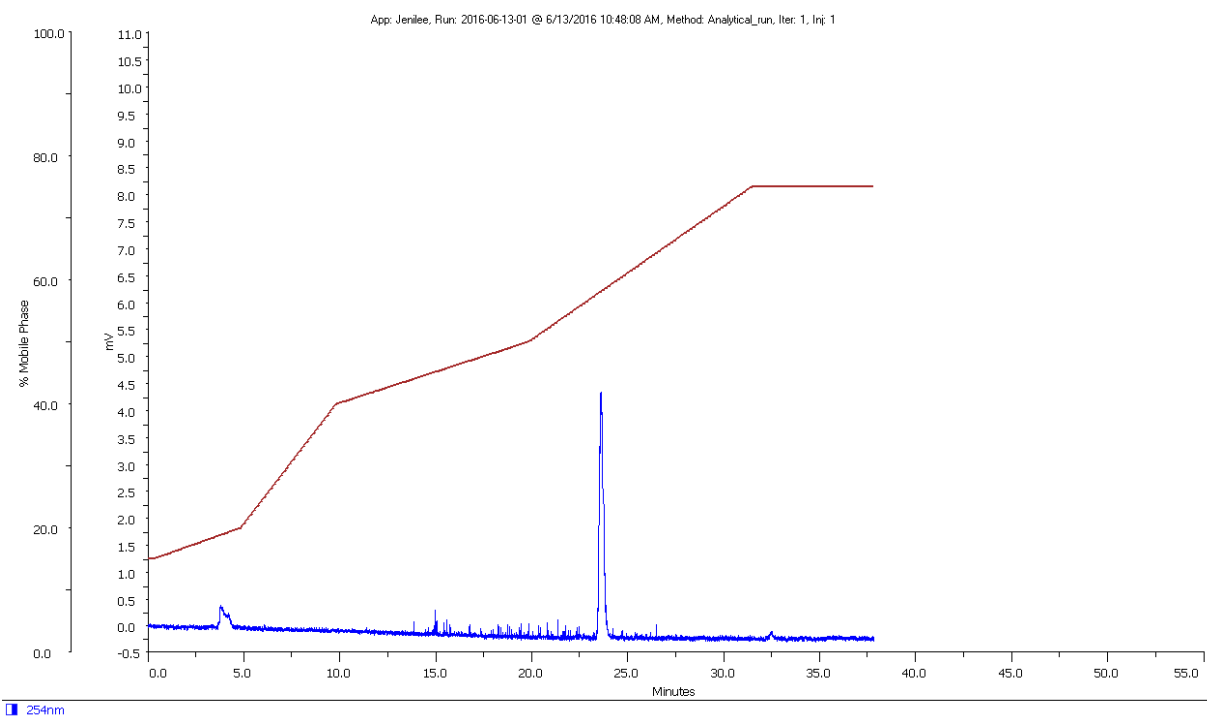


Figure S44. Analytical HPLC for compound **12**.

N-(4-(4-ethynyltoluene)phenyl)-4-((4-(pyridine-3-ylmethyl)piperazin-1-yl) methyl) benzamide, compound 13, supporting data.

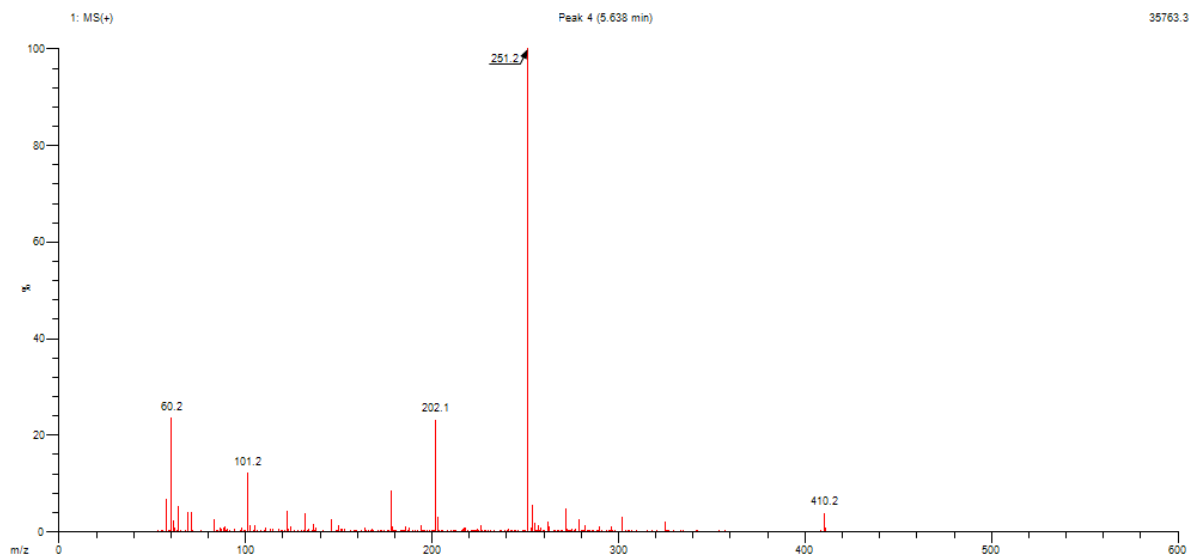
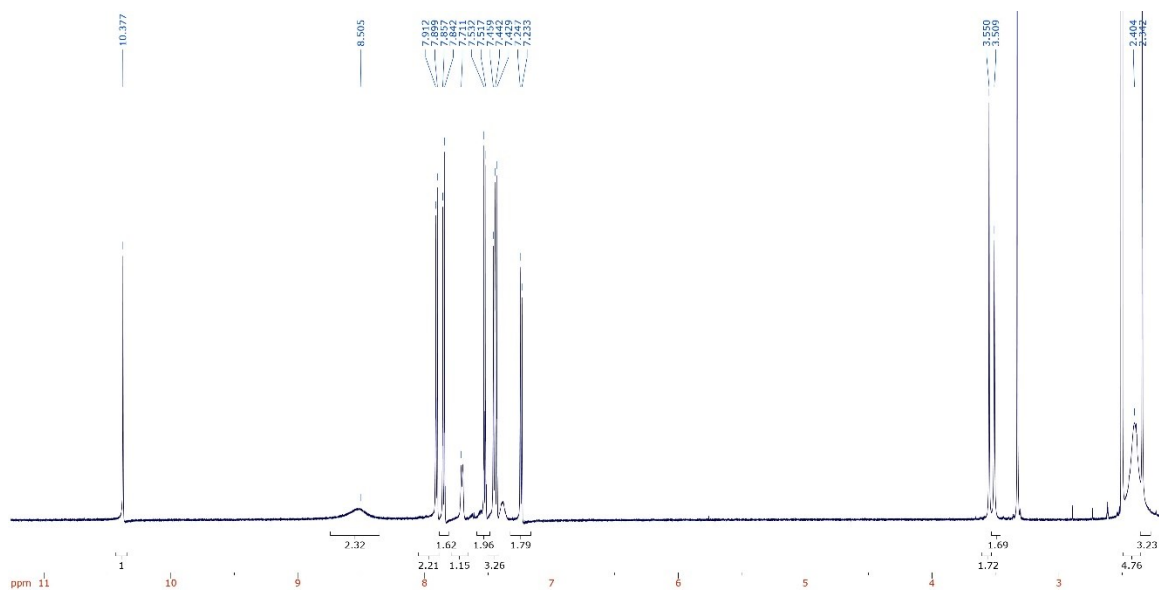


Figure S45. LR-MS for compound 13.



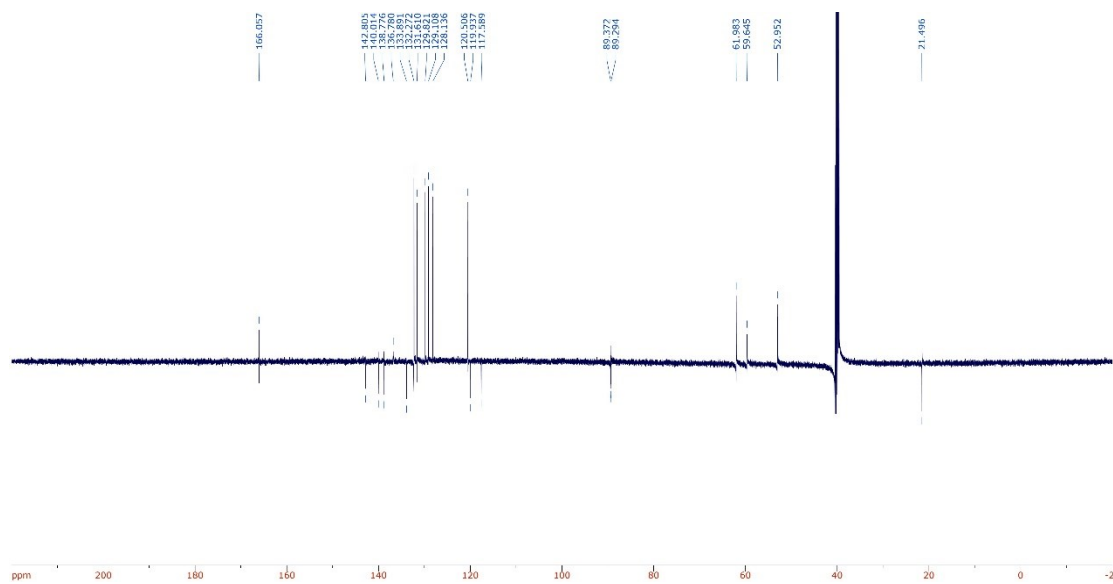


Figure S47.  $^{13}\text{C}$ -NMR for compound **13**.

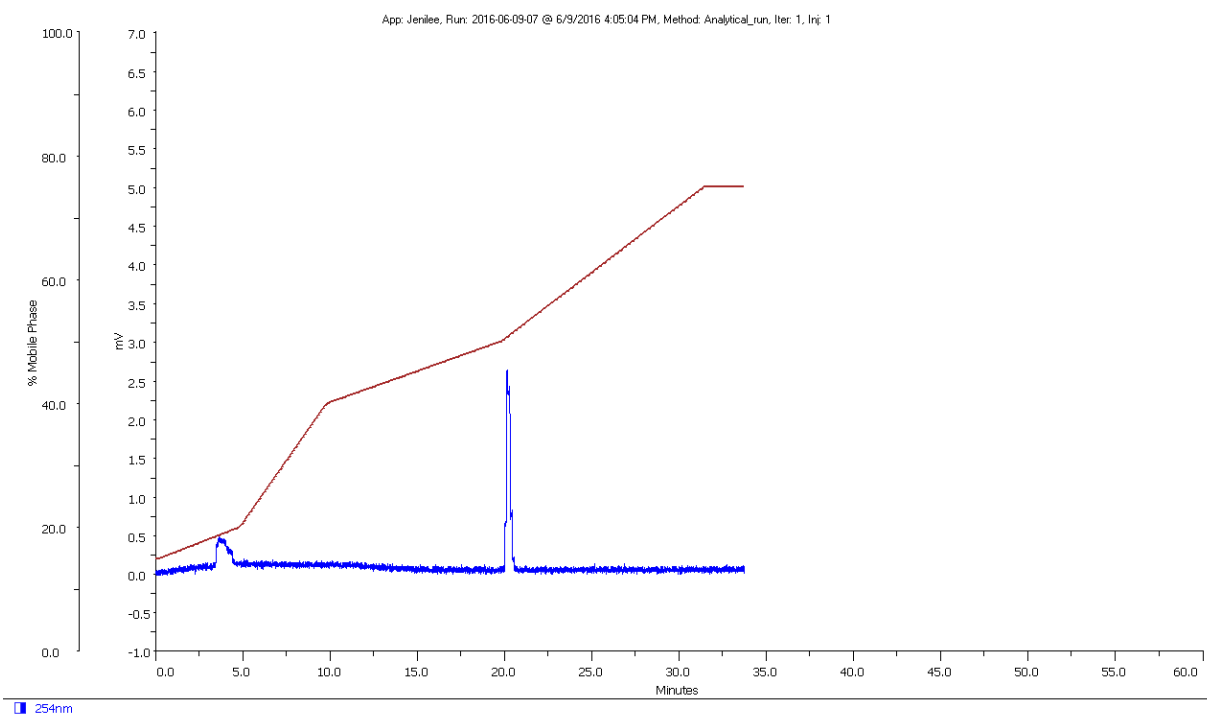


Figure S48. Analytical HPLC for compound **13**.

N-(4-(4-tert-butylphenylacetylene)phenyl)-4-((4-(pyridine-3-ylmethyl) piperazin-1-yl)methyl)benzamide, compound 14, supporting data.

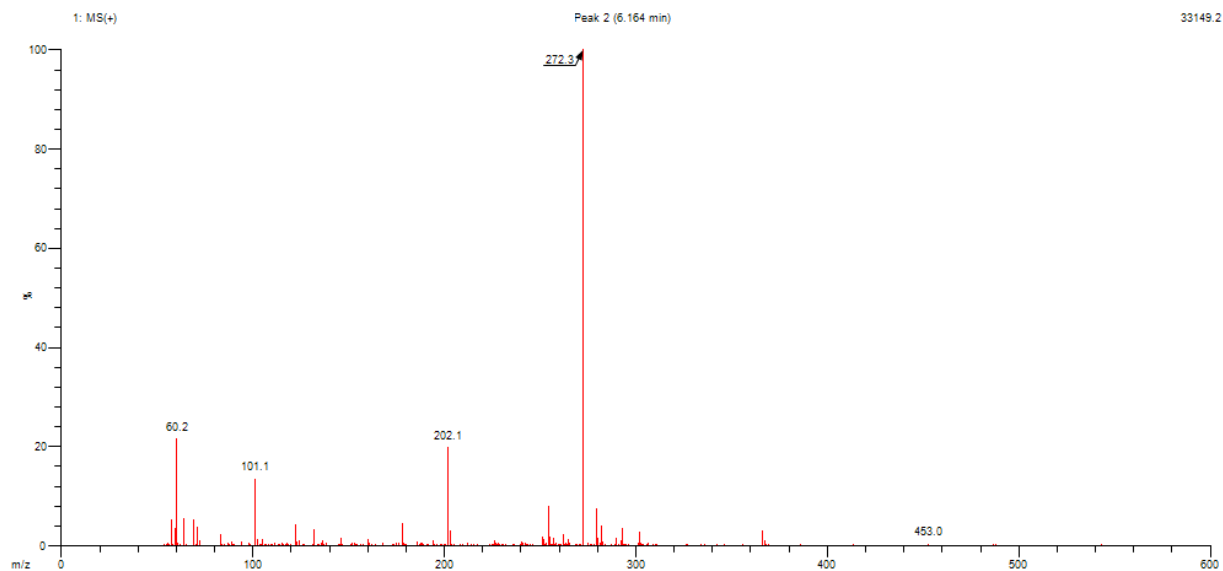


Figure S49. LR-MS for compound 14.

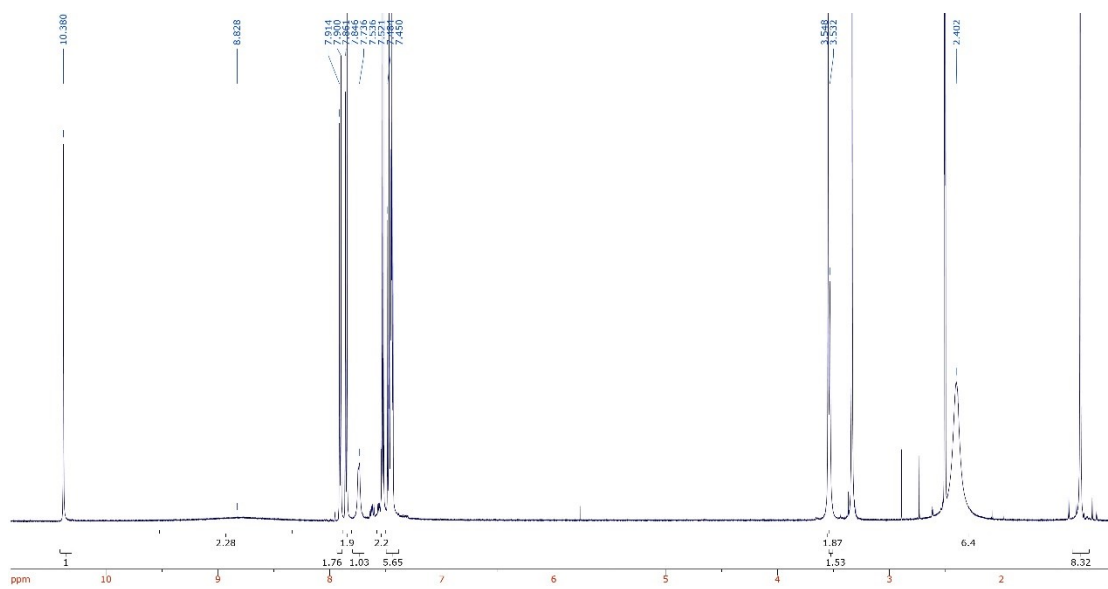


Figure S50.  $^1\text{H-NMR}$  for compound 14.

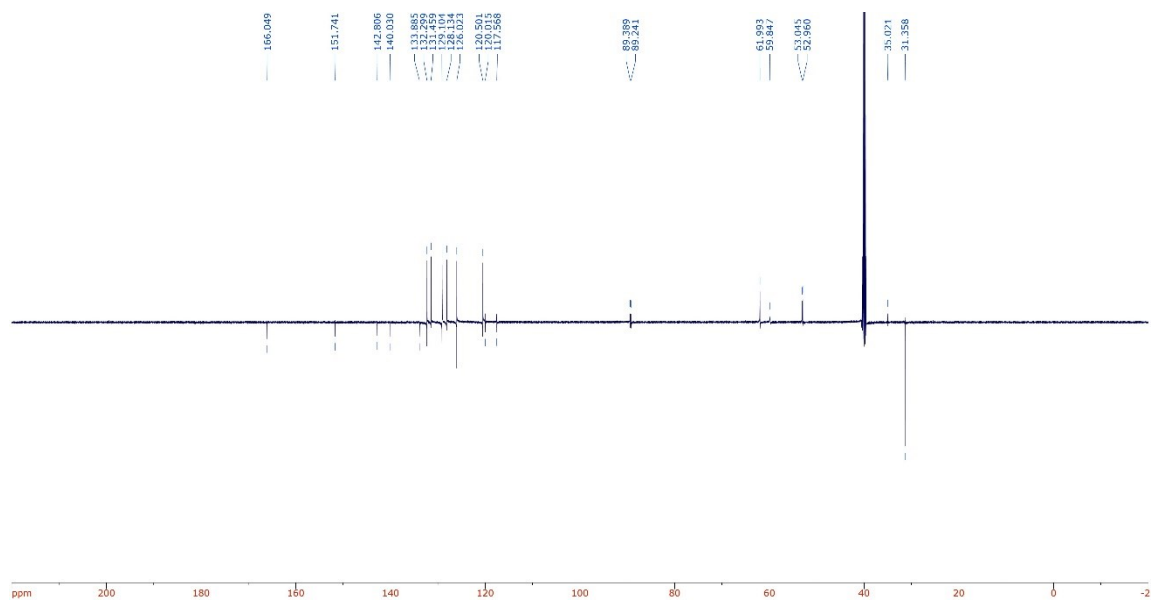


Figure S51.  $^{13}\text{C}$ -NMR for compound **14**.

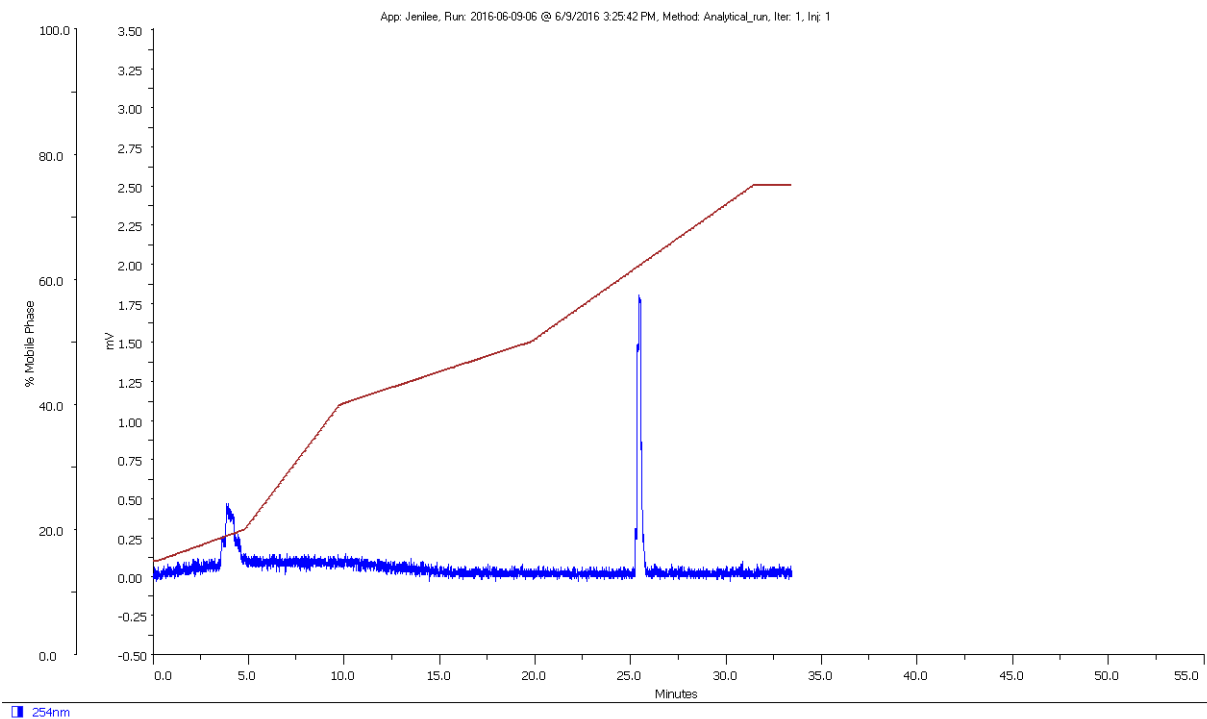


Figure S52. Analytical HPLC for compound **14**.

N-(4-(1-chloro-4-ethynylbenzene)phenyl)-4-((4-(pyridine-3-ylmethyl) piperazin-1-yl)methyl)benzamide, compound 15, supporting data.

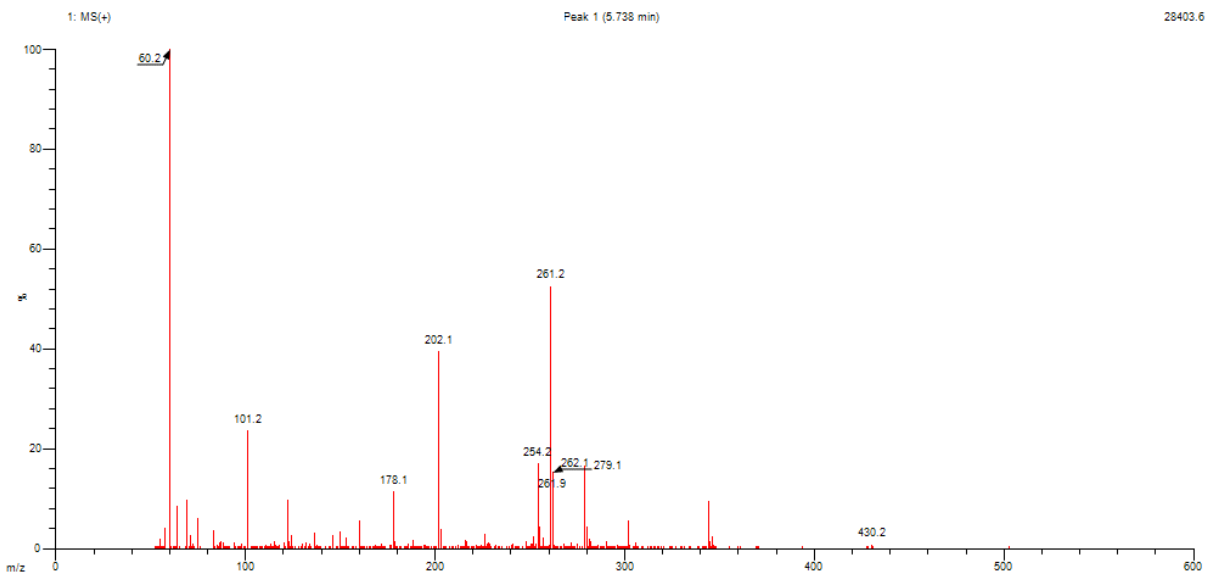


Figure S53. LR-MS for compound 15.

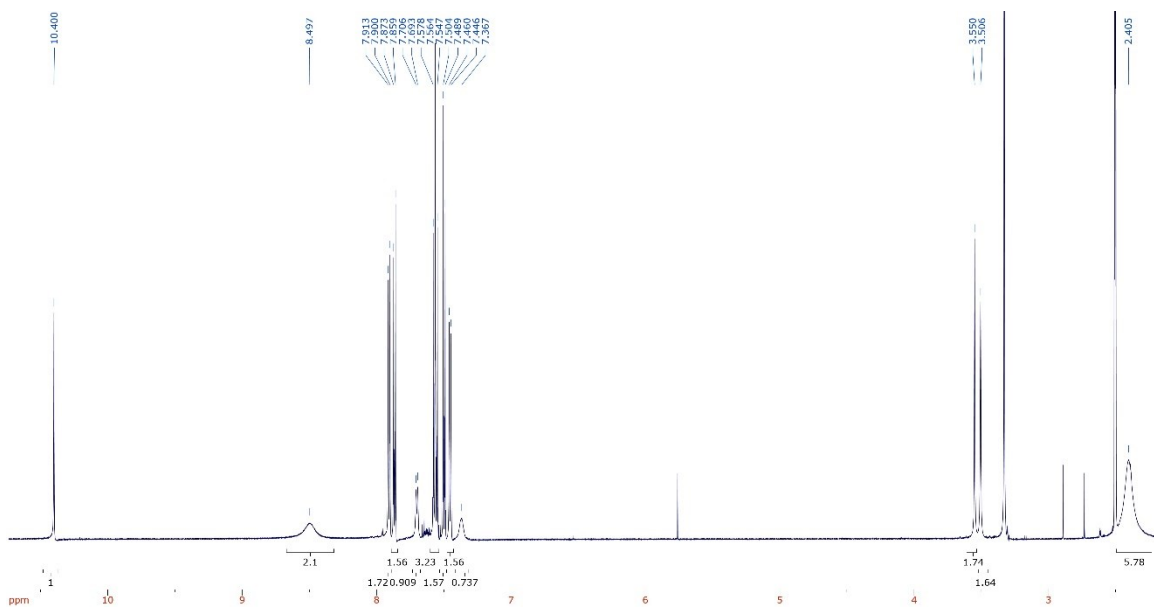


Figure S54. <sup>1</sup>H-NMR for compound 15.

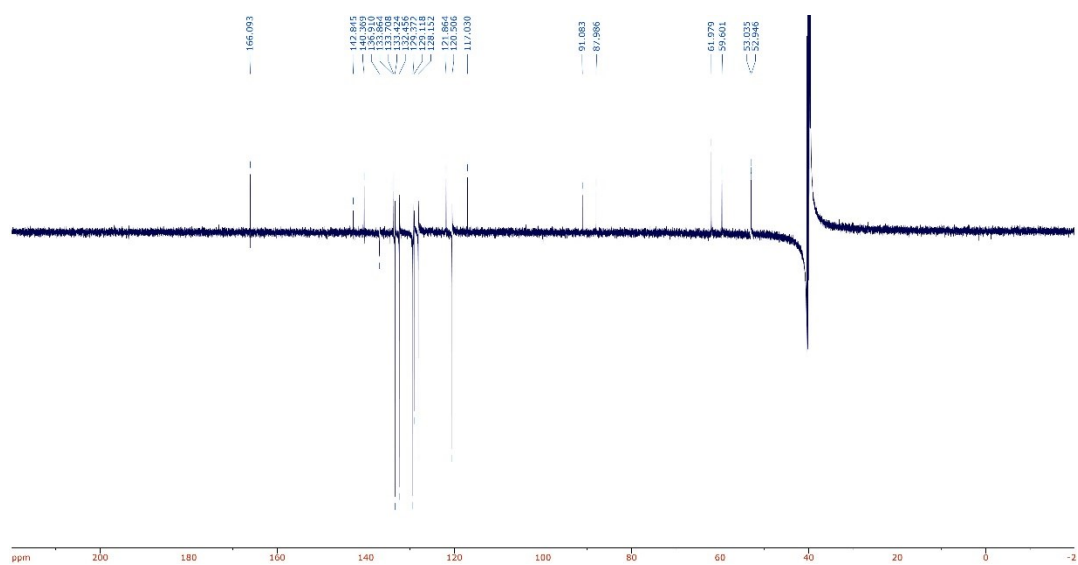


Figure S55.  $^{13}\text{C}$ -NMR for compound **15**.

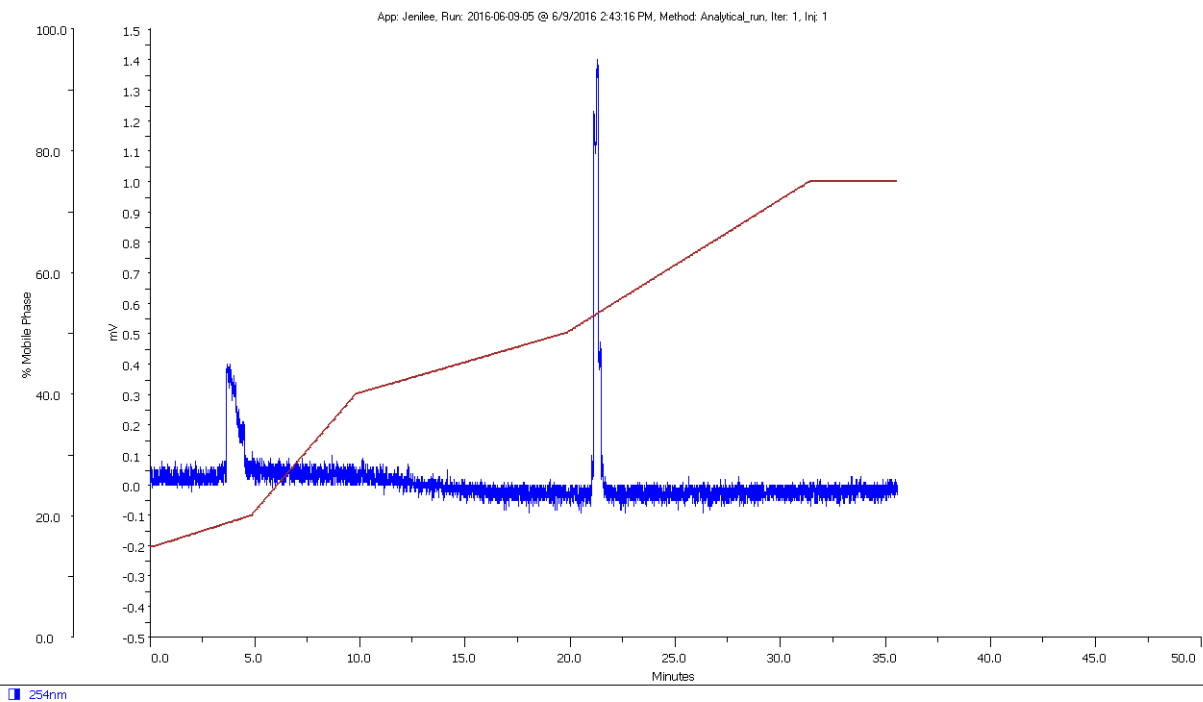


Figure S56. Analytical HPLC for compound **15**.

N-(4-(1-bromo-4-ethynylbenzene)phenyl)-4-((4-(pyridine-3-ylmethyl) piperazin-1-yl)methyl)benzamide, compound 16, supporting data.

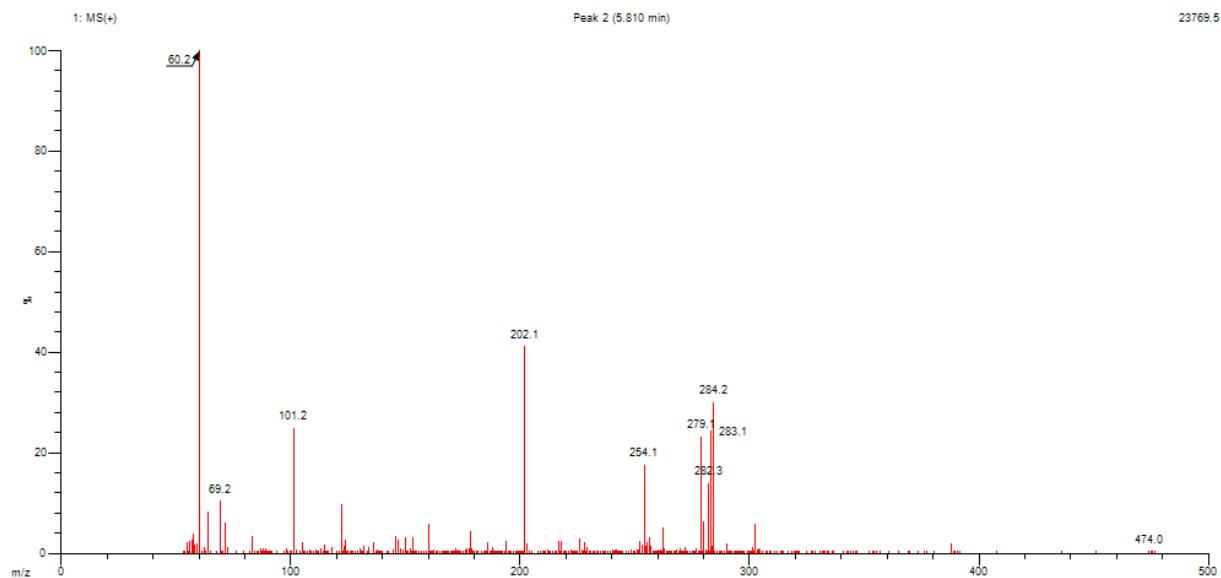


Figure S57. LR-MS for compound 16.

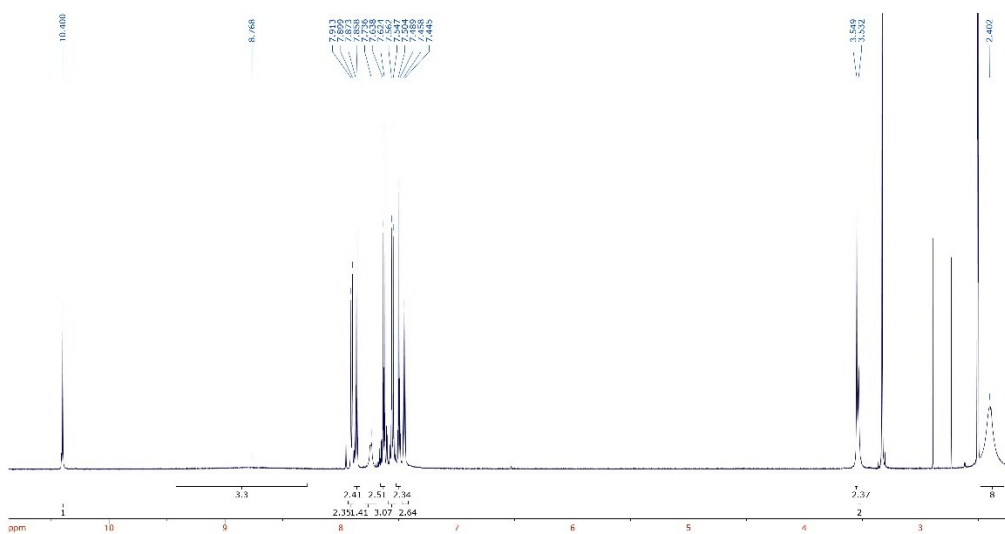


Figure S58. <sup>1</sup>H-NMR for compound 16.

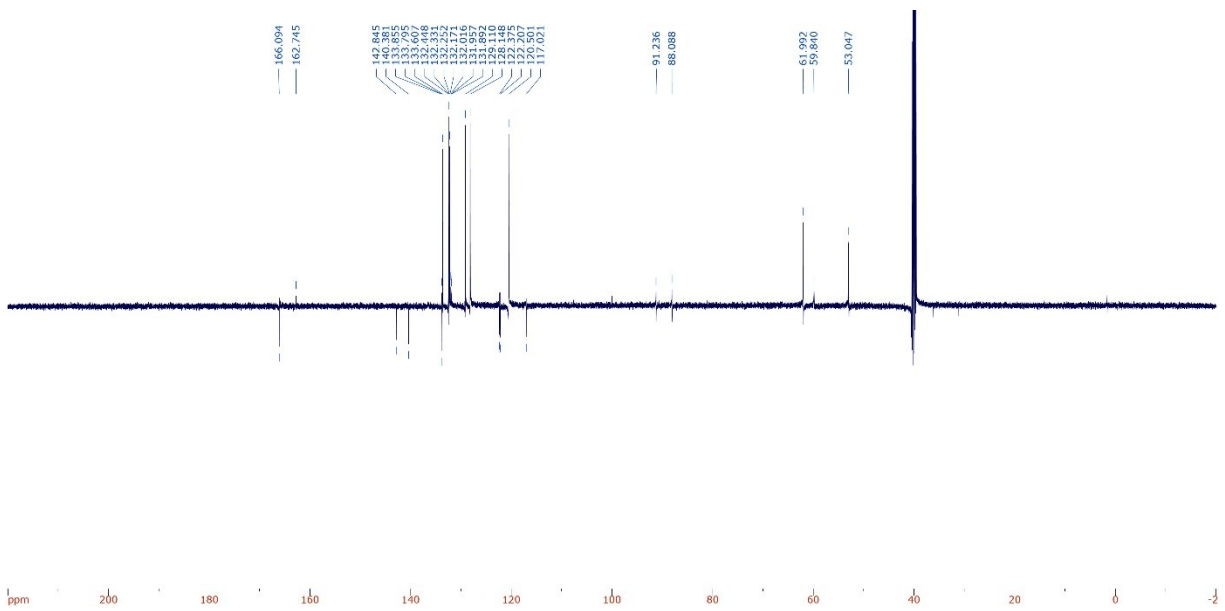


Figure S59.  $^{13}\text{C}$ -NMR for compound **16**.

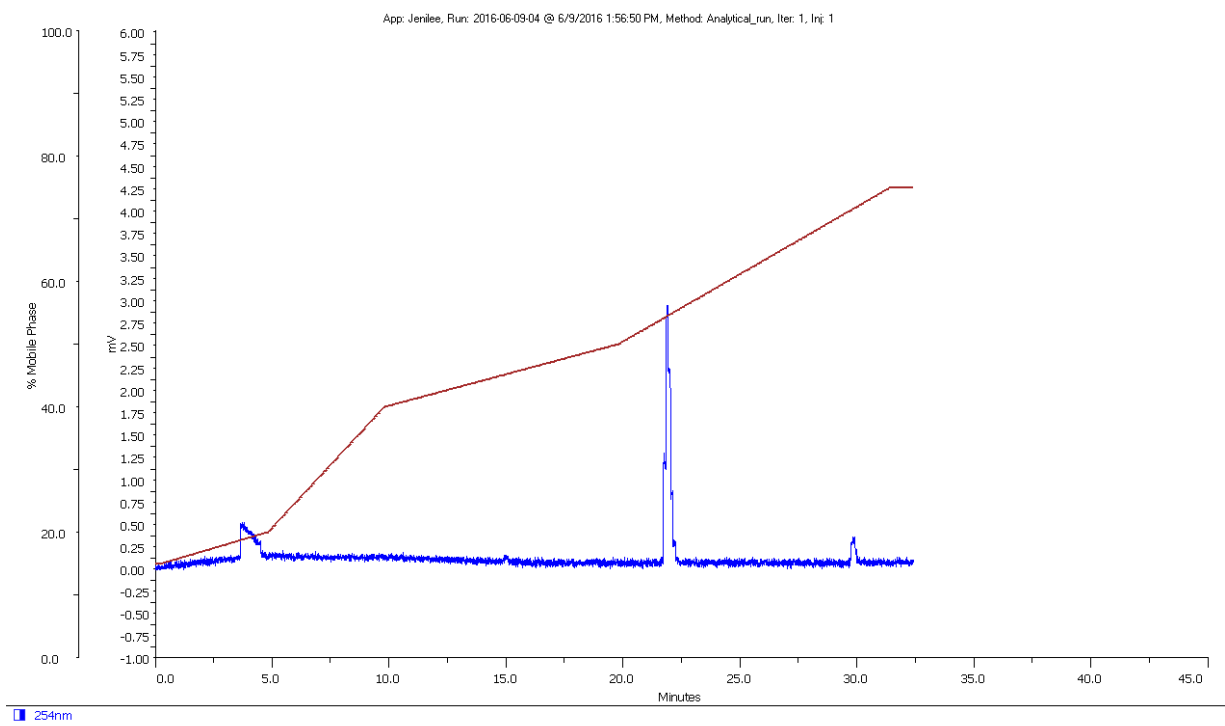


Figure S60. Analytical HPLC for compound **16**.

N-(4-(Phenylethynyl)phenyl)-4-([4-(3-pyridinyl-methyl)-1-piperazinyl)methyl] benzamide compound 17, (ER-400-583-00) , supporting data.

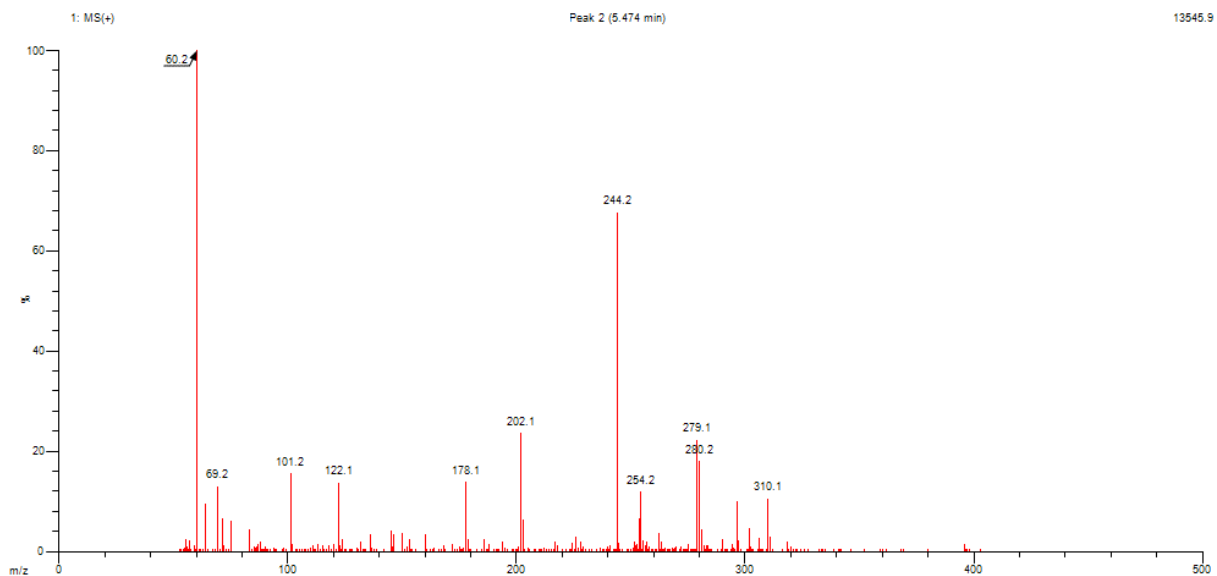


Figure S61. LR-MS for ER-400-583-00.

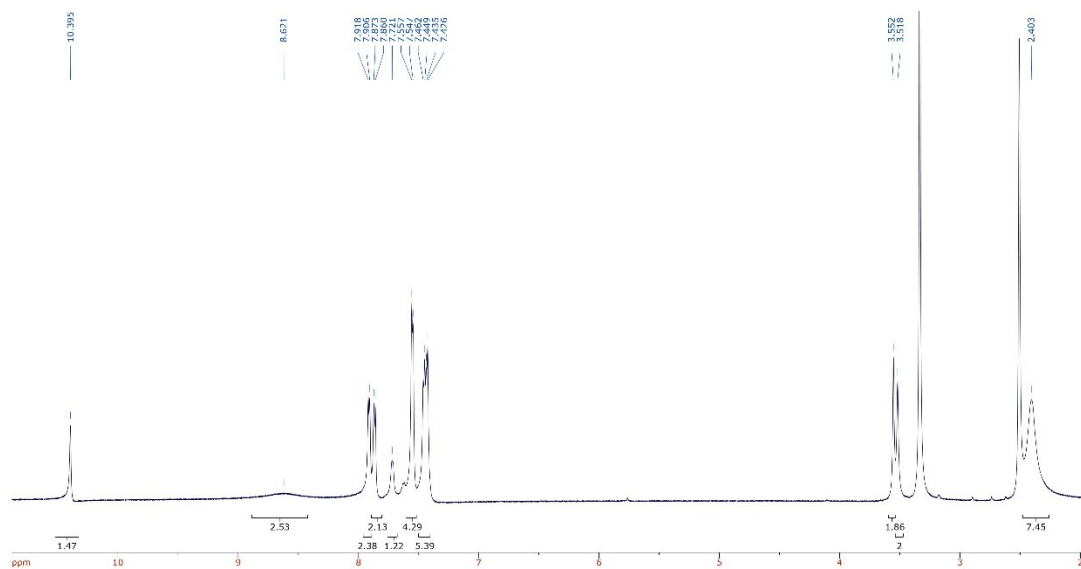


Figure S62. <sup>1</sup>H-NMR for ER-400-583-00.

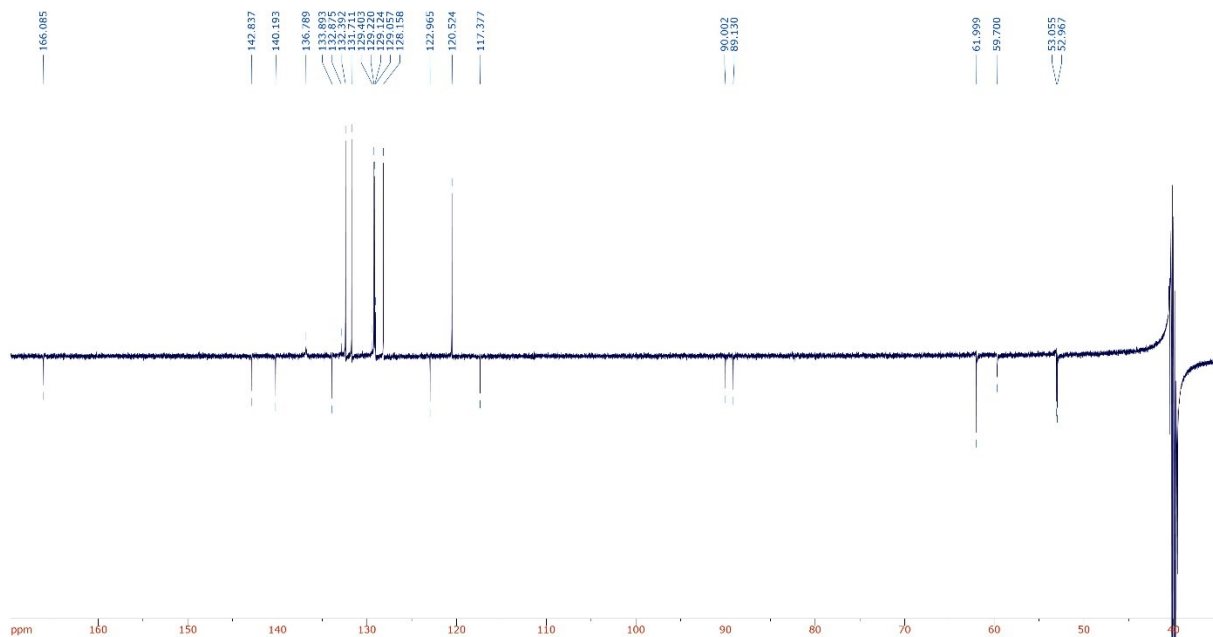


Figure S63.  $^{13}\text{C}$ -NMR for ER-400-583-00.

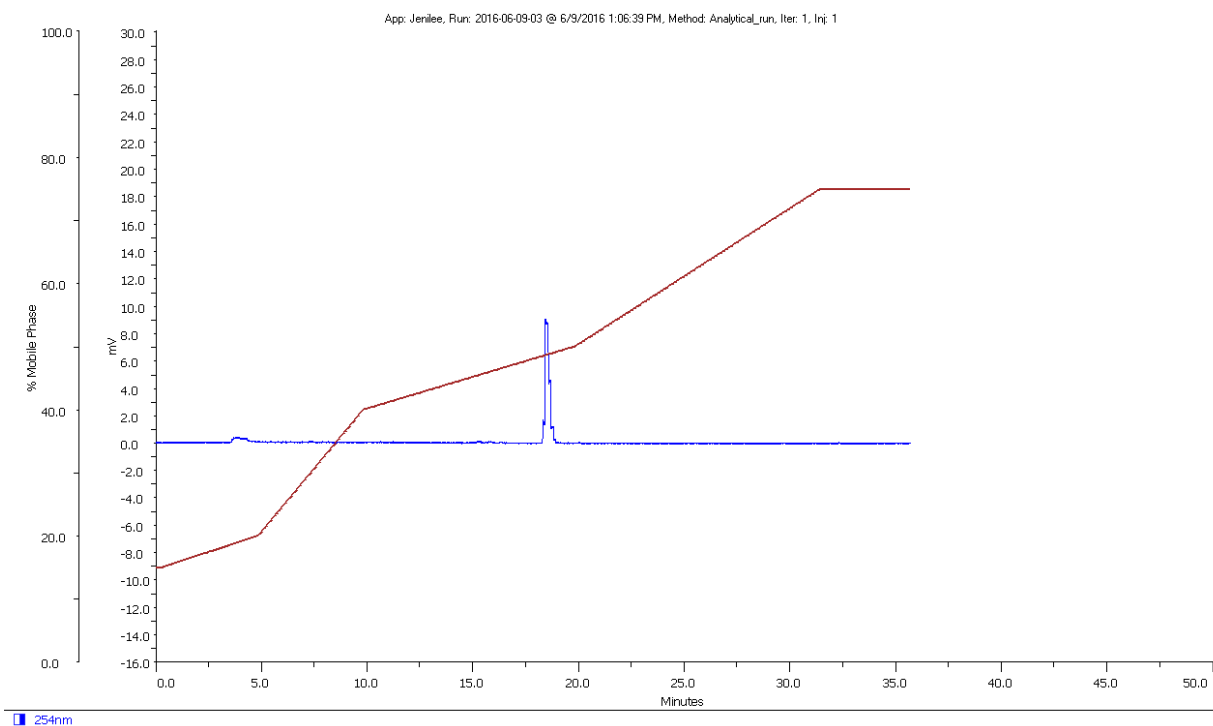


Figure S64. Analytical HPLC for ER-400-583-00.

N-(4-(1-ethyl-4-nitrobenzene)phenyl)-4-((4-(pyridine-3-ylmethyl) piperazin-1-yl)methyl)benzamide, compound 18, supporting data.

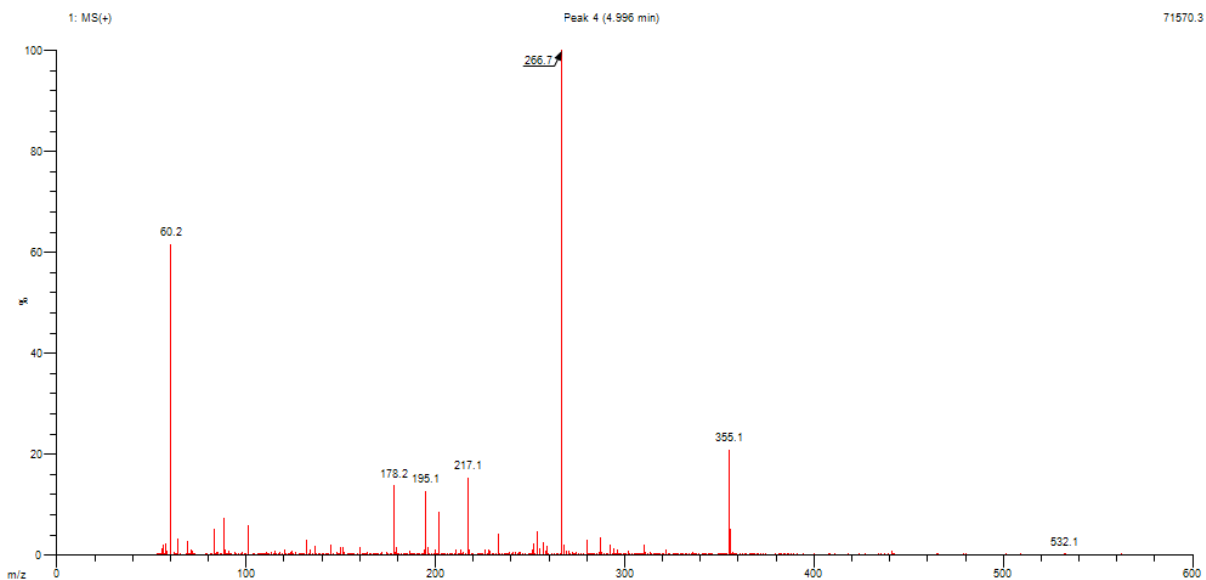


Figure S65. LR-MS for compound 18.

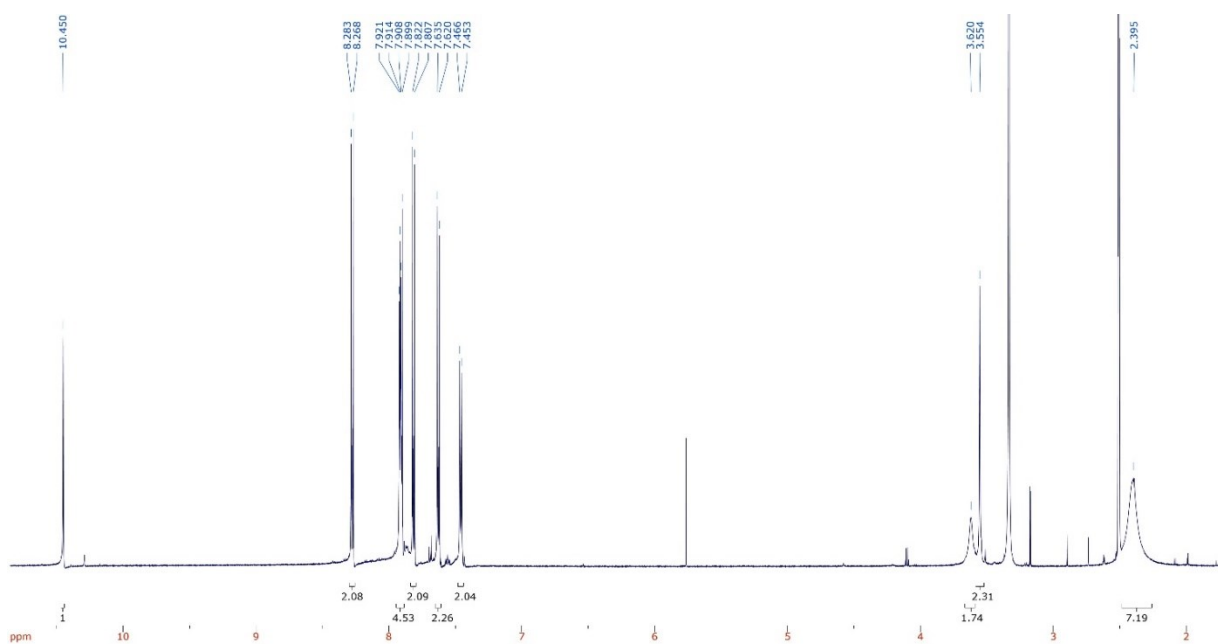


Figure S66.  $^1\text{H-NMR}$  for compound 18.

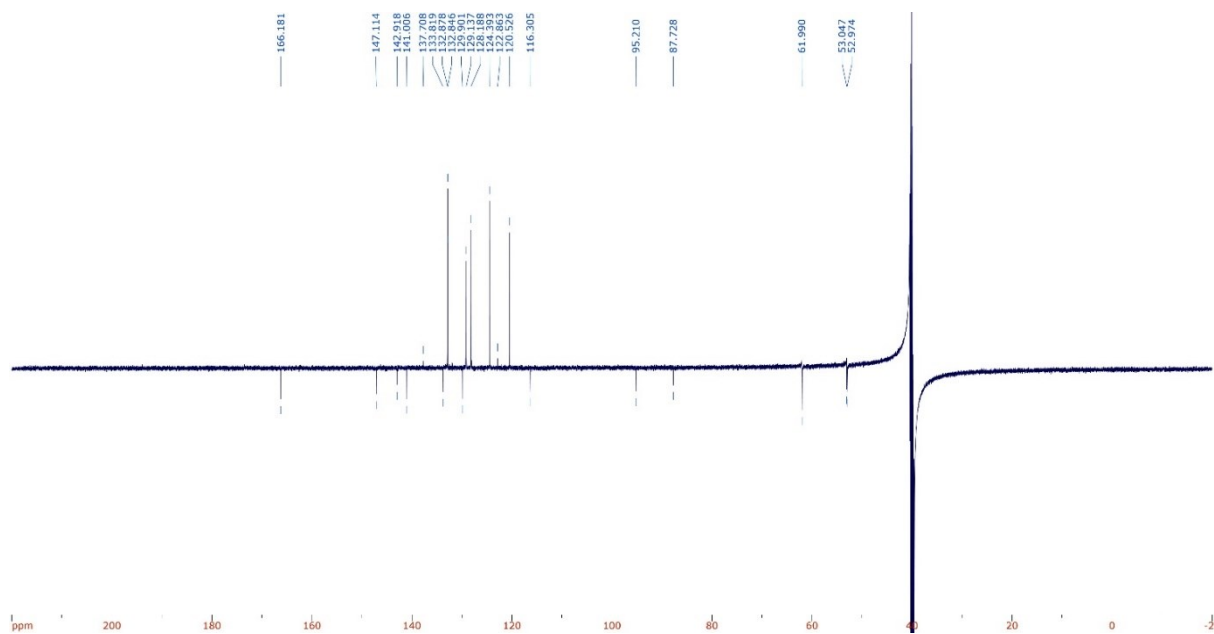


Figure S67.  $^{13}\text{C}$ -NMR for compound **18**.

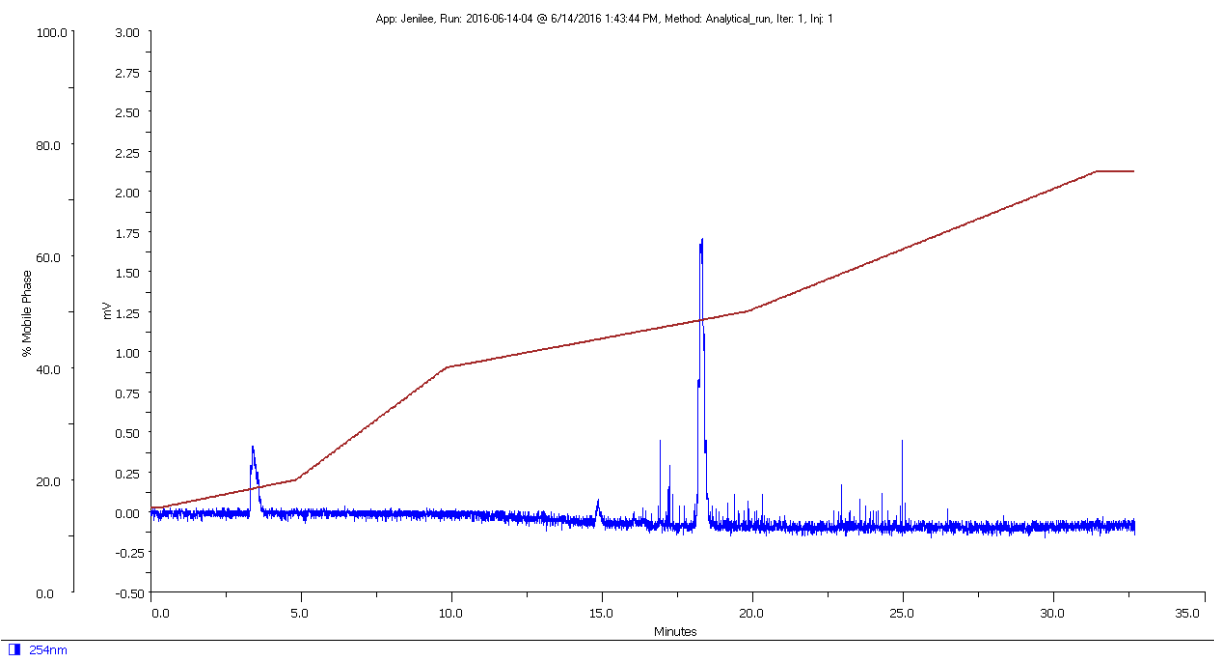


Figure S68. Analytical HPLC for compound **18**.

N-(4-(4-ethylnyl-N,N-dimethylaniline)phenyl)-4-((4-(pyridine-3-ylmethyl) piperazin-1-yl)methyl)benzamide, compound 19, supporting data.

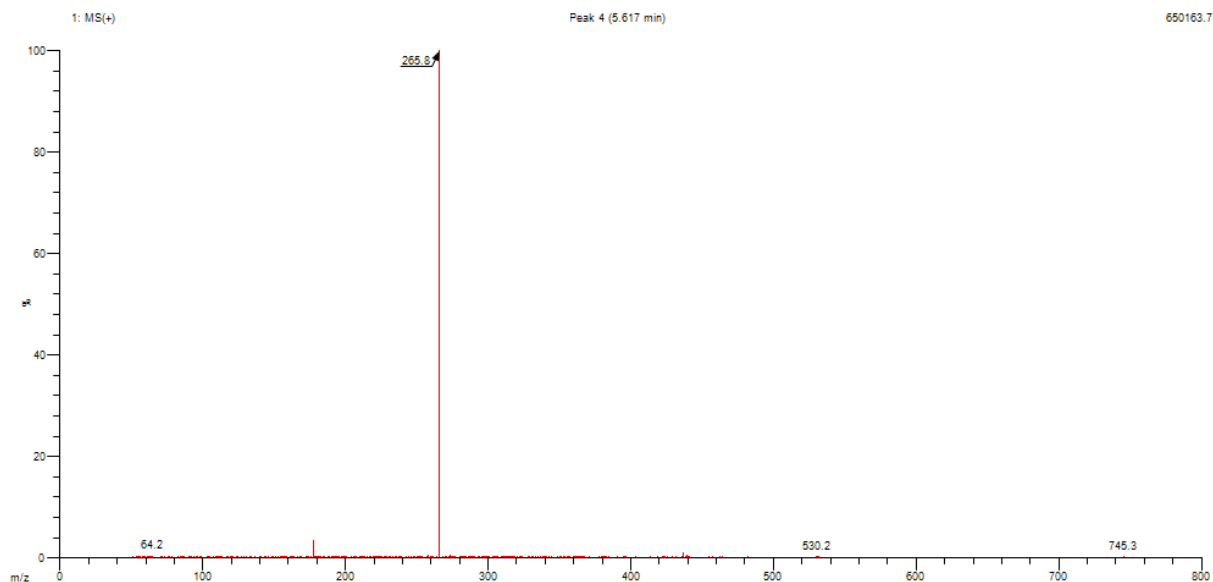


Figure S69. LR-MS for compound 19.

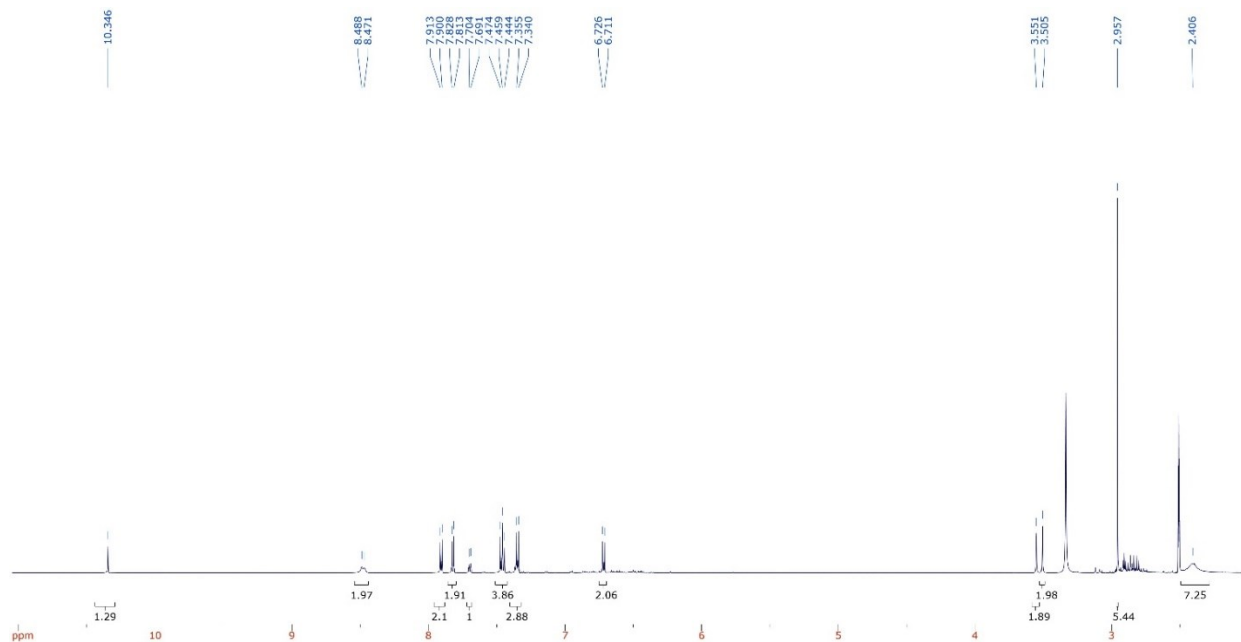


Figure S70. <sup>1</sup>H-NMR for compound 19.

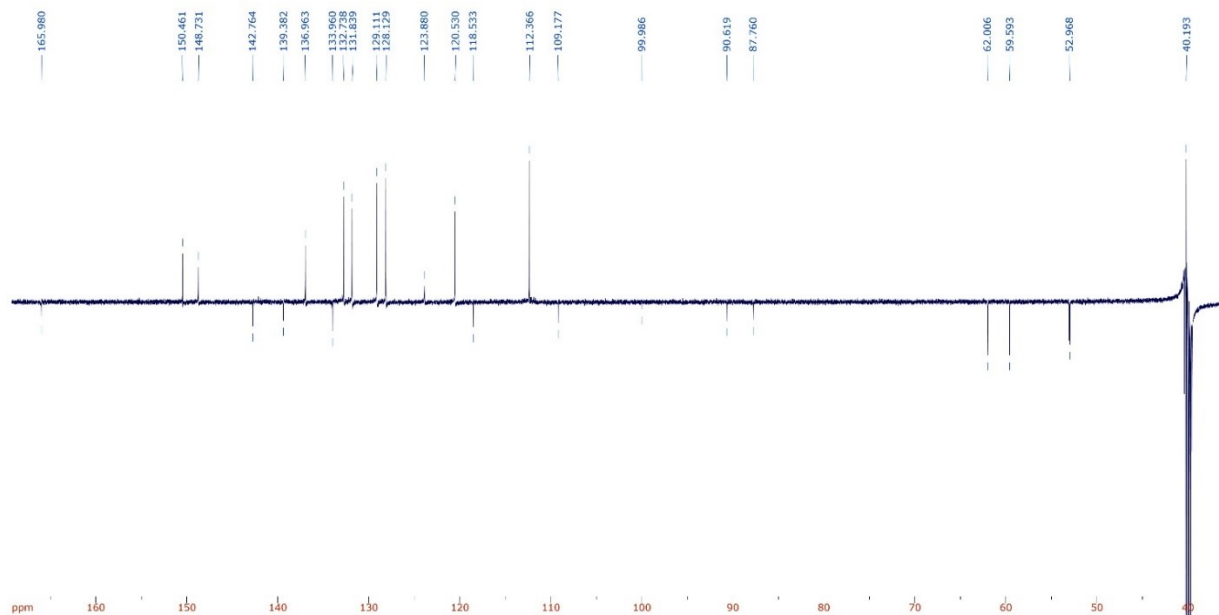


Figure S71.  $^{13}\text{C}$ -NMR for compound **19**.

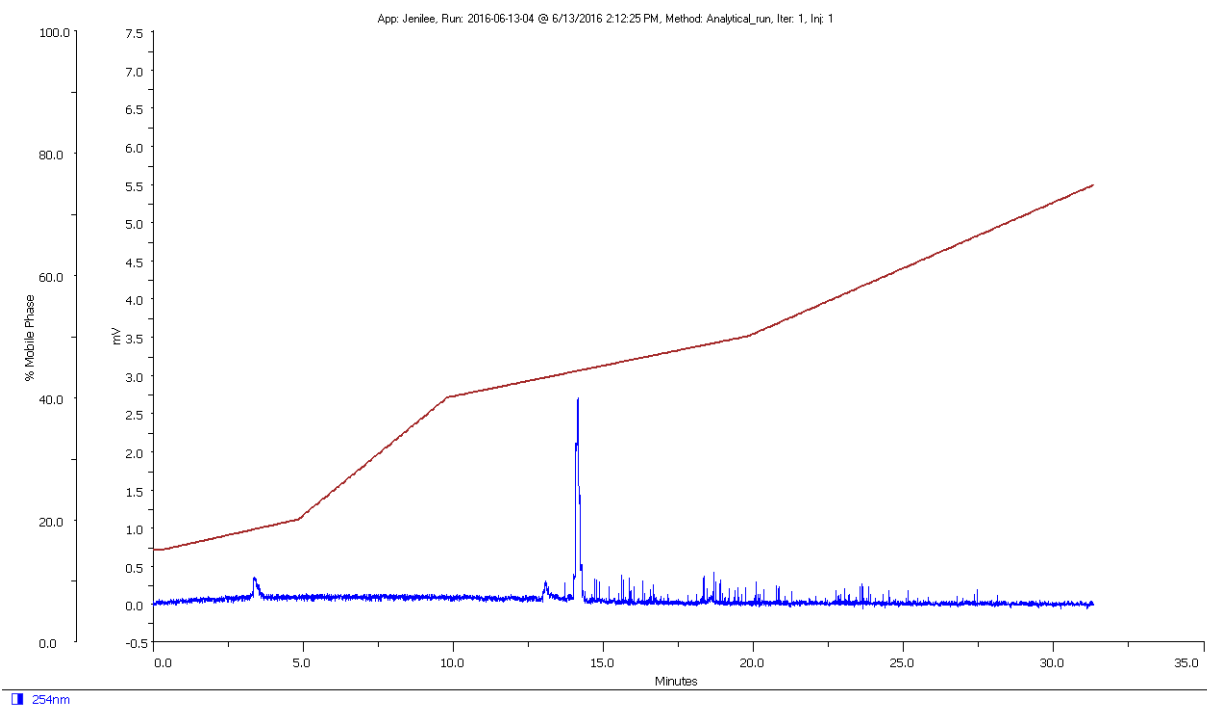


Figure S72. Analytical HPLC for compound **19**.

N-(4-(1-ethynyl-4-(trifluoromethyl)benzene)-phenyl)-4-((4-(pyridine-3-ylmethyl) piperazin-1-yl)methyl)-benzamide, compound 20, supporting data.

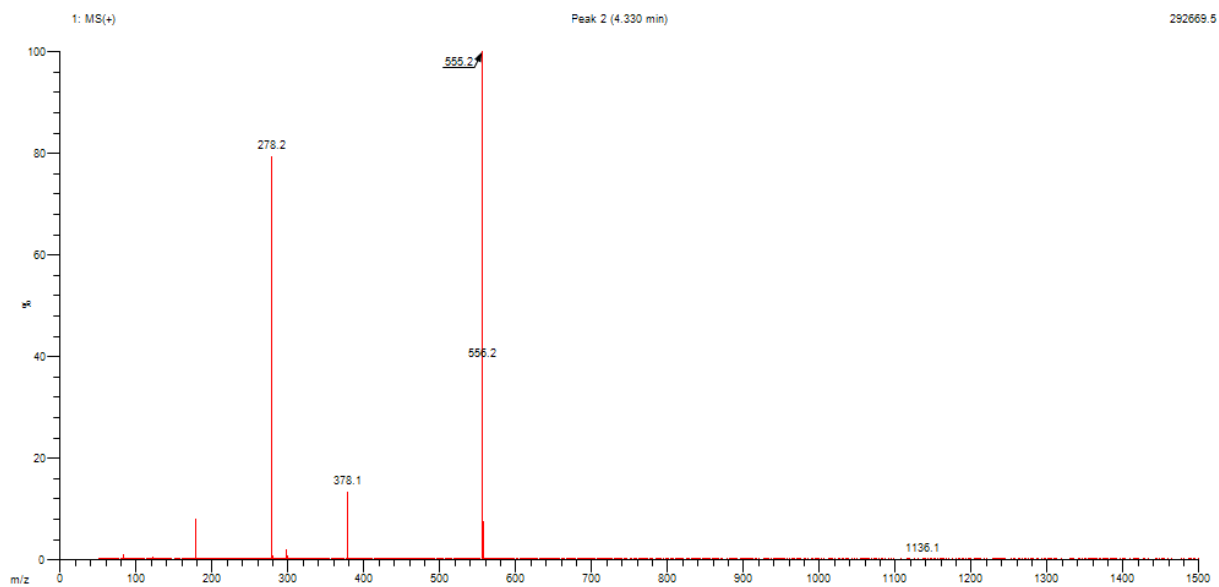


Figure S73. LR-MS for compound 20.

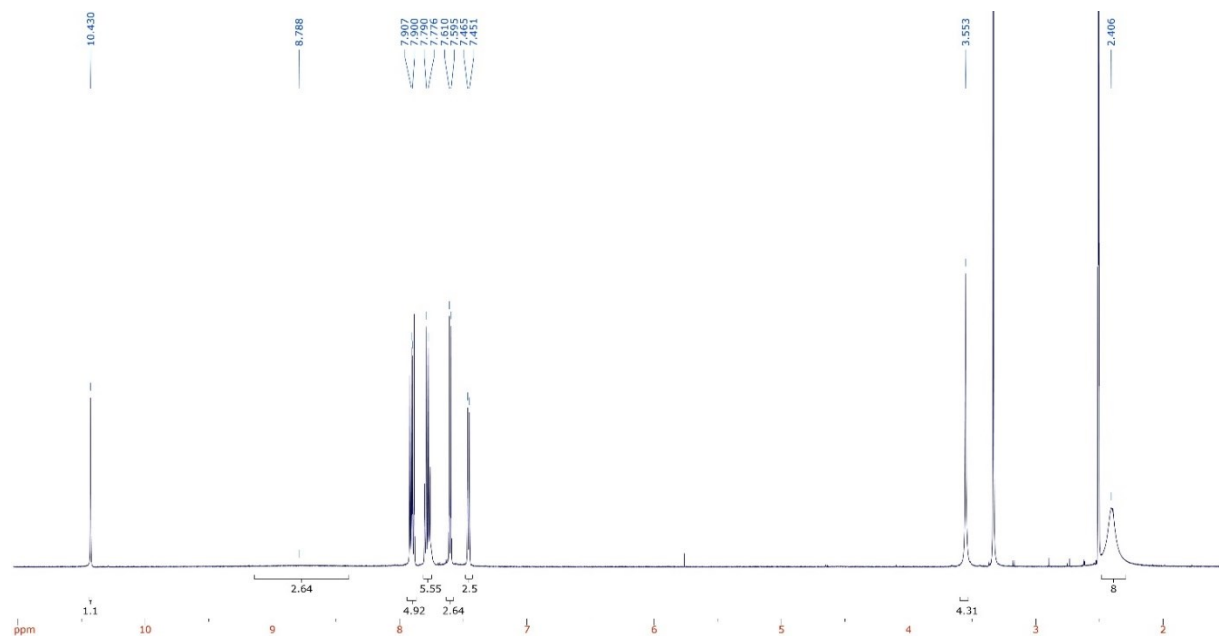


Figure S74. <sup>1</sup>H-NMR for compound 20.



l-(PPg)LLFVY, compound 21, supporting data.

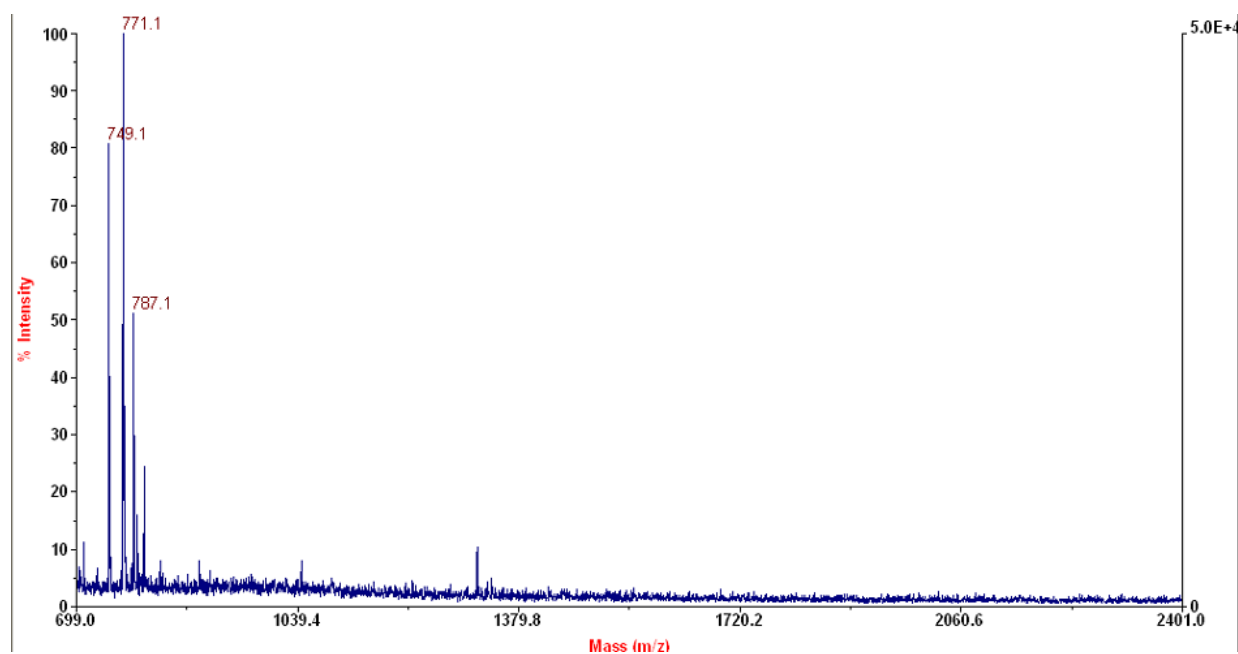


Figure S77. MALDI spectra for l-(PPg)LLFVY.

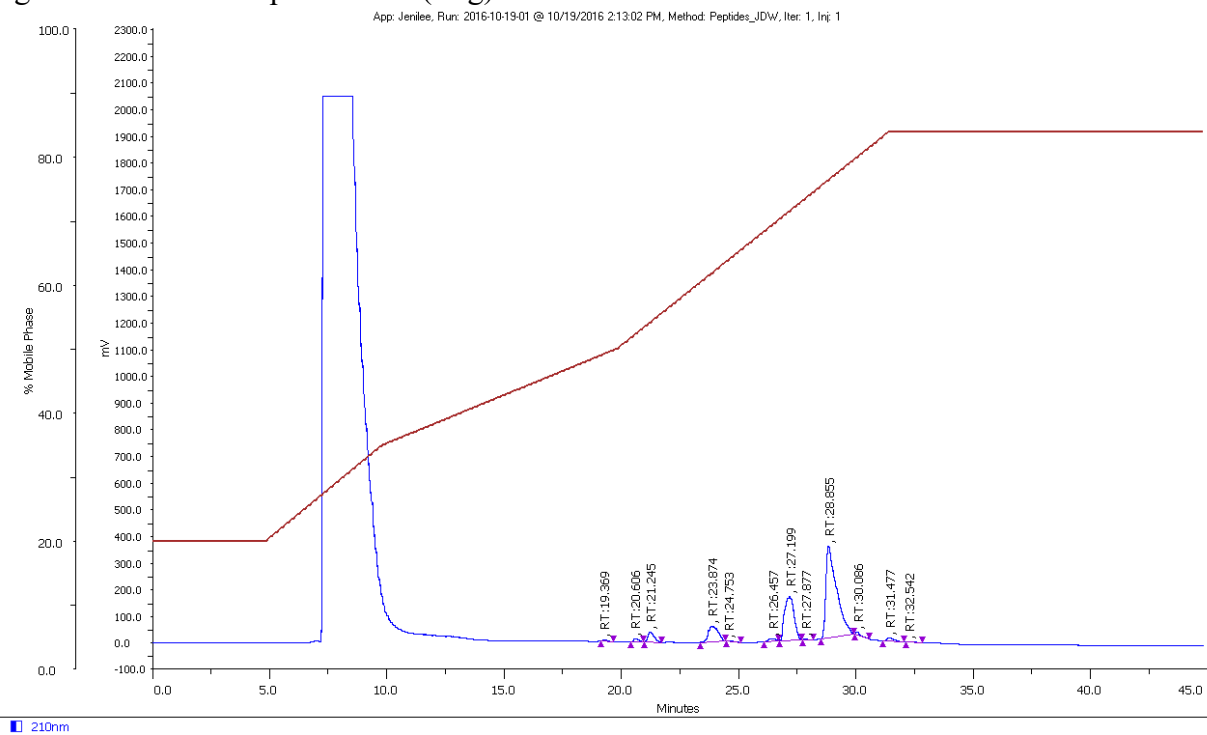


Figure S78. Crude HPLC chromatogram of l-(PPg)LLFVY, product is 28.9 minutes.

l-C(StBu)LLFVY, compound 22, supporting data.

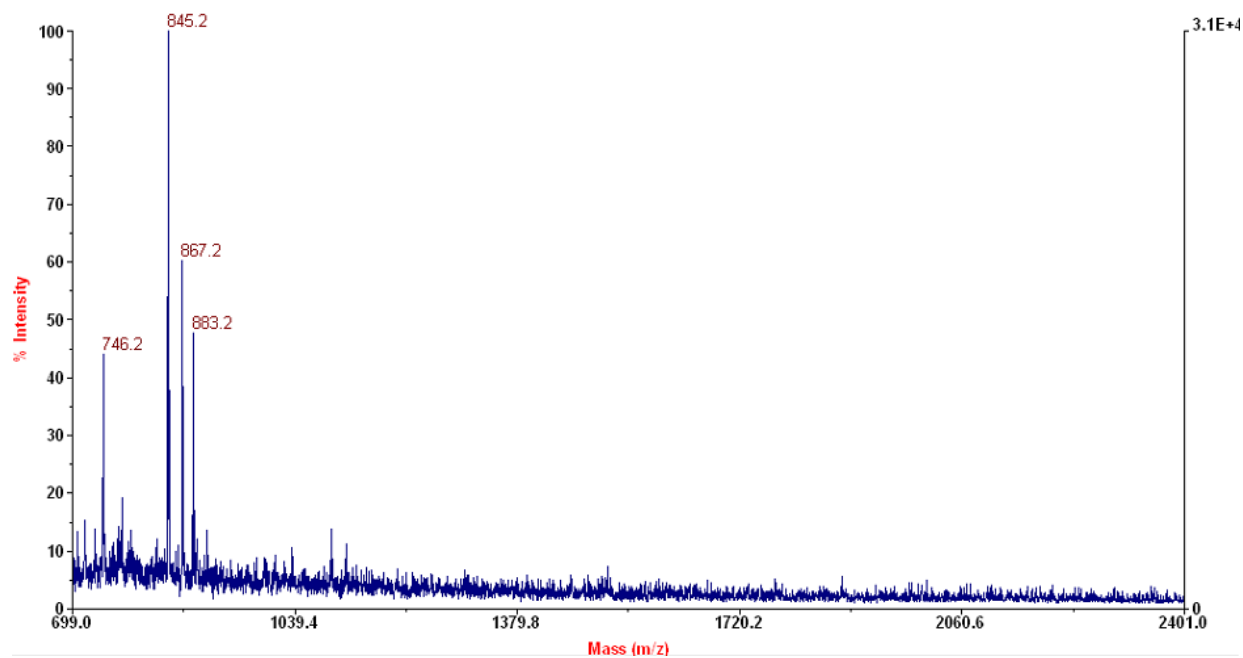


Figure S79. MALDI spectra for l-C(StBu)LLFVY.

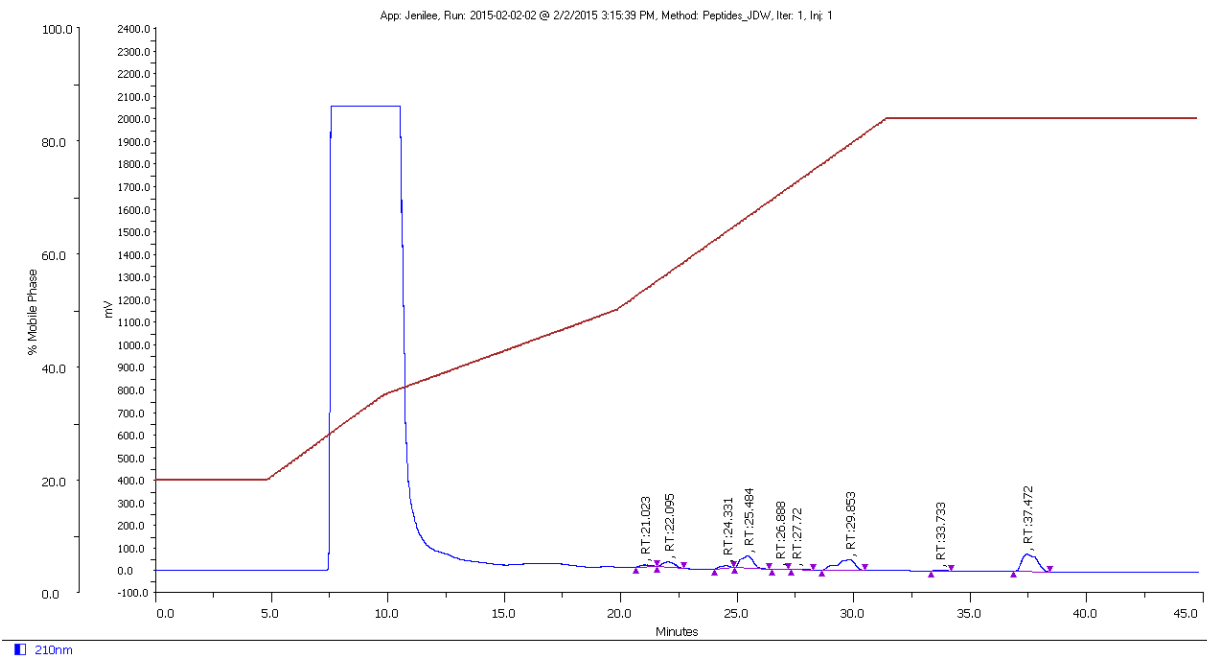


Figure S80. Crude HPLC chromatogram of l-C(StBu)LLFVY, product is 29.5 minutes.

c-(Ppg)LLFVY, compound 23, supporting data.

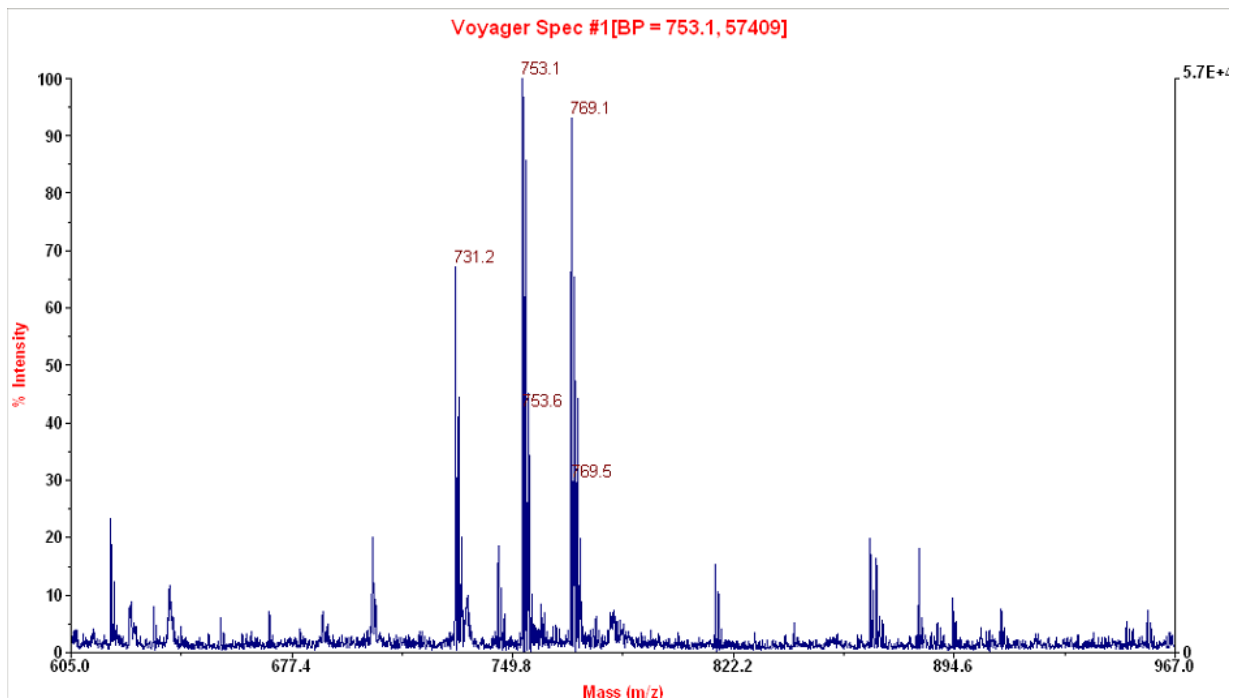


Figure S81. MALDI spectra for c-(Ppg)LLFVY.

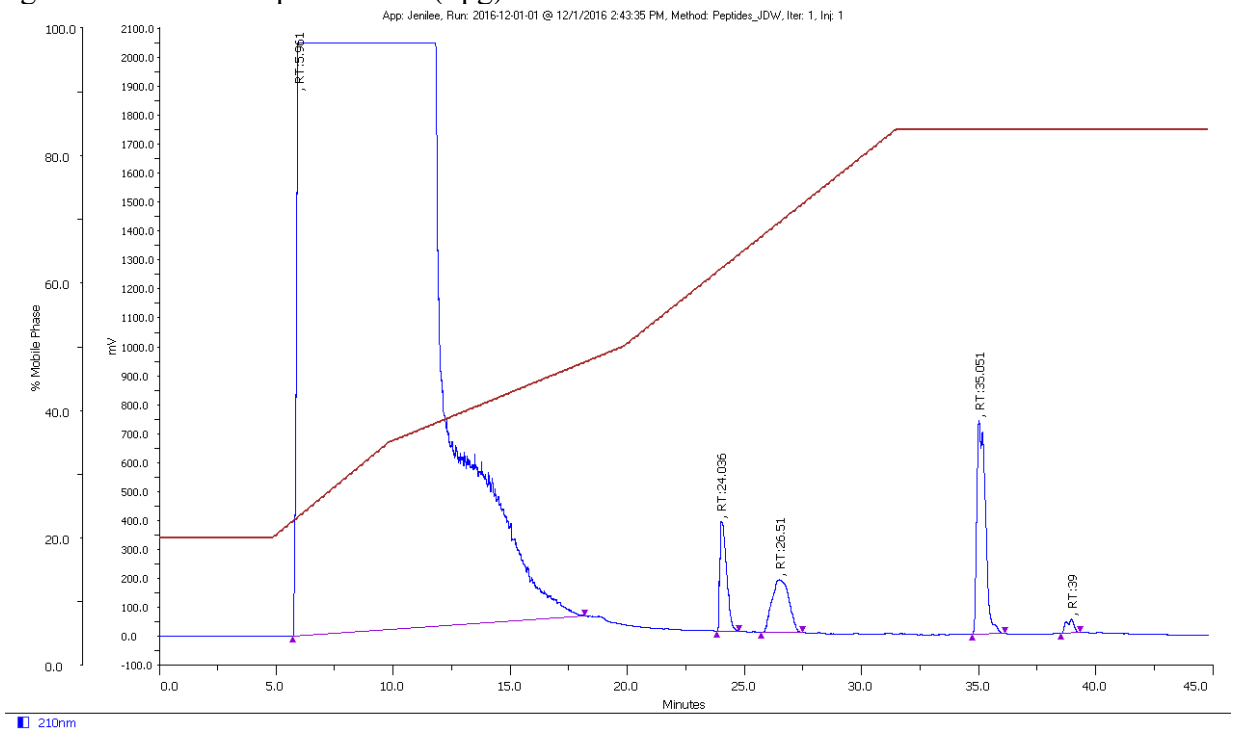


Figure S82. Crude HPLC chromatogram of c-(PPg)LLFVY, product is 35 minutes.

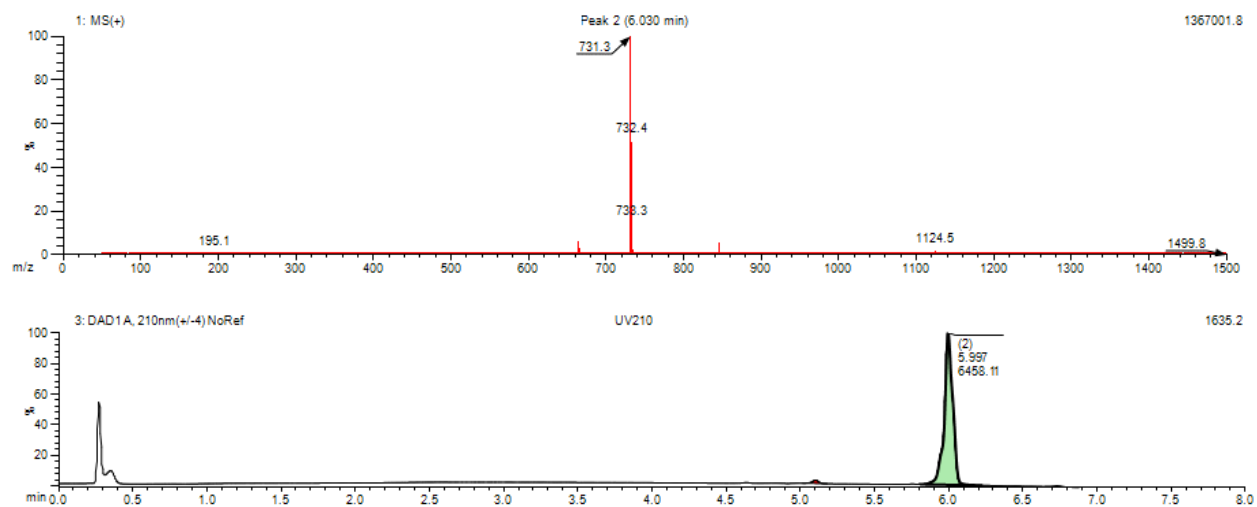


Figure S83. Pure HPLC UV spectra at 210 nm, including LCMS for c-(Ppg)LLFVY.

c-C(StBu)LLFVY, compound 24, supporting data.

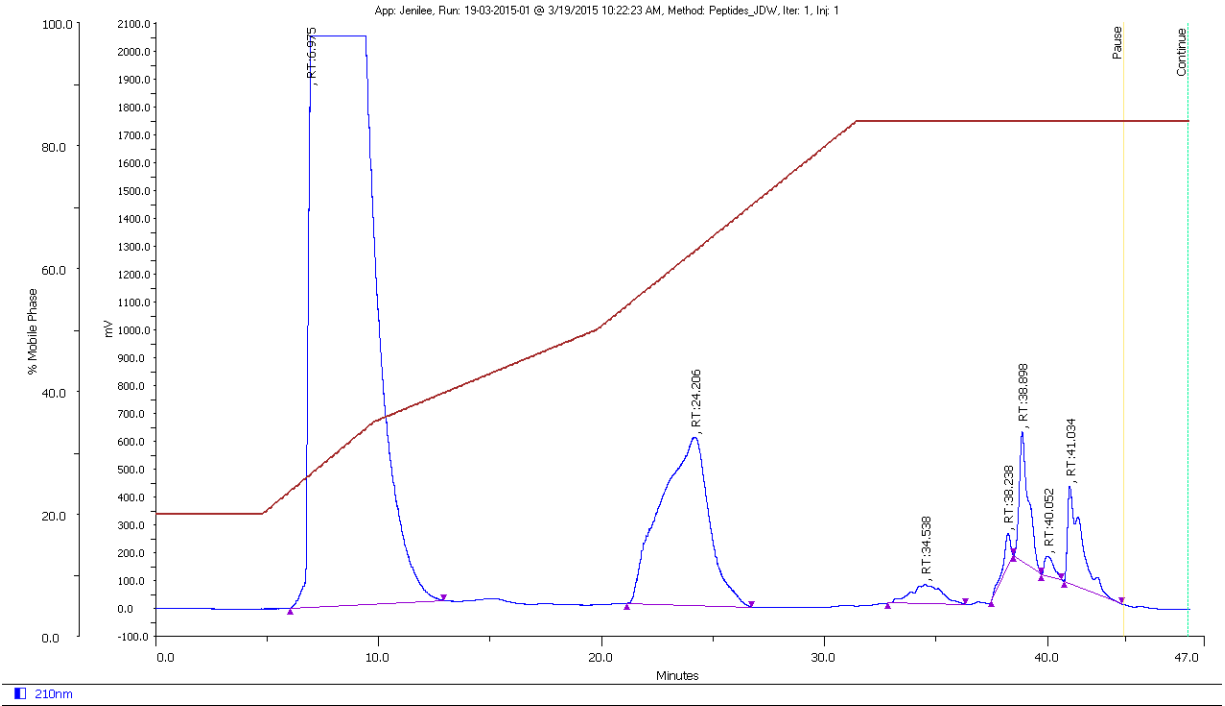


Figure S84. Crude HPLC chromatogram of c-C(StBu)LLFVY, product is 38.9 minutes.

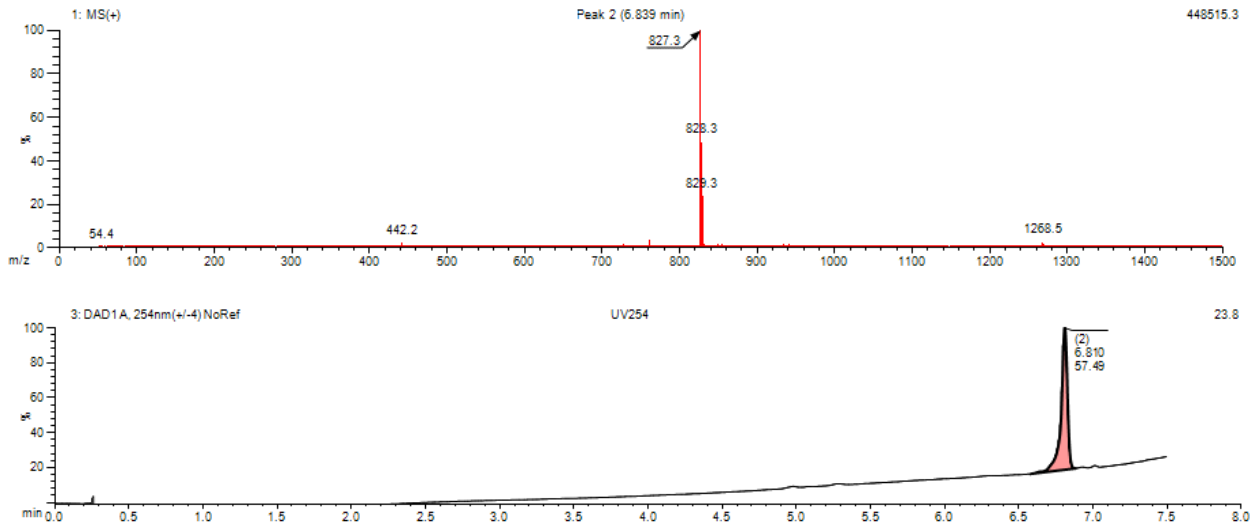


Figure S85. HPLC UV spectra at 254nm, including LCMS for c-C(StBu)LLFVY.

c-CLLFVY, compound 25 supporting data.

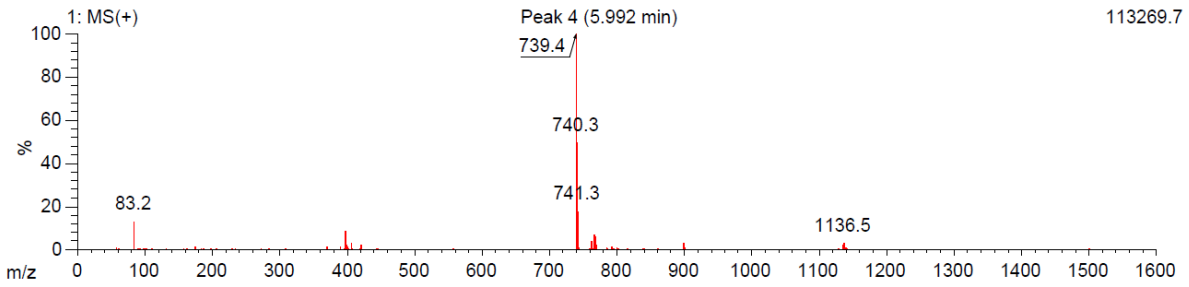


Figure S86. LC-MS for c-CLLFVY.

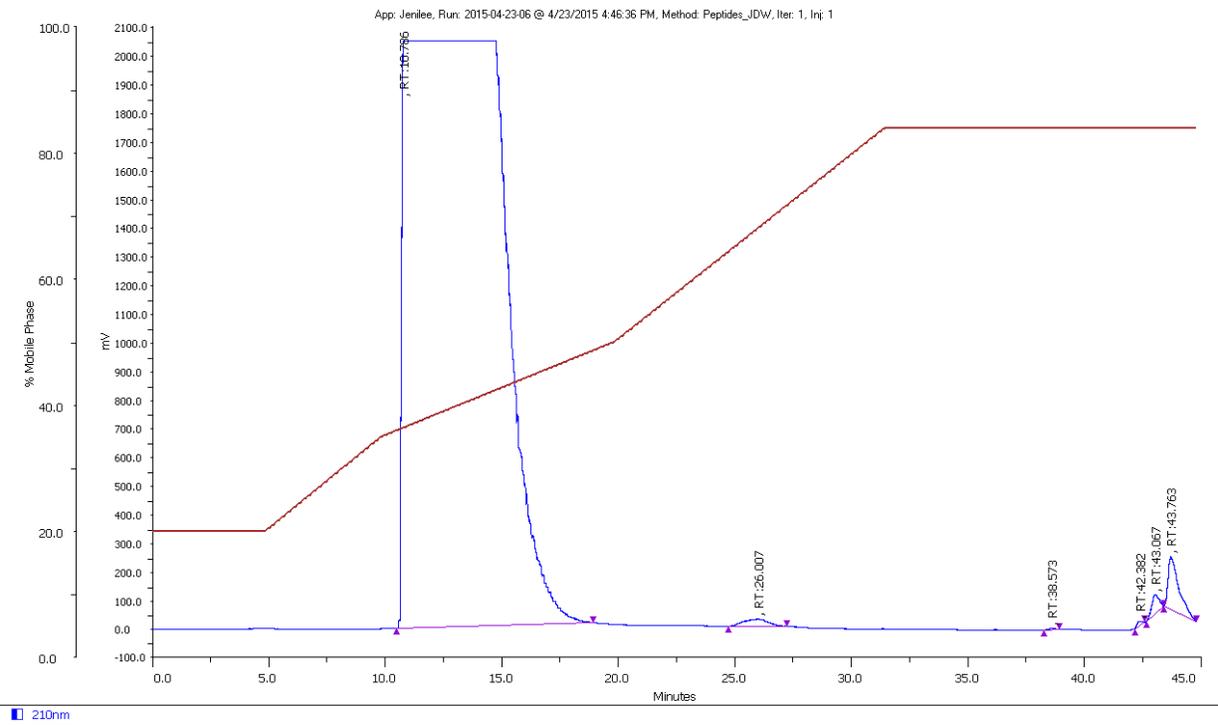


Figure S87. Crude HPLC chromatogram of c-CLLFVY, product is 43.8 minutes.

link-c-(Ppg)LLFVY, compound 26, supporting data.

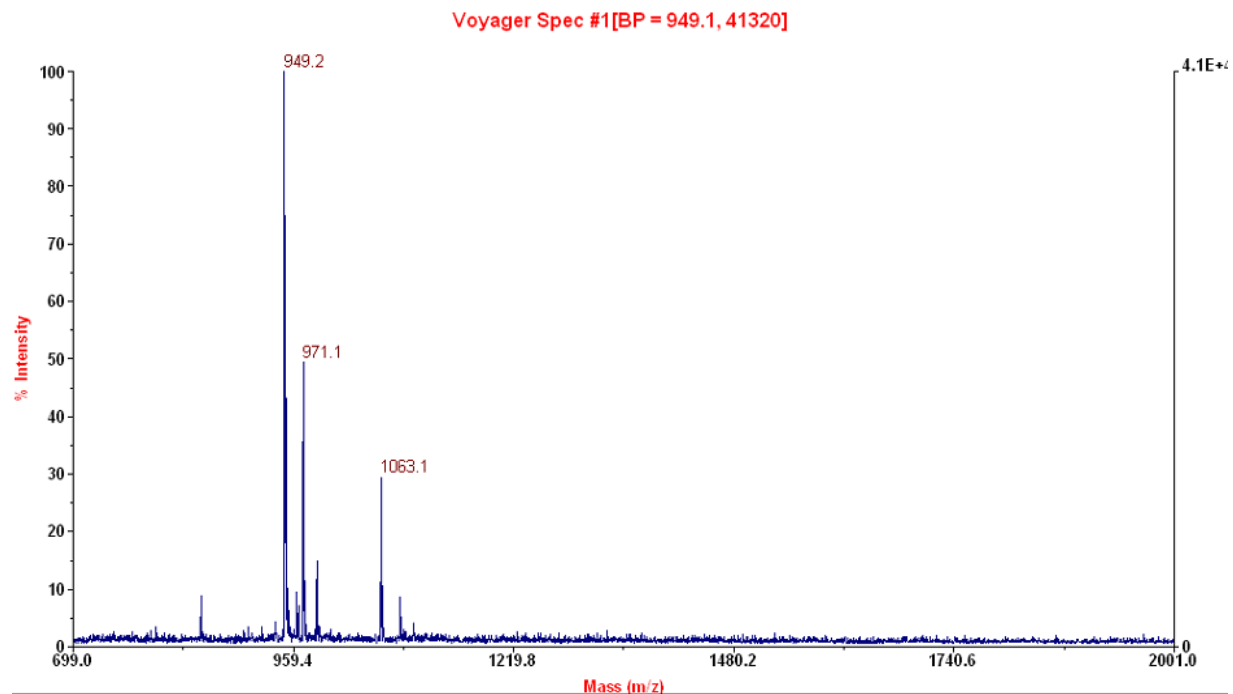


Figure S88. MALDI spectra for link-c-(Ppg)LLFVY.

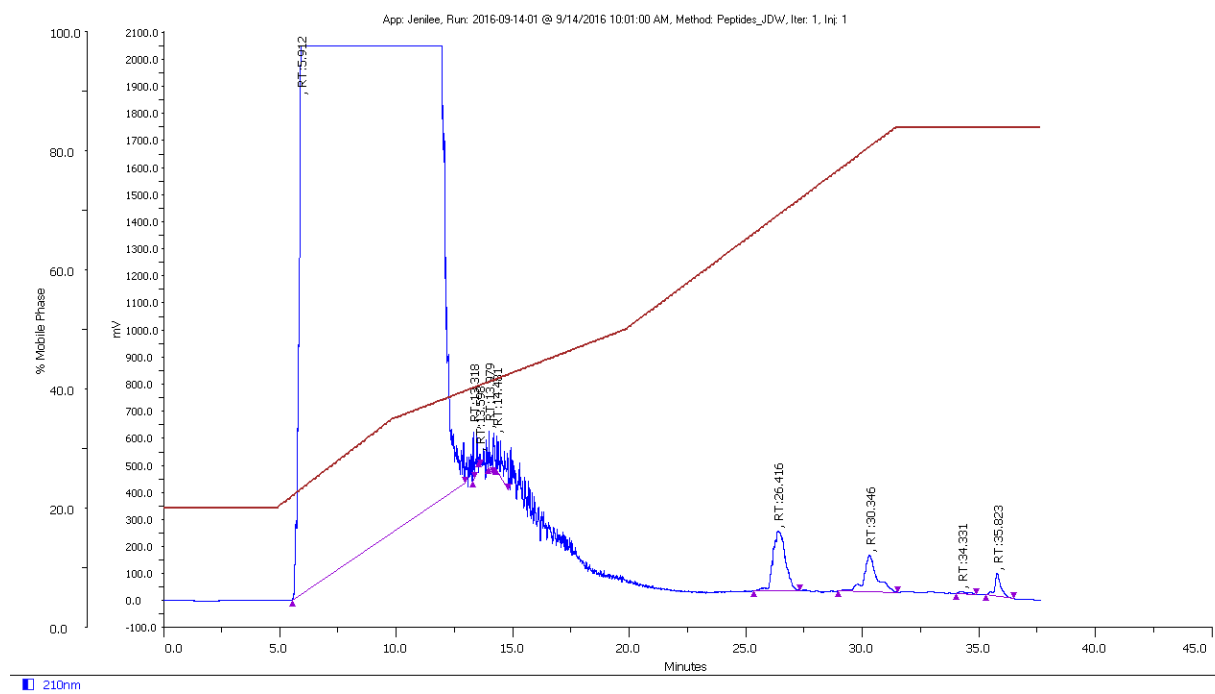


Figure S89. Crude HPLC chromatogram of link-c-(PPg)LLFVY, product is 26.4 minutes.

azido-PEG-4-fluorobenzamide, compound 27, supporting data.

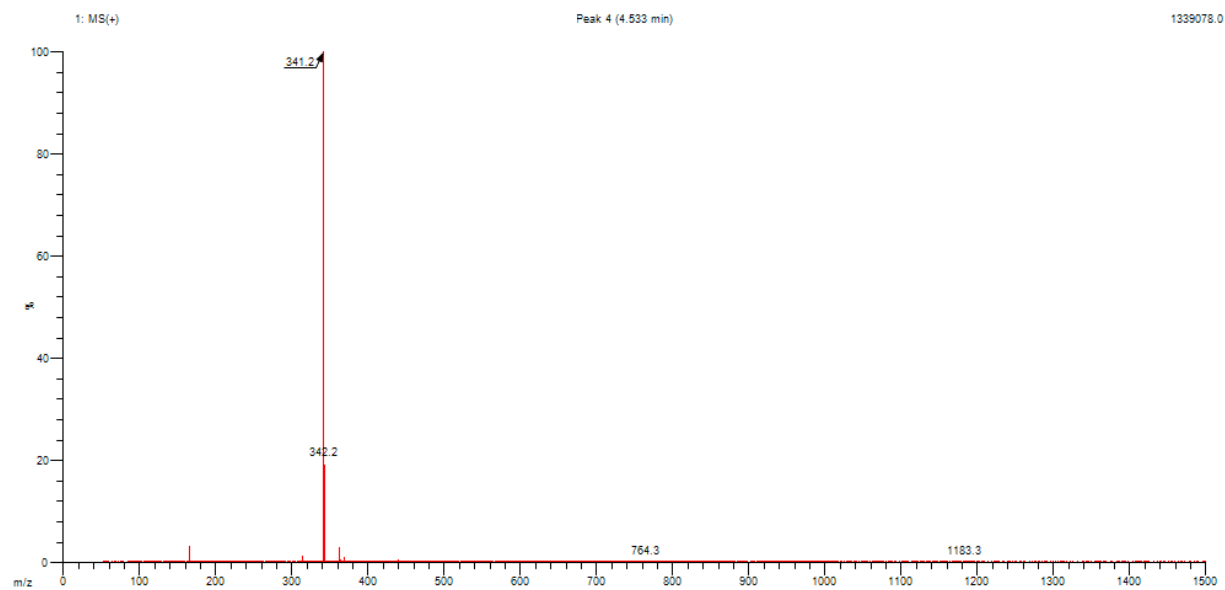


Figure S90. LR-MS for azido-PEG-4-fluorobenzamide.

[<sup>19</sup>F]SFB-link-c-(Ppg)LLFVY, compound **28**, supporting data.

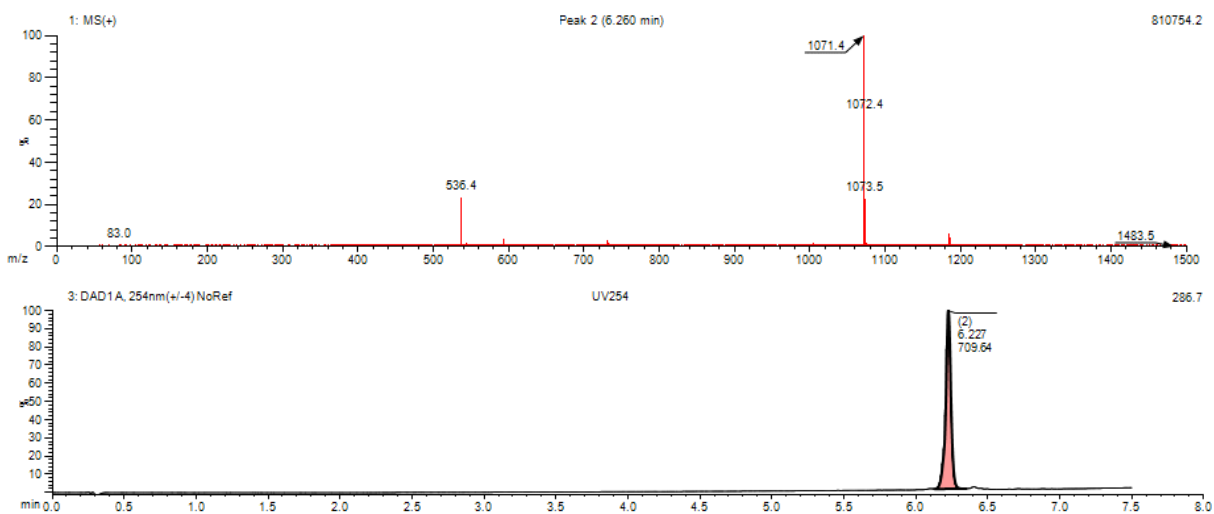


Figure S91. HPLC UV spectra at 254nm, including LCMS for [<sup>19</sup>F]SFB-link-c-(Ppg)LLFVY.

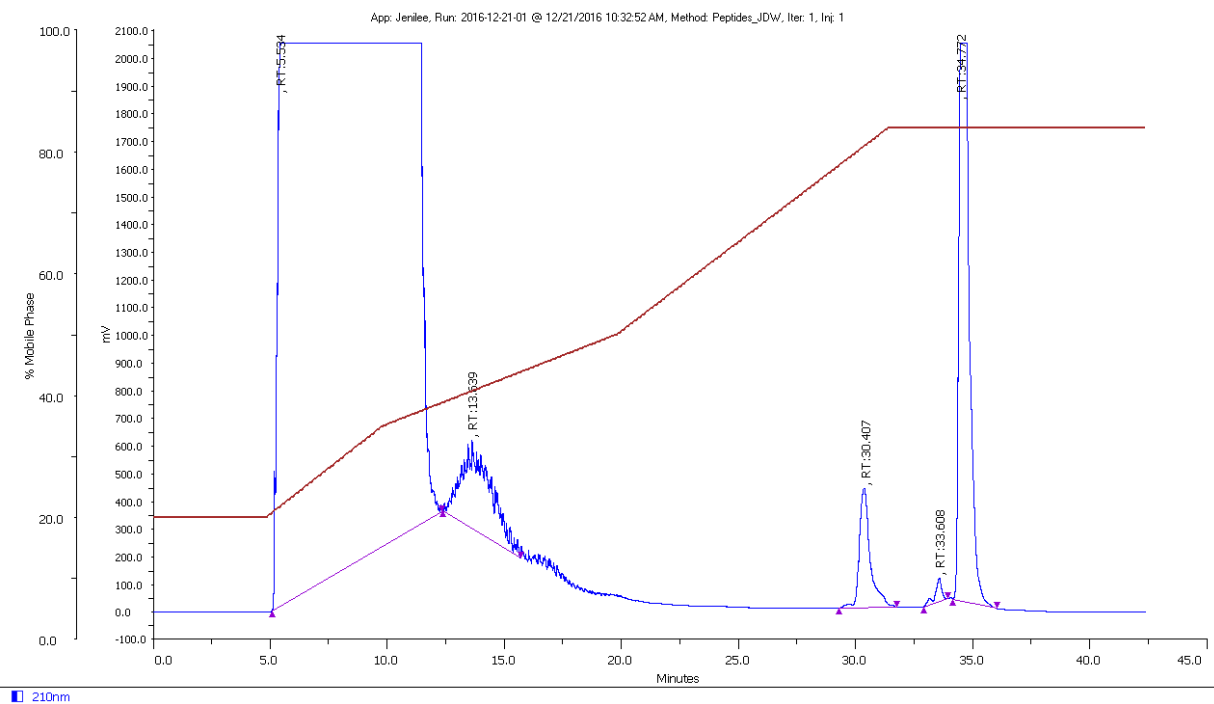


Figure S92. Crude HPLC chromatogram of [<sup>19</sup>F]SFB-link-c-(Ppg)LLFVY, product is 34.7 minutes.

NOTA-Bn-SCN-link-c-(Ppg)LLFVY, compound **29**, supporting data.

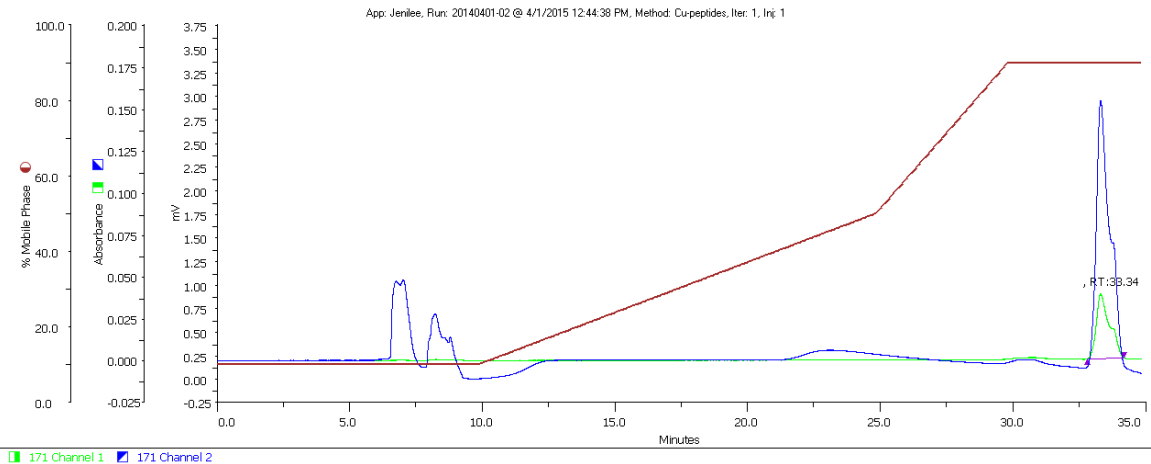


Figure S93. HPLC purification for NOTA-Bn-SCN-link-c-(Ppg)LLFVY.

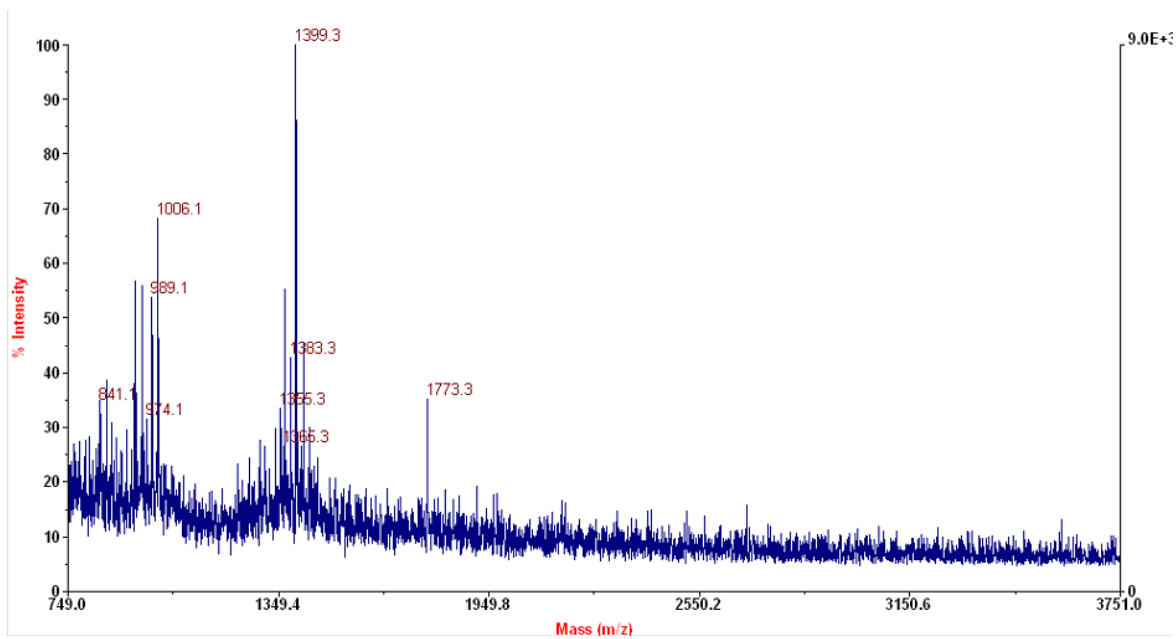


Figure S94. MALDI-MS for NOTA-Bn-SCN-link-c-(Ppg)LLFVY.

DOTA-link-c-(Ppg)LLFVY, compound 30, supporting data.

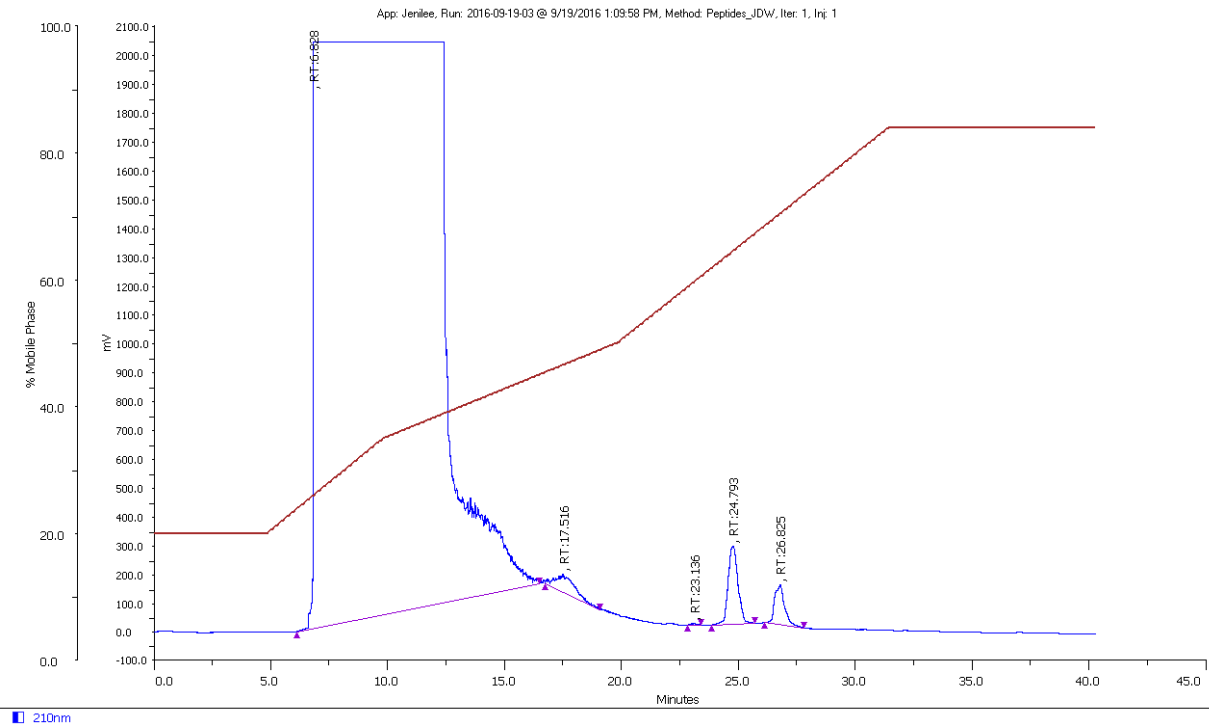


Figure S95. HPLC purification for DOTA-link-c-(Ppg)LLFVY.

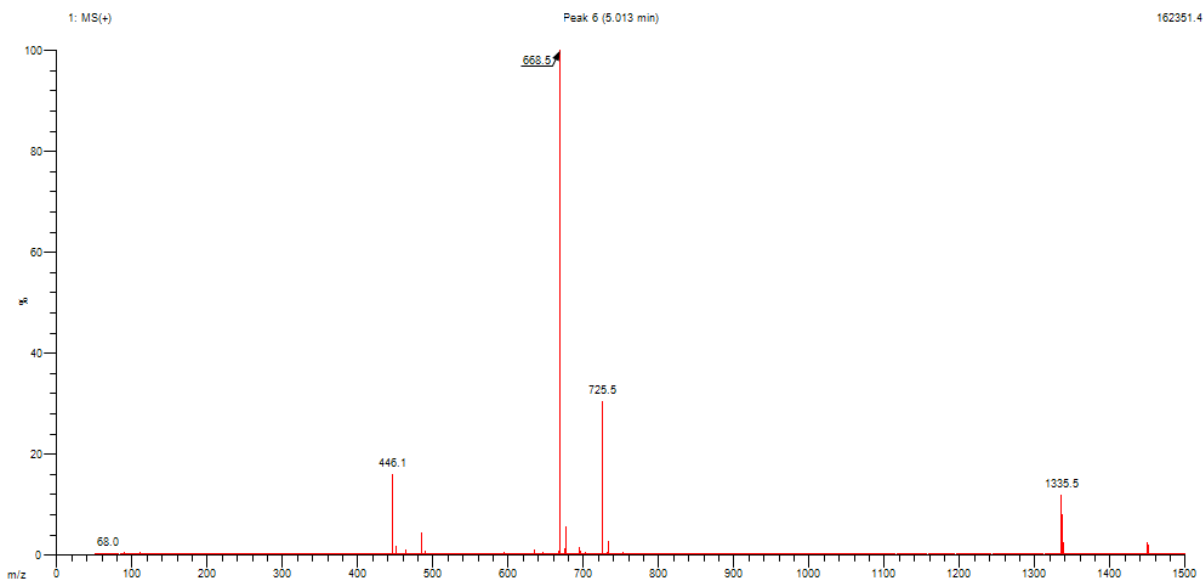


Figure S96. LR-MS for DOTA-link-c-(Ppg)LLFVY.

[<sup>69</sup>Ga]-DOTA-link-c-(Ppg)LLFVY, compound 31, supporting data.

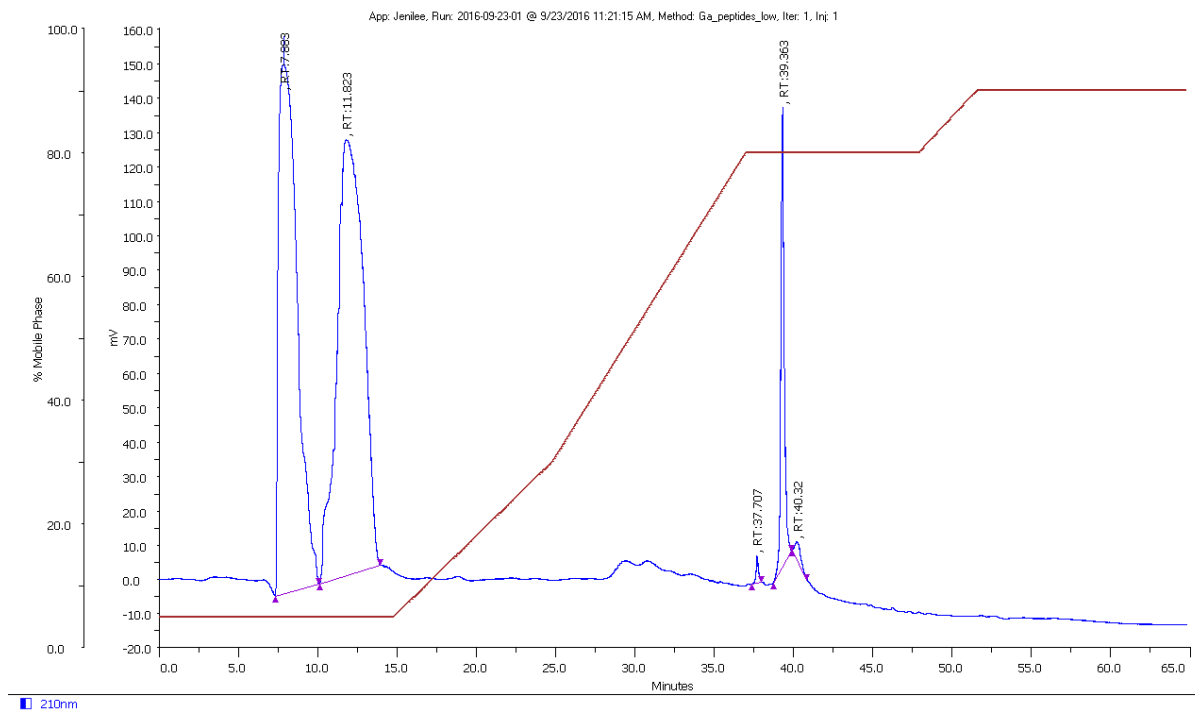


Figure S97. HPLC purification for [<sup>69</sup>Ga]-DOTA-link-c-(Ppg)LLFVY.

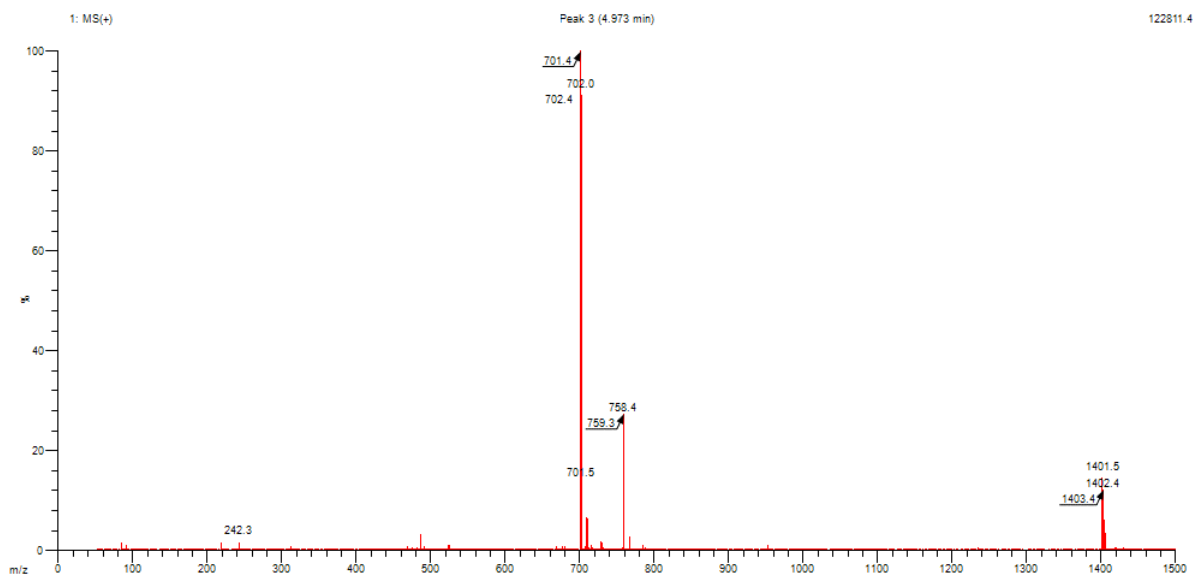


Figure S98. LR-MS for [<sup>69</sup>Ga]-DOTA-link-c-(Ppg)LLFVY.

[<sup>68</sup>Ga]-DOTA-link-c-(Ppg)LLFVY, JDW00816, supporting data.

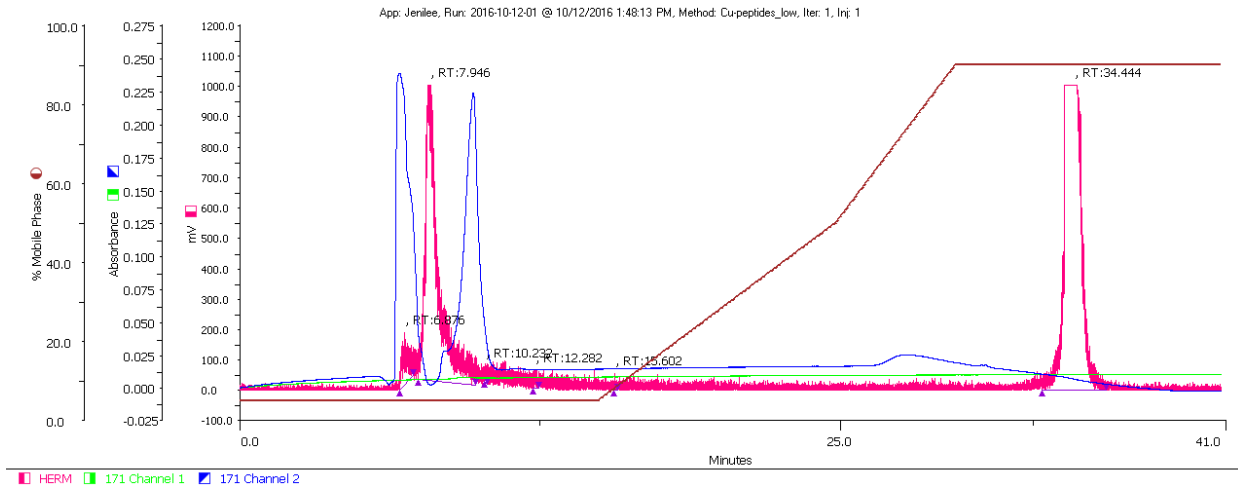


Figure S99. Typical HPLC example of [<sup>68</sup>Ga]DOTA-link-c-(Ppg)LLFVY crude reaction.

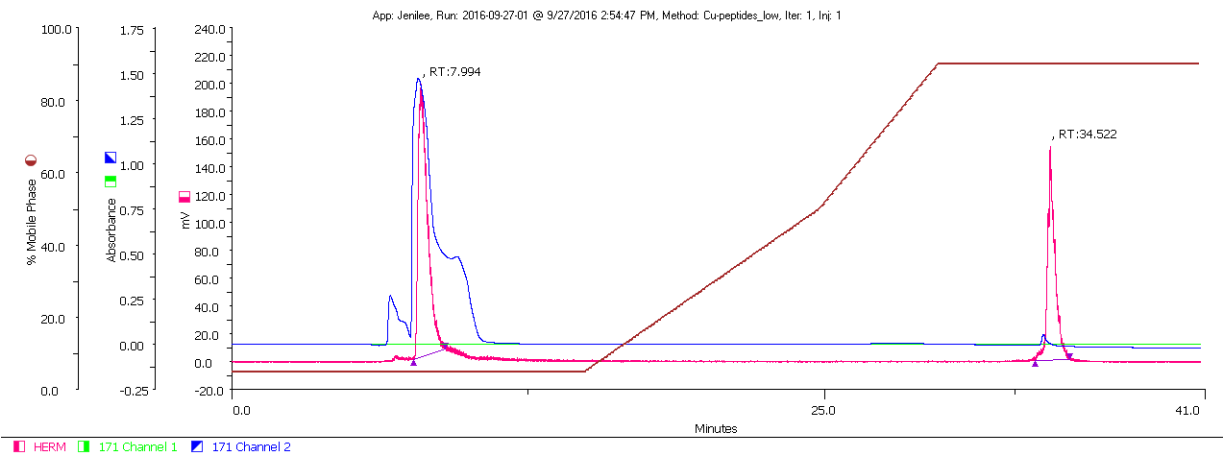


Figure S100. Co-injection of [<sup>68</sup>Ga]DOTA-link-c-(Ppg)LLFVY and [<sup>69</sup>Ga]DOTA-link-c-(Ppg)LLFVY.

N-[2-(2-{2-(2-Azidoethoxy)ethoxy}ethoxy)ethyl]-7-nitro-2,1,3-benzoxadiazol-4-amine, compound **32**, supporting data.

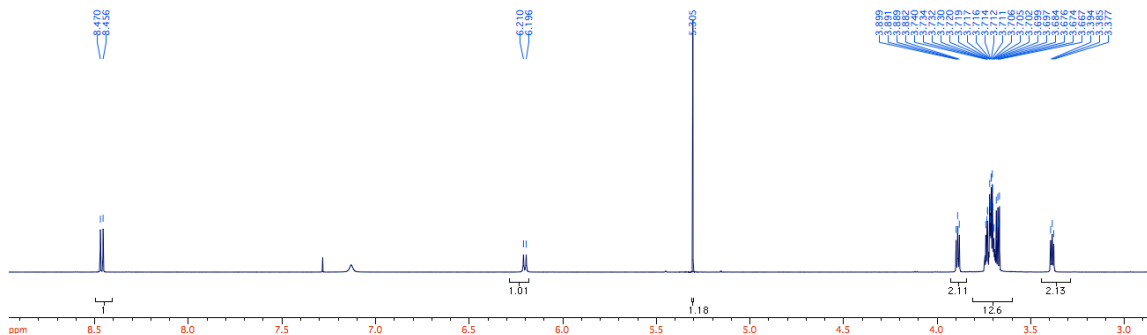


Figure S101. <sup>1</sup>H-NMR for compound **32**.

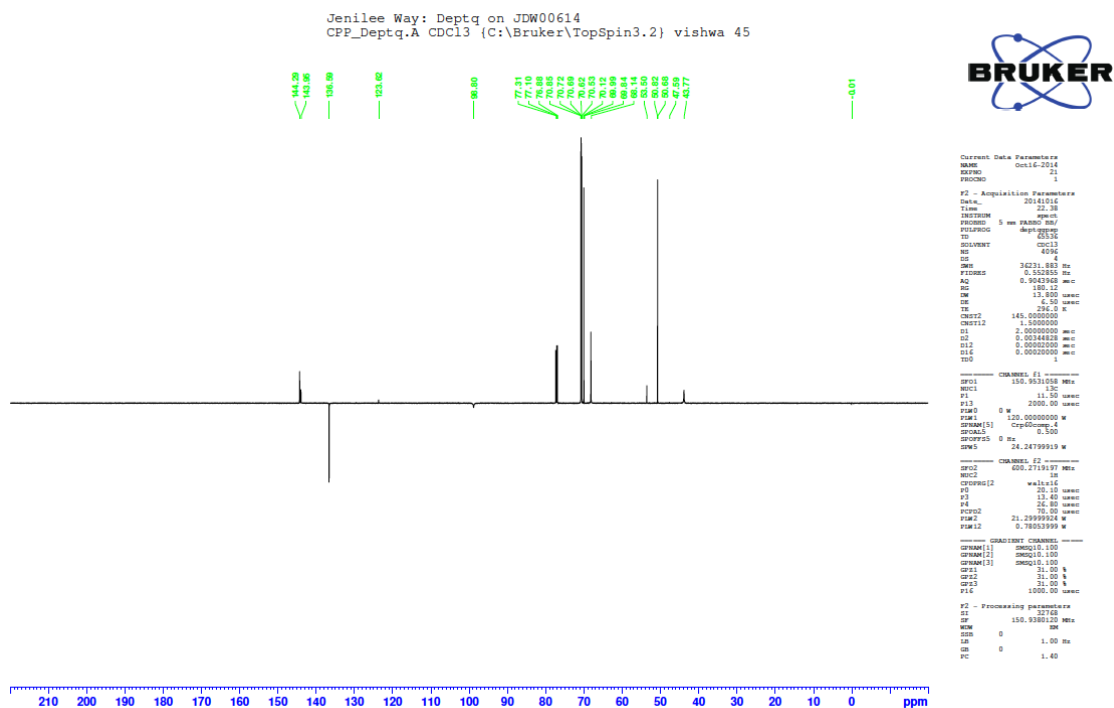


Figure S102. <sup>13</sup>C-NMR for compound **32**.

NBD-link-c-(Ppg)LLFVY, compound **33**, supporting data.

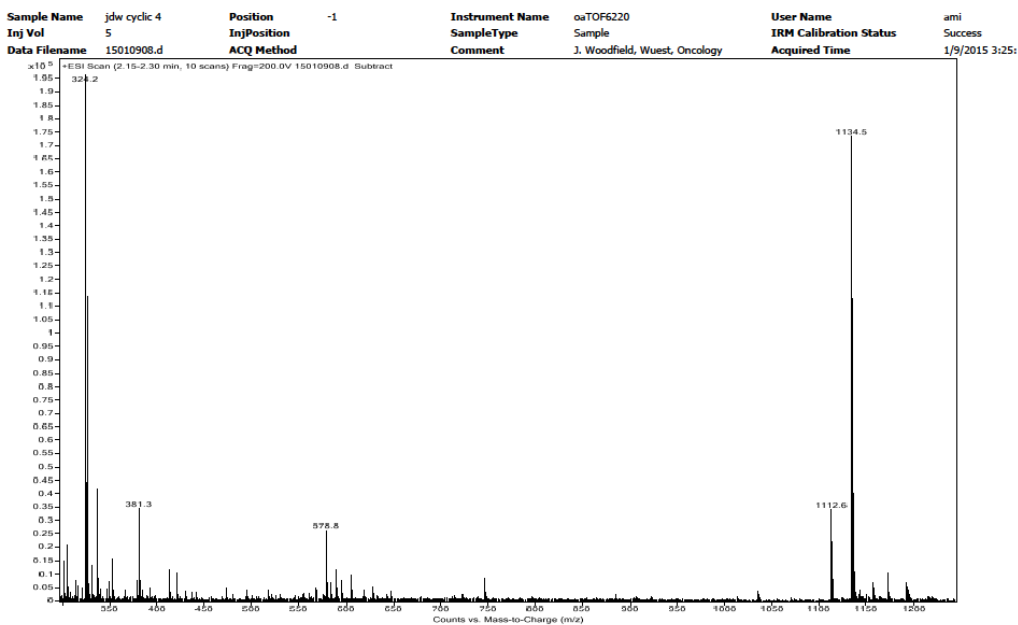


Figure S103. LR-MS for compound **33**.

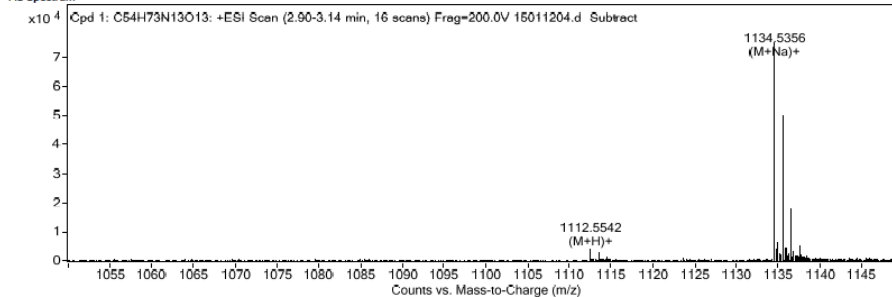
University of Alberta **Qualitative Compound Report** Department of Chemistry

Comment	J. Woodfield, Wuest, Oncology	Sample Name	jdw cyclic 4
Data File	15011204.d	Instrument Name	oaTOF6220
Position	-1	Operator	ami
Acq Method		DA Method	da ami low mass.m

Compound Table

Formula	Mass	Abund
C <sub>54</sub> H <sub>73</sub> N <sub>13</sub> O <sub>13</sub>	1111.5466	75083

MS Spectrum



MS Spectrum Peak List

Ion Formula	Ion type	Measured m/z	Calc m/z	Diff(ppm)	z	Abund
C <sub>54</sub> H <sub>74</sub> N <sub>13</sub> O <sub>13</sub>	(M+H)+	1112.5542	1112.5524	1.67	1	3801
C <sub>54</sub> H <sub>73</sub> N <sub>13</sub> NaO <sub>13</sub>	(M+Na)+	1134.5356	1134.5343	1.17	1	75083

--- End Of Report ---

Figure S104. HR-MS for compound **33**.

(p-Ethynylphenyl)trimethylammonium, compound **34**, supporting data.

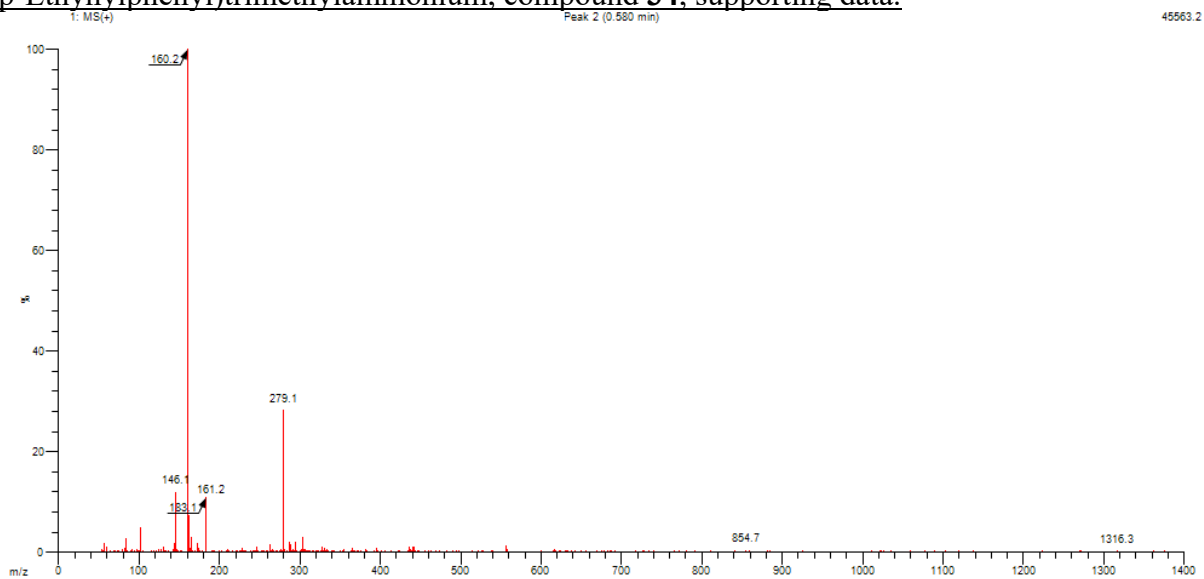


Figure S105. LR-MS for compound **34**.

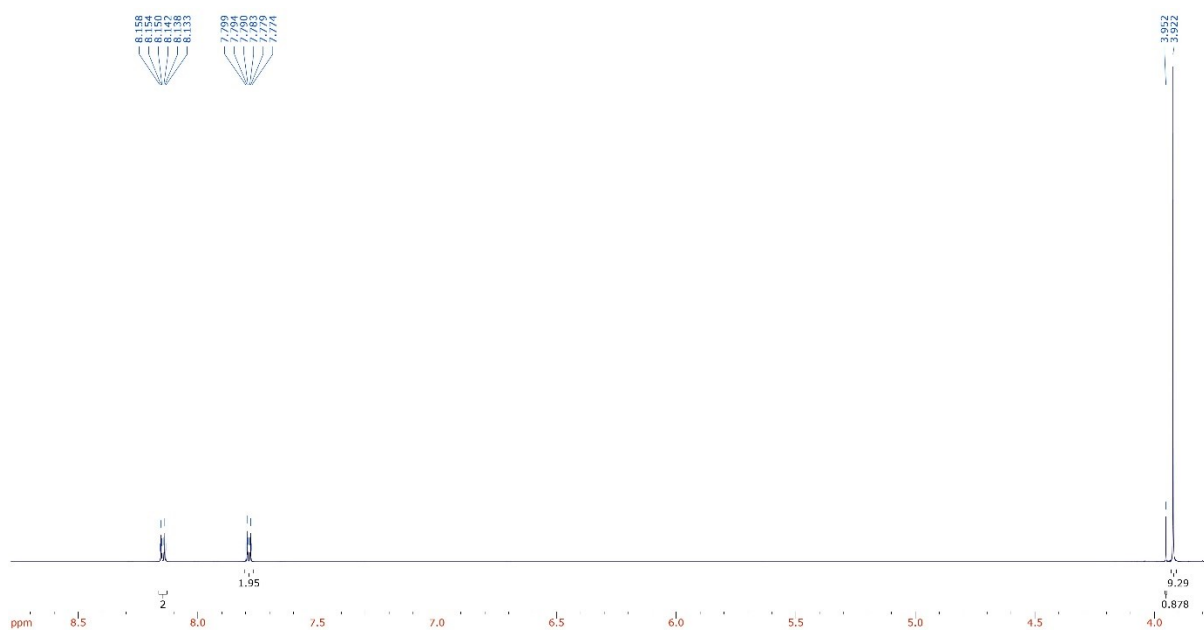


Figure S106. <sup>1</sup>H-NMR for compound **34**.

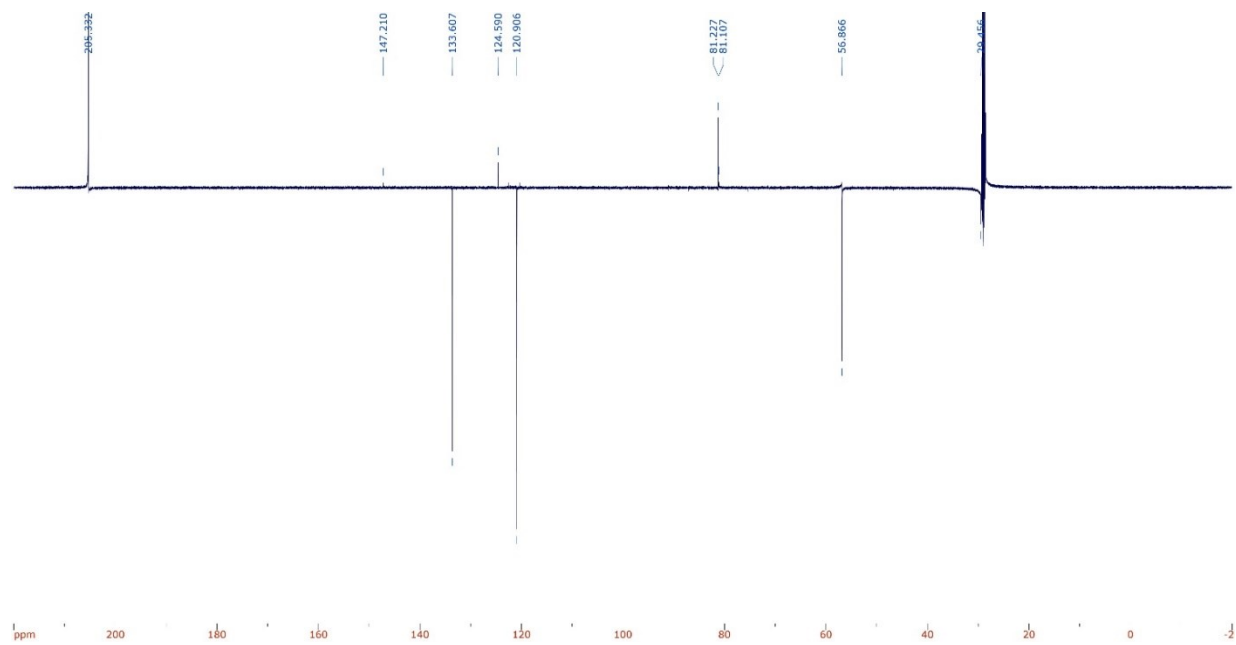


Figure S107.  $^{13}\text{C}$ -NMR for compound 34.

p-(2-(p-(p-((4-(3-Pyridyl)methyl)-1-piperazinyl)methyl)benzylamino]phenyl)ethynyl)(trimethylammonio)benzene, compound 35, supporting data.

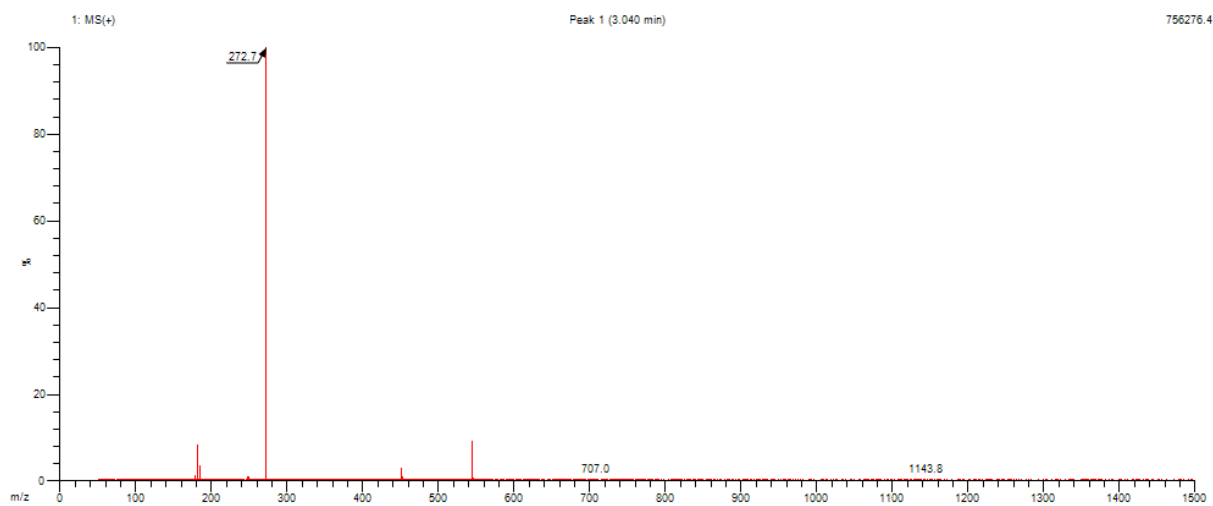


Figure S108. LR-MS for compound 35.

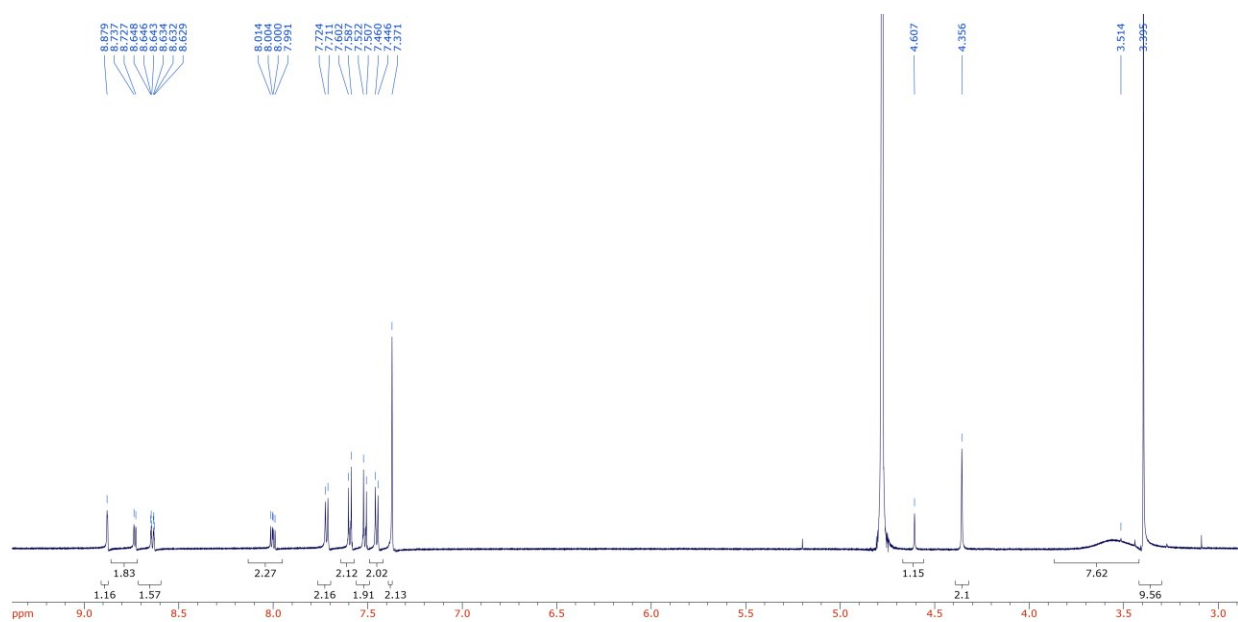


Figure S109. <sup>1</sup>H-NMR for compound 35.

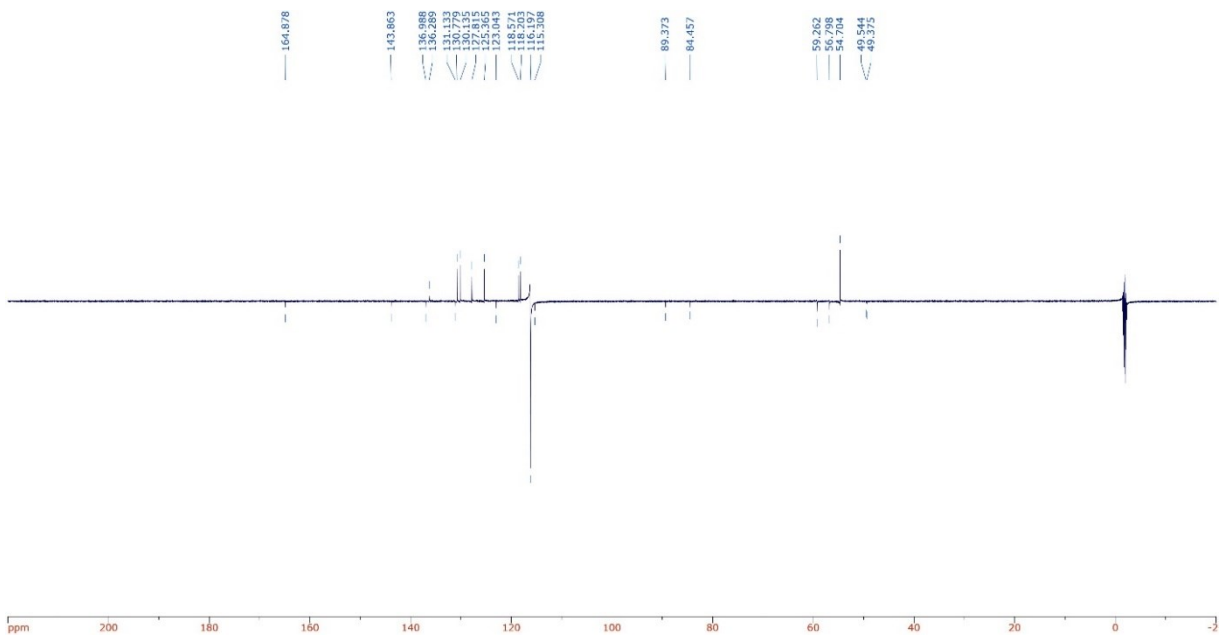


Figure S110.  $^{13}\text{C}$ -NMR for compound **35**.

1-((4-fluorophenyl)ethynyl)-2,4-dimethoxybenzene, compound **36**, supporting data.

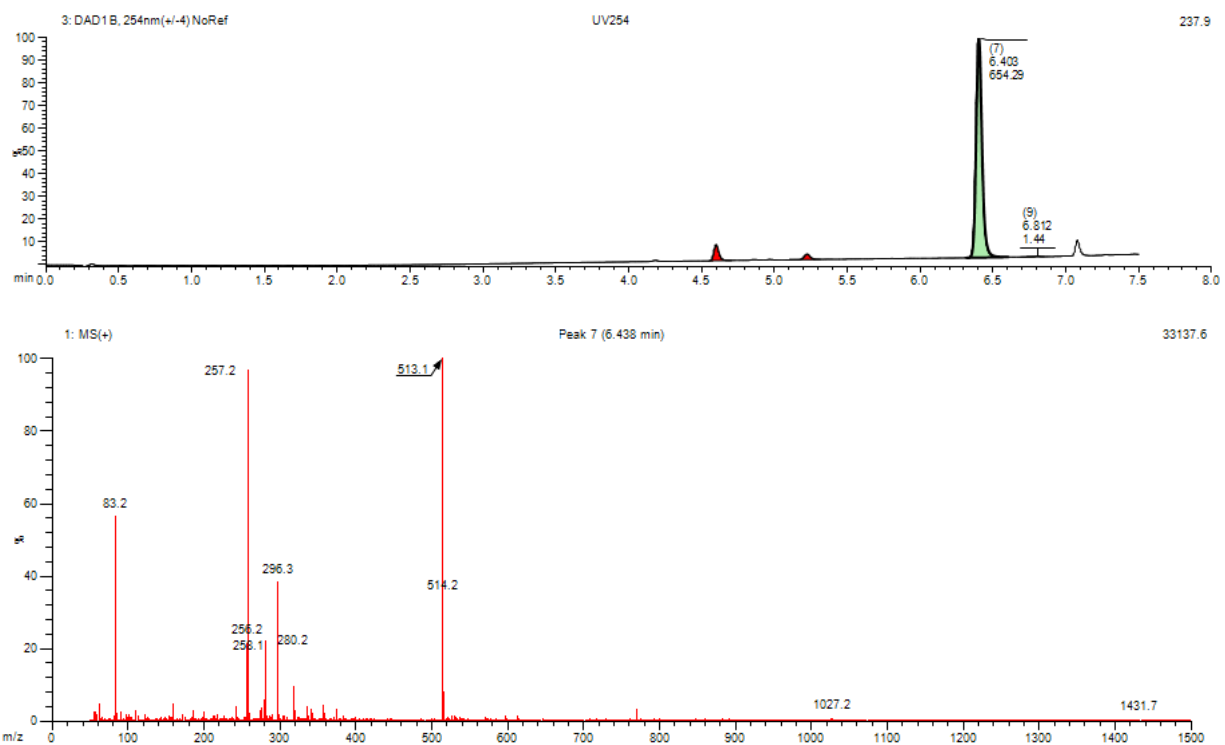


Figure S111. LR-MS for compound **36**.

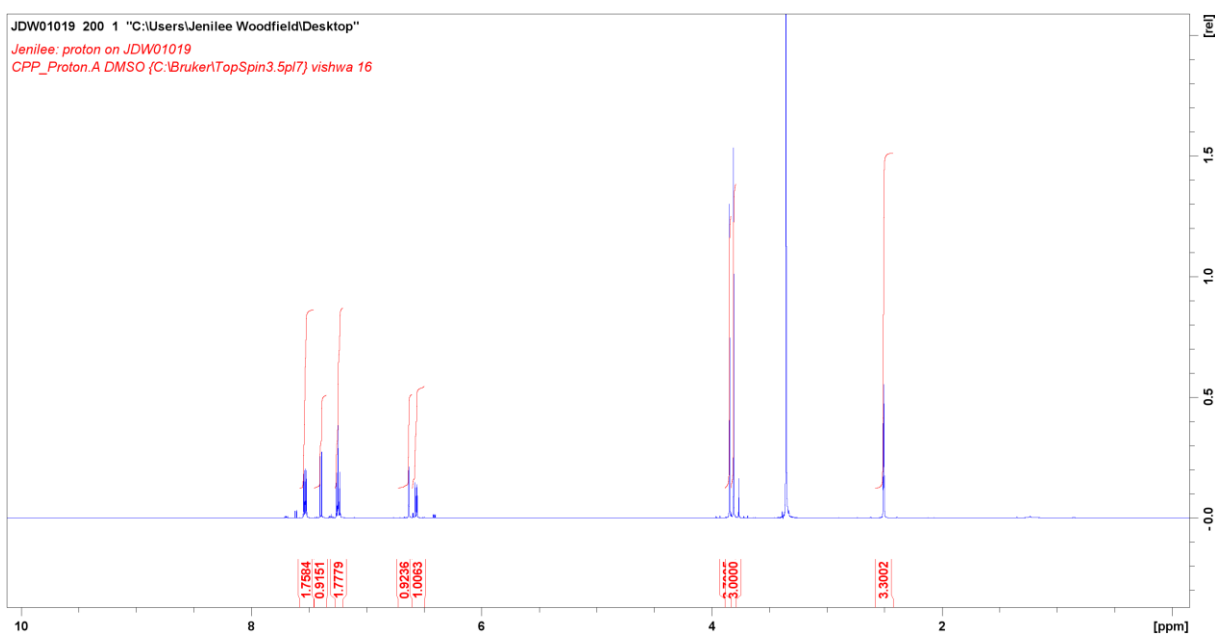


Figure S112. <sup>1</sup>H-NMR for compound **36**.

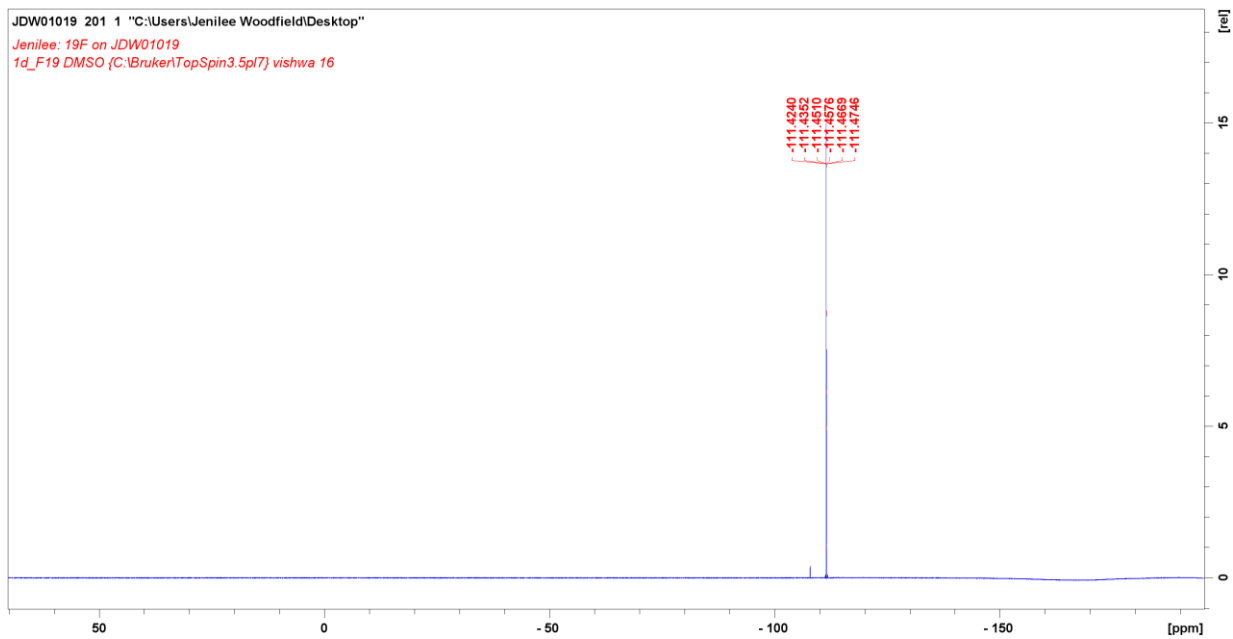


Figure S113.  $^{19}\text{F}$ -NMR for compound **36**.

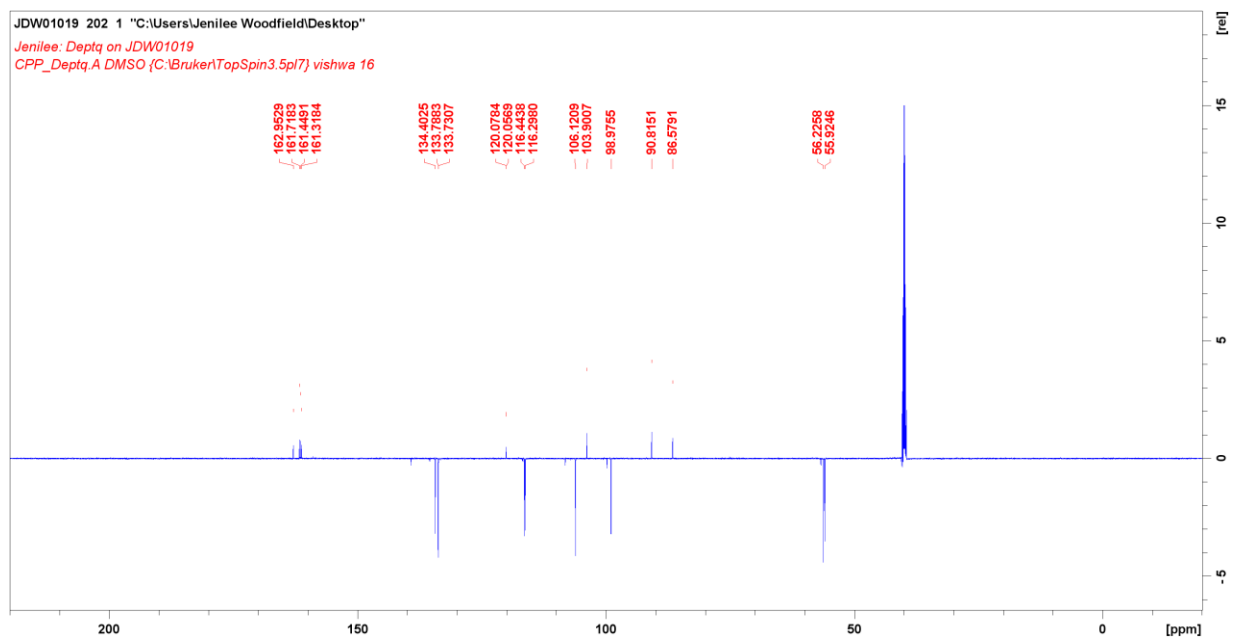


Figure S114.  $^{13}\text{C}$ -NMR for compound **36**.

2-amino-4-[(4-fluorophenyl)ethynyl]benzoic acid, compound 37, supporting data.

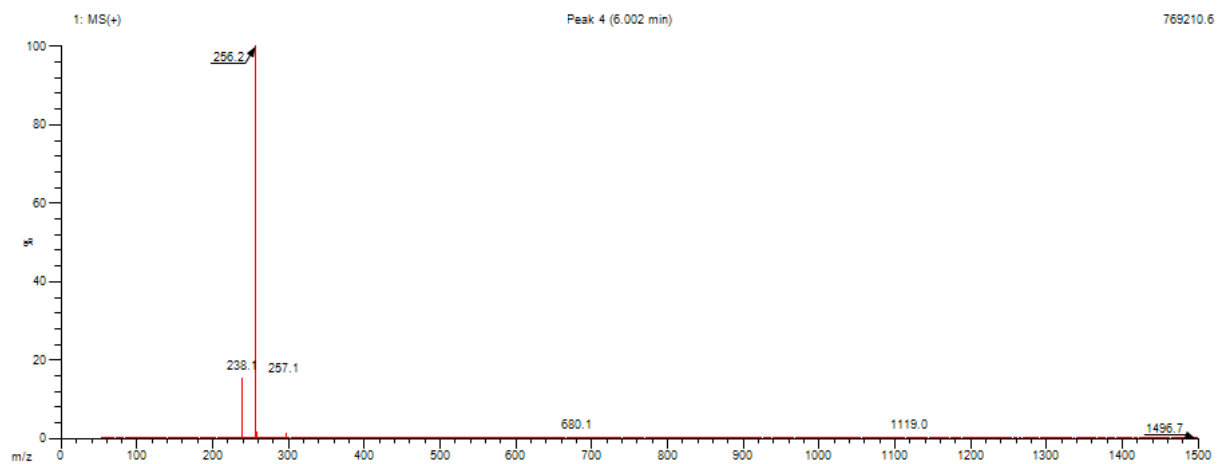


Figure S115. LR-MS for compound 37.

Lane	2	3	4	5	6	7	8	9	10	11	12	13	14	15
HIF-1a	0.150	0.128	0.000	0.001	0.001	0.156	0.187	0.463	0.335	0.005	0.024	0.014	0.479	0.465
B-Actin	0.881	0.445	0.390	0.160	0.493	1.350	1.160	0.607	0.717	1.080	0.743	0.778	0.912	1.369
HIF-1a corrected to protein	0.170	0.288	0.001	0.008	0.001	0.116	0.161	0.763	0.467	0.005	0.032	0.018	0.525	0.340
Treatment	48 hours Opti-MEM		48 hours HIF-1a siRNA			48 hours scrambled		24 hours Opti-MEM		24 hours HIF-1a siRNA		24 hours scrambled		
Average HIF-1a	0.229		0.003			0.138		0.615		0.018		0.432		
Percent of Blank HIF-1a remaining			1.5			60.4				3.0		70.3		
Percent silenced			98.5			39.6				97.0		29.7		

Table S1. Intensity calculations from HIF-1 $\alpha$  silencing in MDA-MB-231 cells.